The Quantification of Pressure and Saturation Changes in Clastic Reservoirs using 4D Seismic data

Veronica Ehinome Ebiweni Omofoma

Submitted for the degree of Doctor of Philosophy

Heriot-Watt University

School of Energy, Geoscience, Infrastructure and Society

June 2017

Abstract

The problem of quantifying pressure and saturation changes from 4D seismic data is an area of active research faced with many challenges concerning the non-uniqueness of seismic data inversion, non-repeatability noise in the data, the formulation of the inverse problem, and the use of appropriate constraints. The majority of the inversion methods rely on empirical rock-physics model calibrations linking elastic properties to expected pressure and saturation changes. Model-driven techniques indeed provide a theoretical framework for the practical interpretation of the 4D seismic response but pressure and saturation separation based on this approach are inconsistent with the observed 4D seismic response and insights from reservoir engineering. The outcome is a bias in estimated pressure and saturation changes and for some a leakage between the two. Others have addressed some of this bias using the causality between the induced-production and the observed 4D seismic response to formulate a direct, quick and less compute-intensive inversion - characterised by data-driven techniques. But challenges still remain as to the accuracy of the causality link- as defined by the reservoir's sensitivity to production effects, and in defining appropriate constraints to tackle non-uniqueness of the seismic inversion and uncertainties in the 4D seismic data.

The main contributions of this thesis are the enhancement of data-driven inversion approach by using multiple monitor 4D seismic data to quantify the reservoir's sensitivity to pressure and saturation changes, together with the introduction of engineering-consistent constraints provided by multiple history-matched fluid-flow simulation models. A study using observed 4D seismic data (amplitudes and time-shifts) acquired at different monitor times on four producing North Sea clastic fields demonstrates the reliability of the seismic-based method to decouple the reservoir's sensitivity specific to each field's geological characteristics. A natural extension is to combine multiple monitor 4D seismic data in an inversion scheme that solves for the reservoir sensitivity to pressure and saturation changes, the pressure and saturation changes themselves and the uncertainties in the inversion solution. At least two monitor 4D seismic datasets are required to solve for the reservoir's sensitivity, and offset stacks (near, mid, and far) are required to decouple pressure, water and gas saturation changes. The generation and use of geologically-constrained and production-

constrained multiple simulation models provided spatial constraints to the solution space, making the inversion scheme robust. Within the inversion, the fitness to spatial historical data, i.e. 4D seismic data acquired at different monitor times is analysed. The added benefit of using multiple monitor data is that it allows for a soft "close-the-loop" between the engineering and the 4D seismic domain. One step in the inversion scheme is repeated for as many history-matched simulation models as generated. Each model provides pressure and saturation input to the inversion to obtain maps of the reservoir's sensitivity. By computing the norm of residuals for each inversion based on each model input, the best model (having the lowest norm of residuals) can be identified, besides the use of a history-matching objective. The inversion scheme thus marks the first step for a seismic-assisted history matching procedure, suggesting that pressure and saturation inversion is best done within the history-matching process.

In addition, analysis of uncertainties in quantitative 4D seismic data interpretation is performed by developing a seismic modelling method that links the shot timings of a real field towed streamer and a permanent reservoir monitoring (PRM) acquisition to the reservoir under production. It is found that pressure and saturation fluctuations that occur during the shooting of monitor acquisitions creates a complicated spatio-temporal imprint on the pre-stack data, and errors if 4D seismic data is analysed in the post-stack domain. Pressure and saturation changes as imaged across the offset stacks (near, mid and far offset) are not the same, adding to the problems in separating pressure and saturation changes using offset stacks of 4D seismic data. The approximate modelling relay that the NRMS errors between offset stacks (up to 7.5%) caused by the intra-survey effects are likely at the limit of 4D seismic measurements using towed streamer technology, but are potentially observable, particularly for PRM technology. Intra-survey effects should thus be considered during 4D survey planning as well as during data processing and analysis. It is recommended that the shot timestamps of the acquisition is used to sort the seismic data immediately after pre-stack migration and before any stacking. The seismic data should also be shot quickly in a consistent pattern to optimise time and fold coverage. It is common to relate the simulation model output to a specific time within the acquisition (start, middle or end of survey), but this study reveals that it is best to take an average of simulation model predictions output at fine time intervals over the entire length of the acquisition, as this is a better temporal comparison to the acquired post-stack 4D seismic data.

This thesis is dedicated to my family and my fiancé

Acknowledgements

"It always seems impossible until it is done", (*Nelson Mandela, South African anti-apartheid revolutionary, politician, and philanthropist, 1918-2013)*…At last, we are finally here, and it has been a journey of growth and self-actualisation. For that, I have a lot to be grateful for.

To my supervisor, Professor Colin MacBeth, how could I have known that meeting you as my external examiner for my MSc Petroleum Geophysics thesis would bring me here, as a proud student of yours? Yes, proud, because you are the epitome of an excellent leader and mentor. It's always amazed me how you've remained dedicated and supportive to every student. Thank you for your wonderful guidance and support throughout my PhD work. It is your scientific curiosity, technical ability, passion and commitment that has helped me to push the boundaries of my knowledge, the outcome of which, is this thesis. I would also like to thank Dr. Asghar Shams for his guidance and support and for teaching opportunities that I have had through him. Thank you also for your many general advices and for the breadth of technical knowledge you shared with me. My gratitude also to Dr Maria-Daphne Mangriotis, the little things you do is noticed! Thank you also for your encouragement. Likewise, to Dr. Romain Chassagne, your attitude to life is quite a unique one. Hamed Amini, you have been a breath of fresh air, thank you for your openness and help through all the times I needed clarity. As a Geophysicist trying my hands in reservoir engineering, I needed someone I could ask silly questions, for that, my special thanks goes to Professor Erick Mackay, whose door was always open for any discussion. Thanks also to Dr. Mojtaba Moradi, who helped in the early days when I took on Eclipse tutorial courses, and to Dr. Ilya Fursov and Dr. Dennis Obidegwu. Special thanks to my PhD examiners – Professor Helmut Jakubowicz, Dr. Rossmary Villegas and Dr. Maria-Daphne Mangriotis for taking their time to examine this thesis, as well as their critical insights and valuable feedback.

I thank the Edinburgh Time Lapse Project (ETLP) sponsors of Phase V and VI, for their support and for providing the datasets used in my research (BG Group, BP, Chevron, CGG, ConocoPhillips, ENI, ExxonMobil, Hess, Ikon Science, Landmark, Maersk, Nexen, Norsar, RSI, OMV, Petoro, Petrobras, Shell, Statoil, Suncor, TAQA, TGS and Total). Thanks to Schlumberger for provision of the Petrel, Eclipse and MEPO software.

I am also grateful to the Society of Exploration Geophysicists (SEG) for awarding me the prestigious SEG/Ian G. Jack scholarship for academic excellence in the Reservoir Geophysics domain in 2015. I am also grateful for the opportunities to present my research at the European Association of Geoscientists and Engineers (EAGE) conferences. Being a member of the EAGE Women in Geoscience (WGE) group and participating in their first mentorship program has been rewarding.

It goes without saying, if you are surrounded by the best people, you will definitely achieve your goals. So to my ETLP colleagues, thank you for the technical discussions, lunch and learn sessions, the positive outlook and the ability to laugh even at stressful times. I will like to show my appreciation to all ETLP colleagues I came in contact with during my PhD: Colin MacBeth, Asghar Shams, Hamed Amini, Erick Alvarez, Reza Falahat, Ilya Fursov, Dhiman Mondal, Sean Shuzhe Tian, Olarinre Salako, Dennis Obidegwu, Zhen Yin, Lu Ji, Zein Wijaya, Ricardo Rangel, Angel Briceno, Ming Yi Wong, Mathieu Chamberfort, Maria-Daphne Mangriotis, Phung Nguyen, Romain Chassagne, Nkechi Obiwulu, Justin Chong Geng, Juliana Santos, Qi Zhang, Miguel Alfonzo, Gustavo Corte, Alejandro Jaramillo, Lee Jean Wong and Ambuj Tyagi. To the IT support team, Alan, Andy, Chris and Chisholm, thank you for always bringing Cayenne back up and running, after the many crashes it observed. Without your professionalism, my MATLAB programs would not have been accomplished on time.

I am grateful to my mum and to my family, for their unwavering support, love and continuous encouragement, right from my undergraduate studies in Electronic Engineering to my PhD. Who are we without our family.

To my fiancé, Chu, how could I have endured this journey without all your love, patience, support and commitment during these last years…You have been my rock, my best friend and my main source of energy. Thank you for inspiring me and for encouraging me. In fact, thank you for being you! I am so excited about the many years ahead, as your wife! To Almighty God, your love for me is beyond my comprehension. My biggest gratitude for your grace and for blessing me through every interaction I have had, for keeping me healthy and giving me a happy mind, full of laughter and positivity.

Veronica Omofoma, June 2017.

Declaration Statement

ACADEMIC REGISTRY
Research Thesis Submission

Name*:*	VERONICA EHINOME EBIWENI OMOFOMA		
School:	School of Energy, Geoscience, Infrastructure and Society		
Version: *(i.e. First, Resubmission, Final)*	Final	Degree Sought:	Doctor of Philosophy Reservoir Geophysics

Declaration

In accordance with the appropriate regulations I hereby submit my thesis and I declare that:

1) the thesis embodies the results of my own work and has been composed by myself
2) where appropriate, I have made acknowledgement of the work of others and have made reference to work carried out in collaboration with other persons
3) the thesis is the correct version of the thesis for submission and is the same version as any electronic versions submitted*.
4) my thesis for the award referred to, deposited in the Heriot-Watt University Library, should be made available for loan or photocopying and be available via the Institutional Repository, subject to such conditions as the Librarian may require
5) I understand that as a student of the University I am required to abide by the Regulations of the University and to conform to its discipline.
6) I confirm that the thesis has been verified against plagiarism via an approved plagiarism detection application e.g. Turnitin.

* *Please note that it is the responsibility of the candidate to ensure that the correct version of the thesis is submitted.*

Signature of Candidate*:*		Date:	21/08/2017

Submission

Submitted By *(name in capitals):*	
Signature of Individual Submitting:	
Date Submitted:	

For Completion in the Student Service Centre (SSC)

Received in the SSC by *(name in capitals):*	

1.1 Method of Submission *(Handed in to SSC; posted through internal/external mail):*			
1.2 E-thesis Submitted (**mandatory for final theses)**			
Signature:		Date:	21/08/2017

Table of Contents

List of Publications

Part of the work presented in this thesis is also presented in the following publications:

- Omofoma, V. and MacBeth, C. (2015). Intra-survey Pressure Variations-Implications for 4D Seismic Interpretation. Paper presented at the 77th EAGE Conference and Exhibition-Workshops, Madrid, Spain, 1 – 4 June, 2015.

- Omofoma, V. E. and MacBeth, C. (2016). Quantification of Reservoir Pressure-sensitivity Using Multiple Monitor 4D Seismic Data. Paper presented at the 78th EAGE Conference and Exhibition, Vienna, Austria, 30 May – 2 June, 2016.

- Omofoma, V., MacBeth, C. and Amini, H. (2017). Intra-survey Reservoir Fluctuations – Implications for quantitative 4D seismic analysis. *Geophysical Prospecting (submitted March 2017, accepted, under review)*

List of Awards

Part of the work presented in this thesis won the following awards:

(Best Presentation Award – Winner).

- Omofoma, V. (2015). Intra-Survey Pressure Variations – Implications for 4-D Seismic Quantitative Interpretation. Presented at the BG Group Geoscience Research Forum 2015, Reading, United Kingdom. September 16 – September 18, 2015.

Chapter 1

Introduction

“A little difference goes a long way.”

-- unknown --

This chapter provides an overview of 4D seismic technology as a reservoir monitoring tool and summarises various advancements to maximise its value, leading to the necessary integration between the 4D seismic domain and reservoir engineering domain. The integration prompts the need for translating 4D seismic data into reservoir dynamic properties for quantitative use. Subsequent sections give an insight into past works of literature concerning the estimation of dynamic properties (such as pressure and saturation changes) by 4D seismic data inversion. The different techniques are discussed, which highlight the progress made and acknowledges the numerous challenges. The work of this thesis is then proposed as a way of expanding the current knowledge base, adding that little different, much needed solution to the current techniques. This chapter concludes with an outline of the subsequent chapters of this thesis.

1.1 A little difference goes a long way

… Somebody once asked me, what do you think is the major advance in the seismic industry in the last 50 years? I answered, "The digital revolution", and the following question was why? And I said, well, it paved the way for '3D seismic imaging' and then the idea of '4D' became conceivable!

The propagation of sound energy in the subsurface depends on the physical properties of all the rocks through which it travels. These properties include mineralogy, fabric (lithology), porosity, fluid content, pressure etc. Some of these can change if production or injection occurs causing as a result a change in the seismic response. The concept of '4D' is a simple one, if one acquires a seismic survey at a specific time, and after a while repeat the same seismic survey, then, a comparative difference between the two seismic data will reveal the changes in the reservoir that have occurred within that production time. Hence, '4D' (or time-lapse) is the fourth dimension, calendar time, to repeated 3D seismic data. '4D' is that little difference (Figure 1-1).

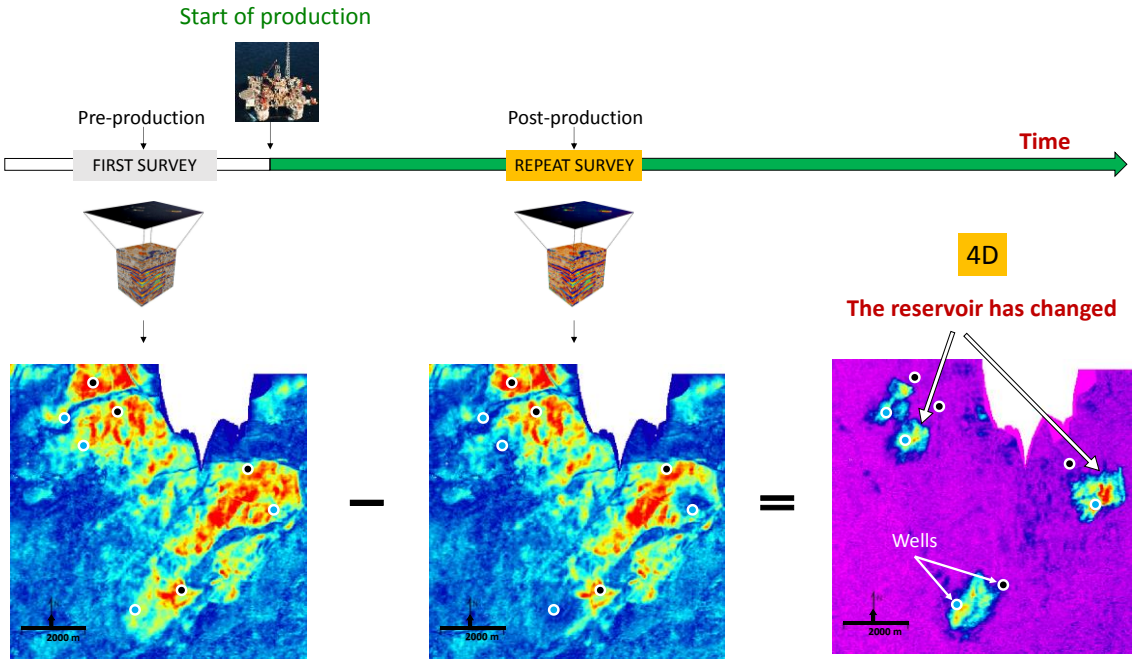

Figure 1-1 The power of '4D'. The difference between mapped data from a seismic survey acquired before production, and a repeat seismic survey acquired another time after production reveals changes in the reservoir resulting from production that are readily visible around wells and far away from wells. It can be expected that subsequent repeat surveys will reveal further changes caused by the production activity up to that time.

Indeed, after the switch from analogue to digital seismic recording in 1953 (Cox and Hibbard 1957; Sharma 2002), the first 3D seismic survey was shot by Exxon over the Friendswood field near Houston in 1957. As early as the 1980s, discussions on the tremendous potential of seismic monitoring techniques to provide lateral information of production-induced changes between wells began (Nur, 1982, Nur et al. 1984, Nur and Wang, 1987). However, it was not until a clear link between seismic observables and reservoir dynamic changes such as fluids, pressure and temperature was established (onshore on the Holt field in north-central Texas in 1987(Greaves and Fulp, 1987); offshore on the Oseberg field in the North Sea in 1991 (Johnstad et al., 1993).), that '4D' began its upward rise (Jack, 1997). 4D seismic technology has since been widely recognised as an effective tool for reservoir monitoring, evaluation and management (Watts et al., 2011), with many successful field case studies from the relatively shallow water depths in the North Sea to more challenging deep water environments in West Africa, Brazil and the Gulf of Mexico (Johnston, 2013). Although a very simple concept, '4D' is not straight forward to implement; the volume of published papers concerned with it alone suggests the active involvement in tackling the challenges brought on by this innovative concept since its pilot in 1987 and the interest in developing the technology

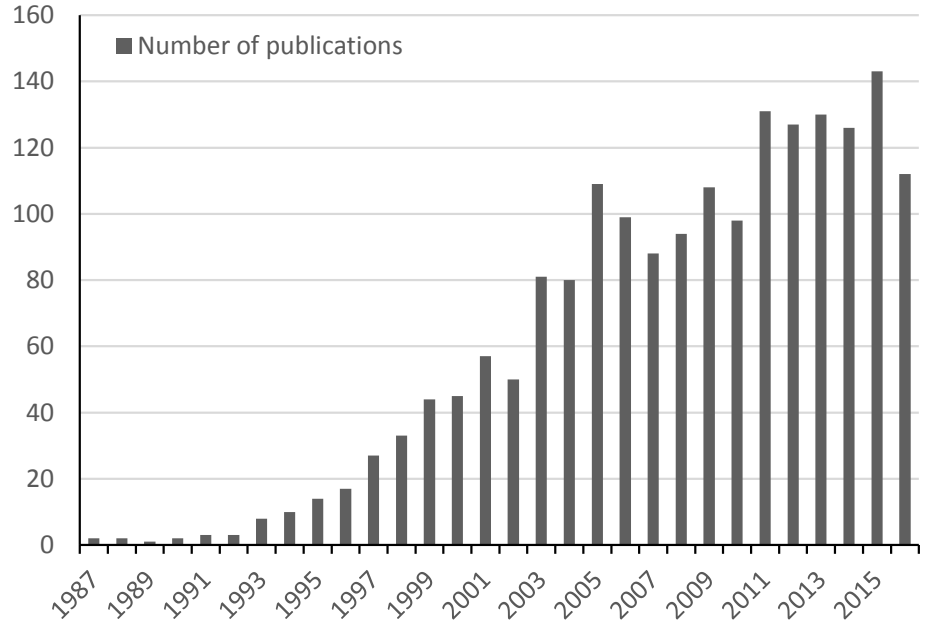

Figure 1-2 Annual scientific research papers whose title included "4D Seismic" or "time-lapse seismic" from 1987 to 2016. Pre-1997 publications were carefully accounted for based on the title "seismic monitoring". Data collected from Google Scholar database. Modified after Floricich (2006) and Yin (2016).

further to maximise practical success (Figure 1-2). In fact the recognition of the usefulness of the '4D' input has motivated advancements in acquisition, processing and interpretation of seismic data, on the back bone of high performance computing capabilities and technology innovation. From the birth of the idea of common-midpoint (CMP) stacking in the 1950's to improve the signal-to-noise ratio of seismic data (Sheriff and Geldart, 1995), complex prestack and poststack seismic processing algorithms for high-resolution 3D imaging (Haugvaldstad et al., 2011) are now a common theme. There are also specialised fast-track ('less than three weeks processing time') and co-processing strategies dedicated to the delivery of high quality 4D seismic data (Campbell et al., 2011; Helgerud et al., 2011; Knapp et al., 2014). Recent reports on 4D full-waveform inversion (Hicks et al., 2016) and illumination concepts beyond the novel idea of CMP stacking (Svay et al., 2013) show just how much the industry has aligned to the demands of '4D' - maximise repeatability between the seismic datasets, preserve and resolve the production-induced changes we so clearly want, and, preserve true amplitudes and arrival times (Johnston, 2013). Campbell et al. (2015) (and also Kvalheim, et al., 2007) show an example of how improvements in processing enhanced the quality of the 4D seismic data (Figure 1-3).

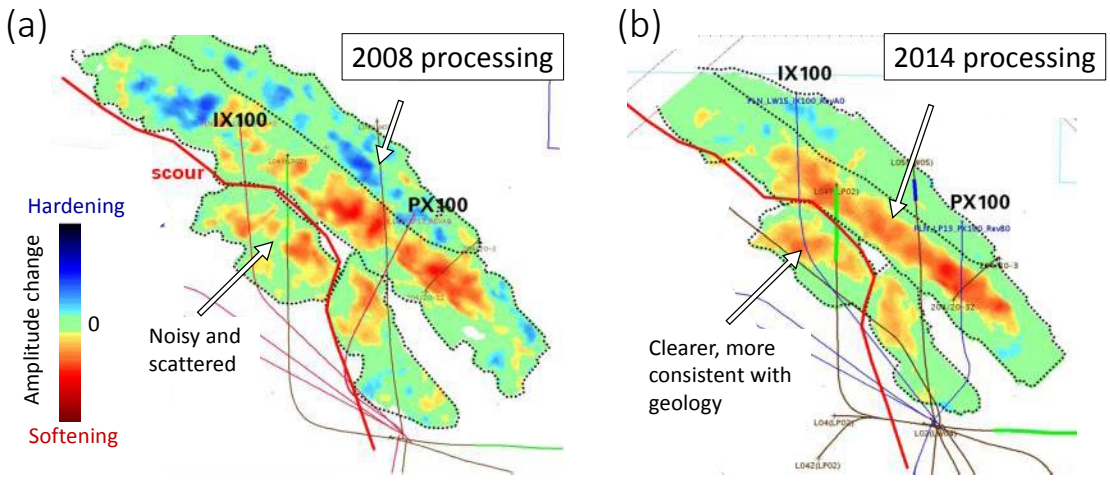

Figure 1-3 The value of good 4D seismic data processing on the Loyal field in the North Sea. (a) shows mapped changes in the reservoir using a processing workflow in 2008 (b) shows the same but using an improved updated workflow in 2014, modified after Campbell et al. (2015).

But of course, the magic from processing begins in the field; improvements in seismic data processing can only go so far, if the acquisitions themselves are not optimally designed for 4D imaging. The best chance of success demands highly repeatable

acquisition geometries, better subsurface imaging (i.e. choice of equipment, source-receiver configuration etc.) and optimal timing of surveys.

Offshore, there has been significant growth in dedicated 4D acquisition methods with the majority of the surveys acquired with towed streamers which are practically difficult to repeat due to currents, streamer feathering, sea state and platform obstructions. Strategies have since been implemented to maximise geometric repeatability (Widmaier et al., 2003; Widmaier et al., 2005), for example, steerable streamers, undershooting using dual-vessel configurations, self-overlapping-systems (Naess, 2005). Figure (1-4) shows the impact of improved geometric repeatability (after Kragh and Christie, 2002) on 4D seismic data acquired on the Forties field in the North Sea due to the use of steerable streamers which facilitated highly repeatable acquisition geometries in 2010 and 2013 compared to 2000 (Singer et al., 2017). Towed streamer surveys, however, are still found lacking with respect to the repeatability of the acquisition geometry; the desire is to repeat the acquisition source and receiver positions exactly.
More advanced technologies such as ocean-bottom-nodes (OBN) or ocean-bottom-cables (OBC) have since been introduced (Ronen et al., 1999). This paved the way for permanent seabed installations for "life of field seismic" (LoFS) monitoring (otherwise known as permanent reservoir monitoring (PRM)) which offer significant improvements in the sensitivity of monitoring, ease and frequency of acquiring repeat surveys (3 to 6 months, compared to towed streamer's 1 to 4 years), but at a cost 3-6 times higher than towed streamer (Watts and Marsh, 2011). Success with the first test on the Foinaven field in 1995 (Cooper et al., 1999) led to the first PRM system installation on the Valhall field in 2003 (Barkved, 2004), and in recent times, over eight fields across the North Sea, Caspian Sea, Offshore Brazil and the Norwegian Sea operate PRMs (WGP, 2010; Eriksrud, 2014; Caldwell et al., 2015). Such surveys provide 4D seismic data of excellent normalised root-mean-square (NRMS) error of around 2 to 15%, in comparison to towed streamers, 15 to 45%.

On land, repeatability of source and receiver locations are generally easier to achieve but the main contribution to data non-repeatability are 4D variations caused by changes in near-surface conditions which can be orders of magnitude higher. The move from explosives (e.g. dynamite sources) to safer, more repeatable vibroseis sources, and the emergence of wireless recording systems allowed single-source single-receiver

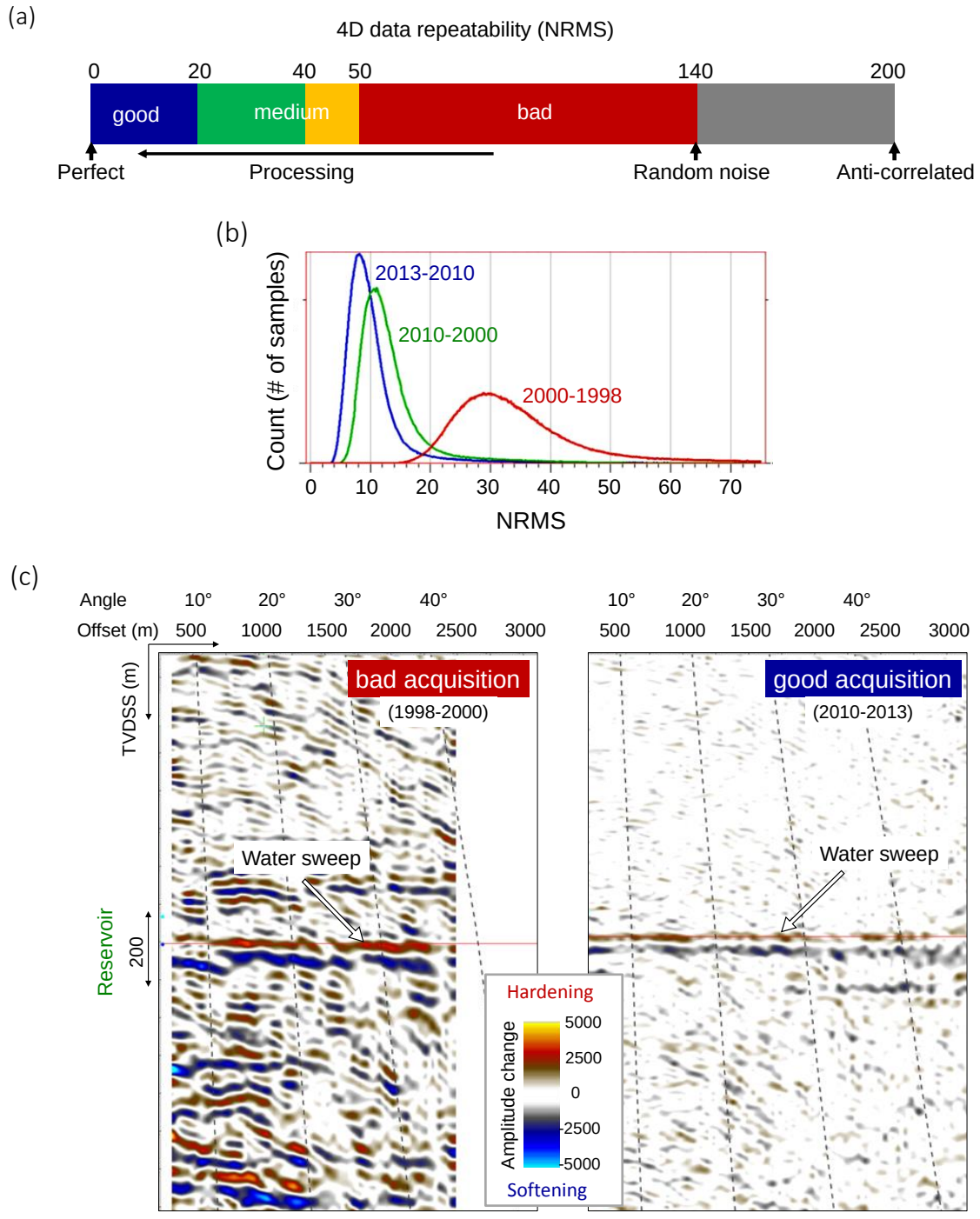

Figure 1-4 ***(a)*** *4D data repeatability (NRMS) chart, illustrating the various levels of data quality, 0 is perfect and 50 is bad. For more information see Appendix A.* ***(b)*** *An example of the impact of increasingly repeatable acquisition geometry, showing the NRMS histograms for various 4D seismic data acquired over the Forties field in the North Sea. Due to the use of steerable streamers in 2010 and 2013, the 4D data repeatability has improved drastically compared to the year 2000 and prior.* ***(c)*** *The value of highly repeatable acquisition geometry is evident. There are strong noise variations above and below the reservoir area which are not related to production effects, whereas, in 2013 (right) even very weak changes due to production (water sweep) are obvious around the reservoir, areas above and below are less noisy in comparison to the left image. Figure 1-3(b) and 1-3 (c) modified after Singer et al. (2017).*

configurations from conventional grouped-receiver arrays. High-density and wide-azimuth land acquisition geometries could thus be achieved which has strong benefits for land 4D (Bagaini et al., 2010) with focused applications in Enhanced Oil Recovery (EOR) such as thermal or CO_2 floods (Byerley et al., 2009; O'Brien et al., (2010)). Advanced automated onshore PRM systems (i.e. buried vibrator sources and receiver arrays), "**SeisMovie**™", the only of its kind, offers unparalleled high quality 4D seismic data with near-perfect data repeatability (< 1%) and continuous daily monitoring of subtle reservoir changes, beyond the limits of offshore PRM systems. The Peace River field in Canada benefits from this system for pro-active thermal EOR production of its heavy oil (Follett et al., 2015).

1.1.1 4D seismic timing and reservoir operations

4D seismic technology therefore has a time-consciousness to it (as Figure 1-1 illustrates), its value is determined by the timely impact it can make on field operations. Different field activities operate over different timescales which can all be impacted by 4D technology (Figure 1-5). In Chapters 4 and 5 we will see how the timescales of the reservoir processes impact the 4D seismic data from the acquisition.

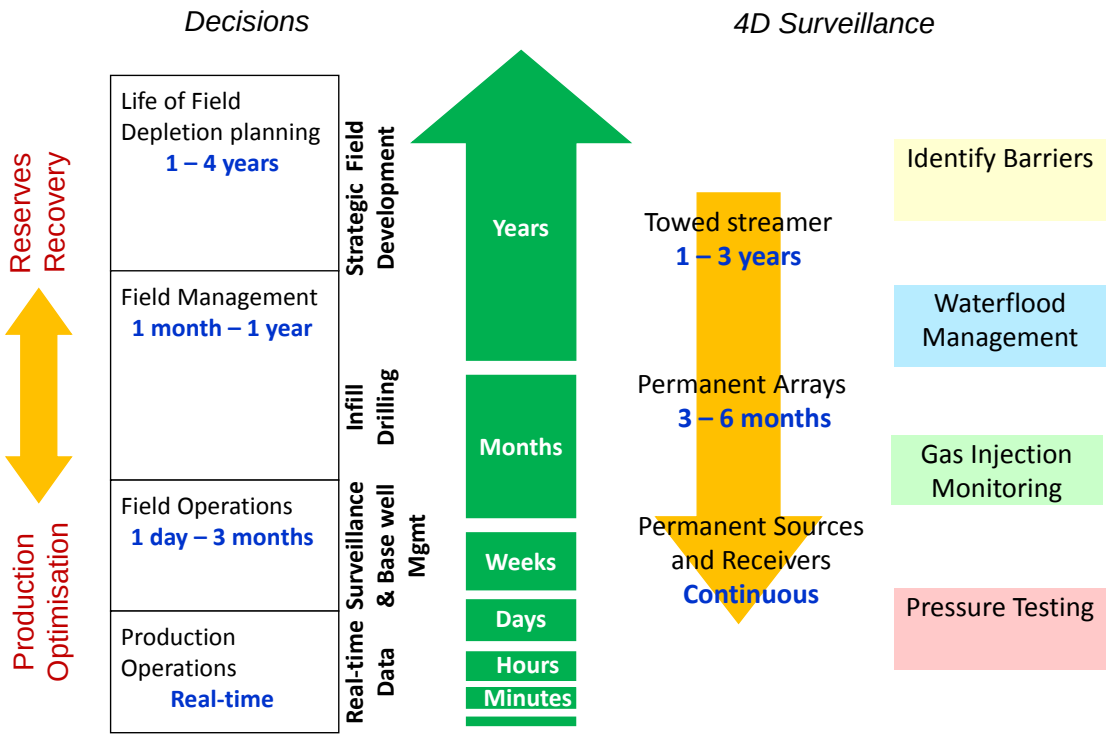

Figure 1-5 Different time cycles of Reservoir Activities, after Watts and Marsh (2011). 4D seismic technology can impact all operational decisions if repeated data is acquired at a similar time scale.

Watts and Marsh (2011) point out that 4D seismic data acquired every 2-3 years (e.g. towed streamers) may be adequate for most infill drilling but may be of little value in managing the wellstock (e.g. decisions to recomplete, frac, reperforate, acidise, workover etc.). More frequent data acquired every 6-12 months (e.g. offshore PRM) and processed within weeks can have a strong impact on well management decisions and even begin to influence daily-weekly production management (for example, decisions to change production chokes, increase/decrease injection rates, change injection pressures and operate smart completions). Indeed, the progression into permanent installations and high frequency of monitoring of the changes in the reservoir (i.e. multiple, repeated seismic monitor surveys), as well as the capabilities of delivering the final processed 4D seismic data quickly (e.g. van Gestel et al., 2007; Grandi et al., 2013, report 3-4 weeks processing time for the Valhall and Ekofisk field PRM data, respectively), is well founded. However, this also depends on how large the reservoir's 4D seismic response to the production changes might be.

1.2 4D seismic data interpretation

In common with many other remote sensing techniques, we cannot measure the properties we are most interested in directly, e.g. pressure and saturation. We have to infer them by measuring other properties which they affect, for example seismic velocity or amplitude. Since the reservoir changes in pressure, saturation etc. are induced by production, the effects captured in 4D seismic data, therefore cannot be interpreted without reservoir engineering knowledge. The industry has since evolved from the isolated 'single-disciplinary' attitude to the practice of 'multi-disciplinary integration' of both reservoir engineering and geophysical data to optimise field production for good return (Lumley and Behrens 1997; Waal and Calvert, 2003). The interpretation across both domains can be done at three main levels depending on the seismically-derived 4D attribute used (Figure 1-6). Comparisons can be performed using mapped (i.e. 4D signals computed along the reservoir interface) or volumetric changes of (1) the direct pre- or post-stack amplitude-variation-with-offset (AVO) / reflectivity data, or (2) elastic properties (such as changes in P- and S-wave impedances, P- and S- wave velocities, time-shifts), or (3) dynamic properties (such as pressure and saturation changes). Inversion is required from the observed seismic amplitudes to the reservoir's dynamic changes. To obtain seismic amplitudes from the reservoir

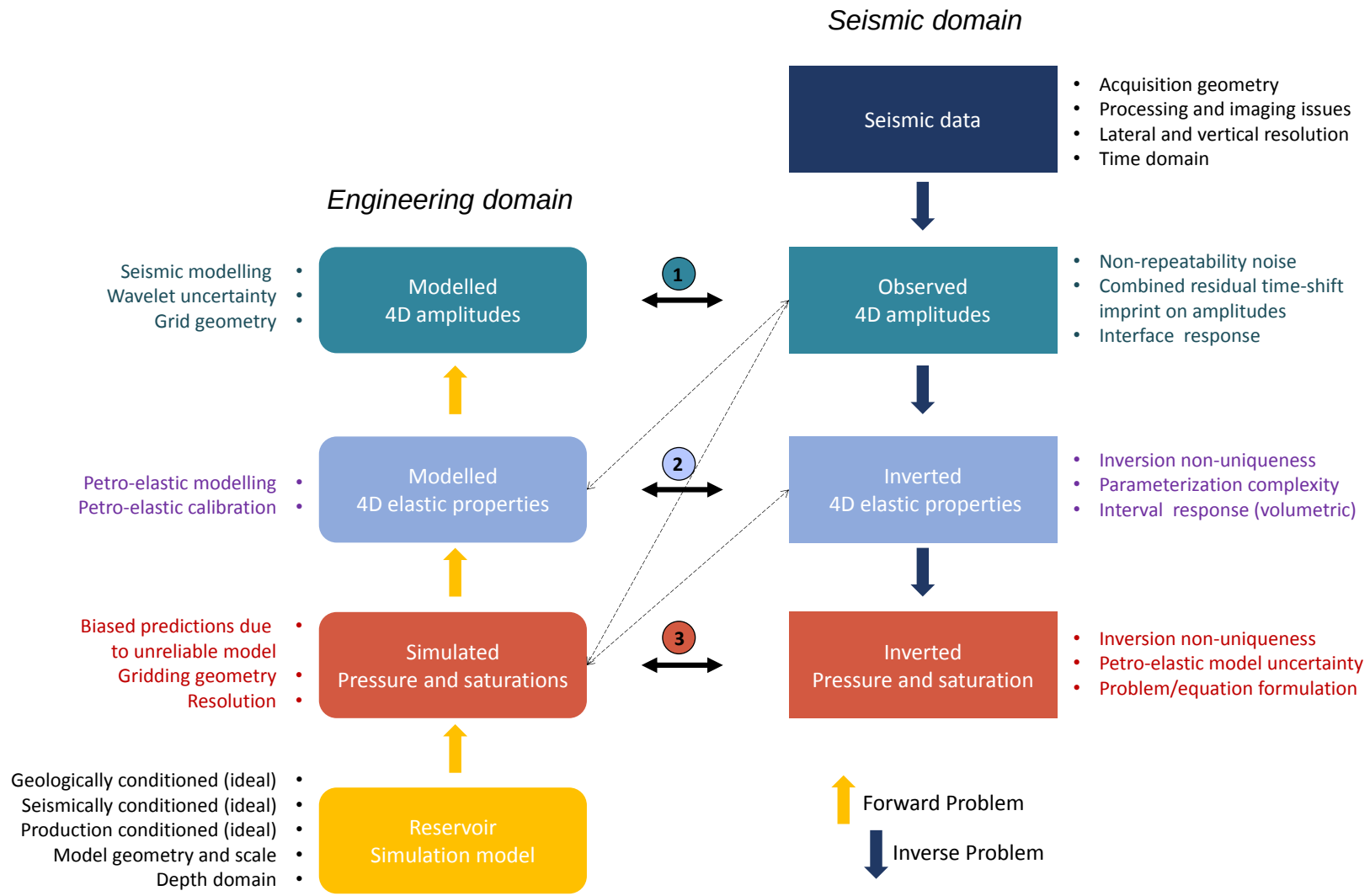

Figure 1-6 Different levels of 4D seismic data interpretation using various 4D attributes. The horizontal arrows (solid line) are concerned with quantitative integration between both domains, where each level has its associated uncertainties. The tilted dashed arrows show possible cross-level comparisons, typical with qualitative interpretation, in this case the comparison is usually done using measured well production and pressure data and predictions from a simulation model, if available.

engineering domain, petro-elastic (or rock-physics) modelling and seismic modelling via the fluid-flow simulation model is required. Uncertainties increase in both directions and each level has its associated issues.

The integration between geophysical and reservoir engineering domains began by qualitative interpretation i.e. using polarity to interpret the predominate effect on the mapped differences aided by well activity. Regions of change in the 4D seismic data are identified and related to changes in saturation, pressure, or temperature guided by well production data and/or predictions from a fluid flow simulation model. Greaves and Fulp (1987) show the first example on the Holtsand fireflood, and early 4D case studies have been reported on the Magnus field (Watts et al., 1995), Foinaven field (Cooper et al., 1999), Meren field in Nigeria (Lumley et al., 1999), Gullfaks field (Landrø et al. 1999; Landrø et al. 2001), Draugen field (Koster et al., 2000), and at Bay Marchand (Behrens et al., 2002). These achieved a variety of goals: identifying pathways of injected water, sealing faults/compartments, bypassed oil, and monitoring water influx.

Qualitative inferences such as these, work on the basis that one production-related effect completely dominates the others, for example, saturation effects may be more visible than pressure or temperature effects. The need for quantitative interpretation is obvious, as two or more production-related effects can impact the reservoir seismic properties which will lead to ambiguities in the interpretation. Fluid saturation, pressure, temperature, compaction effects often overlap to different extents in the reservoir and are likely to compete against each other. In the field example shown in Figure 1-7, pressure increase effects (softening) compete against water saturation increase effects (hardening) in the compartment and beyond it. The presence or dominance of one effect does not mean that others are absent. Numerical estimation of these reservoir changes is therefore necessary to separate the various effects.

To date, the qualitative approach is still widely used with success, but advances in 4D seismic data acquisition and processing has provided incentive for more quantitative integration between both geophysical and reservoir engineering domains, due to improved data quality and deeper knowledge. In such quantitative integration, we try to match the corresponding 4D seismic attribute obtained by modelling from the reservoir engineering domain to that obtained from the observed 4D seismic data (Figure 1-6).

The long-term value of 4D seismic data is fully established if reservoir changes in pressure, saturation, temperature etc. can be directly quantified from 4D seismic data, as

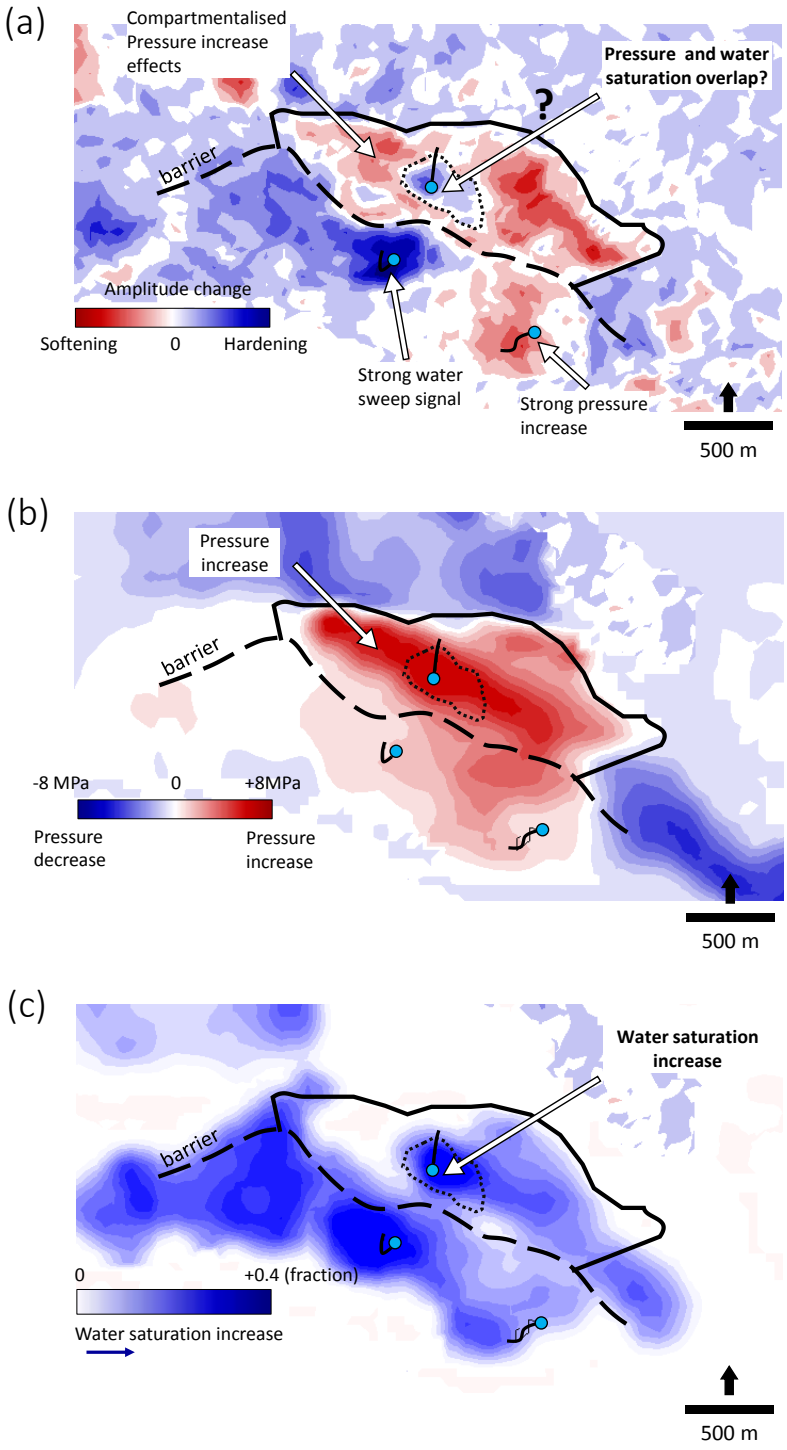

Figure 1-7 The need for pressure and saturation inversion. (a) 4D seismic amplitude map of a reservoir compartment (confined by the black solid line) from a North Sea field (b) and (c) show the corresponding depth-averaged maps of pressure and water saturation changes, respectively, from the history matched simulation model (modified after Huang, 2011). The blue wells are active water injectors during the 4D monitor time. The 4D seismic response in (a) is a combination of pressure and water saturation changes. The waterflood around the injector in the compartment is weakened by the pressure increase, the extent of the water flood is unknown in (a).

this will facilitate commonality with production data. The estimates of pressure and saturation changes from 4D seismic data are closer to the reservoir simulator output, and thus can be directly used to improve/update reservoir models for better forecasting abilities, avoiding any need for petro-elastic or seismic modelling. Johnston (2013) provides an extensive list of seismic measures of reservoir changes versus reservoir property changes that the reservoir engineers would prefer (Figure 1-8). Indeed, the challenge that does present itself is estimating these properties from 4D seismic data. This is a complex, non-unique and scale dependent inverse problem, and it is the quantification of pressure and saturation changes that this thesis is concerned with.

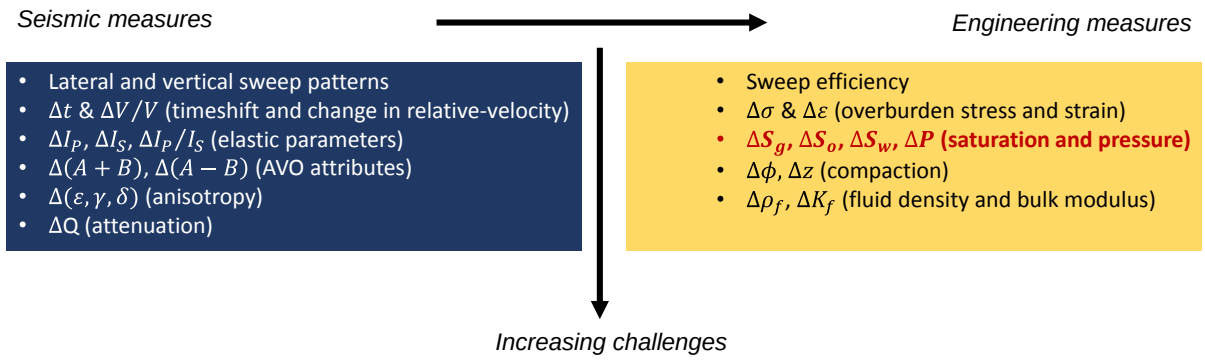

Figure 1-8 The holy grail of quantitative interpretation. Multiple 4D seismic attributes are analysed to estimate engineering measures of reservoir change. The seismic attribute changes are listed in increasing order of the technical difficulty involved in their determination. The engineering measures are listed in increasing order of the difficulty in their quantification from 4D seismic data (after Johnston, 2013). The challenge in this study is the estimation of ΔP and ΔS quantities.

1.3 Developments in ΔP and ΔS inversion in clastic reservoirs

Current techniques for estimating reservoir pressure and saturation changes from 4D seismic data fall into two end members, model-driven and data-driven, and the inversion could be either deterministic or stochastic. A summary of the general progression is shown in Figure 1-9 and a review of the various techniques from 1998 to 2015 follows afterwards.

1.3.1 Model-Driven approach

The majority of published literature focuses on the model-driven approach which constitutes a variety of rock-physics based methods. It involves a two-step process; (1) 3D/4D seismic data are first inverted for elastic property changes and (2) the reservoir

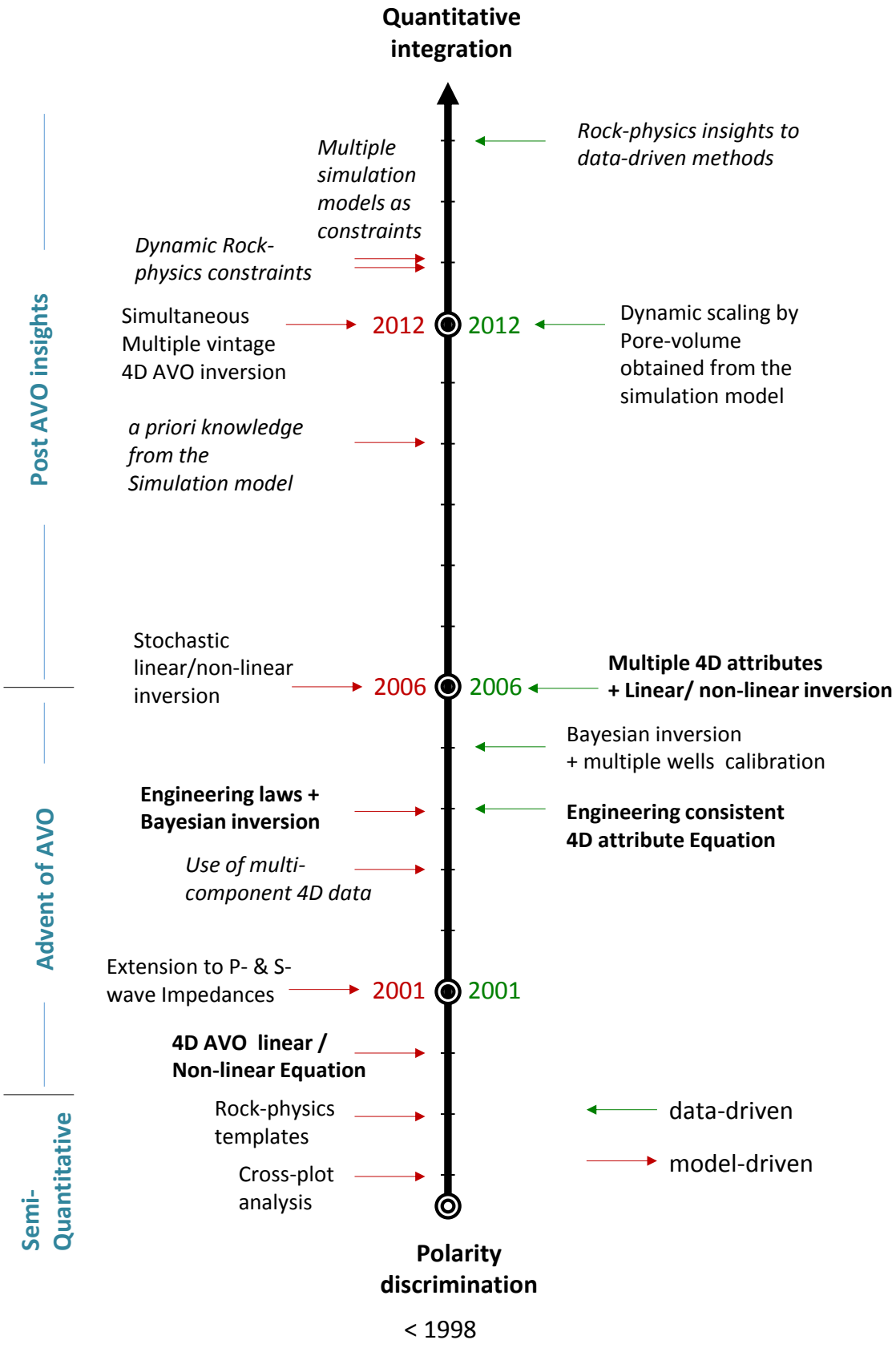

Figure 1-9 Towards quantitative integration with the reservoir simulation model domain. Some key milestones in the developments of model-driven and data-driven techniques in 4D seismic data inversion for pressure and saturation changes. Insights from synthetic studies are in italic.

changes in pressure and saturation are estimated from the elastic properties (time-lapse P- and S-wave) by petro-elastic inversion or from AVO analysis. Such methods rely on a calibrated rock-physics model's ability to predict the changes in the elastic properties that result from reservoir pressure and saturation change. The calibration must be done using well-log data and if available, core analysis to justify its suitability to be used in the inversion for pressure and saturation. In general, such approaches are compute-intensive and can exhibit different levels of complexity.

Tura and Lumley (1998) pioneered efforts through a cross-plot analysis to infer pressure and saturation changes. The workflow involved 3D AVO inversion of monitor and baseline seismic data to obtain P- and S- wave impedances, and subtracting monitor and baseline to obtain 4D changes in impedances. Well-based information is then used in rock-physics modelling of fluid saturation effects (using Gassmann, 1951) together with pressure effects (using empirical equations such as Mavko, 1998) to construct interpretation templates for discriminating pressure and water saturation changes. This was later demonstrated on a realistic synthetic study (Tura and Lumley, 1999). An extension of this approach is presented in Cole et al. (2002) on the Schiehallion field. Gas saturation changes were incorporated in their extensive non-linear rock-physics scheme using a wide variety of pressure and saturation scenarios. Maps of pressure and saturation changes were then obtained semi-quantitatively from a database of 4D seismic impedance cross-plots. It can also be quite attractive to interpret both static and dynamic reservoir properties, for example, Anderson et al. (2009) jointly interpret 3D and 4D AVO inversions through a similar approach of using rock-physics templates to identify areas of potential bypassed oil.

A problem with the cross-plot approach is that the interpretation template must account for all possible effects, as it will be quite easy to incorrectly associate a particular 4D change in the observed data to something else. Moreover, the approach implicitly assumes that honouring distributions observed/modelled at the well locations, would honour the entire data. It is also dependent on the choice of rock-physics model and can be quite sensitive to changes in the parameterisation, as this will lead to different interpretations.

Landrø (1999, 2001) was the first to formulate a mathematical link to pressure and saturation changes, using a reflection coefficient equation for isotropic elastic P-waves. Assuming a single reservoir interface and by combining Smith and Gidlow's (1987) and Shuey's (1985) approximations to the Zoeppritz equation, Landrø (1999) derived the following expressions for the changes in AVO intercept, R_0 and gradient G:

$$\Delta R_0 \approx \frac{1}{2}\left(k_\alpha \Delta S + k_\rho \Delta S + I_\alpha \Delta P + m_\alpha \Delta P^2\right) \tag{1-1}$$

and

$$\Delta G \approx \frac{1}{2}(k_\alpha \Delta S + I_\alpha \Delta P + m_\alpha \Delta P^2) - \frac{4\beta^2}{\alpha^2}\left(I_\beta \Delta P + m_\beta \Delta P^2\right) \tag{1-2}$$

where, α is the P-wave velocity, β is the S-wave velocity, ΔS is the change in water saturation and ΔP is the change in pore pressure. The parameters, k_α, k_ρ, I_α, m_α, I_β, and m_β, weight each pressure and saturation term and define the rock-physics model by linking relative changes in α, β, and density, ρ to pressure and saturation changes as follows:

$$\frac{\Delta\alpha}{\alpha} \approx k_\alpha \Delta S + I_\alpha \Delta P + m_\alpha \Delta P^2 \tag{1-3}$$

$$\frac{\Delta\beta}{\beta} \approx k_\beta \Delta S + I_\beta \Delta P + m_\beta \Delta P^2 \tag{1-4}$$

$$\frac{\Delta\rho}{\rho} \approx k_\rho \Delta S \tag{1-5}$$

They are the regression coefficients of the empirical curve of relative changes in P-wave and S- wave velocity (well-log and/or core data calibrated) versus water saturation and effective stress changes respectively.

By assuming a ratio of 2 between P- and S-wave velocity and small changes in R_0, Landrø (2001) obtained a simplified linear equation to solve for ΔS and ΔP based on empirical measurements on the Gullfaks field as follows:

$$\Delta S \approx 8(\Delta R_0 + \Delta G) \quad (1\text{-}6)$$

and

$$\Delta P \approx 23\Delta R_0 - 35\Delta G \quad (1\text{-}7)$$

where water saturation is measured as a fraction and pressure is in megapascals (MPa). Application of the technique to Gullfaks field (Figure 1-10) gave pressure and saturation which are generally consistent with the pressure measurements at wells and the saturation estimates. However, some unphysical values exist, which may be due to either incorrect rock physics model calibration, spatial variability of this model (which was not accounted for in any way), or lack of repeatability between the seismic surveys. The results proved useful to identify compartments and the extent of saturation patterns, but there are challenges to practical application:

- AVO attributes are noisy
- The rock-physics weighting coefficients are likely to vary spatially, so the assumption of a single set may not be adequate for an entire field
- Leakage from one parameter to the other introduces significant uncertainties in the result
- In theory, gas saturation terms could be included in the equations but it will require an additional AVO term which is difficult to estimate from typical seismic gathers.

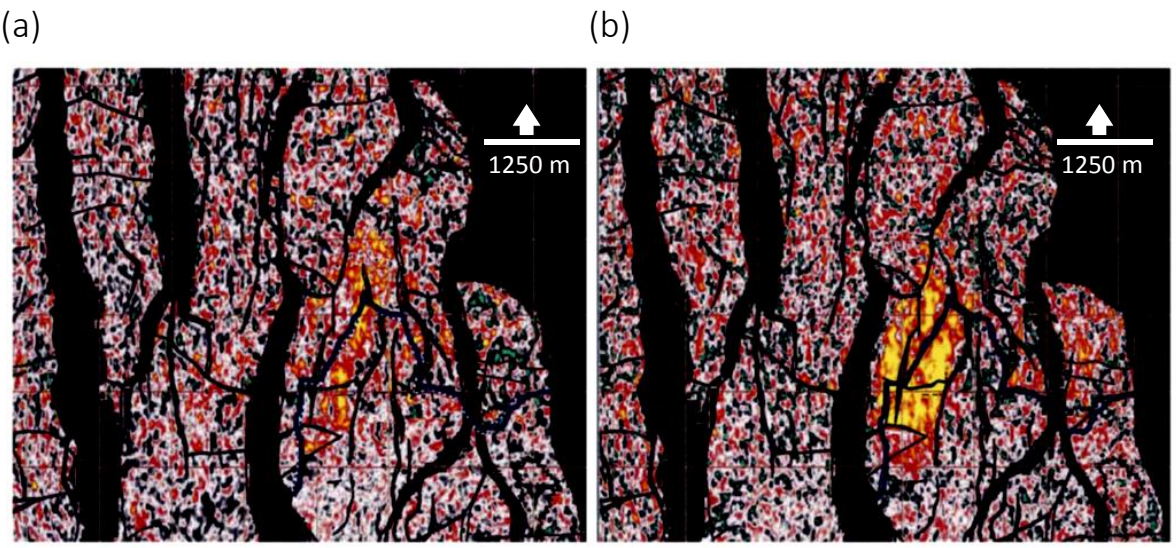

Figure 1-10 Results from Landrø's (2001) application on the Gullfaks field (a) inverted water saturation changes (b) inverted pressure changes. Modified after Landrø (2001). Faults are in black and the biggest changes are in yellow. In (b) pressure is confined within the fault segments indicating a compartment.

To improve on Landrø's approximations, Meadows (2001) makes two modifications, the first uses relative P- wave impedance, $\frac{\Delta I_P}{I_P}$, and S-wave impedance, $\frac{\Delta I_S}{I_S}$, reflectivity changes instead of AVO gradient and intercepts (which can be quite unstable):

$$\frac{\Delta I_P}{I_P} \approx k_\rho \Delta S + k_\alpha \Delta S + I_\alpha \Delta P + m_\alpha \Delta P^2 \tag{1-8}$$

and

$$\frac{\Delta I_S}{I_S} \approx k_\rho \Delta S + k_\beta \Delta S + I_\beta \Delta P + m_\beta \Delta P^2 \tag{1-9}$$

The second modification suggests including in the original expression, higher order terms (with a new coefficient, j_α also added) in order to obtain better empirical fits of the velocity versus pressure, and velocity versus water saturation curves, as follows:

$$\Delta R_0 \approx \frac{1}{2}\left(k_\rho \Delta S + k_\alpha \Delta S + j_\alpha \Delta S^2 + I_\alpha \Delta P + m_\alpha \Delta P^2\right) \tag{1-10}$$

and

$$\Delta G \approx \frac{1}{2}\left(k_\alpha \Delta S + j_\alpha \Delta S^2 + I_\alpha \Delta P + m_\alpha \Delta P^2\right) - \frac{4\beta^2}{\alpha^2}\left(I_\beta \Delta P + m_\beta \Delta P^2\right) \tag{1-11}$$

In theory, Meadows's (2001) modifications better approximate the empirical pressure and saturation curves, and still give a similar result to Landrø's (1999). For real field applications, however, this adds complexity and non-uniqueness to the solutions, and the question remains whether the uncertainty in the rock-physics framework can be justified using high-order approximations. To reduce the uncertainty, Landrø et al. (2003) extend the 4D AVO inversion method to multi-component 4D seismic data in a synthetic study. In addition, Landrø (2002) expresses pressure and water saturation changes using time-shifts and suggests that the problem can be further constrained by combining the same parameter (e.g. water saturation changes) estimated independently from AVO attributes and also from P- and S-wave time-shifts, using weight factors.

In a Bayesian formulation, Veire et al. (2006) study the uncertainty in pressure and saturation inversion on the Gullfaks field using Landrø's (2001) method.

Buland and El Ouair (2006) also implement a stochastic framework on the Norne field, which estimates water saturation changes along with uncertainties.

Trani et al. (2011) extend Landrø's (2001) method by introducing two additional equations that link P- and S-wave time-shifts to pressure and saturation changes in the following formulation:

$$\Delta T_{PP} \approx -\frac{2D}{\alpha_0^r + \delta\alpha_0^r}(k_\alpha \Delta S + j_\alpha \Delta S^2 + I_\alpha \Delta P + m_\alpha \Delta P^2) \quad (1\text{-}12)$$

where, ΔT_{PP} is the P-wave 4D time-shift, D is the reservoir thickness, α_0^r is the baseline reservoir interval velocity, $\delta\alpha_0^r$ is the absolute change in the reservoir velocity between the baseline and monitor, the rest of the parameters have been previously defined as above. The S-wave 4D time-shift, ΔT_{SS} uses the same expression by replacing α with β. Together with Landrø's (2001) equations, the resulting non-linear system solves for pressure and saturation changes using the Gauss-Newton algorithm, which was applied to a synthetic dataset. They note that the inversion improves, if the lateral variations in porosity are known or can be estimated seismically. This is yet to be applied on real field seismic data.

Whilst the inclusion of time-shifts and preservation of non-linearity can improve the quality of the inversion in theory, Blanchard (2012) point out that uncertainties in the inversion for elastic properties from observed 4D AVO data is an intrinsic part of the process, and this could lead to an inability to predict pressure and saturation changes. In a non-linear inversion scheme that combines both observed 4D time-shifts and 4D AVO data, Blanchard and Thore (2013) introduced dynamic constraints to the rock-physics model based on prior information from the reservoir engineer. In their synthetic application, they suggest that by introducing constraints, estimates of pressure and saturation changes are more reliable (Figure 1-11).

Recognising the need for engineering constraints, He et al. (2004) use P-wave impedances within a Bayesian scheme that is constrained by production data and flow principles to tackle non-uniqueness of seismic data in their application to the Draugen Field. Chu and Gist (2010) use a model-based inversion that first inverts for elastic properties and then pressure and saturation at the well locations before propagating the inversion away from the wells using statistical methods such as multivariate regression

or neural networks. Their initial model is based on pressure and saturation changes from a history-matched fluid flow simulation model.

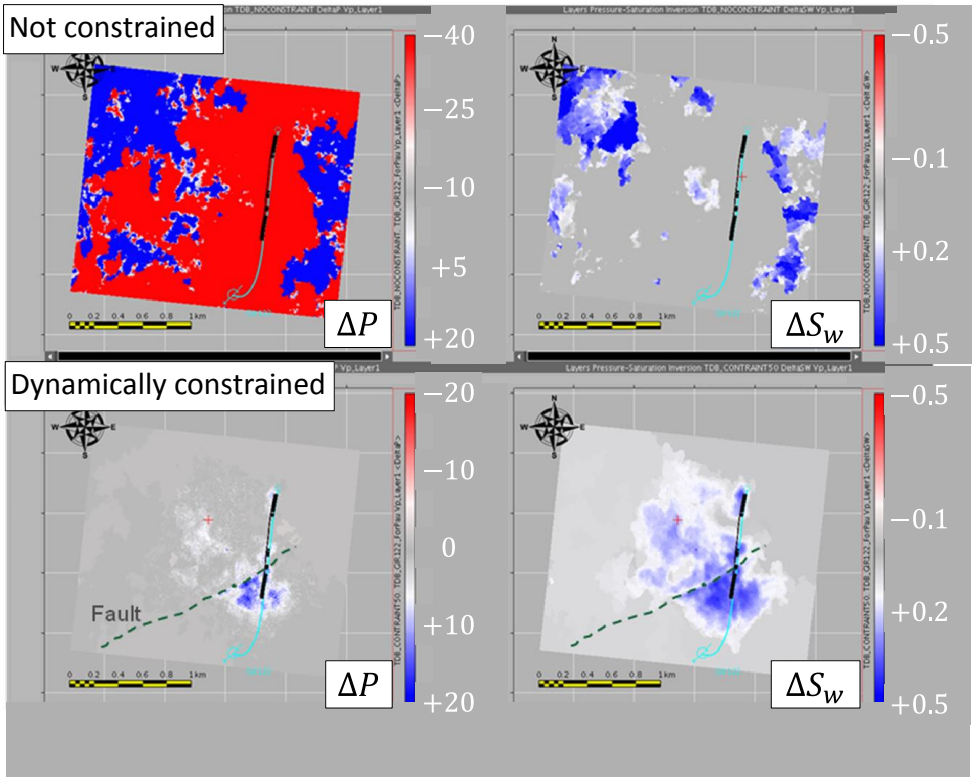

Figure 1-11 Blanchard and Thore's (2013) application of a rock-physics dynamic constraint to synthetic data. A comparison of the changes in Pressure (left, in bars) and Water saturation (right, in fraction of pore space) for the unconstrained (top) and constrained (bottom) inversion results. Dynamically constrained results are quantitatively more realistic, modified after Blanchard and Thore (2013).

In an application to the Schiehallion Field, Floricich et al. (2012) use a Bayesian approach to perform a simultaneous model-based 3D AVO (near, mid and far) inversion of a baseline and seven monitor seismic data which derives estimates of reservoir pressure, oil and gas saturations at the time of each monitor survey and their uncertainties via statistical measures. They achieve this based on a high confidence in the rock-physics model, and in the geologic and simulation model away from wells.

Multiple simulation models have also been used as spatial constraints, for example, on a synthetic study Davolio et al. (2013) generate multiple realisations of reservoir models to account for uncertainties, and uses limits of pressure and saturation values extracted from these realisations at each spatial location to guide their model-driven deterministic

inversion. They note that there are additional difficulties in implementing this on real field data, and suggest using a Bayesian framework to account for known uncertainties.

Perhaps, the reservoir should be used as a laboratory, as an alternative to the biased rock physics models. This is the idea developed within the Edinburgh Time-Lapse Project (ETLP) research consortium where the inversion is driven by what is learnt in the field, making the procedure engineering consistent (Floricich et al., 2005). The basis for this is that the 4D seismic signatures must respond directly to changes in well production and injection during the time periods over which the 4D surveys are shot (Huang and MacBeth, 2009). Thus, by measuring production volumes around wells and measuring the changes in the 4D seismic signals simultaneously, the data-driven method derives its name.

1.3.2 Data-Driven approach

Data-driven approaches are founded on the causality between well production and the 4D seismic responses (Huang et al., 2012). In this technique, known information (i.e. pressure and saturation values) at well locations is calibrated to magnitudes of the 4D seismic signals around the wells, to build training samples. Correlations established with the training set are then used to estimate pressure and saturations at the well locations and also away from well locations which have not been sampled. This circumvents the need for a rock-physics model or detailed core analysis as the estimation procedure is driven by field observations. Thus, the computation is unbiased with respect to the many assumptions implicit in model-driven methods. One short-coming of the data-driven process when compared to model-driven methods that generate 3D volumetric changes in pressure and saturation, is that it has so far been applied using 2D maps. However, the quick computation time, ease and accuracy (as it is determined by measured data) with which the inversion process can be implemented, the 2D maps from the data-driven method are rather useful for timely integration and reservoir management decisions.

MacBeth et al. (2006) define the following engineering-consistent normalised linear approximation for any 4D seismic attribute ΔA,

$$\frac{\Delta A(x,y)}{\bar{A}_b} \approx C_S \frac{\Delta S_o(x,y)}{\bar{S}_{oi}} + C_P \frac{\Delta P(x,y)}{\bar{P}_i} \tag{1-13}$$

where (x, y) is the seismic bin location; $\bar{S}_{oi}$ and $\bar{P}_i$ are the field's average initial oil saturation and average initial pore pressure, respectively; and $\bar{A}_b$ is the average baseline seismic map. The weighting coefficients C_S and C_P are assumed constant (i.e. spatially invariant), to be determined by calibration to production data. For any two or more attributes that are observed to act independently and with a different relation to pressure and saturation effects, the coefficients C_S and C_P obtained from these attributes will also be different, thus, the method can be used to invert for pressure and saturation changes across the field. For a single 4D seismic attribute, Equation 1-13 is organised into matrix form to determine C_S and C_P in a least squares inversion which uses oil saturation, ΔS_o and pressure, ΔP changes measured (or estimated) at chosen wells:

$$\begin{bmatrix} \frac{\Delta A(x,y)_1}{\bar{A}_b} \\ \frac{\Delta A(x,y)_2}{\bar{A}_b} \\ \vdots \\ \frac{\Delta A(x,y)_n}{\bar{A}_b} \end{bmatrix} = \begin{bmatrix} \frac{\Delta S_o(x,y)_1}{\bar{S}_{oi}} & \frac{\Delta P(x,y)_1}{\bar{P}_i} \\ \frac{\Delta S_o(x,y)_2}{\bar{S}_{oi}} & \frac{\Delta P(x,y)_2}{\bar{P}_i} \\ \vdots & \vdots \\ \frac{\Delta S_o(x,y)_n}{\bar{S}_{oi}} & \frac{\Delta P(x,y)_n}{\bar{P}_i} \end{bmatrix} \begin{bmatrix} C_S \\ C_P \end{bmatrix} \tag{1-14}$$

where, $1..n$ denote the well locations; the rest of the parameters are the same as above.

In an application to the Cormorant field (Figure 1-12), Floricich (2006) enhances this approach by performing a multiattribute analysis which determines the most suitable subset from a number of 4D seismic attributes. These include but are not limited to: far amplitude, near amplitude, full amplitude, intra-reservoir time-shift (time-shifts computed in a window below the reservoir minus the time-shifts computed in a window above the reservoir) and instantaneous frequency. To do this, Equation 1-14 is applied simultaneously to different combinations of multiple attributes and the combination with the lowest cross-validation error is selected for the inversion. Principal component analysis is applied to filter out redundancy and interdependencies among the attributes, the results from which are used to determine the most representative C_S and C_P. It was

found that AVO seismic attributes (near, mid and far) and 4D time-shifts yielded the best combination.

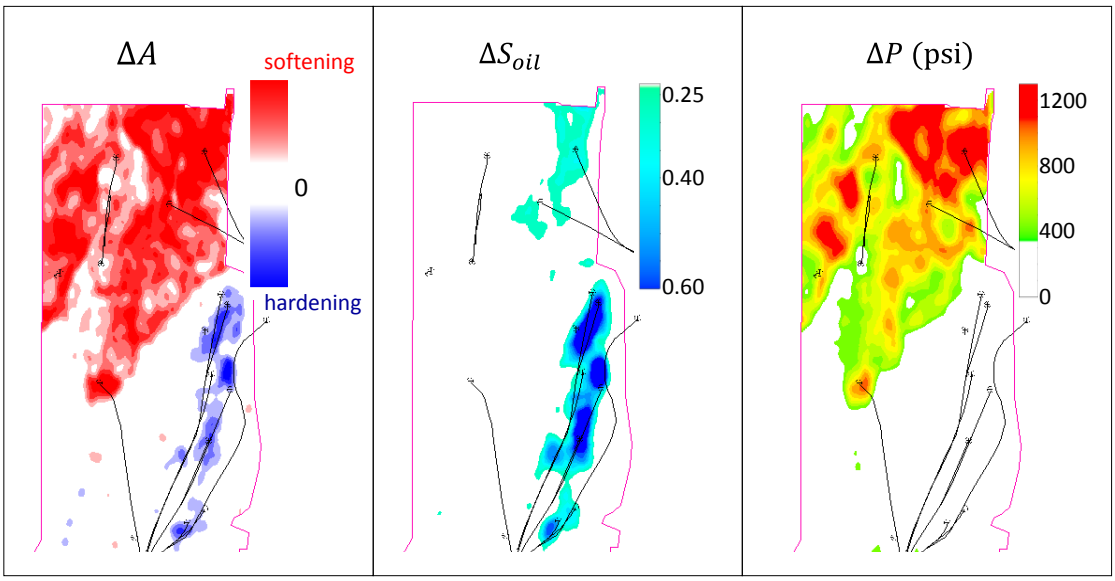

Figure 1-12 Application of the multiattribute analysis and Bayesian inversion using the engineering-consistent approximation, Equation 1-13, on the Cormorant field. The 4D amplitude map response (left), the inverted oil saturation change, in fraction (middle) and the inverted pressure change , in psi (right). In the furthest left image, pressure increase masks the underlying fluid saturation, but the inversion is able to separate the two. Modified after Floricich (2006).

Because the calibration or training data set from the wells are unlikely to cover the entire range of variations in rock properties and production of the reservoir, Floricich et al. (2005) tries to compensate for this by formulating the problem in a Bayesian scheme to account for uncertainties. This outputs probabilities for ΔS_0 and ΔP at each seismic bin location.

Based on a case study from the Schiehallion field, Floricich et al. (2006) proved that the methodology is not restricted to a two-fluid phase system and the approximation is not required to be linear. Incorporating gas saturation changes leads to the non-linear equation for the change in seismic attribute, ΔA

$$\Delta A \approx a\left(e^{b\Delta S_g} - 1\right) + c\Delta S_w + d\Delta P^2 + f\Delta P\,, \tag{1-15}$$

where ΔS_g , ΔS_w and ΔP are the changes in gas saturation, water saturation and pore pressure, respectively. Similarly, the weighting coefficients a, b, c, d, and f are assumed constant, and are again obtained by calibration at the wells.

Like Landrø's (2001) approach and subsequent model-driven cases, Floricich's (2006) data-driven method assumes that the weighting coefficients are invariant across the reservoir. However, they also note that this assumption is invalid, as reservoirs are not homogenous. Although, accounting for uncertainties by utilising a Bayesian scheme is appropriate, weighting coefficients are assumed constant with no physical meaning of their significance. However, Floricich's (2006) approach demonstrated that they are specific to the 4D seismic attribute used in calibrating them.

For thin reservoirs, Falahat et al., (2012) reports that the principal parameters controlling mapped 4D seismic signatures are not the pressure and saturation changes *per se*, but these changes scaled by the corresponding thickness (or pore volume) of the reservoir volume that these effects occupy. By pore-volume scaling and based on the principle of superposition, they derive a three-fluid phase approximation in the form,

$$\begin{aligned}\Delta A(\Delta P, \Delta S_g, \Delta S_w) \\ &\approx a h_p[\phi NTG]\Delta P + b h_g[\phi NTG]\Delta S_g \\ &+ c h_w[\phi NTG]\Delta S_w ,\end{aligned} \tag{1-16}$$

where the square bracketed terms refer to the effective porosity, ϕNTG, averaged over the depth range affected by the particular change at each seismic bin location. Thus, the mapped seismic response is dependent on the changes averaged over the total pore volume. The thicknesses occupied by pressure, water saturation and gas saturation changes, within the reservoir interval are given by h_p, h_w and h_g, respectively. The coefficients a, b, and c are constants obtained around well locations by calibration using pore-volume scaled maps of pressure, ($h_p[\phi NTG]\Delta P$), gas, ($h_g[\phi NTG]\Delta S_g$) and water saturation changes ($h_w[\phi NTG]\Delta S_w$) from a history-matched simulation model. This is similar to Equation 1-13 where the C_S - C_P coefficients now represent the combined terms in Equation 1-16 which weight the pressure, water and gas saturation changes

individually by accounting for the pore volumes. On the Schiehallion field, Falahat et al. (2012) perform a least squares inversion using a number of observed 4D seismic attribute maps (full angle stacks, gradient stacks, envelope weighted frequency and

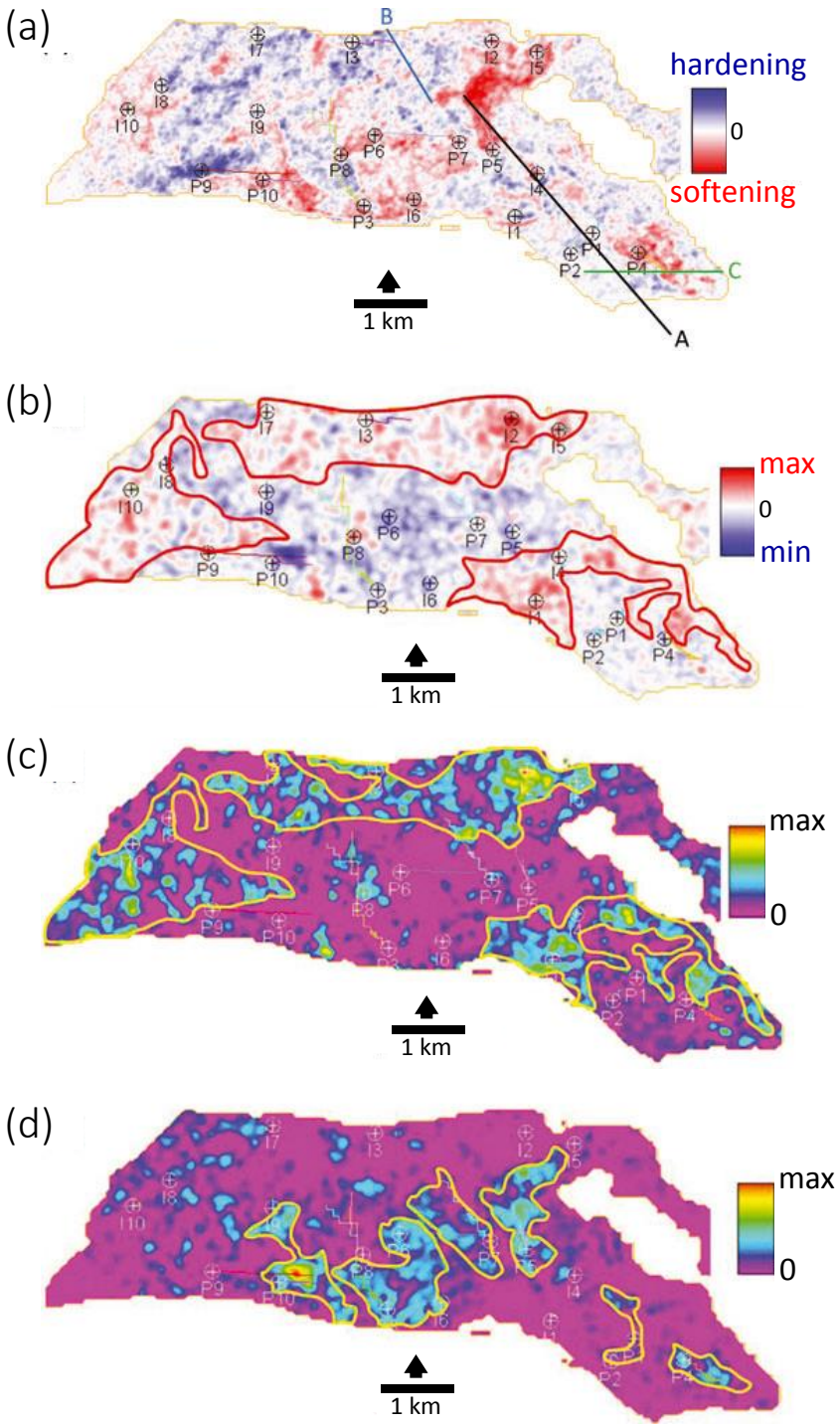

Figure 1-13 Application of the pore-volume scaled least-squares deterministic inversion using the linear approximation in Equation 1-16, on the Schiehallion field. (a) the observed 4D seismic amplitude response (b) the inverted pore-volume scaled pressure change (c) the inverted pore-volume scaled gas saturation change (d) the inverted pore-volume scaled water saturation change. Highlighted areas are for comparison, modified after Falahat et al. (2012).

reservoir thickness in time). Since the reservoir's pore-volume is not known exactly, the results do not yield absolute values of pressure and saturation but a scaled alternative (Figure 1-13), which they show can be semi-quantitatively compared with corresponding pore-volume scaled maps from the simulation model, assuming the simulation model is correct. Landa et al. (2015) also apply Falahat et al.'s (2012) approach in a Bayesian inversion scheme on an offshore turbidite field undergoing water-flood production.

To provide further insights into how pore pressure and saturation changes may combine to affect the 4D seismic signatures, Alvarez and MacBeth (2014) investigated the physical reservoir properties that may control the weighing coefficients presented in MacBeth et al. (2006). By performing extensive sensitivity tests using rock-physics forward modelling, a slight modification to Equation 1-13 expressed as absolute differences, gives

$$\Delta A(x, y, \theta) = C_s(x, y, \theta)\Delta S_w(x, y) - C_P(x, y, \theta)\Delta P(x, y) \quad (1\text{-}17)$$

and,

$$\Delta t(x, y, \theta) = t_i(\, C_s(x, y, \theta)\Delta S_w(x, y) - C_P(x, y, \theta)\Delta P(x, y)) \quad (1\text{-}18)$$

where (x, y) is the seismic bin location; ΔA and Δt are the 4D seismic amplitude and 4D seismic time-shift at a given incidence angle, θ, respectively; and t_i is the initial two-way-time of the reservoir surface. The 4D seismic data could be angle/offset stacks (i.e. AVO stacks) or CMP gathers (i.e. AVO gathers). Note that the sensitivity coefficients/ parameters, C_S and C_P are different for amplitudes and time-shifts, and are also dependent on the AVO data from which they are derived.

Alvarez and MacBeth (2014) confirm what is suspected, that the weighting coefficients, C_s and C_P are indeed related to the in-situ reservoir rock and fluid properties, with effective porosity being a major controlling factor on the magnitudes of the spatially varying C_s and C_P (Figure 1-14). Other reservoir parameters (initial reservoir pressure and saturation, top reservoir contrast, etc.) were found to have minimal influence and acted as groups of parameters rather than as individual contributors to form the 4D seismic signal. In a synthetic application using the

Schiehallion field model, Alvarez (2014) first determines a single C_S and C_P for each AVO amplitude stack (near, mid and far) by calibration to production data, and then accounts for their lateral variability by weighting using maps of porosity and overburden stress computed from the field's fluid-flow simulation model.

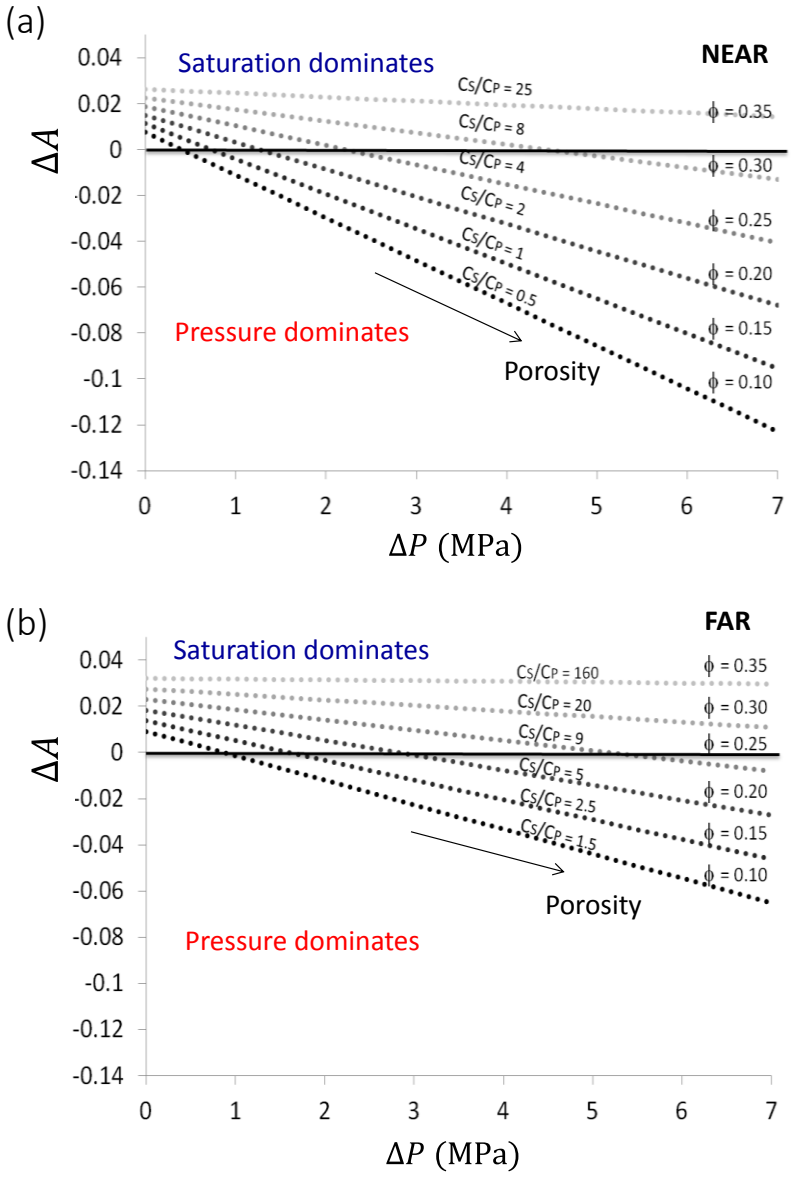

Figure 1-14 Rock-physics modelling insights for an oil-water sandstone reservoir. Effects of pressure increase and water saturation increase compete against each other. For a range of porosity, ϕ , cross-plots are given for (a) amplitude change, ΔA for the near offset stack (angle, Θ = 0° - 10°) versus pressure change, ΔP (at a fixed water saturation value of 0.6) (b) the same as in (a) but for the far offset stack (angle, Θ = 25° - 35°). The weighting coefficients C_S and C_P depend on the reservoir's geology, indicated here by porosity, which are intrinsic to the sensitivity of the offset dependent amplitude changes to pressure and water saturation effects. Pressure increase effects are stronger in the near offset and weaker in the far offset which is the opposite for water saturation effects, and the C_S/C_P ratio, also change according to offset and porosity. As the effects of pressure and water saturation increases compete, the horizontal black indicates the magnitudes of pressure changes that will need to occur, to override water saturation changes and how porosity affects this margin at the near and far offset. Modified after Alvarez and MacBeth (2014).

1.4 Main challenges of the thesis

The progress described above (and as summarised in Figure 1-9) for the estimation of ΔP and ΔS quantities from 4D seismic data are noteworthy as they pave the way for further improvements in this area of active research. Pressure changes in particular are still difficult to estimate with certainty as opposed to water saturation changes. Issues remain regarding uncertainty in the rock physics models and in the degree to which 4D seismic data alone can determine saturation and pressure. It also noted that the fluid flow simulation model can provide additional information (both static and dynamic properties) to aid the inversion process, but that it in itself adds more uncertainty. The various methods appreciate the limitations of their approach, and often utilise a stochastic framework to somehow account for this, but this does not address the issue beyond the well-founded data non-repeatability noise argument and non-uniqueness in the inversion. I seek a more data-driven engineering approach that is concerned with the interpretation of 4D seismic data and its associated uncertainties. The purpose of which is to provide more reliable estimates of pressure and saturation changes from 4D seismic data. The value in this is that such estimates are closest to engineering measures of the dynamic reservoir and are ideal for use in fast and direct model updating through seismic-assisted history matching.

- The first area to address is the quantification of the weighting coefficients (we will call them 'sensitivity parameters (or coefficients)') - these are key for the discrimination between pressure and saturation changes. They represent the reservoir's in-situ sensitivity to pore pressure only and saturation only effects and their meaning is far from empirical. It is also known that the magnitudes of the sensitivity parameters and their spatial variation are determined by the characteristics of the particular reservoir rock – mostly by effective porosity. Rock-physics based methods (together with core data analysis) are far too biased, particularly, in defining the reservoir's rock pressure sensitivity, though such methods provide a good theoretical background. Calibration of the in-situ reservoir response as measured by 4D seismic data is the approach that would be further explored in this thesis.

- There is no clear understanding yet from the observed 4D seismic domain as to how the magnitude of the sensitivity parameters/coefficients differ for pressure and saturation effects, and how they differ with respect to different fields. This is also an area that this thesis aims to clarify using the observed 4D seismic data and reservoir engineering measurements.

- The developments so far are yet to use the information from multiple monitor datasets. The majority of the methods use a single monitor 4D seismic data and where multiple monitor data are inverted, they are treated independently. It is a challenge then to unlock the potential of combining multiple repeated 4D seismic data, not just for the quantification of the sensitivity parameters but for the separation of pressure and saturation changes at one specific monitor time. Utilizing monitor data acquired at different times can help address linearity or non-linearity in the relation between the 4D seismic response and the pressure and saturation changes for a particular field. This can thus determine whether a linear or non-linear equation should be used in data-driven inversion techniques.

- The inversion is non-unique and 4D seismic data is limited mostly by non-repeatability noise and resolution. It is also known that 4D seismic data alone cannot give reliable estimates of the reservoir dynamic properties we seek. The use of sparse well production and pressure data, and material balance engineering laws as constraints has been tried to a great extent. The challenge is to develop a robust inversion scheme that better incorporates reservoir engineering data to guide the inversion of the observed 4D seismic data.

- By investigating the temporal (also termed dynamic) behaviour of reservoirs, we can determine whether any reservoir changes occur during seismic acquisition.

1.5 The work of this thesis

1.5.1 Thesis outline

The remainder of this thesis is divided into seven chapters as follows:

Chapter 2 uses rock-physics modelling to understand the sensitivity of outcrop sandstones and a recovered reservoir sandstone to reservoir changes in pressure and fluid saturation. Zero-offset 4D amplitude and time-shifts are modelled for independent effects of pore pressure increase, pore pressure decrease, gas saturation and water saturation changes.

Chapter 3 implements an interpretation based method that calibrates maps of 4D amplitudes from multiple monitor 4D seismic data (full-offset post stack) and engineering data to quantify the in-situ pressure, water and gas saturation sensitivity of the reservoir, along with its uncertainties. The pressure or saturation sensitivity is expressed in relative amplitude terms as a function of the change in pressure (in MPa) or the change in saturation (in fraction). The method is applied to four producing North Sea clastic fields with different geological environment, production mechanisms, rock properties and simple to complex 4D seismic responses. A different more volumetric 4D seismic attribute, time-shifts is also used. The analysis is done using intra-reservoir time-shifts extracted from the computed 4D time-shift volumes of multiple monitors (full-offset post stack seismic data). Time-shift sensitivity is quantified as the change in two-way-time relative to the reservoir thickness as a function of the change in pressure (in MPa) or the change in saturation (in fraction). This is applied to a geomechanically active high-pressure-high-temperature (HPHT) clastic field and a normally-pressured clastic field.

Chapter 4 addresses the issue of time scales when relating the acquired 4D seismic data to the reservoir engineering data. It examines the spatiotemporal relationship between physical processes in the reservoir such as pressure, water and gas saturation as controlled by field/well operations and the time sequence of shooting of real field North Sea acquisitions from a PRM and towed streamer survey. It suggests that intra-survey reservoir fluctuations (that is, production fluctuations that occur during the shooting of

monitor surveys) might prevent accurate quantitative measurement of the reservoir change using post-stack 4D seismic data.

Chapter 5 assesses the impact of the above intra-survey reservoir fluctuations in the quantification of pressure and saturation changes from 4D seismic data. It reveals that the intra-survey reservoir fluctuations create a complicated spatio-temporal imprint on the post-stack data, and adds to the lack of accuracy in the measurement of reservoir changes using offset stacks from the 4D seismic data, especially pressure changes. It is then recommended that the shot timestamps of the acquisition is used to sort the seismic data immediately after pre-stack migration and before any stacking. The seismic data should also be shot quickly in a consistent pattern to optimise time and fold coverage.

Chapter 6 presents an engineering-constrained, data-driven, map-based inversion scheme to estimate pressure and water saturation changes from 4D seismic data in clastic reservoirs. It is a deterministic least squares inversion that quantifies and uses the uncertainty in the 4D seismic data, as well as the engineering data. Multiple monitor 4D seismic data are combined to estimate the spatially-varying reservoir sensitivity for each sub-offset stack (near, mid and far), which are then used to invert for pressure and water saturation changes at a specific monitor time. The fluid flow simulation model is included to provide soft dynamic constraints. To account for uncertainties with using a single model and lessons learnt from Chapter 4 and 5, multiple realisations of geologically-consistent and history-matched reservoir simulation models are generated, and embedded within the inversion. The added benefit is that the scheme automatically presents the reservoir model that best honours the 4D seismic signals.

Chapter 7 applies the inversion scheme discussed in Chapter 6 on the Heidrun field which has five repeated 4D seismic monitor data. Realistic synthetic data is modelled based on the Heidrun field's reservoir properties, and by extracting the observed 4D seismic noise and adding it to the synthetic data obtained by simulator-to-seismic modelling.

Chapter 8 summarizes the conclusions of the work from previous chapters, and in addition, recommendations are put forward for further future research.

1.5.2 Publications

Parts of this thesis have been independently presented in the following publications:

- Omofoma, V. and MacBeth, C. (2015). Intra-survey Pressure Variations-Implications for 4D Seismic Interpretation. Paper presented at the 77th EAGE Conference and Exhibition-Workshops, Madrid, Spain, 1 – 4 June, 2015.

  --- Chapter 4

- Omofoma, V. and MacBeth, C. (2016). Quantification of Reservoir Pressure-sensitivity Using Multiple Monitor 4D Seismic Data. Paper presented at the 78th EAGE Conference and Exhibition, Vienna, Austria, 30 May – 2 June, 2016.

  --- Chapter 3

- Omofoma, V., MacBeth, C. and Amini, H. (2017). Intra-survey Reservoir Fluctuations – Implications for quantitative 4D seismic analysis. *Geophysical Prospecting (accepted with corrections underway, May 2017)*

  --- Chapter 5

Chapter 2

A rock-physics understanding for the quantification of pressure and saturation sensitivity in sandstones using zero-offset 4D amplitudes and time-shifts

Key to quantitative interpretation of 4D seismic data for the separation of pressure and saturation effects is accurate knowledge of their individual contributions to the 4D seismic signatures. In this chapter I use known rock-physics equations to model zero-offset 4D amplitudes and intra-reservoir time-shift responses in a producing black-oil reservoir. Of particular concern is the sensitivity of normally-pressured sandstones to independent changes caused by pore pressure increase, pore pressure decrease, and water and gas saturation increase. The sensitivity to the reservoir dynamic changes are quantified using the modelled 4D amplitudes and time-shifts, which are found to be complementary attributes. A generalised understanding of the dependence of the time-shift and amplitude sensitivity to lithology variations is also provided by analysing three sandstone samples which ranged from high porosity (18-27%) unconsolidated sandstones to low porosity (5%) cemented sandstones. The modelling also provides insights into the specific nature of sensitivity at various magnitudes of dynamic changes, and the imbalance of sensitivity between pressure and saturation effects.

2.1 Introduction to sensitivity

To separate and quantify reservoir changes in pressure and saturation from 4D seismic data (Figure 1-7), a good understanding of the impact of reservoir dynamic changes on the elastic properties of the reservoir is a prerequisite. This must involve a quantification of the individual contributions of pressure and saturation effects to the overall 4D seismic response (Figure 2-1). In this context, the quantitative metric is given the name 'sensitivity'. Sensitivity is specific to the particular dynamic change e.g. pressure sensitivity, water saturation sensitivity, in addition to the particular elastic or seismic attribute derived from the observed 4D seismic data or modelled. For example, moduli, velocities, impedances, time-shifts, amplitudes, AVO gradient, AVO intercept, etc. Sensitivity is a measure of the change in 4D seismic attribute to a unit change of pressure or saturation. In many works concerned with the separation of pressure and saturation changes in 4D seismic data, the sensitivity is often presented as model-driven regression fits, $k_\alpha, k_\rho, I_\alpha, m_\alpha, I_\beta,$ and $m_\beta,$ (Equations 1-1 and 1-2) or data-driven weighting coefficients C_S and C_P (Equation 1-13). These weighting or regression terms define the balance between pressure and saturation effects for the inversion, and could be viewed as measures of sensitivity to the independent effects.

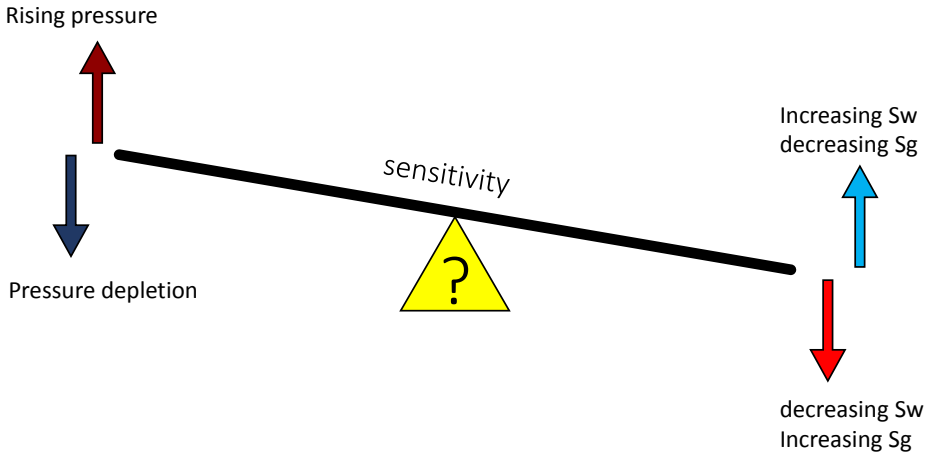

Figure 2-1 Sensitivity is a metric for defining the balance between reservoir dynamic changes such as pore pressure and saturations. Colour-filled arrows indicate the 4D impedance response to any of the changes, softening (red /dark red) and hardening (blue/ dark blue). Softening implies a decrease in impedance and hardening implies an increase in impedance. Arrows facing the same direction illustrate the polarity of pressure and saturation changes that are likely to compete against each other during typical production scenarios. For example, in waterflooding, an increase in water saturation, Sw, is accompanied by an increase in pore pressure, and both effects compete against each other. An increase in gas saturation, Sg, (i.e. gas breakout) could also occur, if pressure drops below the bubble point pressure (Falahat et al., 2014), which both compete. Gas injection could also raise pressure as the gas saturation increases, both effects in this case, will reinforce.

2.1.1 Methods for calibrating sensitivity

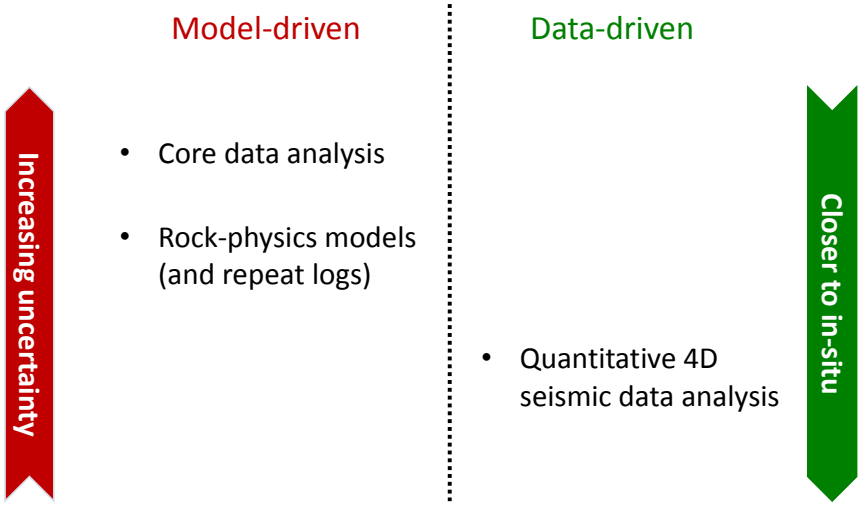

Figure 2-2 The three different methods by which the reservoir sensitivity can be estimated. By moving from laboratory measurements on cores, towards rock-physics models constrained by repeat logs and crossing over to the 4D seismic data domain, the analysis is closer to the in-situ conditions and can be argued to be more accurate, modified after Amini (2014)

The techniques for estimating sensitivity are model-driven or data-driven as it is by these two approaches, pressure and saturation changes are separated from 4D seismic data (Figure 2-2) (see also section 1.3). Part of the model-driven approach as popularised by Landrø (2001), involves (1) estimating pressure sensitivity by laboratory analysis on cores where elastic moduli of the rock are measured under different confining pressures, combined with (2) fluid saturation sensitivity using empirical fluid equations, such as Gassmann's (1951) theory (see section 2.2.1). Although, much of our current knowledge of pressure sensitivity is shaped by laboratory measurements on cores, it is generally acknowledged that such measurements have limited applicability to the in-situ field-scale reservoir response (e.g. Nes, 2000; Eiken and Tøndel, 2005; Alvarez and MacBeth, 2014); contrary to fluid saturation sensitivity which is believed to be adequately explained by Gassmann's model. Alvarez and MacBeth (2014) discuss the issues associated with laboratory experiments which include: statistical sampling of the cores, time-scale of the production relative to the cycle that pore pressure is cycled in the laboratory, core plug damage, frequency dispersion, evaluation of the effective stress coefficient, geomechanical effects, measuring dry-rock response using the Gassmann model, the role of clays and shales, imperfect stress recovery and stress

asymmetry. Laboratory-based measurements can also be boycotted by using repeat logs- where repeat formation tester (RFT) and elastic logs acquired from the reservoir intervals that have undergone production are used to calibrate the pressure sensitivity. The calibration uses rock-physics equations to model and fit the repeat elastic logs. Repeat logs are however not widely available across fields and such analyses are very limited. An excellent example is given in Fürre et al. (2009) which reports weaker pressure sensitivity than those measured in the laboratory, and found that the log-derived calibration compared favourably with the observed 4D seismic response. Of particular concern with rock physics models are that they are grossly uncertain, time consuming and difficult to calibrate sufficiently (Amini, 2014; Briceno et al., 2016).

Many studies point to 4D seismic data as the measure of "truth" to validate log-derived rock-physics models or laboratory measurements (e.g. Eiken and Tøndel, 2005; Fürre et al. 2009; Amini and MacBeth, 2015; Avseth et al., 2016). The 4D seismic data are a direct and spatially-dense measure of the reservoir's response over production time. This allows for the investigation of spatial variations in sensitivity, and across monitor times. The data-driven method thus addresses the gaps in rock-physics models using 4D seismic data as an alternative to calibrate the relationship between observed magnitudes of the 4D seismic response and measured magnitudes of pressure and saturation changes induced by production (for example, MacBeth et al., 2006; Landa et al., 2015). Although 4D seismic data measurements better represent the in-situ behaviour of the reservoir rock and associated fluids, it can be argued that the 4D seismic method can be of higher uncertainty than model-driven methods on the basis of non-repeatability noise. This however, depends on individual field acquisition and processing of the 4D seismic data, but the success so far with the data-driven method is promising as they are more reservoir-consistent. The insights gained from rock-physics models are however essential for the quantification and interpretation of 4D seismic signatures.

In this chapter, 4D rock-physics modelling is used to provide background understanding of the variation of sensitivity in sandstones as well as the sensitivity to pressure and fluid saturation changes. Zero-offset 4D amplitudes and time-shifts are modelled to define and quantify the reservoir sensitivity in sandstones. The aim is to guide the interpretation achieved from quantifying the in-situ reservoir's sensitivity using measured 4D seismic data, to be explored in Chapter 3. Noted earlier in Equations 1-17 and 1-18, the sensitivity depends on the angle of incidence of the 4D seismic data used

for calibration. In Chapter 7 (for example, Figure 7-7) this dependency is shown for the Heidrun field using AVO stacks of the near-offset, mid-offset, far-offset and full-offset to quantify the sensitivity to reservoir changes. It is shown that both the sensitivity to pressure and fluid saturation changes vary with angle of incidence. Also note that full-offset stacks are used to quantify the sensitivity of the various field reservoirs in Chapter 3, and zero-offsets are used in the rock-physics study in this chapter. Ideally, full-offset stack and zero-offset 4D seismic data should be the same after processing, but this is not always true. Seismic acquisitions are strategically designed to image at different offsets, but the propagation effects due to this offset variation are not completely removed in the final processed and stacked (full-offset) 4D seismic data. This means that AVO effects will still interfere and complicate the response observed in the full-offset stack. So, it is to be expected that the sensitivity obtained using zero-offset 4D seismic data will differ from those obtained using full-offset stacks.

2.2 Rock-physics model

Whilst rock physics modelling combined with laboratory measurements on dry cores may not adequately represent the in-situ reservoir response as observed in 4D seismic data (Alvarez and MacBeth, 2014; Amini and MacBeth, 2015; Saul and Lumley, 2015; Fürre et al., 2009), models however provide a theoretical framework by which seismically-derived sensitivity can be better understood. The aim in this section is to develop an understanding of rock and fluid physics and some selected equations that relate seismic changes to changes in reservoir rock properties due to production. The procedure involves performing fluid substitutions and pressure dependence calibration for isolated production-related scenarios, and computing the sensitivity. It is important to mention that this analysis focuses only in sandstones, assuming no change in macro-porosity. This is a reasonable assumption as most sandstones exhibit negligible or no physical thickness changes due to production. The reservoirs are thus non-compacting and there are no geomechanical effects occur in the overburden, hence, only elastic changes are considered. In the following sections I review the relevant equations that form the basis for the 4D rock physics analysis in section 2.3.

2.2.1 Fluid substitution model

The objective in fluid replacement modelling is to replace the initial properties of the reservoir rock with alternate post-production values from which seismic properties such as P-wave velocity, S-wave velocity, and density, and by extension P-wave and S-wave impedances can be computed. The formulas for these basic seismic properties are (Mavko et al., 1998):

$$V_{P_{sat}} = \sqrt{\frac{k_{sat} + \frac{4}{3}\mu_{sat}}{\rho_{sat}}}, \tag{2-1}$$

$$V_{S_{sat}} = \sqrt{\frac{\mu_{sat}}{\rho_{sat}}}, \tag{2-2}$$

$$I_{P_{sat}} = V_{P_{sat}}\rho_{sat}, \tag{2-3}$$

where the subscript sat indicates the fluid-saturated case, V_P is the P-wave velocity, V_S is the S-wave velocity, I_P is the P-wave impedance, ρ is the density, μ is the shear modulus and k is the bulk modulus. The saturated bulk density, ρ_{sat} is governed by porosity, mineralogy and fluid saturations:

$$\rho_{sat} = \rho_{dry} + \phi(\rho_w S_w + \rho_O S_O + \rho_g S_g) \tag{2-4}$$

where $\rho_{dry} = \rho_m(1-\phi)$ is density of the dry rock frame, ϕ is porosity, ρ_m is the mineral bulk density; ρ_w, ρ_O, ρ_g, are the water, oil and gas density respectively and S is the fraction of saturation for each fluid component. The saturated density at pre-production state can either be measured in-situ or computed using Equation 2-4.

Assuming values from the initial state are known, the goal is then to calculate alternate values representing different fluid saturation scenarios. For this, Gassmann equations (Gassmann, 1951) are used to compute the change in bulk modulus associated with a change in the pore fluid phases or a change in the acoustic properties of the existing fluids. These equations assume that the shear modulus is independent of fluid content (but not porosity), written as:

$$\kappa_{sat} = \kappa_{dry} + \frac{(1 - \kappa_{dry}/\kappa_m)^2}{\phi/\kappa_{fl} + (1-\phi)/\kappa_m - \kappa_{dry}/{\kappa_m}^2} \tag{2-5}$$

$$\mu_{sat} = \mu_{dry} \tag{2-6}$$

where κ_{sat} and μ_{sat} are the saturated bulk and shear modulus, κ_m and μ_m are the bulk and shear modulus of the mineral forming the rock, κ_{dry} and μ_{dry} are the bulk and shear modulus of the dry rock (minerals and pores), κ_{fl} is the fluid bulk modulus, and ϕ is the porosity.

For calculating several production scenarios, a practical form of the Gassmann equations is adopted (Equations 2-7 and 2-8) which shows which parameters will change should pore pressure and fluid saturation change:

$$\kappa_{sat}(P, S_{w,o,g}) = \kappa_{dry}(\sigma_{eff}) + \frac{\left(1 - \frac{\kappa_{dry}(\sigma_{eff})}{\kappa_m}\right)^2}{\frac{\phi}{\kappa_{fl}(P, S_{o,g,w})} + \frac{(1-\phi)}{\kappa_m} - \frac{\kappa_{dry}(\sigma_{eff})}{{\kappa_m}^2}}, \tag{2-7}$$

$$\mu_{dry}(\sigma_{eff_i}) \neq \mu_{dry}\left(\sigma_{eff_p}\right), \tag{2-8}$$

The dry rock bulk and shear modulus (κ_{dry} and μ_{dry}) are a function of the effective stress, σ_{eff} (which is linearly dependent on the pore pressure, P, see also Equation 2-18), i and p denote two different pressure states; S is the fraction of saturation for each fluid component and the subscripts w, o, g, indicate water, oil and gas, respectively. As pore pressure changes, the resulting increase or decrease of grain to grain contact of the dry rock frame is measured by the moduli. The bulk modulus of the fluid, κ_{fl}, measures the effect of pore pressure changes on the fluids, as well as the change in the fluid phase, for example, hydrocarbon has been replaced by water or gas break out has occurred due to pressure drop below bubble point. The saturated bulk density (Equation 2-4) is sensitive to fluid saturation changes, and in non-compacting reservoirs (porosity remains constant with production), pressure-related changes in density are only related to the fluids. This is because pore pressure changes only result in a small reduction in the effective pore volume. MacBeth (2004) shows that changes in the dry

rock density due to pore pressure changes (in other words, effective pressure changes) contribute less than 4%. The remaining 96% are controlled by the elastic moduli changes of the dry rock. Therefore, the assumption of constant density for the dry rock frame in response to pressure changes is practically applicable.

Gassmann's theory assumes that the pore space is occupied by only a single fluid phase, but in reservoir rocks different fluid phases are present together in the pore space. To use Gassmann's equations in such practical settings, I use Domenico's (1974) formula to calculate an effective bulk modulus that represents the fluid mixtures based on harmonic averaging assuming a uniform distribution of fluids:

$$\frac{1}{\kappa_{fl}} = \left(\frac{S_w}{\kappa_w} + \frac{S_o}{\kappa_o} + \frac{S_g}{\kappa_g}\right), \tag{2-9}$$

where S_w, S_o, and S_g are water, oil and gas saturations respectively, and κ_w, κ_o, κ_g are the water, oil and gas bulk modulus respectively. Figure 2-3 shows a schematic of fluids in the pore space of the rock (in this case, just oil and water). Fluids in the pore space are of two distinct characters: (1) free fluids (free water and oil, in this case) which are expected to alter the overall seismic properties of the rock during production

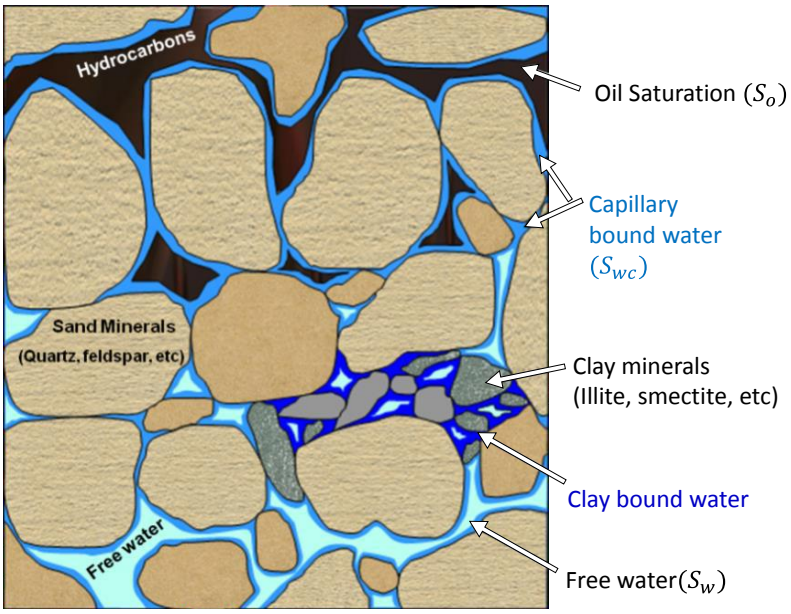

Figure 2-3 Schematic representation of a reservoir rock and the different fluid (shown here for an oil-water system) and solid phases, after Alvarez (2014).

(e.g. a normal water flooding scenario), and (2) capillary bound water and oil, which does not change, except in Enhanced Oil Recovery (EOR) with chemicals etc. The presence of these two distinct characters of fluids, limits the maximum expected saturation change in the rock. For instance, for a water flooding scenario, this yields a practical maximum of $(1 - S_{wc} - S_{or})$, where S_{wc} is the connate water and S_{or} is the irreducible (or residual) oil saturation.

The acoustic properties (i.e. velocity and density, which make up the bulk moduli) of the reservoir fluids (gas, oil and water) are calculated in-situ using Batzle and Wang (1992) equations, which are the state of the art. These describe the empirical dependence of gas, oil and brine properties on *temperature*, pressure and *composition* – (*changes in temperature and composition are not modelled in this study*). This requires knowledge of oil properties (oil API, solution gas-oil ratio and oil-formation volume factor), gas properties, and gas gravity to characterise the hydrocarbon properties, for a gas-oil-water system. Water properties depend on the sodium chloride (NaCl) salinity content. For other fluid systems, for example, modelling the effect of gas saturation of brine (and how much the presence of gas affects brine properties or how much gas can be dissolved in brine), the applicability is questionable (Avseth et al., 2010). In addition, it is not shown how the empirical formulas can be used to model gas condensate reservoirs, but it is expected that the formulas should extend adequately to both gaseous and liquid phases in a condensate situation.

Reservoir temperature	Initial Pore pressure	Water salinity	Oil gravity	Gas gravity	Initial Gas Oil ratio	Bubble point pressure
57.8°C	25 MPa	18000 ppm	25° API	0.5985	62.33 ($^{Sm^3}/_{Sm^3}$)	15 MPa

Table 2-1 Reservoir fluid properties and initial conditions based on a North Sea field to be used in Batzle and Wang (1992) equations for modelling changes in fluid properties for several production scenarios.

These information can be sourced from published empirical relations (Batzle and Wang, 1992), equations of state (fluid flow simulation model), or from pressure-volume and temperature (PVT) measurements taken in the field, which is most common. Table 2-1 details the reservoir properties of the fluids used for the 4D rock physics modelling in this Chapter. Apart from pore pressure, temperature of the reservoir fluids and water

salinity can also change, but for this exercise, I only focus on pore pressure changes. The effects of pore pressure on fluid properties are very subtle, in comparison to fluid saturation-related changes (Figure 2-4).

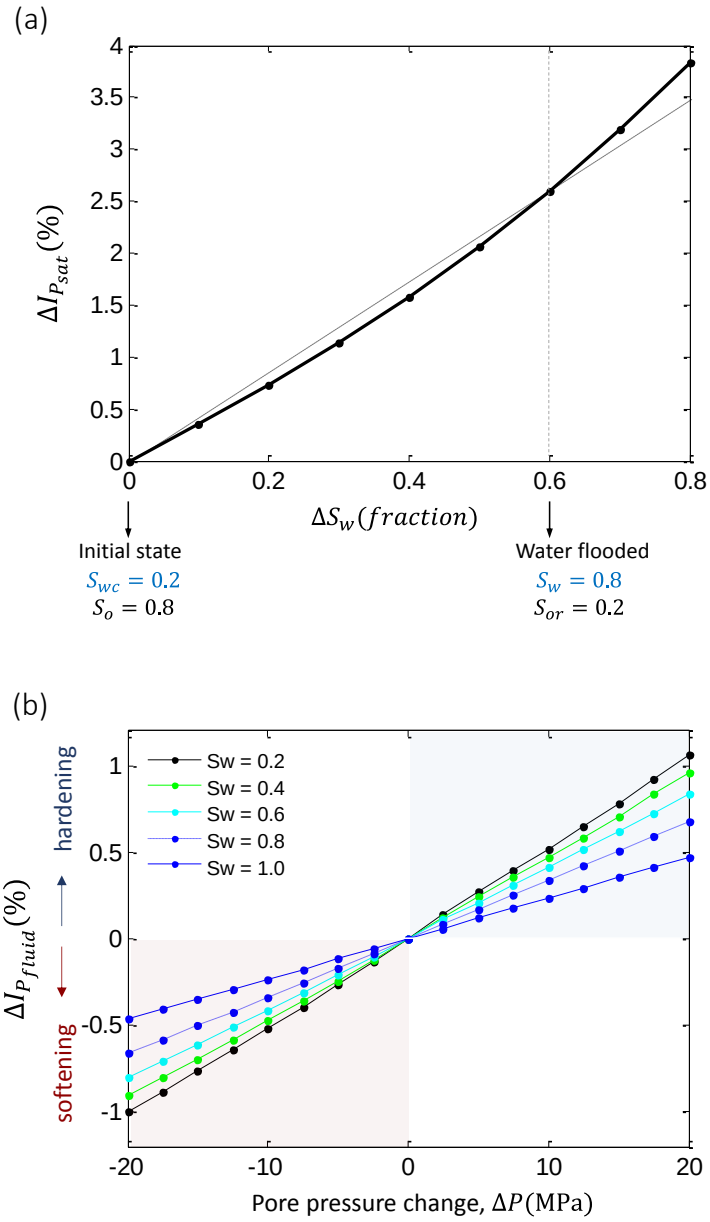

Figure 2-4 (a) Gassmann's fluid substitution prediction for a water flood scenario in a 27.1% porosity North Sea sandstone, showing an approximate linear dependence of the P-wave impedance change, $\Delta I_{P_{sat}}$, (an increase i.e. hardening response), as the rock becomes more water saturated. (b) Linear change of P-wave impedance of fluids, $\Delta I_{P_{fluid}}$, (at different water saturation levels) with pore pressure changes, calculated using Batzle and Wang (1992) equations for a North Sea oil above bubble point (properties in Table 2-1).

Figure 2-4 (a) is calculated for a water flood scenario (with no pressure change) for a 27.1% porosity North Sea sandstone containing only oil and water, and assumed to be above bubble point pressure (Table 2-1). Other properties in Equation 2-4 such as dry rock and mineral moduli remain unchanged and are given later in Table 2-2. An approximate linear response of the P-wave impedance to water replacing oil is predicted by Gassmann's Equations (Figure 2-4 (a)). In Figure 2-4 (b) Batzle and Wang calculations show the linear dependence of the P-wave impedance of the fluids to pore pressure changes at different water saturation levels. As oil is more compressible than water, it is also more sensitive to pore pressure changes than water. Fluids containing more water than hydrocarbons are less sensitive to pore pressure changes. An increase in pressure causes an increase in the impedance of the fluids (hardening), whilst a decrease in pressure yields a softening effect. The magnitude of change in impedance in Figure 2-4 (b) occupies only a small fraction (less than 25%) when compared to Figure 2-4 (a).

2.2.2 Mineral moduli and density model

As with fluids in the pore space, the reservoir rock can contain different minerals (quartz, feldspars, clays, calcite, etc.). An effective mineral bulk modulus which represents the mineral mixtures is found by computing the Voigt–Reuss–Hill average (Hill, 1952). This is simply the arithmetic average of the Voigt upper bound and the Reuss lower bound. This average is expressed as:

$$M_{VRH} = \frac{M_V + M_R}{2}, \tag{2-10}$$

where

$$M_V = \sum_{i=1}^{N} f_i M_i, \tag{2-11}$$

$$\frac{1}{M_R} = \sum_{i=1}^{N} \frac{1}{f_i M_i}, \tag{2-12}$$

The terms f_i and M_i are the volume fraction and the modulus of the ith mineral component, respectively. The modulus M represents the shear modulus, μ_m or the bulk modulus, κ_m, as seen in Equation 2-7.

Similarly, the mineral bulk density, ρ_m (as seen in Equation 2-4) is dependent on the volume fraction of each mineral constituent, and is calculated as:

$$\rho_m = \sum_{i=1}^{N} \rho_i V_i \,, \tag{2-13}$$

where ρ_i and V_i are the bulk density and volume fraction of the ith mineral component, respectively.

2.2.3 Pressure dependence semi-empirical model

As Gassmann's relations show (Equation 2-7), the effect of pore pressure changes on the dry rock frame need also be calculated. I use MacBeth's (2004) equations which describe the pressure dependence of the dry rock bulk modulus κ_{dry} and shear modulus, μ_{dry} in sandstones. The equations are written in the form:

$$k_{dry}(\sigma_{eff}) = \frac{k_\infty}{1 + E_k e^{\left(\frac{-\sigma_{eff}}{P_k}\right)}} \,, \tag{2-14}$$

$$\mu_{dry}(\sigma_{eff}) = \frac{\mu_\infty}{1 + E_\mu e^{\left(\frac{-\sigma_{eff}}{P_\mu}\right)}} \,, \tag{2-15}$$

In each equation, three parameters govern how responsive the rock is to applied pressure: k_∞ and μ_∞ are the maximum values to which the curves asymptote; P_k and P_μ are the characteristic pressure constants that determine the rollover point beyond which the rock frame attains its state of relative insensitivity; E_k and E_μ are constants calibrated from isotropic loading on dry cores and determine how sensitive the rock is to changes in the effective stress, σ_{eff}, and can be considered as summaries of the total rock weaknesses, independently of its origin (MacBeth, 2004). The constants E_k and E_μ are unit-less, P_k, P_μ and σ_{eff} have units of MPa. By testing these equations on 179 sets

of laboratory measurements on different dry core samples from reservoirs as well as outcrop sandstones, MacBeth (2004) justified the fits and also presented evidence of the strong dependence of the dry rock moduli on not only the effective stress, but also on porosity. Equations (2-14) and (2-15) can be adapted to include porosity dependence of k_∞ and μ_∞, based on the constant critical porosity model (Nur et al., 1995; Mavko and Mukerji, 1995):

$$k_\infty = k_m\left(1 - \frac{\phi}{\phi_c}\right), \tag{2-16}$$

$$\mu_\infty = \mu_m\left(1 - \frac{\phi}{\phi_c}\right), \tag{2-17}$$

Where κ_m and μ_m are the mineral bulk and shear modulus, ϕ is the porosity and ϕ_c is the critical porosity, which is the porosity that separates the mechanical and acoustic behaviour into two distinct states. For porosities lower than ϕ_c, the rock is load bearing, whereas for porosities greater than ϕ_c, the rock simply "falls apart" and becomes a suspension (Nur et al., 1998). Under load bearing state, critical porosity in sandstones is between 0.36 and 0.4, and must be greater than the porosity. Equations (2-14) to (2-17) imply that as σ_{eff} increases (i.e. $\sigma_{eff} \to \infty$), the pores and micro-cracks close and the rock becomes tighter ($\phi \to 0$), making both k_{dry} and μ_{dry} approach the values of the pure mineral moduli (k_m and μ_m). Whereas, as the rock approaches surface pressure conditions ($\sigma_{eff} \to 0$), porosity tends towards its critical value ϕ_c (since the rock becomes a suspension), thereby making both k_{dry} and μ_{dry} approach zero. Assuming isotropic loading, the effective stress is estimated using Terzaghi's principle:

$$\sigma_{eff} = \sigma_{ob} - nP, \tag{2-18}$$

$$\Delta\sigma_{eff} = -n\Delta P, \tag{2-19}$$

where σ_{eff} is the effective stress, $\sigma_{ob} = \alpha H$ is the overburden stress (where H is the depth and α is a constant overburden stress gradient), P is the pore pressure, Δ indicates change and n is the effective stress coefficient. Although this is a subject of many debates (Hoffmann, et al., 2005; Gurevich, 2004), a rule of thumb is that $\phi \leq n \leq 1$,

with $n \to 1$ for high porosity poorly consolidated rocks. The constant, α is usually within the range 0.8 – 1 psi/ft at depths of interest down to 4000 m (Fjaer et al., 1992). For the analysis, it is assumed that $\alpha = 1\,\text{psi/ft}$ (equivalent to $0.0226\,\text{MPa/m}$) and $n = 1$.The coefficient n can instead be estimated using the theoretical relation, $n = 1 - \frac{k_{dry}}{k_m}$ (for k_{dry} at an arbitrarily high effective pressure, i.e. $k_{dry} \to k_\infty$) which is equivalent to the empirical formula, $n = \frac{\phi}{\phi_c}$ (Simm, 2007). The negative sign in Equations (2-18) and (2-19) implies that pore pressure effects on fluids counteract the effects on the rock frame due to overburden stress (Figure 2-5).

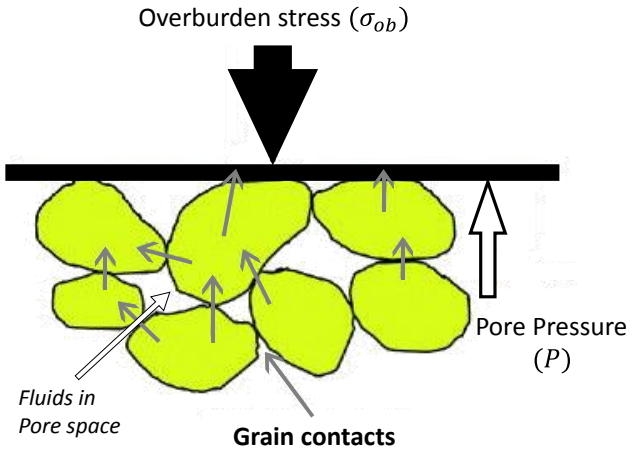

Figure 2-5 Schematic representation of different isotropic pressure acting on the reservoir rock. Pore pressure effects (affecting the fluids) counteract changes in the overburden stress (affecting the rock frame i.e. grain to grain contact).

For instance, an increase in pore pressure decreases the density of the fluids, and increases the fluid velocity, which leads to an impedance increase (hardening). Whereas, the same increase in pore pressure (equivalent to a decrease in effective pressure) leads to a decrease in grain to grain contact in the rock frame, hence, a decrease in impedance (softening). In general, the fluid response to pore pressure changes is small in comparison to the impact of the equivalent effective pressure on the dry rock frame. This may also depend on the value of n (Alvarez and MacBeth, 2014).

Figure 2-6 plots the change in the P-wave impedance of a dry rock in response to changes in the effective pressure calculated using MacBeth (2004) equations, for a

North sea unconsolidated sandstone (SST. A) with porosity of 27.1% and at an initial effective pressure of 31.5 MPa. Properties for the dry roc, are given in Table 2-2

(a)

SST.	Geology (field)	Porosity ϕ (%)	Dry rock seismic properties		
			$V_P(\mathrm{km/s})$	$V_S(\mathrm{km/s})$	$\rho_{dry}(\mathrm{kg/m^3})$
A	Unconsolidated Paleocene (WoS)	27.1	2.24	1.35	1910
B	Unconsolidated Cretaceous (Lochaline, outcrop)	18.0	3.67	2.22	2170
C	Cemented Cretaceous (Lochaline, outcrop)	5.0	4.88	2.77	2520

(b)

SST.	Geology (field)	Porosity ϕ (%)	Mineral rock properties		
			$k_m(\mathrm{GPa})$	$\mu_m(\mathrm{GPa})$	$\rho_m(\mathrm{kg/m^3})$
A	Unconsolidated Paleocene (WoS)	27.1	34.65	27.02	2620
B	Unconsolidated Cretaceous (Lochaline, outcrop)	18.0	26.39	32.02	2646
C	Cemented Cretaceous (Lochaline, outcrop)	5.0	42.36	36.48	2653

(c)

SST.	Dry rock Pressure-dependence parameters					
	$P_k(\mathrm{MPa})$	$E_k(\mathrm{unitless})$	$k_\infty(\mathrm{GPa})$	$P_\mu(\mathrm{MPa})$	$E_\mu(\mathrm{unitless})$	$\mu_\infty(\mathrm{GPa})$
A	6.32	1.00	9.94	7.23	1.222	7.75
B	6.14	1.3256	13.89	7.75	1.439	16.85
C	0.0753	4.49	36.79	6.94	0.6393	31.68

Table 2-2 Sandstone (SST.) dry rock properties (at zero-pressure) of a recovered reservoir rock from the West of Shetland (WoS) and a Lochaline outcrop of two samples (unconsolidated and well-cemented), taken from MacBeth (2004). (a) P-wave, S-wave velocity and density seismic properties (b) Bulk and shear moduli and density of the mineral forming the rock, estimated using Equations (2-4), (2-16) and (2-17), with critical porosity, $\phi_c = 0.38$, (c) Pressure-dependence parameters for the sandstones (MacBeth, 2004).

The typical non-linearity of the pressure dependence curve is observed, with a decrease in effective pressure yielding a bigger magnitude of change (softening) than the opposing increase in effective pressure response (hardening). Compared to fluid pressure response (in Figure 2-4 (b)), the dry rock pressure response is the over-riding effect, but a more balanced competition is expected as effective pressure reduces significantly. The composite effect of pore pressure changes on the saturated reservoir

rock (rock frame and fluids) is what is being considered for the analysis, as this is what is measured in 4D seismic data.

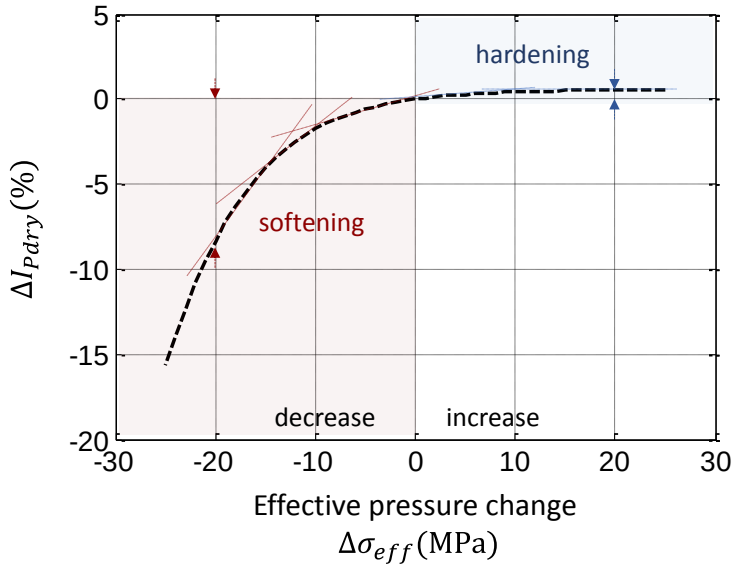

Figure 2-6 Dry rock P-wave impedance pressure dependence calculated using MacBeth's (2004) equations for a recovered reservoir sandstone in the North Sea, with a porosity of 27.1%. Decrease in effective pressure causes a decrease in velocity (impedance softening) which yields a stronger change than an opposing increase in effective pressure response (impedance hardening), revealing the asymmetry with pressure effects on the rock frame. Compare with fluid pressure sensitivity (Figure 2-4(b)).

2.3 Rock-physics modelling of zero-offset 4D amplitude and time-shift sensitivity in sandstones

In section 2.2 I reviewed the rock-physics models and equations for fluid saturation and pressure dependency in normally –pressured sandstone reservoirs. The aim now is to use the rock-physics models to quantify the reservoir sensitivity in relation to various production effects. To provide a generic understanding of the zero-offset 4D seismic responses, two standard attributes necessary for 4D seismic data interpretation, 4D time-shifts and amplitudes will be modelled and used to measure the sensitivity (Figure 2-7). The effect of AVO on the sensitivity is not considered, but it is considered in Chapter 7 (see Figure 7-7). Only zero-offset 4D amplitudes and time-shifts are modelled which limits the generalisation of the results to AVO effects. However, As post-stack (full offset) 4D seismic data is used for calibrating the field observations in Chapter 3, the

zero-offset sensitivity response is used as an approximation to aid the interpretation of the full-offset post-stack sensitivity responses in Chapter 3. Two scenarios are considered, the first relates to the lithology, and the second to various production effects. Using sandstones of different porosity, geological age and environment helps to provide some insights as to how the rock fabric affects the sensitivity. The different production scenarios (pressure changes, and water and gas saturation changes) gives insight as to which production effects the reservoir rock is most and least sensitive to. The range of pressure changes to be modelled (up to +/- 20 MPa) actually do not cover the wide range observed in the field responses in Chapter 3 (see Figure 3-1), particularly, for the high-pressure-high-temperature (HPHT) sandstone fields which experience pressure changes of up to -60 MPa. This is because the modelling here is done for normally-pressured sandstones only, and as such, there is a limit to the

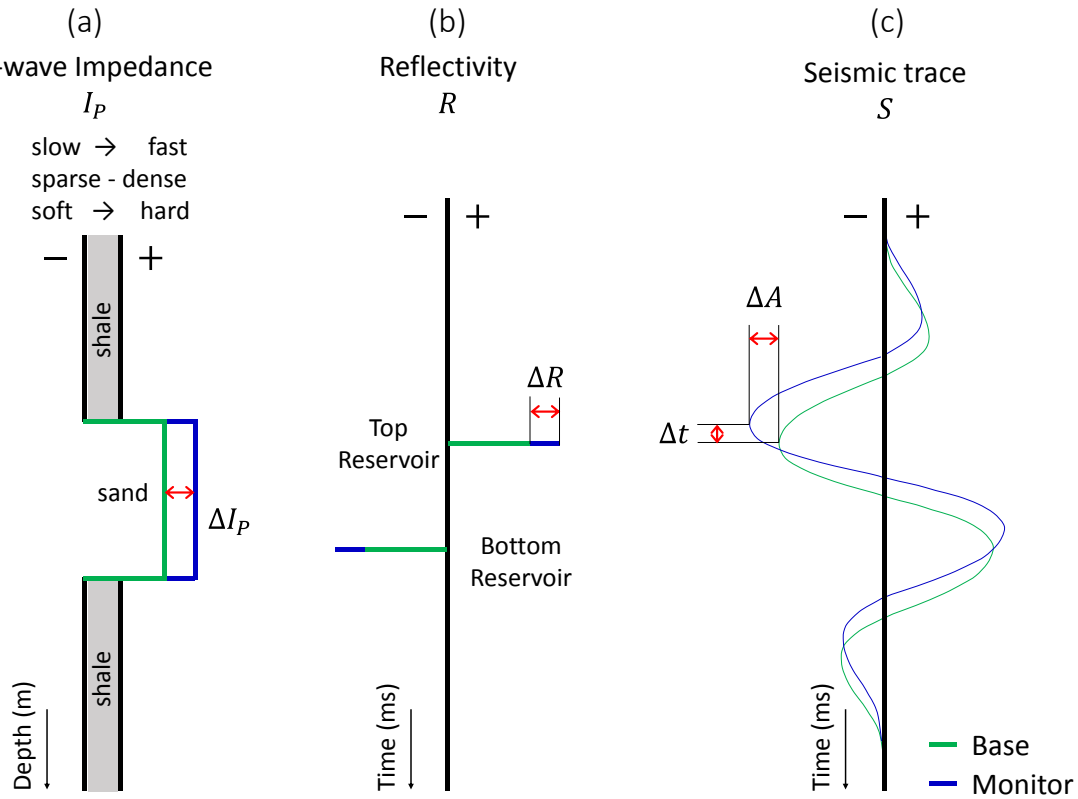

Figure 2-7 Schematic diagram linking (a) impedance changes, ΔI_P, and (b) reflectivity changes, ΔR, to (c) the seismic trace which is obtained by convolving (b) with a wavelet (not shown). In (c) changes in amplitude, ΔA and vertical time-shift, Δt, are annotated. Changes refer to a monitor minus baseline response (red arrows). Two attributes are used to quantify sensitivity, Δt (a function of velocity changes) and ΔA (a function of velocity and density changes). Note that ΔA has been represented as having the opposite polarity convention to ΔI_P.

magnitude of pressure changes that the rocks can experience under load bearing state (Avseth et al., 2010). This suitably describes the sandstones of the Heidrun, Norne and Schiehallion fields studied in Chapter 3. However, in the applicability to HPHT fields, the modelling results to follow (Section 2.3.4) show that the modelled time-shift sensitivity range (Figure 2-13 (b)) still covers the quantified sensitivity obtained in Chapter 3 for the HPHT Shearwater field, which experiences pressure changes of up to -59 MPa (see Figure 3-22(b), Section 3.4).

2.3.1 4D amplitude sensitivity equations

The pressure dependence model (section 2.2.3) together with Gassmann theory (section 2.21), can be applied to calculate the P-wave impedance changes for a reservoir rock as a function of pore pressure and fluid saturation changes. From this, amplitude changes (i.e. reflectivity changes) at top reservoir can be estimated, assuming a single sand-shale interface (Figure 2-7). Stammeijer and Hatchell (2014) detail the conversion between the change in impedance and the change in reflectivity; this is repeated here for clarity.

At zero-offset, the 3D reflectivity of a sand-shale interface at baseline time, R_{base}, can be approximated using the P-wave impedance, I_P, as:

$$R_{base} = \frac{{I_P}^{sand} - {I_P}^{shale}}{\overline{I_P}^{sand} + \overline{I_P}^{shale}} \cong \frac{1}{2}\frac{dI_P}{\overline{I_P}}, \tag{2-20}$$

where $\overline{I_P}$ represents the average P-wave impedance for sand and overlying shale. Since 4D impedance changes, ΔI_P, primarily affect the reservoir (sand), the contribution of ΔI_P to I_P, can be neglected. The change in reflectivity, ΔR, (at zero-offset) between the monitor and baseline values can be expressed as:

$$\Delta R = R_{monitor} - R_{base} = \frac{dI_P + \Delta I_P}{2\overline{I_P}} - \frac{dI_P}{2\overline{I_P}} = \frac{1}{2}\frac{\Delta I_P}{\overline{I_P}}, \tag{2-21}$$

Equation 2-21 implies that the 4D change in reflection coefficient equals half the 4D relative impedance change. The 4D seismic signals are independent of the 3D reflectivity. Stammeijer and Hatchell (2014) note that this approximation is practically

applicable to a wide range of realistic shale impedances, as the shales are unlikely to change.

How strong the relative change in reflectivity is, compared to the 4D relative impedance change depends on the strength of the sand/shale interface, R_{base}. This is typically a larger number than the impedance change, as follows:

$$\frac{\Delta R}{R_{base}} = \frac{\Delta I_P \Big/ 2\overline{I_P}}{dI_P \Big/ 2\overline{I_P}} = \frac{\Delta I_P \Big/ \overline{I_P}}{dI_P \Big/ \overline{I_P}}, \tag{2-22}$$

The relative change in the 4D reflection coefficient equals the 4D relative impedance change scaled by the inverse of the sand-shale impedance contrast (Equation 2-22). If the sand-shale impedance contrast is zero (as can happen, e.g., North Sea Forties sands and similar, Singer et al. (2017)), the $\frac{\Delta R}{R_{base}}$ measure becomes instable, while the 4D signal itself, ΔR, remains stable. The relative change in reflectivity, $\frac{\Delta R}{R_{base}}$, is equivalent to the relative change in amplitude, $\frac{\Delta A}{A_{base}}$. This measure can also be determined from 4D and 3D (baseline) seismic cubes using for example, root-mean-square (RMS) values extracted in gates inside the reservoir zone. Also note that Equation 2-22 has no offset dependency, thus, the amplitude changes computed are of zero-offset amplitudes.

In the schematic shown (Figure 2-7), an increase in impedance between baseline and monitor is a positive change, likewise for the reflectivity change at top reservoir, whereas, the amplitude change is negative. When using the rock-physics modelled $\frac{\Delta A}{A_{base}}$ (or in this case, $\frac{\Delta R}{R_{base}}$), I maintain this European reverse polarity as this is the convention in the North Sea 4D seismic datasets to be used in Chapter 3.

Following this, the 4D amplitude sensitivity, ${c_X}^{\Delta A}$, of the reservoir rock to various production effects can be quantified as the percentage change in amplitude per unit change of the specific dynamic property, X, causing the response:

$$C_X{}^{\Delta A} = \frac{100\left(\Delta A/A_{base}\right)}{\Delta X}, \tag{2-23}$$

where X indicates pore pressure, P (in MPa) or fluid saturation S_w , S_o or S_g measured as a percentage (%) and Δ denotes change (i.e. monitor-baseline). Equation 2-23 applies if using zero-offset, partial-offset (near, mid, far) or full-offset 4D seismic amplitudes. $C_X{}^{\Delta A}$ varies with offset, since ΔA (and A_{base}) is offset-dependent.

2.3.2 4D Time-shift sensitivity equations

4D time-shifts are the difference in two-way travel time between a monitor and baseline data (Figure 2-7). Though physical thickness changes can contribute to this, it is predominantly caused by velocity changes; a practically applicable assumption for non-compacting reservoirs i.e. sandstones. The time-shifts can be estimated from velocity changes as a function of pore pressure and fluid saturation changes. Considering a pre-production (base) and post-production (monitor) state, the 4D time-shift is given by (Asveth, 2013):

$$\Delta t = t_{monitor} - t_{base} = 2\,Z\left[\frac{1}{V_{P,\,monitor}} - \frac{1}{V_{P,\,base}}\right] \tag{2-24}$$

where Δ indicates change, t is the two-way travel time (in seconds), Z is the reservoir depth (in metres) and V_P is the P-wave velocity (in m/s) of the saturated rock at a given pore pressure and fluid saturation.

To honour depth trends and geological variability within a reservoir zone, Equation 2-24 can be modified as:

$$\Delta t(z) = 2\int_{z,\,top}^{z,\,bottom}\left[\frac{1}{V_{P,\,monitor\,(z)}} - \frac{1}{V_{P,\,base\,(z)}}\right]dz, \tag{2-25}$$

where the terms have been earlier defined as in Equation 2-24. This is particularly useful when estimating Δt from the top to bottom of the reservoir or sample-by-sample for a well.

Equations (2-24) and (2-25) imply that 4D time-shifts are a cumulative change with depth (Figure 2-8). Time-shifts taken at a particular depth, say at point A or B, is the sum of all travel-time differences above that point (Rickett et al., 2007). Thus, direct interpretation of time- shifts as shown, is problematic as it cannot be related to a specific interval. To obtain time-shifts within a particular interval of interest (e.g. inside the reservoir), the time-shift at the bottom of the interval, Δt^{B} is subtracted from the time-shift at the top of the interval, Δt^{A}. The subtraction makes 4D time-shifts an interval property which can be directly related to the reservoir rock. This is so called "intra-reservoir" time-shift, Δt^{res}, which is particularly useful when interpreting the reservoir's response in the observed 4D time-shift volumes.

In the schematic (Figure 2-8), the intra-reservoir time-shift, Δt^{res} is a positive response which implies a velocity increase at monitor time (also known as a speed-up), meaning a shorter travel time. This corresponds to an increase in impedance of the rock

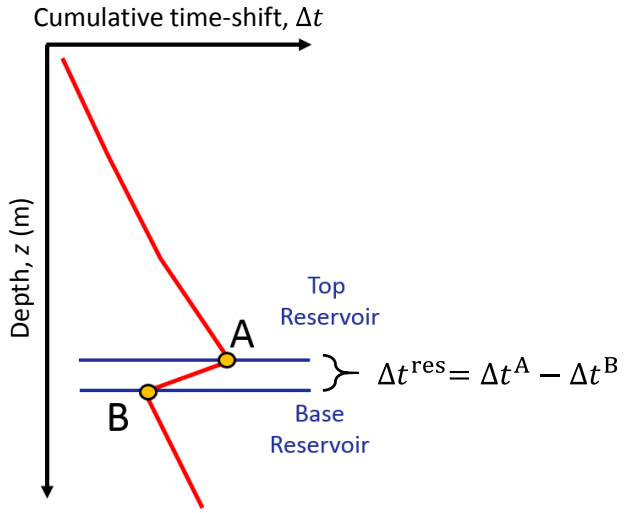

Figure 2-8 A schematic diagram of the cumulative 4D time-shifts change with depth. The 4D time-shift, Δt, is the difference in two-way travel time between monitor and baseline seismic data. The intra-reservoir time-shift, Δt^{res}, is extracted as the difference in Δt between point A and B.

(hardening). A negative Δt^{res}, implies a velocity decrease at monitor time (i.e. slow-down) which can be interpreted as a decrease in impedance (softening). In the overburden i.e. above point A, the time-shift is very small in non-compacting normally-pressured sandstones (e.g. Snorre field and the Visund Field (Røste et al., 2015; Avseth et al., 2016)) and it is considered zero in the modelling, as only the reservoir interval is calculated. This, however, is significant in highly geomechanically active compacting

fields where both changes in velocity and physical thicknesses occur (e.g. chalk fields of Valhall and Ekofisk (Guilbot and Smith, 2002; Hatchell and Bourne, 2005) and for high-pressure, high-temperature (HTHP) fields, e.g., Elgin and Kristin (Dybvik et al., 2009; Grandi et al., 2010)). Also note that this time-shift attribute, Δt^{res}, has the same polarity convention as impedance changes (Figure 2-7).

Once the intra-reservoir time-shift is computed, the reservoir 4D time-shift sensitivity, ${C_X}^{\Delta t}$, to different production effects can be quantified as the time-shift, Δt^{res}, (in microseconds) per unit thickness (in metres), $\frac{\mathrm{us}}{\mathrm{m}}$ (or $\frac{\mathrm{ms}}{\mathrm{km}}$) per unit change of the dynamic property, X:

$$ {C_X}^{\Delta t} = \frac{\Delta t^{\mathrm{res}}(\mu\mathrm{s}) \Big/ d(\mathrm{m})}{\Delta X} , \tag{2-26} $$

where, Δt^{res} is the intra-reservoir time-shift, d (in metres) is the reservoir thickness. This implies that the time-shift is first normalised by the thickness of the reservoir, d, before computing the sensitivity, ${C_X}^{\Delta t}$. The denominator X indicates pore pressure, P (in MPa) or fluid saturation S_w , S_o or S_g measured as a percentage (%) and Δ denotes change (i.e. monitor-baseline). The numerator can also be expressed as milliseconds per kilometre, (ms)/(km). Equation 2-26 applies if 4D seismic time-shifts are computed from zero-offset, partial-offset (near, mid, far) or full-offset 4D seismic data. ${C_X}^{\Delta t}$ will also vary with offset, if Δt^{res} is offset-dependent.

2.3.3 Rock-physics modelling for reservoir 4D sensitivity quantification

Here, I perform the 4D rock-physics analysis to quantify the sensitivity of the reservoir rock to pore pressure, water and gas saturation changes, using 4D time-shifts (Equation 2-26) and relative amplitude changes (Equation 2-23). Two categories are considered; the first relating to the lithology and the second, to the various production effects. For the lithology category, one recovered reservoir sandstone and two samples from a Lochaline outcrop taken from MacBeth (2004) are considered. Table 2-2 (Section 2.2.3) gives the initial elastic properties and pressure dependence relationships of the dry

sandstones as published in MacBeth (2004). The reservoir and outcrop sandstones were carefully selected to represent end members, as their pressure dependence curves suggest (Figure 2-9). The reservoir rock (A) is a Palaeocene-age deep water unconsolidated sandstone with a high porosity of 27.1% taken from the West of Shetland (WoS) area in the North Sea. The outcrop Lochaline sandstone is a Cretaceous-age shallow-marine sandstone with two samples, (B) clean unconsolidated with 18% porosity and (C) well-cemented, extracted from hard lenses of rock containing postdepositional silica cement, with 5% porosity. For the calculations, the overburden rock is a water saturated shale with initial elastic properties: $V_P = 2602\ \mathrm{m/s}, V_S = 1113\ \mathrm{m/s}$ and $\rho = 2291\ \mathrm{kg/m^3}$ based on a North Sea field. It is assumed that the overlying shale does not change during production, so, there are no 4D changes in the overburden. The reservoir is 30 m thick, and at a depth of 2400 m.

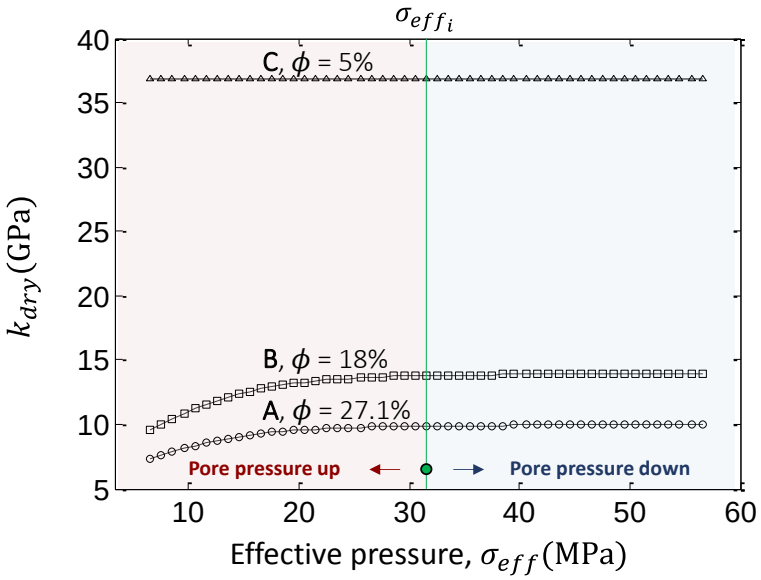

Figure 2-9 Dry-rock bulk moduli pressure dependence curves for the recovered WoS reservoir sample (sandstone A, with 27.1% porosity) and the Lochaline outcrop samples (sandstone B and C) at two different physical states (18% and 5% porosity, respectively). Predictable trends can be observed as the unconsolidated sandstones (A and B) are more pressure sensitive than the cemented sandstone C. The green line represents the starting point (i.e. initial effective pressure, $\sigma_{eff_i} = 31.5\ MPa$) for the 4D calculations.

The three different sandstones could be taken to represent lateral heterogeneity across a reservoir or the hypothetical case of three separate sandstone reservoirs that are homogenous with the same overlying shale properties and depth. Whilst three sandstone samples is insufficient to make a general conclusion about all sandstone

reservoirs, the sandstones A, B and C have been carefully chosen such that an end-member range of sensitivity responses is satisfied. The quantified sensitivity for these sandstones can help give a general understanding of the typical sensitivity levels one could expect for high porosity unconsolidated sandstones versus low porosity cemented sandstones.

The computations begin by populating the dry rock at zero-pressure (Table 2-2) with initial fluid saturations, assumed to be 80% oil saturated, and 20% water saturated (S_{wc}, or otherwise denoted, S_{wi}). The seismic properties of the initial fluid-saturated rock are then calculated for an initial pore pressure of 25 MPa. Following this, several production scenarios are calculated, these include (1) pressure decrease, (2) gas replacing oil, (3) pressure increase and (4) water replacing oil, which are modelled independently. For the fluid substitution scenarios, the rock is kept at the initial pressure, and for the pressure scenarios, the rock is kept at the maximum water saturation ($1 - S_{wc} - S_{or}$), and $S_{or} = 20\%$. Pressure changes are modelled in the range 5 to 20 MPa, at coarse increments of 5 MPa, to mimic the temporal coarseness with which pressure might be observed in multiple monitor 4D seismic data, which are typically acquired at 3 months to 3 years interval. Similarly, water saturation changes are modelled at 10%, 40% and 60% ($1 - S_{wc} - S_{or}$), and gas saturation changes at 5%, 10%, 20%, 50% and 80% (maximum, assuming all oil is replaced by gas and only water at $S_{wc} = 20\%$ remains). The 4D relative change in amplitude (Equation 2-22) and intra-reservoir time-shifts (Equation 2-25 and Figure 2-8) are then calculated for each modelled scenario and for the three sandstone samples, A, B and C (detailed in Table 2-2).

Figure 2-10 shows the modelled 4D changes in amplitude and intra-reservoir time-shifts to the different magnitudes of pore pressure increase and decrease, and water and gas saturation changes. Each scenario falls on a different quadrant, labelled 1 to 3, depending also on whether the effect is hardening (blue) or softening (red). The three different sandstones provide upper and lower range of expectations as indicated. In general, the unconsolidated reservoir sandstone, A, which has the highest porosity, responds with the biggest changes. The response of the outcrop unconsolidated sandstone B is also close to and sometimes bigger than that of sandstone A, due to the nature of their pressure-dependence curves (Figure 2-9). Effects due to gas saturation

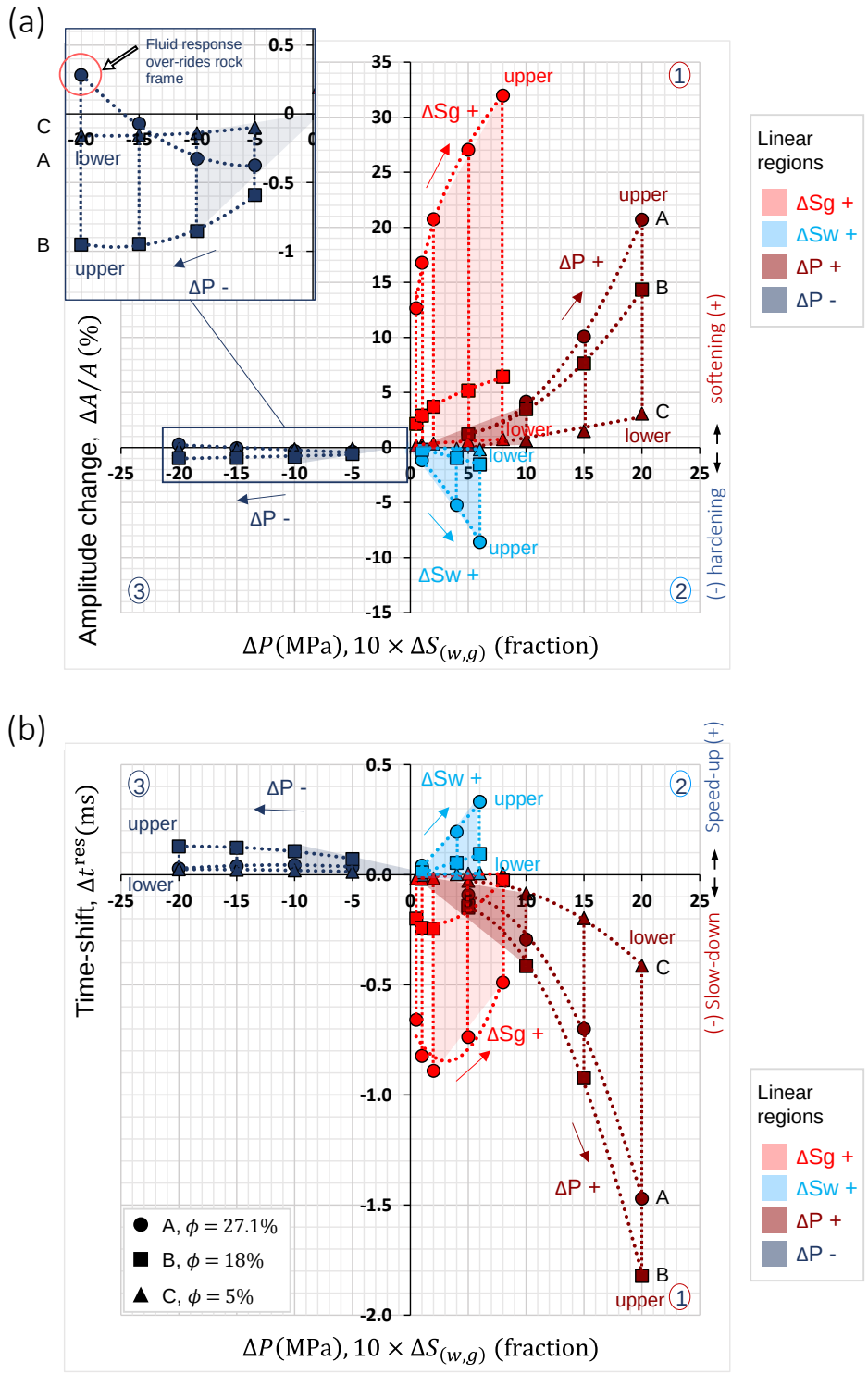

Figure 2-10 Rock-physics 4D response for a typical range of production scenarios using the three sandstone samples, A,B and C (see Table 2-2) (a) 4D relative amplitude changes (in percentage) (b) Intra-reservoir 4D time-shifts . The horizontal axis shows pore pressure changes (in MPa), water saturation, ΔSw, and gas saturation changes, ΔSg (in fraction, multiplied by 10). Each scenario has been modelled separately of others and falls on a different quadrant, labelled, 1, 2 and 3, predetermined by the production-induced change and the 4D polarity for a hardening (or speed-up) and a softening (or slow-down) response. Each magnitude of change on the horizontal axis could represent changes observed at different monitor times. Filled regions identify an approximately linear response if the production changes relative to baseline across monitor time are within the range highlighted.

and pressure increase are highly non-linear and for water saturation changes, approximately linear. Regions where both amplitude and time-shift responses are approximately linear have been highlighted on the plots. This is only satisfied when the magnitudes of pressure and fluid saturation changes relative to baseline (i.e. the zero axes) are within a limited range as shown. Pressure decrease induces very small changes compared to pressure increase. Such a small response could also be viewed as a linear effect even for a pressure decrease of -10 MPa or more.

In Figure 2-10 (a) fluid saturation changes impact bigger amplitude changes than pore pressure changes that occur in the 0 to 10 MPa range, with gas saturation changes inducing the biggest response. For the given range of changes modelled, the magnitude of amplitude response to pressure increase and gas saturation is comparative across the sandstones. As to be expected, pore pressure increase yields a stronger response (softening) than pore pressure decrease (hardening) due to the asymmetry of the pressure dependence relationship (Figure 2-9). Whilst a 10% water saturation change and a 5 MPa pressure increase may produce the same magnitude of amplitude change which counteract each other, a 15 MPa pressure increase will easily dominate over a 60% water saturation change, in sandstone A. Higher competitive advantage to pressure effects in sandstones B and C, also suggests that the response to pressure changes becomes more dominant than saturations in lower porosity sandstones. Notice for the high porosity sandstone A, fluid response to pore pressure decrease (at $\Delta P \leq$ -20 MPa) over-rides the hardening response expected. This is because at such pore pressures, the dry rock is relatively insensitive (Figure 2-9) and the competing fluids in the pore space (Figure 2-4 (b)) dominate the pressure response.

For 4D time-shifts, (Figure 2-10 (b)), however, the dry rock prevails and the expected hardening response at $\Delta P =$ -20 MPa occurs, though the time-shift is almost zero. In addition, the impact of pressure increase on time-shifts are unrivalled by the next strongest effect, gas saturation changes. This suggests that time-shifts are a more sensitive metric for pressure changes than for saturation changes, contrary to amplitudes. The non-linearity with gas is however more complex for time-shifts than for amplitudes. Taking data points for sandstone A, a 10% increase in gas (which is a 16.8% relative change in amplitude) yields a time-shift of -0.82 ms, whereas, an 80%

increase in gas (which is a 32% change in amplitude) yields a mere -0.49 ms in time-shifts. Pressure increases are also non-linear but in the forward direction. As with amplitudes, an approximate linear time-shift response occurs for water saturation changes, and pressure decrease could also be assumed as having a linear effect.

2.3.4 Quantification of modelled 4D amplitude and time-shift sensitivity in sandstones

The modelled 4D responses agree with expectations of variation of changes in amplitude and time-shifts with lithology as evident across the three different sandstones (properties detailed in Table 2-2). In addition, the amplitude or time-shift sensitivity could also depend on the magnitude of the pressure or saturation change currently being observed. Transforming Figure 2-10 (a) into amplitude sensitivity using Equation 2-23, and also Figure 2-10(b) into time-shift sensitivity using Equation 2-26, gives, Figure 2-11 and Figure 2-12, respectively. The vertical axis is sensitivity, which measures how much amplitudes (in %) or time-shift (in ms/km) will change for the smallest unit of change in pressure (i.e. for every 1 MPa) and fluid saturation (i.e. for every 1%). The horizontal axis clarifies that the sensitivity has been calculated for a specific magnitude of change in pressure or saturation that was observed in Figure 2-10.

In Figure 2-11 gas saturation changes impact the highest amplitude sensitivity compared to water saturation changes, pressure decrease or increase. This is true for the higher porosity sandstones, A and B, but not for sandstone C which is more sensitive to pressure changes. Sensitivity varies with the magnitude of gas saturation increase, for example, for sandstone A, in the range $0 < \Delta S_g \leq 5\%$, the amplitude sensitivity is 2.53%, which implies that for every 1% increase in gas saturation, a 2.53% or more increase in relative amplitude change will occur (softening effect), whereas, in the range $\Delta S_g \geq 80\%$, the amplitude sensitivity is 0.40% or lower. So, when calibrating the 4D seismic response to gas saturation changes using several monitor data, the sensitivity could vary from one monitor time to the next depending on how far apart the magnitude of gas saturation changes are that have occurred at the monitor times. The magnitude of water saturation changes across monitor times could also impact the magnitude of amplitude sensitivity. This variation may be negligible and thus assumed constant for lower porosity sandstones, as observed in C and B, but for sandstone A, the sensitivity

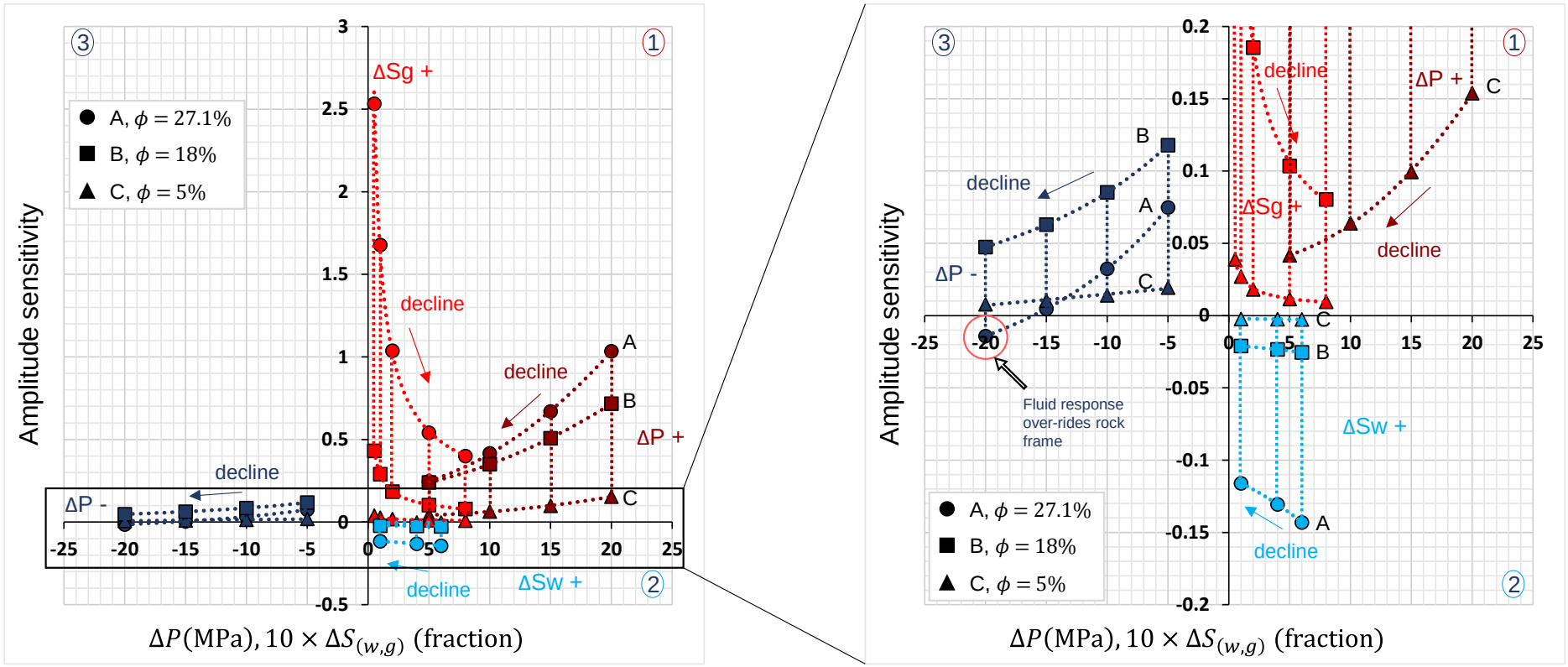

Figure 2-11 Rock-physics quantified amplitude sensitivity (Equation 2-23) to a specific magnitude and polarity of change in pressure, water and gas saturation observed in Figure 2-10(a). The amplitude sensitivity (vertical sensitivity) is the relative change in amplitude (monitor- baseline, in %) per unit change of pressure (in MPa) or fluid saturation (in %). Sensitivity is significantly controlled by the lithology of the three sandstones A, B, C (see Table 2-2). The arrows indicate the direction of decline in sensitivity, which suggests that sensitivity is specific to the magnitude of the production induced change relative to pre-production state (horizontal axis), especially for non-linear effects of pressure changes, and gas saturation increase.

decreases (from -0.14% to -0.12%) with decreasing magnitude of water saturation changes (from 60% to 10%), which is the reverse direction to gas.

For pressure up, the same is observed, the amplitude sensitivity decreases with decreasing pressure change. Sandstone B for example, has an amplitude sensitivity of 1.04% or greater for $\Delta P \geq +20$ MPa, whereas in the range $0 < \Delta P \leq +5$ MPa, the amplitude sensitivity is 0.24% or lower. Pressure down shows the reverse to pressure up, with smaller magnitudes of pressure decrease having higher amplitude sensitivity than bigger magnitudes. Taking sandstone B, the amplitude sensitivity is 0.12% or higher when pressure decrease is in the range -5 MPa $\leq \Delta P < 0$, but for $\Delta P \leq -20$ MPa the amplitude sensitivity is less than half at 0.05%; this disparity is wider for the higher porosity sandstone, A. This is because the pressure dependence curves (Figure 2-9) reach an asymptote as effective pressure increases (i.e. when pore pressure decreases). How big the pore pressure decrease must be before an asymptote is reached depends on the starting point along the curve, i.e. the initial effective pressure ($\sigma_{eff_i} = 31.5$ MPa), which has been modelled for a normally pressured reservoir at initial pore pressure of 25 MPa and at a depth of 2400 m. The curves also indicate that under load-bearing state, rocks can only experience a limited range of pressure changes (Avseth et al., 2010). At -20 MPa pressure decrease, the amplitude sensitivity for sandstone A is of opposite polarity (-0.014%), driven by the fluid pore pressure response and not the rock frame. At lower magnitudes of pore pressure decrease, however, the rock frame pressure response dominates.

In Figure 2-12 the resulting 4D time-shift sensitivity is shown (see also Equation 2-26). The horizontal axis relays that the sensitivity has been calculated for a specific magnitude and polarity of change in pressure or saturation currently being observed. Time-shift sensitivity echo the general trend observed for amplitude sensitivity (Figure 2-11). The main difference between the two attributes is that the time-shift sensitivity to pressure changes can be much higher than that to fluid saturation changes. For pressure decrease and gas saturation changes, the sensitivity decreases with increasing magnitude of change, whereas, for changes due to pressure increase and water saturation increase, the sensitivity decreases with decreasing magnitude of change. For example, sandstone A, has a sensitivity of -4.4 ms/km or greater when the gas saturation is in the range

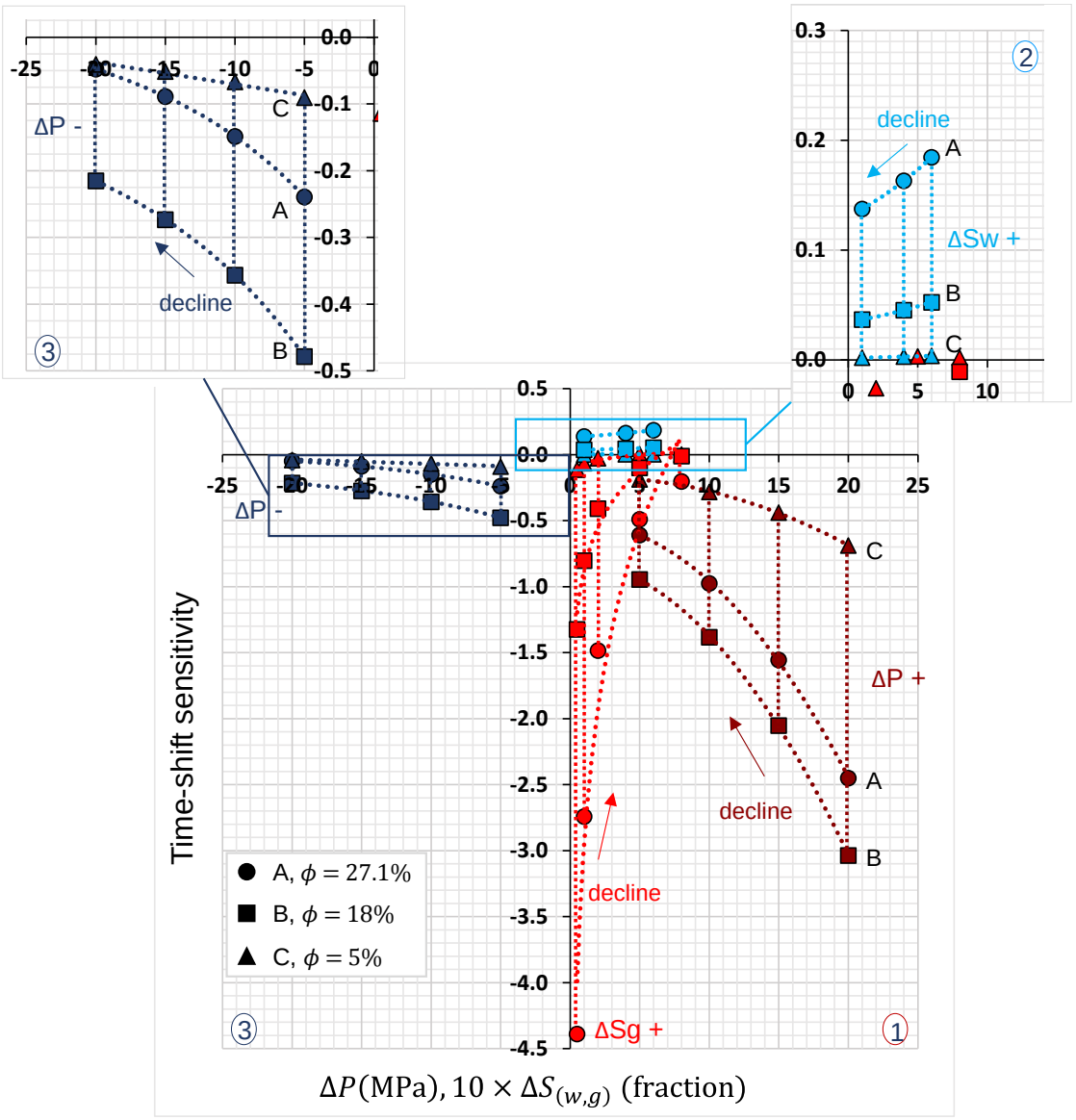

Figure 2-12 Rock-physics quantified time-shift sensitivity (Equation 2-26) to a specific magnitude and polarity of change in pressure, water and gas saturation observed in Figure 2-10(b). The time-shift sensitivity (vertical axis) is the 4D time-shift (monitor-baseline) per kilometre (in ms/km) per unit change of pressure or fluid saturation. Sensitivity is significantly controlled by the lithology of the three sandstones A, B, C (see Table 2-2). The arrows indicate the direction of decline in sensitivity, which suggests that sensitivity is specific to the magnitude of the production induced change relative to pre-production (horizontal axis), especially for non-linear effects of pressure changes, and gas saturation increase.

$0 < \Delta S_g \leq$ 5%, but only -0.20 ms/km or lower for $\Delta S_g \geq$ 80%. For pressure up, the sensitivity is -0.61 ms/km when in the range $0 < \Delta P \leq +5$ MPa, and is more than four times higher with a value of -2.5 ms/km when the pressure increase is equal to or greater than 20 MPa. A similar but subtle opposing trend can also be concluded when comparing the sensitivity due to changes in water saturation and pressure decrease. The overall minimum and maximum observations from the rock-physics modelling of time-

shift and amplitude sensitivity are summarised in Figure 2-13 , and given in Table 2-3. In Figure 2-13, the vertical axis shows the absolute magnitude of sensitivity contributed by the three sandstones, which represent the upper and lower range of expectations. The sensitivity range has been determined using pore pressure changes of 0 to 20 MPa, water saturation changes of 0 to 60% and gas saturation changes of 0 to 80%.

For sensitivity to fluid saturation changes, the unconsolidated reservoir sandstone, A, with 27.1% porosity contributes to the upper limit. For sensitivity to pressure changes, the upper limit is contributed by both the reservoir sandstone and the unconsolidated sandstone, B, of 18% porosity from the Lochaline outcrop. The lower range for pressure and saturation sensitivity is occupied by the well-cemented sandstone of the Lochaline outcrop, which has a porosity of 5%. It is expected that most reservoir sandstones can be adequately explained within this end-member range. Relative amplitude changes, however, will rely on the reflection strength of the reservoir interface (Equation 2-20) which vary from field to field. In addition, initial PVT properties of the fluids also vary across fields and within reservoirs themselves, as well as reservoir thicknesses, all could result in sensitivity numbers far outside the end-member range modelled.

Sensitivity is therefore expected to vary across different reservoir sandstones, and also laterally within a reservoir due to inhomogeneities. MacBeth's (2004) empirical study on the pressure sensitivity of dry cores of sandstones recovered from 12 reservoirs reported that sensitivity varied from 1% (the lower-porosity cemented sandstones) to 10% (the higher porosity unconsolidated sandstones). MacBeth (2004) also suggests that at realistic initial effective pressure, reservoir depth and for a fluid saturated rock (as is the case modelled), the sensitivity range disclosed will be much lower. "*The laboratory-measured stress sensitivities rapidly diminish with increasing effective pressure, so that at 24 MPa (corresponding to a normally pressured reservoir at 2000-m depth), most of the rocks in the current database are predicted to have a sensitivity of less than 1% per MPa*" (MacBeth, 2004).This agrees with observations in the current work. For example, for the 27.1% porosity West of Shetland sandstone, MacBeth (2004) reports a dry-rock bulk moduli sensitivity of 7.9% at zero- effective pressure, whereas, when subjected to in-situ pressure conditions as modelled in this rock-physics study, a maximum amplitude sensitivity of 1.04% per MPa change was calculated.

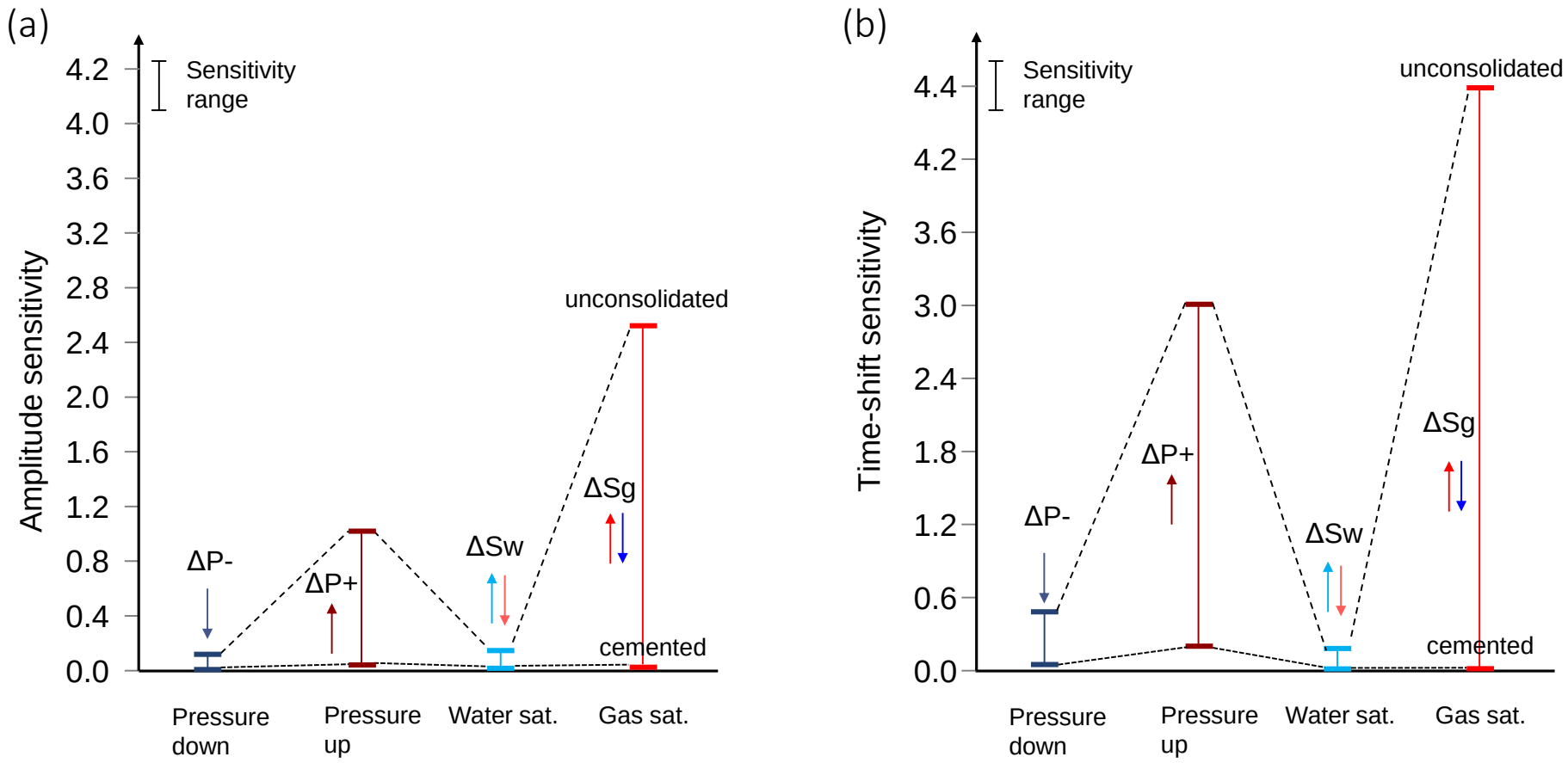

Figure 2-13 Summary of absolute values for (a) Amplitude sensitivity (Equation 2-23) and (b) time-shift sensitivity (Equation 2-26) based on rock-physics modelling of pressure and fluid saturation changes, separately. The lower and upper ranges are contributed by the low porosity (5%) cemented sandstone C, and the unconsolidated sandstones A (of 27% porosity) and B (of 18% porosity), respectively (see Table 2-2). Note that sensitivity to pressure has been calculated for a unit change in MPa, and sensitivity to fluid saturation for a unit change in saturation in percentage (%). Downward arrows indicate a decrease, and upward arrows, an increase in pressure or saturation.

Reservoirs under induced production can experience significant pressure or saturation changes that are far apart between monitor times. Relative to the pre-production state, the estimated sensitivity at each of these monitor times will differ, alluding to a non-time-constant sensitivity in sandstones. This does not mean that the fabric of the rock changes, since porosity and net-to-gross are unlikely to change in sandstones, but instead that the reservoir's elastic properties are changed due to different magnitudes of production changes (see Figure 2-11 and Figure 2-12). For approximate linear effects due to water saturation changes, the sensitivity calculated at different monitor times should be very similar, but, for more non-linear effects associated with gas or pressure increase, it may be considerably different, particularly for higher porosity sandstones which are more sensitive. A change in sensitivity between monitor times indicates a non-linear response to that particular reservoir dynamic property. The reservoir could undergo different pressure and fluid saturation changes, causing it's response across monitor times to lie outside the linear regions as indicated in Figure 2-10. However, the sensitivity can change as a result of a change in the rock fabric. During production, for example, mechanical weakening of cemented sandstones due to high pressure injection could induce fractures around the well bore, thus, altering the rock properties in a non-elastic manner (Saul and Lumley, 2015). Thus, if the sensitivity is quantified over the magnitudes of pressure and fluid saturation changes at different monitor times, this allows one to assess whether a data-driven linear or non-linear equation earlier discussed in Chapter 1 should be used to separate pressure and saturation changes for the specific reservoir.

Figure 2-13 and Table 2-3 suggest that 4D amplitudes and time-shifts are complementary attributes, although the former offers a more balanced sensitivity to fluid saturation changes, and the latter offers pressure changes some advantage over saturation changes. The results also indicates that at typical magnitudes of pressure and saturation changes, the 4D amplitude and time-shift response in well-cemented sandstones of low porosity will be very small (lying below the 2% amplitude detectability limit for the 4D seismic method, MacBeth (2004) compared to those of the unconsolidated sandstones. This offers a useful understanding for 4D feasibility predictions to address detectability of production-induced changes in sandstones considering non-repeatable 4D noise. Also note that in Figure 2-13 the relative scale

between pressure and fluid saturation sensitivity is not one-to-one. The sensitivity has been calculated with pressure change in MPa and saturation change in percentage (%). A fairer comparison can be achieved by expressing the denominator in Equation 2-23 and Equation 2-26 as a relative percentage change, $\left(\frac{\Delta S}{S_i}\right)$ or $\left(\frac{\Delta P}{P_i}\right)$, where P_i and S_i are the initial pressure and saturation, respectively. Whilst this is stable for pressure and water saturation (since for any reservoir $S_{wi} \neq 0$), the suggested calculation will become instable if S_{gi} is equal to or near zero; the same condition applies to S_{wi}. For better insights of the balance between pressure and saturation effects on 4D amplitudes and time-shifts, Figure 2-10 has been earlier discussed.

Production Scenarios		Sandstones (ϕ)	Rock-physics limits	Amplitude sensitivity (Equation (2-23))	Time-shift sensitivity (Equation (2-26))
Pressure up +ΔP (MPa)		Unconsolidated (18-27%)	Max.	1.04	-3.04
			Min.	0.24	-0.61
		Cemented (5%)	Max.	0.154	-0.69
			Min.	0.042	-0.19
Pressure down -ΔP (MPa)		Unconsolidated	Max.	-0.12	0.48
			Min.	0.014	0.05
		Cemented	Max.	-0.02	0.09
			Min.	-0.0079	0.04
Water sat. ΔSw (%)		Unconsolidated	Max.	-0.143	0.18
			Min.	-0.028	0.04
		Cemented	Max.	-0.0026	0.0037
			Min.	-0.0022	0.0020
Gas sat. ΔSg (%)		Unconsolidated	Max.	2.53	-4.39
			Min.	0.08	-0.011
		Cemented	Max.	0.039	-0.114
			Min.	0.0096	-0.0020

Table 2-3 Summary of amplitude and time-shift sensitivity based on rock-physics calculations for pressure and fluid saturation scenarios modelled independently. Minimum and maximum values are provided based on the three sandstone samples of 27.1%, 18% (unconsolidated) and 5% porosity (cemented) (see also Table 2-2).The sensitivity values have been signed based on the modelled 4D polarity of the amplitude and time-shift response to an increase in impedance (hardening) or a decrease in impedance (softening). The table is obtained for pressure changes in the range 0 to 20 MPa, water saturation increases of 0 to 60% and gas saturation increases of 0 to 80%. Notice for pressure down, the row entry for minimum amplitude sensitivity provided by the unconsolidated sandstone (27.1% porosity) is of opposite polarity to the rest of the entries for pressure down. This is due to fluid pressure effect (softening) over-riding the rock frame effect (hardening) at a pore pressure decrease of -20 MPa or lower.

2.4 Summary

In this chapter, rock-physics modelling provided insights to the sensitivity of saturated sandstones to induced production effects such as changes due to pore pressure increase, and decrease, and water and gas saturation. An understanding of the dependence of the sensitivity to lithology variations was also achieved by analysing three sandstone samples which ranged from high porosity (18-27.1%) unconsolidated sandstones to a low porosity (5%) cemented sandstone. Properties for these sandstones were obtained from MacBeth (2004). The reservoir's sensitivity was quantified using two standard attributes for 4D seismic data interpretation, amplitudes and time-shifts. The amplitude sensitivity measures the relative change in amplitude in percentage (i.e. relative to baseline) to a unit change of dynamic property. The time-shift sensitivity measures the intra-reservoir 4D time-shift (in microseconds normalised by the reservoir's thickness, in metres) to a unit change of dynamic property, expressed as (ms/km) per dynamic change. The dynamic property is either pressure change (in MPa) or saturation change (in percentage), where change is simply monitor-baseline (i.e. pre-production state).

Both amplitude and time-shift sensitivities were of complementary trends. Amplitudes offer a more balanced sensitivity to pressure and fluid saturation changes, whereas, time-shifts show more dispersion between pressure changes and water saturation changes. This suggests the usefulness of combining both attributes for discriminating pressure from saturation effects in 4D seismic data. Sensitivity decreases significantly from the unconsolidated sandstones (highest) to the cemented sandstone (lowest). The cemented sandstones are more sensitive to pressure changes than to saturation changes, whilst the unconsolidated sandstones provide a balance. For the higher porosity sandstones, sensitivity to gas saturation changes can be up to 20 times greater than that for water saturation changes, but typically are around 2.5 to 3.5 times greater. An asymmetry in pressure sensitivity was also observed, where the sensitivity to pressure increase can be up to 14 times greater than the sensitivity to pressure decrease (in unconsolidated sandstones), but this disparity has a lower margin in cemented sandstones - only 2 times greater.

These findings offer a foundation for interpreting production-induced 4D effects and the balance between them. However, it is all based on a rock-physics model, properties of an outcrop sandstone sample and a recovered sample from a West of Shetland reservoir, and a narrow range of pressure changes of up to 20 MPa. The effective-medium model applied (i.e. Gassmann theory), has limitations with regards to its assumptions, namely: the rock is isotropic, pore spaces are well connected and completely saturated and low seismic frequency (< 100 Hz) of observation. The latter is practically applicable to the seismic experiment. The low frequency assumption implies that pore pressures are equilibrated throughout the pore space and the fluids can flow easily through the pore space, otherwise, at high frequencies (> 100 KHz), fluids do not have enough time to flow and this will increase the stiffness of the rock. The limitations of Gassmann's (1953) assumptions mostly affect low porosity cemented sandstones. In any saturated rock, fluids are not homogenously distributed throughout the pore space, a patchy saturation model which spans the range of fine-scale (homogenous) to patchy mixing is recommended (for example, Brie et al., 1995). In addition, rocks are not isotropic, relations such as those detailed in Brown and Korringa (1975) must be used to account for anisotropy. In terms of the rock mineral moduli, the Voigt-Reuss-Hill average (Hill, 1952) was used, but Hashin-Shtrikman bounds (Hashin and Shtrikman, 1963) can also be applied, or a modified version by combining it with Dvorkin's contact cement model (Dvorkin and Nur, 1996) and this may be widely applicable to a variety of unconsolidated and cemented sandstones. Asveth et al. (2010) details the various rock-physics models that could be applied, but it is expected that similar conclusions on the sensitivity for the sandstones used, as well as the relative magnitudes between pressure and saturation sensitivity will be reached. On a reservoir-constrained modelling on three different fields (two clastic fields and one carbonate field), Briceno (2017) shows that different rock-physics models give similar results, and it is the parameterisation of the various rock-physics models that affect the results. The purpose of the generalised rock-physics modelling performed in this chapter is to provide some guidelines, and it is not intended to try to match any observations on real field studies; this is beyond the scope of this thesis.

In the next chapter, the observed 4D seismic data will now be calibrated to quantify the reservoir's sensitivity on four different clastic fields.

Chapter 3

Quantification of the sensitivity of sandstone reservoirs to pressure and saturation changes using full-stack 4D seismic amplitudes and time-shifts

In Chapter 2 rock-physics modelling provided basic understanding of the pressure and saturation sensitivity of different sandstones. In this chapter, the in-situ reservoir's sensitivity is quantified directly from the observed 4D seismic data. The main motivation for this is to provide an alternative to laboratory measurements on core plugs or rock-physics models. This complementary technique for estimating pressure and saturation sensitivity compares 4D seismic and pressure/saturation measurements. This is possible in selected areas around and away from wells where pressure or saturation variations contribute predominantly to the 4D seismic signatures. Multiple monitor 4D seismic data are used to sample these areas as a function of field production time. The technique is applied to 4D seismic amplitudes and time-shifts across four producing North Sea clastic reservoirs (Shearwater, Norne, Heidrun and Schiehallion). The results indicate that pressure and saturation sensitivity varies according to the geology of each reservoir. This also indicates the reliability of the approach to better tackle the separation of pressure versus saturation for improved reservoir management.

3.1 Introduction

The pressure sensitivity of sandstone reservoirs (due to pore pressure change) though a mature subject lacks proper in-situ calibration. Contrary to fluid saturation sensitivity which is believed to be adequately explained using empirical fluid equations (such as Gassmann, 1951). In Chapter 2 I reviewed the typical techniques (model-driven and data-driven) by which the reservoir sensitivity can be estimated. The model-driven approach is concerned with rock physics modelling (which can be constrained using repeat logs (e.g. Fürre et al., 2009) and /or laboratory experiments on core plug samples (e.g. MacBeth, 2004). Many studies have since raised concern with laboratory measurements and their suitability for replicating the in-situ reservoir response (e.g. Nes 2000; Eiken and Tøndel 2005; Alvarez and MacBeth 2014) as well as the field-scale accuracy of rock-physics models. As Saul and Lumley (2015) point out, "*the magnitudes of observed time-lapse seismic anomalies associated with pore pressure changes are sometimes not explainable by velocity-pressure relationships determined by fitting elastic theory to core data. This can lead to difficulties in interpreting time-lapse seismic data in terms of physically realizable changes in reservoir properties".* Similar findings are also reported in Eiken and Tøndel (2005), Fürre et al. (2009), and Amini and MacBeth (2015).

The data-driven approach estimates sensitivity by an integrated interpretation of 4D seismic data and production data. One of the first examples is given by Eiken and Tøndel (2005) where interval time-shifts estimated from a single 4D seismic data (and measured pressure changes in the well), are used to quantify the reservoir's pressure response which was found to be 2-3 times weaker than the sensitivity measured from dry core plugs. Concerned with the separation of pressure and saturation changes, Floricich (2006) maps 4D seismic signals (amplitudes and time-shifts) around wells to known pressure and saturation changes around the same wells, but combines all wells in a least-squares inversion to estimate a single value of sensitivity for the reservoir, each for pressure and saturation. Amini and MacBeth (2015) inferred the sensitivity by comparing observed 4D seismic amplitude data with synthetic data from a simulator-to-seismic study at water-flooded areas around water injectors where pressure changes dominate. It was found that after perturbations of laboratory-measured pressure

sensitivity on dry cores combined with forward rock-physics modelling, the observed 4D seismic response could not be adequately reproduced.

The purpose of this current study is to investigate the sensitivity of sandstone reservoirs to pore pressure and saturation (water and gas) changes observed in 4D seismic data. The data-driven concepts in Foricich (2006) and Amini and MacBeth (2015) is further developed and generalised beyond just wells. The investigation of sensitivity will involve:

- Using not just a single 4D seismic data but multiple monitor 4D seismic data to quantify the reservoirs sensitivity across its life time of production. This will of course depend on the availability of monitor seismic data and production measurements at these times. The use of multiple monitors is not a first. For example, Huang et al. (2011) and Yin et al. (2015) correlate pressure and water saturation induced amplitude signatures from multiple monitor surveys and well engineering data to directly update reservoir connectivity. To produce smooth transitions of the CO_2 front movement in-between surveys, Kiær et al. (2016) uses multiple monitor seismic data for calendar time interpolation of amplitude maps. Barkved et al. (2009) constructs seismic PLTs for horizontal wells by linking production data to multiple monitor 4D seismic changes acquired at frequent time intervals. The reservoir's sensitivity can thus be calibrated both in areas further away from well control and for seismic data acquired at different times. Calibrating for sensitivity using several monitor data allows for a better understanding of the changes in sensitivity over time. This also helps to reveal the linearity or non-linearity in the 4D seismic response to induced production.

- Using multiple attributes such as 4D amplitudes (as an interface map) and time-shifts (as an interval map) estimated from stacked (full offset) pre-stack time migrated seismic data to measure the reservoir's sensitivity. These two 4D seismic attributes are a standard for quantitative studies (Stammeijer and Hatchell, 2014).

- Applying to four North Sea clastic fields that differ in geology (structure, stratigraphy, rock fabric and environment), fluid properties and production

mechanism. A quantitative measure of sensitivity using 4D seismic data across real fields will bring realistic insights into sensitivity-dependency on various field characteristics.

3.1.1 A discussion of pressure responses observed in 4D seismic data

A collection of observations of clear 4D seismic amplitude responses to production-induced pressure changes published in the literature (some with estimated interval time-shifts indicated on the histograms) for various producing reservoirs motivates this study (Figure 3-1). The chart is generated for some clastics, chalk and carbonate fields in the North/Norwegian Sea, Gulf of Guinea, Gulf of Mexico, offshore Malaysia, offshore North Western Australia and onshore Canada (see Appendix B for table and references

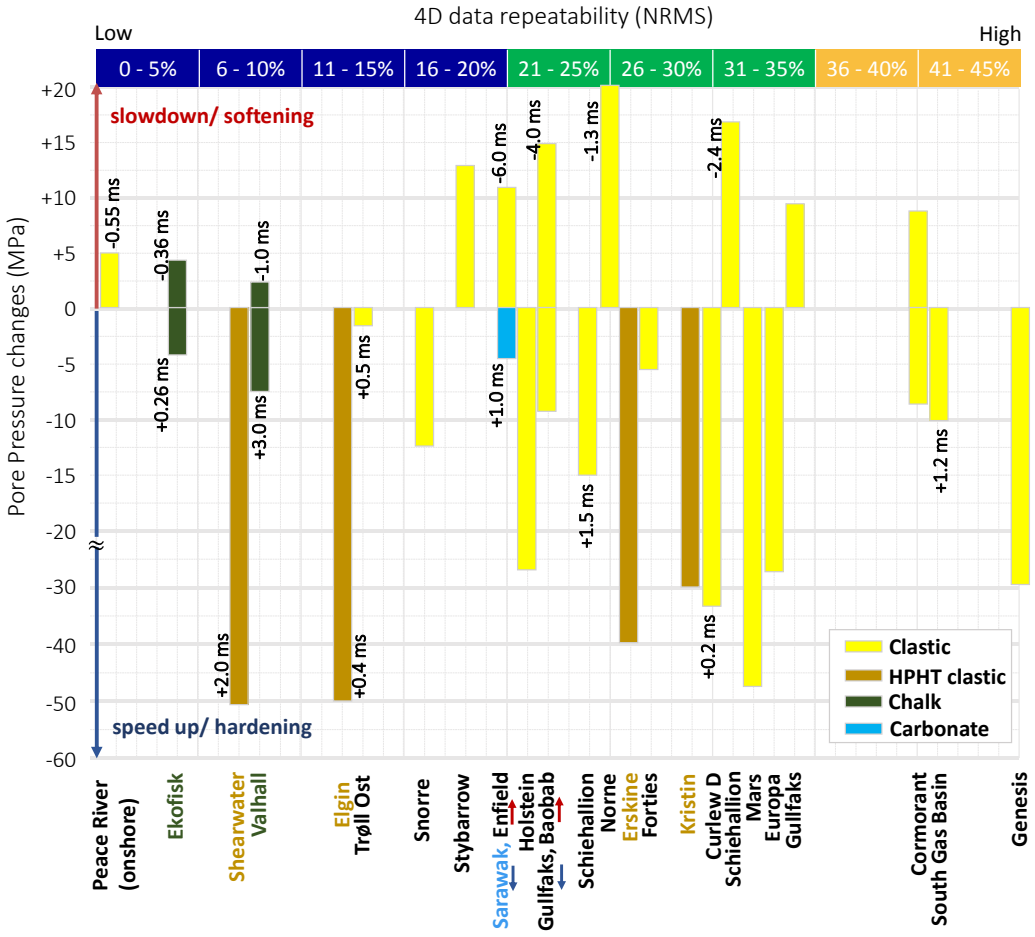

Figure 3-1 Reservoir pressure effects observed in 4D seismic amplitude data for various producing fields taken from published papers where the magnitude of the pressure change (MPa) and the data noise levels expressed as"normalised RMS"(root-mean-square) were reported. The observed reservoir interval time-shifts (ms) is also provided for some cases. Datasets from PRM surveys include Peace River (land), Ekofisk and Valhall. Others are from a variation of towed streamer acquisitions. Field names are written in black for normally-pressured "clastics", and are color-coded for other field types, "HPHT clastic", "Chalk", and "Carbonate".

from which Figure 3-1 was derived). The legend "clastic" indicates normally-pressured sandstones, and "HPHT clastic" indicates high-pressure-high-temperature sandstones. The 4D seismic data quality as measured by the NRMS (low–very good quality, and high – bad quality) is a good indicator of the reported magnitudes of pressure changes causing the hardening or softening response which was observed across the various fields. Data for the North Sea chalk fields of Valhall and Ekofisk have been acquired using PRM technology. With the exception of the Peace River onshore field in Canada which boasts the *"*SeisMovie^{TM}*"* PRM system, data for the remaining offshore fields were acquired using towed streamer technology. Looking at the histograms for each field type (e.g. clastics), there is a general indication that the higher the data non-repeatability, the bigger the magnitude of pressure changes need to be so that the effect is interpretable in 4D seismic data. For example, for pressure down response, compare the unconsolidated gas sands of Trøll Ost (at -1.5 MPa, and NRMS of 13%) versus the tight cemented gas sands of the South Gas basin (at -12.4 MPa, and NRMS of 41%). For pressure up response, also compare the clean unconsolidated sandstones of Enfield (at +11.7 MPa, and NRMS of 20%) with the turbidite sands of the Schiehallion field (at +17 MPa, and NRMS of 31%).

The fields shown exhibit different magnitudes of 4D time-shifts (the same for their amplitude responses) depending on their rock fabric, porosity, thickness, and the magnitude of induced pressure change. The intra-reservoir time-shifts reported for some of the fields range from as a low as 0.2 ms to as high as 6 ms. Although a small collection, it is noteworthy that 4D seismic time-shifts due to pore pressure increase causing a softening/slow-down (-0.3 to -6 ms) are observed to be generally bigger than those due to pore pressure decrease causing a hardening/speed-up (+0.2 to +3 ms). This asymmetry is expected as rocks are more sensitive to slow-down effects due to pore pressure increase than to speed-up effects due to pore pressure decrease (Hatchell and Bourne, 2005). This also agrees with insights from rock-physics modelling in sandstones (see Figure 2-10, Section 2.3.3).

Time-lapse reservoir time-shifts associated with gas saturation increase (i.e. gas/ steam injection and gas breakout) are generally observed to be between -2 to -20 ms (see Bergmann and Chadwick, 2015; Falahat, 2012; Jenkins et al., 1997; Benguigui et al,

2012; Alsos et al., 2009; Ivanova et al., 2012; Grude et al., 2013; Zadeh et al., 2010; Ng, 2005; La Follet et al., 2015).

For water saturation increases, this is reported to be between +0.2 to +3 ms (La Follet et al., 2015; Aarre, 2006; Floricich, 2006; Falahat, 2012; Folstad et al., 2013).
These observations and many more across various fields show the capabilities of 4D seismic data as a direct in-situ measure of the reservoir's response, considering the data non-repeatability and the magnitude of induced production. Estimating the reservoir's sensitivity using 4D seismic data can thus fill the gaps in rock-physics derived or core plug measured pressure sensitivity and can help to better separate pressure from saturation changes in 4D seismic data. Knowledge of seismic pressure and saturation sensitivity could also improve planning of future surveys, as accuracy requirements and detectability limits can be assessed in a practical sense. Further, similar reservoirs could also benefit, as such knowledge may also be used to predict their 4D seismic response to pressure and fluid saturation changes.

3.1.2 Some considerations for quantifying sensitivity using 4D seismic data

Whilst the seismic–based approach appears promising for quantitative measures of the reservoir's sensitivity, there are challenges with 4D seismic data that should be of note, both for amplitudes and time-shifts.

4D seismic amplitudes

Seismic amplitudes are affected by acquisition geometry/shot variation, equipment, propagation effects and processing algorithms/workflows, and, as such, are non-unique (Sheriff, 1975; Simm and Bacon, 2014) (see also Figures 1-3 and 1-4, in Section 1.1). For the interpretability of 4D seismic data, one criterion is data repeatability (Kragh and Christie 2002) which is believed to be affected mainly by acquisition-geometry differences, near-surface conditions, environmental conditions, noise, geology etc. as discussed in Johnston, 2013. Whilst co-processing algorithms and parameters for 4D processing (Helgerud et al., 2011) aim to preserve the 4D signal (amplitude and phase) and improve repeatability, the 4D signal is not always preserved in processing. Migration, in particular, has a complex averaging effect on the 4D signature and may

also introduce additional noise (Canning 2010) that will impact quantitative 4D amplitude studies. More important is the use of appropriate velocity models for 4D imaging. Brain et al. (2009) reveals better 4D signal preservation and interpretation using a pre-stack depth migrated data (which requires more accurate velocity models) compared to that of a time migrated data. In addition, intra-survey reservoir fluctuations results in a lack of accuracy in the measured amplitude response (in post-stack 4D seismic data) to reservoir changes as they are found to be in error (Omofoma and MacBeth, 2015; see also Chapters 4 and 5). Such irreconcilable spatio-temporal discrepancies between the acquisition itself and the dynamic reservoir during shooting of the seismic surveys also makes small pressure or saturation induced signals difficult to detect in stacked data and may appear as noise, besides the usual factors affecting data non-repeatability. The analysis in this chapter is thus limited to areas of genuine production-induced signals caused by fluid saturation or pore pressure changes that are sufficiently large.

As is common with map-based techniques, this brings problems associated with interpreting the horizon, defining a target window, selecting a method for averaging etc. and each carries its own uncertainty.

- The root-mean-square, RMS, amplitude averaging method has been chosen for the map-based calibration. This is because the resulting RMS values are always positive irrespective of whether the reservoir reflectivity interface is represented by a trough or a peak. This will thus be appropriate for any field. The RMS amplitude is also a recognised standard for 4D seismic interpretation (Stammeijer and Hatchell, 2014). As the RMS uses windowed measurements, it is also robust with respect to noise and horizon mispicks, and is suitable for a wide range of field seismic datasets with different repeatability measures. Other methods for averaging such as Amplitude Envelop, Sum of Negative Amplitudes, and Sum of Positive Amplitudes etc. can also be used, but may not be as robust as the RMS. These other averaging methods must also be selected appropriately for a negative or positive or near-zero reflectivity interfaces.

- Appropriate time windows are required to compute the RMS amplitude maps along the top reservoir interface and this is done for both baseline and for each

monitor data individually. In this work the top reservoir picks are used because these are generally well defined and easier to pick than the bottom of the reservoir. This is most suited to seismically thin reservoirs (usually < 50 m thick) of half a wavelength. The window size for averaging the amplitude signals is straightforward as this is typically the same as half the wavelength (i.e. peak to trough). Thus, there is some tolerance allowed in the mispositioning of the window to produce a reliable RMS amplitude signal. In thick reservoirs (i.e. reservoirs represented by one or more wavelength cycles), considerations have to be given to the particular effect that can best be captured at top reservoir or at the bottom of the reservoir. Falahat et al. (2013) suggest that the effects of pressure and fluid saturation changes occupy different volumes in the reservoir. Pressure effects are likely to be laterally extensive, occupying the entire thickness of the reservoir until barriers are intercepted, whereas, water or gas saturation effects may concentrate in the deeper and shallower areas, respectively, depending on gravity, pressure gradients, mobility ratios and reservoir heterogeneity.

- It is also suggested to test different search windows and the final window choice should be selected based on improved focusing of the mapped 4D signatures and good window coverage over the reservoir interface. Larger windows will be found to be poorer focus and resolution due to too many destructive and constructive events being averaged out, but smaller windows will not capture adequately all the 4D changes. The choice of window for averaging will thus affect the magnitude of the 4D amplitude signals in the resulting maps, which adds to the non-uniqueness in amplitude sensitivity estimates.

As this study quantifies sensitivity across monitor times, it is best to use the same window size for the monitor and baseline seismic datasets belonging to a field. The RMS 4D amplitude maps are the difference between each monitor RMS map and the baseline RMS map. Differencing in the maps domain, rather than directly from volumes (from which 4D maps can then be computed) reduces the influence of residual time-shifts which are known to corrupt the amplitude information (Hughes, 2000; Alsos et al., 2009). This is common practise when the monitor and baseline seismic datasets have not been adequately time-shift corrected (Johnston, 2013). Processing of 4D

seismic data usually aims to reduce such time-shifts as much as possible. These time-shifts refer to the time misalignment between baseline and monitor traces which can be caused by production (genuine 4D signals) and noise (which is what should be removed). Time-shifts due to noise originate from non-repeatable acquisition geometries, variations in source and receiver coupling, and near-surface variations. Such near-surface variations are caused by weathering layer changes and water column changes (including those that affect the elevation of the sea surface (tides, weather and currents) and those that result in variations in water velocity (temperature and salinity changes)). Therefore, cross-equalisation and local as well as global (and trace by trace) matching filters are commonly applied to the baseline and monitor data (for example, Rickett and Lumley (2001); Kristiansen et al. (2000); Magesan et al. (2005)). Nevertheless, such time-shifts cannot be completely removed for several reasons - acquisition geometry, processing algorithms, velocity models, and parameterisation (Johnston, 2012), hence the name, residual time-shifts. For example, residual time-shifts in the range of ±1.0ms are observed above the reservoir of the Curlew D field, located in the Central North Sea and are suspected to be caused by the differences in source and receiver positioning between the surveys, but cannot be removed during processing (Fehmers et al., 2007). In such cases of poor time alignment (as is the case for the various seismic datasets in this study), the 4D amplitude signatures on maps computed separately for baseline and monitor seismic data (using the same window size), and then differenced, are better interpretable than on 4D seismic vertical sections. If the time misalignments are large between baseline and monitor times, then it is best to repick the reservoir's horizon, or apply a bulk shift to the horizon from the baseline seismic data or adjust the window centre while keeping the same window size, before computing maps. However, within the window interval, residual time-shifts still affect the mapped RMS 4D amplitudes.

4D seismic time-shifts

Unlike 4D amplitudes which can be directly calculated from the processed seismic data simply by taking the difference between two 3D seismic amplitude volumes, or the difference between amplitude maps, time-shifts have to be estimated from the seismic volumes. The manual way of doing this is by picking the reservoir interface on baseline and monitor data, and taking the difference between the two horizons, which results in a

time-shift map. This however is affected by the consistency and accuracy of picks, which is not easy to manage even in noise-free data. Besides, it is not a very sensitive way of capturing travel-time differences, as 4D time-shifts within the reservoir interval are small (Figure 3-1) compared to seismic wave periods. Other non-manual, more sensitive, and volumetric methods for measuring time-shifts exists and are also susceptible to noise, thus, will trade spatial and temporal resolution against noise suppression. The most common way of measuring time-shifts is by cross-correlation methods (Rickett and Lumely 2001; Hatchell et al. 2003; Hall et al., 2005; Hale, 2009; Naeini, 2013). A key parameter for such methods is the size of the cross-correlation window which is not always straightforward to choose. For example, time-shift measurements over long windows may not be sufficiently accurate, whereas, estimates over short windows can be unstable as they are more affected by noise and non-repeatability. It is thus suggested to test for an appropriate window size (see for example, Williamson et al., 2007; Pazetti et al., 2016).

Other non-cross-correlation based methods include: non-rigid matching (Nickel and Sonneland, 1999) and time shift inversion based on formal Taylor expansions (Rickett et al., 2007; Williamson et al., 2007; Zabihi Naeini and Hoeber, 2008; Grandi et al., 2009; Zabihi Naeini et al., 2009; Whitcombe et al., 2010; Lie, 2011). These inversions work by minimizing an objective function obtained from the monitor-base difference seismic cubes and are non-linear ill-posed problems with non-unique solutions that require careful regularisation. Such inversions can be very effective if the time shifts are small, although the methods usually assume that the wave propagation is vertical, that the seismic traces are nearly zero offset and that changes in the reservoir are mainly influenced by velocity and not by density (Williamson et al., 2007). However, stability is to a greater extent a problem when large enough time shifts are encountered and such methods also require balanced amplitudes (Lie, 2011). In addition, in some thick reservoirs, time shifts may be large enough to cause cycle skipping (for example in Mitchell et al., 2009, where overburden time-shifts greater than 30 ms are observed), in which case, Rickett et al. (2007) emphasize that the inversion can become more non-linear. More expensive global optimisation techniques will thus be required as steepest-descent solutions will fail. Grandi et al. (2010) uses a priori information (production data, structural interpretation or other geological information) to carefully regularize the inverse problem in an iterative Gauss-Newton optimisation scheme. This they consider

a more stable inversion with better resolution which addresses stress-sensitive reservoirs with time shifts that are induced both by 4D velocity change and compaction (see also Chu et al., 2012; Zabihi Naeini et al., 2009).

Using MATLAB codes developed within ETLP, a few of these methods (Rickett et al., 2007; Hale, 2009; Whitcombe et al., 2010) have been tested to compute 4D time-shifts between observed monitor and baseline seismic data. The tests suggest that the different methods will output estimates that are of varying degrees of resolution and magnitude, but the character of the time-shift responses related to strong production-induced signals are usually consistent across the methods. Kanu et al. (2016) evaluate the accuracy of a number of these time-shifts methods and document their strengths and weaknesses. Time-shifts estimated from seismic data are therefore non-unique as the different methods suggest, and are also influenced by amplitude/phase changes (Hoeber et al., 2008).

For this study, I use the fast cross-correlation technique detailed in Hale (2009) which uses a Gaussian window to quantify vertical time-shifts between the baseline and monitor seismic volumes. Although other methods for time-shift estimation may be more accurate, their use in determining time-shift sensitivity is beyond the scope of this thesis. The cross-correlation technique was preferred mainly because of its robustness to noise and its fast computation time. Longer windows can be used to achieve better stability in noisy data and big time-shifts will still be preserved but poorer resolution means that the magnitude of the time-shifts are of lower accuracy. However, this may not present any significant impact on the time-shift interpretation (Tigrek and Hatchell, 2006; Pazetti et al., 2016), but will influence the magnitude of the quantified time-shift sensitivity. Since the quality of the cross-correlation is determined by the window size, time-shift volumes from several Gaussian windows were first evaluated for meaningful information (particularly around known well locations), lateral consistency and vertical smoothness before suitable window parameters are chosen. For consistency, the same window sizes is used for cross-correlation of the baseline and each monitor seismic volume, and was also found to be appropriate for the various field seismic datasets in this study.

Production induced 4D time-shifts are of two sources, 1) fluid saturation changes (with accompanying fluid contact movement in the reservoir) which causes seismic velocity changes and 2) changes in the stress-strain state due to pore pressure changes which cause both seismic velocity and physical thickness changes inside and outside the reservoir. For reservoir changes associated with fluid saturations, time-shifts associated with the velocity changes affects the reservoir as well as everything below it, whereas, the accompanying fluid contact movement impacts only the reservoir experiencing the fluid saturation changes. Attempts have also been made to quantify the two assuming that the effects of pore pressure changes are negligible (Aarre, 2006), and this is beyond the scope of this thesis.

For effects due to pore pressure changes, 4D seismic time-shifts capture the combined effects of velocity and thickness changes, within the reservoir interval; the former being the main contributor in sandstones. Separating the two effects remains practically challenging (Røste et al., 2006 and 2007). In this study, I make no attempt to separate time-shifts due to velocity changes from those due to thickness changes (i.e. physical compaction and dilation). The estimated time-shifts across the four offshore clastic fields in this study are thus assumed to be caused purely by velocity changes. So that a speed-up anomaly (i.e. positive time-shifts), may be caused purely by an increase in seismic velocity in the monitor time relative to baseline, and a slow-down anomaly (i.e. negative time-shifts) may be caused purely by a decrease in seismic velocity in the monitor time relative to baseline.

When interpreting the observed 4D seismic data, the time-shifts are not only caused by production but also by noise (i.e. residual time-shifts as discussed in the "4D seismic amplitudes" section above), such that the quantified time-shifts is a contribution from both sources. One ought to be cautious how processing algorithms affect the time-shifts in preserving the 4D seismic signals (Johnston, 2013).

3.2 Interpretation method for calibrating sensitivity in 4D seismic data

The method uses multiple repeated seismic monitor surveys shot across a field undergoing production and recovery. The interpretation is map-based and uses intra-reservoir time-shift maps extracted from pre-computed time-shift volumes and 4D amplitude maps calculated as the root-mean-square (RMS) average along the top

reservoir interface. The magnitude of the mapped 4D (monitor-baseline) seismic signals at different monitor times are collected at specific locations in the reservoir where any of the dynamic effects (pressure increase/decrease, water saturation or gas saturation changes) are verified to be the over-riding influence and considered to be large enough 4D signals. This is then cross-plotted against known pressure or saturation changes at these locations. Following this, the amplitude and time-shift sensitivity is quantified as described in Equations 2-23 and 2-26, respectively (see section 2.3). In the numerator of Equation 2-23, the 4D amplitude response is expressed as a fractional change weighted by the baseline seismic amplitude. This allows for a direct comparison of sensitivity across different fields where amplitudes are of different scales. This could also be the case for a particular field where monitor and a matched baseline seismic data have been processed with different amplitude scales, compared to other baseline/monitor datasets for the same field. Likewise, in Equation 2-26, the intra-reservoir time-shift is normalised by the average thickness of the reservoir formation. As this study is concerned with the response of the reservoir rock, the normalisation removes the influence of thicknesses in the time-shifts (since thick reservoirs will appear to have bigger time-shifts than thin reservoirs). This therefore allows for a balanced comparison across different fields which have different reservoir thicknesses.

The 4D interpretation workflow is given in Figure 3-2. Well production data (co-located in space and time with the seismic response) together with reservoir model depth-averaged maps of simulated pressure and saturation changes at the same dates are used to validate the 4D seismic signatures for a causal effect. Simulator-to-seismic modelling can also be performed as a data QC/validation step to further assess the 4D seismic response (Amini, 2014). For consistency and clarity, it is best to maintain the same polarity for the 4D seismic response across monitor times i.e. a consistent polarity for amplitudes and a consistent polarity for time-shifts. For each monitor time and for each selected area, both attribute maps are compared to ensure that their 4D responses are in agreement. The mapped 4D amplitude signals are used to guide the interpretation of the intra-reservoir time-shift maps.

Sensitivity calibration requires that strong saturation or pressure-induced signals across monitor surveys are interpretable and that the magnitude of the saturation or pressure changes at the selected locations are known. Pore pressure changes can be obtained

from three sources: bottom-hole-pressure (BHP) build-up tests for wells (injectors and producers) perforated in the reservoir formation, repeat-formation-tester (RFT) logs, Drill-stem test (DST) shut-in pressures and/or depth-averaged maps from a history-matched fluid-flow simulation model. These pressure data sources carry their own uncertainties, with the measured (historical) BHP, RFT or DST pressure generally preferred to simulated data (Beaumont et al., 1999). Saturation changes are usually obtained as depth-averaged maps from the simulation model or can be inferred from historic gas-oil-ratios (for gas saturation changes) and water-cut (for water saturation changes) in producing wells in the reservoir formation (for example, Floricich, 2006).

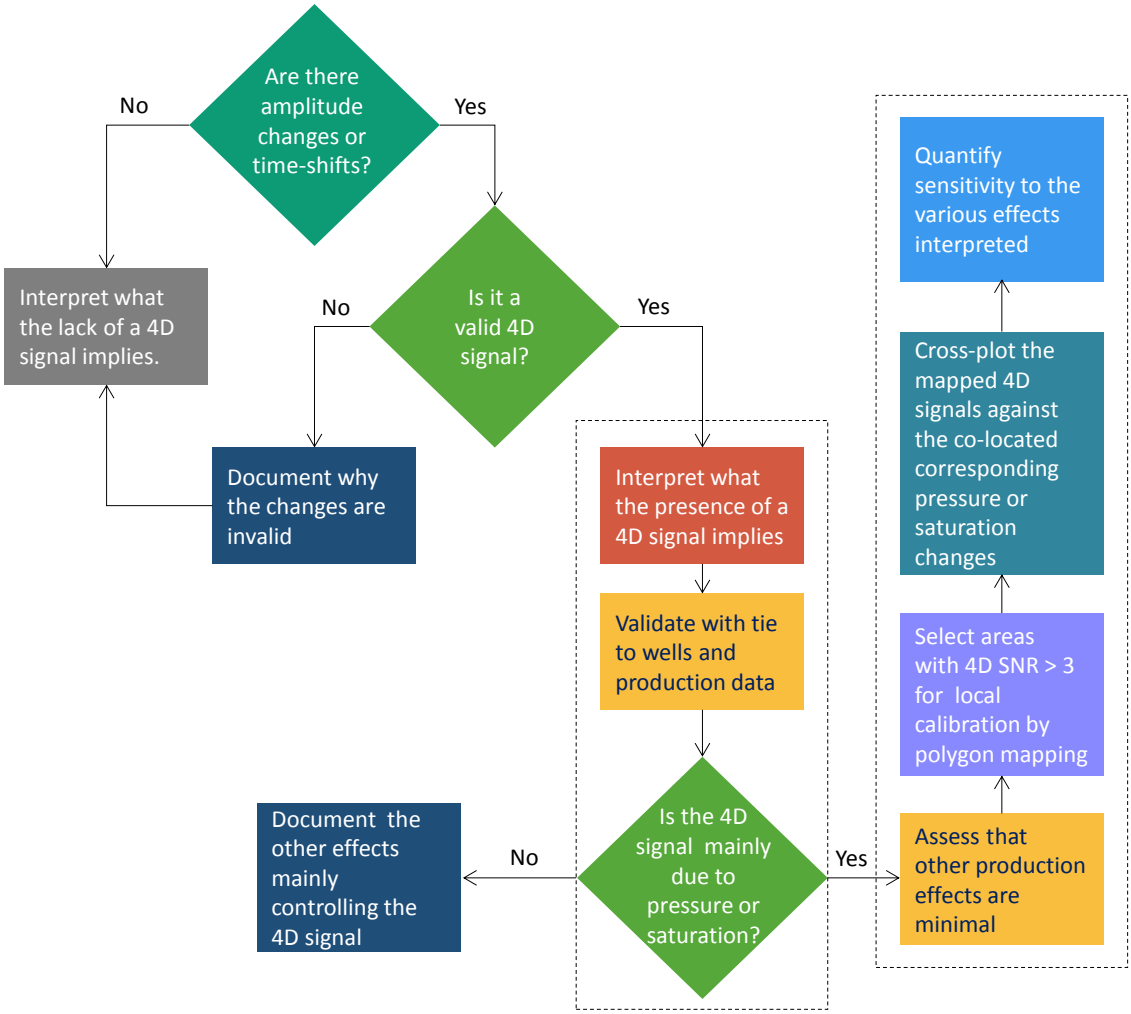

Figure 3-2 Conceptual 4D seismic interpretation workflow (modified after Johnston, 2013) for the map-based calibration of the reservoir's sensitivity in 4D seismic data. The workflow is repeated for each 4D seismic data across the monitor times, with 4D amplitudes and intra-reservoir time-shifts maps interpreted side-by-side. For selecting areas for calibration, the map-based signal-to-noise (SNR or S/N) ratio in 4D seismic data is the inverse of the noise-to-signal ratio (N/S) which is calculated as shown in Appendix A.2.

The uncertainty in the quantification of sensitivity comes from the 4D seismic data and the measured/simulated dynamic production data. The uncertainty in 4D seismic data is simply given by a measure of the data non-repeatability, and the signal-to-noise ratio, SNR, (or noise-to-signal ratio, N/S) can also be computed based on non-repeatability noise, NRMS (see Appendix A.2). For a confident interpretation, only pressure or saturation dominant areas with 4D signal-to-noise ratios greater than the value of 3 are used for sensitivity estimation; a quantitative criterion suggested in Behrens et al. (2002). For the dynamic pressure or saturation data, if simulated data are used (due to a lack of data i.e. historical well BHPs or repeat logs), the uncertainty is estimated using the percentage error between historical measurements of key field production data and their simulated alternative. Key field production data are water-cut and gas-oil-ratio, which are considered as first order parameters for material balance (Dake 1997). If measured data such as historical BHPs for wells are used, the uncertainty is simply the standard deviation of the measurement error. This is regarded as unbiased observation error and the magnitude will vary from field to field depending on well operators and practices. Yin et al. (2015) provides a number of 5% based on reservoir engineering information on a specific North Sea field. This number is assumed here, as it is not available for the North Sea fields in this study.

3.2.1 Some suggestions on where best to calibrate the various effects

Although areas where pressure and saturation changes dominate are likely to be strongly field dependent, some generalisations are possible to guide this study:

(i) ***Inside water-flooded areas or regions of undisturbed fluid saturations*** **-** areas water-flooded at a previous monitor time are likely to show pure pressure-induced signals in subsequent monitor surveys. This result may however be biased by fractures existing around the borehole. I start by calibrating signals around water-flooded wells and expand outwards to larger water-flooded regions. Areas in the natural water or gas leg are useful as initial saturation levels are likely to remain fixed over time.

(ii) ***Outside areas undergoing significant saturation changes*** **-** whilst theoretically small, pressure-induced signals should still exist away from injectors

and outside the influence of a growing water-flood front. Likewise, in areas away from producers undergoing depletion but no associated gas breakout (in an oil-water system reservoir) or negligible gas condensation effect (in gas condensate reservoirs). These areas could be significant if the injection or depletion response is inside a compartment (For example, see Figure 1-7 in section 1.2). One assumption is that other changes such as temperature or salinity changes are negligible; checked from knowledge of field production mechanisms and modelling.

Saturation-induced 4D signals can be found anywhere outside the water leg. Water saturation induced signals can easily be observed around water injectors perforated in the hydrocarbon leg, sometimes around producers and also in between injectors or producers. Gas saturation induced signals are likely to concentrate around producers and/or in shallower parts of the reservoir if a new gas cap is formed or the existing gas cap expands, all dependent on pressure gradients, gravity, mobility ratios and reservoir heterogeneity. Likewise, other effects caused by temperature or salinity changes are assumed negligible. This is also validated from knowledge of field production mechanisms and modelling.

3.3 Application to four North Sea/ Norwegian Sea Clastic fields

Four North Sea clastic fields where 4D seismic technology is the main surveillance tool for reservoir management are interpreted for their sensitivity to pressure and saturation changes, using amplitudes and time-shifts. The fields include the Shearwater field (a highly geomechanically active HPHT gas condensate) and three normally-pressured oil-water-gas fields (Norne, Schiehallion and Heidrun field) (Figure 3-3). The monitor and baseline seismic data for all fields have been acquired using towed streamer technology. All seismic data in this chapter are post-stack (full offset) data. Specifically, these are stacked pre-stack time migrated seismic data. For pressure sensitivity using amplitudes, I consider all four fields and for time-shifts, this could only be resolved for two fields, the Shearwater and Norne fields. Time-shifts for Heidrun and Schiehallion fields could not be reliably resolved (believed to be mainly due to poor data quality and too small a time-shift response). The ETLP Reservoir Geophysics MATLAB code based on the fast

cross-correlation technique (Hale, 2009) is used for computing the vertical time-shifts between the baseline and monitor seismic volumes. The technique requires the Gaussian window parameters: vertical window length in two-way time, number of traces in the x-direction and number of traces in the y-direction. These parameters have been tested and appropriately defined as 8 ms by 10 traces by 10 traces for the calculations on both the Shearwater and Norne field seismic datasets.

Figure 3-3 Location of the four offshore clastic fields considered for 4D seismic sensitivity calibration. Shearwater, an HPHT gas condensate above dew point pressure, Schiehallion a normally-pressured black-oil reservoir very close to bubble point pressure, and Heidrun and Norne are also normally-pressured oil-water-gas reservoirs but are below bubble point pressure.

The fields have more than one reservoir formation, and for the sensitivity analysis I focus only in the main producing formation, which is usually the top reservoir. I briefly introduce and interpret each field separately. A table of the seismically-quantified sensitivity is provided at the end of each field case, with a summary across the four fields provided in section 3.4. The available datasets for this study are given in Table 3-1. The amplitude attribute map, ΔA, is the root-mean-square (RMS), which requires appropriate time windows above and below the top reservoir horizon for averaging the amplitude signals. This is given in Table 3-2 for the four reservoir formations studied in this Chapter. For the time-shift attribute, Δt, time-shift maps are obtained by extracting

from the 4D seismic time-shift volume, time-shift values along the top and bottom of the reservoir formation. The intra-reservoir time-shift map is then computed from the two maps (Figure 2-8 illustrates this).

Fields	4D seismic vintages (Full stack)			Reservoir engineering data			
				Historical well data		Simulated data	
	Number of monitors	Data repeatability (NRMS)	4D attribute maps	Well pressures	Other production profiles	Simulated production profiles for wells	Fluid flow simulation results on 3D grid
Shearwater	2	5 - 15%	Δt and ΔA	all wells	no	no	yes
Norne	3	25 - 45%	Δt and ΔA	no	yes	yes	yes
Schiehallion	3	30 - 60%	ΔA	one well	yes	yes	yes
Heidrun	5	20 - 40%	ΔA	no	yes	yes	yes

Table 3-1 Summary of field 4D seismic data and reservoir engineering data available for this study. Some fields have more monitor surveys than others, and NRMS repeatability varies across the datasets. Both 4D amplitudes, ΔA and time-shifts, Δt, attributes are computed and used for sensitivity quantification on two fields, and only amplitudes are used on the other two fields. Apart from pressure, other production profiles refers to field/well liquid production rates, gas-oil-ratio, water-cut, etc. History-matched fluid flow simulation models are available for all the fields.

Clastic fields	Reservoir	RMS averaging window length	Horizon window partitioning above (+) / below (-)
Heidrun	Garn Formation	12 ms	6 ms (+) / 6 ms (-)
Schiehallion	T31A sands	20 ms	0 ms (+) / -20 ms
Norne	Garn Formation	21 ms	5 ms (+) / 16 ms (-)
Shearwater	Upper Fulmar	70 ms	20 ms (+) / 50 ms (-)

Table 3-2 Time window parameters for computing the 4D amplitude attribute map, ΔA. The root-mean-square (RMS) is the averaging method used. RMS maps are computed using a defined window above and below the top reservoir horizon. The RMS maps are computed separately for the baseline and monitor seismic data. The maps are then differenced to produce, ΔA.

3.3.1 Sensitivity calibration on the Shearwater field

The Shearwater Field is located 250 km east of Aberdeen in in the central graben area (Block 22/30b) of the Central North Sea in water depths of 90 m (Figure 3-3). The graben structure partitions the field into a fragmented western block, a central downthrown block, and an un-faulted eastern block (Figure 3-4). This makes a rotated fault block with the reservoir stratigraphy divided between two major intervals (Figure 3-4 (a)). The Pentland formation makes up the basal unit which is up to 550 m thick and comprises of variably stacked fluvial sand channels, crevasse splay and overbank shales and coals of Middle Jurassic age. The overlying unit is the Fulmar formation which consists of clean stacked shoreface and shallow marine sandstones of Upper Jurassic age, with a thickness of around 219 m. Buried in deep water (with top reservoir at 4700-5000 m), the Fulmar sands are poorly consolidated for their burial depth due to premature diagenetic and consolidation processes. A laterally extensive marine shale (21 to 30 m thick), the Lower Heather Shale, separates the Pentland and Fulmar formations.

The Fulmar itself represents the main reservoir unit in Shearwater and can be broken down into the Upper Fulmar which is of very high porosity (20 to 30%) and permeability from which major production is attained from it 92 m thick sands, and the Lower Fulmar of low to moderate porosity with some dispersed shale and calcite cemented intervals. The Fulmar reservoir sandstone accumulations are a condensate and gas with a ratio of 170 barrels of condensate per million cubic feet of gas. The burial depth, coupled with challenging reservoir conditions of high pore pressures of 106.8 MPa, temperatures of around 180 °C (HPHT) and a high salinity aquifer, the Fulmar reservoir only began producing in October 2000 after a comprehensive reservoir appraisal process, since its discovery in 1991 (Gilham et al., 2005). The gas condensate is initially above dew point pressure of 46.9 MPa and production mechanism is by pressure depletion.

The substantial pressure decline roughly after 4 years of depletion results in the compaction of the producing Fulmar sands due to both layer thickness and seismic velocity changes, which leads to overburden stress and strain reduction (stress arching) (Staples et al., 2007). The reduction in the overburden stress is evident as big slow-

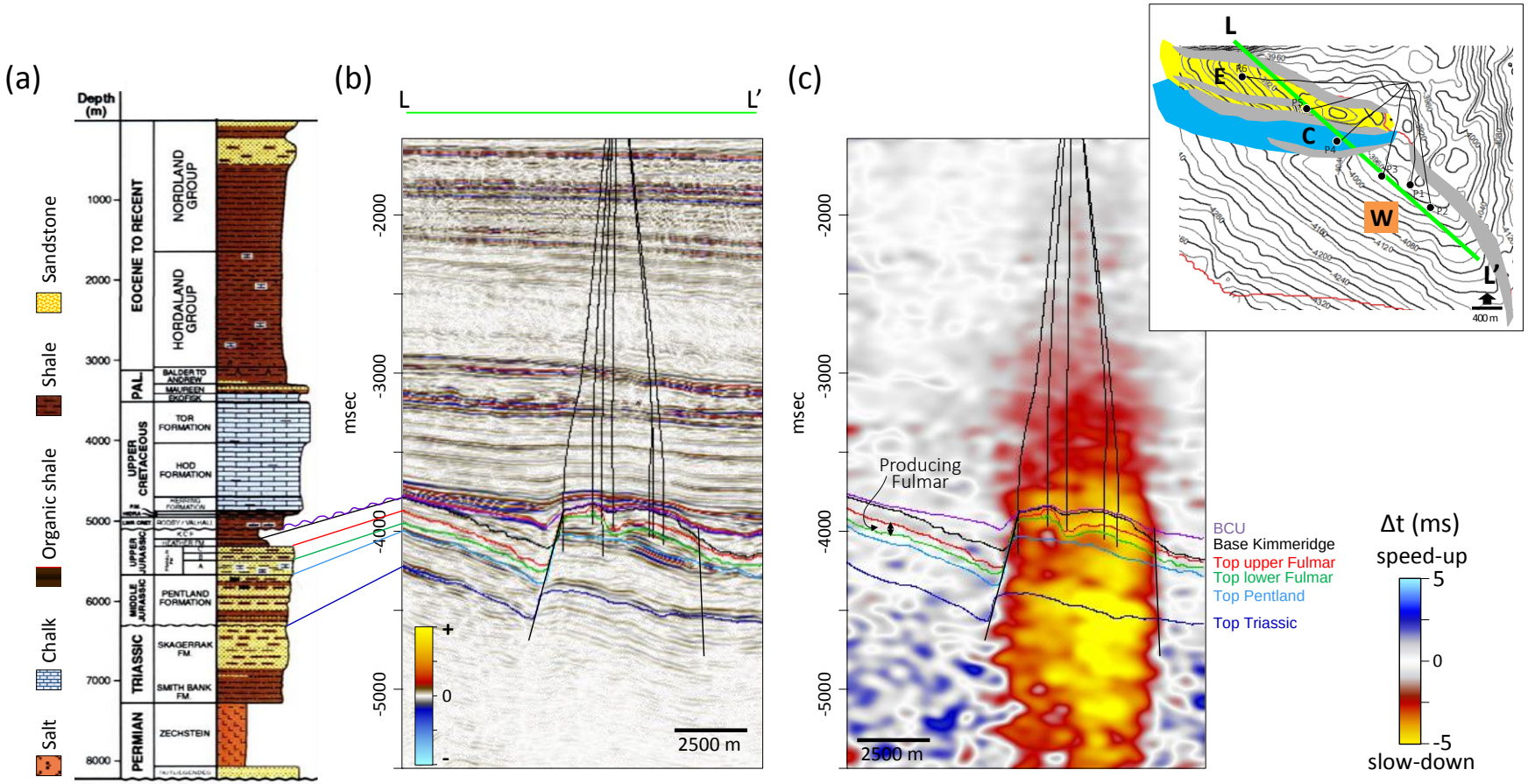

Figure 3-4 (a) Stratigraphic column for the Shearwater Field (after Lasocki et al., 1999) (b) Vertical seismic section through inline L-L' showing main structural components (c) 4D seismic time-shifts after approximately 4 years of production by pressure depletion, revealing the high geomechanical response of this HPHT gas condensate field bounded by the major faults. Inset map highlights the east, central and west (largest) blocks. The production itself is from the Upper Fulmar which is the focus for sensitivity calibration. The rocks surrounding the reservoir do not deplete but as they are connected to the reservoir, these rocks undergo stress and strain changes and deform as well. The Fulmar formation compacts, though this is unclear here as the time-shifts in the vertical section are effectively an integral function of depth (see Figure 3-7 for interval maps). The overburden and underburden undergo extension (i.e. slow-down) which are expected to diminish further away from the Fulmar reservoir.

down effects with negative time-shifts of up to -6 ms at top reservoir (Upper Fulmar) with the time-shift signals degrading as seabed is approached (Figure 3-4 (c)). As the field is within a highly stressed region, large time-shifts are observed in the immediate overburden due to the highly sensitive and compacting nature of the thick chalk units, the Hod and Tor Formation which lie above the reservoir (Figure 3-4 (a)). The immediate underburden (i.e. just below the Fulmar formation), also shows the expected slow-down with similar time-shift magnitudes which appear to diminish, but the expected decline towards the Pentland formation and below is not observed. Figure 2-8, showed a typical time-shift response for highly geomechanically active fields, the likes of HPHT clastic and chalk fields. The larger negative time-shifts in the Pentland Formation are unexpected (Figure 3-4 (c)), as the lithostatic weight of the entire rock column should not allow either considerable compaction or expansion in the underburden; thus, the expected time-shift signals should diminish and not grow, which is the opposite of what is observed here, and has been reported in Staples et al. (2007). As the 4D seismic time-shifts accumulate along the ray path, it is difficult to highlight the intervals of the most dramatic change which is within the producing Fulmar sands. The speed-up (positive time-shifts) inside the Fulmar sands are masked in the vertical sections, but the intra-reservoir time-shift calculated between the top Upper Fulmar and the top Lower Fulmar (later given in Figure 3-7 (d)) reveals the reservoir's compaction with positive time-shifts of up to 3 ms, caused by pressure depletion.

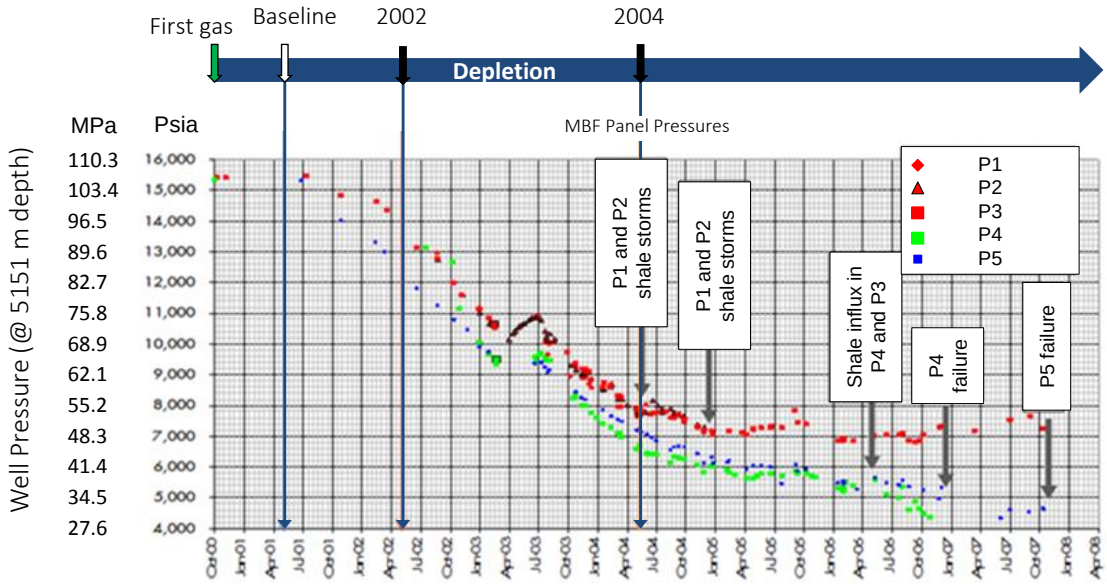

Figure 3-5 Shearwater pressure decline measured from wells with 4D seismic survey timings in 2002 and 2004, apart from the baseline, highlighting also the various well failures reported (Brain, 2011).

Four wells (P5, P3, P6 and P2) were drilled in the Upper Fulmar formation and a fifth to appraise the Pentland Formation (not shown), before production start-up. A sidetrack, P1 and also a new well, P4 were drilled in 2002, both are also perforated in the Upper Fulmar. As a result of the significant pressure decline (Figure 3-5), many of the wells have since failed almost simultaneously due to massive shale influx in the Kimmeridge Clay. It is believed that overburden fault reactivation or interface slip caused the shearing of the boreholes, which allowed passage of debris of up to 1 cm scale (J. Brain, personal communication, 11 November, 2015).

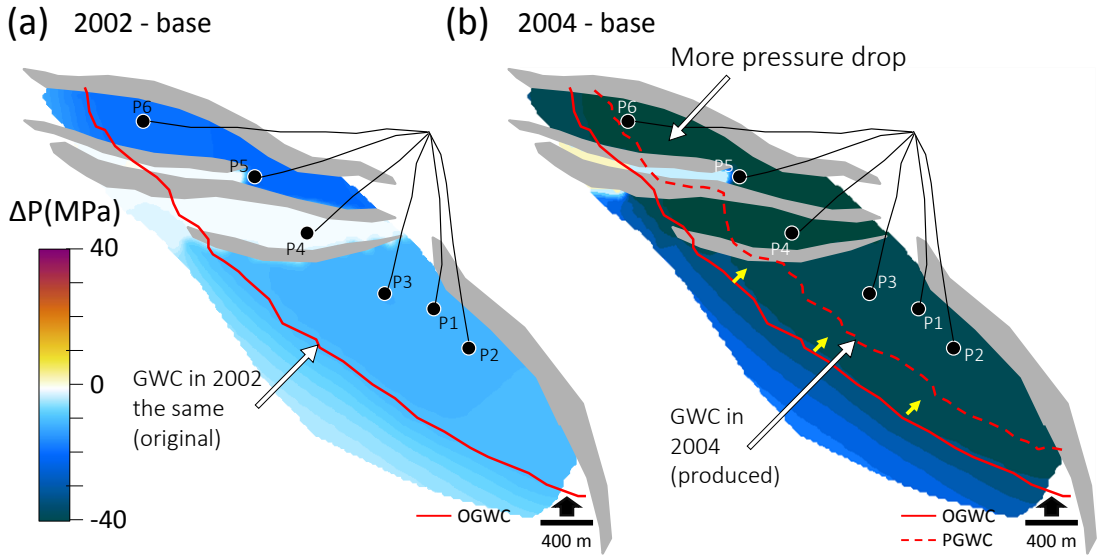

Figure 3-6 Depth-averaged maps of simulated pressure changes in the Upper Fulmar sands (Top reservoir). The significant pressure decline is also accompanied by a gas-water contact movement in the later 2004 monitor time, as predicted by the model. Producers are in black.

Three seismic monitor surveys acquired in 2001 (treated as baseline), 2002 and 2004 of very good data quality (with data non-repeatability 5 to 15%) have been acquired. A fourth seismic survey was acquired in 2013 but it is not used in this study as all wells in the study area had been shut-in by 2008. Albeit the significant well pressure changes recorded at the gas-water contact (5151 m TVDSS) of between -13 to -25 MPa in 2002, and -49 to -59 MPa in 2004, the induced pressure gradients were just above the reservoir's dew point pressure (46.9 MPa). The only changes of saturation involved in the reservoir are thus related to the upward movement of the gas (condensate)-water contact as predicted by the history-matched fluid flow simulation model (Figure 3-6) and possible water breakthrough towards the producing wells, though the latter is

suspected to have occurred far beyond the 2004 monitor time. The calibration of 4D seismic data for the sensitivity of the Upper Fulmar sands to pressure depletion is thus restricted to the remaining gas leg, and just around the producing wells. Figure 3-7 shows the top reservoir 4D seismic amplitude changes and the intra-reservoir time-shift maps for the 2002 and 2004 monitor times. Both attributes (Figure 3-7) convey similar 4D response, the amplitudes, a hardening response and the time-shifts a speed-up,

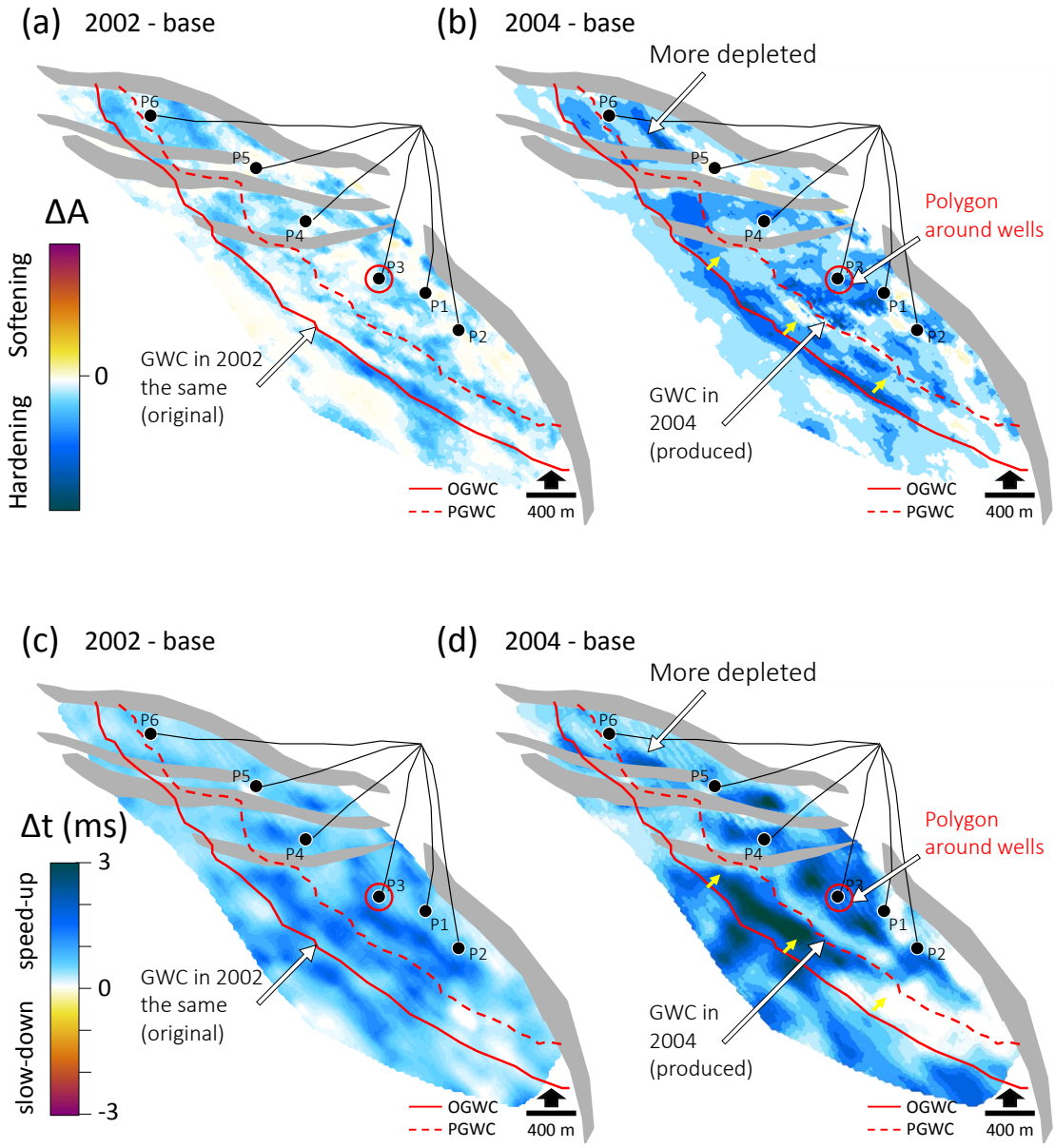

Figure 3-7 (a)-(b) Mapped 4D seismic amplitudes around the top Upper Fulmar showing a hardening response to pressure depletion (c)-(d) The extracted intra-reservoir 4D time-shifts calculated between top Upper Fulmar and top Lower Fulmar showing a speed-up response, both shown here for the 2002 and 2004 monitors. Both attributes are complementary. Producers are in black.

due to pressure decline, with the magnitude of the 4D signals increasing from 2002 to 2004 monitor time, in line with bigger magnitudes of pressure depletion that occur (Figure 3-5 and Figure 3-6). The mapped 4D seismic signatures are not uniform, and are imprinted by the character of the stacked shoreface sands. Areas of no significant changes are due in part to the difficulty in picking the specific reflection event of the top Upper Fulmar which pinches-out and is partially or totally eroded.

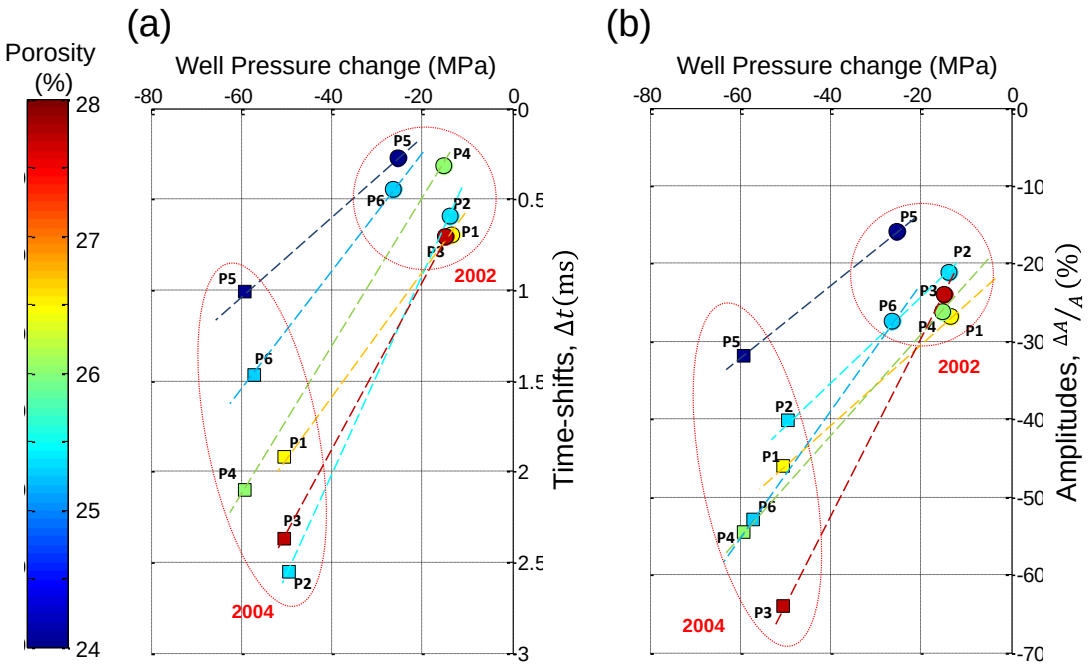

Figure 3-8 Cross-plot of (a) 4D seismic intra-reservoir time-shifts and (b) 4D relative amplitude changes (b) versus measured ΔP decrease (top x-axis) for the 2002 (circles) and 2004 (squares)4D times taken around the six production wells perforated in the Upper Fulmar. Colour bar is the effective porosity at these well locations which highlights the influence of porosity on the magnitudes of 4D amplitudes and time-shifts across the wells.

Polygons with a radii of 200 m around the perforation points of each of the six wells are used to extract the mean value of mapped 4D signals which are then cross-plotted against the measured well pressure changes for both the 2002 and 2004 monitor times (Figure 3-8). The computed amplitude and time-shift sensitivity is provided in Table 3-3. In Figure 3-8, as the magnitude of the pressure drop increases from 2002 to 2004 monitor times, the reservoir's 4D seismic response captured around each well react accordingly. Both time-shifts and amplitudes are correlating in the same way for all the wells, but differ slightly for the P2 and P6 wells at the 2004 monitor time. The plot has also been colour coded by the effective porosity taken around each well. The strong dependence on effective porosity can be observed, with some wells exhibiting bigger

magnitudes of 4D seismic signals, even for a similar magnitude of pressure drop across the wells in both monitor times, for example, well P3 in the West block versus well P5 in the East block. This confirms the lateral variation in sensitivity from well to well.

In Table 3-3, the mean value of amplitude sensitivity to pressure depletion across all six wells shows a decline in sensitivity from the 2002 monitor time (1.41% amplitude change per 1 MPa pressure drop) to the 2004 monitor time (0.90%). Such a trend was earlier observed from the generalised rock-physics model calculations (Figure 2-11). As the pore pressure decreases to bigger magnitudes of change, the rock approaches its asymptote, making it less pressure sensitive. The time-shift sensitivity for the Upper Fulmar sands relays the same with a decrease in mean value from 2002 (0.34 ms/km change per 1 MPa pressure drop) to 2004 (0.28 ms/km change) as the pressure drops from -13 to -25 MPa in 2002, to -49 to -59 MPa in 2004. Despite the large pressure decreases observed on the Shearwater field, the observed time-shift sensitivity of its Fulmar sands to pressure depletion (Table 3-3) still lies within the lower and upper range determined from the general rock-physics modelling in Chapter 2 (Figure 2-13 (b)) (although the modelling was performed for pressure decreases only up to -20 MPa, and for normally pressured sandstones with the same overburden shale). For the observed amplitude sensitivity to pressure depletion (Table 3-3), this is higher and lies outside the general range determined by rock-physics modelling (Figure 2-13). This is mainly because amplitude sensitivity is an interface property quantified using relative amplitude changes which rely on the reflection strength of the reservoir interface (Equation 2-20), and are thus, specific to the particular field.

Mechanism	4D seismic calibrated	Amplitude sensitivity (Equation (2-23))	Time-shift sensitivity (Equation (2-26))
Pressure depletion -ΔP (MPa)	Max.	1.97	0.56
	Min.	0.54	0.12
	Mean (2002)	1.41	0.34
	Mean (2004)	0.90	0.28

Table 3-3 Summary of quantified amplitude and time-shift sensitivity of the Upper Fulmar sands (92 m thick) to pore pressure decreases of -15 to -59 MPa, calibrated using multiple monitor 4D seismic data (2002 and 2004) on the HPHT Shearwater field. The sensitivity is not the same in 2004, as is in 2002.

3.3.2 Sensitivity calibration on the Norne field (segment G)

Located in the southern part of the Nordland II area in the Norwegian Sea approximately 100 km north of Aasgard Field, is the Norne Field, a horst block of approximately 9 x 3 km (Figure 3-3). The reservoir is enclosed and segmented by major faults with three segments (C, D and E) making the main field area, and the fourth segment, G, forming a small compartment disconnected from the main field area (Osdal et al., 2006). The reservoir rocks are sandstones of Lower and Middle Jurassic age dominated by fine-grained and well to very well sorted sub-arkosic arenites consisting of the Garn, Ile, Tofte and Tilje Formations.

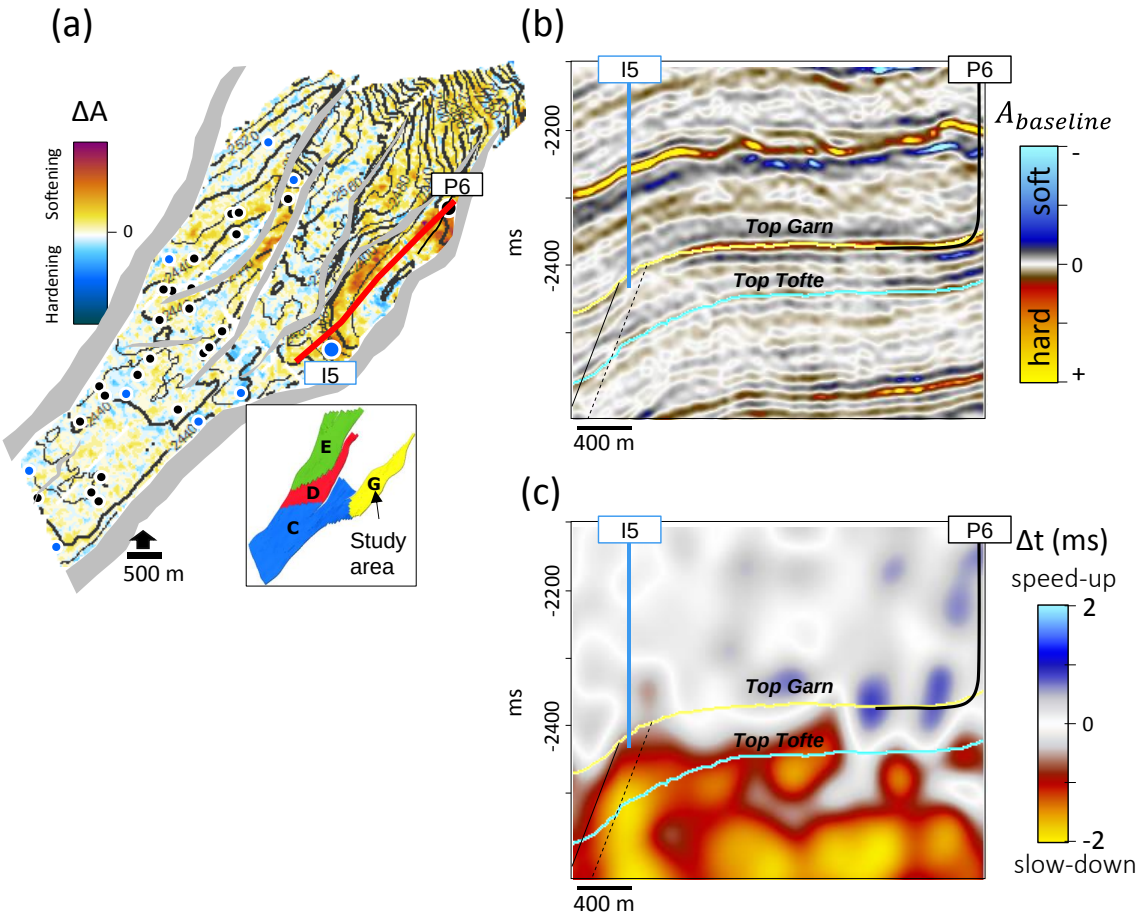

Figure 3-9 4D amplitude response (2006-baseline) map at top reservoir (Garn Fm.) showing strong softening signatures (dark red) due to pressure increase in compartment G along water injector I5 and producer P6. Inset map shows the reservoir segments (b) Vertical seismic section showing stratigraphy and a major fault (solid black) which separates segment G from other segments (c) Estimated 4D time-shifts showing speed-up anomalies from the injector, I5, due to pressure up. The time-shifts accumulate from top reservoir, with no observable time-shifts above the reservoir, other than noise-related artefacts.

The Garn formation was deposited near shore with some tidal influence and the Ile formation are shoreface sands. The Tofte formation are marine sands deposited foreshore to offshore and the Tilje formation was deposited in a marginal marine, tidally affected environment (Verlo and Hetland, 2008). The sandstones are buried at a depth of 2500-2700 m and are affected by diagenetic processes. Mechanical compaction is the most important process which reduced the reservoir quality. Reservoir quality reduces with depth but with porosities and permeabilities of 25–32% and 200–2000 mD, respectively, most of the sandstones are good reservoir rocks. Net-to-gross is close to 1 for most reservoir units but some are carbonate cemented.

In the top most reservoir unit, the Garn formation, all segments are gas filled except in segment G which contains oil in the upper most part, with near constant sand thickness of 30 m. Majority of the oil in the main segments (C, D and E) is found in the lower units, Ile and Tofte formations with a combined oil leg of 110 m, and together with the Garn formation, a gas cap of 75m. In the Ile, Tofte and Tilje formations, segment G is water filled. Reservoir connectivity in the main segment and in segment G is good, but shale and calcite permeability barriers and faulting have a major impact on reservoir production (Aarre, 2006). With the reservoir initially oversaturated, production strategy is pressure maintenance by water injection and water-alternating-gas (WAG) injection which started concurrently with first oil in 1997.

The first dedicated survey for 4D monitoring was acquired in 2001 and is the baseline survey. Subsequently, three monitor surveys in 2003, 2004 and 2006 have been acquired with data non-repeatability 20 to 40%. The reservoir unit of interest is the Garn formation with a thickness of around 30 m. The study area is segment G which initially contained oil and is the only area where strong pressure effects have been observed (Figure 3-9 (a) and (c)), causing a strong slow-down time-shift response from top reservoir downward. The segment has a horizontal producer in the oil leg and a vertical water injector in the water leg. Both wells are perforated only in the Garn formation, and there are no other wells in underlying reservoirs in this segment. Pressure drop from the producer which began producing in mid-2000 caused significant gas exsolution. The producer was intermittently shut down and a water injector was introduced in late-2001 to raise the pressure (Figure 3-10 (a) and (b)). Re-pressurisation from the injector caused gas dissolution back into oil with some of the gas also being produced. Validated

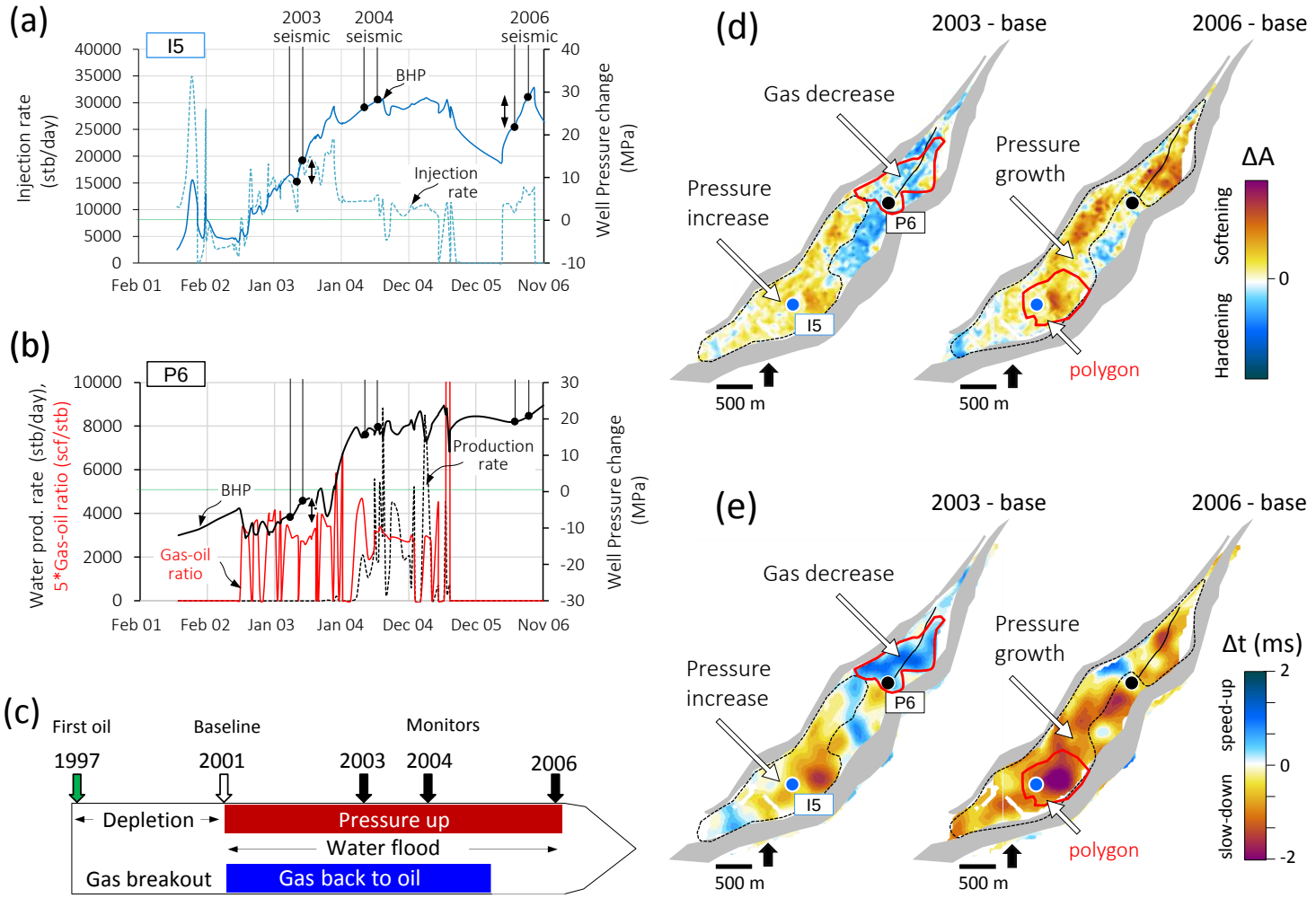

Figure 3-10 Linking well production to the 4D seismic response in segment G (a) Historical water injection rate (left y-axis) and simulated BHP change (right y-axis) for the injector, I5 (b) Historical Water production rate and gas-oil ratio multiplied by 5, both on the left y-axis, and simulated BHP change (right y-axis) for the producer, P6. (c) Timeline illustrating the production mechanisms that occur in this segment across the monitor survey times, filled areas are effects that dominate the 4D seismic amplitude responses in (d) and the intra-reservoir 4D time-shift responses in (e) , shown here for the 2003 and 2006 monitors. Polygons around the strongest signatures around wells for pressure increase and gas decrease are mapped for sensitivity calibration. Producer in black and water injector in blue.

by the water production rate from the producer which indicated water breakthrough in late 2003, there is also a water-flood front emanating from the injector towards the producer, but the effect of gas saturation decrease masks the effect of water in the 2003 monitor time (Figure 3-10 (d) and (e)). However, at this monitor time, strong pressure effects are observed firstly around the injector. The pressure signal grows over time and spreads further towards the producer in the later 2004 and 2006 monitor times, and with the producer being shut-off, the gas goes back into solution two years before the 2006 survey.

Further, using the history-matched simulation model predictions of pressure, water and gas saturation changes, the spatial extent and possible over-lap of the various effects was inferred (Figure 3-11). For example, the waterflood from the injector overlaps gas

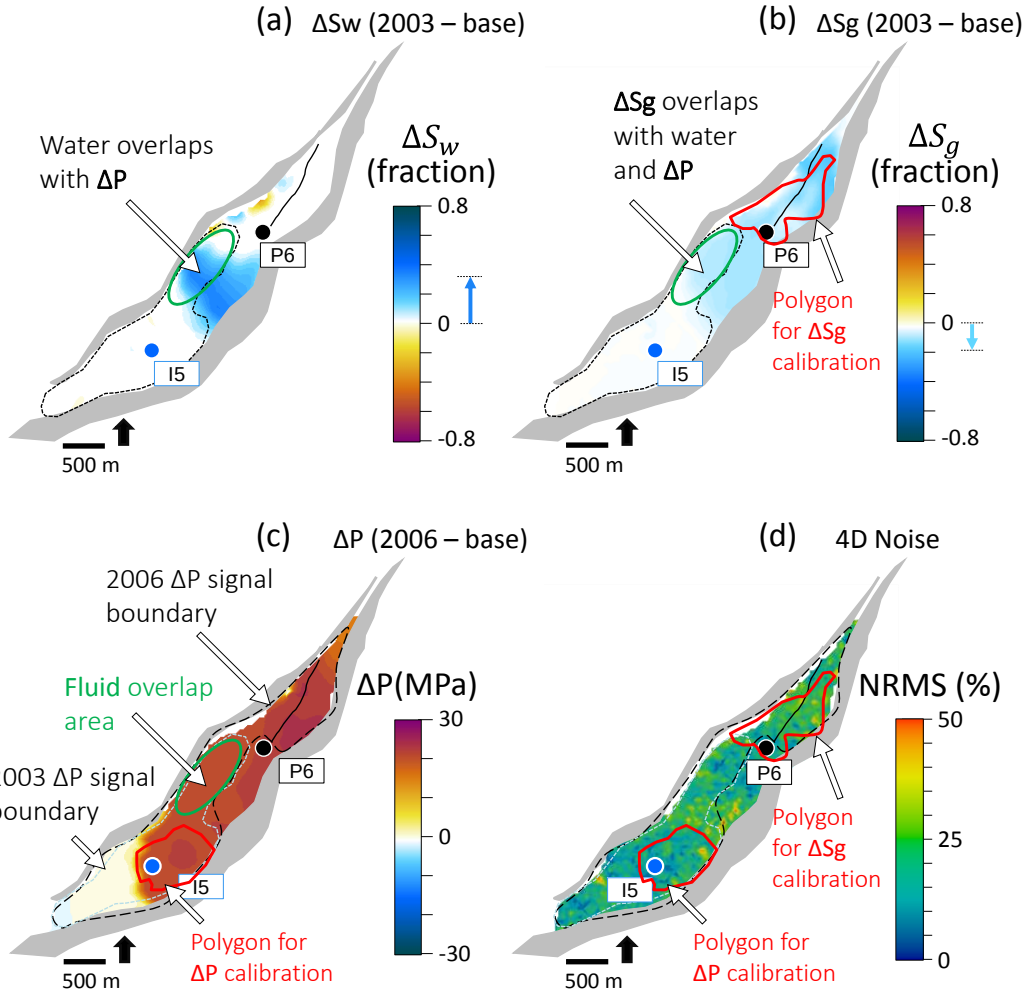

Figure 3-11 Depth-averaged maps over top reservoir of (a) water saturation increase (b) Gas saturation decrease and (c) pore pressure increase from the simulation model show over-lapping effects. The area for calibrating sole effects of ΔSg and ΔP is carefully selected. (d) NRMS values in this area. See also Figure 3-10.

saturation decrease towards the producer, which reinforces each other, but competes the pressure increase. Data quality in this segment G area is not optimum as the moderate non-repeatability noise levels suggest (Figure 3-11(d)), but the strong 4D seismic signatures gives confidence. Polygons were carefully mapped to highlight only areas with sole effects of pressure increase and gas saturation decrease, effects which contribute predominantly to the 4D seismic signatures in (Figure 3-10 (d) and (e)). Pressure increase effects can be observed in both 2003 and 2006 4D monitors, but gas saturation decrease effects are observed around the producer only 2003.

Cross-plots of the mapped 4D signatures versus the mapped changes in gas saturation and pressure from the simulation model are then obtained (Figure 3-12), with 4D amplitude and time-shift sensitivity computed using Equations 2-23 and 2-26. Summary of the range of sensitivity observed on the Norne field in segment G is provided in Table 3-4. In Figure 3-12, notice the magnitude of amplitude and time-shift responses to the simulated magnitudes of pressure increase around 15 MPa in 2003 and 26 MPa in 2006. Despite the extra 11 MPa pressure increase at the 2006 monitor time, the amplitude response (softening effect) shows little change between 2003 and 2006, but time-shifts however, show an increasing slow-down effect as pressure increases, which suggest that the time-shifts are more reliable. This observation is however tied to the amplitude maps appearing noisier than the estimated time-shift maps which are

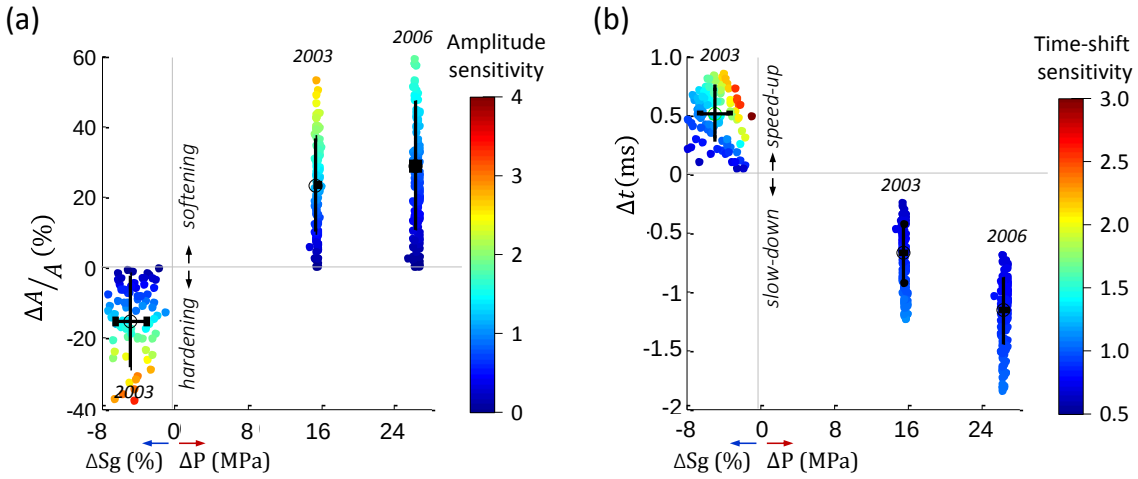

Figure 3-12 Cross-plot of (a) 4D relative amplitude changes and (b)4D intra-reservoir time-shifts, versus ΔSg decrease (left x-axis) and ΔP increase (right x-axis) for the 2003 and 2006 4D times in filtered polygon area shown in Figure 3-10 and Figure 3-11. Colour bar is the computed sensitivity (see Equations 2-23 and 2-26). In (a) and (b) the colours indicate that pressure sensitivity at the 2003 and 2006 monitor time are of similar scales, despite the big pressure increase from 15 MPa change in 2003 to 26 MPa change in 2006, relative to 2001 baseline time.

smooth and spatially consistent within the area calibrated, as indicated by the polygon (see Figure 3-10 (d) and (e)). Although, gas saturation decrease is less than 10%, similar magnitudes of amplitude and time-shift responses are observed in comparison to the big pressure changes, this is expected based on rock-physics understanding (Figure 2-10). Each data point has been colour coded by their respective sensitivity to pressure increase and gas saturation decrease.This is almost monotonic for pressure, suggesting near-homogenous sands in the small polygon area used. Likewise, even across the two monitor times, 2003 and 2006 a similar range of sensitivity is obtained, with a few outliers tied to noise variations across the monitor surveys.

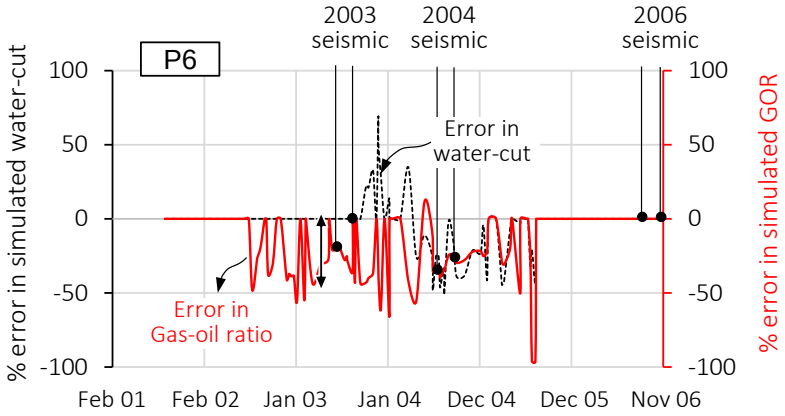

Figure 3-13 Estimating the uncertainty in simulation model predictions using percentage error. Shown is the percentage error in water-cut (left y-axis) and percentage error in gas-oil ratio (right y-axis) for the producer. The percentage error between the simulated and historic well production data is calculated relative to the historic data as, $\left(100\,\frac{simulated-historical}{historical}\right)$.

This implies that pressure sensitivity is relatively constant for the magnitude of pressure increases induced in the Garn Formation. The uniform effective porosity is 21% in this area as computed from the fluid-flow simulation model. This may be the case as the time-shift sensitivity (and amplitudes to some extent) suggests. Sensitivity to gas saturation decrease also shows some variability, the scatter along the horizontal axis is controlled by the spatial distribution of the gas saturation from the simulation model, the true gas distribution and magnitude in the area calibrated around the producer is not known with certainty. Figure 3-13 shows the error between the simulated and historic gas-oil ratio and water-cut for the producer, during the 2003 monitor survey, the average error in simulated gas-oil ratio is around 25%, and this is considered to be the uncertainty here.

The vertical axis in Figure 3-12 indicates different 4D seismic response to a similar change in gas saturation, suggesting inhomogeneous reservoir sands. Trends can be better observed in time-shifts. Effective porosity from the simulation model is however, a near homogenous value of 19%. Apart from reservoir heterogeneity, the variations are likely to be contributed by data non-repeatability noise, the magnitude of gas which is not completely known and intra-survey reservoir fluctuations (see Chapters 4 and 5).

Mechanisms	4D seismic calibrated	Amplitude sensitivity (Equation (2-23))	Time-shift sensitivity (Equation (2-26))
Pressure up +ΔP (MPa)	Max.	1.9	1.30
	Min.	0.32	0.33
	Mean	1.1	0.67
Gas sat. down -ΔSg (%)	Max.	3.1	2.5
	Min.	0.25	1.0
	Mean	1.67	1.8

Table 3-4 Summary of quantified amplitude and time-shift sensitivity of the Garn formation sands (30 m thick) to pore pressure increase and gas saturation decrease, calibrated using multiple monitor 4D seismic data on the Norne field.

3.3.3 Sensitivity calibration on the Heidrun field

The Heidrun field is located in the Haltenbanken region (blocks 6507/7 and 6507/8) off the coast of mid-Norway in water depths of 350 m (Figure 3-3). The field is a large fault-bounded structural closure dipping towards the south at angle of -5°, covering an area of approximately 75.7 km^2 (Figure 3-14). The reservoir is formed by a complex network of faults trending NNE-SSW and ESE-WNW, which divides the field into several segments and compartments. An analysis of the seismic data by Kahar et al. (2006) proposes faults as one of the fluid flow mechanisms controlling drainage. Seismic resolution allows the detection of faults with throws down to 10 m, but typically between 30 to 80 m (Reid et al., 1995). At depths ranging from 2175 m to 2475 m below sea level, the hydrocarbons are trapped in a triangular shaped, south dipping horst block (Figure 3-14(b)) and comprises of three reservoirs of Jurassic age grouped into two clastic sequences: the middle Jurassic Fangst Group containing the Garn and Ile Formations with exceptionally good reservoir characteristics and the early Jurassic Båt group containing the more heterogeneous Tilje and Åre Formations, which

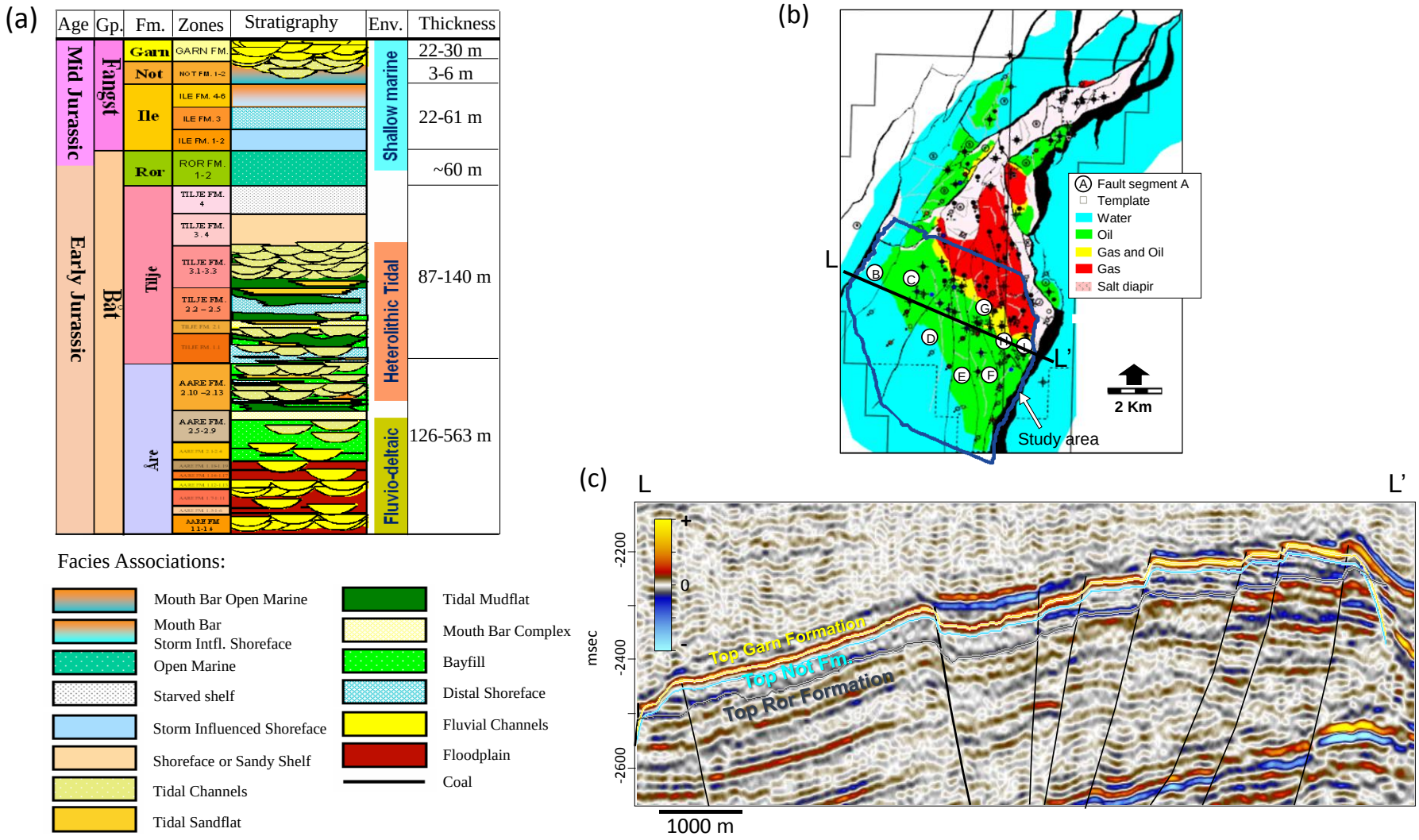

Figure 3-14 (a) Stratigraphic column of the Heidrun Field showing the two main groups Fangst and Båt and depositional environments of the four reservoir sands, Garn, Ile, Tilje and Åre (Modified from Statoil internal report) (b) Compartmentalisation and initial fluid distribution map of the Fangst Group (Benguigui, 2010) (c) Seismic section showing structural elements. Top reservoir (Garn Formation) is the focus for sensitivity calibration

are of substantially lesser reservoir (Harris, 1989) (Figure 3-14(a)). A thin shale, the Not Formation separates the Garn sands from the Ile sands and a thick shale, the Ror Formation separates the Fangst group from the Båt group.

The Garn formation, which is top reservoir, is the focus for sensitivity calibration. The Garn Formation consists of medium to coarse-grained, moderate to well- sorted sandstones, with some mica rich intervals, cross-bedded laminations, and occasionally carbonate cemented. The fluvial deposits represent a mixture of wave-dominated upper to middle shoreface sediments with progradations of braided delta lobes (Harris, 1989) and are the best quality sands with high permeability of 2500 to 5000 mD and high porosity of 24 to 32%. Discovered by Conoco and partners in 1985, the Heidrun field's recovery reserves are an estimated 186 million cubic metres of oil and 46.5 billion cubic metres of gas. The reserves consist of live oil (28° to 34.4° API) and primary gas cap accumulations (Figure 3-14(b)).

As the over-saturated oil reservoirs are initially at a pressure of around 26 MPa, a pressure maintenance strategy was implemented to drain the oil column which is up to 190 m thick. This included up-flank gas injection at the crest of the structure and down flank water injection, coupled with primary gas cap expansion, which began simultaneously with first oil in October 1995. During several campaigns, an intense infill drilling (77 producers, 25 water injectors and 2 gas injectors until 2011, of which only 17 producers and 8 water injectors perforate the Garn formation) has been conducted to accomplish an effective oil sweep. However, due to the fault complexity of the field, the prediction of drainage pattern, fluid saturations and contact movements has proven difficult. With the success of the first 4D seismic monitor in 2001, which helped to identify the remaining infill drilling targets (Furre et al., 2003), four additional seismic monitor surveys have been acquired in 2004, 2006, 2008 and 2011, with a merged baseline acquired in 1986/1991 prior to production start-up. The data quality is a moderate non-repeatability of 20 to 40% across the five monitors (Figure 3-15(a)), shows the spatial distribution of the computed NRMS for the 2001 and baseline seismic data, over an area of interest.

The 4D seismic amplitude signatures of the Garn formation is a clear example of a fluid saturation driven response over the 15.8 years of production history, from 2001

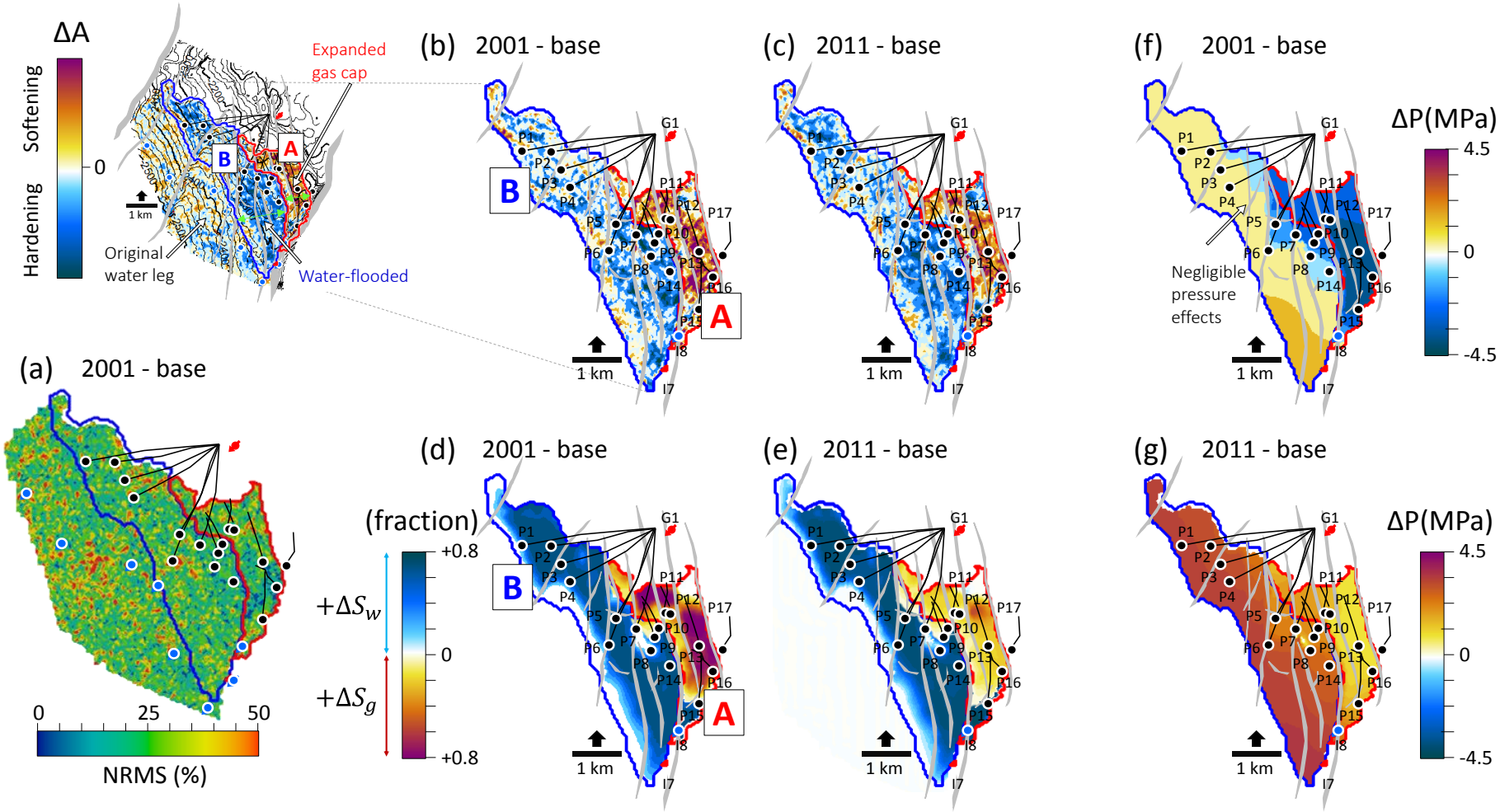

Figure 3-15 (a) Measure of 4D seismic data repeatability, NRMS map showing 10 to 50% variations. (b)-(c) 4D amplitude response over top reservoir (Garn Formation) showing hardening response due to water-flooding and softening response due to gas cap expansion for the 2001 4D monitor, and a slight reduction after 10 years of production for the 2011 4D monitor. Polygons B and A outline the extent of the water flood, and the extent of the gas cap expansion. (d)- (e) Depth-averaged maps of fluid saturation changes for both monitor times from the history-matched fluid-flow simulation model. Gas saturation maps overlain on water saturation maps to highlight the distinct areas each effect covers, both are positive changes. (f)- (g) Depth-averaged maps of pressure changes from the simulation model. Inset map in top left corner show the full study area, including the original (pre-production) water leg. Producers (in black), water injectors (in blue) and gas injector (in red).

(monitor) to 2011 (monitor) (Figure 3-15 (b) and (c)). Two large regions are mapped with polygons A and B, which represent the gas saturation dominated area (softening response), where gas saturation increases occur, expanding the gas cap, and the water saturation dominated area (hardening response) where oil has been drained and replaced by water, respectively. The predictions from the history-matched simulation model support the flood patterns seen in the 4D seismic amplitude maps (Figure 3-15 (d) and (e)). Water saturation increases occur in region B and gas saturation increases in region A. From 2001 to 2011, it can be observed that the water-flood signals remain of similar magnitudes (region B), but the 4D signals for gas diminish (region A) due to a decrease in gas saturation as a result of pressurisation and also due to the area being water-flooded by 2011 (see also Figure 6-8). As it is common for other effects to overlap, mild pressure changes (Figure 3-15 (f) and (g)) also compete against the strong saturation effects, although, severely disproportionate. Historic gas-oil ratios and water-cut for the producers in region A and B show the earliest gas breakout (higher than the initial 117 Sm^3/Sm^3 gas-oil ratio) and water breakthrough (non-zero water-cut) at the wells (Figure 3-16). In region A, producer P15, being the earliest activated well, shows higher gas-oil ratio prior to and at the 2001 monitor time, with more newly activated wells following suite (Figure 3-16(a)). As producer P15 is closest to the original oil-water contact, it also experiences water-breakthrough just after the 2001 monitor time (Figure 3-16(b)).

So, region A is certainly only gas saturation driven, apart from weak and negligible effects of pressure decreases of -5 MPa or lower. This agrees with the generalised rock physics modelling in Chapter 2 (Figure 2-10(a)). The 4D amplitude response of the high porosity unconsolidated sandstones A and B (which are similar to the Garn Fm.) to pressure decrease is much weaker than that to pressure increase or gas saturation increase. The gas saturation driven response of the Garn Fm. (Figure 3-15) is the case at the 2001 monitor time, and also at the 2004 monitor time which marks the onset of water-flooding in region A (see also Figure 7-10). As majority of the first producers were drilled in region B, water breakthrough at most of the wells occur prior to the 2001 monitor time (Figure 3-16(c)) which supports the water-flooded 4D signatures in both 2001 and 2011 monitor time relative to baseline (Figure 3-15 (b) and (c)). Much of the oil in region B has been drained prior to the 2001 monitor time, with five early producers shut by this time due to water breakthrough, leaving only five producers

which are intermittently active. The mismatch between the simulated GOR and historic GOR for producers in region A was calculated to be an underestimate of around 34%., although good consistency between the observed amplitude change (softening response)

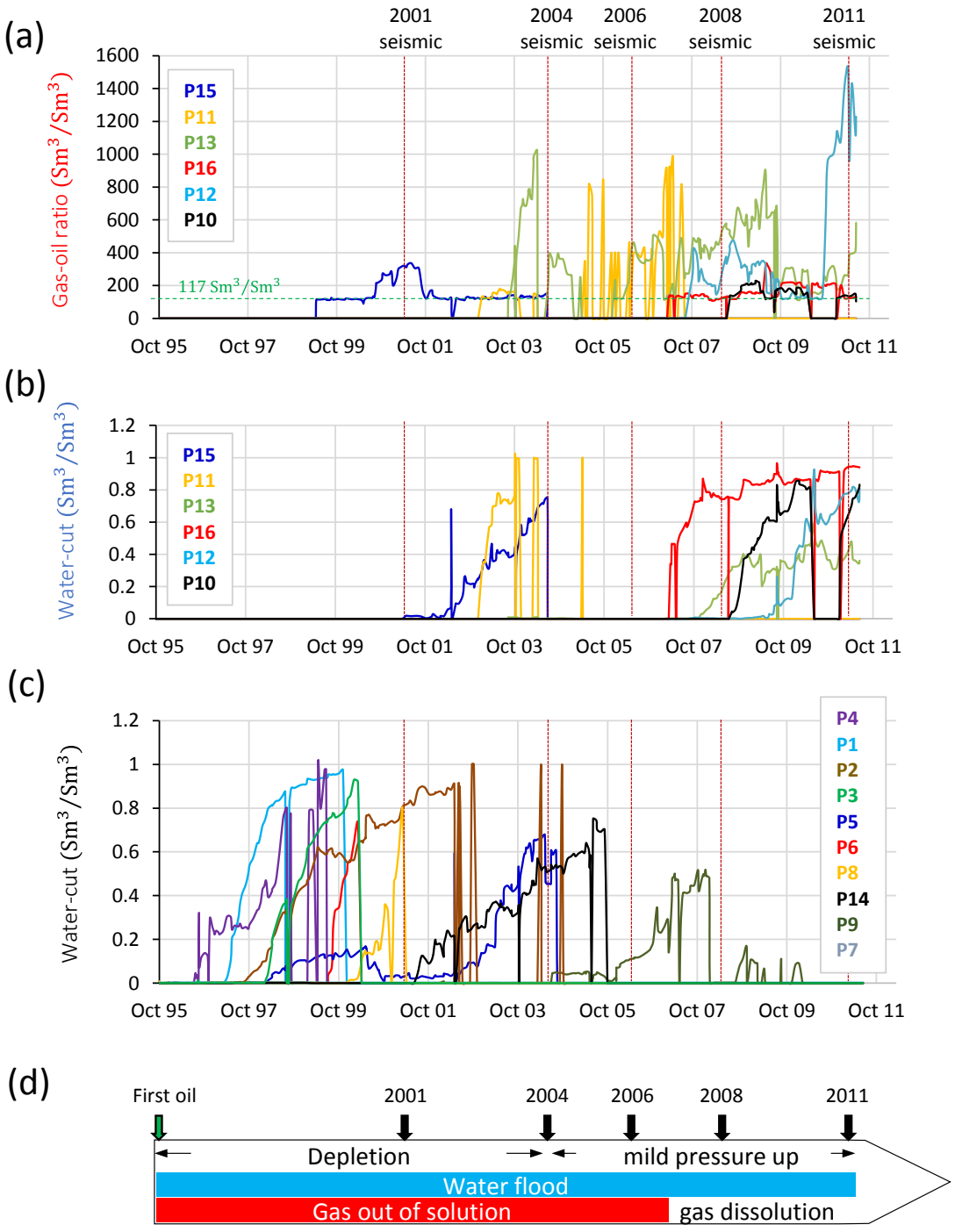

Figure 3-16 Historic production profiles for the producers perforated in the Garn Formation from production start in October1995 to last history date in July 2011, showing also the time of acquisition of the five monitor surveys. (a) Gas-oil ratio for producers in the gas dominated region A (b) Water-cut for same wells in (a) (c) Water-cut for producers in the water-flooded region B (d) Timeline of various mechanisms, filled areas are effects that dominate the 4D seismic signatures relative to baseline (see Figure 3-15).

and the predicted gas saturation change has been observed. For producers in the waterflooded region B, the water-cut mismatch was found to be around 30%. The best monitor times for calibrating both gas and water saturation sensitivity are the 4D seismic data from the 2001 and 2004 monitors because the influence of pressure change is minimum at these times. As pore pressure increases are very mild < +2 MPa in region B during these times, the water saturation responses are more authentic. In region A, pore pressure also increases after the 2004 monitor time, and water breakthrough prior to this time reveals that water saturation signals become more spatially extensive at monitor times later than 2004. Later monitors will thus yield a competing response against gas saturation effects (see also Figure 6-8 and 7-10). In the original water leg (outside regions A and B) which is perforated by water injectors, the softening response to pore pressure increases of up to 4 MPa are very weak and unclear, as the 4D amplitude response in this area appear to show similar patterns to the non-repeatability noise which is higher here (Figure 3-15).

For calibration, polygons with a radii of 200 m are used to extract the mean value of the 4D amplitudes around the producers in region A and B, as well as the mapped changes in gas and water saturation predicted from the simulation model during the 2001 and 2004 monitor times, cross-plots are given in Figure 3-17. In Figure 3-17(a), a rightward increase in water saturation should reflect a downward increase in the 4D amplitude magnitudes for a clean sand. However, porosity variations from well to well partially indicate that wells in lower porosity areas are less sensitive (with a lower 4D amplitude response) than wells in higher porosity areas, for example, from well P2, to P8 and to P7. Well P7 appears to have the lowest water saturation change but the biggest 4D amplitude response. Perhaps, the simulation model fails to predict the correct magnitude of water saturation at the 2001 monitor time, though this prediction agrees with the near-zero water cut in this well (Figure 3-16 (c)) which also suggests an erroneous historical measurement. Other wells cluster around water saturation changes of 60 to 70%, but exhibit varying magnitudes of amplitude changes.

In Figure 3-17(b) 4D amplitude signals around the five producers in region A show a general upward trend, with increasing amplitudes correlating to increasing gas saturation changes predicted from the simulation model. Correlations can also be found for specific wells, for example data points for well P11 and P12 at the 2001 and 2004 monitor time. The cleaner sands in this region are near homogenous with little

variations in porosity and are of generally higher porosity than in region B (Figure 3-17(a)).

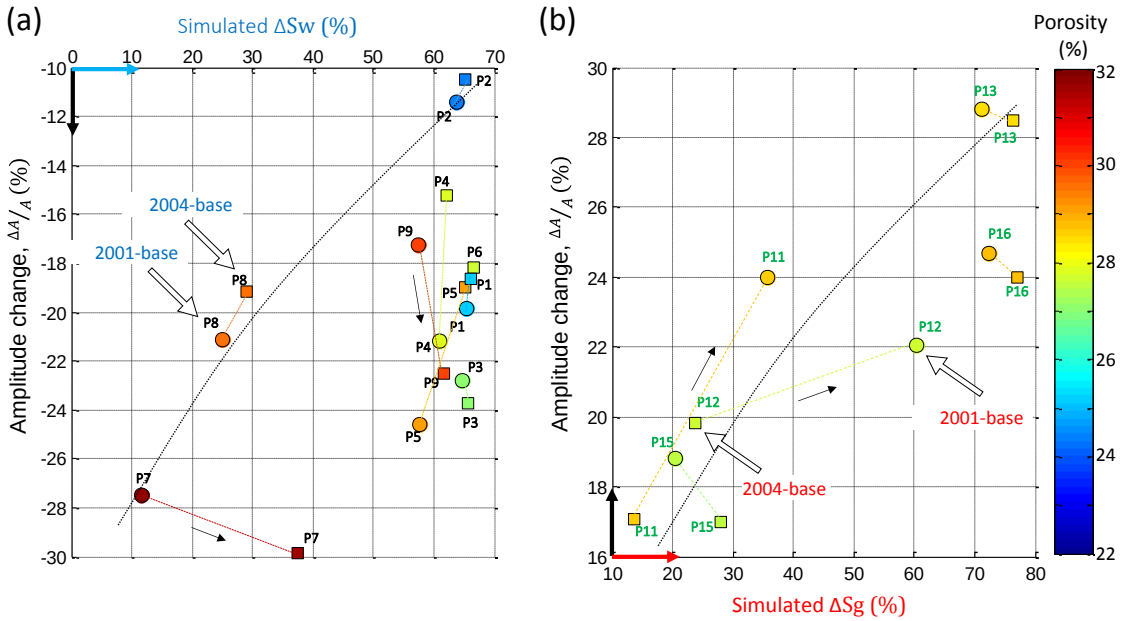

Figure 3-17 Cross-plot of (a) 4D relative amplitude changes versus water saturation changes, ΔSw, for producers in region B and (b) 4D relative amplitude changes versus gas saturation changes, ΔSg, for producers in region A. Data points are shown for the 2001 (circles) and 2004 (squares) 4D monitors. For regions A and B see Figure 3-15. Notice also the similar range of water and gas saturation increase in both times. Coloured lines connect data points for a specific well, and thin black arrows suggests trends.

Mechanisms	Areas	4D seismic calibrated	Amplitude sensitivity (Equation (2-23))
Water sat. up +ΔSw (%)	around wells	2001	0.34
		2004	0.32
	Map B	2001	0.31
		2004	0.28
Gas sat. up +ΔSg (%)	around wells	2001	0.64
		2004	0.77
	Map A	2001	0.55
		2004	0.71

Table 3-5 Summary of mean value of the quantified 4D seismic amplitude sensitivity for the Garn formation sands (30 m thick) to water and gas saturation increase. This was calibrated using two monitor 4D seismic data (2001 and 2004) on the Heidrun field both around wells and using a mapped region (see Figure 3-15). Between 2001 and 2004, the saturation sensitivities are of similar scales, both for gas and water saturation.

The average 4D seismic amplitude sensitivity to water and gas saturation increase for the Garn Formation sands are summarised in Table 3-5. The sensitivity is calculated

using the data just around wells, and also calculated using the filtered regions in polygon A and B earlier shown in Figure 3-15. At the 2001 monitor time, active producers in region A and B also experience a pressure decrease, which reinforces the hardening response due to water saturation increase and opposes the softening response due to gas saturation increase, so sensitivity for water saturation appears stronger in 2001 than in 2004, and sensitivity for gas saturation appears weaker in 2001 than in 2004. As a quality check, areas where pore pressure changes are expected to be strongest, particularly around the producers were eliminated from the maps to reduce the uncertainty from the water and gas saturation sensitivity estimations. These are compared against estimates around the wells, and are observed to be slightly smaller and bigger for water and gas saturation, respectively. The 4D seismic amplitude sensitivity to gas saturation changes is twice as big as that to water saturation changes.

3.3.4 Sensitivity calibration on the Schiehallion field

The final field for sensitivity calibration is the Schiehallion field which is located approximately130 km west of the Shetland Islands in the south-western part of the Faeroe-Shetland basin in water depths of 350 - 450 m (Figure 3-3). It was formed as a result of the Late Jurassic/ Early Cretaceous rifting of the north-western margin of Europe. The field is heavily compartmentalised and divided into four main segments by hydraulically uncommunicating faults, of which segments 1 and 4 are the focus in this study (Figure 3-18). The Schiehallion field was discovered in 1993 and production commenced in 1998, with estimated recoverable reserves between 425 and 600 million barrels (2 billion barrels in place), out of which 270 million barrels of oil have been produced as of 2010 (Gainski et al., 2010), and is operated by BP on behalf of the Schiehallion field partners (Shell - 55%, BP - 33.5% and OMV -11.8%).

Production of oil and associated gas comes from relatively thin, multiple stacked Paleocene turbidite channel and sheet-like sands (deposited in a slope/proximal basin floor setting) ranging in thickness from 5 to 30 m (Chapin et al., 2000). The majority of the clastic input to the Schiehallion field's reservoirs occurred during the Lower Palaeocene T30 sequence which is approximately equivalent to the Lista Formation in the North Sea (Freeman et al., 2008). The T30 sequence comprises of siliciclastic turbidites sands with the main oil bearing sands occurring (from bottom to top), in the

T25, T28, T31, T34 and T35 sequences (nomenclature based on the BP operational Tertiary nomenclature for the West Shetland Basin) (Gainski et al., 2010).

Much of the oil is produced from the T31 sequence subdivided into T31B and T31A (Figure 3-18(b)). The main focus for this study is the T31A sequence which is laterally more extensive, thicker and is of higher quality sand facies (high porosity of 25-30% and permeability 200-1000 mD) than the underlying T31B sands. A thin shale interval separates the two sequences.

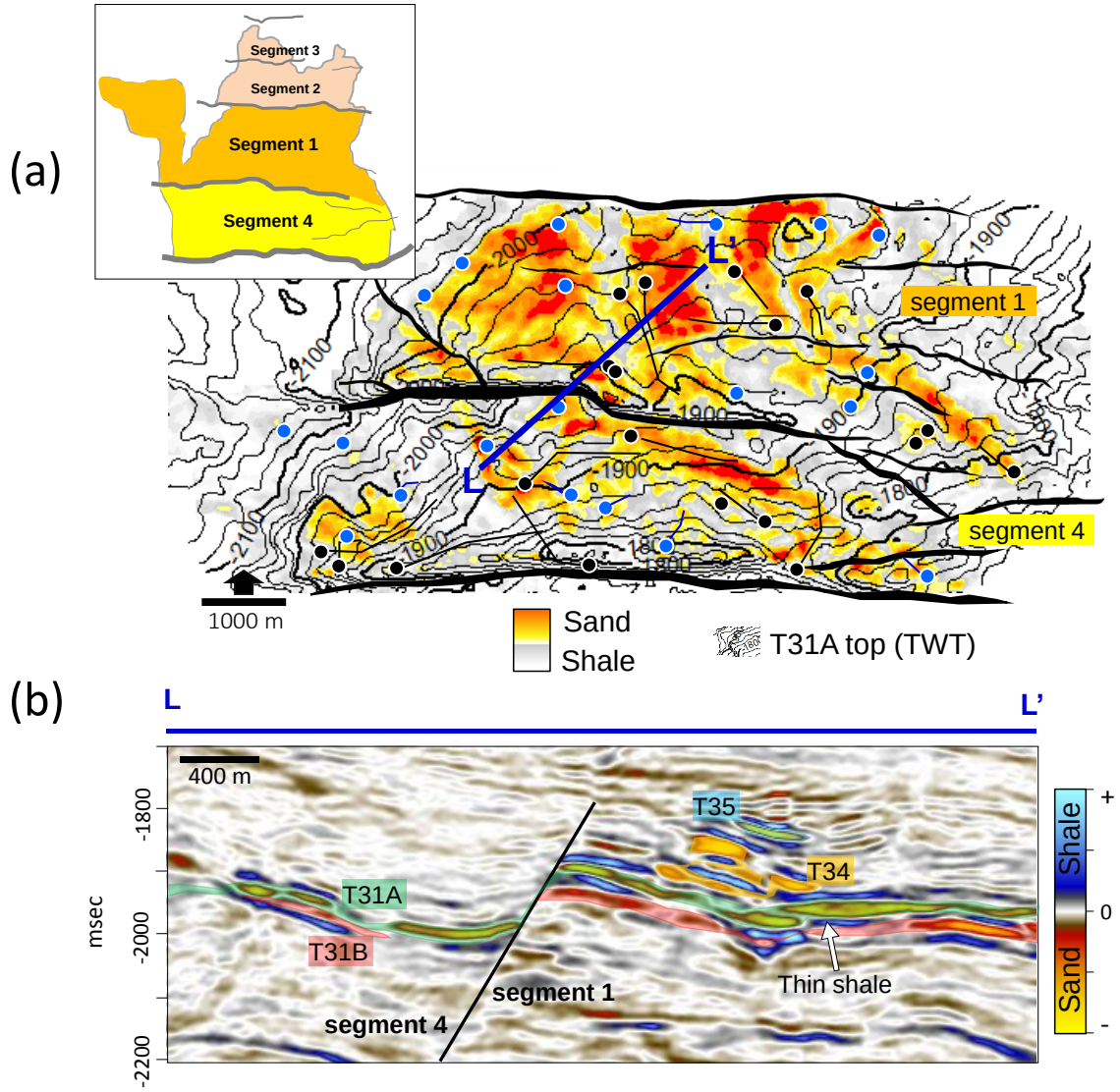

Figure 3-18 (a) RMS amplitude map of baseline seismic data over the T31A sequence (reservoir of interest) showing the sand channels in warm colours and well locations (water injectors in blue, and producers in black). Inset map shows the four main segments of the Schiehallion field (segments 1 and 4 are used in this study) (b) Vertical seismic section showing the distribution of the turbidite channels' sequences T31B, T31A, T34 and T35 in segments 4 and 1.

As the Schiehallion reservoirs contain live black oil accumulations (25° API) at an initial pressure of 20 MPa at 1940 metres TVD (top reservoir), very close to the bubble point pressure (19.4 MPa) and also small local gas caps, a pressure maintenance production scheme was implemented to develop the field. This involved a waterflood regime using down-dip water injectors and up-dip producers. As of 2010, around 22 oil producers and 24 water injectors have been drilled. Five monitor surveys (1999 to 2008) have been acquired with average non-repeatability noise 30 to 60% in post-stack (full offset stack) seismic data. Production mechanism has been to maintain the reservoir above bubble point pressure through water injection but connectivity is a main problem. In the early monitor surveys acquired (1999, 2000 and 2002), gas exsolution occurred and during these times, gas saturation signals dominated the 4D seismic amplitude signatures, but these are not available for this study. In the later monitor surveys (2004, 2006 and 2008), which are available for this study, new infill water injectors induced re-pressurisation causing some of the gas to go back into solution. It is therefore these later monitor surveys that are calibrated for both pressure and water saturation sensitivity.

Figure 3-19 shows the 4D amplitude response of the T31A sands at the 2004 and 2008 monitor time together with depth-averaged maps of pressure and water saturation from the fluid flow simulation model. At the 2004 monitor time, pressure increase responses have been identified using polygons A and B in both segments 4 and 1, respectively, which appear to be compartmentalised. Areas of strong water saturation effects (hardening) are particularly located around the many injectors in this field (for example, I2, I1, I3, I4) and at the 2008 monitor time, this is more wide spread as the flood front grows from the original oil-water contact (OOWC), evident also around injector I17 which had been switched off after the 2004 monitor survey. Notice also the weaker hardening response to water saturation effects in segment 4 compared to segment 1, which corroborates the smaller magnitude of water saturation changes in segment 4. Some softening effects due to gas saturation increase which occurred in the early stages of production can still be observed in areas dominated by producers, but this is dampened by the competing effects of both pressure and water saturation changes.

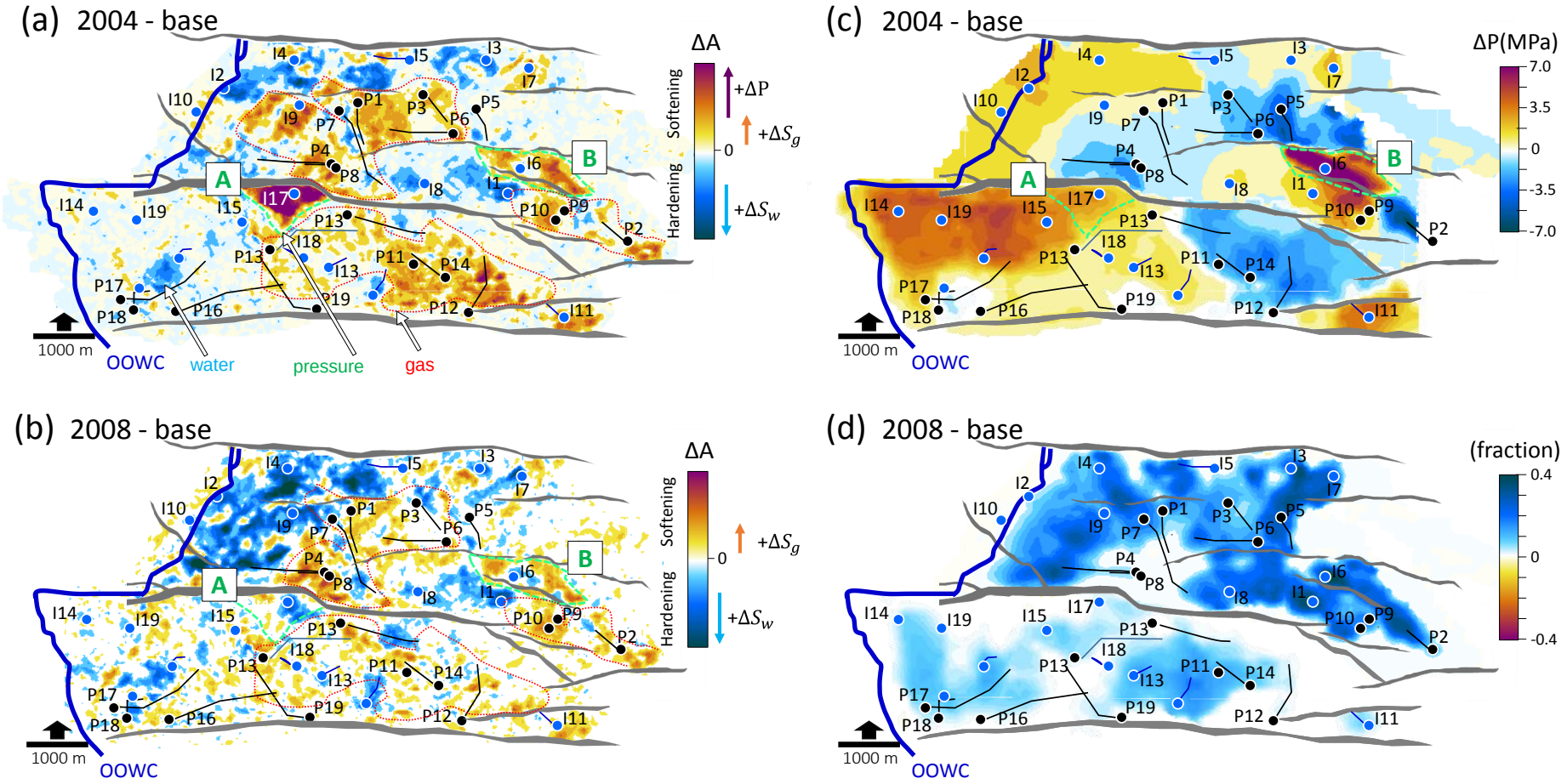

Figure 3-19 (a)-(b) 4D amplitude response of the T31A sands of the Schiehallion field shown for the 2004 and 2008 monitor time (c) Depth-averaged map of pressure changes at the 2004 monitor time predicted by the history-matched fluid flow simulation model (c) Depth-averaged map of water saturation changes at the 2008 monitor time predicted by the history-matched fluid flow simulation model. In (a) the green dashed polygons, marked A and B, highlight two compartmentalised pressure injection response (softening effect) with a single water injector I17 (in segment 4) and I6 (in segment 1). Competing effects of underlying water saturation changes can be inferred developing around I6, giving a near zero 4D amplitude response around the well. In (b) the I17 well is turned off a year after the 2004 monitor time, and thus only water saturation effects which was previously obscured by the strong pressure increase response can now be observed. Water saturation increase effects (hardening) are wide spread around injectors, and particularly, in segment 1. Water injectors are in blue and producers are in black.

The injection activity and BHP pressure changes for the two wells, I17 and I6 associated with the compartmentalised pressure response (annotated in Figure 3-19) are given in Figure 3-20 and Figure 3-21, respectively. Water injection from injector I17 starts in 2003, and the biggest magnitudes of pressure change is 17 MPa which occurs during the 2004 monitor time, with the well shut down just one year later in 2005 (Figure 3-20(a)). In the 4D seismic responses (Figure 3-20(b)), the associated big amplitude changes (softening response) can be observed, overriding any onset of waterflood around the well. However, as the well is switched off long before the 2008 monitor time, the opposite polarity of the 4D amplitude response (hardening) is observed, revealing the pure water saturation increase effects localised around the well which were previously over-ridden by pressure effects.

Likewise, injector I6 starts-off months earlier than I17 and is injecting at almost twice the rate (Figure 3-21(a)), meaning that the flood front around I6 has had some time to expand before the 2004 monitor. In the 4D seismic response for 2004- baseline (Figure 3-21 (b)), what is observed around I6 is a cancellation effect as water saturation increase competes against pressure increase, but elsewhere within the compartment, the amplitude response corresponds to pressure increases of around 11 MPa. At later monitor times, I6 injects intermittently, but the slight up rise just before the 2008 monitor time (after which it is switched off) causes a softening response outside the vicinity of I6. However, the hardening effect due to the developing flood front is now stronger around the well; owing also to the smaller induced pressure of magnitude of around 5 MPa. Both effects still compete around the well. Using these two compartments as examples, pressure sensitivity is best quantified at the 2004 monitor time and outside the vicinity of the wells where water saturation competes. As I7 is switched off a year and some months before the 2006 monitor time, the water saturation effects are unbiased as there are no induced pressures at the 2006 or 2008 monitor time. Since the compartments are quite small (<0.8 km^2), the sands can be assumed to be experiencing the same pressure as at the wells.

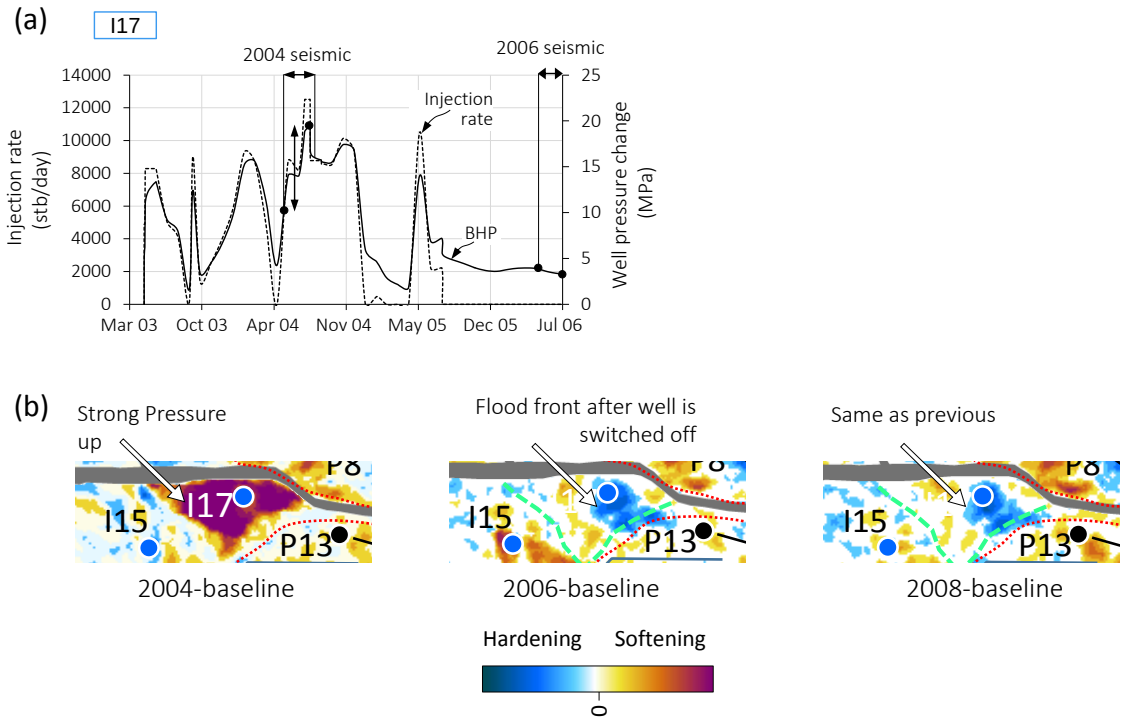

Figure 3-20 Linking (a) well injection activity to (b) the compartmentalised 4D seismic response annotated as polygon A in segment 4 in Figure 3-19. Well profile is for historical water injection rate (left y-axis, dashed lines) and historic BHP change (right y-axis) for the injector, I17 in compartment A.

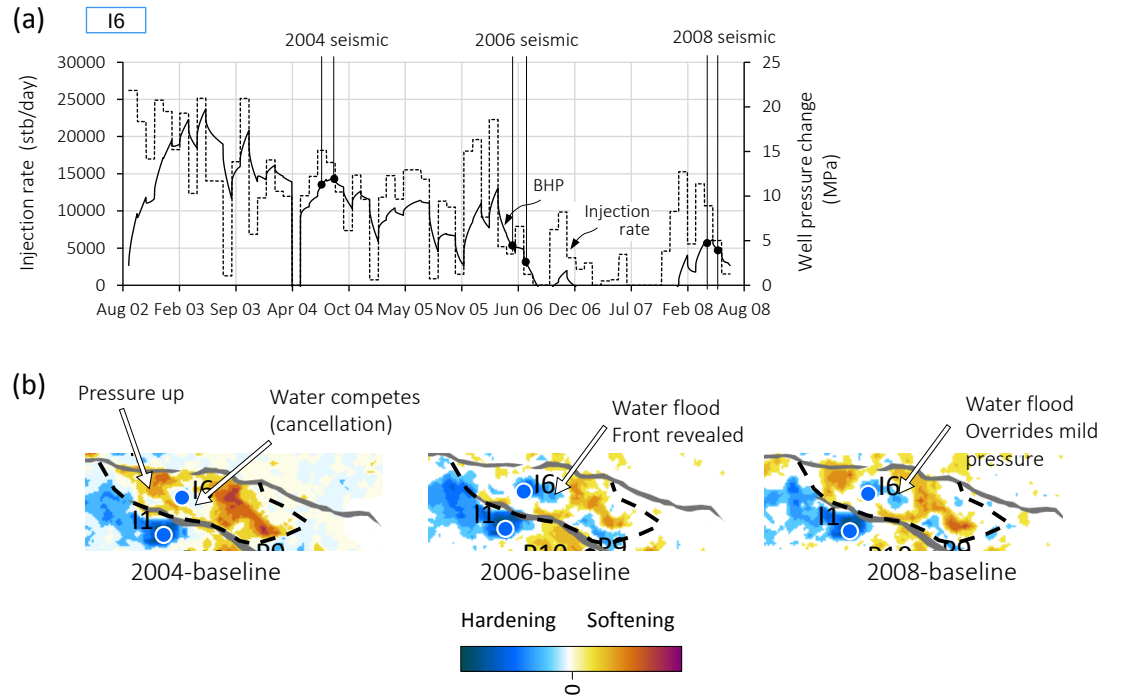

Figure 3-21 Linking (a) well injection activity to (b) the compartmentalised 4D seismic response annotated as polygon B in segment 1 in Figure 3-19. Well profile is for historical water injection rate (left y-axis, dashed lines), and simulated BHP change (right y-axis) for the injector, I6 in compartment B.

Table 3-6 details the quantified sensitivity with very similar water saturation sensitivity across the 2006 and 2008 monitors, as to be expected.

Mechanisms	4D seismic monitors	Amplitude sensitivity (Equation (2-23))	Standard deviation
Pressure up +ΔP (MPa)	2004	1.56	0.88
Water sat. up +ΔSw (%)	2006	0.44	0.05
	2008	0.49	0.11

Table 3-6 Summary of quantified 4D seismic amplitude sensitivity (mean value) of the T31A sand sequence (5 to 30 m thick, mostly around 25 m thick) to pressure increase and water saturation increase, calibrated using three monitor 4D seismic data on the Schiehallion field in the compartment regions (see Figure 3-20 and Figure 3-21). The standard deviation is simply the variation of sensitivity in the areas calibrated.

3.4 Summary of quantified sensitivity using 4D seismic data on four fields

In this chapter a data-driven map-based interpretation method was applied on four North Sea fields to quantify the in-situ reservoir's sensitivity to pressure, water and gas saturation changes using 4D seismic data. The fields included a high-pressure-high temperature (HPHT) gas condensate (the Shearwater field) and three normally-pressured oil-water-gas fields (Schiehallion, Norne and Heidrun) (Table *3-7*).

Clastic fields	Reservoir	Environment	Rock type	Thickness (m)	Porosity
Heidrun	Garn Formation	Shallow marine	Unconsolidated	25 - 30	24 to 32%
Schiehallion	T31A sands	Turbidite deep water	Heterogeneous stacked soft sands	5 - 30	25 to 30%
Norne	Garn Formation	Near Shore	Slightly consolidated	20 - 35	18 to 24%
Shearwater	Upper Fulmar	Shoreface deep water	HPHT poorly consolidated	92	20 to 30%

Table 3-7 Properties of the reservoir formation used for sensitivity quantification across the four fields.

Both 4D seismic amplitudes and intra-reservoir time-shifts from multiple monitor seismic data were used to calibrate the 4D seismic response to different production effects observed in the field. Figure 3-22 shows the range of 4D seismic amplitude and time-shift sensitivity observed across the fields. Thus the quantified seismic sensitivities

can be linked to the specific geology of the field. In Figure 3-22(a), the soft turbidites of the Schiehallion field are more sensitive to pressure increase than the consolidated Norne sands, as to be expected.

On the asymmetry between pressure decrease and pressure increase, the sensitivity to pressure increase is expected to be at least twice that of pressure decrease, the HPHT shearwater field overturns this expectation. As it is in a highly stressed state, its amplitude sensitivity to pressure depletion lies on a similar scale, if not higher than those of the normally–pressured Schiehallion and Norne field which respond to pressure increase. Contrarily, the expected asymmetry is maintained using the 4D seismic time-shifts (Figure 3 22(a)). The Norne field's time-shift sensitivity to pressure increase is of a slightly higher sensitivity than those of the Shearwater's field to pressure decrease. Despite the big magnitudes of pressure decrease of up to -59 MPa observed on the Shearwater field, it is interesting to see that the time-shift sensitivity falls in the higher end, but still within the generalised rock-physics modelling in Chapter 2, which was calculated for pressure decreases of up to just -20 MPa. Although in a highly stressed environment, the Upper Fulmar sands still behave like a normally-pressured sandstone, when the intra-reservoir time-shifts are analysed. Physical thickness changes (i.e. compaction) lies between 0 and 1 millistrain (Staples et al., 2007), which is negligible.

Although just on two fields, the time-shift sensitivity falls within the wide range obtained from the generalised rock-physics results Chapter 2, whereas amplitudes do not, even for water saturation. This is because the amplitudes are an interface property, and as they are expressed as a percentage change relative to baseline, they are dependent on the reflection contrast, specific to the particular reservoir and different interfaces. This reveals that time-shifts are a more robust attribute when linking the observed 4D seismic response to the rock-physics modelled response, for a number of reasons; seismic velocity changes in a producing reservoir may be observed as either time-shifts of reflections below the reservoir or amplitude changes of reflections from within the reservoir or at its boundaries. Amplitude changes are caused by altered impedance contrasts in the vicinity of the bounding reservoir interfaces. Such a response could therefore be influenced by local anomalies and intra-reservoir inhomogeneities.

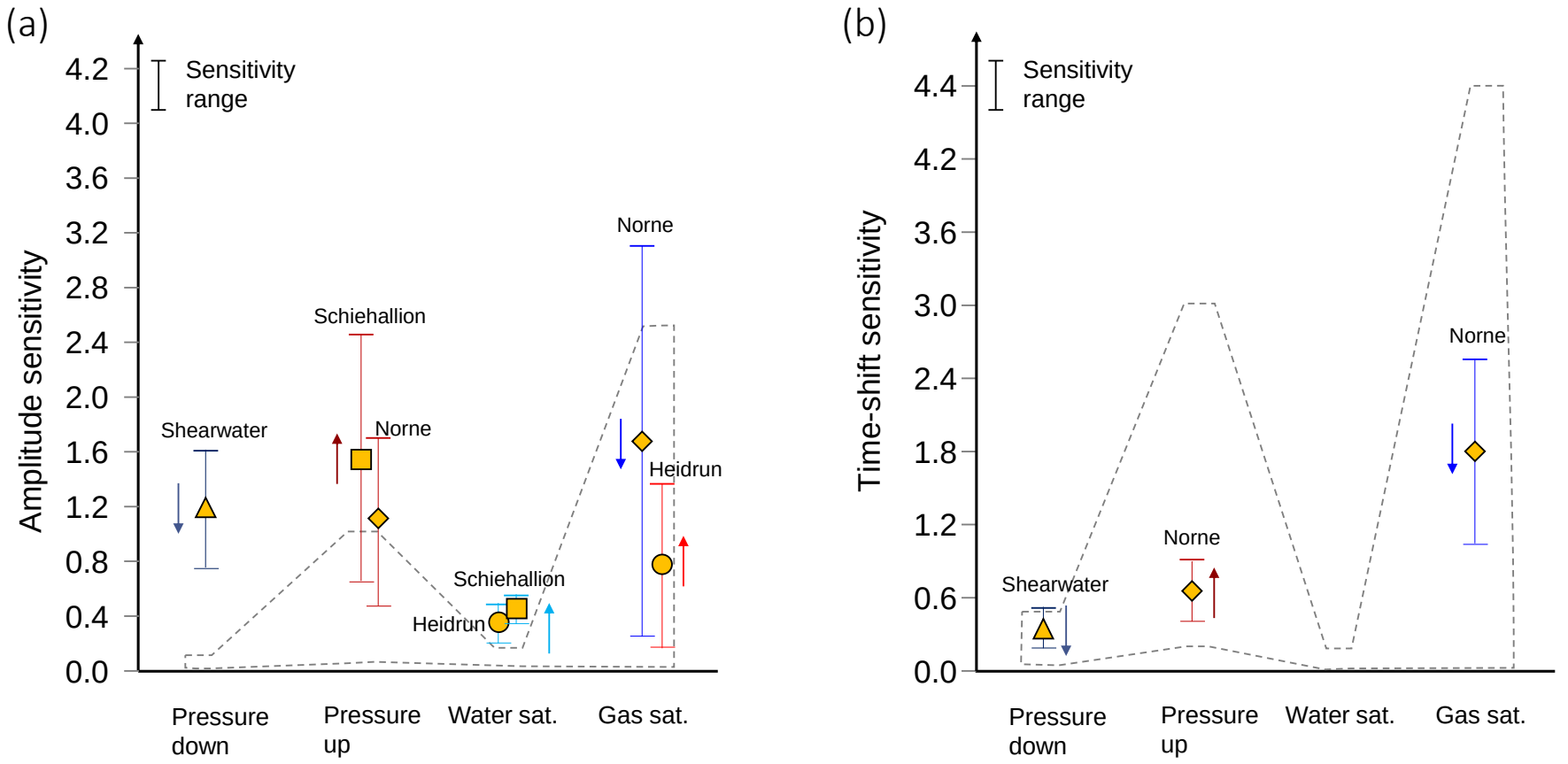

Figure 3-22 Summary of quantified values for (a) 4D amplitude sensitivity (Equation 2-23) and (b) 4D time-shift sensitivity (Equation 2-26) obtained for four North Sea fields by quantitative interpretation of multiple monitor 4D seismic data to pressure and saturation measurements (or predictions). The dots represent the mean value from the areas calibrated for each field. The spread from the mean is also shown, suggesting variations in reservoir sensitivity within a field and from field to field. The grey dashed outline is the range obtained from the generalised rock-physics modelling in Chapter 2 (see Figure 2-13). Note that sensitivity to pressure has been calculated for a unit change in MPa, and sensitivity to fluid saturation for a unit change in percentage (%). Downward arrows indicate a decrease, and upward arrows, an increase in pressure or saturation.

For thin reservoir intervals, the response will depend significantly on the reservoir thickness, which needs to be precisely known for a correct quantitative interpretation. Time-shifts of seismic waves which have passed through the entire reservoir integrate the local velocity changes and can potentially provide a more robust measure of the average changes in the reservoir. The intra-reservoir time-shifts are in effect an interval property, and thus, a more volumetric attribute. Sensitivity to gas decrease or increase are much higher than those associated with water saturation changes. The dispersion in gas saturation sensitivity across Heidrun and Norne fields, compared to water saturation sensitivity on the Schiehallion and Heidrun field confirms this.

3.5 Some remarks

A technique for quantifying pressure, water saturation and gas saturating sensitivity using multiple monitor seismic amplitude and time-shift data has been successfully applied to four offshore clastic reservoirs. This method is transferable to other field types e.g. carbonates and could fill the gaps in rock-physics derived or laboratory-based measurements of pressure/ saturation sensitivity. This is due to the value of 4D seismic data as an in-situ field-scale measurement of the reservoir's response with better reliability over the production life time of the field. The practical limitations of the technique are that only production mechanisms that occur and are interpretable on the 4D seismic signatures can be used, overlapping effects of pressure and saturation changes adds to the complexity, and the need for an acquired monitor survey. The uncertainties concerned with sensitivity quantification are measurement errors from historic production / well pressure data, predictions from the fluid flow simulation model (where used), and 4D seismic data non-repeatability. Finally, I note the implications of using post-stack seismic data for pressure and saturation related studies (as to be addressed in the next chapter) but justify this practical approach to be effective in areas with sufficiently large 4D seismic signals. A natural extension of this technique for sandstone reservoirs is to combine multiple monitor 4D seismic data in an inversion scheme to estimate the reservoir's sensitivity at each seismic bin location and for different offset stacks (to be addressed in Chapters 6 and 7).

Chapter 4

Intra-survey reservoir fluctuations- the reservoir dynamic domain from the perspective of the seismic acquisition

"The cure for boredom is curiosity. There is no cure for curiosity."

-- Dorothy Parker, US author, humorist, poet, & wit (1893 - 1957) --

With a simple question, "what is the reservoir doing during shooting of monitor seismic data?" this chapter investigates the ability of typical seismic surveys to accurately capture the fluctuating changes that occur in the reservoir during the acquisition. Seismic data acquisition takes many weeks to complete, pressure and saturation may fluctuate spatially due to field production and operational procedures within this time. The spatiotemporal relationship between such physical processes in the reservoir and the time sequence of shooting and geometry of the acquisition is examined here through a reconstruction exercise. This uses real field monitor acquisitions of a towed streamer and a permanent reservoir monitoring (PRM) survey shot in the North Sea, and fine timescale simulator predictions from the history-matched Norne field model. The work reveals that the pre-stack distribution in any CMP location is a combination of the reservoir changes acquired at different times during the shooting, and thus the resultant post-stack (i.e. average) is not a true representation of the reservoir change at any location. This analysis continues in Chapter 5.

4.1 Timescale of seismic surveys

Seismic surveys (onshore or offshore) are not shot instantaneously. Apart from areal coverage, the time taken to acquire seismic data depends on a broad range of practical operational and logistical considerations, which also influence to some extent the sequence and timing with which the surveys are shot.

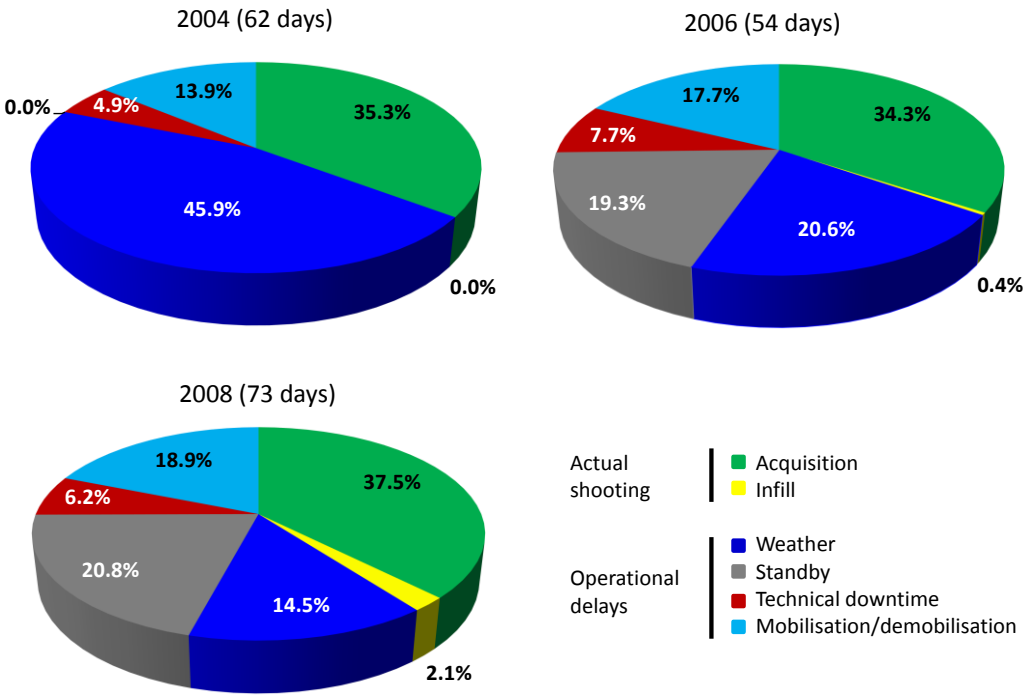

Figure 4-1 Breakdown of survey activity for three consecutive towed streamer monitor surveys shot over the Schiehallion field, covering an area of 420 km^2. Data sourced from BP internal report by Western Regent (2004), Western Monarch (2006) and MV Geowave Master (2008). A number of operational factors especially weather sea conditions determine the duration of the surveys.

For example, towed streamer data are dependent on boat speed, boat turn-around, offset coverage, the effect of tides, platform and facility obstructions, additional field activity and bad weather downtime. Figure 4-1 provides further detail on the general contributions of such factors to the survey duration for three 4D dedicated towed streamer (dual source and 10 x 3000 m streamer configuration) surveys shot over the Schiehallion field. The three surveys are acquired two years apart and lasts for 62 days (2004), 54 days (2006) and 73 days (2008), covering an area of 430 km^2. The actual shooting (acquisition plus infill) takes less than 40% of the total survey time. Bad weather delays appear to be the main contributor to this delay, compared to technical downtime or other operational restrictions. On the Heidrun field, for example, a

monitor towed streamer data acquired between April and July 2011 takes around 84 days for an area of 224 km^2. Breaks in the acquisition of more than 25 days in June occurred, due to other activities in the area, which led to the survey being completed later in July of the same year (Fischer et al. 2013). As a consequence, mostly due to bad weather, a typical North Sea towed streamer survey of 250 km^2 can take six to eight weeks to complete (Campbell et al. 2005, Ross et al. 2010).

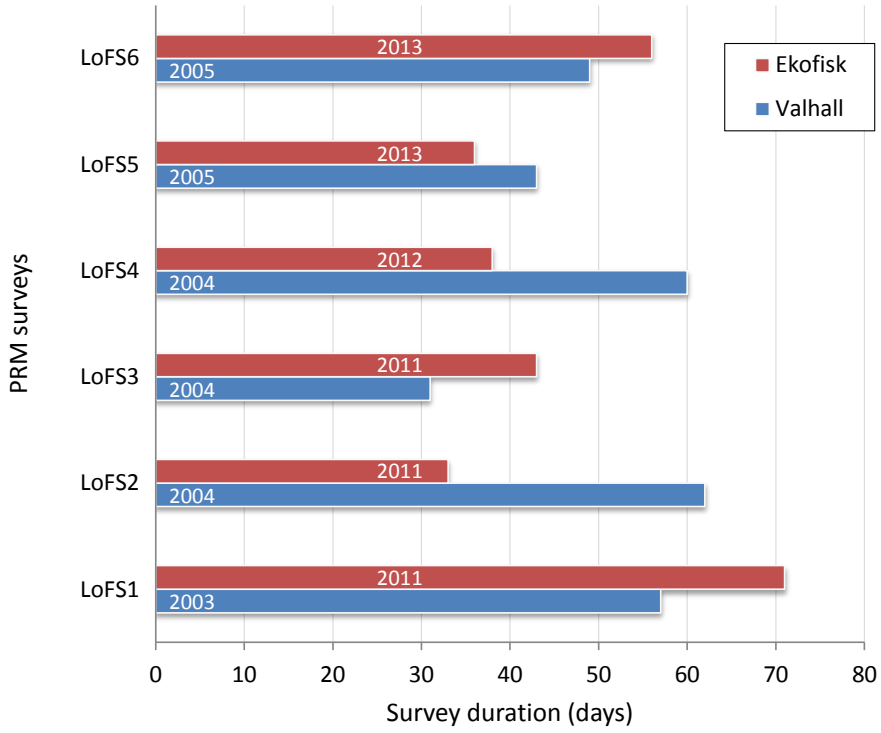

Figure 4-2 Acquisition year and durations (including weather delays) of the first six consecutive Life of field seismic (LoFS) surveys at two North Sea fields, Valhall field (in blue) and Ekofisk field (in red). Data sourced from Corzo 2009 for the Valhall field and Bertrand et al. 2014 for the Ekofisk field.

Permanent reservoir monitoring (PRM) with ocean-bottom cables cover a smaller area but with a higher shot density, and thus, will also take months to complete (Corzo, 2009, Bertrand et al. 2014). Whilst permanent reservoir monitoring with ocean-bottom nodes is not restricted by large streamer or cable dimensions, nevertheless such surveys can still take a few months to cover similar but higher fold area of 20 km^2 to 120 km^2 due to weather and operational restrictions (Eriksrud 2014, Farmer et al. 2015, Vaxelaire et al. 2007, Thedy et al. 2015, Vieira et al. 2011). On the Valhall field, six consecutive PRM surveys (also known as Life of Field Seismic, LoFS) acquired three months apart take 31 to 62 days to shoot an area of 45 km^2. Almost a decade later, six LoFS surveys acquired six months apart on the Ekofisk field take 33 to 71 days for an

area of 60 km^2 (Figure 4-2). On land, survey time is strongly affected by the complexity of terrain, weather conditions, equipment availability, physical obstructions and environmental constraints. Land surveys are clearly expected to take longer than towed streamers to cover a comparable area (Aouad et al. 2012, McWhorter et al. 2012). New onshore PRM technologies like SeisMovie™ cover a much smaller area, and take less than a day to complete (Hornman and Forgues 2013) which could be considered instantaneous and are unlikely to be impacted by intra-survey reservoir fluctuations.

Reservoir Processes	**Timing**
Depletion	
Pressure falling	Years
Gas out of solution at bubble point	Days
Aquifer movement	Years
Water coning leading to rise in watercut	Months
Baffles and compartments appearing	Days/weeks
Water Injection	
Repressurisation	Months
Movement of flood front through well	Days/months
Reservoir seal failure	Days
Gas integrity at surface	Months
Water overrun	Months
Gas Injection	
Repressurisation	Months
Reservoir seal failure	Days
Gas integrity at surface	Months
Gas underrun	Months
Enhanced Oil recovery (EOR)	
High/low salinity flood	Years
Miscible/immiscible gas injection	Months
Polymer injection	Months
Thermal flood	Months

Table 4-1 Familiar reservoir processes and timelines (Watts and Marsh 2011). Of particular interest are those effects with similar time scales to the 4D surveillance.

4.2 Timescale of reservoir processes

In the reservoir, several processes possess a similar time scale to the acquisition (Table 4-1), and are controlled by operations management, specific to the well and field under consideration. Activities such as injector or producer well shut-off or re-start/start, alteration of a rate/choke setting, well tests, bumping/slugging, and squeeze treatment (Watt and Marsh 2011) occur independent of the acquisition and are known to cause reservoir pressure fluctuations, which will also affect saturations as well. Pressure is also affected by turn-around, production optimisation, work-overs, evolving water cuts, and the introduction of new wells or re-introduction of old wells.

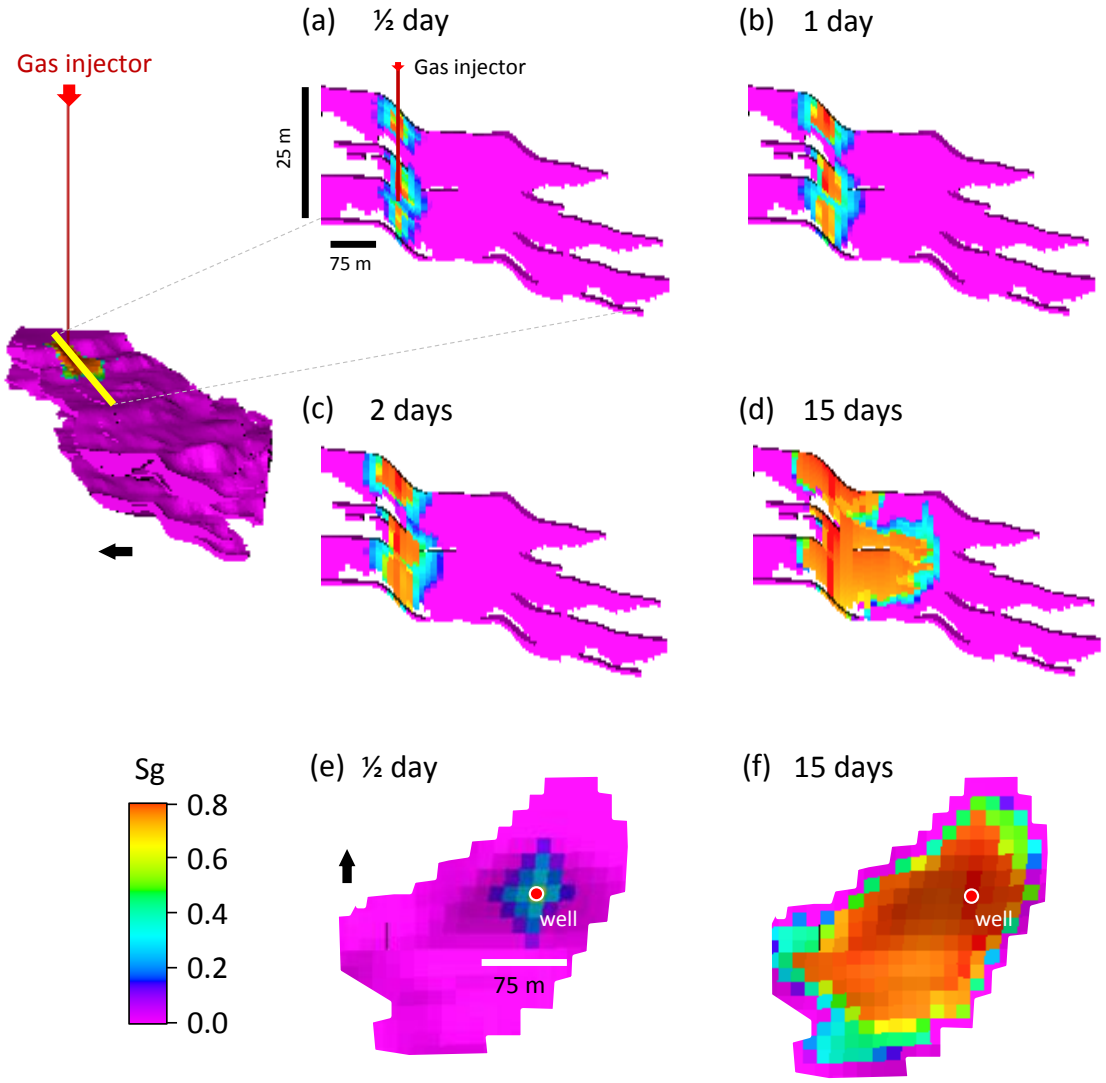

Figure 4-3 Model based simulations of fine time scale movement of injected gas through fluvial channel sands over 15 days (a) to d) Cross-section view showing heterogeneous flood front. Aerial view of the injected gas after (e) 12 hours and (f) 15 days. The edge of the gas flood may be particularly difficult to sharply define in seismic post-stack data due to the irregularity of the gas front, which moves quicker at the flood front than behind it. Within 15 days, the gas saturation change is greater than 80%.

Field average or bottom-hole pressure fluctuations due to natural day to day field operations are usually between 0.05 and 0.5 MPa/day, and therefore small enough to be below the seismic noise levels (Omofoma and MacBeth, 2016). However, well operations that involve well shut-off, restart or variation in choke setting can generate changes of as much as 1.5 to 15 MPa for typical offshore fields injecting between 10,000 and 30,000 stb/day. Production or injection into small compartments or isolated zones will induce bigger changes than those in larger compartments. For each distinct pressure change due to a fluid volume discontinuity, there emerges a pressure transient that spreads across the reservoir. Over time this is followed by a semi-steady state and then subsequently an equilibration period (Dake 1997). Whilst pressure is generally detected quickly and established across the entire connected volume in a matter of hours, the phenomenon of pressure diffusion takes much longer to stabilise. Eventually pressure is expected to be uniform across a compartment and evolve linearly in time for constant rate wells after equilibration. However pressure can take tens to hundreds of days to equilibrate, depending on the dimensions of the reservoir boundaries and compartments, easily as long as, or longer than, the seismic survey acquisition time.

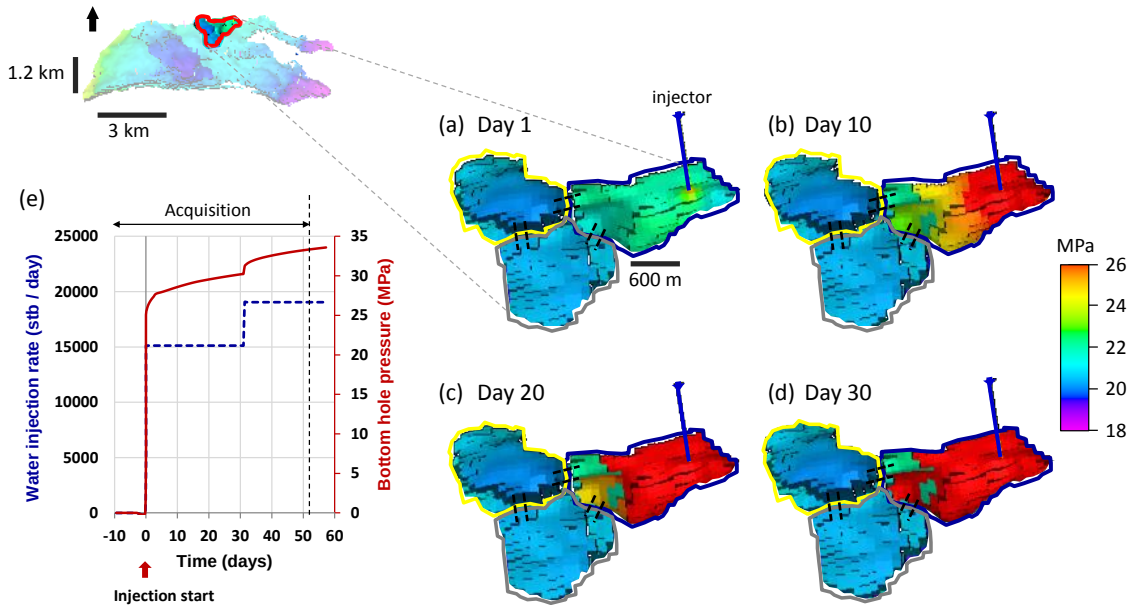

Figure 4-4 Simulation model of the Schiehallion field with highlighted area showing (a)-(d) Sequence of fine time scale pressure growth in a compartment (highlighted in blue) within the first 30 days of water injection. (e) Simulated water injection rate, dashed line (left y-axis) and bottom-hole-pressure, solid line (right y-axis) for the well. The pressure change within the first 30 days is only 5 MPa, and after 52 days about 9 MPa relative to start of injection. See also Figure 4-5 for water saturation image.

By comparison to pressure, fluid saturation changes generally evolve laterally at a

slower but nevertheless significant rate. For example, depending on the mobility (relative permeability divided by viscosity), gravity effects and vertical and horizontal permeability, waterfronts may move typically at a velocity of 0.3 to 1.5m/day (Tjetland et al. 2007), whereas hydrocarbon gas, steam or CO_2 fronts propagate at around 6m/day (Michou et al, 2013, Lu et al. 2012). It is observed that in some cases CO_2 propagation can exceed 12m/day (Lu et al. 2012). For example, a fine time scale model of hydrocarbon gas injection into thin (< 25 m) fluvial channel oil sands show that the injected gas moves at a relatively quick rate of around 12.5m/day (Figure 4-3). The gas is injected at an average rate of 1245 tonnes/day (oil equivalent of 9323 stb/day). Within the first 2 days, the gas front reaches a 75 metre distance from the well and over a 15 day window, gas fully saturates within 187.5 metres from the well, covering an approximate area of 0.45 km^2. Vertical sections between 12 hours and 15 days of injection show a heterogeneous flood front as the gas meanders through the sands. Only the boundary of the fluid distribution will experience significant change during the survey; in this case over the entire area of the gas flood. Thus, considering only the acquisition geometry itself, the acquisition survey will generally sample movement in a halo of 50 to 500m in width (2 to 20 seismic bins) during the acquisition itself. This event may be difficult to adequately capture at the flood front, as the gas moves quicker at the edge of the flood front than behind the front. In reality, seismic measurements relate to the full region of the wavefield between the source and receivers, not just

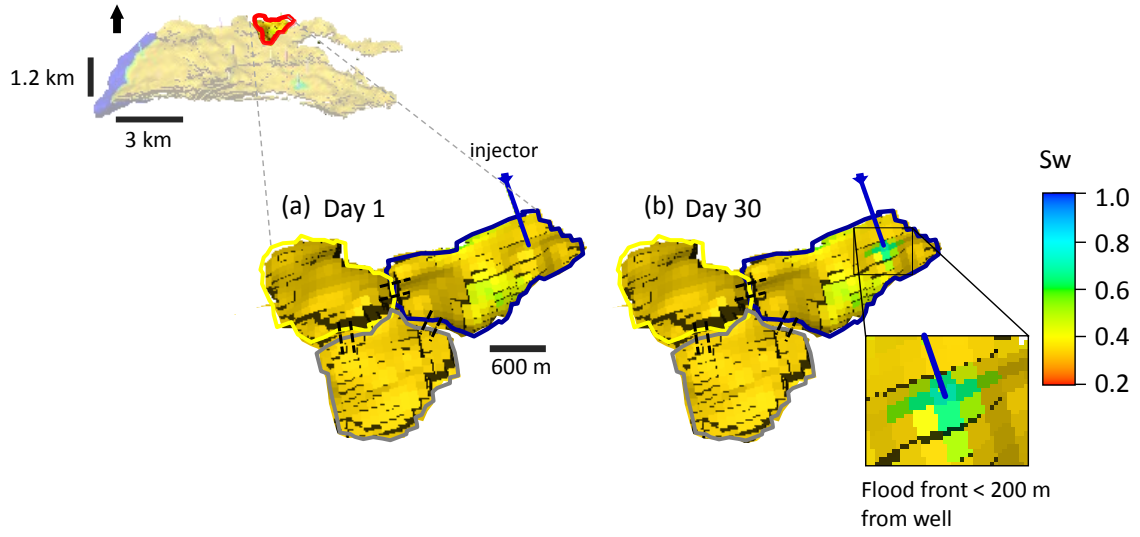

Figure 4-5 Simulation model of the Schiehallion field with highlighted area showing (a)-(b) Flood front movement from the injector in a compartment at day 1 and day 30 of water injection (corresponding image for pressure is shown in Figure 4-4). After 30 days of injection, the water saturation change away from the water injector is around 30%, and at the water injector, full saturation occurs.

localised areas of the reservoir. Indeed, because of the migration aperture, reservoir effects will generate differences at large lateral distances from the changes themselves (H. Jakubowicz, personal communication, 4 July, 2017).

In Figure 4-4, snapshots within a 30 day period of water injection at a constant rate show the evolution of pressure in a compartment with size of around 0.67 km^2. This is taken from the simulation model predictions for an injector activity in the Schiehallion field model. As introduced in section 3.3.4, the field is a stacked turbidite reservoir with poor lateral connectivity across bodies of stacked sands (Gainski et al., 2010). Two nearest compartments to the injection compartment are also highlighted. Within this time, pressure moves smoothly and quickly reaches the boundaries of the compartment within days. Well pressure transients last for around three days of first injection and attempts to achieve semi-steady state flow (i.e. linear growth of pressure with time) are disturbed by an alteration in rate after 32 days (Figure 4-4(e)). Spatially the pressure information grows with time and within a few weeks inter-compartment pressure communication is likely.

By contrast, water saturation is localised with a sharp flood front building up just within 200 metres from the well (Figure 4-5). When compared to pressure behaviour, the water flood could be viewed as stationery during the acquisition. Vertical fluid contacts will move much more slowly and are unlikely to change much during the survey duration. For example, in the Nelson field, the oil-water contact moved vertically by 30 to 60 m after 10 years of production (MacBeth et al. 2005) and in the Troll field, the gas-oil contact moved by 10 to12 m after 5 years of production (Bertrand et al. 2005). Another example is in a chalk field where the gas-water contact is interpreted to have moved by 25 m in 4 years (Barker et al. 2008). Gas out of solution is a separate process, it is relatively quick and responds immediately to pressure drop below the bubble point pressure within hours (Falahat et al. 2014), and thus there can be significant variations in gas caps, trapped gas or gas remaining at critical saturation within the reservoir during a survey period of 60 days. Other processes that might be relevant to this study include compaction in highly porous chalk reservoirs (Barkved et al., 2005), evolution of strain deformation in geomechanically active reservoirs, the sudden breakdown in faults due to depletion which may occur in days, or the creation of baffles during fluid flow which could appear in weeks.

As Figures 4-3, 4-4 and 4-5 illustrate, common reservoir processes (Table 4-1) such as gas saturation, pressure and water saturation changes occur over similar and even shorter time scales than typical seismic acquisitions discussed in Section 4.1. Changes in gas saturation greater than 80% can occur within 15 days or shorter. Pressure changes of 5 MPa or greater are not uncommon within 30 days, and for water saturation, changes between 20% and 50% over a 30 day period should be expected during the monitor acquisitions. Whether or not these changes will be detected in the acquired 4D seismic data depends on non-repeatability noise and the sensitivity of the reservoir to these changes. The latter determines how big the elastic properties will change (e.g. amplitudes and time-shifts) given the magnitudes induced by production. In light of the generalised rock-physics modelling in Chapter 2 on sandstones (Figure 2-10, 2-11 and 2-12), it can be concluded that the above mentioned magnitudes are potentially detectible in unconsolidated sandstones of 18% porosity or higher. Such magnitudes in pressure and fluid saturation changes are likely to yield 4D seismic amplitude responses (Figure 2-10(a)) greater than the 2% detectability limit of the 4D seismic method (MacBeth, 2004) outside any influence of non-repeatability noise.

To address the above, real acquisitions and a field model are used to access the reservoir domain based on how the surveys have been shot. Specifically, reservoir pressure and fluid saturation changes are simulated using a history-matched simulation model of a structurally complex field. The geometry and time sequence of shooting from a towed streamer and PRM monitor survey acquired in the North Sea are then used to reconstruct the reservoir dynamic changes. The reconstruction is solely based on the source and receiver coordinates of the acquisition geometry, and the shot times of the monitor survey. This does not consider survey illumination, propagation effects of seismic waves, positioning non-repeatability or data processing effects. Thus, the analysis in this chapter can only provide a crude estimation of the reconstructed reservoir changes based on the acquisition shooting sequence. Likewise, in the analysis to follow in Chapter 5, only a rough estimate of the magnitudes of the 4D seismic responses of these effects can be obtained through 1D convolution seismic modelling. A comprehensive scheme for modelling the seismic data as the reservoir changes during the acquisition using finite difference modelling, and including the effects of data processing is discussed in Chapter 8 (section 8.2.3). Implementing the full scheme is beyond the scope of this work.

4.3 Intra-survey analysis using the Norne field model

4.3.1 Acquisition dataset and timings

Two real field towed streamer and permanent reservoir monitoring (PRM) seismic surveys are available for this study. The towed streamer surveys were acquired in 2000 (baseline) and 2003 (monitor) on a North Sea field, and the PRM surveys were acquired six months apart in 2014, on a different North Sea field. The earlier PRM survey is taken as baseline and the later, the monitor. The acquisition data are initially received as navigation files which require pre-sorting to extract information on shots and receivers coordinates, and more importantly, the timings of each shot during the survey. Shot geometry (including the timings of each shot), and histograms of shooting activity are shown in Figure 4-6 for the PRM survey and in Figure 4-7 for the towed streamer survey. The towed streamer shooting covers an approximate area of 240 km^2, taking 72 days for the baseline and 58 days to shoot the monitor survey. For the PRM surveys, this is a smaller shot area of 143 km^2 which takes 30 days for the baseline and 45 days for the monitor. The monitor surveys have a different time sequence of shooting from their baseline. For the towed streamer, a 'race-track' pattern is observed, whereas the PRM survey follows a more randomised pattern, and is also not shot in sequence.

Histograms of shooting activity (Figure 4-6 (e)-(h)) show down-times due to the many factors discussed in section 4.1. Survey acquisitions aim to optimise the time available and negotiate field operations and weather windows and it is not uncommon for weather down time to be 20 to 40% of the overall survey duration (Figure 4-1). The surveys are thus not shot in a smooth pattern covering the subsurface in sequence, but according to the practicalities, which is specific to the acquisition. The towed streamer experiences delays of up to 30 days for the monitor and up to 40 days for the baseline survey. The PRM acquisitions achieve a fairly continuous shooting with shorter down time windows of up to 5 days. The implication here is that the monitor surveys will miss any information on the changes in the reservoir when no data are acquired. I therefore expect that monitor surveys will also not capture the changes in the reservoir in the same way.

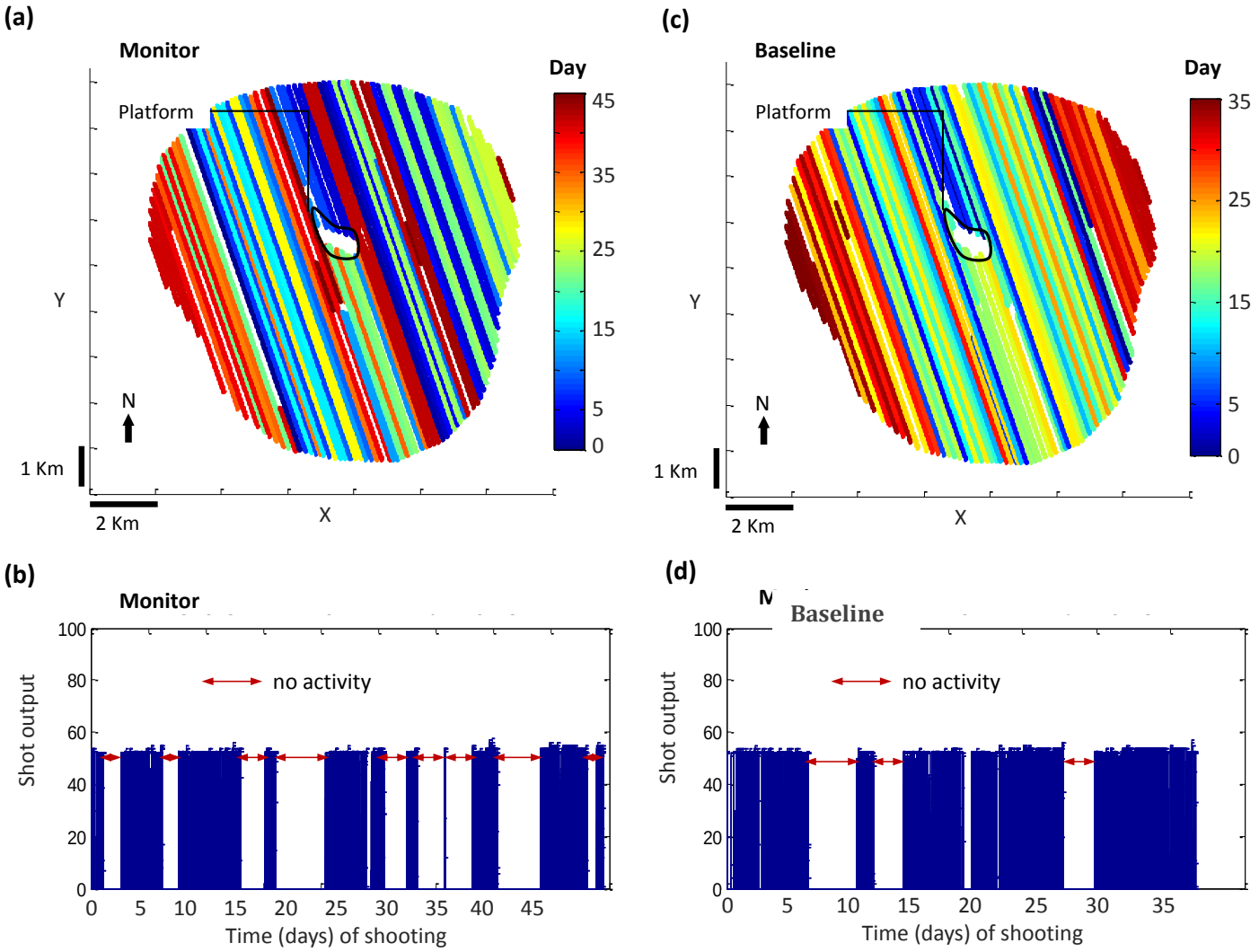

Figure 4-6 (a) and (c) Shot geometry (colour coded by the time sequence of shooting (in days) of each shot line for the PRM monitor and baseline acquisitions in the North Sea. Acquisition activity histogram from the start to end of the surveys are shown in (b) and (d). The baseline and monitor surveys do not follow the same order of shooting.

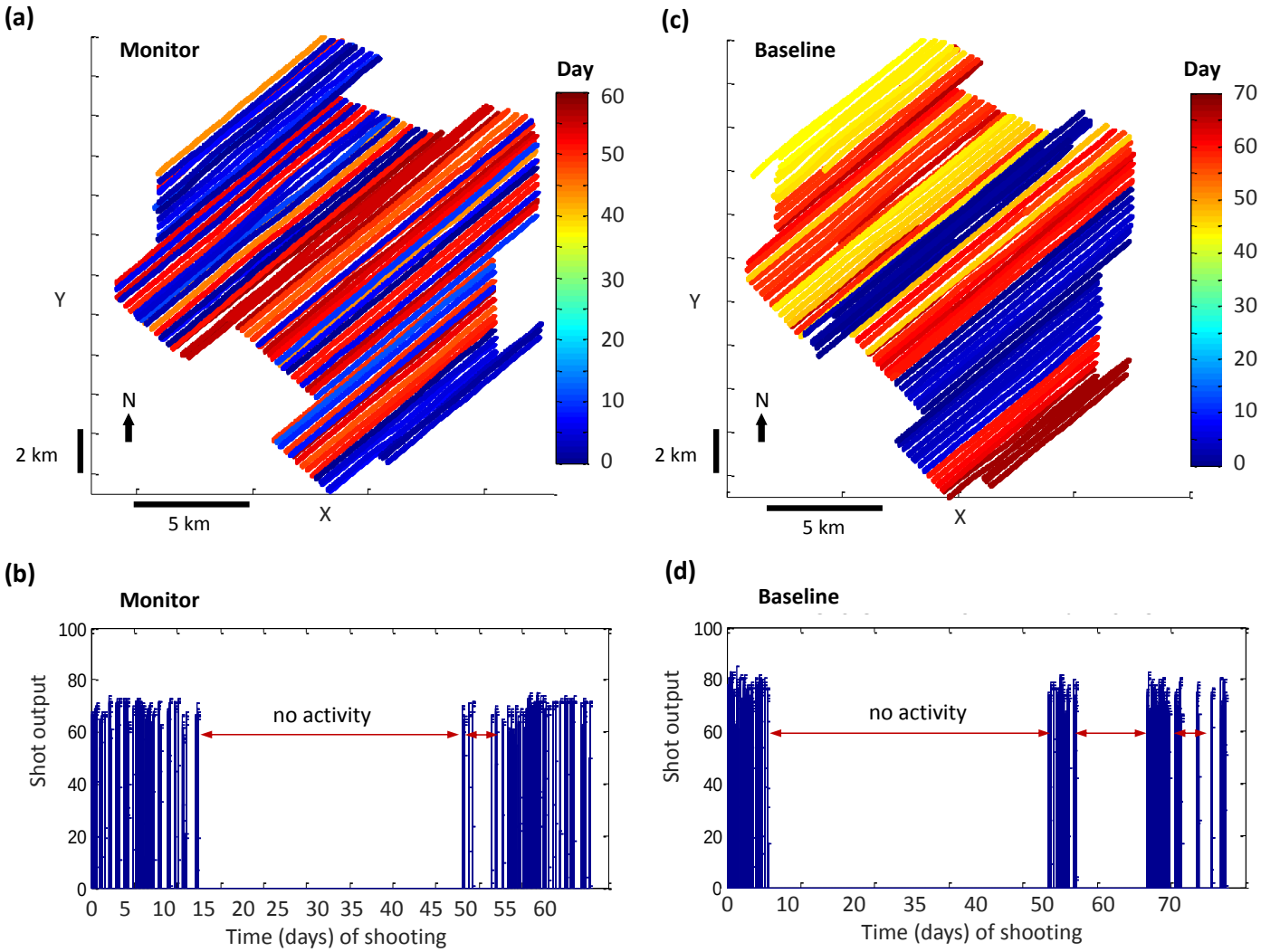

Figure 4-7 (a) and (c) Shot geometry (colour coded by the time sequence of shooting (in days) of each shot line for the towed streamer monitor and baseline acquisitions in the North Sea. Acquisition activity histogram from the start to end of the surveys are shown in (b) and (d). The baseline and monitor surveys do not follow the same order of shooting.

4.3.2 Reservoir details and simulation

The simulation model for this study is that of the Norne field (which has been earlier introduced in section 3.3.2).

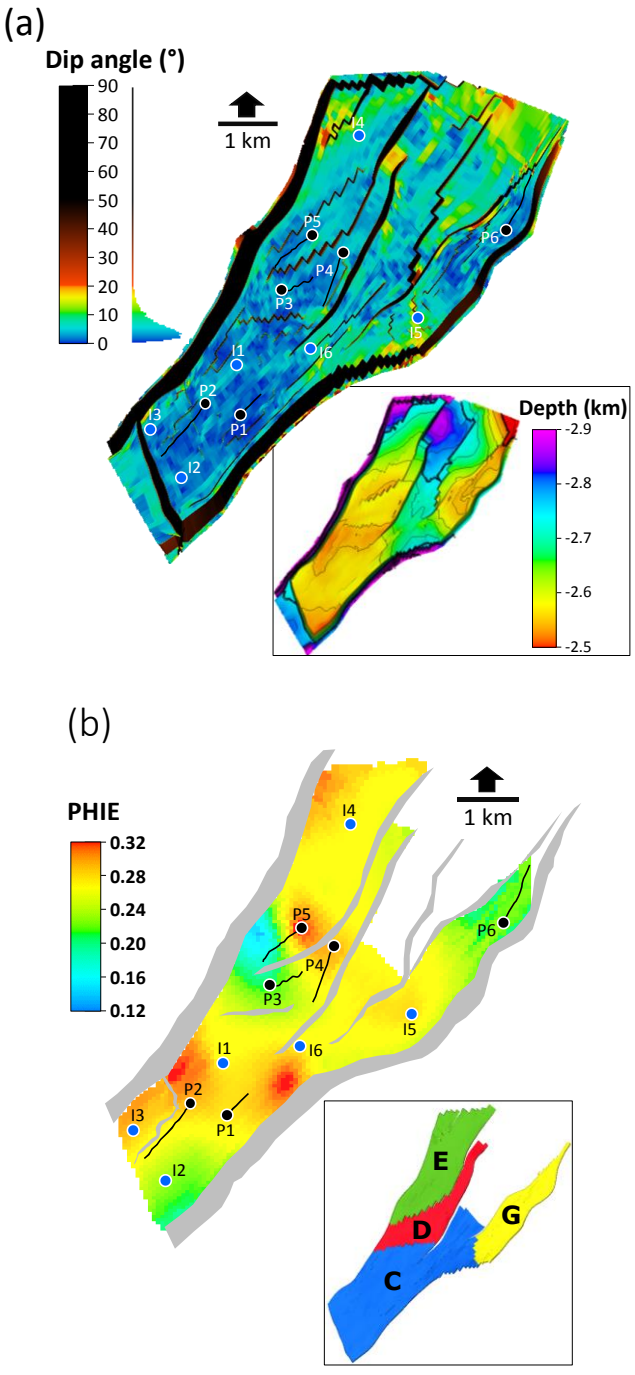

Figure 4-8 (a) Dip angle (in degrees) of top reservoir surface in depth (shown as the inset map) capturing the main structural features of the Norne field simulation model with faults possessing a higher dip angle (> 40°) than the formation (~ 4°) – shown by the histogram. (b) Variations in effective porosity (PHIE) for top reservoir of the simulation model showing wells used in this study. Blue wells are water injectors and black wells are producers. Inset map in (b) shows the reservoir fault segments, C, D, E and G.

The simulation model is a horst block of approximately 9 x 3 km, has dimensions 230 x 560 x 22 (making 2,833,600 grid cells) with an average cell size of 24.3 x 25.8 x 8.4 m and contains 41 faults. The model is built to be consistent with the geological features, flow units and fault planes; hence, the grid uses non-vertical pillars and irregular cells (corner-point geometry (CPG)). There are 23 geological horizons and 22 geological layers in the model, which are distributed across the four sandstone formations (Garn, Ile, Tofte and Tilje) of Middle and Lower Jurassic age.

The reservoir lies at a depth of 2500 m to 2900 m and is enclosed and segmented by major faults with three segments (C, D and E) in the main field area and the fourth segment, G, an isolated compartment of size 3.6 km^2 (Figure 4-8). The steepest angle between the reservoir's top surface and the horizontal plane is computed using the dip angle attribute map (Figure 4-8(a)). This shows a skewed distribution of the dip population for the top reservoir horizon. Steep dips with an angle greater than 40° are associated with faults, whereas, the formation itself rests at a mild dip angle of approximately 4°.

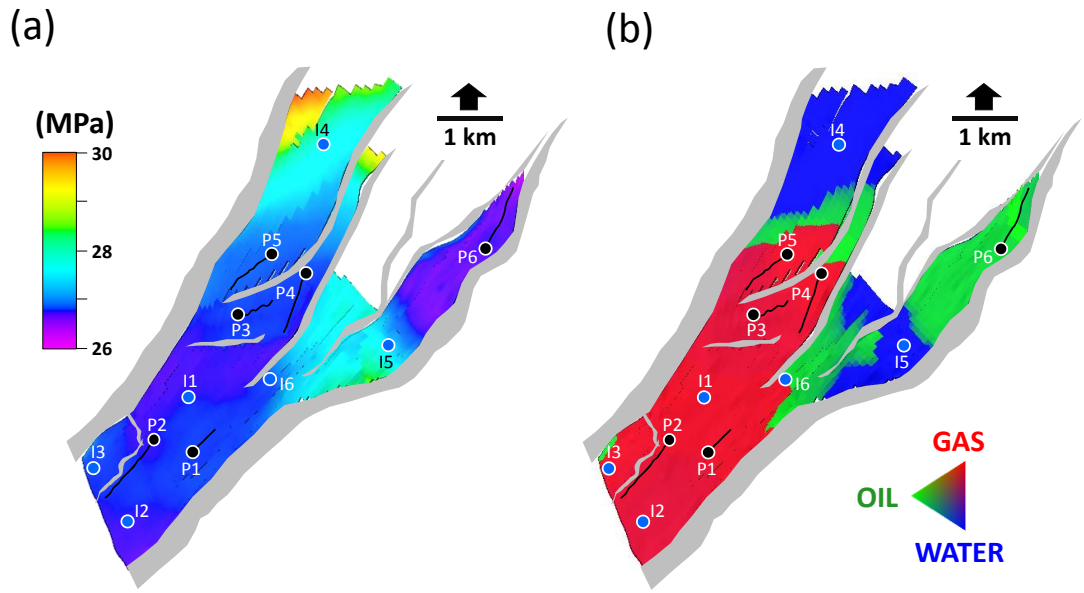

Figure 4-9 Pre-production conditions of top reservoir from the Norne field model (a) Initial pressure (b) Initial fluid distribution. Producers are in black and water injectors are in blue. Higher initial pressure is associated with the water leg which lies deeper than the hydrocarbon leg (see also Figure 4-8(a)).

My analysis uses properties from the top layer of the top reservoir (the Garn Formation, represented by the first three layers of the model). The Garn Formation covers an area of 18 km^2, has an average thickness of 28 m and shows variations in effective porosity from 12 to 32% in the model (Figure 4-8 (b)). Horizontal and vertical permeability also vary from 80 to 1300 mD and 10 to 250 mD respectively. Segments C, D and E predominantly contain gas with most of the oil (with an API gravity of 32.7°) in segment G (Figure 4-9).

For the simulations, six water injectors and producers with a well spacing of 500 to 2000 m in the field model are chosen and a pressure maintenance scheme is operated. The baseline state is the same as pre-production. Production and water injection (from injectors 12 and I3) starts two years prior to the monitor survey. Additionally, water injection in the new wells I1, I4 and I5 is scheduled to commence close to the time of the monitor acquisition. For the field acquisitions considered in this study, this takes 45 or 58 days to complete. Within this time, Injector I1 starts on day one as a consequence of injector I6 being turned off five days before the acquisition and Injector I4 is started on day twelve to support producers P4 and P5. Finally, Injector I5 is introduced twenty one days later to support producer P6, where mild gas breakout occurred prior to the monitor time.

In Figure 4-10, the injection and production rates during the acquisition are shown. For gas production, this is on average 479,000 sm^3/day (oil equivalent of 3,012 stb/day), with day-to-day fluctuations of up to 195,478 sm^3/day (oil equivalent of 1,230 stb/day). Across the producers, only well P6 contributes to oil production with an average rate of 1,120 stb/day and day-to-day fluctuations of up to 700 stb/day. Likewise, well P2 contributes predominantly to water production with an average rate of 1,190 stb/day and day-to-day fluctuations of up to 155 stb/day during the survey. All water injectors operate at an average rate of 16,800 stb/day but fluctuations of up to 4,180 stb/day occur. As a result, pressure also fluctuates at these wells; with injectors I4 and I5 exhibiting the biggest changes when compared to the start of the survey (Figure 4-11).

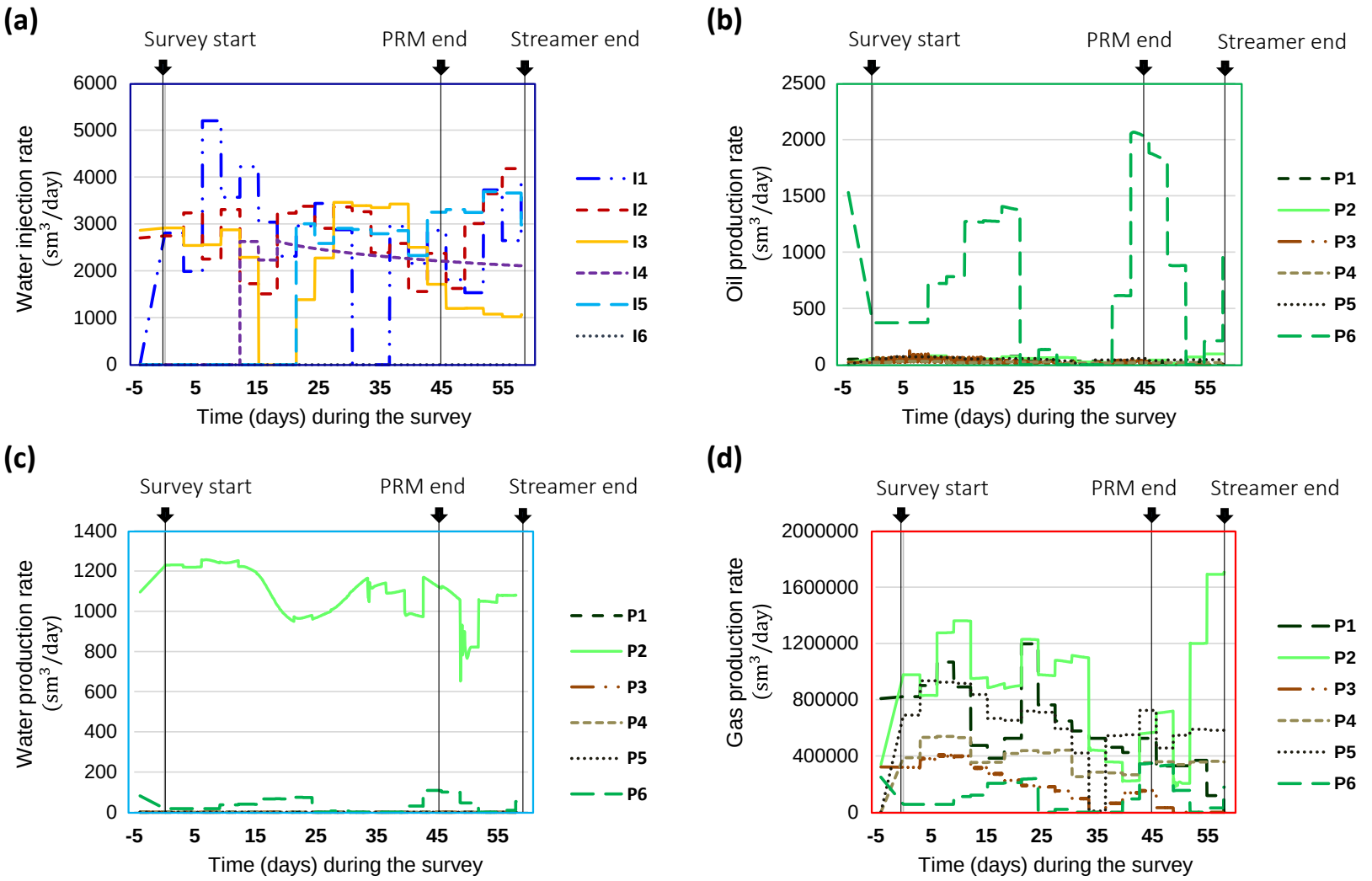

Figure 4-10 Simulated well rates in the Norne field model during the acquisition of the PRM and towed streamer monitor surveys (a) Water injection rate (b) Oil production rate (c) Water production rate (d) Gas production rate. Water injectors, I1, I4 and I5 are started on day 1, day 12 and day 21 respectively. Injector I6 is switched off five days before the survey.

With the exception of well P6 from which most of the oil is produced, pressures at the remaining predominantly gas producers are similar to the overall field average pressure which is relatively constant during this time due not only to their smaller liquid rates but to the pressure support from the injectors. During this period, the wells remain in transient flow.

Figure 4-12 shows the simulated reservoir changes that occur between the start and end of this acquisition time frame which marks a monitor acquisition of 58 days. Spatially, pressure fluctuations are smaller in the gas leg (segment C and D) with the majority of the pressure changes being in segment E and G where injectors I4 and I5 are located. Flood front growth can also be tracked from the two mature injectors I2 and I3, and the new injectors I1 and I5.

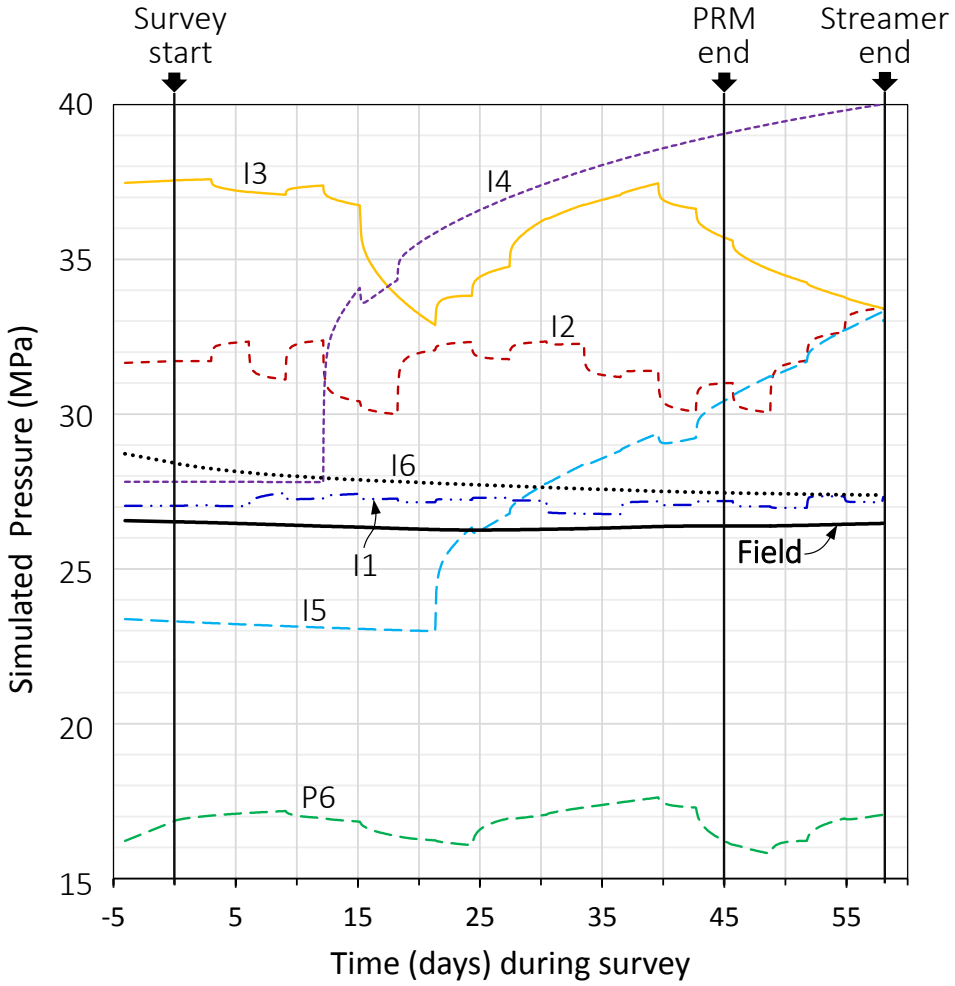

Figure 4-11 Simulated bottom-hole-pressure (BHP) fluctuations and overall field average pressure (in black) from the Norne field model. Water injectors, I1, I4 and I5 are started on day 1, day 12 and day 21 respectively, within the time frame of a monitor acquisition for the PRM and towed streamer survey. Larger pressure fluctuations are induced from the water injectors than the producers. With the exception of P6, the remaining five producers fluctuate only mildly around the field average pressure.

In segment G, mild gas breakout is also observed, although pressure increase at injector I5 restricts the exsolved gas to lie close to the producer P6. During the acquisition time frame, the average magnitudes of the pressure fluctuations ranges from 0.15 to 4.5 MPa for the injectors, but are less than 0.1 MPa for the producers. By comparison, the saturation floods progress at a rate of between 0.9 and 2.3 m/day.

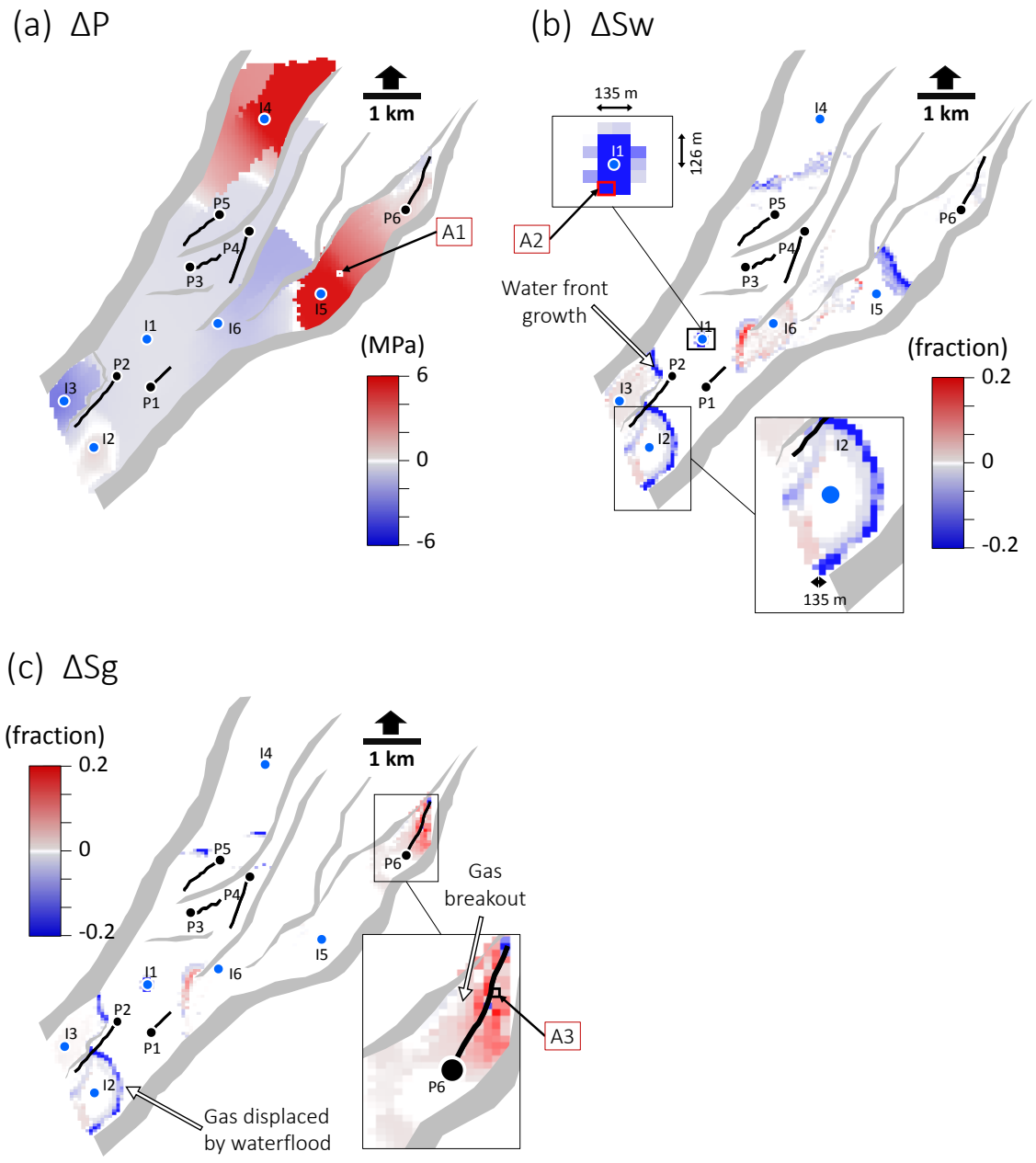

Figure 4-12 Differences between simulated predictions at the start and end of a monitor survey which took 58 days. Displayed for (a) Pressure changes, ΔP (b) Water saturation changes, ΔSw (c) Gas saturation changes, ΔSg. Water injectors are in blue and producers in black. Fluid front changes are localised to within 200 m, whereas pressure changes are widespread. The annotated bin locations A1, A2 and A3 are later analysed in Figure 4-19, Figure 4-20, and Figure 4-21.

4.3.3 Spatio-temporal binning workflow and implementation

To investigate the intra-survey phenomenon, Figure 4-13 details the workflow which reconstructs the pressure and saturation changes as acquired by the monitor surveys, by spatio-temporal binning. It combines the fluid flow simulator predictions from the Norne field model sequenced according to the timings of the shots for the PRM and towed streamer survey. The spatio-temporal binning is performed firstly by CMP binning of the acquisition source-receiver midpoints. This is then followed by timestamp sorting of the simulator predictions by allocating pressures and saturations to each midpoint on the reservoir grid according to the time that each midpoint was shot during the survey.

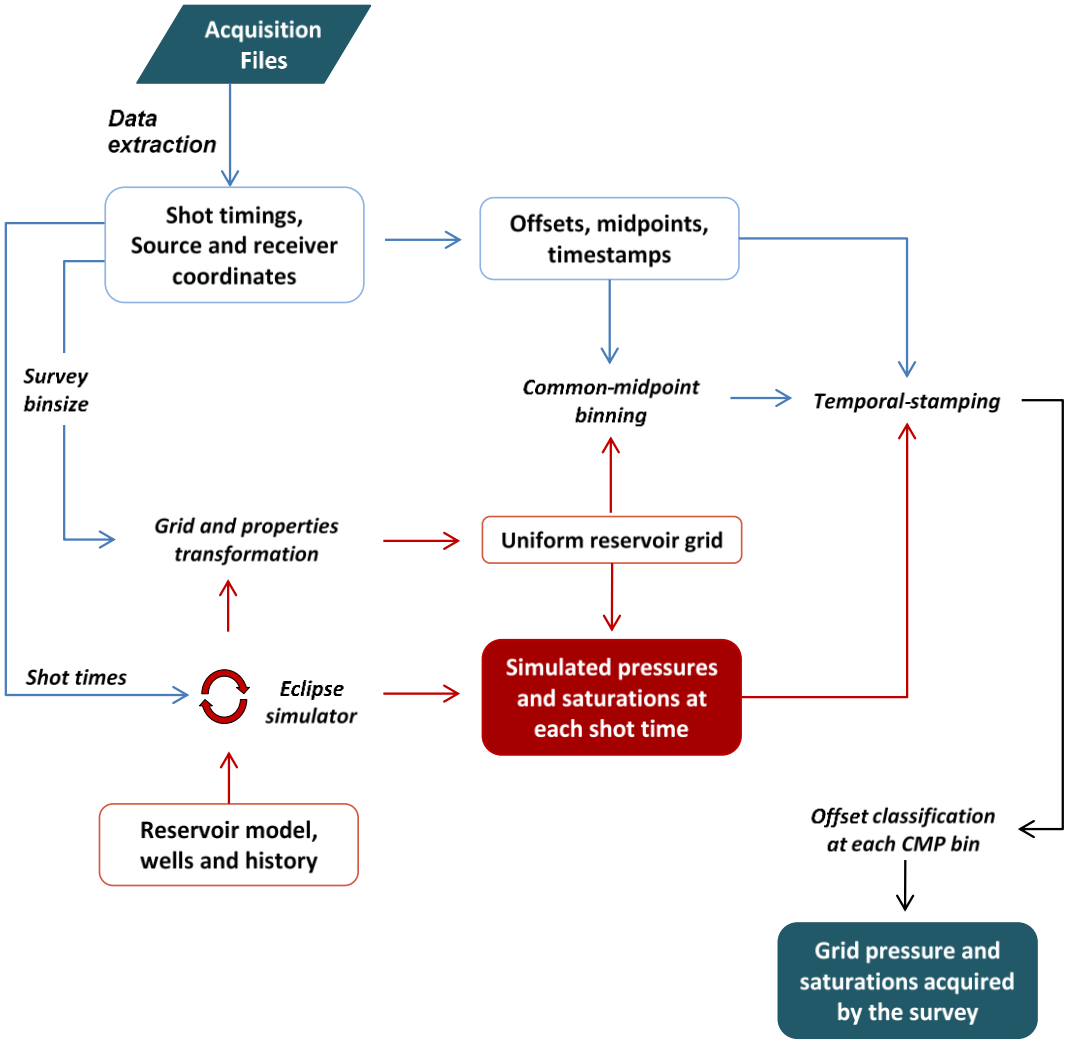

Figure 4-13 Workflow for spatio-temporal binning of the acquisition data and simulation model dynamic predictions, aimed to reveal the reservoir dynamic changes acquired by the survey. Apart from Eclipse simulations for each shot time, the workflow is implemented in MATLAB. This workflow forms the first part of the analysis. The second part of the analysis is performed via 1D convolution seismic modelling using the reconstructed grid pressure and saturation changes acquired by the survey, (See Section 5.2, Figure 5-2).

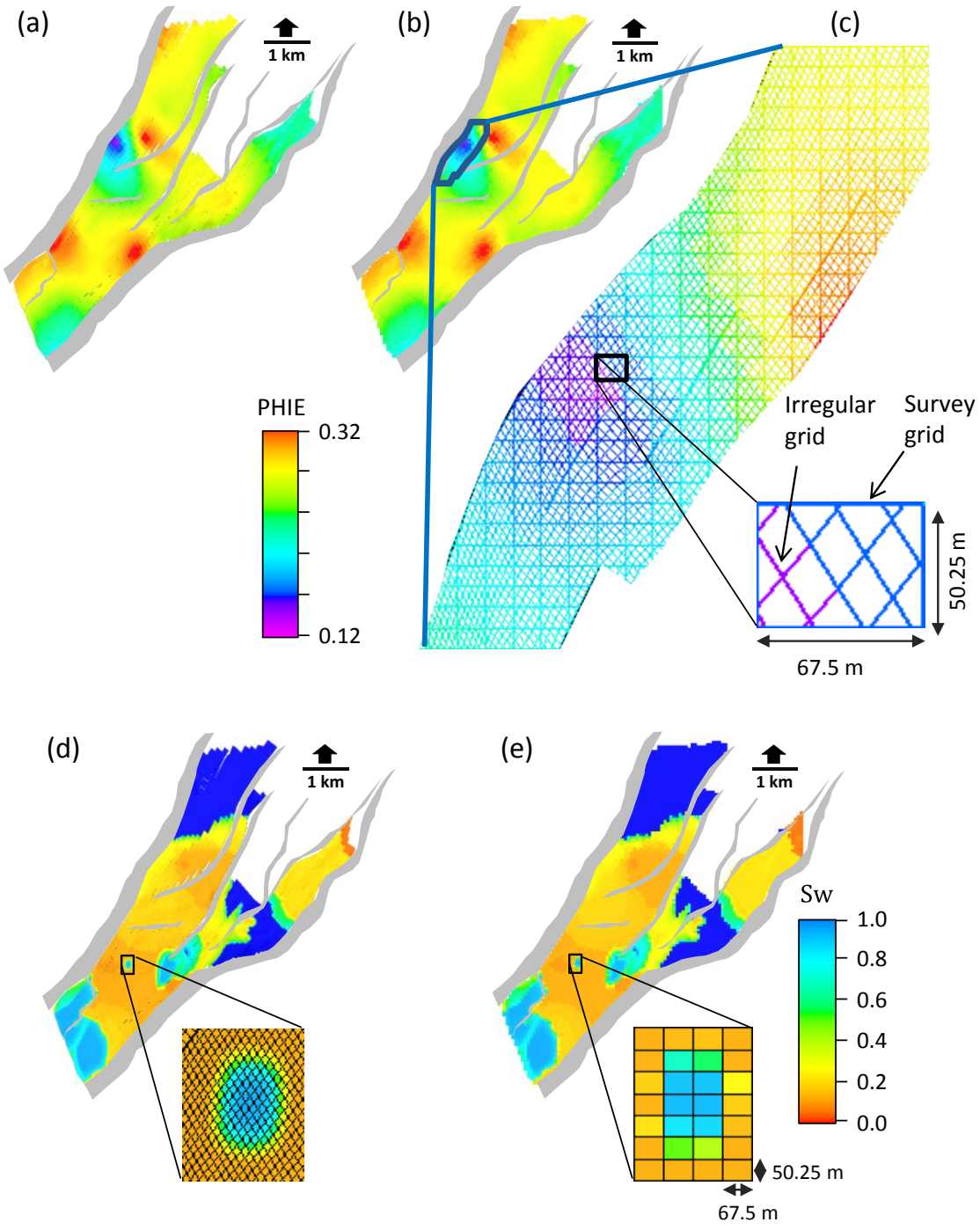

Figure 4-14 Reservoir grid to survey grid transformation. Static property distribution for effective porosity on (a) the irregular reservoir grid (b) the transformed uniform grid based on the binsize, 67.5 x 50.25 m from the acquisition. (c) Zoomed in portion showing the overlap of the irregular reservoir and uniform grid lines colour coded by the property values for effective porosity, PHIE. Dynamic property distribution for water saturation predicted on day 45 of the monitor acquisitions are also shown on (d) the reservoir irregular grid (e) the transformed uniform grid used in this study.

The simulator predictions are output at 10 minute timesteps and predictions at finer times (determined by the shot time intervals) are obtained by linear interpolation. The

workflow assumes perfect geometry between the monitor and baseline, thus ignoring any impact of non-repeated source and receiver positions. This process yields time sensitive pressure and saturation changes at each midpoint on the grid and these can be grouped according to the geometric source-receiver offset classes: near offset - 0 to 1500 m, mid offset - 1500 to 3000 m, and far offset - 3000 to 4500 m, in addition to the full offset (up to 5600 m for the towed streamer, 14600 m for the PRM).

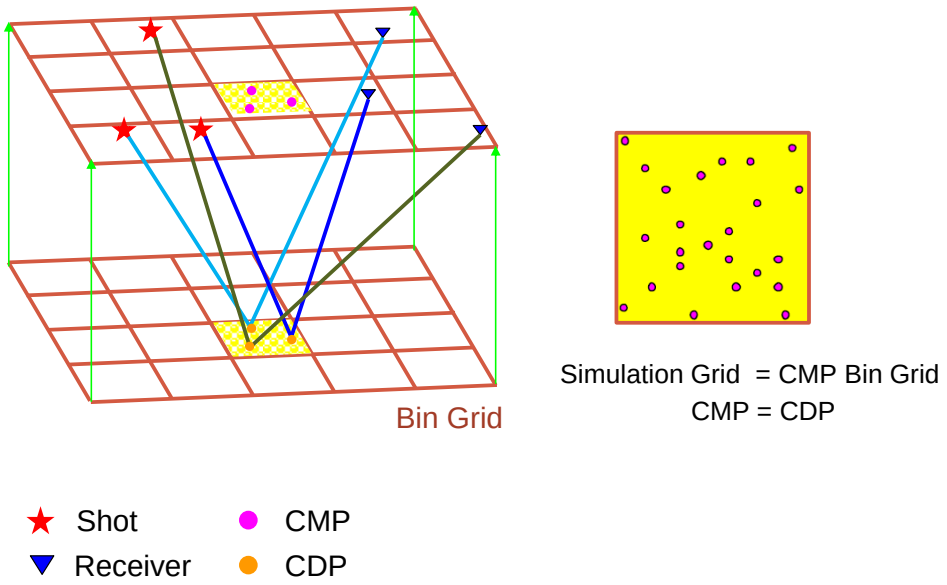

Figure 4-15 An illustration of common-midpoint (CMP) binning of the acquisition at the surface and the reservoir below, where both share a common grid. The assumption is that a CMP location (which is the halfway point between shot points and receiver locations at the surface) is the same as a common-depth point (CDP) at the reservoir level. The limitations of this simplistic assumption are discussed in Section 4.3.4, and recommendations for future work are provided in Section 8.2.3.

For the above, the properties on the irregular reservoir grid are transformed to a rectangular CMP grid from the acquisition by lateral interpolation. This results in a uniform reservoir grid where the size of each cell is the bin size, 67.5 x 50.25 m, from the source-receiver geometry from the survey. Figure 4-14 shows the reservoir properties on the original irregular grid and transformed uniform grid. As the reservoir grid is transformed after the simulations, the dynamic properties are adequately preserved, but at a much coarser scale.

The grid transformation makes common-midpoint (CMP) binning straightforward, as both the bin grid of the acquisition and the simulation model share a common grid (Figure 4-15). For each bin grid of the reservoir, all the midpoint coordinates with their

corresponding offset and time of shots are extracted. Each midpoint is allocated a pressure and saturation change value, based on the time of shot during the monitor acquisition. The baseline sequence of shooting and timestamp (Figure 4-6(c) and Figure 4-7(c)) is not considered in the spatio-temporal binning workflow (Figure 4-13) because it is assumed to be acquired pre-production, and so, there are no intra-survey reservoir fluctuations, as the reservoir is in pressure equilibrium. In addition, baseline and monitor acquisition geometry are assumed to be exactly repeated. The limitations and assumptions of the workflow for the first part of the analysis in Figure 4-13 are discussed in detail in Section 5.2.1. This also applies to the second part of the analysis carried out in Section 5.2 (Figure 5-2) which uses the output from Figure 4-13. These outputs are the reconstructed grid pressure and saturation changes acquired by the survey in the presence of intra-survey reservoir fluctuations (Figure 4-13). As seen in Figure 5-2, a 1D convolution-based seismic modelling with a migration operator considers the intra-survey reservoir fluctuations by using these outputs to model the 4D seismic response.

4.3.5 Fold and shot timestamp coverage of the acquisitions

Table 4-2 details the survey statistics for the towed streamer and PRM monitor acquisitions. The towed streamer survey was originally shot on a field four times bigger than the Norne field and to achieve a suitable configuration for the size of the field model, the acquisition geometry was compressed, guided by a real survey shot on the Norne field (WesternGeco, 2007). This real 4D survey on the Norne field in 2004 consisted of a 6 x 3200 km streamer and a single source configuration with streamer cable separation of 50 m and shot point spacing of 25 m. The overall streamer/survey area covered was 146 km2. For the compression of the towed streamer geometry available for this study, shot line spacing was reduced from 350 m to 80 m and streamer cable separation from 100 m to 50 m. This reduced the shot coverage from 240 km^2 to 67 km^2, resulting in an overall streamer/survey coverage of 110 km^2. This is similar to the dimensions of the real survey acquired on the Norne field described above. For the PRM data, the only alteration made is the rotation of its acquisition geometry to align with the orientation of the Norne field model.

Survey statistics	PRM		TOWED STREAMER	
	Original	Reduced	Original	Reduced
Receiver coverage per shot	≈60 km^2	≈60 km^2	≈3.8 km^2	≈3.8 km^2
Shot coverage	143 km^2	143 km^2	67 km^2	67 km^2
Reservoir size	18.5 km^2	18.5 km^2	18.5 km^2	18.5 km^2
Survey duration	45 days	45 days	58 days	58 days
# of shots (total)	117,525	44,589	54,704	16,047
Shot time interval	≈11 seconds	≈30 seconds	≈8 seconds	≈30 seconds
# of receivers per shot	3,966	1,966	3,456	1,152
# of midpoints (total)	430 ,842, 984	87, 661, 974	68, 735, 520	18, 486, 144
Bin size	12.5 x 25 m	33 x 50.25 m	19 x 6.25 m	67.5 x 18.75 m
Minimum offset (minimum, average)	0.54 m, 167.4 m	1.1 m, 173.4 m	215.2 m, 256 m	216.3 m, 262.4 m
Maximum offset (maximum , average)	14.6 km, 13.1 km	14.6 km, 13.1 km	5.65 km, 5.61 km	5.65 km, 5.61 km
Average offset	5.51 km	5.52 km	2.91 km	2.91 km
Shot line spacing	56 m	56 m	80 m	80 m
Shot point spacing	25 m	66 m	38 m	135 m
Receiver spacing	50.25 m	100.5 m	12.5 m	37.5 m
Cable separation	304 m	304 m	50 m	50 m
Cable length	554 to 6,585 m	503 to 6,585 m	5400 m	5400 m
# of cables (total)	48	48	8	8
Receivers per cable	12 to 131	6 to 66	432	144

Table 4-2 Survey statistics for the PRM and towed streamer monitor surveys, highlighting the reduced number of parameters after decimating the original shot time interval to every 30 seconds and the receivers accordingly. Bin size is chosen as half the shot point spacing and half the spacing between receivers on a line. An optimum fixed bin size of 67.5 × 50.25 m was used for the reduced (i.e. decimated) acquisition geometry, giving a total of 5,404 CMP bins which represent the reservoir grid cells.

The shot interval on each line was increased from the original 8 to 12 seconds to around 30 seconds, to reduce storage space in the computation (Table 4-2). As a consequence, receivers on each cable were reduced whilst maintaining the ratio of shot point spacing to the receiver spacing, originally designed in the acquisitions. Figure 4-16 shows the final layout of the shots and receivers, and the timings of the shots overlapped on the reservoir. Notice the high density of shot points to compensate for the sparse sensor layout of the PRM. Receiver layout for the towed streamer is the overall streamer coverage from the shooting.

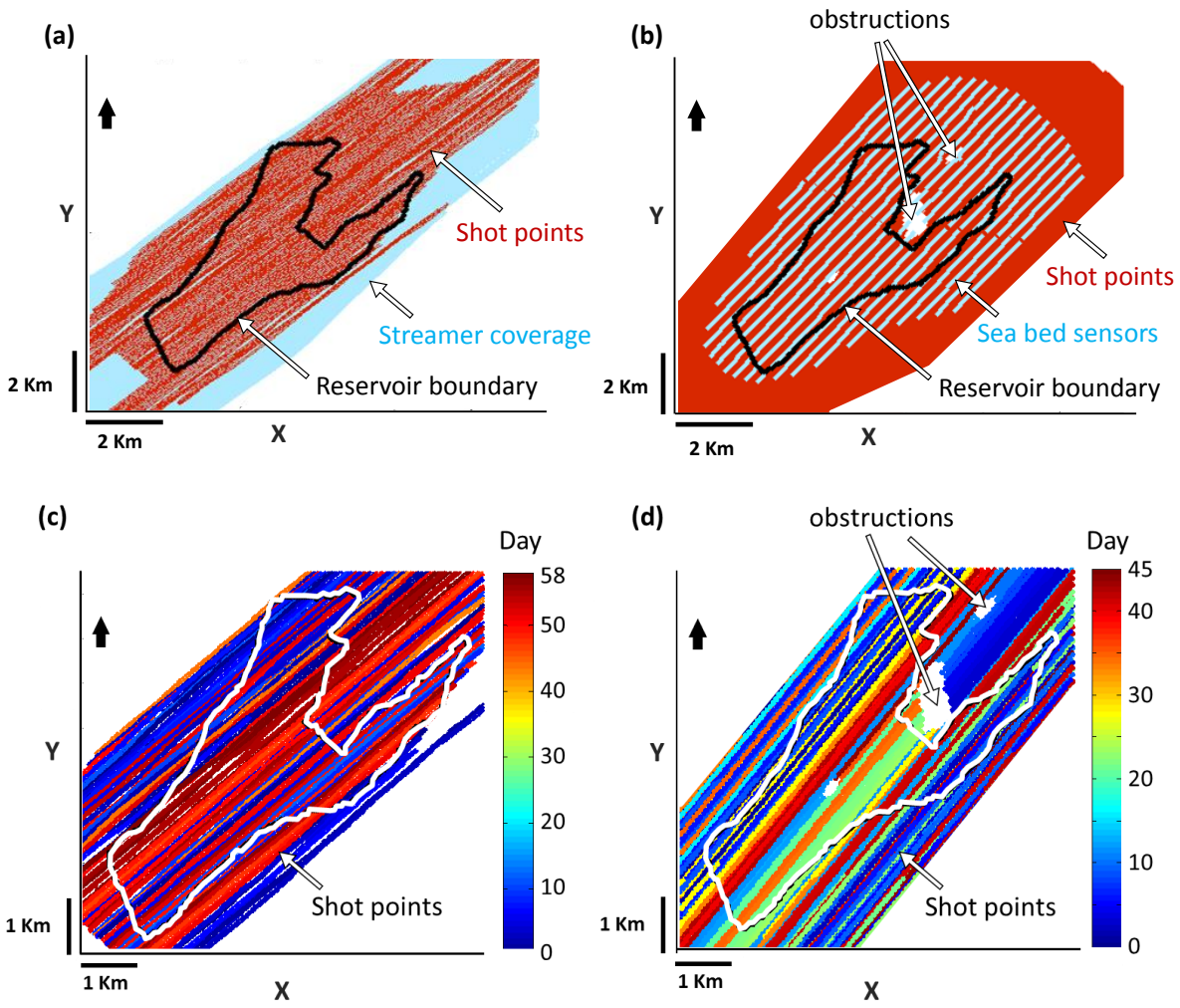

Figure 4-16 Layout of the shots and receivers over the Norne field model (a) the towed streamer acquisition (b) the PRM acquisition. The time sequence of the shots are also shown in (c) for the towed streamer and in (d) for the PRM.

In Figure 4-17 the resulting fold distribution for each offset class for both acquisitions is obtained after implementing the workflow. From a data coverage point of view, the fold per offset class is restricted for the towed streamer due to its limited cable dimension but the PRM design allows larger variability across offsets and much higher fold, with the near offsets having the lowest fold for both surveys.

Of particular concern, however, is the resultant timestamp over the reservoir (Figure 4-18). This is simply the mean of the shot times from all midpoints in each bin location, classified, also according to offsets. Because the PRM survey is designed to cover the entire area per shot; its timestamp coverage for full-offset is far less irregular across bin locations than the towed streamer.

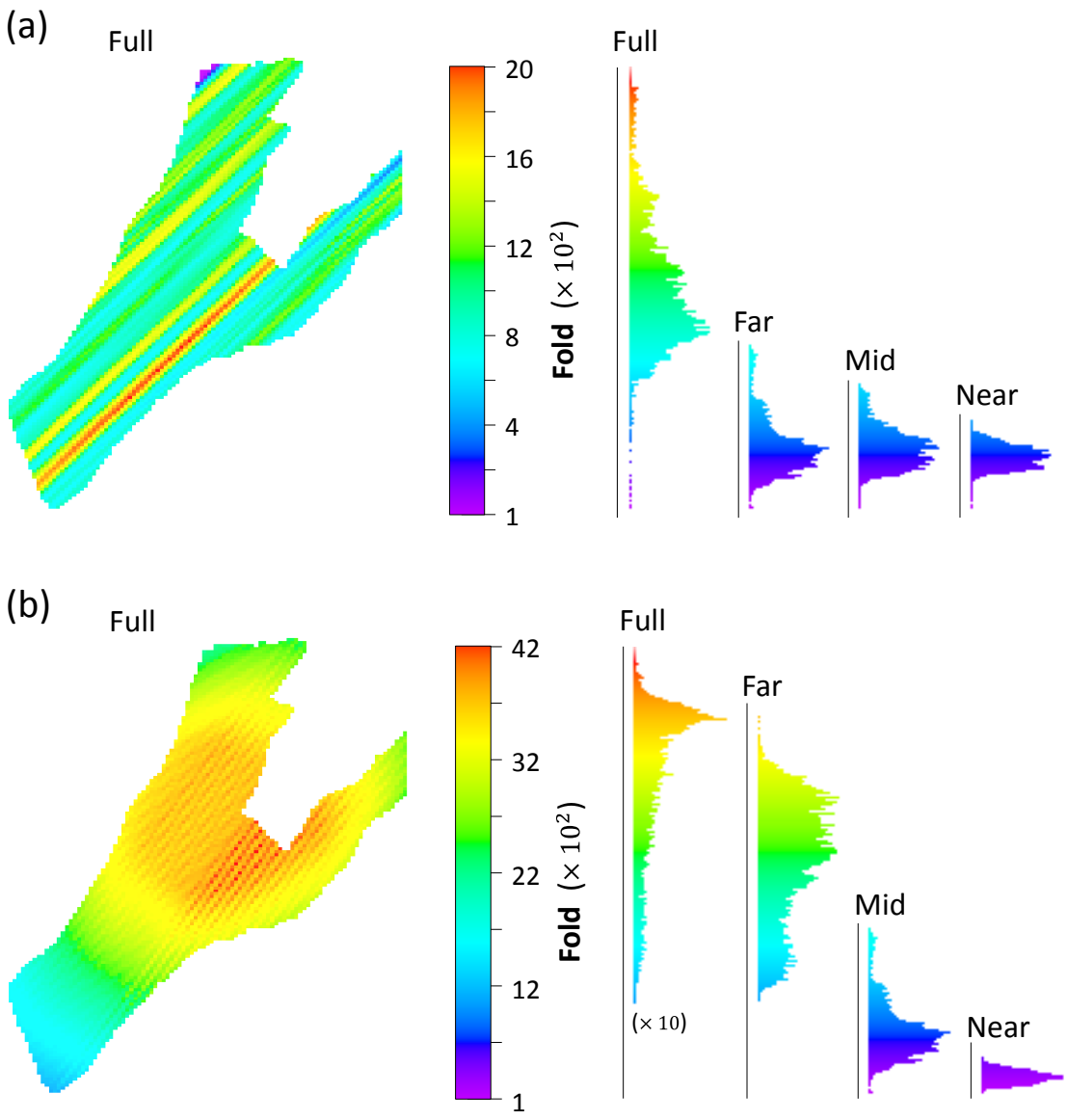

Figure 4-17 Fold coverage over the reservoir for full offset along with histograms across offsets (near, mid, far and full) shown for (a) the towed streamer survey (b) the PRM survey. The PRM full-offset fold is ten times the scale used.

Moreover, the single mean of all shot times from the acquisition is around day 22 for the PRM and day 29 for the towed streamer. Notice how skewed the towed streamer is from its single mean due to its restricted coverage per shot. The histograms also indicate that the timestamp varies across the different offset class which is also of significance since the reservoir pressures and saturations also change with time during the acquisition (see also Figure 5-12 and Figure 4-8).

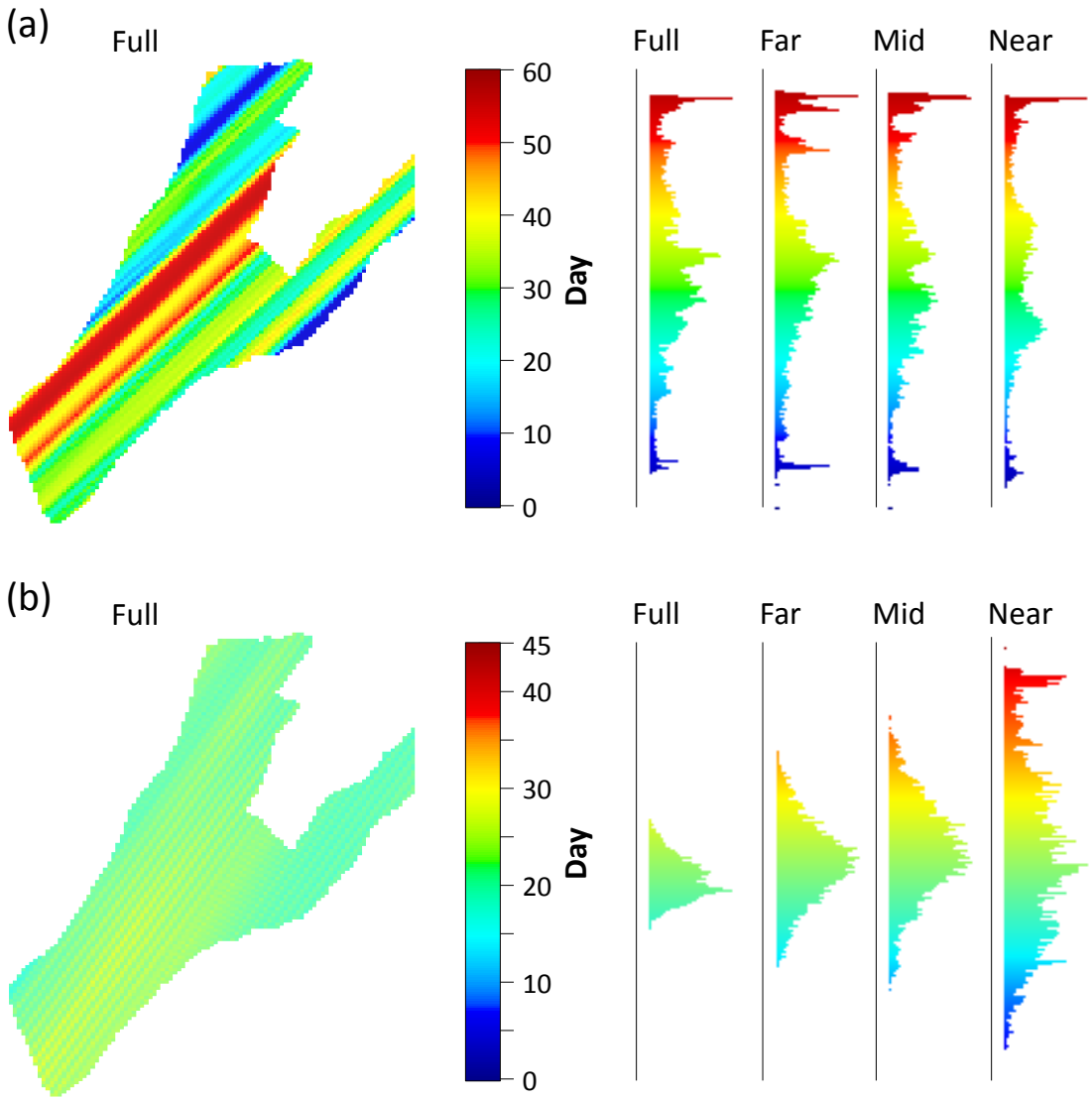

Figure 4-18 Average shot timestamp (in days) coverage at each bin location over the reservoir for the full offset along with histograms for the offset classes (near, mid, far and full) shown for (a) the towed streamer survey (b) the PRM survey.

4.4 Proof of concept

Based on the spatial positions of the acquisition source-receiver midpoints, and the principle of common-midpoint binning, midpoints located within a CMP bin will have been acquired at different times during the acquisition. Assuming that a CMP bin crudely represents an image location, then, in a "pre-stack" sense the image location has been acquired at different times within the same acquisition. Consequently, the image location associated with the acquired midpoints (in a CMP bin) will also correspond to the reservoir changes that occurred at the time that each midpoint was shot. Figure 4-19

shows a particular CMP bin located close to injector I5 in segment G. The midpoints respond to different pressure changes due to their different shot timestamp.

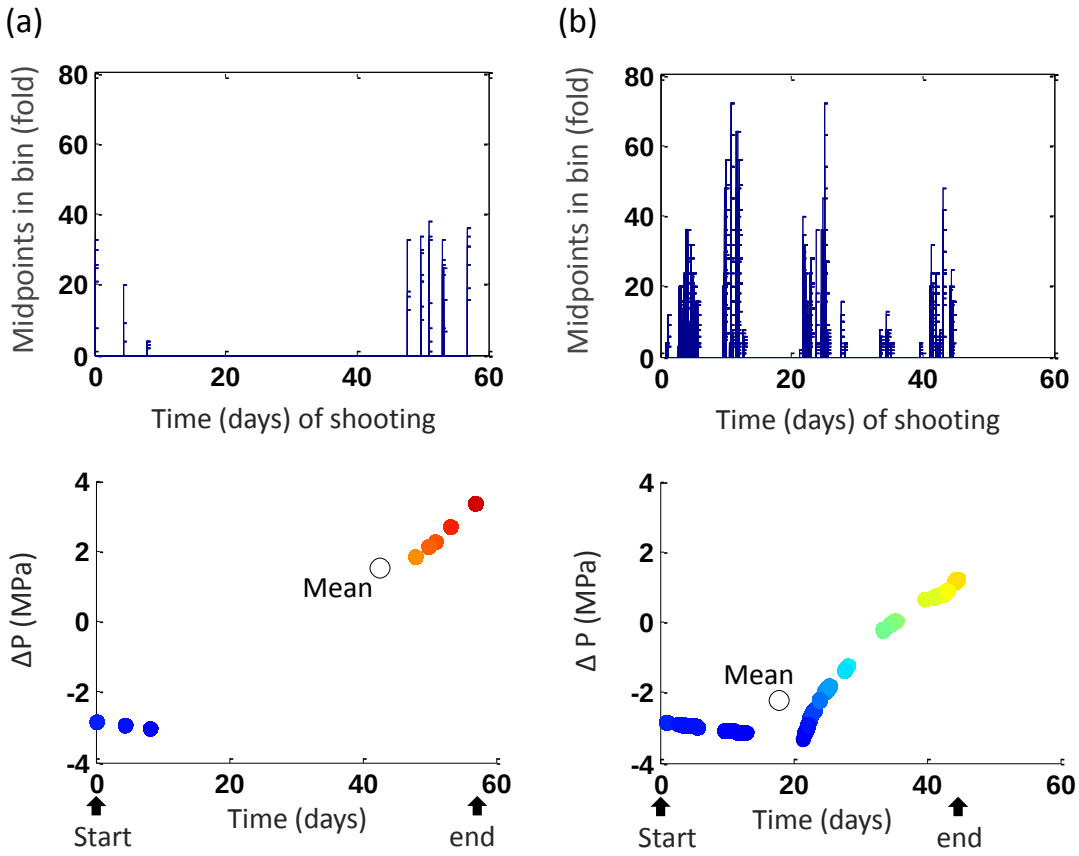

Figure 4-19 Histogram of timestamped midpoints in a bin (fold) using the decimated acquisition bin size of 67.5 × 50.25 m (see Table 4-2) showing the time variability across a particular CMP bin ('pre-stack') and corresponding fluctuations in pressure change (monitor-preproduction) during the acquisition for the (a) towed streamer survey (c)-(d) PRM survey. The location of the CMP bin is annotated in Figure 4-12(a) as A1. Assuming a linear 4D seismic response to pressure change (see Figure 2-10) since ΔP < 5 MPa at any time during both surveys, the mean value of the pressure change (synonymous to 'CMP stacking') does not represent the pressure changes at any time during the monitor acquisition

Both the PRM and towed streamer survey capture certain parts of the pressure behaviour and are also different in magnitudes because of their different time sequence of shooting. The towed streamer captures additional 13 days beyond the time frame of the PRM survey. The midpoints show that pressure changes (relative to pre-production) at this bin location fluctuate between ±4 MPa during the PRM and towed streamer survey (Figure 4-19). The 4D seismic response to pressure changes will also fluctuate. By observation, the pressure change at any time during the acquisition is less than 5 MPa at this bin location. Therefore, a linear response to pressure should be expected based on rock-physics calculations (Figure 2-10). This linearity supports the conclusion

that in a 'post-stack' sense, the CMP stack 4D response would represent the mean of the pressure change (indicated on Figure 4-19), which is not true of the real pressure changes at this bin location.

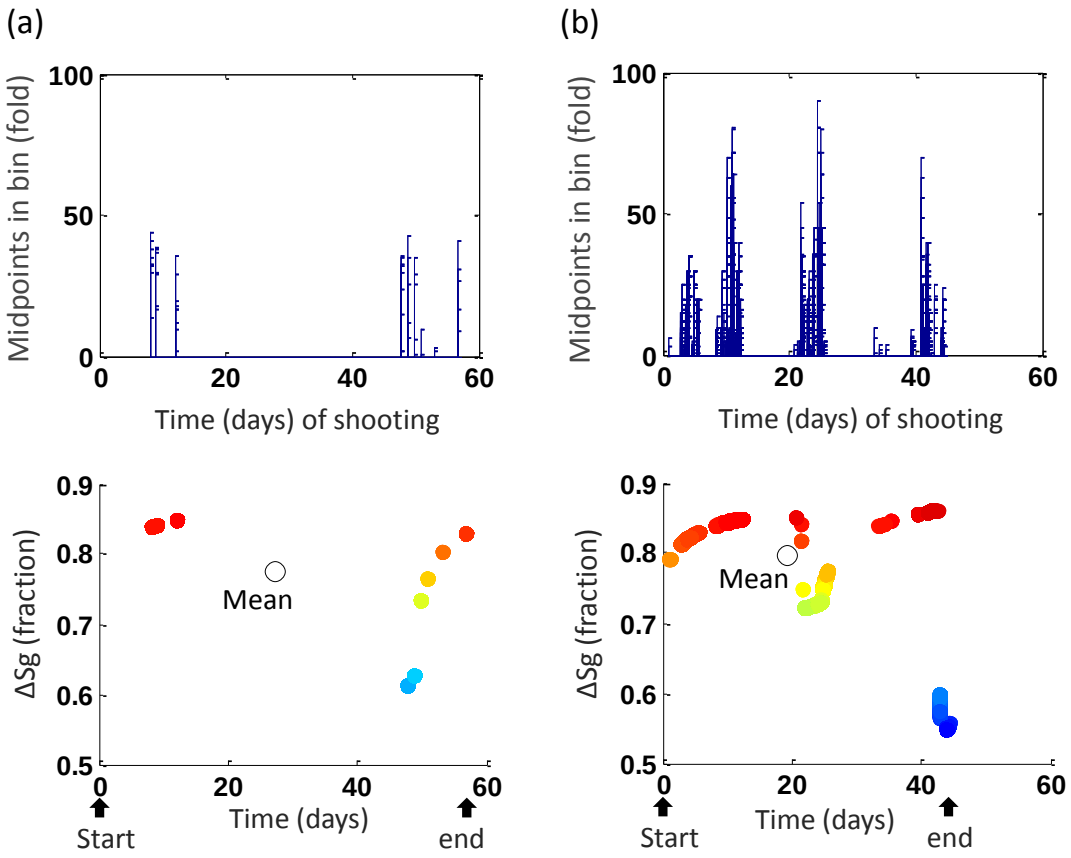

Figure 4-20 Histogram of timestamped midpoints in a bin (fold) using the decimated acquisition bin size of 67.5 × 50.25 m (see Table 4-2) showing the time variability across a particular CMP bin ('pre-stack') and corresponding gas saturation change fluctuations (monitor-preproduction) during the acquisition for the (a) towed streamer survey (b) PRM survey. The location of the CMP bin is annotated in Figure 4-12(c) as A3. The colours, blue to red, indicate increasing gas saturation change. As the fluctuations in gas saturation change lie within the linear region of the rock-physics modelled 4D seismic response (see Figure 2-10), the mean value of the gas saturation change can be considered as the CMP stacked response, and this does not represent the situation at any time during the acquisition.

The same is observed for other reservoir processes, for example, in the gas breakout area close to the producer, P6 (Figure 4-20). The PRM shooting is better able to capture some of the complex gas saturation fluctuations that the towed streamer misses (due to its long down-time). In Figure 4-21, a time distribution of water saturation changes at a CMP bin located around the new injector I1 (which started on day 1 of the acquisition) is shown. As the waterfront grows with time, both the PRM and towed streamer survey acquire different magnitudes. If the 4D seismic response to pressure change or gas

saturation change lies outside the linear region (as indicated on Figure 2-10), this non-linearity implies that the CMP stack 4D response is not the mean of the pressure or gas saturation change (as assumed on Figures 4-19 and 4-20) but the mean of the 4D seismic response from each midpoint.

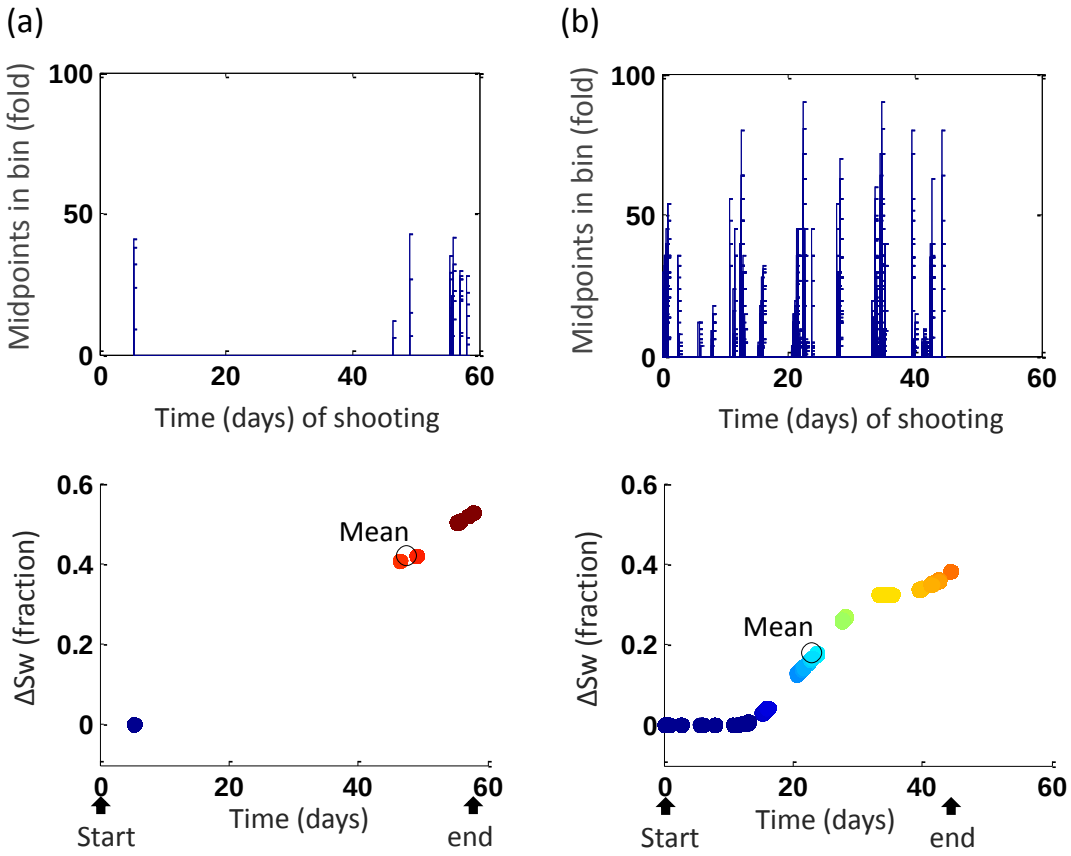

Figure 4-21 Histogram of timestamped midpoints in a bin (fold) using the decimated acquisition bin size of 67.5 × 50.25 m (see Table 4-2) showing the time variability across a particular CMP bin ('pre-stack') and corresponding water saturation change fluctuations (monitor-preproduction) during the acquisition for the (a) towed streamer survey (b) PRM survey. The location of the CMP bin is annotated in Figure 4-12(b) as A2. The colours, blue to red, indicate increasing water saturation change. Since the 4D seismic response to water saturation changes is approximately linear (see Figure 2-10), it can be concluded that the mean value of the water saturation change is synonymous to 'CMP stacking' and this mean value (or resultant stack) does not represent the entire water saturation changes during the acquisition.

Assuming a linear 4D seismic response to reservoir changes, it is possible to visualise the CMP stack response (i.e. "post-stack" response) in terms of the reservoir changes at each CMP bin location. Figure 4-22 (a) and (c) show the resulting 2D map of the acquired pressure change over the reservoir based on the mean from the distribution of pressure changes at each CMP bin, from the towed streamer and PRM surveys, respectively. For comparison, a reference 2D map of pressure change, based on the mean of the simulator predictions (output at fixed 30 seconds time steps from start to

end of the survey) at each CMP location is provided in Figure 4-22(b) and Figure 4-22(d) for the towed streamer and PRM time frame, respectively.

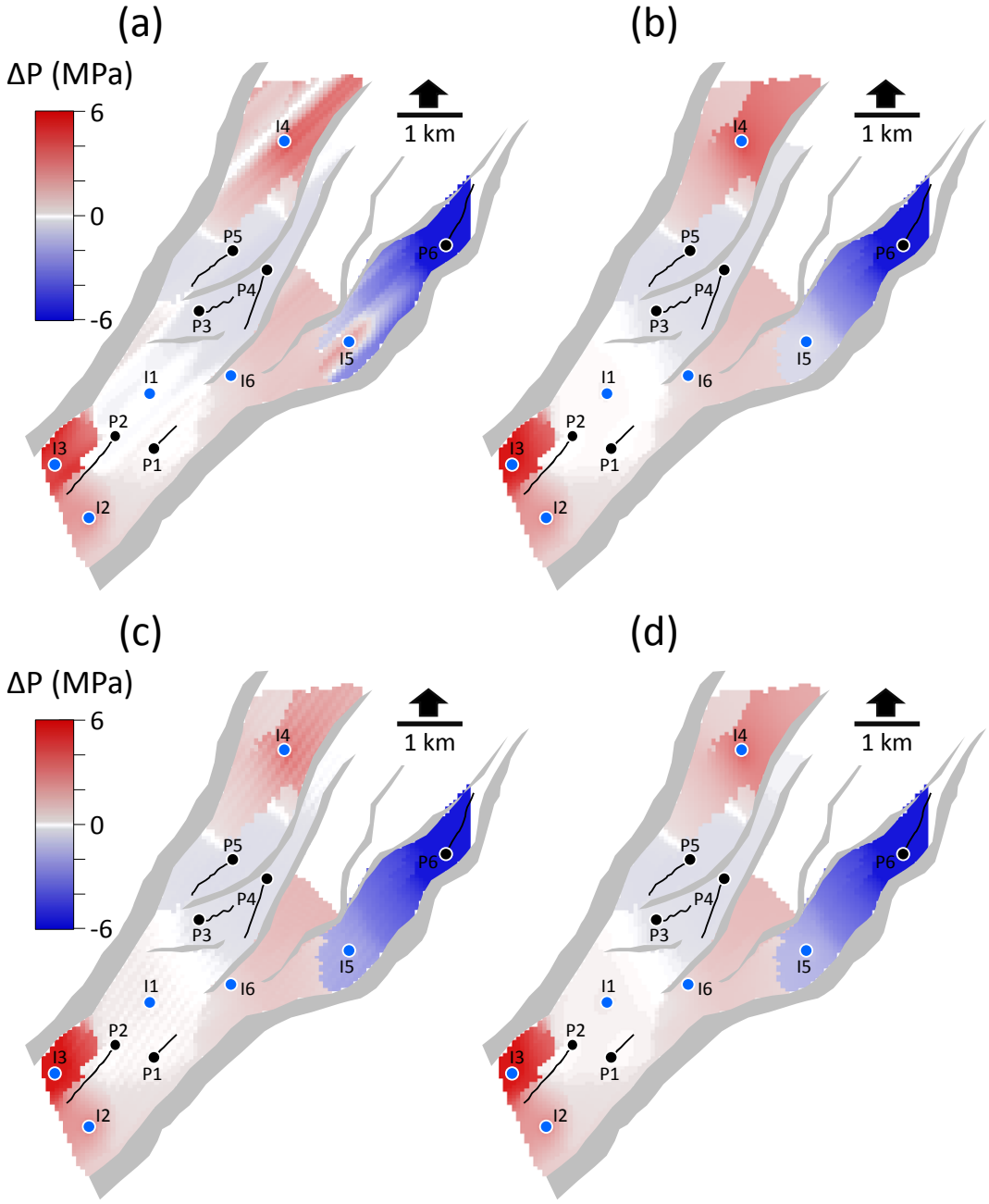

Figure 4-22 2D map of pressure change (monitor-baseline) acquired by the towed streamer (top) and PRM (bottom) surveys based on the spatio-temporal binning process. Displayed in (a) or (c) mean of pressure changes from the distribution of pressure at each CMP bin and (b) or (d) the reference determined from the average of predictions from the simulator over the survey duration at each CMP location. In (a) and (c) both surveys fail to capture the true nature of pressure relative to (b) and (d), worse for the towed streamer.

These reference maps represent the truth. By visual comparison, the spatial character of the representative post-stack pressure change acquired by the towed streamer in Figure 4-22(a)) relative to its reference (Figure 4-22(b)) is not the real nature of pressure.

This is due to timing of the shooting relative to the pressure fluctuations during the survey. The PRM survey (Figure 4-22 (c)) is much closer to its reference (Figure 4-22 (d)), and this is because of its specific design. With the sensors laid out on the sea bed, the PRM survey is able to acquire more midpoints per shot and over a much larger area per shot, but again, the spatio-temporal imprint of the timings of the shot relative to the pressure fluctuations are still visible as strips.

4.5 Summary

- In this chapter, a fundamental aspect of seismic survey acquisitions in terms of the time scales of common reservoir processes was discussed. Often, reservoir pressure is not in equilibrium during monitor surveys, if at all during the field's life time of production, and surveys are not shot instantaneously. Wells and field operations during the shooting will cause fluctuations at the well and spatially across the reservoir over the many weeks of the monitor acquisition and this has consequences for the acquired data.

- To investigate the above, a self-developed integrated workflow was implemented. Monitor acquisitions of a PRM and towed streamer survey in the North Sea were used to reconstruct pressure, water and gas saturations changes based on the time-sequence of the shooting and CMP locations of the survey data, by spatio-temporal binning. The simulator predictions were obtained from the Norne field model and output at very fine time scales sequenced according to the timings of each shot from both surveys. The spatio-temporal binning provided access to the reservoir dynamic domain based on how the survey is being shot.

- Focusing on key locations where gas breakout had occurred, waterflooding had commenced around the time of the survey and also where pressure changes occurred, a preliminary analysis of both acquisitions was performed.

- From this, it was revealed that the pressure, water or gas saturation changes acquired by the surveys is a consequence of the time sequence of the shooting in relation to the reservoir behaviour and this is specific to the particular acquisition.

- Both surveys capture different magnitudes of the reservoir changes due mainly to their different shooting sequence. This particular towed streamer is more affected than the PRM due to the prolonged down times experienced. The PRM survey shoots more continuously and it is better able to capture the reservoir changes across the time of the acquisition. In general, towed streamer surveys will be more affected than PRM surveys because of their very limited streamer (cable) dimension compared to the PRM's seabed sensor system.

- Although CMP stacking (i.e. averaging for post-stack data) is generally inadequate for 4D seismic studies, the occurrence of intra-survey reservoir fluctuations adds to the inaccuracies in post-stack 4D seismic data. This is because the same location will have been acquired at different times during the shooting, and therefore will have captured different reservoir changes. By averaging, there is a lack of truth in the resultant reservoir change.

In the next chapter I conclude this study by performing a seismic modelling exercise which uses the pressures and saturation changes obtained after performing the spatio-temporal binning of the towed streamer and PRM monitor acquisitions. The aim, thereof, is to investigate what impact such dynamic reservoir fluctuations that occur during the acquisition, may have on quantitative analysis using the acquired post-stack 4D seismic data.

Chapter 5

Intra-survey reservoir fluctuations – An assessment of its impact for quantitative 4D seismic interpretation

To get the most value from 4D seismic technology, quantitative estimates of the reservoir changes (for example, pressure and saturations) from 4D seismic data are often desired for reservoir management purposes. Magnitudes of 4D seismic signals (amplitudes, time shifts or other 4D attributes) are therefore relied upon for their accuracy. In Chapter 4, the reservoir changes were reconstructed based on how the acquisitions have been shot. This revealed that the pre-stack intra-survey reservoir fluctuations are important and cannot be neglected. Following this, the impact of the intra-survey reservoir fluctuations in the post-stack seismic domain is assessed here by seismic modelling via 1D convolution and a migration operator. It is found that the final migrated post-stack 4D seismic response does not directly represent the true absolute reservoir changes, but is a mixed version of reality that depends on the sequence and timing of seismic shooting. The outcome is a lack of accuracy in the measurement of reservoir changes using post-stack or offset sub-stacks from the 4D seismic data, as they are found to be in error. It is recommended that pre-stack 4D seismic data should be analysed using the time stamp of the acquisition, and the data shot in a consistent pattern to optimise aerial time coverage.

5.1 Introduction

Measurements of pressure change across the reservoir are useful for evaluating well performance, and in particular the reservoir connectivity that relates to the degree of aquifer/injector pressure support, barriers, fault seal/non-seal, and compartments. Saturation measurements are also useful for assessing sweep efficiency, barriers, the risk of breakthrough, and optimal monitoring of production and recovery. This information is typically provided by production logging tools, down-hole gauges, and/or subsurface fluid-flow simulation models. As discussed in Chapter 1, 4D seismic technology has been used extensively to sense these changes, with the added benefit of access across the inter-well space. However, despite significant improvements in processing and acquisition over the past ten years, accurate quantitative estimation of changes in the reservoir using 4D seismic data (using amplitudes, time-shifts or some other attribute), especially that of pressure, remains technically challenging (Eiken and Tøndel, 2005; Røeste et al., 2015) for a wide variety of accepted reasons (Alvarez and MacBeth, 2014). The limitations for pressure include most significantly the uncertainty in obtaining a precise description of the rock stress sensitivity and geomechanical response. The ability of 4D seismic data to detect pressure and saturation changes is believed to be dependent on 4D seismic data non-repeatability (i.e. magnitude of non-production related artefacts, 'noise') and 4D seismic signal (i.e. the magnitude of the change in reservoir's elastic properties due to the induced production) which not only depends on how significant the production is but mainly on the seismic properties of the reservoir (Johnston, 2013). As observed in Chapter 3, data from a number of case studies indicate that large increases in pressure of 5 to 15 MPa from fluid injection into isolated compartments are readily visible, whilst field-wide pressure fluctuations of less than 5 MPa or more may be difficult to detect with accuracy in many reservoirs (Landrø and Øyvind, 2002; Hurren et al., 2012; Domes, 2010; Omofoma and MacBeth, 2016). Fluid saturation, on the other hand, is measured with better accuracy in general - although the impact of pressure uncertainty on saturations remains unclear.

To contribute to this research topic, another factor of relevance is suggested. This concerns the time scale of the seismic data acquisition relative to that of the reservoir fluctuations themselves which was conceptualised in Chapter 4. During seismic acquisition (either offshore or onshore) over many weeks, the inevitable rapid

fluctuations induced in the field are captured in a non-obvious and irregular way across the pre-stack domain (Figure 4-19). The post-stack migrated data (and stacked pre-stack migrated data) therefore do not accurately reflect the spatial distribution of the true absolute pressure, but provide instead a complicated, smeared and distorted average over the survey duration. The purpose of this chapter is to assess the impact this may have on current 4D seismic interpretation and suggest possible changes to the acquisition and processing to reduce and possibly exploit this. If the intra-survey effects are significant, they could be used to provide more detailed information on the reservoir response, especially if the seismic acquisition is coordinated with the production, or vice versa. The work uses seismic modelling on the Norne field model based on pressures and saturations obtained after the spatio-temporal binning of the towed streamer and PRM acquisitions in Chapter 4.

5.2 Seismic modelling of the acquisitions

Seismic modelling is performed to compute the expected 4D seismic data acquired in the presence of the intra-survey fluctuations on the Norne field model. This is achieved by firstly converting pressure and saturation changes acquired by the PRM and towed streamer surveys into elastic parameters (P-wave velocity, V_P, S-wave velocity, V_S and density, ρ) using a petroelastic model specifically calibrated with well log data from the Norne field (Briceno et al., 2016). "*The petroelastic model consist of two parts: first the static rock components by which the saturated rock frame moduli and density in their initial (baseline) state are specified, and secondly the dynamic component which is defined by the fluid substitution model, effect of pressure changes on each fluid phase, and finally the stress dependency of the rock frame density and moduli"*, Briceno et al. (2016). The matrix moduli for clean sand and pure shale for the reservoir are given in Table 5-1.

	Sand	Shale
Matrix bulk modulus	29 GPa	16 GPa
Matrix shear modulus	25 GPa	7 GPa
Matrix density	2728 kg/m^3	2637 kg/m^3

Table 5-1 Sandstone and shale matrix elastic properties for the Norne Field, after Briceno et al. (2016).

The definitive value for each reservoir cell is calculated by its porosity and NTG, applying a sand-shale mixing average method (Backus, 1952) in Section 2.2.2. Pressure-dependent stress-sensitivity relationships (MacBeth, 2004) in Section 2.2.3 are then used to compute the elastic moduli of the rock frame. To account for saturation changes, fluid properties are calculated for their elastic moduli (Batzle and Wang, 1992) and the fluid mixtures are represented with an effective value by harmonic averaging (Domenico, 1974) as in Equation 2-9. The pressures and saturations from the acquisition in each CMP bin output their corresponding elastic parameters via Gassmann's model (1952), Equations 2-7 and 2-8. Reflectivity series are then computed using Zoeppritz equations (Aki and Richards, 2008), assuming uniform overburden and underburden properties (Table 5-2). After this, synthetic seismic volumes are obtained by 1D convolutional modelling using a data-derived wavelet (Figure 5-1).

Reservoir temperature	98.3°C
Water salinity	50000 ppm
Oil gravity	32.7° API
Gas gravity	0.8618
Overburden properties	P-wave velocity = 3350 m/s; S-wave velocity = 1800 m/s; Density = 2450 kg/m^3
Underburden properties	P-wave velocity = 3200 m/s; S-wave velocity = 1600 m/s; Density = 2300 kg/m^3

Table 5-2 Reservoir parameters (fluid properties, temperature and earth model) used for synthetic seismic modelling based on the Norne Field.

For each CMP bin, modelling is performed using the same angle range, 0 to 40° for the time-sensitive pressure and saturation changes obtained per offset class after the spatio-temporal binning of the acquisitions. At each CMP bin location, the mean of the pre-stack traces corresponding to the offset class from the acquisition geometry are then calculated to yield a single trace per offset class. Over the survey area, these mean traces represent offset stacks for post-stack seismic data. The same angle range (a single angle could also be used, instead of a range) is used so as to assess solely the temporal sampling of the intra-survey fluctuations by the acquisition (at each offset class), outside any influence of amplitude-variation-with-angle (or offset (AVA/AVO)), which would superimpose on the effect currently being studied. For the monitor acquisition geometries used for this work, this process yields time-lapse seismic volumes

corresponding to the offsets classes 0 to 1500 m (near), 1500 to 3000 m (mid), and 3000 to 4500 m (far), in addition to the full stack (up to 5600m for the towed streamer, 14600 m for the PRM). The baseline seismic data is assumed to be acquired pre-production, so the petro-elastic modelling and 1D convolution at a fixed angle of incidence is also done at the pre-production state of the reservoir. Since the baseline is acquired pre-production, its shot times are not considered as the reservoir is in equilibrium, and there are no intra-survey reservoir fluctuations prior to production.

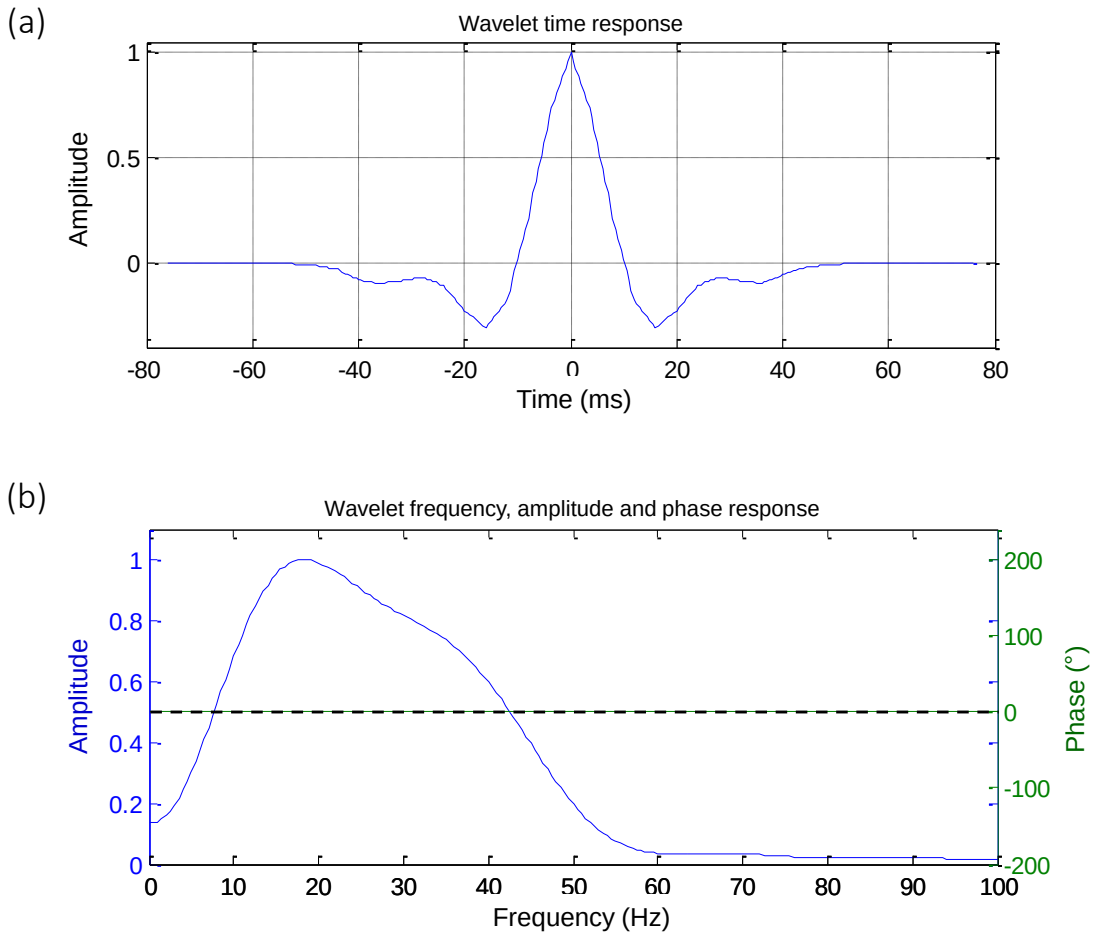

Figure 5-1 (a) Statistical wavelet (with normal polarity) extracted from the baseline seismic data (full-stack) from the Norne Field, (b) The amplitude spectrum in the frequency domain with peak frequency around 19 Hz.

In the context of integrating the seismic domain and the reservoir engineering domain, attributes modelled from the fluid-flow simulation model are often compared to those obtained from the seismic domain (see Figure 1-6). In this modelling work, the 4D seismic volumes from the seismic domain are modelled based on the acquisition geometry and shot timestamps (i.e. the combined workflows in Figure 4-13 and Figure

5-2 to follow) through the use of the fluid-flow simulation model. A monitor seismic volume for the PRM and towed streamer survey can also be modelled directly from the simulation model and this can be used to provide a reference 4D seismic volume for comparison. The two reference monitor volumes are obtained as described above by simulator-to-seismic modelling. In this case, instead of modelling the simulator predictions according to the shot timestamps of the acquisition to account for the intra-survey effect, an average is used. This average is obtained from all the predictions of pressures and saturations output from the simulation model. The predictions are output at 30 seconds linear intervals from start to end of the monitor acquisitions.

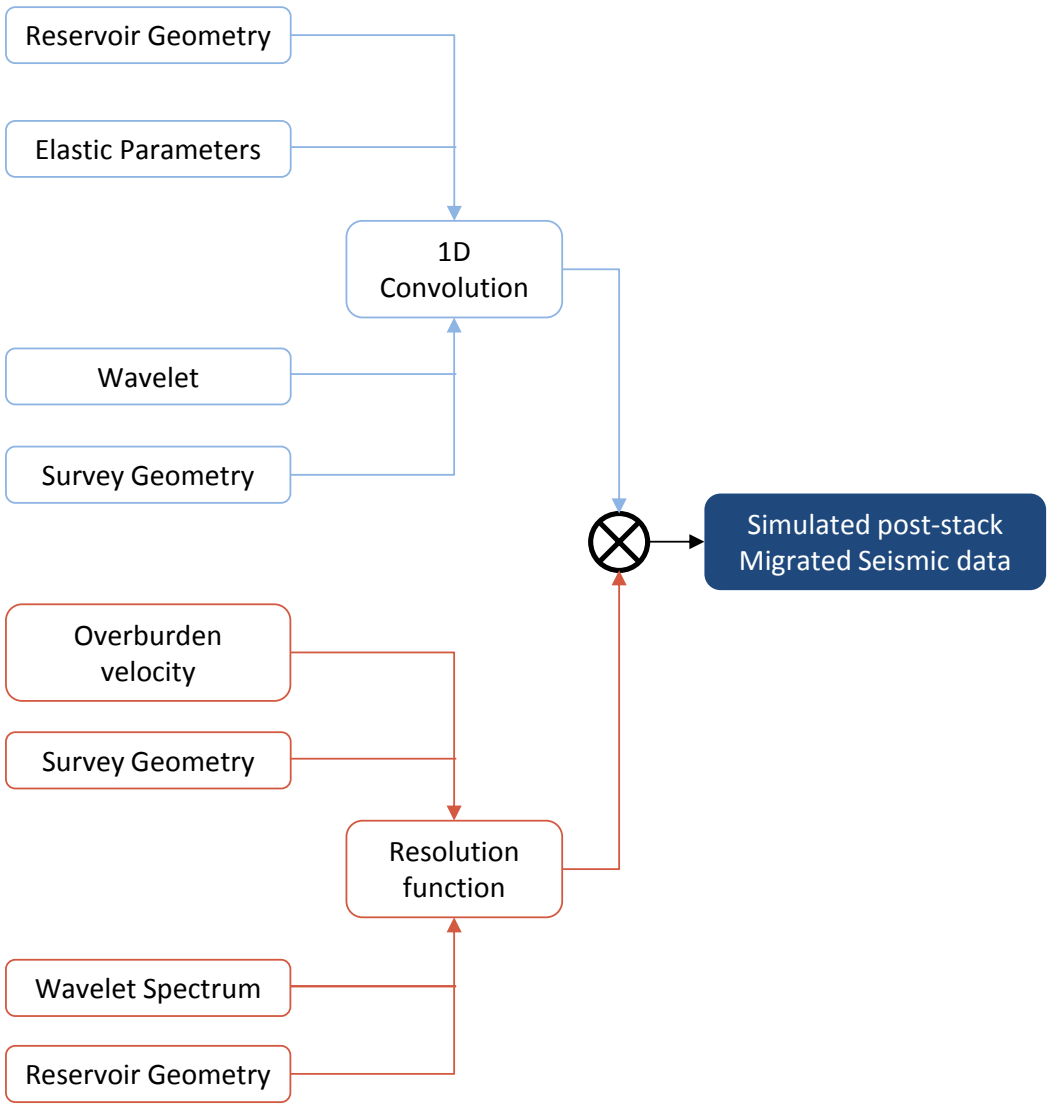

Figure 5-2 Key components of the seismic modelling 1D convolution algorithm with a resolution function (migration operator) to simulate a post-stack time migrated seismic data, after Amini (2014). The elastic parameters are modelled using the static and dynamic (reconstructed pressure and saturation acquired by the acquisition, see Figure 4-13) reservoir properties. The assumptions of this workflow are discussed in Section 5.2.1, and a proper seismic modelling scheme is presented in section 8.2.3 (Figure 8-3) for future studies of the intra-survey effect.

Prior to the above modelling, properties defined on the reservoir grid had been earlier transformed onto a rectangular grid, defined by the bin size (67.5 x 50.25 m) from the acquisition, so the size of a reservoir cell corresponds to a CMP bin (Figure 4-14).

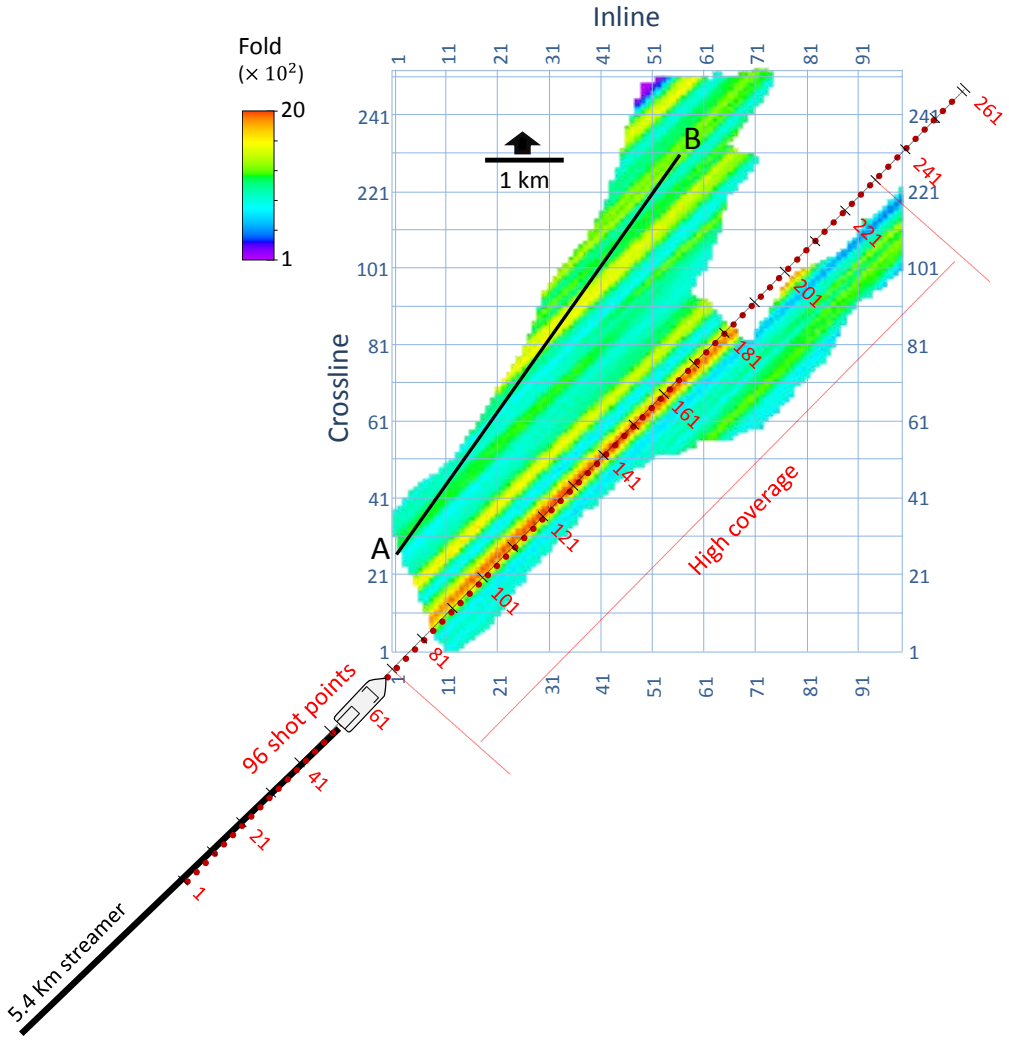

Figure 5-3 Schematic of the 2D geometry (one source with a streamer towed behind it) used for resolution function calculation showing the location of the shot line (with annotated CMP numbers), overlaid on the actual full offset fold from the towed streamer acquisition showing irregular coverage. Inline and crossline layout from the 1D convolution are as shown. Line A to B is used in Figure 5-6.

After this, following Amini (2014) a realistic post-stack time migration data is simulated by convolving the seismic volume from the 1D convolution with a migration operator (otherwise called, 'resolution function'). The algorithm for creating the migrated seismic data based on 1D convolution is shown in Figure 5-2.

Shot line length	12960 m
Number of shot points	96
Shot point spacing	135 m
Streamer length	5400 m
Number of receivers	54
Receiver spacing	100.5 m
Number of CMP locations	258
CMP spacing	50.25 m
Maximum fold	20
Dominant frequency	19 Hz
Depth image point in TWT	1.575 s
Background velocity	3350 m/s

Table 5-3 Parameters used for computing the resolution function based on the reduced acquisition geometry used in this study (see also Table 4-2).

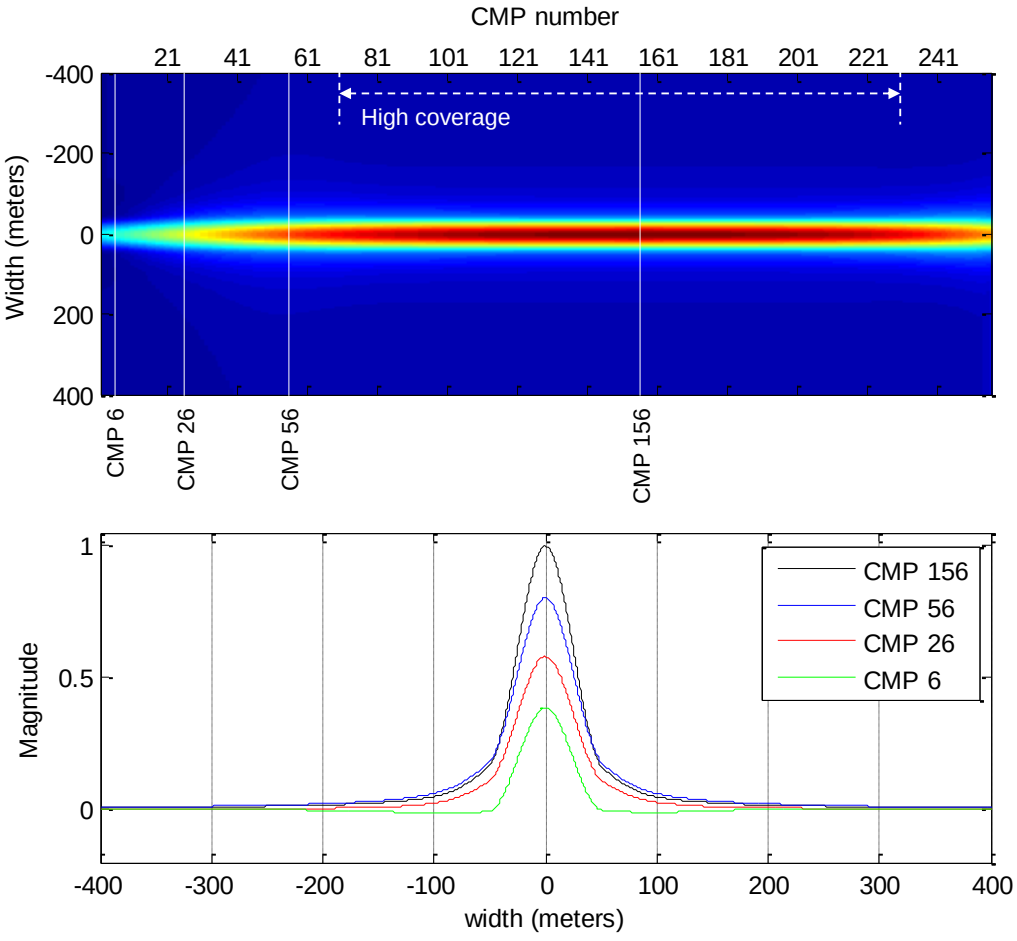

Figure 5-4 The variations of the resolution function at different CMP locations on the 2D line in Figure 5-3. The resolution function changes from the central high fold area to the edges of the line with low fold.

Amini (2014) shows that this modelling approach yields similar results to the more sophisticated finite difference (FD) modelling and processing workflow proposed in Section 8.2.3. However, the similarity (see Figure 8-4) was achieved under certain FD modelling assumptions such as: thin reservoir, uniform overburden, and noise-free seismic data.

For the simulated migration in this work (Figure 5-2), the resolution function depends on the acquisition geometry, reservoir depth, wavelet frequency spectrum and overburden velocity (Toxopeus et al. 2003) and it is calculated using the equation of Chen and Schuster (1999) for post-stack seismic data. For the calculation of the resolution function, a 2D line from the acquisition assuming a single streamer towed behind a source is used (Figure 5-3). The length of the shot line and number of shots on a line is the average from the towed streamer survey. Parameters used for computing the resolution function are also given in Table 5-3.

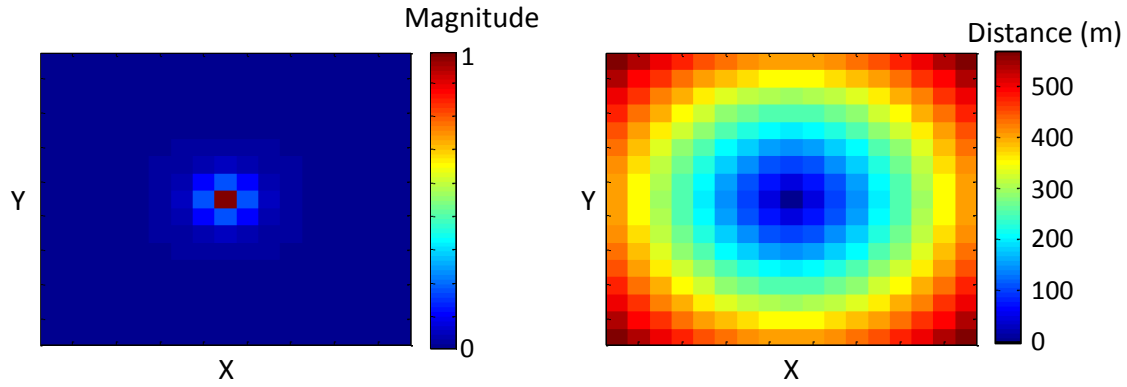

Figure 5-5 The resolution function at CMP 156 (Figure 5-4) represented as a spatial filter with magnitude and lateral distance (in meters). This is applied to time slices of the 3D seismic volume by 2D (i.e. lateral) convolution.

Similar to observations in Amini (2014), the shape and magnitude of the resolution function varies across different locations on the shot line depending on the coverage (Figure 5-4). The lateral variation is not very strong due to the modelled case of a uniform overburden and thin reservoir. A single resolution function will thus suffice in the reservoir area and a good choice would be in a high fold location, CMP 156 for example. Finally, the resolution function is transformed into a spatial filter (Figure 5-5), and applied to both baseline and monitor post-stack seismic volumes from the 1D convolution.

Figure 5-6 shows a seismic section of the baseline data before and after applying the resolution function. As discussed in Section 4.3.4, the modelling assumed a uniform overburden and horizontal layers. Thus, the 1D convolution applied here assumes that the image point of reflection at the reservoir level is directly below the geometric midpoint of the trace at the surface. In reality, the subsurface is complex and the reflected information could have been generated from anywhere in the subsurface with the same two-way travel time (Sheriff and Geldart, 1995).

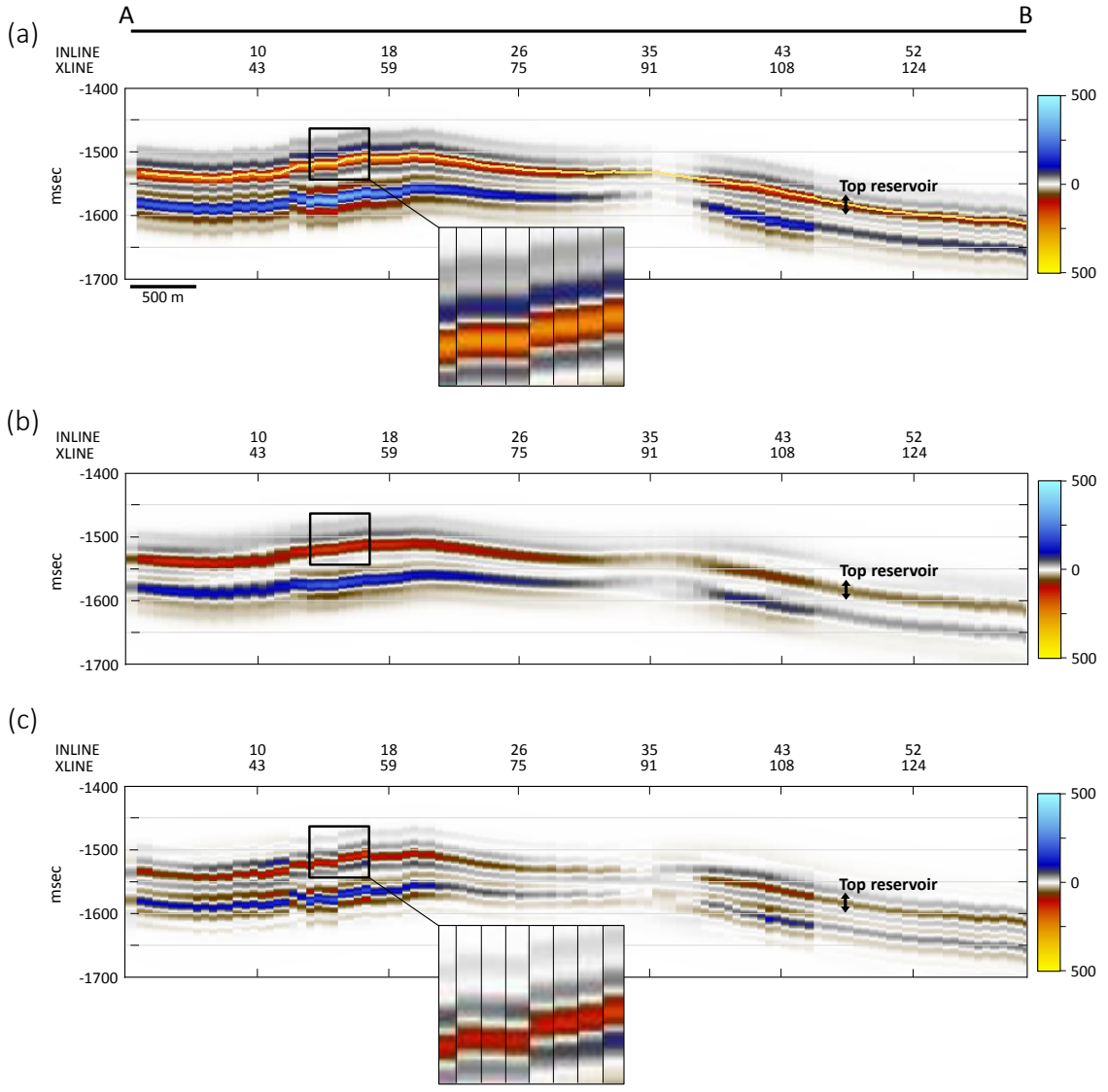

Figure 5-6 The 1D convolution versus the simulated migrated stack. (a) the baseline seismic section before application of the resolution function, (b) the baseline seismic section after application of the resolution function, and (c) the difference between (a) and (b). Line A-B is indicated in (Figure 5-3).

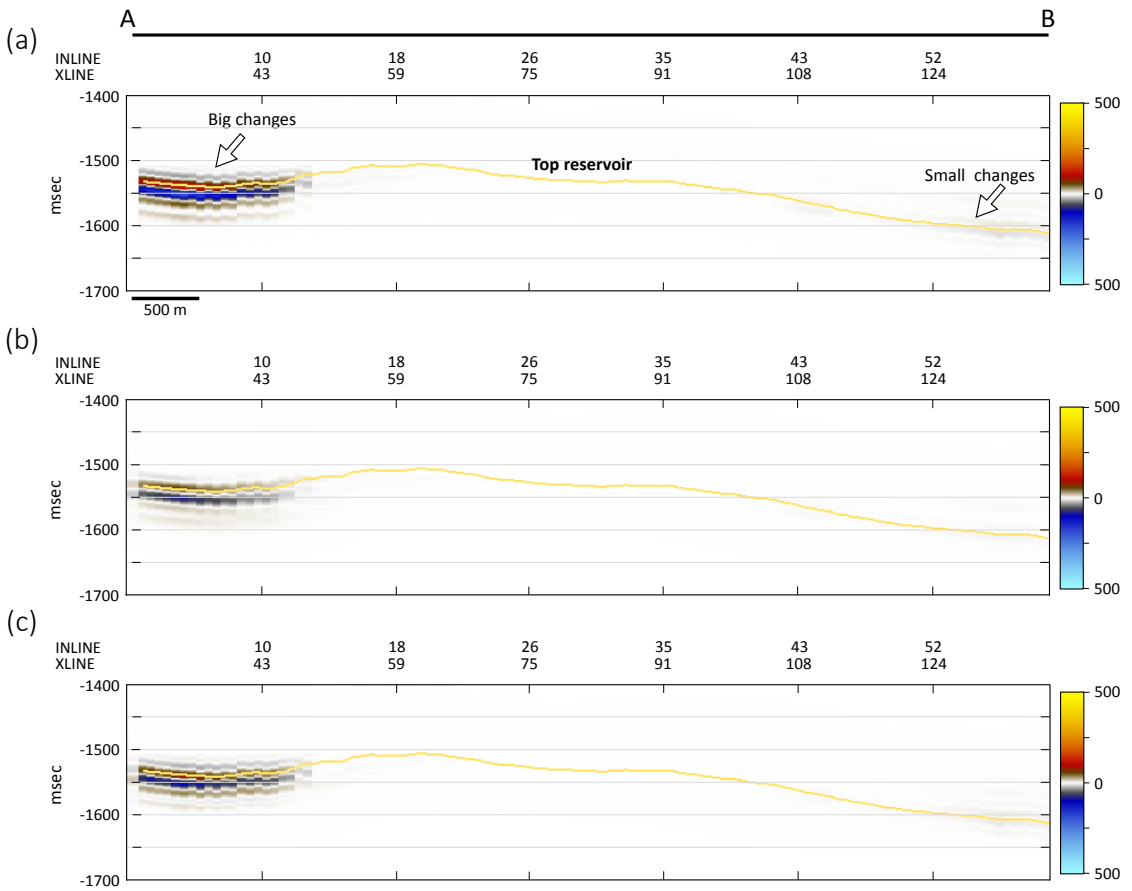

Figure 5-7 Time-lapse (monitor-baseline) response to pressure changes only. Comparison is made between the 1D convolution versus the simulated migrated section, using the reference monitor (full stack), softening (red-yellow), hardening (blue-cyan), (a) the 4D amplitudes before application of the resolution function, (b) the 4D amplitudes after application of the resolution function, and (c) the difference between (a) and (b). Line A to B is indicated in (Figure 5-8).

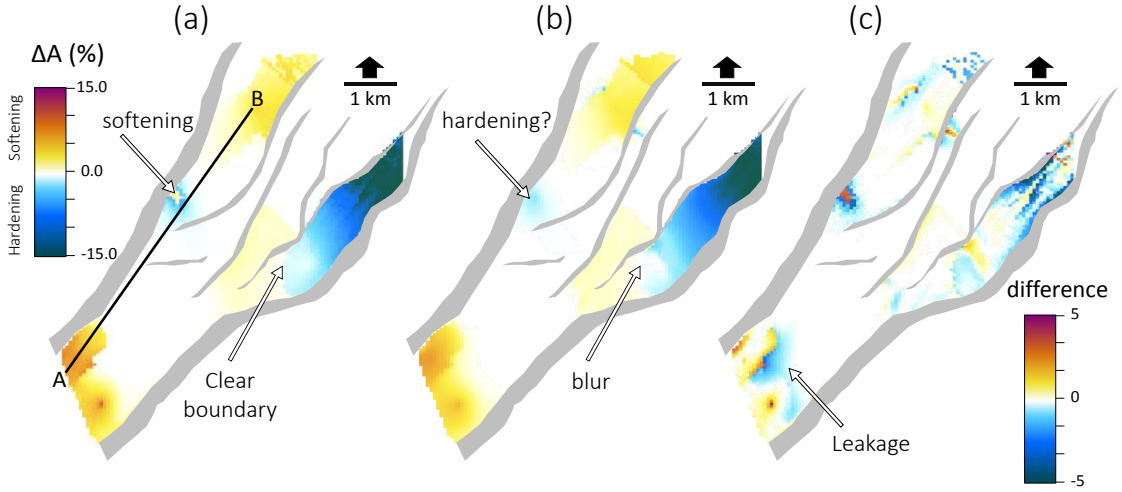

Figure 5-8 Top reservoir 4D amplitude response to pressure changes only, comparing the 1D convolution versus the simulated migrated stack. The amplitude response is expressed as a percentage change relative to baseline, using the reference monitor seismic data, (a) the 4D response before application of the resolution function, (b) the 4D response after application of the resolution function, and (c) the direct difference, (a) -(b).

The resolution function applied (Figure 5-5) is simply a filter which describes the spatial impulse response of the migration operator. It applies to all image points (i.e. CMP locations) in the post-stack seismic data obtained from the 1D convolution, irrespective of where the reflections are generated. Discontinuities at the cell boundaries from the simulation model appear smoothed in Figure 5-6 (a) compared to Figure 5-6 (b). Consequently, the amplitudes of the migrated section (Figure 5-6 (b)) are also dampened, the difference in Figure 5-6 (c) shows this. This is however, not an uncommon observation, as Canning (2010) suggests that migration could introduce some amplitude distortions.

In the modelled 4D seismic data, the amplitude response of the simulated migrated stack difference (monitor-baseline) show weaker magnitudes than the 1D convolution stack (Figure 5-7). Areas with the biggest 4D changes appear to be more dampened, but both small and big 4D signals are smoothed in the same degree; the 4D amplitudes are weakened by up to 30% in the simulated migrated stack. Along the top reservoir (Figure 5-8), it is shown that identifying barriers (e.g. compartments) can become more problematic using the signature of the 4D maps from the simulated migrated stack. Such features are unclear due to the smoothing by the applied resolution function. The smoothing also imposed 'false' polarities, and amplitude leakages, as areas where no 4D changes occurred, now show changes (Figure 5-8(c)).

It may be argued that the applied migration could magnify the intra-survey effect by introducing more distortions; however, the migration only smooths the 4D seismic response. A pilot result from the spatio-temporal binning in Chapter 4 (Figure 4-22) is a good approximation of the spatial character of the 4D seismic response when only pressure changes are considered, assuming that only 1D convolution is performed. Compare Figure 4-22 (a) and (c) to the actual 4D seismic amplitude response to pressure changes only, obtained after 1D convolution and migration (Figure 5-10 (a) and (c), respectively). It can be concluded that the applied resolution function does not significantly affect the response caused by intra-survey reservoir fluctuations. Also, by comparing Figure 4-22 (b) and (d) to Figure 5-10 (b) and (d) respectively, the same conclusions can be reached.

5.2.1 Assumptions of the intra-survey modelling workflows in Section 4.3.3 and Section 5.2

The spatio-temporal binning workflow (Figure 4-13) and 1D convolution seismic modelling workflow (Figure 5-2, Section 5-2) are geometric CMP-based (Figure 4-15) approaches, and, as such, are a crude way of analysing the intra-survey problem. Propagation effects of the seismic wavefield (amplitude loss, attenuation/absorption, diffractions, scattering, Amplitude Variation with Offset (AVO)), intrinsic noise of data acquisition contributed mostly by acquisition geometric non-repeatability, other noise such as multiples and statics, and effects of seismic data processing, especially migration, are not considered. In real seismic experiments and processing, all of these effects including the intra-survey reservoir fluctuations combine to affect the acquired 4D seismic data, and it is difficult to separate one from the other. The assumptions described below highlight the limitations of the modelling workflows adopted in this chapter and in Chapter 4. However, these workflows (Figure 4-13 and Figure 5-2) achieve the main aim of the analysis, which is to study purely the intra-survey problem outside other effects mentioned above.

(1) Homogeneous overburden earth model:

To perform 1D convolution, seismic reflectivity from the surface down to the reservoir (the overburden), in the reservoir, and below the reservoir (the underburden) is required at each bin location. The reflectivities are computed using Zoeppritz equations (Aki and Richards, 2008) which require a 3D earth model containing the elastic properties (P-wave velocity, V_P, S-wave velocity, V_S and density, ρ). These are calculated using the rock-physics equations in Section 2.2, with some simplifications. The overburden and underburden consist only of shale with homogenous elastic properties i.e. a single V_P, V_S and ρ (see Table 5-2). The overburden remains unchanged during production. The reservoir sands remain heterogeneous, with lateral variations in V_P, V_S and ρ provided by the static and dynamic properties of the simulation model. It is also only the reservoir (with a thickness of 28 m and at a depth 4500 m) that is affected or changed during production.

(2) Horizontal reflectors (no dipping layers):

As the interest is the reservoir's response, the overburden and underburden are not just homogenous (with no diffractors), but are also flat. This implies a horizontal and continuous overburden/reservoir interface, and the reservoir is structurally simple such that the dip is negligible. As seen in Figure 4-8(a), the reservoir layer is not flat, but is dipping at angles of 0° to 10°, but mostly at 4° which should not be neglected. In addition, abrupt discontinuities due to faulting will cause diffractions and scattering. The 1D convolution to be performed here handles only reflected energy, and not diffracted energy.

(3) *Common-midpoint (CMP) maps directly to common-depth point (CDP) (or common-reflection point (CRP) or common-image point (CIP)):*

The assumptions in (1) and (2) imply straight ray-paths from source to reflector and back to the receiver at the surface. So, the recorded location which is the point at the surface halfway between the source and receiver is shared by numerous source-receiver pairs, and is called the common midpoint. Thus, a CMP location recorded at the surface is assumed to be the same CMP location in depth vertically down to the reservoir reflector (Figure 4-15). This allowed the development and implementation of the spatio-temporal binning workflow (Figure 4-13).

In the real earth, strata are dipping with complex geology including faulting, folding, (some) fracturing, salt bodies, different lithology/rock type and unconformities, and other velocity anomalies in the overburden. Where dip is present, the CMP method breaks down since traces do not all reflect from the same mid-point location, likewise, where other geological complexities exist. As is the case with imaging the real subsurface, multi-channel processing techniques such as Dip Move out (DMO) and Migration are required to accurately reposition/move the seismic data from the recorded surface locations to the locations in depth with the correct CMP. This correctly located CMP is otherwise called common-depth point (CDP) or common-reflection (CRP) or more appropriately, common-image point (CIP). Migration corrects the flat-geological-layer assumption by a numerical, grid-based spatial convolution of the seismic data to account for dipping events (where geological layers are not flat) and collapse diffractions (Yilmaz, 2001). Such

imaging techniques work by combining many traces from different CMP locations. This contradicts the 1D convolution method applied in Section 5-2, which embodies a single channel seismic reflection system. Although, a migration operator (see Figure 5-4) based on Chen and Schuster's (1999) equations is applied on the post-stack seismic data obtained after 1D convolution, it only crudely emulates the smoothing effect of migration (see Figure 5-6), and the reservoir's dip is ignored (assumptions (1) and (2) above). It is simply the spatial impulse response of the migration operator and is applied to all image points (i.e. in this case, CMP bin locations) irrespective of where the reflections are generated.

(4) Perfect geometric repeatability between baseline and monitor acquisition:

This implies source and receiver positions (Figure A-2) are the same in the baseline and monitor acquisition, which is not always the case. Source positioning errors, *ΔSource*, between the baseline and monitor PRM survey (Figure 4-6) are +/-5 m or lower, but with permanently installed sensors on the seabed, the receiver positioning error, *ΔReceiver*, is zero. However, for the towed streamer acquisitions in Figure 4-7, the monitor and baseline positioning errors combined, *ΔSource +ΔReceiver*, are a maximum of 180 m, but on average around 65 m (calculated from the 1500 m to 3000 m mid-offset locations). The influence of such degree of non-repeatable acquisition geometry in the intra-survey analysis in Section 5.3 is not modelled and is considered negligible for two reasons. The first is that a common grid with a large CMP bin size (i.e. grid size) of 67.5 x 50.25 m is used, which was found to be the optimum for both the PRM and towed streamer acquisition data (see Table 4-1). The second and most important is that a horizontal, homogenous and non-changing overburden is modelled based on the assumptions in (1) to (3). In the real subsurface, the overburden can be very complex and near-surface velocity variations including sea tide, water bottom and weathering layer changes occur, making even the smallest positioning errors between baseline and monitor acquisition cause high non-repeatable noise (non-production-induced time-shifts, amplitude and phase changes), which is problematic for imaging the true 4D seismic response at the reservoir interval.

Smit et al. (2005) compile a chart of NRMS versus *ΔSource +ΔReceiver* measure

for processed 4D seismic data acquired in several North Sea fields (Figure 5-9). The NRMS error was computed above the reservoir and away from any intervals affected by production.

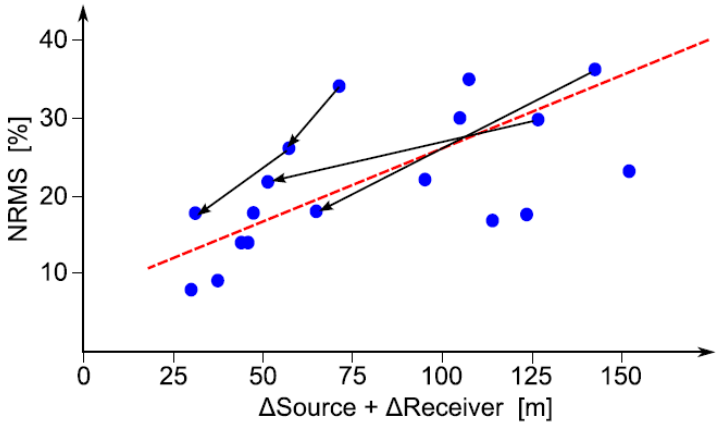

Figure 5-9 Geometry repeatability for towed streamer surveys. The relationship between NRMS values and the average positioning error in source plus receiver location, ΔSource +ΔReceiver, for 4D surveys in the North Sea. Each blue dot represents one acquired 4D survey. Arrows connect repeat surveys shot over the same field. The dashed red line marks the trend of the data (after Smit et al. (2005)).

Each dot in Figure 5-9 represents one 4D seismic survey. Black lines connect points corresponding to the same field in cases where multiple surveys are acquired over the same field. A clear trend of decreasing NRMS values with decreasing positioning errors (Figure 8-3, dashed red line) can be observed. This is evident for the three fields (black lines) where multiple 4D seismic surveys are shot. For the latter case, however, it is assumed that all 4D seismic surveys acquired over the same field are reprocessed so that the decrease in NRMS is solely attributable to the decreasing positioning error and not to an improvement in the data processing. An important observation is that mispositioning of source and receiver locations during 4D seismic acquisition is a controlling parameter which affects the overall NRMS measure.

This NRMS error due to geometric non-repeatability is rather high (Figure 5-9), compared to the resulting NRMS error caused by intra-survey reservoir fluctuations causing genuine production induced 4D signals in the reservoir - up to 7.5% is observed between the near and far offset stacks (Table 5-4, see Section 5-

3). However, positions of sources and receivers are increasingly well controlled now, such that geometric non-repeatability can lead to an NRMS of as low as 2 to 5% (for example, in PRM acquisitions; see also Figure 3-1). If such is the case, then the problem of intra-survey reservoir fluctuations in stacked 4D seismic data is likely to be dominant at the reservoir level.

(5) *Planar wave assumption and no attenuation:*

Geometrical spreading which causes amplitude loss with distance, and attenuation does not occur. This is not true of the seismic energy which behaves as spherical waves that spread-out over a spherical surface of ever increasing size as they propagate through the earth from the point source. In addition, as with elastic wave propagation, high frequencies are absorbed rapidly than low frequencies because of the intrinsic attenuation in rocks. So that deeper reflectors are of much lower resolution and lower amplitude than shallower reflectors. In addition, scattering attenuation which causes the energy of the seismic wavefield to be scattered in different phases when it encounters different rock properties does not occur. This also leads to amplitude loss and dispersive effects. This assumption of a planar wave is however not far-fetched. One of the fundamental techniques in processing is True Amplitude Recovery which accounts for amplitude loss (using a scaling function of velocity, offset and time), in an attempt to recover the true amplitude. Deconvolution, time-variant spectral whitening and inverse-Q filtering are also routine methods that try to remove the effect of attenuation by modifying the amplitude spectrum of the seismic signal (Yilmaz, 2001).However such effects cannot be completely compensated for in processing.

(6) Fixed Amplitude Variation with Offset response:

In typical angle-dependent seismic modelling, the incidence angle (equivalent of offset) is used to calculate the amplitude variation with angle (AVA) or offset (AVO) response. However, in the seismic modelling (Section 5.2) of the results from the spatio-temporal binning workflow in Figure 4-13, the amplitude dependency on the angle of incidence is omitted by calculating the reflectivity using the same angle of incidence as further discussed in Section 5.2. This is done so as to separate the intra-survey effect from the 4D AVO response. The workflow

(Figure 4-13) reconstructs the reservoir changes in pressure and saturation according to the acquisition geometry (source-receiver midpoint and offset) and timings of shots, based on the many assumptions above. As a result, the reconstructed pressure and saturation changes could be obtained for all midpoints at each CMP bin for a range of offsets from the acquisition geometry. Therefore any differences between the computed reflectivity (and convolved seismic traces) for the range of offsets at a CMP bin is solely due to their different time of shots. Different time shots imply different pressure and saturation changes as these are fluctuating during the acquisition (in Section 4.4 the results of implementing the workflow in Figure 4-13 are shown). If the AVO response was to be modelled by including different angle of incidence with respect to the different offset groups from the acquisition, then this will amplify the resulting NRMS measure of the intra-survey effect between offset stacks in Section 5.3. As real acquisitions and seismic wave propagation are naturally designed for the AVO effect, it is not possible to separate the intra-survey fluctuation problem from such effects in the acquired 4D seismic data. This is perhaps one of the perks of being able to study such a problem through a fixed-angle 1D convolution seismic modelling.

Based on the above assumptions, the intra-survey modelling results in this chapter provide only a rough estimate of the magnitudes of the 4D seismic response obtained through 1D convolution seismic modelling. A comprehensive scheme for modelling the seismic data as the reservoir changes during the acquisition using finite difference (FD) modelling, and including the effects of data processing is discussed in Chapter 8 (Section 8.2.3). The FD modelling is performed only once for the baseline survey as it is assumed to be acquired pre-production. For the monitor, this will need to be repeated for as many shot times acquired (Figure 8-3). This is because intra-survey reservoir fluctuations occur during the monitor acquisition, and the reservoir might be changing at each shot time. Seismic shot gathers for the entire survey area are output from the FD scheme for the baseline, but for the monitor, these should be obtained for each shot time. Typical 4D seismic processing workflows (Figure 8-5(b)) can then be applied on the modelled shot gathers, and the shot timestamp preserved for the reconstruction of the acquired 4D seismic data through spatio-temporal binning. Applying the full scheme (Section 8.2.3) is beyond the scope of this thesis and it recommended for future studies.

5.3 An assessment of the impact of intra-survey reservoir fluctuations

In Section 4-2 (Figures 4-4 and 4-5), it was understood that pressure behaves more like a wave and diffuses quickly, but the waterflood front moves slowly during the time frame of a seismic acquisition. The seismic modelling described in Section 5.2 was therefore performed separately for pressure changes and for fluid saturation changes (water and gas combined), so as to investigate the monitoring of these different character of reservoir changes by the towed streamer and PRM acquisitions.

5.3.1 Monitoring pressure changes

During the monitor acquisition, the wells exhibit pressure transient behaviour due not only to fluctuating flow rates but also near-well interferences and boundary conditions (see Figure 4-11). Even if constant well rates are maintained, the field would equilibrate well beyond the survey duration. Traces in each seismic bin will therefore sample the pressure field during different stages of its evolution (see Figure 4-19). Importantly, the time sampling of the reservoir vary across bin locations and also across offsets (see Figure 4-18). Therefore, the process of stacking mixes together distinctly different pressures, and the resultant seismic image does not represent the pressure at one particular time, but is a complex pre-stack combination of all pressure changes that have occurred during the shooting. This weighting of these pressures is a function of the spatio-temporal sampling across the survey, which depends on the particular survey and how it has been shot.

Acquisition imprints due to the time-sequence of shooting can be seen on the top reservoir full-stack responses (Figure 5-10 (a) and (c)). This appears as smearing, which is severe for the towed streamer but weaker for the PRM - both could easily be mistaken for genuine reservoir features. When interpreting the towed streamer response for example, the softening signals surrounded by the hardening signals in segment G could instead indicate a local compartment. To the south west of the field, around injector I3, notice that the PRM survey (Figure 5-10 (c)) captures bigger magnitudes of pressure than the towed streamer (Figure 5-10 (a)). This is solely due to the different timings of both acquisitions relative to the injection activity at the time. The towed streamer shoots for an extra 13 days beyond the PRM survey, and thus images other changes during this

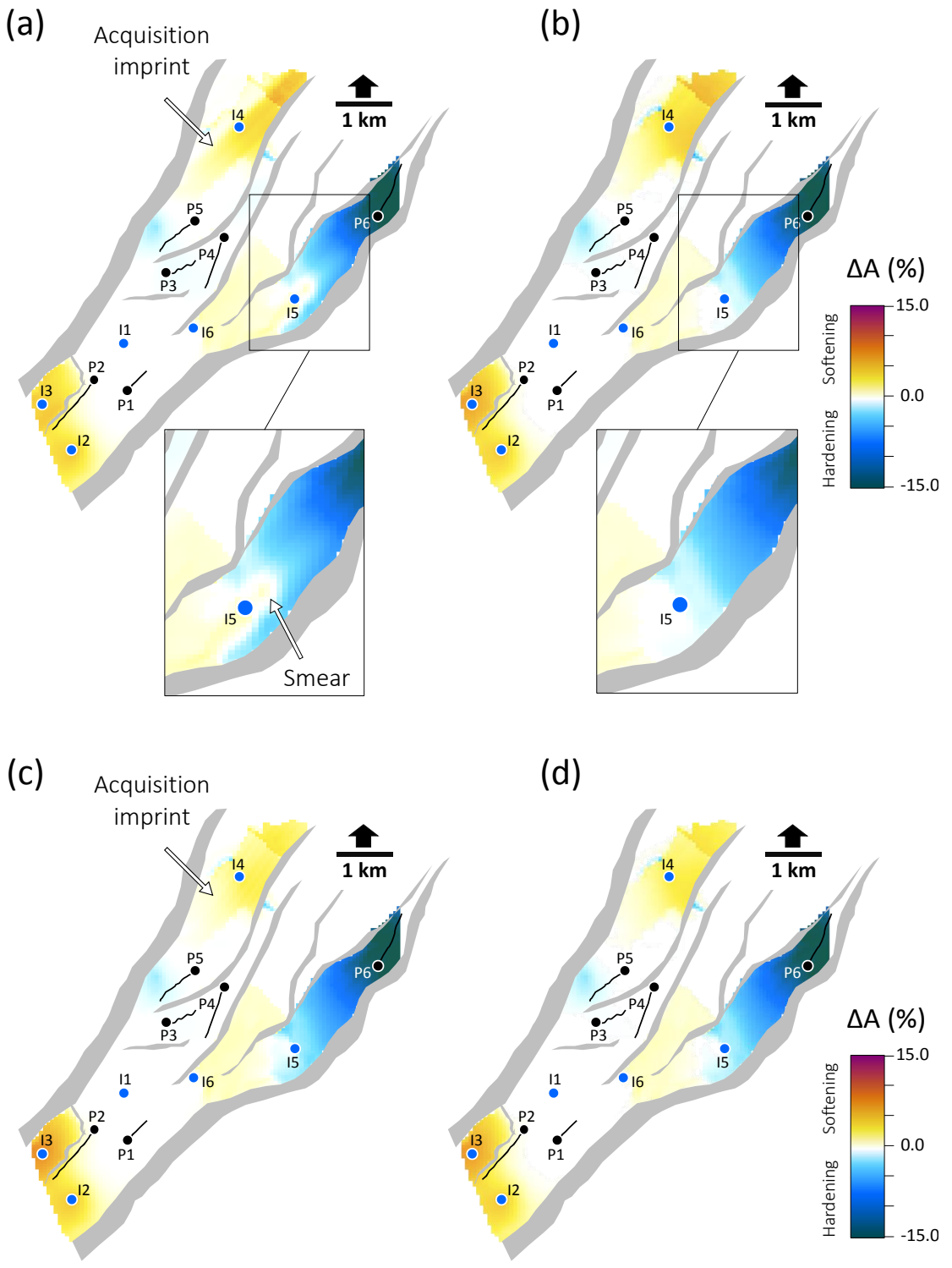

Figure 5-10 *Modelled Post-stack migrated time-lapse amplitudes for the pressure-only response for towed streamer (top) and PRM (bottom) surveys. The 4D amplitudes are expressed as a percentage change (monitor-baseline) relative to baseline. Displayed in (a) or (c) full offset stack response and (b) or (d) the reference determined from the average pressure response from the simulator over the survey duration. Smearing and striping is evident on (a) and (c) relative to (b) and (d).*

extra time, resulting in the observed post-stack 4D seismic responses. A quantitative comparison is made against the reference seismic dataset (Figure 5-10 (b) and (d)) obtained by modelling using an average of the saturation and pressures over the acquisition time-frame (Figure 5-11, see also Table 5-4). The NRMS* error is up to 16.3% for the towed streamer and 5.2 % for the PRM survey. Intrinsic noise due to data acquisition can be as low as an NRMS of 2% in offshore PRM systems and is usually around 15% or higher for towed streamer systems (see Figure 3-1). Comparing the magnitudes of the NRMS error due to the intra-survey effect to those introduced by data acquisition leads to the conclusion that the intra-survey effect might be measurable by PRM surveys, but is likely obscured by the intrinsic noise in current towed streamer technology.

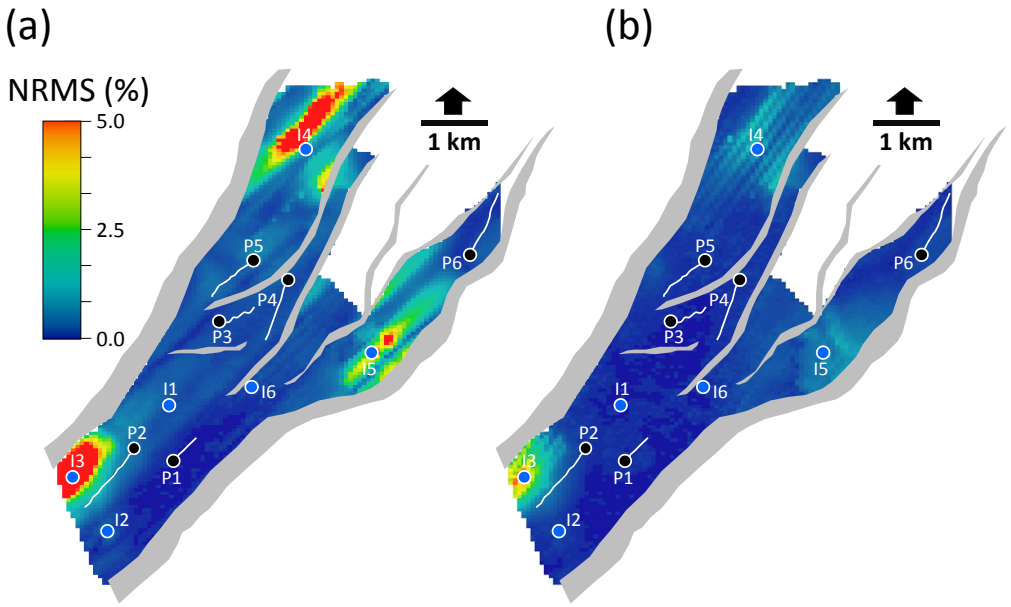

Figure 5-11 NRMS error in pressure response between full stack response and the reference as a result of intra-survey pressure fluctuations shown for (a) the towed streamer (b) the PRM acquisition. Areas experiencing larger pressure fluctuations result in larger errors (see also Figure 4-12).The colour scale has been chosen to emphasize the smaller errors. In the red areas, the NRMS error goes up to 16 %.

**The normalized root mean square, NRMS, error (Kragh and Christie 2002) calculates the normalized difference between two datasets (see also Appendix A). Typical NRMS values for non-repeatability noise are around 15 to 45% for towed streamer and 2 to 15% for PRM (see also Figure 3-1).*

Also, Figure 5-11(b) emphasizes that the PRM full-stack result (Figure 5-10(c)) more closely resembles its reference dataset (Figure 5-10(d)) than the towed streamer, and this is related to the way in which these particular surveys have been shot. The PRM experiences short but repetitive downtimes of up to 5 days, whilst the towed streamer has a long downtime of 30 days that misses some of the pressure signal. Additionally, the PRM survey provides a much wider aperture of the recording array and denser sampling over the reservoir.

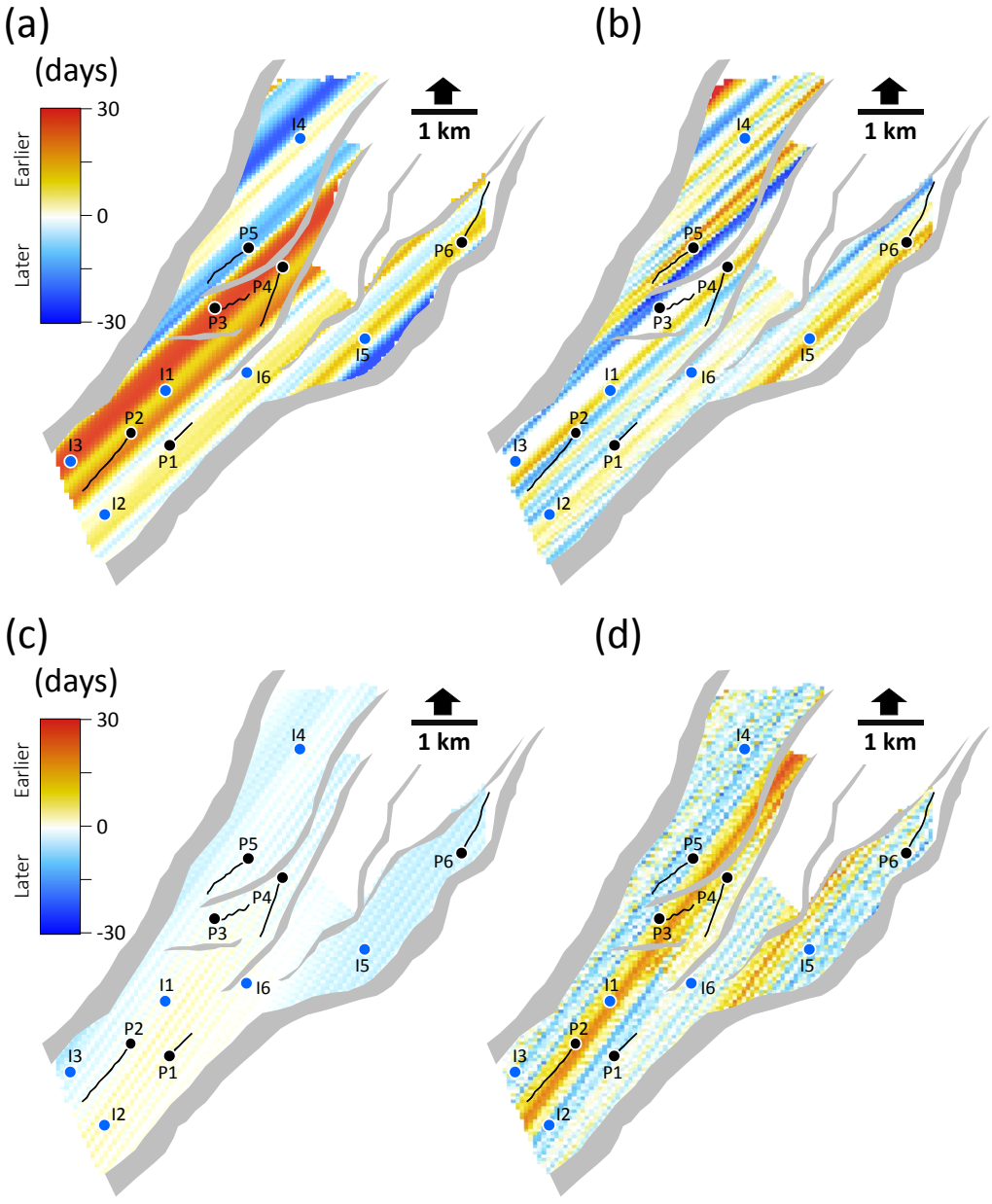

Figure 5-12 Discrepancy in timestamps (in days) across offset stacks for the towed streamer (top) and PRM (bottom) acquisition. (a) or (c) compare the shot time mean at each bin location for the full stack traces. (b) or (d) compare shot time mean between the near offset and far offset stacks.

Figure 5-12 (a) and (c) compare timestamp differences between the modelled data for both acquisitions by differencing the mean of the shot times in each bin with a single mean for the entire survey (day 29 for the towed streamer and day 22 for the PRM). The shot time mean for the full-stack data differ by up to 27 days for the towed streamer whilst the PRM shows less divergence with 6 days.

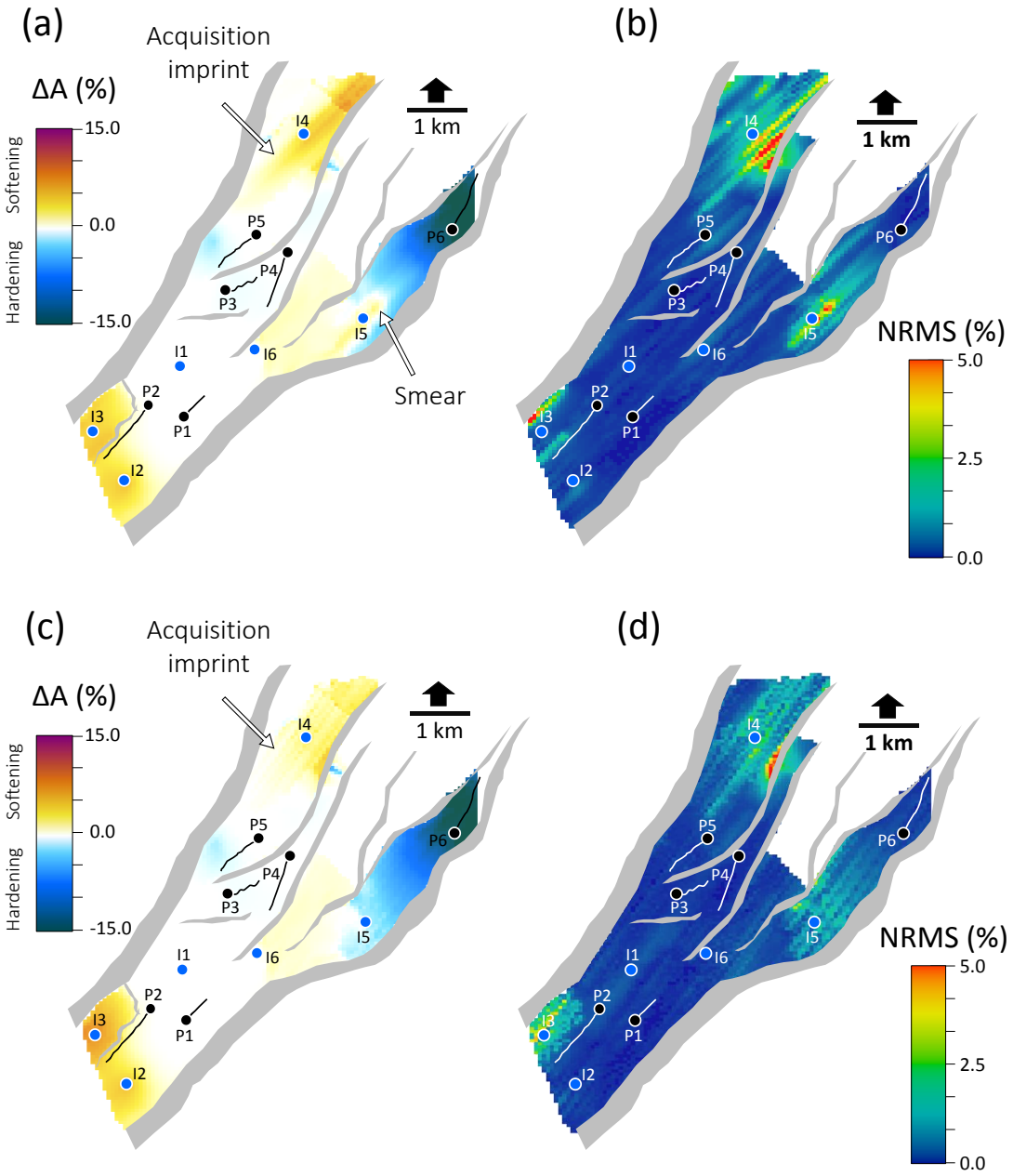

Figure 5-13 Modelled Post-stack (Near offset) migrated time-lapse amplitudes for the pressure-only response for (a) the towed streamer survey (c) the PRM survey. The 4D amplitudes are expressed as a percentage change (monitor-baseline) relative to baseline. The NRMS error between the near offset and far offset stack response modelled for the same incidence angle are shown in (b) for the towed streamer and (d) for the PRM survey. Stripping and smearing is more severe in the offset sub-stacks than in full stack. Near and far stacks acquire different pressures, evident in the NRMS error.

Next, the pressure-only, top reservoir amplitude responses for the near and far offset stacks are compared. The image of pressure on the nears and fars is observed to be quite different as indicated by the NRMS error between them (Figure 5-13(b) and (d)). This is also due to large timestamp discrepancies between these offset stacks **(**Figure 5-12 (b) and (d)). Acquisition timestamp smears are also more severe than on the full stack response due to greater sampling irregularity by the acquisitions in the offset sub-stacks (Figure 5-13 (a) and (c)). The NRMS error between the near and far offset amplitude responses is up to 7.3% for the towed streamer response and 7.5% for the PRM response. Areas of very small pressure fluctuations still show an error of 0.5% which may add to the "noise floor" associated with 4D seismic data.

Pressure fluctuations have also been analysed for a variety of different scenarios of injection before and during the seismic surveys, and for varying compartment sizes in the modelling. All yield similar conclusions to the above, thus suggesting these findings can indeed be generalized. The biggest impact is for large compartments in the earliest stages of production, as pressure in this case is not stabilised. For a single injector in a small isolated zone of pressure around the well location, the pressure signal will be imaged accurately in space, but the absolute magnitude of pressure will remain poorly determined. For equilibrium established in a compartment, pressure is now uniform but evolves linearly with time according to the well rate. In this case a variation in pressure measurement error across the compartment is still observed due to the time sampling of the surveys. This error is proportional to the daily pressure change induced by the well rate and survey duration, and inversely proportional to the compartment pore volume. For example, a constant rate of 16,400 stb/day injected into a 6 km^2 reservoir of thickness 25 m and porosity 25%, gives a pressure rise of 0.2 MPa/day.

Figure 5-14 and Figure 5-15 show two North Sea field examples of post-stack 4D seismic data acquired from towed streamer systems, where injectors are active in compartments. In both cases the effects discussed above are superimposed on the non-repeatability noise effects, and this is more prominent than the intra-survey effect which introduces small NRMS errors of 16% or lower (Table 5-4), whereas, the data non-repeatability noise is around 25% to 45% for the two examples shown.

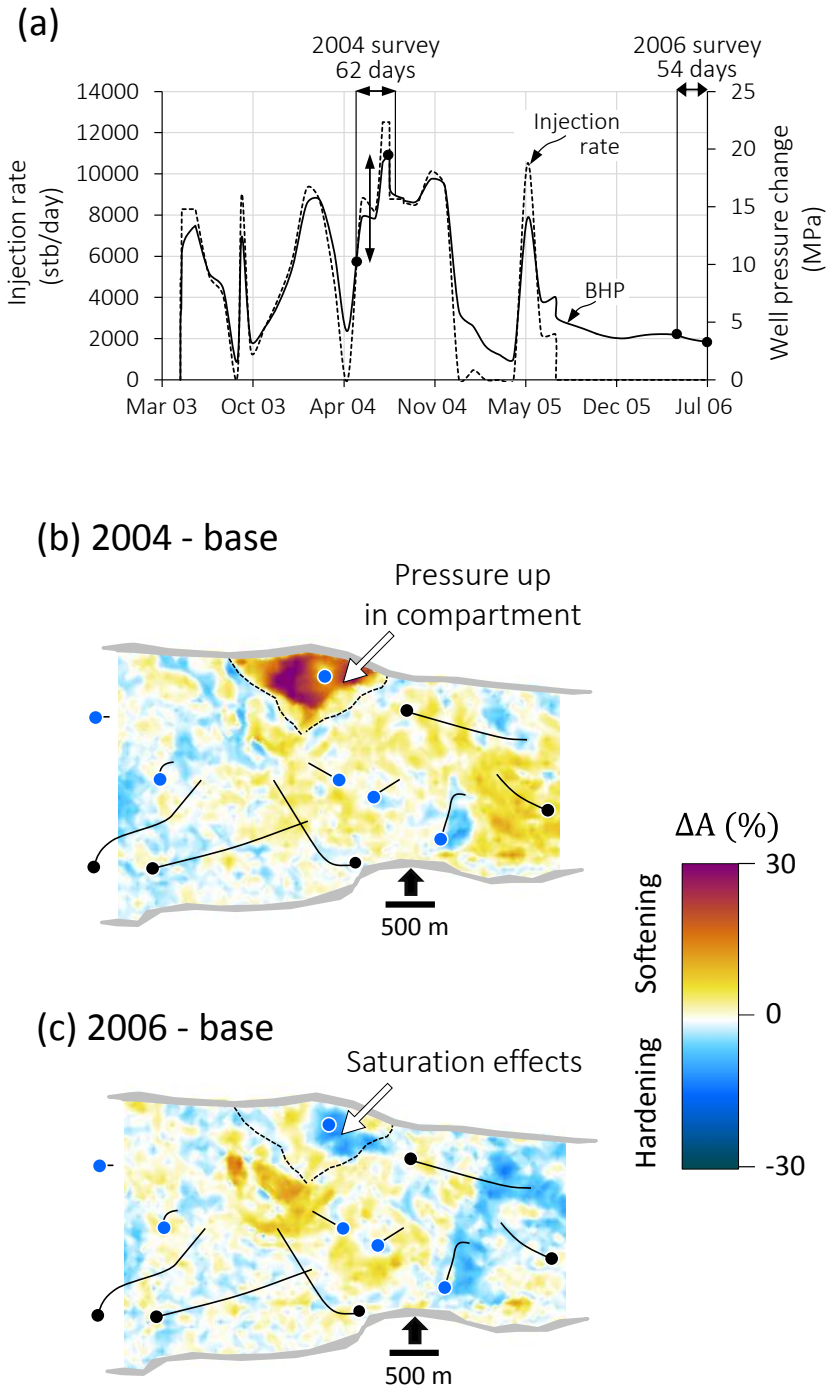

Figure 5-14 Observations of pressure injection into a small compartment in the Schiehallion field. (a) Simulated bottom-hole pressure fluctuations and historical water injection rate for an injector active during two monitor acquisitions. Maps of the percentage difference (relative to baseline) in RMS amplitude for full stack data are shown for (b) 2004 minus baseline seismic data (c) 2006 minus baseline seismic data.

The first example is from the Schiehallion field (segment 4) with a compartment of relatively small area of 0.7 km^2. Here the water injector is switched on 14 months before the first monitor survey (2004) and switched off 8 months before a second

monitor survey (2006). The pressure is therefore in equilibrium before both monitor surveys. The water injection rate and resultant pressure fluctuations are shown in

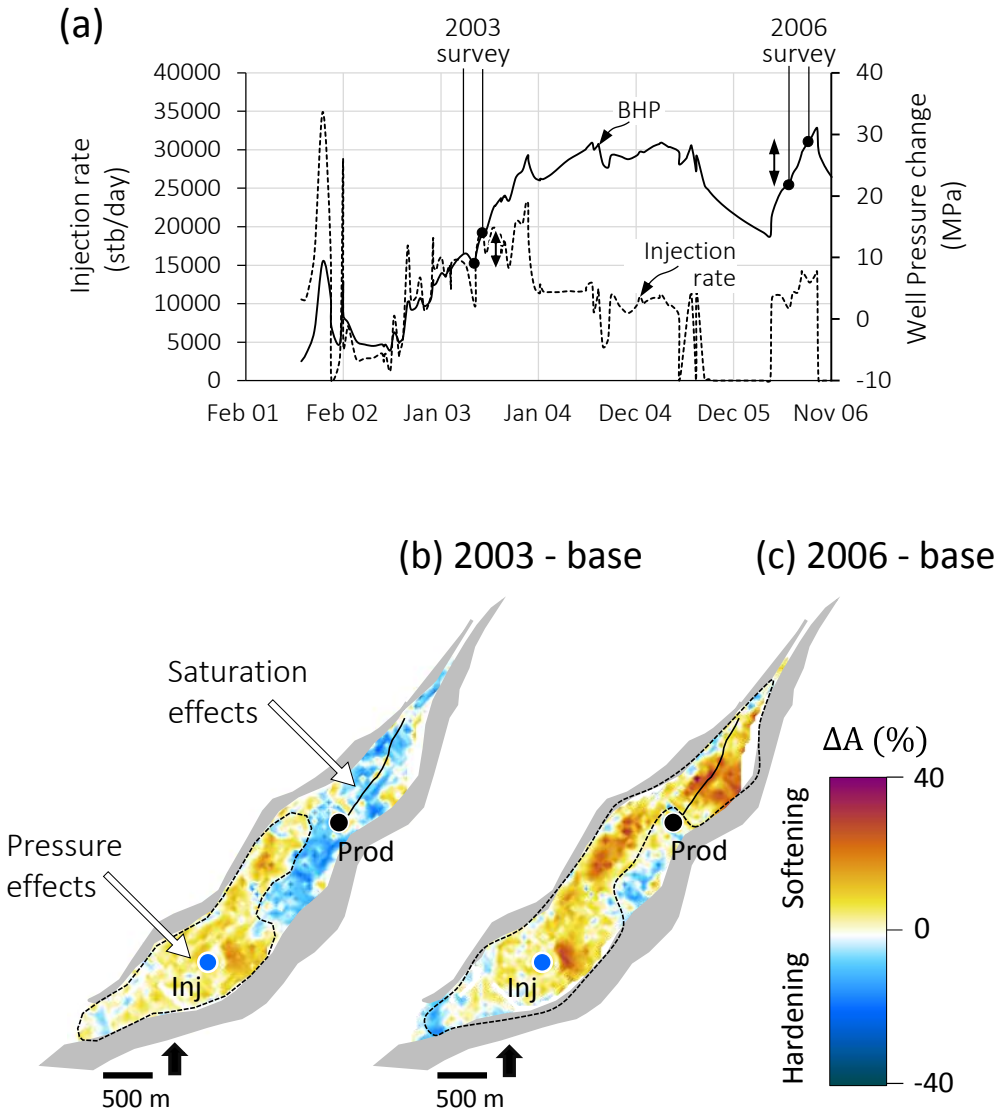

Figure 5-15 Field example of pressure injection into a large compartment in a clastic reservoir. (a) Simulated bottom-hole pressure fluctuations and historical water injection rate for the injector active during two monitor acquisitions. Maps of the percentage difference (relative to baseline) in RMS amplitude for the full stack data are shown for (b) 2003 and baseline seismic data (c) 2006 and baseline seismic data. The pressure-dominated seismic signals are enclosed by the dashed black polygons.

Figure 5-14(a), with the corresponding time-lapse seismic images in Figure 5-14(b) and Figure 5-14(c). Pressure fluctuations of up to 4 MPa (as observed from bottom-hole pressure and simulation model predictions) are present during the first monitor acquisition. A spatially varying measurement error of 2 MPa for the high pressure in this compartment (discounting the effects of water saturation) can therefore be expected,

and this may account for some of the observed variations that may be inadvertently attributed to geology. For the second monitor acquisition the compartment pressure is much lower, and errors are at most 0.6 MPa.

The second example in Figure 5-15 is for a larger compartment of 3.6 km^2 in the Norne field (segment G), where the water injector has already an established injection rate prior to the first monitor survey in 2003 and continues beyond the 2006 survey. There are injection rate fluctuations during the survey acquisition, and corresponding pressure changes. Pressure drops during 2003 and linearly increases by 10 MPa during the 2006 survey when the pressure change (monitor – preproduction) at the well is 26 MPa. On the 4D seismic maps a softening is observed due to pressurisation from the injector. It is suggested that the observed variability in the softening response however is not just a function of reservoir heterogeneity but a combined spatially-variant intra-survey noise floor plus non-repeatability noise.

5.3.2 Monitoring fluid saturation changes

Images for the saturation-only top reservoir amplitudes from the modelling are shown in Figure 5-16. Errors are again calculated for the full stack data relative to the reference. In this case the errors are localised to the flood front edges where saturations are changing during the survey - the waterflood front moves by between 50 and 135 m during the shooting of both acquisitions. Movement of gas in segment G is confined to the structural high close to the horizontal producer P6, from which most of the exsolved gas is immediately produced (due also to the action of I5, (see Figure 4-12). Consequently, only small errors (< 0.7 %) result from mild gas breakout (Figure 5-16 (c) and 10(d)). In segments C, D and E, the initial gas is displaced by water flood during the shooting. NRMS errors are only 0.8% for the PRM survey but up to 3.3% for the towed streamer survey. The mismatch between the near and far offset stacks is now up to 2% (PRM) and 2.5% (towed streamer), which is smaller than the pressure errors (Figure 5-16 (d)). New floods which commence as the survey is being shot are likely to show larger errors behind the flood-front than a more mature flood. The above errors suggest true quantitative evaluation of saturation change from offset stacks from 4D seismic data should take timestamp variations into consideration. These results also have strong implications for the imaging of fluid movement along high permeability

channels, where fluid moves rapidly and for which the exact position may not be accurately determined with current time-lapse seismic data. This is particularly important for a more mobile fluid such as injected or liberated gas.

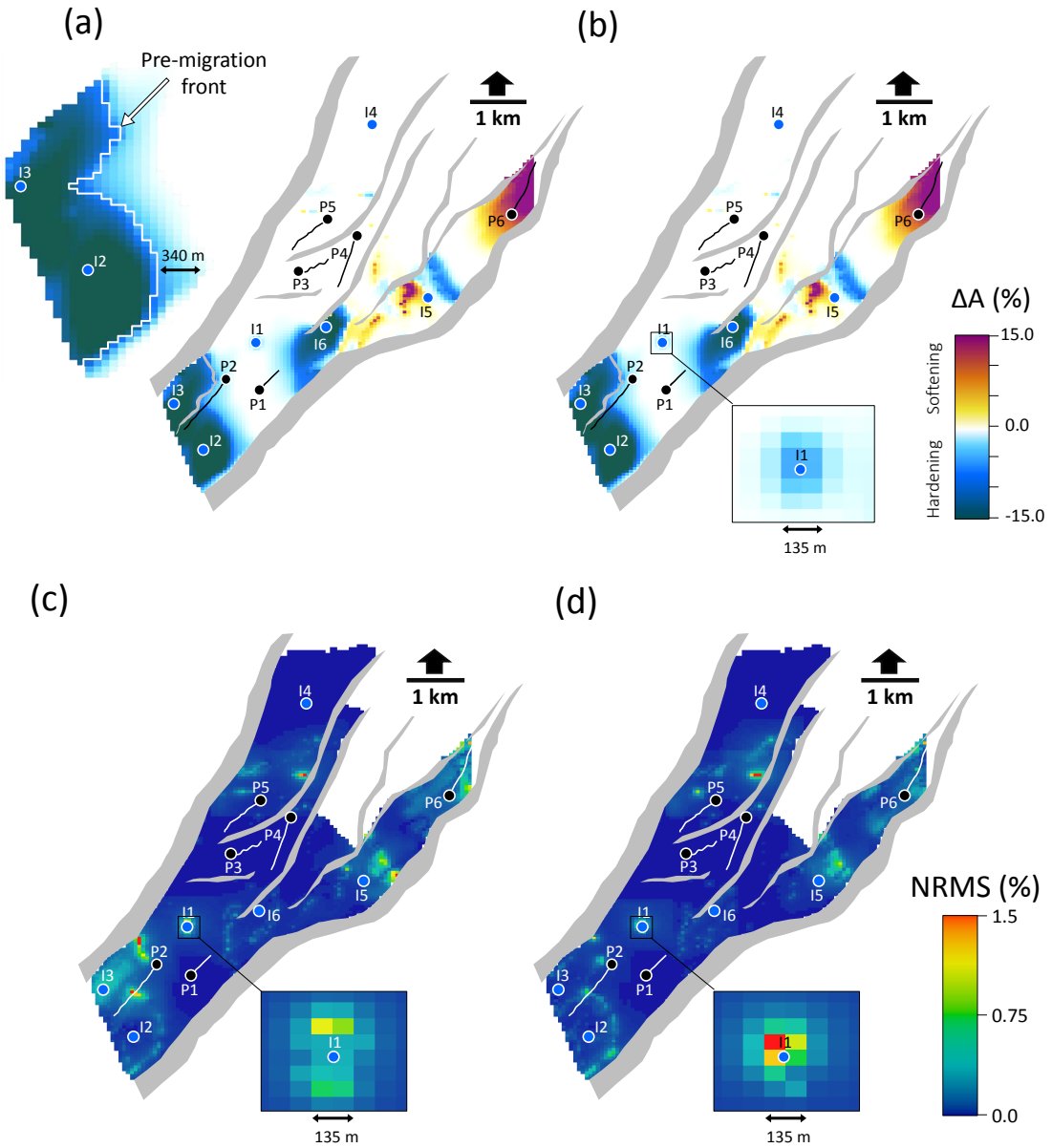

Figure 5-16 Post-stack migrated time-lapse amplitudes for saturation-only response from the modelling shown for the towed streamer survey. The 4D amplitudes are expressed as a percentage change (monitor-baseline) relative to baseline. Displayed are (a) full offset stack response (b) near offset stack response. Note that the simulated migration blurs the flood front. The resultant errors are shown in (c) for full stack response compared against the simulator reference (d) for near offset compared against far offset stack response. Errors are largest at the fluid fronts, and for new floods activated during the acquisition (for example, I1).

.

Error in 4D seismic imaging		Pressures		Saturations	
		ΔP error (MPa)	NRMS (%)	ΔS error (fraction)	NRMS (%)
FULL - AVERAGE	PRM	2.09	5.30	0.033	0.8
	Towed streamer	6.42	16.3	0.136	3.3
NEAR - FAR	PRM	2.95	7.50	0.082	2.0
	Towed streamer	2.90	7.30	0.103	2.5

Table 5-4 Maximum NRMS errors in post-stack seismic imaging of pressure and saturation changes for PRM and towed streamer surveys, evaluated over the reservoir area. The top two rows are for the full stack seismic response against the simulator response from the average of predictions over the survey duration and the bottom two rows are for the near offset and far offset stacks.

5.4 Shooting sequence and timestamp binning stacking solutions

The analysis above has shown that the presence of intra-survey reservoir fluctuations during monitor acquisitions adds to the uncertainty in 4D seismic data interpretation, both in spatial description and magnitude. If analysing post-stack 4D seismic data (full stack or offset stacks), the estimates of the reservoir changes often sought after cannot be accurately obtained using data that has been stacked the conventional way. By 'conventional', I mean stacking by CMP location only (as is the case for the modelled data above). The sequence of the shots over the reservoir for both the towed streamer and PRM acquisitions follow an irregular pattern (Figure 4-12) and it was also shown that midpoints in each CMP bin acquire different reservoir changes due to the different times they were shot during both acquisitions (Figures 4-19 to 4-21).

To reduce the complex imprint of the intra-survey fluctuations in the acquired 4D data, it is necessary to use the monitor timestamp of the data. The suggestion is to incorporate 'time binning' immediately after pre-stack migration and before any CMP stacking i.e. additional binning of the data in each CMP bin according to its shot timestamp. This will yield a subset of time-grouped data for each CMP location, which can then be classified by offsets and stacked. Figure 5-17 shows how the data can be grouped into independent time bins based on the shot activity from both acquisitions. For the PRM

shooting, this gives a total of nine timestamp groups (T1 to T9) and for the towed streamer, this is only four (T1 to T4).

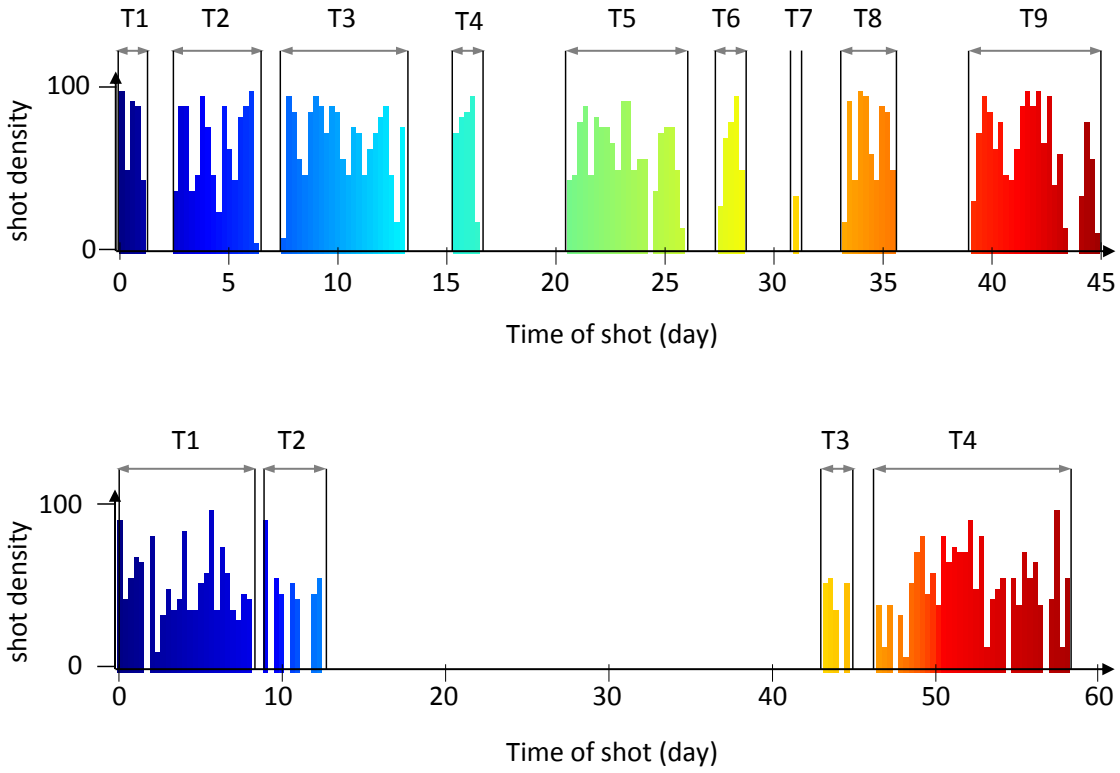

Figure 5-17 Histograms of shooting activity colour coded by time (in days) for (a) the PRM (b) the towed streamer, illustrating the different number of shot timestamp groups, Tx, (where x is an integer) by which the acquired 4D data can be binned. See also Figure 4-18 for the time coverage histograms for each offset group, and also Figure 4-16 for how these time groups are spatially distributed over the reservoir.

In practice, the real concern with time binning is the resultant fold of the data which may not be very useful in improving the signal-to-noise ratio of the stacked data. Data from some time groups will possess a higher fold than other groups, and thus may be the default choice for further processing and interpretation. However, it is of greater value to use data from all time groups as these provide additional intra-survey time-lapse information in areas covered by such time groups. Figure 5-18 compares the full-offset fold resulting from the time group with the minimum fold and the time group with the maximum fold. Data gaps exist due to the sparse spatial time sampling of the survey, towed streamer being more affected than the PRM. Compared to the fold from conventional CMP stacking, the maximum fold from the timestamp stacking is about half for the towed streamer, and one-fifth for the PRM, which is still much higher than towed streamer's conventional stacking fold, (Figure 5-18 (c) and (f)).

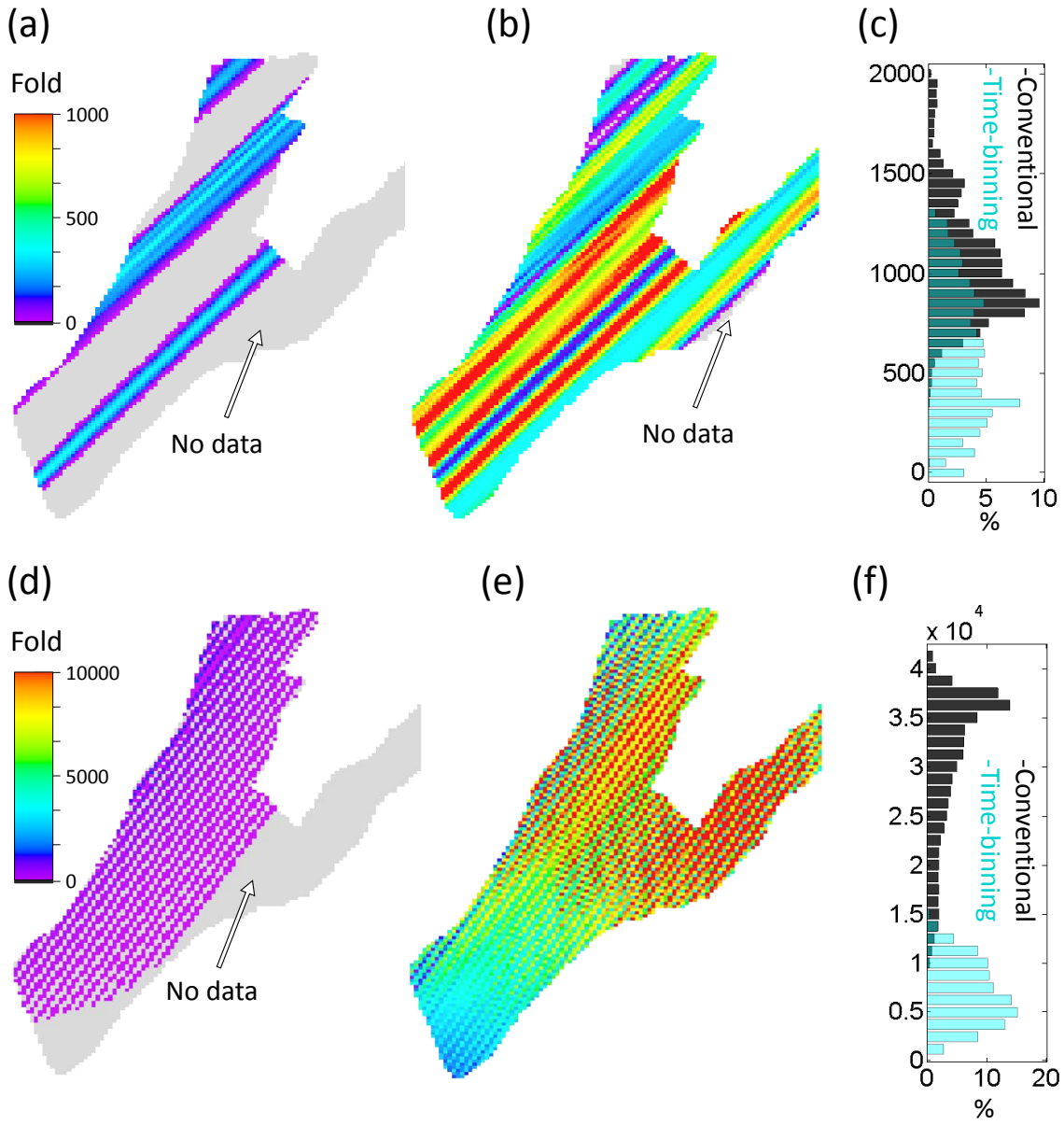

Figure 5-18 Full-offset fold coverage from the time binning, shown for the towed streamer (top) and PRM survey (bottom). (a) or (d) the time groups with the poorest coverage, (T3 for towed streamer or T7 for PRM). (b) or (e) the time groups with the best coverage (T4 for the towed streamer or T3 for PRM). (c) or (f) histograms of full-offset fold from the conventional stacking (in black) versus the timestamp stacking (in cyan) using the group with the best coverage. Y-axis is the fold and X-axis is the count in percentage. For reference of time groups, see Figure 5-17.

To optimise the proposed time binning method, monitor surveys should perhaps be shot to aim for better time sequence consistency, covering the entire survey (or reservoir) area as quickly as possible without breaks Two patterns of shooting are suggested in Figure 5-19, and the shot lines are colour coded by the time of shot from the start (blue) to the end (red) of the acquisition. To achieve the sequence in Figure 5-19(a) practically, shot lines can be spaced sparsely during each continuous shooting before the next down

time, as indicated by the "sequence" shot line spacing. For the next shooting sequence, new shot lines are placed in between the shot lines of the first sequence, and are also acquired continuously. Subsequent shot sequences are acquired on new lines which need also be placed in between the previous lines (Figure 5-19(a)). The acquisition is distributed over the time scale of a typical survey but shot to cover the entire area during each sequence. Thus, the shooting achieves the designed final shot line spacing for data fold considerations, and also, regular time coverage to minimise the error due to the intra-survey fluctuations. Ideally, each shooting sequence should be completed as quickly as possible, and a short down time, if required, can be observed. This scenario provides sufficient sampling to address spatial aliasing for multichannel processing since the final shot line spacing is the same as the typical shot line spacing shown in Figure 5-19(b). This shooting sequence will however be ideal for acquisitions designed for high fold data, PRM/OBN surveys, if timestamp binning is to be performed. Towed streamers with smaller streamer dimension will still not be ideal for timestamp binning, although the actual shooting of the survey will be made easier due to the designed large shot line spacing when implementing each lap of sequence shooting. In addition, one can repeat the same shot line positions during each continuous sequence, but the towed streamer would be worse off in terms of fold.

Alternatively, the continuous shooting sequence in (Figure 5-19(b)) can be implemented. This scenario will also provide sufficient sampling to address spatial aliasing for multichannel processing. Neighbouring shot lines are acquired within a short a time difference as possible. Different parts of the survey would then represent different time groups across the reservoir. Although the shooting pattern is orderly, from left to right, the problem with this is that only a section of the reservoir area is imaged within a time sequence. This will lead to spatially irregular time coverage over the survey area, and can result in spatial gaps in fold for some time groups if timestamp binning is performed (see Figure 5-18 for an illustration of this problem). In practice, it is also quite difficult to shoot continuously and in an incremental sequence as shown in Figure 5-19(b). Again, PRM systems would still be better off than towed streamers.

One thing to bear in mind is that the sequence of shooting of the acquisition is not a standalone. It is the interplay between the spatio-temporal behaviour of the reservoir during the acquisition, and the time sequence of shooting that result in the acquired 4D

seismic response. Both shooting sequences in Figure 5-19 could also be coordinated with production activities to provide direct assessment of resulting fluid movement and/or pressure changes. This coordination would be easier to achieve for Figure 5-19(b) than for Figure 5-19(a).

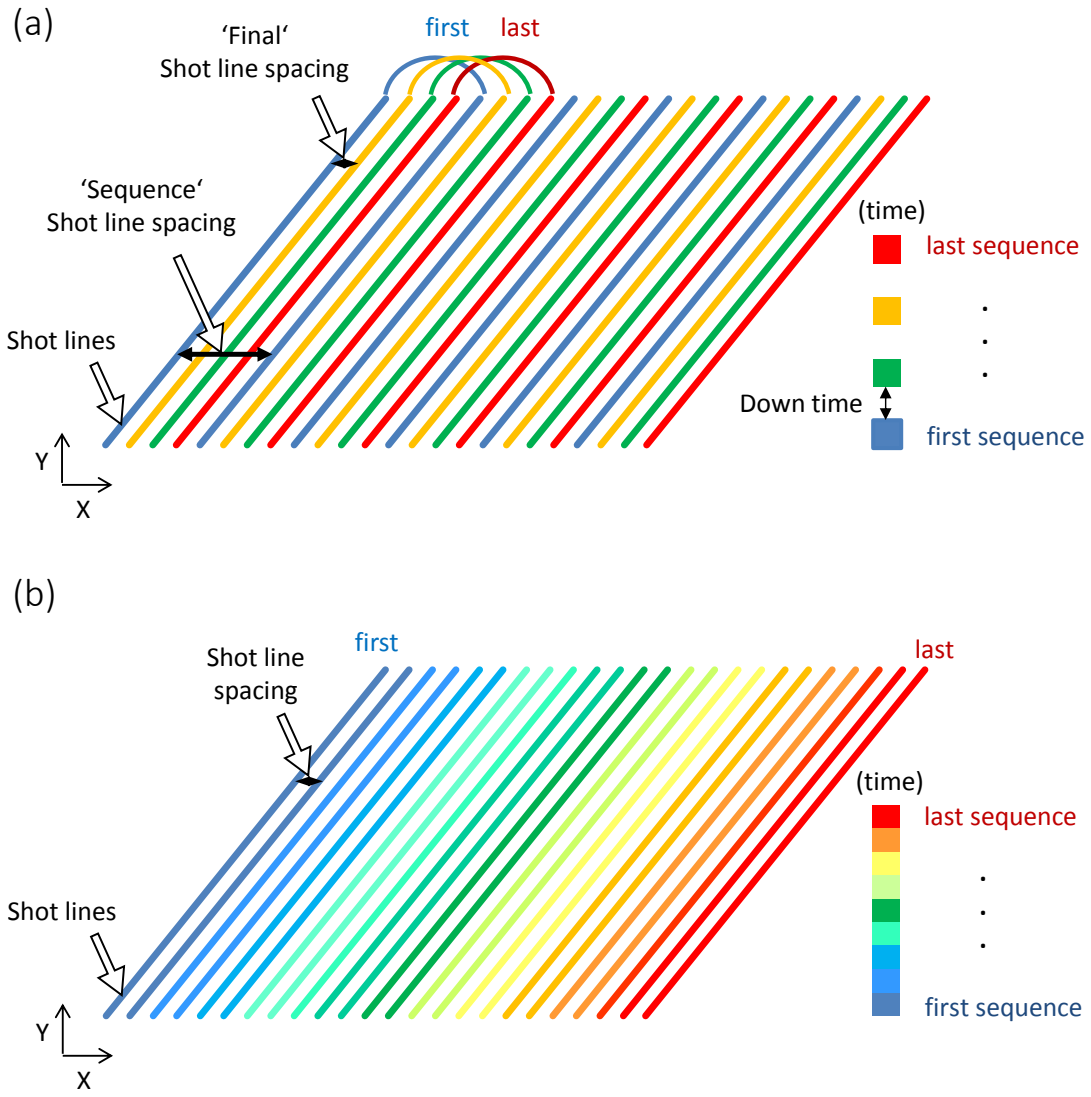

Figure 5-19 ***(a)*** *Proposed time sequence of shooting of each monitor survey (both PRM and towed streamer systems) to optimise the shot times coverage over entire area. The final shot line spacing is what is typically designed in conventional shooting, whereas the sequence shot line spacing can be sparse during each round of continuous shooting (shown here for four sequences), so that a regular spatial coverage with time can be achieved within the acquisition time frame.* ***(b)*** *Alternative shooting pattern following a linear and continuous sequence in time from left to right, with little or no breaks in the acquisition. Unlike (a), the time coverage in (b) are not regularly distributed over the survey area. Figure 5-19(b) courtesy of H. Jakubowicz (personal communication, 4 July, 2017).*

5.4.1 Benefit of timestamp binning

Stacking the modelled data in each CMP bin according to their shot timestamp is proposed to yield better results than conventional CMP stacking. By time binning (Figure 5-17), the timestamped 4D data can be directly related to instantaneous times from the fluid-flow simulation model. Figure 5-20 shows the pressure-only amplitude response for full offset stack for data binned according to time groups, T3 (for PRM) and T4 (for towed streamer). From the simulation model, these time groups correspond to day 10.5 (for PRM) and day 50.5 (for towed streamer) during the acquisitions, which now represent a reference instantaneous snapshot, for the basis of comparison.

Compared to conventional stacking (Figure 5-10 (a) and (c)), there is a dramatic improvement in the spatial character of the 4D signals (Figure 5-20 (a) and (d)). Imprint of the acquisition timestamp which introduced smears in the data have been removed, simply by timestamp stacking. The NRMS error between the full-offset and the instantaneous reference is now around zero but not exact because it is still not a one-to-one relationship between the acquired time-grouped data and one specific time from the simulator (Figure 5-20 (c) and (f)). The timestamp of each trace in each time group are similar but can be up to a few days apart, as Figure 5-17 illustrates. In addition, it is shown that the error between the near and far offsets stacks have been greatly minimised because their timestamps are now in better agreement, a clear benefit of time binning (Figure 5-21; see also Figure 5-13 for comparison). However, data gaps are more prevalent due to more irregular sampling by the acquisition across the sub-offsets.

Apart from the reservoir fluctuations themselves, other non-production-related changes which possess a similar timescale to the acquisition (for example, the effects of tide, weather and currents which affect the water-column, salinity and temperature changes which affect water velocity etc. (Lacombe et al., 2009; Wang, 2013), can also benefit from time binning and thus improve the overall 4D data quality. It is therefore emphasised that seismic data processing for 4D applications should take to account the shot timestamp of the monitor acquisitions; this information is yet to be applied in typical processing workflows.

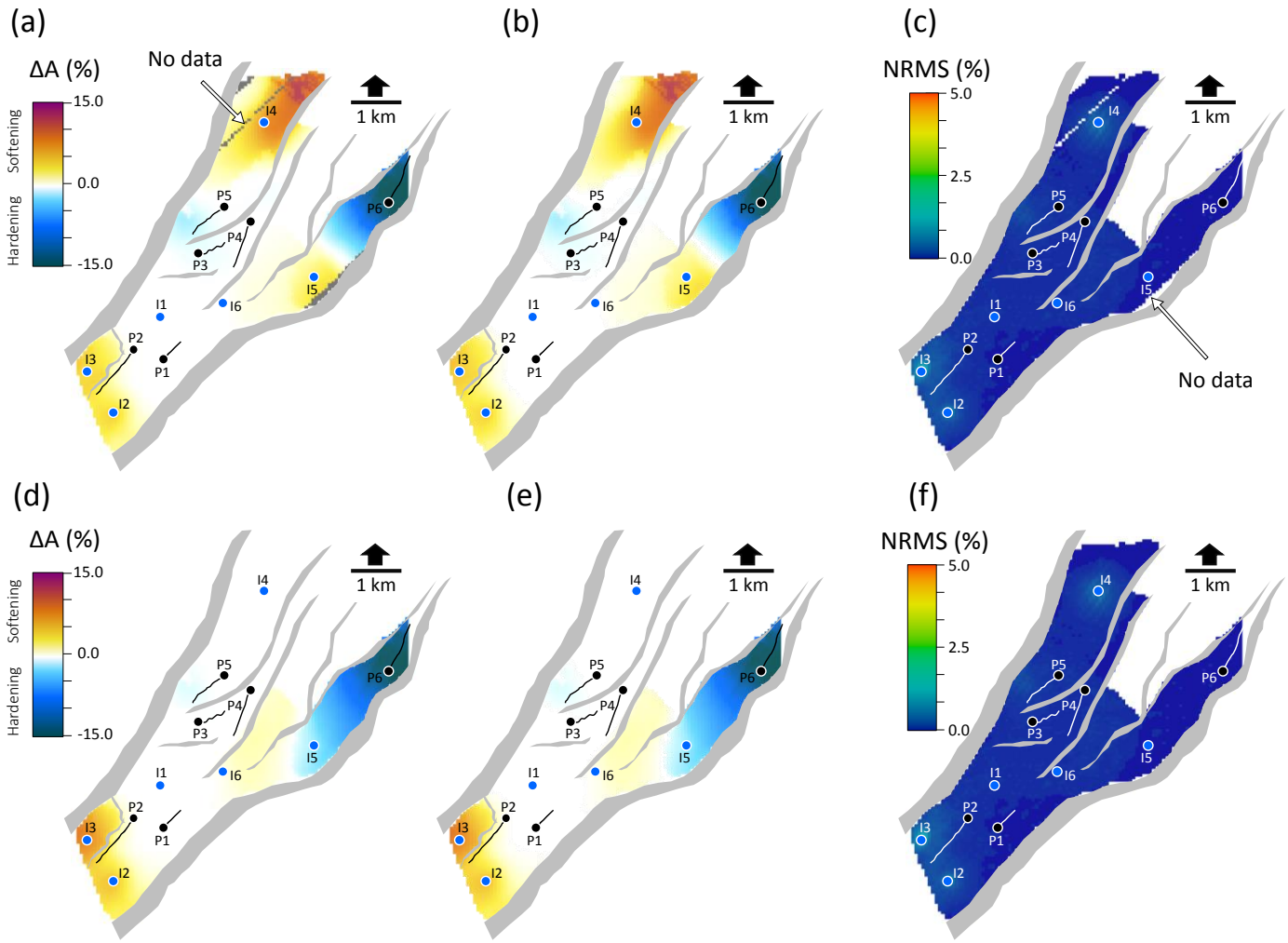

Figure 5-20 Time-binned Post-stack migrated time-lapse amplitudes for the pressure-only response for towed streamer (top) and PRM (bottom) surveys. Displayed in (a) Data from the timestamp groups, T4 for the towed streamer and (d) T3 for the PRM. For time-group information, see Figure 5-17. Reference instantaneous response from the simulator, corresponding to the time groups are shown in (b) Day 51.5 for towed streamer (e) Day 10.5 for the PRM. Displayed in (c) or (f) the NRMS error between the time-binned full stack response and the reference. Smearing and stripping observed earlier in Figure 5-10 have been removed and the match between (a) or (d) relative to (b) or (e) is exemplary, evident in (c) or (f).

5.5 Discussion

It is common in practice for well production and injection rates to fluctuate or for wells to be shut-in, re-started or turned off during acquisition of seismic data for time-lapse studies. Additionally, in any field numerous wells affect pressure locally and at field-scale while the seismic survey is ongoing. This means that the reservoir is typically not in pressure equilibration during the acquisition (if at all during its lifetime), and pressure will fluctuate in and around wells, and also between wells. As the reservoir always remains active, there are also many fluid changes occurring during the duration of the survey. I therefore believe that the intra-survey effect observed in this study is possibly widespread across many 4D seismic field datasets but remain at background noise levels due to the dominance of data non-repeatability noise. As data repeatability improves, as is currently achievable by PRM technology (NRMS ~ 2%), such intra-survey effects will become prevalent, and could remain unobserved due to the coarse way in which we compare time-scales between the simulator and seismic domains. This may add a general floor of small-scale fluctuations within the non-repeatability noise attributed to processed 4D seismic data. For wells with significant responses during or close to the start of the survey, the impact has been demonstrated to be significant. It is typical to match the simulation results to the start, middle or end time of the seismic survey, however, it is suggested in this study that perhaps the best comparison may be achieved by averaging fine-scale simulation predictions between the start and the end of the survey.

The range of possible significant reservoir IOR/EOR mechanisms that have time constants smaller than the seismic survey acquisition time open up the question of what might be the ideal survey to measure these phenomena for geomechanics, pore pressure, water, hydrocarbon gas, CO2 or steam injection? Most 4D seismic surveys tend to be large and have field-wide coverage that takes months to complete and are repeated every few years. Permanent reservoir monitoring offers the alternative of a smaller survey size, more frequent repeats and higher fold. In practice the lower non-repeatability noise of the PRM would also make such acquisitions attractive.

This study suggests that an ideal seismic survey should be very quick to acquire with little or no gaps during the shooting, high coverage with each shot, and repeated

frequently to sample the rapid reservoir changes adequately. Possible choices for such surveys include the specialised i4D surveys (instantaneous 4D using a sparse and highly repeatable OBN) that take only a day to a few weeks depending on the survey size (Stammeijer et al., 2013; Hatchell et al, 2013).

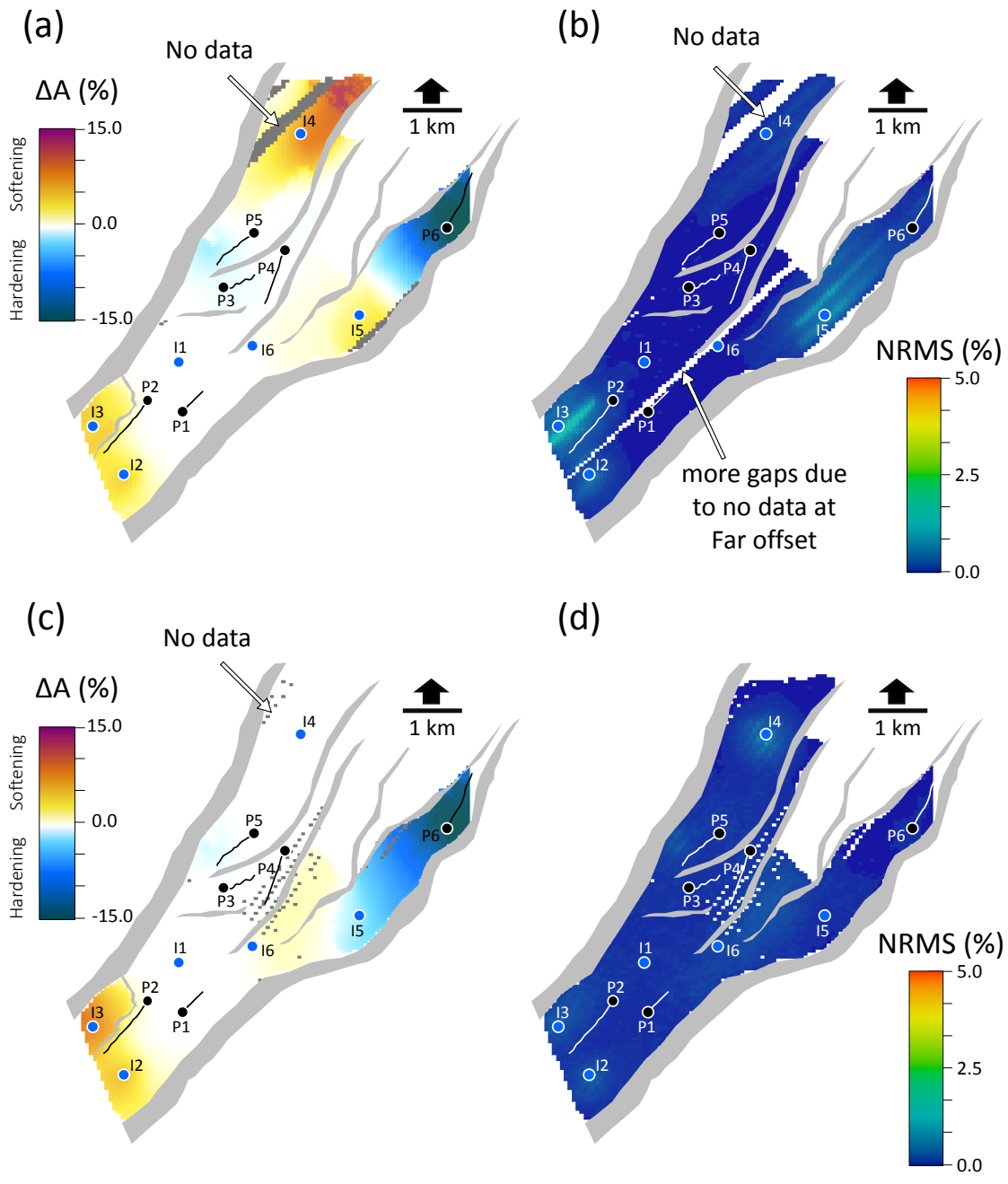

Figure 5-21 Time-binned Post-stack (Near offset) migrated time-lapse amplitudes for the pressure-only response for (a) the towed streamer survey using timestamp group T4 (c) the PRM survey using timestamp group T3. For time-group information, see Figure 5-17. The 4D amplitudes are expressed as a percentage change (monitor-baseline) relative to baseline. The NRMS error between the near offset and far offset stack response modelled for the same incidence angle are shown in (b) for the towed streamer and (d) for the PRM survey. By time binning, the NRMS error due to the intra-survey fluctuations between near and far stacks have been significantly reduced (see the conventional stacks in Figure 5-13 for comparison).

These would provide a more reasonable temporal sampling of reservoir changes than a full 4D survey. A further possibility involves the use of time-lapse (3D) VSP to provide highly accurate images over a small image area (Tøndel et al. 2014; Pevzner et al. 2015). Another acquisition possibility where rapid physical effects may be more sharply defined than in normal surveys is highlighted on land with the SeisMovie technology enabling six hour sweeps and four shots per day in an almost continuous sequence over a small localised pad of reservoir activity (Hornman and Forgues, 2013).

The analysis using the Norne field simulation model has shown that fine-scale fluctuations can lead to errors in detecting consistent pressure or saturation signals across sub-stacks of seismic data, and should not be neglected. Of particular concern here therefore is the quantitative inversion approach for pressure and saturation change (as popularised by for example: Landrø 2001; Lumley et al., 2003; MacBeth et al., 2006) all of which could be adversely affected by this phenomenon. This is because they require that the near, mid and far offsets will measure the same pressure and saturation signals, which is not the case. This study has indicated that the saturation flood front is difficult to position accurately in post-stack migrated data, and the timestamp of the acquisition can imprint false features in the 4D pressure response which could be mistaken for genuine geological variations. Finally, stacking according to the shot timestamps in the modelled data on the Norne field demonstrates that it is possible to reduce the uncertainty in 4D seismic data analysis (full stack and offset sub-stacks) introduced by these intra-survey fluctuations, compared to conventional stacking.

5.6 Summary

Reservoir fluctuations that occur during the shooting of a monitor seismic acquisition can create a complicated spatio-temporal imprint on the pre-stack CMP data, and errors when interpreting the time-lapse seismic data quantitatively in the post-stack domain. This signature does not translate into a clear post-stack seismic image of the pressure, even when geometric repeatability is perfect. Both pressure and fluid changes are affected by this phenomenon – both suffer from lack of spatial location of the change, and quantification of the absolute value of that change. With fluid changes the main errors are concentrated around the fluid fronts, but with pressure the errors are more

widely spread across field compartments due to its quick diffusive nature. Near and far-offsets sample pressure and saturation differently and this affects the ability of time-lapse analysis to accurately separate changes of saturation and pressure.

This modelling study with real field acquisition data from a PRM and towed streamer North Sea survey and fluid flow simulation from the Norne field model reveals a number of important considerations:

- Quantitative analyses of reservoir changes are best performed in the pre-stack CMP domain, as they are smeared in the post-stack volume.

- The time-scale of the survey relative to the well behaviour and simulation time period needs to be precisely defined in a time-lapse project – usually only one exact time is quoted for the survey, which is incorrect. The reservoir changes acquired by the acquisition cannot be associated with instantaneous predictions from the simulator at any time during the survey. It is best to use an average of fine timescale predictions over the acquisition time frame, than to use simulator predictions for a specific day (for example, start, middle or end) of the survey. The simulation domain is linear over time, but the acquisition has a complex time distribution across bin locations.

- Pressure and saturation (gas, water, steam) change separation using offset stack data should be avoided in situations of rapid change during the acquisition. The reservoir changes acquired by the survey in the near and far offsets are different, due to the irregularity of the timestamp coverage across the offsets at each CMP location. Near and far offsets appear to have been shot at different days and so cannot capture the same reservoir changes.

- Ideally time-lapse acquisition should be performed during a quiet period of pressure equilibration in the reservoir lifecycle, i.e. sufficiently far away from well start-up or shut-down. However, fluid fronts will still continue to move due to pressure gradients and production. Consequently, production activity of wells should be properly observed during the acquisition. Coordination between production and 4D monitor surveys could be an opportunity for more detailed

understanding and observation of reservoir changes. This will require rapid data acquisition focussed on specific parts of the reservoir, not just carpet shooting to cover the whole field area. This in turn requires survey design/illumination study for the target area.

- If a quiet period of pressure equilibration cannot be guaranteed, it is recommended that the seismic data should be sorted differently for quantitative time-lapse studies. The sorting strategy should not only account for the location of each image gather but also for the timestamp of each trace during the acquisition. It is emphasised that seismic data processing for 4D applications should take to account the shot timestamp of the monitor acquisitions; this information is yet to be utilised in typical seismic processing workflows. This will involve an additional timestamp binning of traces immediately after pre-stack migration and just before stacking. Ideally, the data would have been shot continuously in a consistent pattern and more frequently, both, for regular time distribution at each bin location over the reservoir area, and for high fold coverage. The time-binned data can thus be directly compared with instantaneous predictions from the simulation model domain. In terms of fold, PRM systems are more ideal for the timestamp binning due to their high density coverage. Data acquired using towed streamer systems can still be used but with limited sensor coverage and coarse sampling, the fold would be severely affected.

- Finally, the approximate modelling relay that the NRMS errors between offset stacks (up to 7.5%) caused by the intra-survey effects are likely at the limit of 4D seismic measurements using towed streamer technology, but are potentially observable, particularly for PRM technology.

- The intra-survey effect raises particular concerns when interpreting post-stack 4D seismic data, and, thus, should be considered during 4D survey planning as well as during data processing and analysis.

Chapter 6

Introducing an engineering-constrained inversion scheme for the quantification of pressure and saturation changes

In this chapter I introduce and describe a multi-cycle inversion scheme which integrates 4D seismic data with engineering data from fluid-flow simulation models. The inversion scheme is characterised by a multi-monitor inversion, a multi-offset inversion, and the quantitative use of dynamic properties from history-matched multiple fluid-flow simulation models. Specifically, simulated pressure and saturation changes from the multiple models are used to guide the inversion process and provide more reliable estimates. In addition, the model that best honours the 4D seismic response and historical production data can be found via the inversion scheme. This can thus be viewed as a soft 'close the loop' at the dynamic level using multiple simulation models. The first part of the inversion scheme is implemented here on the Heidrun field model, where uncertain static properties are combined, and the original reservoir model is perturbed to generate multiple models. The next part of the inversion scheme uses these multiple models to constrain the inversion, to be presented in the next chapter.

6.1 Introduction

To improve reservoir characterisation, the integration of datasets with different characteristics, such as flow simulation and 4D seismic data is a common practice. The simplest, most direct form is by qualitatively determining barriers and baffles (Helgerud et al., 2011; Tuttle et al., 2009). Quantitatively, the integration between the geophysical and reservoir engineering domain is done via history matching; a conditioning procedure that matches both measured well data (pressure and production data) and the observed 4D seismic data. Because, well data are temporarily dense and spatially coarse, whereas, 4D seismic data are temporarily coarse and spatially dense, combining both types can be quite powerful to optimise reservoir models for better forecasting (Castro et al., 2009). This requires inversion and modelling to link the engineering and geophysical domains (Figure 1-6). Thus, the same type of attributes can be derived from both domains, but the choice of a stable attribute has been one of much debate.

For example, Dadashpour et al. (2009) quantitatively matches production and seismic data in the form of zero-offset amplitudes and AVO gradients on a semi-synthetic model. Fahimuddin et al. (2010) used both amplitudes and impedances for comparing both domains and finds that the observed and modelled data are better matched using impedances. They find that the uncertainty is better understood in the context of forward modelling problem rather than the inversion. Many field case studies on integrating both domains have therefore been performed using impedance attributes (Waggoner et al., 2002; Aanonsen et al., 2003; Gosselin et al., 2003; Mezghani et al., 2004; El Quair et al., 2005; Haverl et al., 2005; Stephen et al, 2006; Stephen and MacBeth, 2006; Roggero et al., 2007; Dong et al., 2008; Tolstukhin et al., 2012). It is considered by some to be the optimal level for data comparison in history matching due to less computational effort and straightforward interpretation of data as no forward seismic modelling is needed. However, Souza and Lumley (2015) emphasise that matching time-lapse seismic and fluid flow data using amplitudes may be more reliable than impedances if the observed seismic data has strong noise, which can lead to significant errors and non-uniqueness in the inversion for impedances. This is however, the most difficult to implement in an integration workflow because the seismic amplitudes cannot be quantitatively associated with reservoir properties directly (Kumar and Landa, 2008;

Landa and Kumar, 2011). Synthetic amplitudes are also usually of different order of magnitudes compared to the observed data (Amini, 2014), which has made the integration problematic, and many resort to normalisation. For directly updating the reservoir model, Feng et al., 2012; Alerini et al., 2014 and Ayzenberg and Liu, 2014) apply a variety of elastic properties (velocities, time-shifts, and amplitudes) via petro-elastic modelling and seismic modelling by representing the attribute changes as a ratio. Kazemi et al. (2011) and Stephen et al. (2014) present a normalisation technique that uses RMS repeatability of amplitudes for improving the matching process.

Most of the methods that use petro-elastic modelling and/or seismic modelling to generate the 4D seismic attribute, raise concern with the calibration complexity, time inefficiency, unreliability with regards to laboratory stress sensitivity measurements which are prone to errors, as well as Gassmann's equation assumptions (Landrø, 2001; Gosselin et al.; 2003; Stephen et al., 2006; Floricich, 2006; Wen et al., 2006; Amini, 2014).

Fursov (2015) and Obidegwu (2016) circumvent the need for such modelling by using MacBeth et al.'s (2006) data-driven approximations to model the 4D seismic amplitude maps for fast model updating. Attempts have also been made at the dynamic level using information on pressure and saturation effects inferred from 4D seismic data, Landa and Horne (1997) present one of the earliest applications through image analysis. Gervais and Roggero (2010) show the possibility of using saturation information from 4D seismic data to perform local parameterisation in a synthetic study, and Trani et al. (2013) in their synthetic 3D case use interpreted fluid fronts as an attribute for matching. In a real field case study, Jin et al. (2011) uses seismically-extracted water-front patterns as an attribute to match both domains. Obidegwu et al. (2015) generate binary maps based on the observed 4D signatures attributed to saturation effects and matches these to binary maps of predicted saturations for direct model updating. Huang et al. (2011) present a technique for evaluating and updating reservoir connectivity by combining multiple monitor observed 4D seismic data with well pressure and production data to produce a single robust 2D map attribute. This is advanced to volumetric attributes incorporating water saturation effects in Yin et al. (2015).

6.1.1 Inversion strategy for 4D seismic data integration with the engineering domain

There is a strategic preference for translating 4D seismic data into more reservoir engineering attributes. Readily available pressure and saturation attributes from the observed 4D seismic data will thus yield a quicker and more efficient integration with the reservoir simulation model. Whilst inverted pressure and saturation changes may provide convenience of intuitive attributes, estimating them from the observed 4D seismic data is by no means easy and the techniques described in Chapter 1 provides a basis for more work.

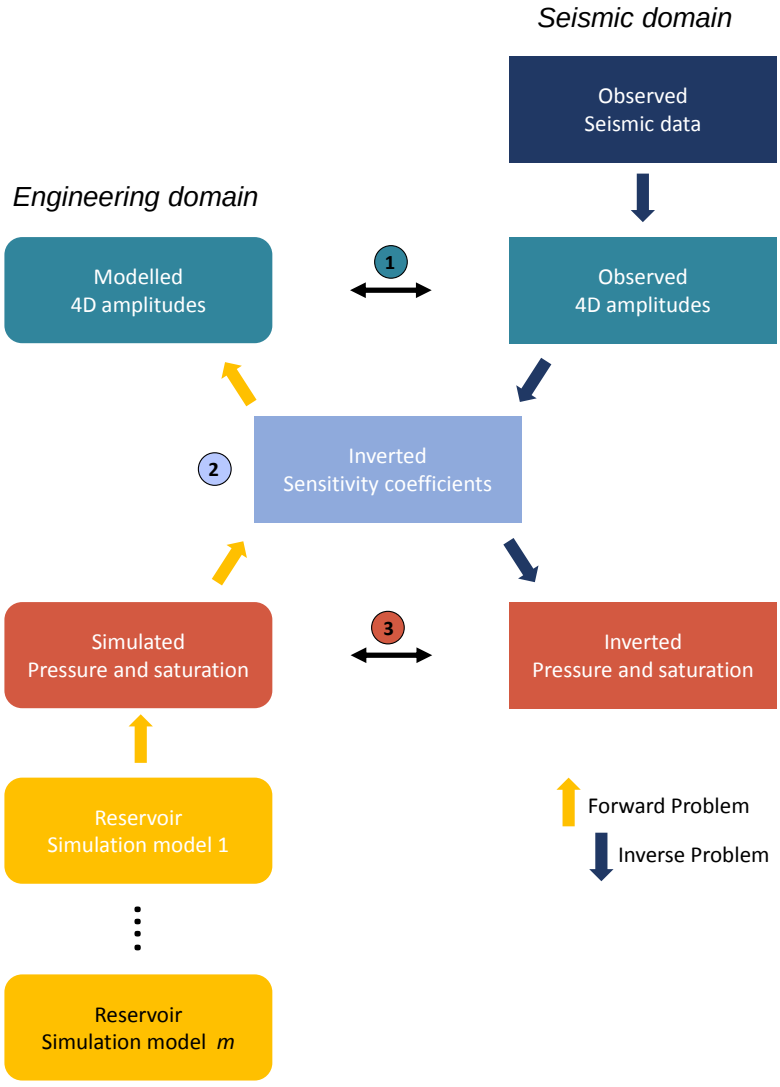

Figure 6-1 Different levels of 4D seismic data interpretation in the proposed inversion scheme which is a modified version of Figure 1-6. It has been modified to highlight the key feature for pressure and saturation estimation which is the reservoir's sensitivity as they define pressure and saturation effects. The philosophy presented is thus one of an interactive loop via the multiple models engineering domain (models 1 to m) and 4D seismic data inversion domain for the sensitivity coefficients, and secondly, the inversion for pressure and saturation changes.

As Figure 1-9 illustrates, the developments point towards the necessity for the 4D seismic data inversion for pressure and saturation to be constrained by engineering data, in order to tackle the inherent non-uniqueness in the inversion, as well as errors due to 4D seismic non-repeatability noise. Such information is generally obtained from a single history-matched flow simulation model and/or measured well production/pressure data. Because of this necessity, such quantitative analysis for pressure and saturation changes might best be done as a component of the reservoir – simulation history matching process.

The work to be presented here uses reservoir engineering data based on multiple realisations of history-matched fluid-flow simulation models to guide the inversion process (Figure 6-1). Compared to Figure 1-6, another difference is that the key driver for the integration is by inverting the 4D seismic data for the reservoir's sensitivity as a natural extension from Chapter 3. The sensitivity coefficients can then be later used for separating pressure and saturation changes (more on this in section 6.2). This avoids the need for petro-elastic/rock-physics modelling which are time consuming and carry considerable uncertainty. The scheme thus provides a flexible and direct integration between both domains via inversion. Apart from the integration at the dynamic level, the sensitivity coefficients can also be used as a proxy model to obtain synthetic 4D seismic amplitudes from the simulation model, which can then be compared with the observed 4D seismic amplitudes for fast model updating in history-matching.

6.2 Methodology

The methodology is divided into two main parts, first the inversion procedure (covering sections 6.2.1 to 6.2.4), followed by how the multiple models are generated, analysed and used in the inversion scheme (section 6.2.5).

6.2.1 Description of a map-based multiple-monitor, multiple-offset inversion scheme

Within the seismic domain loop as shown in Figure 6-2, the data-driven approach is a two-step inversion:

1) Step 1 is to invert the 4D seismic data for the reservoir's sensitivity to pressure, water saturation and gas saturation changes. These will be collectively referred to as sensitivity coefficients.
2) Step 2 takes the inverted sensitivity coefficients from step 1 and performs a second inversion to estimate pressure and saturation changes using offset stacks.

Step 1 above combines 4D seismic data acquired at different monitor times in an inversion for the sensitivity coefficients, C_S and C_P - the name "multi-monitor inversion" is adopted here. Combining two or more monitor 4D seismic data provides the opportunity to compute the sensitivity coefficients not just at each well, but between the inter-well spaces. This is an extension of Chapter 3 where the reservoir's sensitivity was calibrated independently at each monitor time, but at sparse locations of genuine and strong 4D seismic signals. The motivation here is to extend this approach such that the reservoir's sensitivity can be obtained at each seismic bin location. This could also be viewed as a further development from MacBeth et al. (2006) where a single value for the sensitivity coefficients, C_S and C_P was obtained (Equation 1-14). MacBeth et al. (2006) note that this assumption of a spatially invariant C_S and C_P is unrealistic as reservoirs are not homogenous, and variations in the physical static properties are common from one well location to another. As has been shown in the work of Alvarez (2014) (Figure 1-14) and Falahat et al. (2013), the sensitivity coefficients are dependent on the reservoir heterogeneity (influenced mainly by porosity and NTG), which in turn defines the reservoir's 4D seismic response.

In Chapter 2, rock-physics modelling using cemented and unconsolidated sandstones of 5% and 18-27% porosity, respectively, showed significantly different sensitivities to pressure, water saturation and gas saturation changes (Figures 2-11, 2-12 and 2-13). In Chapter 3, variations in the quantified reservoir sensitivities using acquired 4D seismic data on four sandstone fields (Figure 3-22) were observed in localised areas around wells (for example, Figure 3-12), and from one well location to another (for example, Figure 3-8). Floricich (2006), Falahat et al. (2013) and Alvarez (2014) also note that assuming a single value of C_S and C_P is not representative of reservoir facies variation and introduces errors when finally estimating pressure and saturation changes in step 2 as outlined above. In Chapter 7.2.2, it is shown how this assumption of a uniform C_S and C_P causes leakages in the final inversion solution, particularly for estimates of

pressure and gas saturation changes where they overlap (Figure 7-14 (d) to (f)). In Floricich's (2006) least squares inversion (Equation 1-14), a priori (measured or estimated using material balance calculations) pressure and saturation changes were known only at the well locations and were combined with a single monitor 4D seismic response at such well locations to obtain the sensitivity coefficients, C_S and C_P. Each well location experiences some pressure and saturation change depending on the activity of the particular well at the monitor time. However, the problem is that the reservoir's static properties also varies spatially and is different from one well location to another. Therefore, the obtained sensitivity coefficients C_S and C_P represent some smeared average of the reservoir's sensitivity from the combined well locations.

To address the challenge of estimating the reservoir's sensitivity, C_S and C_P as spatial quantities, Floricich's (2006) approach as seen in Equation 1-14 is modified such that each well could represent 4D seismic data, each for a monitor time. Similar to the wells, each monitor time will experience some pressure and saturation changes across the reservoir depending on the production activity at the monitor time. The induced production at each monitor time also act independently of other monitor times. Fundamentally, the static properties of the reservoir which mainly controls C_S and C_P (such as porosity, NTG), are unlikely to change over the production time. This is a valid assumption for non-compacting rocks, such as sandstones. Thus, the reservoir's sensitivity at each seismic bin location remains the same for each monitor time, and can be obtained by combining data from several monitor times as they are independent of each other. The reservoir's sensitivity, particularly, in well consolidated and cemented sandstones can however change, if for example, fractures are induced around the well bore due to high pressure injection (Saul and Lumley, 2015). Xu et al., (2006) show that the low porosity (~ 7% porosity) Lyons sandstone under induced fractures exhibit a higher sensitivity to pressure changes and a different stress path than before the sandstones were fractured.

For C_S and C_P to be estimated spatially, data required at each seismic bin location are (1) the 4D seismic response across monitor times, and (2) pressure and saturation changes at the monitor times. The problem is that the latter (2) is also unknown, and this is where the engineering domain in Figure 6-2 plays its part in the inversion scheme.

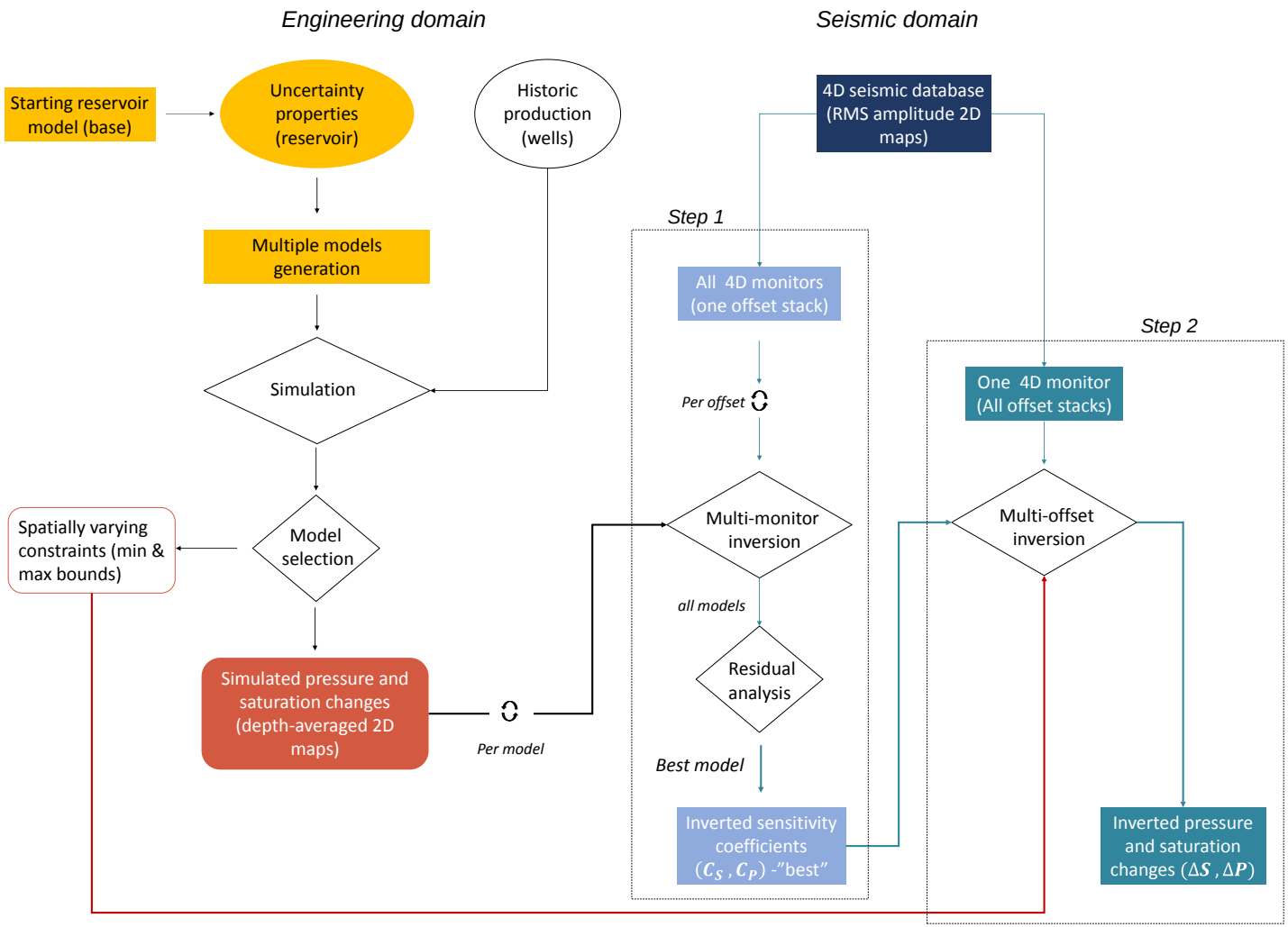

Figure 6-2 Internal architecture of the proposed inversion scheme. Multiple models that honour historical data are generated based on reservoir static properties that are uncertain from an original (base) model. Models that fit certain history-match quality criteria are selected to provide pressure and saturation input to step 1 - the multiple-monitor inversion which is repeated for each pressure and saturation model. The residual norm from the inversion using each model identifies the sensitivity coefficients that best honour the 4D seismic data, hence the specific model. The best estimate of the sensitivity coefficients are then used in step 2 - the multiple-offset inversion which is constrained by limits extracted from the multiple model realisations to estimate reliable pressure and saturation changes at any monitor time.

This a priori knowledge of pressure and saturation changes at the monitor times are taken from history-matched fluid flow simulation models. Multiple reservoir models that honour the geology of the reservoir are generated based on a perturbation of a starting model. The reservoir models are simulated and selected based on their match to production history of the field (see also section 6.2.5 and section 6.3.4). Although all models are wrong, this inversion scheme opens the possibility of using several models in order to compensate for the uncertainties in using only one model. Although, the simulation model can be inaccurate in its relative spatial predictions when in the early stages of development, the cumulative statistics of material balance remain honoured and thus, most of the models should provide robust measures of pressure and saturation changes for use in 4D seismic data calibration. Each simulation model predicts its own pressure and saturation changes, which are used one by one in the multi-monitor inversion to estimate the sensitivity coefficients, C_S and C_P. So, if 100 models are generated, there will be 100 estimates of C_S and C_P based on the 100 scenarios of pressure and saturation changes from the models. With the objective of minimising the misfit with the observed 4D seismic data, the inversion outputs the residuals from each model scenario, and thus gives the simulation model that predicted the pressure and saturation changes, with which the estimated sensitivity coefficients best honours the 4D seismic data (section 7.3.1 details the results of this application). This model and its corresponding C_S and C_P estimate is identified as "best" from the multi-monitor inversion. It is this best C_S and C_P that is used in the final inversion in step 2 to obtain pressure and saturation changes. As seen in Equations 2-23 and 2-26, the sensitivity is dependent on the 4D seismic attributes used to calibrate it. If using interface attributes such as amplitudes, the sensitivity would also depend on whether the data is full stack or partial-offset stack (such as near, mid and far offsets) – see for example, Figure 7-7. Likewise, if using interval attributes such as the intra-reservoir time-shifts, these can also depend on the offset seismic data from which they are calculated.

My approach in step 2, which is the final goal, is to estimate pressure and saturation changes from the seismic domain, and this requires the use of different offsets of 4D seismic data. The near, mid and far offsets have been proven to act independently in relation to pressure and saturation effects, (Landrø, 2001; Floricich, 2006; Alvarez, 2014) and will thus be sufficient for separating these effects in this current work. As a

result, in order to perform step 2, the sensitivity coefficients in step 1 of the inversion scheme (Figure 6-2), will need to be obtained for each type of 4D seismic attribute and offset data. The inversion procedure in step 2 combines multiple offset 4D seismic data at a monitor time, together with the best estimate of C_S and C_P for each offset stack - hence, the name "multi-offset inversion" is adopted here. This multi-offset inversion estimates pressure and saturation changes at the specific monitor time.

The inversion scheme (Figure 6-2) is implemented in Chapter 7 using 2D maps. So, from the seismic domain, the root-mean-square (RMS) amplitudes computed using time-windows along the top reservoir interface is the 4D seismic attribute used (see appendix A for RMS definition). Firstly, the RMS amplitude is calculated separately in baseline and monitor seismic data and a difference of the two maps (monitor-baseline) is obtained, which represents the 4D seismic amplitude maps. Other 4D seismic attributes such as intra-reservoir time-shifts maps could also be used in addition to amplitudes, but in this implementation, only amplitudes are used. From the engineering domain, depth-averaged maps of pressure and saturation changes (co-located with the seismic bin locations) are used. The depth average is evaluated over the reservoir interval of interest, and the seismic horizon at top reservoir is used for the co-location. So, for a particular location, and for a particular effect, say pressure change, this may occur over a thickness h out of the total reservoir interval of thickness, d, the depth average $(h/d)\Delta P$ is mapped. It is understood that h will vary from one monitor time to the next, as will ΔP, whilst d is a function of the reservoir geology and remains the same. It is an expectation that the 4D seismic signatures must respond to this depth-averaged property and so the depth-average can be used in the 4D seismic inversion equations (Equation 6-1). The rationale is that seismic energy, due to its wave behaviour senses a depth average of the reservoir properties, so the depth average is compatible with the 4D seismic maps. Using Petrel software, 2D maps of data from the seismic domain and reservoir engineering domain can be computed.

6.2.2 The data-driven seismic-to-reservoir engineering inversion equations

In Chapter 3, the reservoir's sensitivity to pressure, and water and gas saturation changes was quantified using the observed 4D seismic amplitudes and time-shifts at

each monitor time. This attested that the 4D seismic signatures are consistent with general well activity over production time, which embodies a data-driven approach introduced in Chapter 1.3.2. As Equations 2-23 and 2-26 show in Chapter 2, the sensitivity are symbolised as, C_P - for pressure sensitivity, C_{S_w}- for water saturation sensitivity and C_{S_g}- for gas saturation sensitivity, and measure the unit change in 4D seismic signals to a unit change of the individual pressure or saturation changes. Where both pressure and saturation changes overlap in the reservoir, the composite 4D seismic response represents the sum of their individual contributions (MacBeth et al., 2006; Falahat et al., 2013; Fursov, 2015). This sum is the data-driven formulations, Equation 6-1, developed within ETLP over the last 12 years. Starting with the two-fluid phase equation (Equation 1-13) derived in MacBeth et al. (2006); an extension to three-fluid phase reservoirs is presented in Fursov (2015), which was earlier validated by Falahat et al. (2013). Driven by the causality between well production and the 4D seismic response, the relationship between the mapped 4D seismic signatures and depth-averaged maps of reservoir dynamic properties (pressure, water saturation and gas saturation changes) is expressed in the following linear (Equation 6-1a) and non-linear (Equation 6-1b) forms (Fursov, 2015):

$$\Delta A(x,y) \approx \Big\{C_P(x,y)\Delta P(x,y) + C_{S_w}(x,y)\Delta S_w(x,y) + C_{S_g}(x,y)\Delta S_g(x,y)\Big\}\, A_b(x,y) \tag{6-1a}$$

$$\Delta A \approx \Big\{C_P\Delta P + C_{S_w}\Delta S_w + C_{S_g}\Delta S_g + C_{PP}\Delta P^2 + C_{PS_w}\Delta P\Delta S_w + C_{S_wS_w}\Delta {S_w}^2 + C_{PS_g}\Delta P\Delta S_g + C_{S_gS_g}\Delta {S_g}^2\Big\}\, A_b) \tag{6-1b}$$

where, ΔA is any 4D seismic attribute map, which could be of an interface property (e.g. amplitude maps) or an interval property (e.g. time-shift maps). If using amplitudes, this is simply monitor minus baseline RMS amplitude maps, but for time-shifts, ΔA is replaced by the intra-reservoir time-shift, Δt^{res} in two-way time (for definition, see Figure 2-8). The reservoir dynamic properties: ΔP is the change in pore pressure, ΔS_w is the change in water saturation and ΔS_g is the change in gas saturation. The baseline seismic attribute map, A_b, normalizes the equations so that the left-hand side and the

right-hand side of Equation 6-1 are of the same unit. The attribute map, A_b represents either the RMS amplitude computed along top reservoir using the baseline seismic data or the two-way travel time thickness of the reservoir interval (that is, top reservoir horizon minus bottom reservoir horizon) picked on the baseline seismic data. For amplitudes, A_b captures the effects of the reservoir geology, porosity, net-to-gross and general static seismic properties, and for time-shifts, A_b captures the reservoir's structural components and thickness variations. For time-shifts, the two-way time thickness, A_b, replaces d as seen in Equation 2-26 because the reservoir's thickness, d (in metres) is not usually known at each seismic bin location (x, y). Note also that for the 4D seismic attributes, ΔA, both 4D amplitudes and intra-reservoir time-shifts will depend on the offset stack used (such as near, mid, and far offsets). Also note that if A_b is defined using amplitudes, it will also depend on the offset stack of the baseline seismic data, whereas, if A_b is defined by the two-way time thickness picked on the baseline seismic data, it should in theory remain the same, regardless of whether the near, mid, far or full offset stack data is used for interpreting the baseline horizons. C_P, C_{S_w} and C_{S_g} are the seismically-derived sensitivity coefficients, which as an extension from Chapter 3, will now be estimated at each seismic bin location. Also, as described in Chapter 2, the reservoir pressure sensitivity, C_P accounts for the rock stress sensitivities and fluids response to pore pressure change, water saturation sensitivity, C_{S_w} accounts for the difference in bulk modulus and density between the water and other reservoir fluids, and gas saturation sensitivity, C_{S_g} accounts for the difference in bulk modulus and density between the gas and other reservoir fluids – shown here as spatially-varying quantities and can also be viewed as rock-physics parameters describing the reservoir's 4D seismic response. Equation 6-1b describes a quadratic equation, such that 2nd order terms of the sensitivity coefficients C_{PP}, C_{PS_w} $C_{S_wS_w}$, $C_{S_wS_g}$ and $C_{S_gS_g}$ weight the corresponding ΔP^2, $\Delta P \Delta S_w$, $\Delta {S_w}^2$, $\Delta P \Delta S_g$, and $\Delta {S_g}^2$, respectively – all variables are spatially varying. Also note that all terms in Equation 6-1 can also be volumetric, (x,y,z), where z represents the vertical direction.

By multiplying using the baseline seismic map, A_b (amplitudes or two-way time thickness), instead of a division to the right-hand side of Equation 6-1 in the form $\Delta A / A_b$, the inversion is less unstable should A_b approach zero, either for amplitudes or two-way travel time thickness. For two-way travel time thickness, top and

bottom reservoir horizons may cross each other, possibly across faults, where this occurs, their values should be replaced with zero. It is also recommended that A_b should be represented in its absolute values, so as not to alter the polarity in ΔA.

6.2.3 When to use a linear or non-linear $\Delta P, \Delta S$ inversion equation for sandstones

It is always recommended to apply the inversion using the quadratic formula (Equation 6-1b) over the linear approximation (Equation 6-1a), as this is a more accurate formulation of the 4D seismic response. However, Falahat et al. (2013) and Fursov (2015) in a synthetic application to the Schiehallion field, show that using the linear equation results in only a 2% error compared to the quadratic equation. The question of whether to use the linear (Equation 6-1a) or non-linear (Equation 6-1b) formulation depends on whether the induced production causes pressure and saturation changes that differ significantly across the monitor times. Relative to baseline (pre-production) conditions, this will cause the reservoir to lie in the linear or non-linear region in each of the quadrants in Figure 2-10 at any monitor time.

The question of linearity can be better defined by data calibration of the reservoir's sensitivity (as carried out in Chapter 3). If the sensitivity changes significantly between monitor times, this is indicative of a highly non-linear response, whereas, if the sensitivity is quite similar, then a linear approximation would be sufficient. This will require monitoring of wells so that measurements of pressure, water saturation and gas saturation changes can be taken at each monitor time. On the four fields studied in Chapter 3, the calibration was restricted to specific areas (both around wells and away from wells) with sufficiently strong 4D seismic signals either caused solely by pressure or saturation effects observed across multiple monitor surveys. By calibrating the same location at several monitor times relative to baseline, it was shown that the range of pressure and saturation changes observed in the normally-pressured sandstones yielded a near constant sensitivity across monitor times (Norne, Figure 3-12, Heidrun, Table 3-5 and Schiehallion, Table 3-6). The exception is the HPHT shearwater field whose Fulmar sands become less sensitive at a pressure drop of between -49 to -59 MPa in 2004, compared to a pressure drop of -13 to -25 MPa earlier in 2002 (see Table 3-3). Such a huge gap in pressure decrease of around -35 MPa between the two monitor times causes a decline in pressure sensitivity in 2004 of around 36% relative to the pressure

sensitivity in 2002. This decline in sensitivity to pressure depletion is evident of a slightly non-linear 4D seismic response as the HPHT rocks become closer to their asymptotic state within this huge scale of pressure drop. In the other direction, i.e. pore pressure increase, the sensitivity will rise at a more significant rate for a significant magnitude of pressure increase, compared to a magnitude that is closer to the initial pressure state (see for example, Figure 2-6). For normally-pressured sandstones, this non-linearity can be approximately linear if the changes in pressure (increase or decrease) across monitor times are not far apart, say, within 10 MPa, relative to the baseline (Figure 2-11 and Figure 2-12). Hence, for the same location, the pressure sensitivity calculated at several monitor times will be approximates of each other. This was observed for the Norne Field (Figure 3-12), although in this case an additional 11 MPa pressure increase occurred between the 2003 monitor (at ΔP = 15 MPa) and the 2006 monitor time (at ΔP = 26 MPa). Thus, the assumption of linearity will introduce negligible errors.

For water saturation changes, this could in effect be assumed linear for any magnitude of change (Figure 2-10). Within the typical 10% to 60% range for water saturation changes relative to baseline, the reservoir's sensitivity to water saturation changes differs only slightly at -0.12% to -0.14% amplitude sensitivity, respectively (Figure 2-11). The increase in water saturation change from ΔS_w= 10% to ΔS_w= 60% yields a rise in sensitivity of around 17% relative to the sensitivity at a water saturation change of 10% (Figure 2-11 and Figure 2-12). Unlike pressure changes, this 17% rise in water saturation sensitivity leads to only subtle discrepancies in relative amplitude changes. For example if ΔS_w= 50%, then using a sensitivity of -0.12% gives an amplitude change of -6%, whereas, using the other sensitivity value of -0.14% gives an amplitude change of -7%. Comparing both sensitivity values, the discrepancies in their resulting amplitude change when ΔS_w= 50%, is only 1%. This 1% is considered to be below the amplitude detectability limit of the 4D seismic method, which is suggested to be 2% (MacBeth, 2004). The same calculations using the two sensitivity values can be performed for other magnitudes of practically expected water saturation changes, and so, if calculating at ΔS_w< 50%, the discrepancy will be found to be lower than 1% and if ΔS_w > 50%, it will be found that the discrepancy is still less than 2%.

For gas saturation effects, consideration needs to be given depending on the range of gas saturation changes across monitor times at each seismic bin location. If between monitor times, the magnitude of gas saturation changes occupies the entire range modelled, 0% to 80%, in Figure 2-10, then the 4D seismic responses to gas saturation is non-linear. This non-linearity is particularly severe if using the intra-reservoir time-shift (Figure 2-10 (b)), compared to using amplitude attributes (Figure 2-10 (a)). The sensitivity to gas saturation changes decreases significantly when the gas saturation change is in the 5% to 50% range, whereas between a gas saturation change of 50% and 80%, the sensitivity is relatively stable (Figure 2-11 and Figure 2-12). Within this latter range of 50% and 80%, gas saturation changes would impact an approximately linear effect for both amplitudes and time-shifts.

In Chapter 3, where the acquired 4D seismic amplitudes at two different monitor times (2 years apart for the Schiehallion field and 3 years apart for the Heidrun field) was used, it was observed that the sensitivity to water saturation changes is almost constant across the monitor times. For the Schiehallion field (Table 3-6), the water saturation sensitivity between the two monitor times differed by up to 11.4%. Likewise, for the Heidrun field (Table 3-5), the water saturation sensitivity between the two monitor times differed by up to 9.6%. However, for the calibrated sensitivity to gas saturation increase using the observed 4D seismic data, it was found that the sensitivity differs by 20 to 30% between the two monitor times on the Heidrun field. This suggests a slightly non-linear effect of gas saturation changes, which are not too far apart between monitor times.

For the inversions to be performed in Chapter 7 using 4D seismic amplitudes of the top reservoir formation of the Heidrun field, the linear approximation (Equation 6-1a) has been found to be appropriate based on the observations in Chapter 3.3.3, as discussed in the above paragraph (see also Figure 7-6). Gas saturation changes (monitor-baseline) are above 10%, and the fluctuations in magnitudes across monitor times are within 50% of each other (Figure 3-17(b)). Water saturation changes lie within 10% and 70% (Figure 3-17(a)), and only mild pressure changes of up to 5 MPa in magnitude occur across all monitor times. Though the influence of pressure facilitates the saturation dominated response of the reservoir, such pressure effects could not be solely observed

in the 4D seismic amplitude response, which is strongly saturation driven (see Figure 6-8).

6.2.4 Multi-monitor and multi-offset inverse problem formulation

For step 1 of the inversion procedure (Figure 6-2), consider $\boldsymbol{z}$ number of 4D seismic offset stacks, and $\boldsymbol{v}$ number of monitor vintages, Equation 6-1a yields $\boldsymbol{z}$ number of linear equations (each, a multi-monitor equation) to solve for the sensitivity coefficients, C_P, C_{S_w} and C_{S_g} which also depend on offsets, θ:

$$\begin{bmatrix} \Delta A_{\mathbf{1}}(\theta_1) \\ \Delta A_{\mathbf{2}}(\theta_1) \\ . \\ . \\ \Delta A_{\boldsymbol{v}}(\theta_1) \end{bmatrix} = \begin{bmatrix} A_b(\theta_1)\Delta P_{\mathbf{1}} & A_b\Delta S_{w_{\mathbf{1}}} & A_b\Delta S_{g_{\mathbf{1}}} \\ A_b(\theta_1)\Delta P_{\mathbf{2}} & A_b\Delta S_{w_{\mathbf{2}}} & A_b\Delta S_{g_{\mathbf{2}}} \\ . & . & . \\ . & . & . \\ A_b(\theta_1)\Delta P_{\boldsymbol{v}} & A_b\Delta S_{w_{\boldsymbol{v}}} & A_b\Delta S_{g_{\boldsymbol{v}}} \end{bmatrix} \begin{bmatrix} C_P(\theta_1) \\ C_{S_w}(\theta_1) \\ C_{S_g}(\theta_1) \end{bmatrix} + \begin{bmatrix} e_{\mathbf{1}}(\theta_1) \\ e_{\mathbf{2}}(\theta_1) \\ . \\ . \\ e_{\boldsymbol{v}}(\theta_1) \end{bmatrix}$$

$$\vdots$$

$$\vdots \qquad (6\text{-}2)$$

$$\begin{bmatrix} \Delta A_1(\theta_{\mathbf{z}}) \\ \Delta A_2(\theta_{\mathbf{z}}) \\ . \\ . \\ \Delta A_v(\theta_{\mathbf{z}}) \end{bmatrix} = \begin{bmatrix} A_b(\theta_{\mathbf{z}})\Delta P_1 & A_b\Delta S_{w_1} & A_b\Delta S_{g_1} \\ A_b(\theta_{\mathbf{z}})\Delta P_2 & A_b\Delta S_{w_2} & A_b\Delta S_{g_2} \\ . & . & . \\ . & . & . \\ A_b(\theta_{\mathbf{z}})\Delta P_{\boldsymbol{v}} & A_b\Delta S_{w_{\boldsymbol{v}}} & A_b\Delta S_{g_{\boldsymbol{v}}} \end{bmatrix} \begin{bmatrix} C_P(\theta_{\mathbf{z}}) \\ C_{S_w}(\theta_{\mathbf{z}}) \\ C_{S_g}(\theta_{\mathbf{z}}) \end{bmatrix} + \begin{bmatrix} e_1(\theta_{\mathbf{z}}) \\ e_2(\theta_{\mathbf{z}}) \\ . \\ . \\ e_{\boldsymbol{v}}(\theta_{\mathbf{z}}) \end{bmatrix}$$

where, θ_1 to $\theta_{\mathbf{z}}$ denote different offsets (or angle), in this case there are $\mathbf{z}$ number of offsets, and the inside subscript $1, 2, \ldots, \boldsymbol{v}$ denote the 4D monitor vintages, from first monitor, 1, to last monitor, $\boldsymbol{v}$. Each monitor time has its own pressure and saturation changes, and its own 4D seismic amplitude response, ΔA, which are inputs to the multi-monitor inversion. Other inputs include the baseline seismic amplitude, $A_b(\theta_{\boldsymbol{i}})$ which is different for each offset data, is independent of the monitor time, and scales the pressure and saturation changes across all monitors. The 4D seismic amplitude noise, $\boldsymbol{e}$, varies for each monitor data and is also different at each offset. Offset/angle gathers can be used, but in this application, restricted offset stacks are used, and these include only the near, mid, and far offset amplitude stacks, so, $\mathbf{z}$ = 3. Note also that all terms in each row/line of the matrix equations in Equation 6-2 are 2D maps and each row in a particular matrix equation corresponds to a specific monitor time i where $i =$

$1, 2, \ldots, \boldsymbol{v}$. For information on how the matrices are set up in the inversion, see Appendix C.1. The output are the sensitivity coefficients C_P, $C_{S_w}$and C_{S_g} which are obtained for each offset $\theta_i = \theta_1, \ldots, \theta_{\mathbf{z}}$. This means that there are $\boldsymbol{z}$ number of sets of equations to solve for C_P, $C_{S_w}$and C_{S_g}. Equation 6-2 indicates that at least two monitor surveys are required to solve for the sensitivity coefficients per offset stack. Addition of data from more monitor surveys could thus help to reduce redundant information. By combining multiple monitors, the 4D seismic response can be transformed into the sensitivity coefficients. As discussed in section 6.2.1, note that pressure and saturation changes for all the monitor times are taken a priori from multiple fluid-flow simulation models (see also section 6.2.5). So, for "m" number of simulation models (i.e. "m" number of pressure and saturation changes for all monitors), Equation 6-2 is implemented "m" times, for each offset stack θ_i, (see also Equation 6-4).

In step 2 of the inversion procedure (Figure 6-2), the final estimation of the unknown pressure and saturation changes from 4D seismic data at different monitor times, $1, 2, \ldots, \boldsymbol{v}$, re-arranges Equation 6-1a into the multi-offset form:

$$\begin{bmatrix} \Delta A_1(\theta_1) \\ \Delta A_1(\theta_2) \\ . \\ . \\ \Delta A_1(\theta_{\mathbf{z}}) \end{bmatrix} = \begin{bmatrix} (A_b C_P)(\theta_1) & (A_b C_{S_w}) & (A_b C_{S_g}) \\ (A_b C_P)(\theta_2) & (A_b C_{S_w}) & (A_b C_{S_g}) \\ . & . & . \\ . & . & . \\ A_b C_P(\theta_{\mathbf{z}}) & (A_b C_{S_w}) & (A_b C_{S_g}) \end{bmatrix} \begin{bmatrix} \Delta P_1 \\ \Delta S_{w_1} \\ \Delta S_{g_1} \end{bmatrix} + \begin{bmatrix} e_1(\theta_1) \\ e_1(\theta_2) \\ . \\ . \\ e_1(\theta_{\mathbf{z}}) \end{bmatrix}$$

$$\vdots$$

$$\vdots \qquad (6\text{-}3)$$

$$\begin{bmatrix} \Delta A_{\boldsymbol{v}}(\theta_1) \\ \Delta A_{\boldsymbol{v}}(\theta_2) \\ . \\ . \\ \Delta A_{\boldsymbol{v}}(\theta_{\mathbf{z}}) \end{bmatrix} = \begin{bmatrix} (A_b C_P)(\theta_1) & (A_b C_{S_w}) & (A_b C_{S_g}) \\ (A_b C_P)(\theta_2) & (A_b C_{S_w}) & (A_b C_{S_g}) \\ . & . & . \\ . & . & . \\ A_b C_P(\theta_{\mathbf{z}}) & (A_b C_{S_w}) & (A_b C_{S_g}) \end{bmatrix} \begin{bmatrix} \Delta P_{\boldsymbol{v}} \\ \Delta S_{w_{\boldsymbol{v}}} \\ \Delta S_{g_{\boldsymbol{v}}} \end{bmatrix} + \begin{bmatrix} e_{\boldsymbol{v}}(\theta_1) \\ e_{\boldsymbol{v}}(\theta_2) \\ . \\ . \\ e_{\boldsymbol{v}}(\theta_{\mathbf{z}}) \end{bmatrix}$$

where for a given monitor time, i, where $i = 1, 2, \ldots, \boldsymbol{v}$ number of 4D monitor vintages, the multi-offset inversion combines 4D seismic amplitude data, ΔA, at different offsets θ_1 to $\theta_{\mathbf{z}}$ (or otherwise called angles), together with the best estimate of the sensitivity coefficients, $C_P(\theta_i)$, $C_{S_w}(\theta_i)$, and $C_{S_g}(\theta_i)$, which have been obtained for each offset

$\theta_{\boldsymbol{i}} = \theta_1, \ldots, \theta_{\mathbf{z}}$ using Equation 6-2. For a given monitor time, the 4D seismic noise, $\boldsymbol{e}$ corresponds to each offset. The seismic amplitude map, $A_b(\theta_{\boldsymbol{i}})$ is computed using the baseline seismic data and is also calculated for each offset stack, and is independent of the monitor time. Offset/angle gathers can be used, but in this application, restricted offset stacks are used, and these include only the near, mid, and far offset amplitude stacks, so, $\mathbf{z}$ = 3. Note also that all terms in each row/line of the matrix equations in Equation 6-3 are 2D maps and each row in a particular matrix equation corresponds to specific offset $\theta_{\boldsymbol{i}}$. For information on how the matrices are set up in the inversion, see Appendix C.1. The unknowns are pressure and saturation changes, which can now be estimated from the observed 4D seismic data for each available monitor time, $i = 1, 2, \ldots, \boldsymbol{v}$. If estimating for all monitor times, this means that there are $\boldsymbol{v}$ number of sets of equations to solve for their respective ΔP, ΔS_w and ΔS_g. So, for a two-fluid phase system, at least two independent offset stacks (e.g. near and far offset) are needed to solve for $\Delta P \& \Delta S_w$ or $\Delta P \& \Delta S_g$, but for a three phase system (oil, water and gas) as is the example shown, this expands to three offset stacks (near, mid and far offset).

For the multi-monitor inversion (Equation 6-2), the inversion needs to be repeated for each simulation model generated, as each model provides its own pressure and saturation changes (Figure 6-2). Equation 6-2 can be represented as several general linear system for "*m*" number of simulation models, Equation 6-4:

$$\begin{aligned} \mathbf{d} &= \mathbf{G}^{[\mathbf{1}]}\mathbf{m}^{[\mathbf{1}]} + \mathbf{e} \\ \mathbf{d} &= \mathbf{G}^{[\mathbf{2}]}\mathbf{m}^{[\mathbf{2}]} + \mathbf{e} \\ &\vdots \\ &\vdots \\ \mathbf{d} &= \mathbf{G}^{[\boldsymbol{m-1}]}\mathbf{m}^{[\boldsymbol{m-1}]} + \mathbf{e} \\ \mathbf{d} &= \mathbf{G}^{[\boldsymbol{m}]}\mathbf{m}^{[\boldsymbol{m}]} + \mathbf{e} \end{aligned} \tag{6-4}$$

where, $\mathbf{d}$ is the data vector which contains all 4D seismic RMS amplitude maps including all monitors and their offset stacks, $\mathbf{e}$ contains 4D seismic noise maps corresponding to the monitors and their offset stacks**.** The matrix mapping operator, $\mathbf{G}^{[\boldsymbol{i}]}$**,** where $[\boldsymbol{i}] = [\mathbf{1}], \ldots, [\boldsymbol{m}]$ number of simulation models, contains depth-averaged maps of simulated pressure and saturation changes, ΔP, ΔS_w and ΔS_g for all

monitor times predicted from the model,$[\boldsymbol{i}]$. As a result, the output, $\mathbf{m}^{[\boldsymbol{i}]}$ which contains maps of the sensitivity coefficients C_P, $C_{S_w}$and C_{S_g} for all offset stacks, is obtained for the specific simulation model $[\boldsymbol{i}]$**,** from which $\mathbf{G}^{[\boldsymbol{i}]}$ is obtained**.** Note that the maps of ΔP, ΔS_w and ΔS_g contained in $\mathbf{G}^{[\boldsymbol{i}]}$ are pre-multiplied by the baseline seismic amplitude maps, A_b computed for each offset stack, as in Equation 6-2.

By computing the norm of the difference $\left\|\mathbf{d} - \mathbf{G}^{[\boldsymbol{i}]}\mathbf{m}^{[\boldsymbol{i}]}\right\|_{\mathbf{2}}^{\mathbf{2}}$**,** it is then possible to identify the solution estimate $\mathbf{m}^{[\boldsymbol{i}]}$ that sufficiently fits the data, $\mathbf{d}$, based on all "*m*" simulation models of $\mathbf{G}^{[\boldsymbol{i}]}$.This then helps to also identify the specific simulation model by which the best estimate of $\mathbf{m}$ was obtained, which resulted in the lowest norm of the difference. A "sufficient" fit to the data is used here as the inversion will be constrained (as discussed in subsequent pages) so as not to over-fit the noise in the data. To bring this to full picture, Equation 6-2 corresponds to one linear system of equations in Equation 6-4. Each linear system of equation is a matrix/ vector combination which is solved simultaneously, and not element-wise. In Figure 7-16(b), I show the resulting norm of residuals for this multiple simulation models, multi-monitor inversion scheme.

For the multi-offset inversion as shown in Equation 6-3, a single linear system in the general form ensues, Equation 6-5:

$$\mathbf{d}' = \mathbf{G}'\mathbf{m}' + \mathbf{e}' \tag{6-5}$$

where, the data vector $\mathbf{d}'$ contains 4D seismic amplitude maps for all offset stacks combined, with each combination arranged according to monitor times and $\mathbf{e}'$ contains 4D seismic noise maps for all offset stacks combined, and arranged according to monitor times. The matrix mapping operator, $\mathbf{G}'$ contains the best estimate of the sensitivity coefficients C_P, $C_{S_w}$and C_{S_g} for all offset stacks (after implementing Equation 6-4). This $\mathbf{G}'$ is now used for estimating pressure and saturation changes, ΔP, ΔS_w and ΔS_g, for all monitor times, which are the unknowns in $\mathbf{m}'$. Also note that the maps of C_P, $C_{S_w}$and C_{S_g} contained in $\mathbf{G}'$ are pre-multiplied by the baseline seismic amplitude maps, A_b computed for each offset stack, as in Equation 6-3. This is a matrix/ vector combination which is solved simultaneously, and not element-wise.

For matrix/vector dimensions, I refer back to each set of linear equations in Equation 6-2 and Equation 6-3, and denote each set as $\boldsymbol{d} = \boldsymbol{Gm} + \boldsymbol{e}$. So, for M number of seismic bin locations (x, y), subset $\boldsymbol{G}$ is the $cM \times nM$ matrix mapping operator where n is the number of unknown variables to be estimated (such as C_i or $\Delta i, where\ i = P, S_w, S_g$) in $\boldsymbol{m}$ which is a vector with dimension, nM, containing the unknown variables; $\boldsymbol{d}$ is the 4D seismic data vector with dimension $cM \times 1$ which could be offset stacks for a particular 4D monitor time or 4D monitor vintages for a particular offset stack; and $\boldsymbol{e}$ is the 4D seismic noise which is estimated from 4D seismic data. It is a vector with dimension $cM \times 1$, which forms the diagonal elements of the error covariance matrix $\boldsymbol{C_d}$. See also Appendix C.1 for how the matrices/vectors are set up.

In the case of Equation 6-2, $c = \boldsymbol{v}$ number of 4D monitor vintages, and for Equation 6-3, $c = \mathbf{z}$ number of 4D seismic offset stacks. If $\boldsymbol{v} > n$ or $\mathbf{z} > n$, the inversion problem will be over-determined (i.e. an exact solution does not exist). However, having more knowns allows for a reduction in the influence of biased data in the solution. Such an over-determined problem needs to be solved through a least squares process. The objective is then to estimate the variables in $\boldsymbol{m}$ such that they agree with the 4D seismic data, $\boldsymbol{d}$. I chose an L_2 norm as an appropriate measure of the goodness of data fitting, as it balances errors of different magnitudes, a higher order norm emphasises larger errors or outliers (Menke, 1989). The L_2 norm implies that the solution to the inverse problem is given by the solution to the objective function,

$$f(\boldsymbol{m}) = \|\boldsymbol{e}\|_2^2 = (\boldsymbol{d} - \boldsymbol{Gm})^{\mathbf{T}} \boldsymbol{C_d^{-1}} (\boldsymbol{d} - \boldsymbol{Gm}) \tag{6-6}$$

where $\boldsymbol{C_d}$ is the data error covariance matrix with dimension $cM \times nM$. Its diagonal elements contain an estimate of the spatially varying noise in the observed 4D seismic data. Only the diagonal elements are defined, thus assuming that 4D seismic data measurement errors are independent. Each diagonal element in $\boldsymbol{C_d}$ represents a seismic bin location, each with a different noise estimate defined by variance, $\sigma_{\mathbf{d}}^2$ (i.e. a normal distribution of data errors with zero mean and non-zero standard deviation, σ).

If a least-squares solution to the inversion problem in Equation 6-4 or Equation 6-5 exists, it can be found by minimizing the objection function, $f(\boldsymbol{m})$ in Equation 6-6 by taking its partial derivatives with respect to $\boldsymbol{m}$ and setting it to zero, giving the least-squares solution (Menke, 1989):

$$\boldsymbol{m} = \left(\boldsymbol{G^T C_d^{-1} G}\right)^{-1} \left(\boldsymbol{G^T C_d^{-1} d}\right) \tag{6-7}$$

and the error covariance matrix for $\boldsymbol{m}$ is

$$\boldsymbol{C_m} = \left(\boldsymbol{G^T C_d^{-1} G}\right)^{-1} \tag{6-8}$$

where the variance of the model variables, $\sigma_{\mathbf{m}}^2$ is given by the diagonal elements of $\boldsymbol{C_m}$ **.**

In practise, simply solving Equation 6-2 may not always yield physically meaningful signs of the values of the sensitivity coefficients. For example, if the reservoir's pore pressure increases ($\Delta P > 0$), leading to a softening effect, and the mapped attribute responds to the reservoir's softening by increasing its value ($\Delta A > 0$), then the resulting derivative, $\partial \Delta A / \partial \Delta P$ should be positive, i.e. $C_P > 0$. In the case of a water saturation increase ($\Delta S_w > 0$) leading to a hardening effect, the mapped attribute responds by decreasing its value ($\Delta A < 0$), then the resulting derivative $\partial \Delta A / \partial \Delta S_w$ should be negative, i.e. $C_{S_w} < 0$. As it is common for the 4D seismic data to be noisy, the inversion may output the wrong sign for the sensitivity coefficients and the causality relationship in Equation 6-1a becomes rather meaningless. It is necessary then to impose constraints such that the expected signs are maintained:

$$\partial \Delta A / \partial \Delta P \geq 0;\ \partial \Delta A / \partial \Delta S_w \leq 0\ ;\ \partial \Delta A / \partial \Delta S_g \geq 0 \tag{6-9}$$

The signs are defined by the polarity of the mapped 4D seismic signatures at each offset stack in response to the different dynamic effects. This is dependent on the baseline polarity of the reservoir interface and thus an appropriate choice of a mathematical operation (for example, root-mean-square (RMS), sum-of-negative amplitudes (SNA), sum-of-positive amplitudes (SPA) etc.) by which the baseline and monitor seismic amplitudes are averaged over the reservoir interval, and then differenced to produce 4D maps. In this case, the RMS amplitudes are used.

In addition, the inverse problem in Equation 6-2 or 6-3 is inherently ill-posed as it is common for the resulting determinant of the matrix $\left[\boldsymbol{G^T C_d^{-1} G}\right]$ to be equal to zero, meaning that the matrix is singular and its inverse does not exist, hence the least-squares

solution fails. This implies that the 4D seismic signals are highly correlated as several combinations of ΔP, ΔS_w and ΔS_g can affect the magnitude and polarity in ΔA in the same way. For example, both an increase in pore pressure and an increase in gas saturation will give the same softening effect. So also that the solution does not over-fit the noise in data, it is therefore necessary to introduce additional constraints and a priori information to obtain stable estimates of ΔP, ΔS_w and ΔS_g.

One way to introduce a priori information is to impose upper, $\boldsymbol{m^{upper}}$ and lower, $\boldsymbol{m^{lower}}$ bounds for ΔP, ΔS_w and ΔS_g so as to constrain the solution space of the multi-offset inversion in Equation 6-5, the objective then becomes to minimize:

$$f(\boldsymbol{m}) = (\boldsymbol{d} - \boldsymbol{Gm})^{\boldsymbol{T}} \boldsymbol{C_d^{-1}} (\boldsymbol{d} - \boldsymbol{Gm})$$

subject to the constraints (6-10)

$$\boldsymbol{m^{lower}} \leq \boldsymbol{m} \leq \boldsymbol{m^{upper}}$$

Analytically, the solution of the linear programming problem in Equation 6-10 is not straightforward but various algorithms in numerical methods exist that allow solving this type of problem (e.g. Björck, 1988; Coleman and Li, 1993). The algorithm selected is that by Coleman and Li (1993), which has a built-in function in MATLAB. Further descriptions are given in Appendix C.

The upper and lower bounds (Equation 6-10) serve as a priori information which could be either uniform (i.e. the same for each seismic bin location) or spatially varying. Uniform bounds are based on engineering material balance laws and/or global well bottom-hole-pressure and saturation measurements, which may not be adequate to constrain each spatial location. To honour the 4D seismic data, I chose the more realistic spatially-varying constraints which is a key point of the proposed inversion scheme. These upper and lower bounds for pressure and saturation changes will be provided from multiple reservoir simulations, as will be discussed in the next section. Such spatial constraints are also quite necessary, as Figure 2-10 (b) shows that a gas saturation change of 50% may be confused for one of 10%. Uniform bounds can also be

used in the multi-monitor inversion in Equation 6-3 to obtain the sensitivity coefficients, C_P, C_{S_w} and C_{S_g}. These bounds are obtained via data calibrated sensitivities (as carried out in Chapter 3). The bounds will ensure that the signs as in Equation 6-9 are maintained and a solution can be found with such minimum a priori information. In Figure 7-7 (see section 7.1.3), I show the uniform bounds used for the multi-monitor inversion for C_P, C_{S_w} and C_{S_g}(specific to each offset stack) – see also some results in Figure 7-9. In Figures 7-5 and 7-6 (see section 7.1.2) I show the spatially varying bounds used for the multi-offset inversion for ΔP, ΔS_w and ΔS_g (specific to the particular monitor time)- see results in Figure 7-10(a) to (c) and Figure 7-14(a) to (c). Uniform bounds are also tested for the multi-offset inversion (see for example, Table 7-1, and results in Figure 7-14(d) to (f) and Figure 7-15(a) to (c)).

6.2.5 Multiple flow simulation models

Multiple models allow some uncertainty in the static reservoir properties to be accounted for. This concept was first implemented by Davolio (2013) on a synthetic model, which demonstrated its usefulness. By combining different uncertain properties such as porosity, permeability, fault transmissibility, etc. multiple simulation models can be generated. The results from the multiple simulation models can then be used to constrain the solution space of the multi-offset inversion for pressure and saturation changes. Thus, a statistical database can be obtained by computing the maximum, minimum, mean and the standard deviation at each spatial location based on the contribution from the generated models, which can then be used as spatially varying constraints. Figure 6-3 illustrates how the statistical database is extracted. As Davolio (2013) explains, first, uncertain reservoir properties are identified and assigned a distribution, in this case assuming there are "p" number of uncertain reservoir properties. These properties are then combined to build "m" number of reservoir simulation models. After simulating all the models, there will be "m" number of scenarios of pressure and saturation changes as predicted by the models. Every spatial point on the map or grid will thus have a minimum, maximum, mean and standard deviation assigned to it, based on all possible "m" number of model scenarios. The idea is to guide the inversion using limits from the simulation results, optimising the estimates to fall within these limits (Appendix C.2 describes how the optimisation

within the constrained inversion works).

In the inversion scheme (Figure 6-2), multiple simulation models from the engineering domain are applied in two ways. Firstly, in the multi-monitor inversion, each simulation model provides its own predicted pressure and saturation changes, which are used to estimate C_S and C_P for the specific model prediction (Equation 6-4). Secondly, in the multi-offset inversion, maximum and minimum values at each seismic bin location are extracted from all the predictions of pressure and saturation changes from the generated "m" number of models combined. These are then used to constrain the solution estimates for pressure and saturation changes (as seen in Equation 6-10), where minimum represents $\boldsymbol{m}^{\boldsymbol{lower}}$ and maximum represents $\boldsymbol{m}^{\boldsymbol{upper}}$).

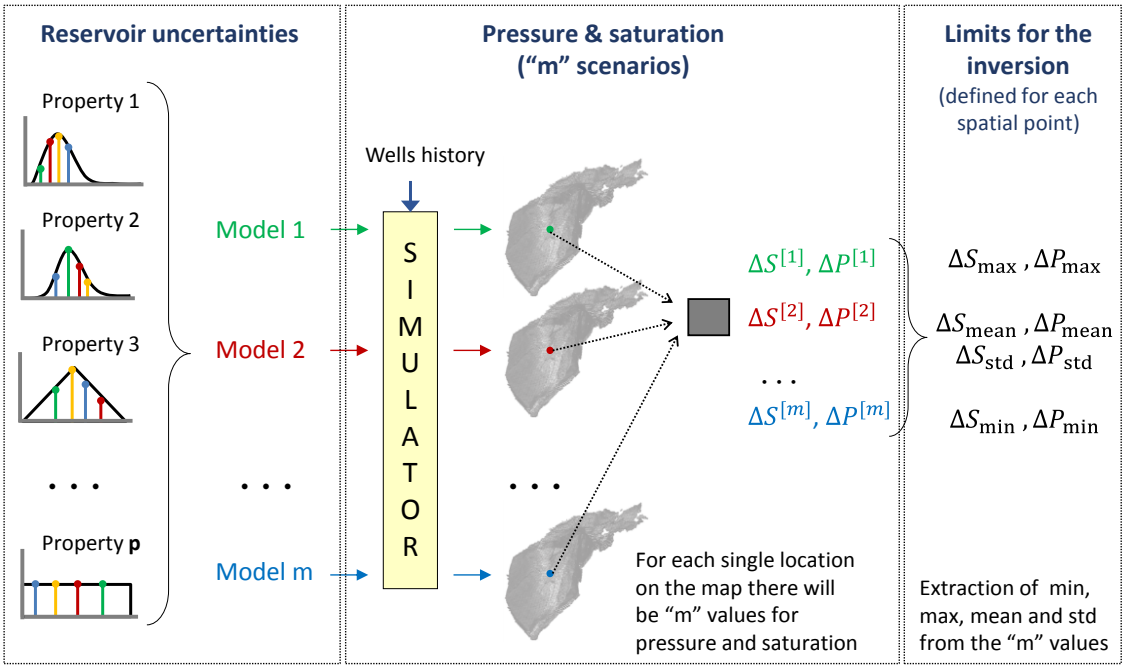

Figure 6-3 General procedure used to define limits of pressure and saturation change for each spatial point on the depth-averaged maps. 'Property 1'; 'Property 2'; 'Property p' are generic representations of the reservoir uncertainty and 'Model 1'; 'Model 2' and 'Model m' are generic reservoir models generated from the combination of the reservoir uncertainties, modified after Davolio (2013).

Three main reasons why the procedure in Figure 6-3 is proposed in the inversion scheme:

- The 4D seismic data is noisy and the inversion is inherently non-unique. Spatially varying engineering-consistent constraints to the inversion solution space will help yield inversion estimates that better honour material balance and flow conditions.

- Errors/uncertainties in reservoir static properties from using a single model. As, by definition, all models are wrong but some can be useful (Box et al., 2005), using many history-matched models allows for better uncertainty characterisation. In addition, as has been shown in Chapters 4 and 5, intra-survey reservoir fluctuations add to the uncertainty when linking acquired 4D seismic data to fluid flow simulation models. Many predictions from the models can thus help to reduce this, but, historical production data input into the simulation model are typically at coarse time scales of weekly to monthly intervals (Aanonsen et al., 2003).

- Multiple models offer flexibility, as several scenarios of pressure and saturation changes can be input to the multi-monitor inversion to estimate the sensitivity coefficients C_P, C_{S_w} and C_{S_g}, as well as an opportunity to find models that better honour the 4D seismic signals across the combination of 4D monitor times and also, models that better match historical data.

If an original (i.e. base) reservoir model already exists, then a perturbation of its uncertain static properties will facilitate the generation of many model realisations, which will in turn output predictions of pressure and saturation changes across the history of the field. The assumption here is that the base reservoir model is conditioned to 3D seismic data, well log data, engineering data and other data sources (Dubrule, 2003).

Historic production data is used as a quality indictor for the generated simulation models. This allows for a reduction of the dispersion across the models, such that only those models that honour historic data are selected to provide input to the inversion. The generated models undergo a validation process which assesses the match between the simulated predictions, $\boldsymbol{d^{sim}}$ for each model and historic observations, $\boldsymbol{d^{hist}}$ using the global objective value, $\mathbf{OF}_{\boldsymbol{model}}$, defined as:

$$\mathbf{OF}_{\boldsymbol{model}} = \sum_{\boldsymbol{d=1}}^{\boldsymbol{K}} \boldsymbol{X_d} \tag{6-11}$$

and the partial objective value, $\boldsymbol{X_d}$ is calculated as

$$\boldsymbol{X_d = w_d \sum_{i=1}^{N} w_i \left(\frac{d_i^{sim} - d_i^{hist}}{\sigma_d} \right)^2}$$

where

$\boldsymbol{K}$ is the number of different types of production data, $\boldsymbol{d}$,

$\boldsymbol{w_d}$ is the Global Weight (ranging from 0 to 1) for each type of production data, $\boldsymbol{d}$

$\boldsymbol{N}$ is the number of data points in the series (from start to end of production)

$\boldsymbol{w_i}$ is the normalised weight for data point $\boldsymbol{i}$

$\boldsymbol{d_i^{sim}}$ is the simulated value for data point $\boldsymbol{i}$

$\boldsymbol{d_i^{hist}}$ is the historic (observed) value for data point $\boldsymbol{i}$

$\boldsymbol{\sigma_d}$ is the Standard Deviation of the particular production data, $\boldsymbol{d}$

The production data, $\boldsymbol{d}$, usually includes one or more of the following: gas production, oil production, water production (in rates or cumulative measures), gas-oil-ratio (GOR), water-cut (WCT), and well pressures (if available). So, $\boldsymbol{X_d}$ is calculated for each production data, and $\mathbf{OF}_{\boldsymbol{model}}$ is the sum. For any simulation model, the smaller the result of $\mathbf{OF}_{\boldsymbol{model}}$, the better the match to the historic data. For the application in section 6.3.4, the field GOR and WCT are the two production data used to compute $\mathbf{OF}_{\boldsymbol{model}}$ and both are given equal weights, with $\boldsymbol{w_d} = 1$. More details of how multiple simulation models are generated are also given in section 6.3.4.

The criterion used to qualify or reject a model is based on the percentage difference between the global objective value from the generated model, $\mathbf{OF}_{\boldsymbol{generated}}$ and the global objective value from the original (base) model, $\mathbf{OF}_{\boldsymbol{base}}$ such that:

$$\text{Qualifying criterion : } -100\% \leq Q \leq 50\%$$

$$\text{where } Q = 100\left(\frac{\mathbf{OF}_{generated} - \mathbf{OF}_{base}}{\mathbf{OF}_{base}}\right) \qquad (6\text{-}12)$$

Note that in Equation 6-11, the global objective function value, $\mathbf{OF}_{\boldsymbol{model}}$, is calculated for both the generated models and the base model. Equation 6-12 implies that all generated models which match historic data better than the base model are qualified

(i.e. Q is negative), and models which surpass the global objective function value from the base model beyond 50% are excluded. The selected models are then used to extract the limits for pressure and saturation for the multi-offset inversion (this is part of step 2 of the inversion scheme, as Figure 6-2 illustrates). If a base model is not available, then the criteria could be to select models with a global objective function value smaller than some percentage, in relation to the model with the maximum global objective function value. For the multi-monitor inversion, pressure and saturation predictions from the qualified models are then used in turn (Equation 6-4), to estimate the sensitivity coefficients (this is step 1 of the inversion scheme, as Figure 6-2 illustrates).

6.3 Multiple models application to the Heidrun field

This section introduces the Heidrun field and details how the multiple simulation models were generated for the Heidrun field which are then applied later in the inversion scheme in Chapter 7. The Heidrun field has been earlier introduced in Chapter 3.3.3.

6.3.1 Description of the Heidrun field simulation model

The simulation model has dimensions 154 x 146 x 66 (making 1,483,944 grid cells, with only 264,701 active grid cells), having an average cell size of 100 x 100 x 9.6 m and contains 1000 faults. The model is built to be consistent with the geological features, flow units and fault planes; hence, the grid uses non-vertical pillars and irregular cells (corner-point geometry (CPG)). The simulation model is a large fault-bounded structural closure dipping towards the south at angle of -5°, forming a complex network of faults, and covers an area of approximately 75.7 km^2 (Figure 6-4 (a)). The reservoir is composed of sandstones. The model porosity ranges between values of 0.01 and 0.38 and the permeability along X, Y and Z direction ranges between 0.0001 and 5000 mD. Vertical to horizontal permeability ratio ranges from 0.01 to 1.5. The static properties are well constrained by the large amount of well data. Data from wells and an acoustic impedance background trend were used in the porosity modelling. There are 67 geological horizons and 66 geological layers (otherwise called zones) in the model.

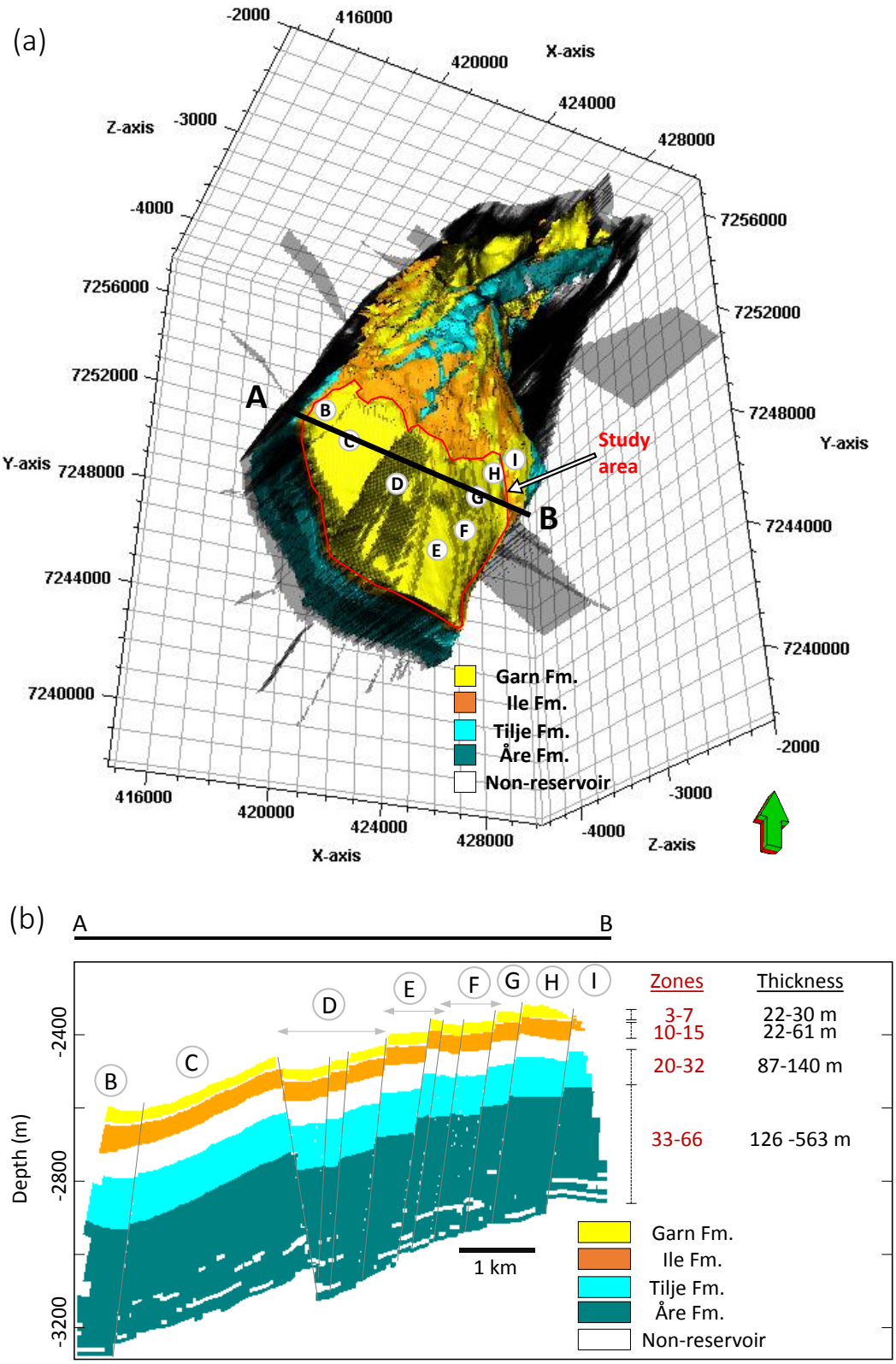

Figure 6-4 (a) Fluid-flow simulation model of the Heidrun field with a fault-bounded structure with ~1000 faults. The study area over which the inversion is performed for the Garn formation is highlighted in red, with several fault segments B to H in this area. (b) Vertical section of the simulation model along line A-B illustrating the zone allocations and average vertical thicknesses according to the four reservoirs (Garn, Ile, Tilje and Åre Formation). Non-reservoir units i.e. Shales are inactive in the model.

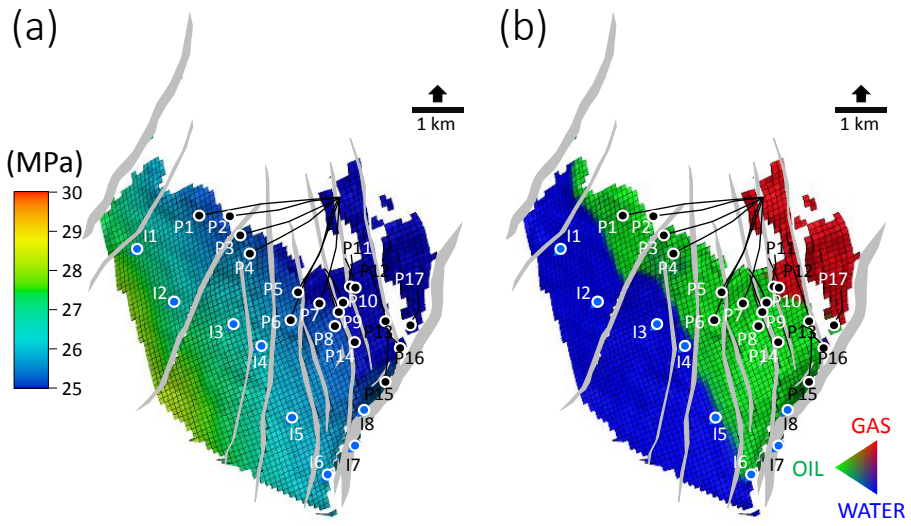

Figure 6-5 Pre-production conditions of top reservoir (Garn Fm.) study area from the Heidrun field model (a) Initial pressure (b) Initial fluid distribution. Producers are in black and water injectors are in blue.

Property	Description
Black oil system	Gas, oil, water, dissolved gas in live oil
Oil gravity	34.4° – 20° API
Initial reservoir pressure (P_i)	22.5 – 34.6 MPa
Temperature	85°C
Oil viscosity	0.53 – 2.27 cp
Gas gravity	0.7534 – 0.6036
Salinity	44,210 ppm
Gas density	0.9182 – 0.7243 kg/m^3
Oil density	853 – 930 kg/m^3
Water density	1033 kg/m^3
Rock compressibility (at P_i = 24.5 MPa)	0.000682 – 0.001060 MPa^{-1}
Residual oil saturation (S_{or})	0.2 – 0.15 fraction
Connate water saturation (S_{wi} or S_{wc})	0.13 – 0.19 fraction
Original gas-oil ratio (GOR)	630 – 390 scf/stb
Critical gas saturation*(S_{gc})	0.038 – 0.041 fraction
Residual gas saturation*(S_{gr})	0.24 – 0.15 fraction

*Table 6-1 Fluid reservoir properties and initial reservoir conditions used in the Heidrun field's simulation model. * indicates that the input applies only to the Tilje and Åre formation which make up the Båt Group reservoirs. Apart from pressure, where a range of values is provided, values closer to the first entry are more representative of the shallower Fangst Group reservoirs (Garn and Ile formation) and values closer to the last entry are more representative of the deeper Båt Group reservoirs.*

The 66 zones are distributed across the four reservoirs, Garn, Ile, Tilje and Åre Formations (Figure 6-4(b)). The non-reservoir parts make up the remaining zones which are inactive i.e. the Not shale (< 8 m thick) which lies in-between the Garn and Ile Fm., making the Fangst Group and the Ror shale (~60 m thick) which separates the Fangst Group from the Båt Group reservoirs, comprising of the Tilje and Åre Formations. These are all preserved when generating the multiple simulation models, as well as the cell thicknesses. The top reservoir is the focus for the inversion, and so, only simulation results of pressure and saturation changes from the Garn Fm. which covers zones 3 to 7 are used. Figure 6-5 shows the initial pressure and fluid saturation distribution in the Garn formation, over the study area. Higher initial pressure in the water leg where water injectors support the aquifer, and lower initial pressure in the hydrocarbon leg situated in the shallower areas, with an initial gas cap present before the start of production in 1995. The fluid properties and initial reservoir conditions are given in Table 6-1.

6.3.2 Heidrun field 4D seismic data quality

Repeated towed streamer monitor surveys between 2001 and 2011 have been acquired over the field, spaced around 2 to 3 years apart, since the 1986/1991 merged baseline survey. Full stack time-migrated seismic data are available for all monitor times, 2001, 2004, 2006, 2008 and 2011, and offset stacks (near, mid and far) are provided for the 2006, 2008 and 2011 surveys for this study. All monitor surveys boast identical single-source and six cable configuration, and were acquired using Q-marine technology for repeatable positioning, by WesternGeco. Monitor seismic data from 2006 onward were co-processed along with the baseline seismic data in 2010 using a revised processing workflow which improved the data quality. The 2011 survey was also processed using the revised 2010 processing flow (Fischer et al., 2013).

Figure 6-6 shows the calculated NRMS data repeatability in the study area for the near and far stacks of the 2006, 2008 and 2011 monitor data relative to the baseline seismic data. This was calculated using a window of 100 ms above and below a relatively flat non-producing reflector, located 350 ms above top reservoir and 1540 ms below the sea bed. Across the monitor datasets, the NRMS values range from 25% up to 70%, and are typically around 38% for the far offsets and 58% for the near offsets, which is rather

poor. For confidence in quantitative analysis, Behrens et al. (2002) suggest that the 4D signal-to-noise ratio (SNR or S/N) equal to 3 is a minimum. For the 4D seismic data from the Heidrun field, S/N is estimated to be between 1.3 and 4.8 (mean value of 2.3)

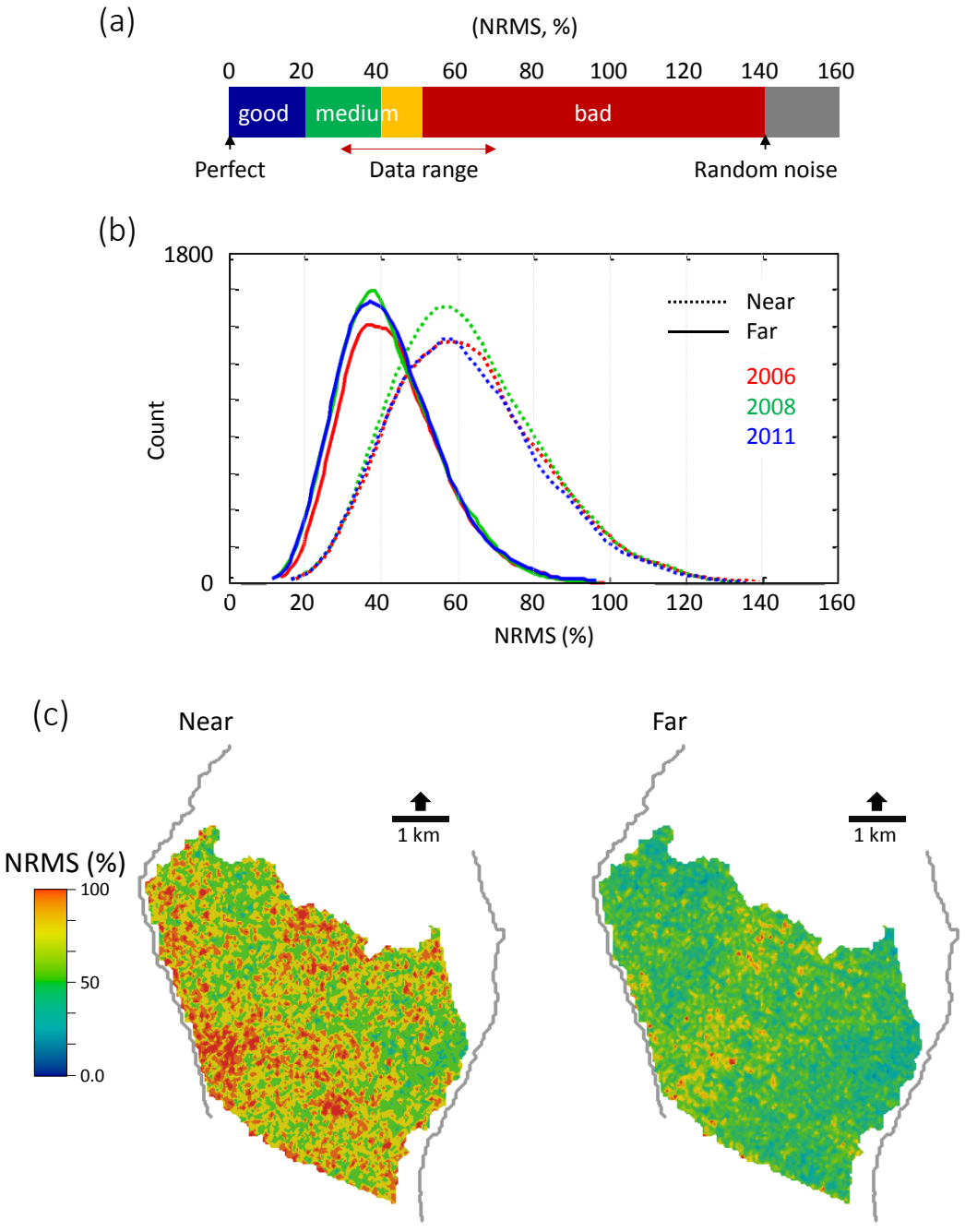

Figure 6-6 (a) NRMS chart indicating the 4D data repeatability range (30 % to 70%) for the offset stacked data shown in (b). In (b) the NRMS histograms across the 4D monitor times (2006, 2008 and 2011) for the near and far offset data from the Heidrun field. (c) A 2D map of the NRMS in the study area calculated for the 2011 monitor and baseline seismic data, showing high variations in the near offset (left) when compared to the far offsets (right). Data repeatability for both offsets are quite bad, and in (b) marginal improvements from 2006 to 2011 are observed.

for the near offset stacks, and for the far offset stacks, S/N is between 2.2 and 5.1 (mean value of 3.6). Such low signal-to-noise ratio (S/N) is a clear limitation for the inversion. The solution is thus to introduce engineering-consistent pressure and saturation limits through the use of multiple fluid-flow simulation models (see Appendix A-2 for definition of NRMS and noise-to-signal ratio (N/S), which is the inverse of S/N).

6.3.3 Heidrun field 4D seismic response and production history

As of 2011, 77 producers and 25 injectors have been drilled since the start of production in October 1995. This constitutes 17 producers and 8 water injectors perforated in the top reservoir in the study area (Figure 6-5). By the 2011 monitor time, only water injectors I4, I5 and 18 are active and producers P13, P12, and P17. Observations across the 16 years of production history for water cut and gas-oil ratio for the Fangst Group, suggests an early water break through, accompanied by gas cap expansion prior to the first monitor survey in 2001 (Figure 6-7). Subsequent monitor times imply further increase in water cut due to continuous water flooding, and some fluctuations in gas-oil ratio which attempts to settle to a value closer to the start of production, by 2011, indicating that some of the gas dissolves back into solution.

The 4D seismic response (monitor – baseline) at the 2011 monitor time, together with the fluid flow simulator output of pressure, water and gas saturation changes from the base model, validate the general understanding from the historical profiles (Figure 6-8). Water-flooding effects (hardening) can be observed, with a significant movement of the oil-water contact by the 2001 monitor time. Gas saturation increase effects (softening) are also very clear, from the original gas-oil contact. All of the five monitor surveys show consistent 4D signals related to gas saturation increase and water flood. Pressure increase effects in the water leg are not very clear due to mild pressure increases coupled with high non-repeatable noise which is an intrinsic issue within the interpretations. Overall, the 4D seismic response is characterised by very weak unclear pressure effects with strong saturation dominance. The simulated changes are mostly in agreement with the observations from 4D seismic data.

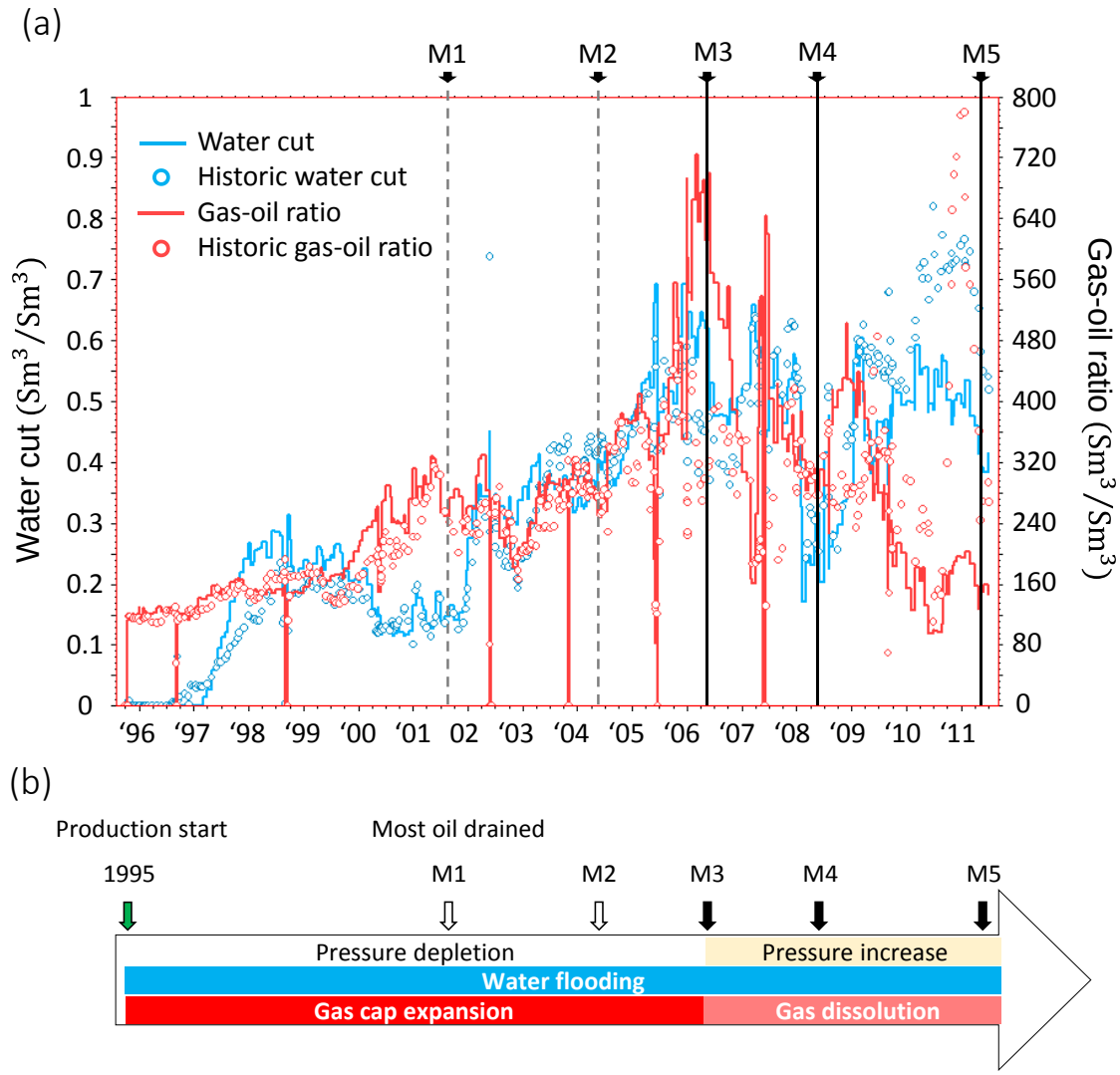

Figure 6-7 (a) Fluctuations in Water cut (left y-axis) and Gas-oil ratio (right y-axis) across 16 years of production from October 1995 (start) to 2011 for the Fangst Group. The predicted profiles from the base (original) simulation model tries to match the historical measurements. The times of the acquisition of the monitor surveys M1 to M5 are also shown. Offset stacks for the near, mid and far are only available for 2006, 2008 and 2011 seismic data.(b) A timeline of the different reservoir processes in the Fangst group across the five monitor surveys. Coloured coded areas within the arrow indicate the effects that are most interpretable in the observed 4D seismic data, relative to pre-production (i.e. baseline).

6.3.4 Generating multiple models for the Heidrun field

To generate multiple simulation models, a number of reservoir static properties from the base (original) model were selected that have the strongest influence on the reservoirs sensitivity coefficients C_P, $C_{S_w}$and C_{S_g}. Faults are the main feature in this field for recovery optimisation, as a better understanding of the connectivity between the various segments will aid strategic drainage of the reservoir. However, the faults themselves do not control the reservoir,s sensitivity to pressure and saturation effects, but determine

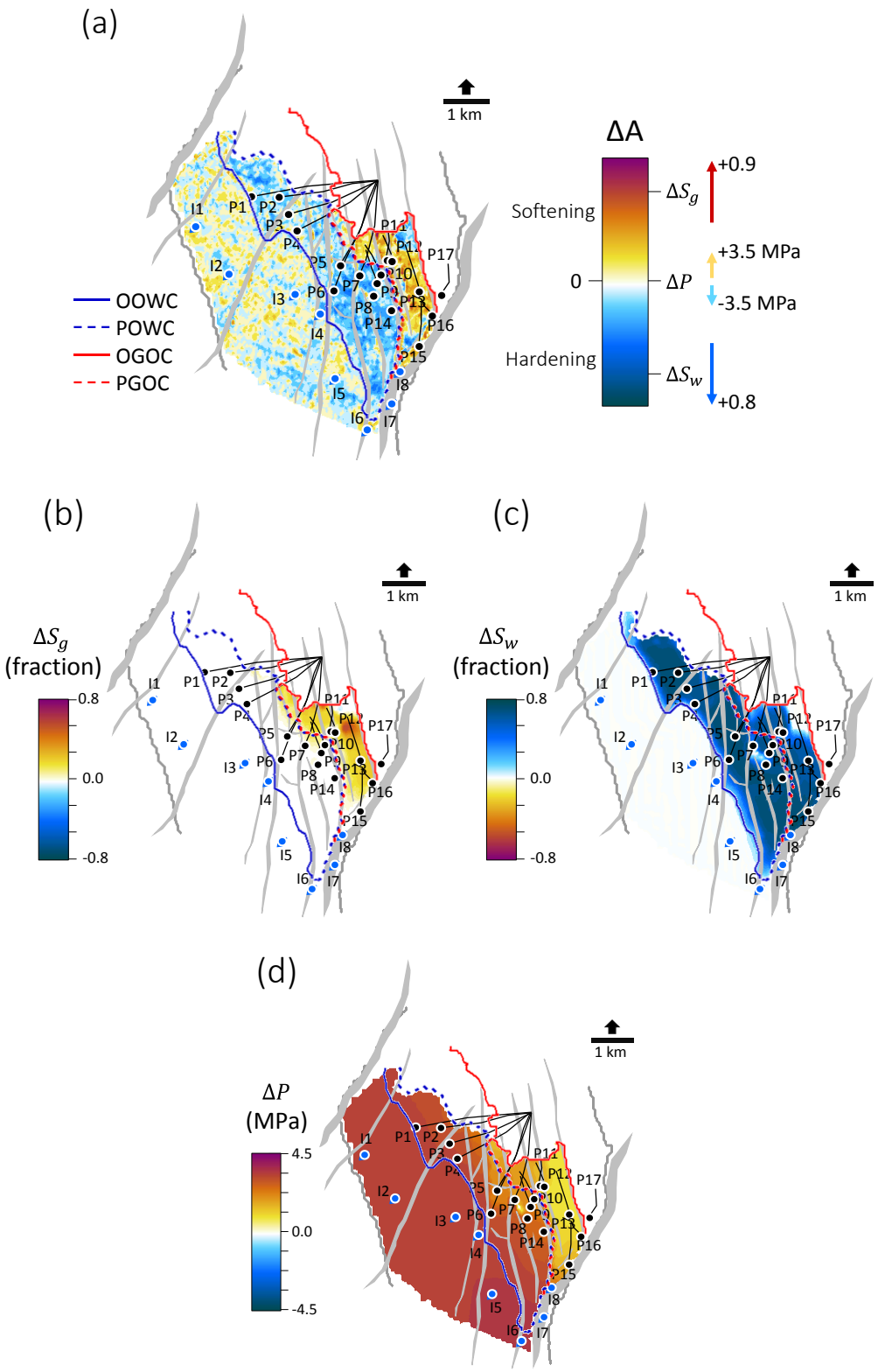

Figure 6-8 Top reservoir observed 4D seismic amplitude response, full-stack (monitor-baseline) shown for 2011-baseline monitor time. Interpretations have been made in the maps for the original oil water-contact (OOWC), original gas-oil contact (OGOC), post-production oil-water contact (POWC), and gas-oil contact (PGOC) as of the 2001 monitor time. The colour scale highlights the dominance of saturation changes over pressure changes. Depth-averaged maps for top reservoir for gas saturation, water saturation and pressure changes (2011-1995) from the base (starting) fluid flow simulation model are given in (b), (c) and (d) respectively. Note that the response is highly saturation driven. The softening signatures in the water leg (dominated by water injectors) are not due to the mild pressure change, but as a result of noise.

the pressure communication and fluid flow across the segments. Structural compartmentalisation affects the lateral and vertical extent of the dynamic changes represented by the 4D seismic signatures (Furre et al., 2006). The faults appear to define the extent of the water-flooding and gas cap changes (Figure 6-8). However, for this study, the fault transmissibility are kept as originally defined in the base model, assuming they are already well defined.

A comparison of the base model predictions to historic data shows that the base model is able to replicate the overall production, and the volumetrics are close to reality (Figure 6-7). In addition, predictions of pressure and saturation changes from this base simulation model correspond with the interpretations of the 4D seismic response (Figure 6-8). This gives confidence to the above assumption. The base reservoir model is therefore a good starting point for generating other models.
The uncertain static reservoir properties thus considered in this work on the Heidrun field, defined by global multipliers are as follows:

- Porosity and net-to-gross (NTG)
- Permeability X, Y and Z

For the base reservoir model of the Heidrun field, only porosity variations are defined and NTG is assigned a value of 1. This means that the model captures the fields NTG variability within its porosity distribution. So, a perturbation of the porosity, also accounts for NTG.

The implementation of the procedure in Figure 6-3 is detailed in Figure 6-9 which are of three main stages. Firstly, the perturbation of the base model to generate the model ensembles, followed by a validation of the generated models against historic data, and, then the evaluation of the limits from the validated models. The static properties from the base model are perturbed using global multipliers defined for each parameter as shown in Table 6-2, assuming a uniform distribution. This means that all models maintain similar static property distribution as the base model, in the sense that the models are a scaled version of the base model (Figure 6-10). In stage 1 (Figure 6-9), the models are generated using the Multiple Reservoir Optimizer (MEPO) platform. To create the model ensembles, MEPO gives the option of several Experimental Design

methods for sampling the initial parameter space (given in Table 6-2). These methods include: Plackett-Burman, Latin Hypercube Experimental Design (LHED) or Factorial Design (Schulze-Riegert and Ghedan, 2007; Zubarev, 2009). The method chosen is LHED which ensures that the entire multiplier distribution is represented and produces a set number of model simulations (for example, as presented in Tewari et al., 2014; Maschio et al., 2010).

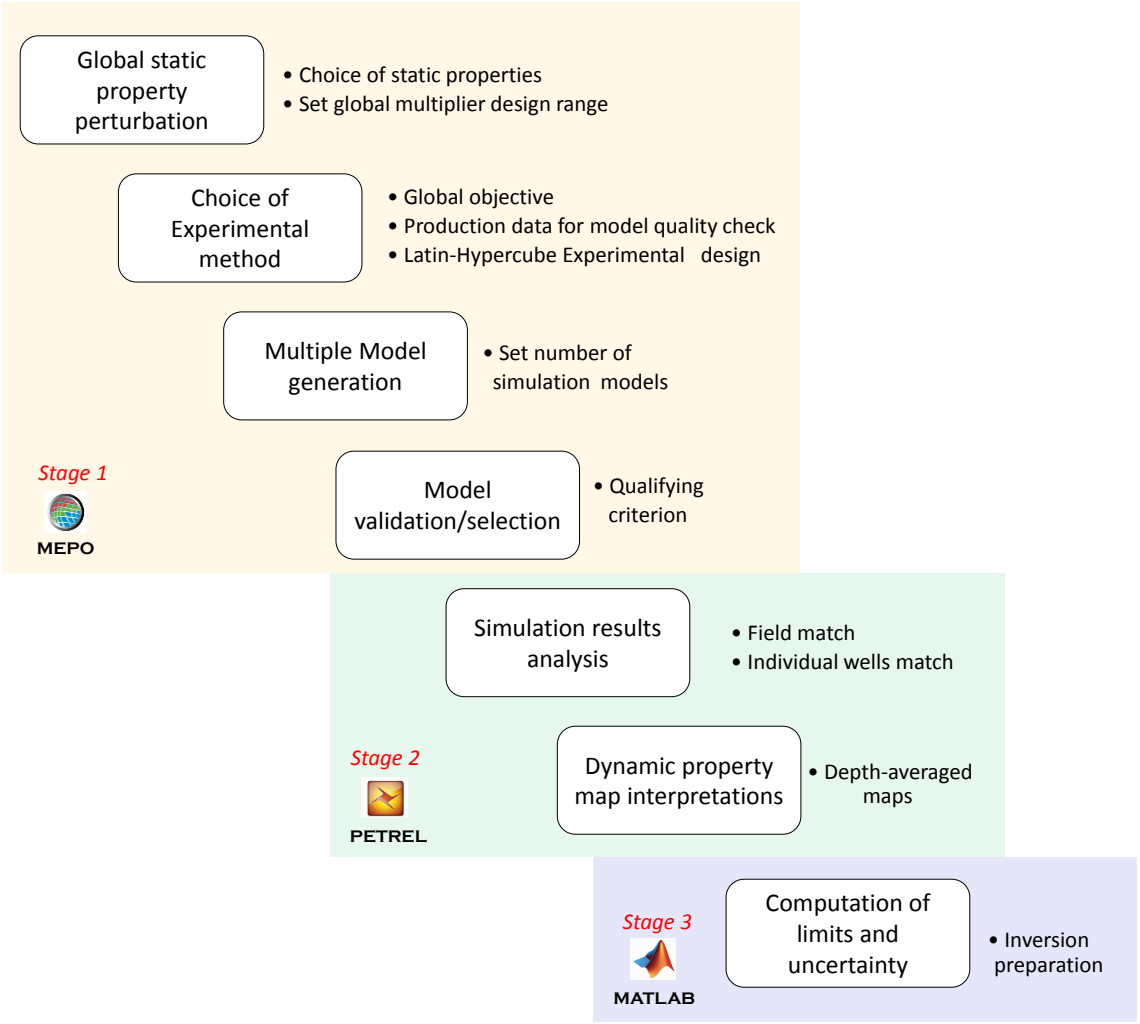

Figure 6-9 Workflow formed of three stages for generating the multiple simulation models on the Heidrun field and extracting limits of simulated pressure and saturation changes to be used in the inversion. Each stage uses a different software from the Multiple Reservoir Optimizer (MEPO) platform to MATLAB.

The LHED is a statistical method for generating a sample of plausible collections of parameter values from a multidimensional distribution, and it is useful for exploring the uncertainty range (Schulze-Riegert and Ghedan, 2007; Risso et al., 2011; Maschio and Schiozer, 2014). So, to generate "m" experimental models, LHED calculates cumulative

probability distributions for every input parameter in Table 6-2, and proposes "m" uniformly distributed points for each of them. Values of input parameters, corresponding to those points are then randomly combined to define models of the sample. The multiplier distribution for the input reservoir parameters does not have to be uniform or of the same type, as Figure 6-3 illustrates, but a uniform distribution is explored here, as Table 6-2 indicates. As multiple models have extensive coverage of the search spaces, LHED delivers robust results (Roggero et al., 2007). In addition, any value of an input parameter is found only once in all the models of the dataset.

In Table 6-2, the starting values of the properties are the initial values, which is the base model, while the ranges are selected generally based on engineering judgement, and such that the perturbed model remains physically and geologically meaningful and consistent with the initial understanding of the field (Figure 6-10)). For example, the porosity multiplier range is given stricter bounds compared to the permeability multipliers. This is chosen such that apart from ensuring that the reservoirs cells are not de-activated due to unfeasible pore volume at the lower limit, porosity values at the upper limit should also lie below the critical porosity in sandstones, which is 40% (Nur et al., 1998). As porosity is the key parameter which has a high influence on the 4D seismic response, it was important to do a sensitivity test by perturbing porosity alone using the LHED method. This also allowed for a clear definition of the multiplier range chosen (as in Table 6-2), guided by well log information, but mostly by a reasonable match to historic data. The upper limit of the permeability multipliers is around 1.5 times their initial value, which is high but explores such possibilities, while the lower limit is 0.45.

Apart from the design parameters (Table 6-2) and historic production data for all wells, input to the MEPO platform is the ECLIPSE .DATA file of the base simulation model. The .DATA file includes the following: model unit (unit is METRIC), production start date, model dimensions, grid geometry (3D), permeability (X, Y, Z) and porosity (as grid properties), fault properties (position of faults through cells on the 3D grid and fault connectivity defined by transmissibility values), PVT properties of reservoir fluids (including: oil API, relative permeability curves, critical water saturation, variation of solution-gas oil ratio with depth, variation of solution-gas oil ratio/oil formation volume factor/ oil viscosity with pressure, variation of gas formation volume factor/ gas

Static Properties	Lower Limit	Start Value	Step increment	Upper Limit
Global Porosity Multiplier	0.85	1	0.05	1.25
Global Permeability X Multiplier	0.45	1	0.10	1.55
Global Permeability Y Multiplier	0.45	1	0.10	1.55
Global Permeability Z Multiplier	0.45	1	0.10	1.55

Table 6-2 Model parametrisation using global property multipliers which are perturbed over the entire reservoir. The starting point is the base (original) reservoir model from which other models are generated.

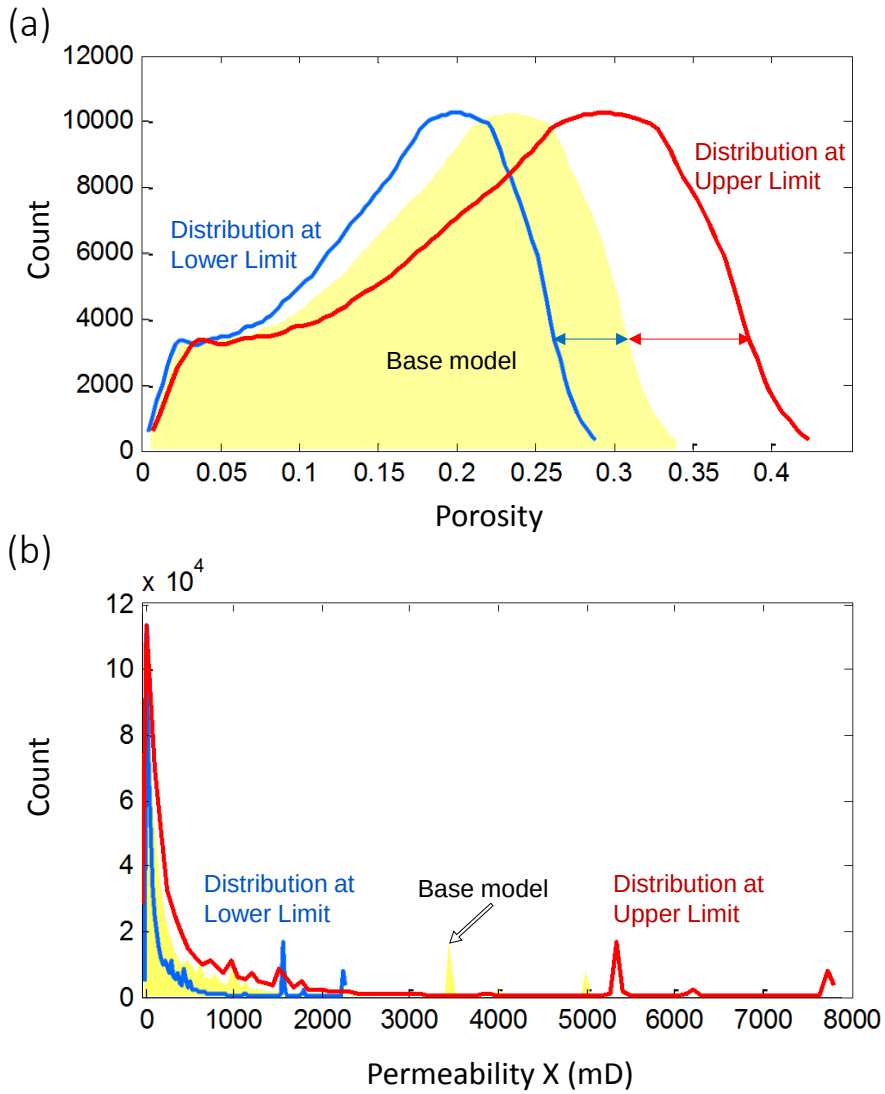

Figure 6-10 Distribution bounds for reservoir static properties shown for (a) Porosity (b) Permeability X, for the generation of multiple models using global multipliers as in Table 6-2. Histogram for the Base (original) model is in yellow.

viscosity with pressure, fluid density and fluid compressibility), rock compressibility, aquifer properties, equilibrium conditions, fluid contacts, tracer information, and well information recorded to date (well locations, well trajectory, well completions, well schedule history and injection/production rates). The base model ECLIPSE .DATA file is modified to include a .MINC file which contains the multiplier keywords for the design parameters (Table 6-2), ready for MEPO using the ECLIPSE 100 black oil simulator.

For computing the global objective value, $\mathbf{OF}_{\boldsymbol{model}}$ in Equation 6-11, the production data used are field gas-oil-ratio (FGOR) and field water-cut (FWCT) which are first order parameters for assessing the match to historic data, in addition to the overall material balance (Dake, 1997). Both are given equal weights with $\boldsymbol{w_d} = 1$. Using the Latin-Hypercube Experimental Design method, all four static parameters: porosity and permeability X, Y and Z, were perturbed using global multipliers (Table 6-2) and simulations run. This generated a set number of 200 simulation models, out of which 95 models satisfied the criterion in Equation 6-12, removing poor fit models. Results for the global objective and partial objective value (Equation 6-11), and the qualifying criterion value (Equation 6-12) for the 95 models are tabulated in Appendix D.

For stage 2 in Figure 6-9, the simulation results from the 95 models are imported into Petrel E&P software platform and depth-averaged maps of pressure, water and gas saturation changes for each model and across the five monitor times are computed. Stage 3 is completed by exporting the depth-averaged maps of simulated pressure and saturation changes across all monitors and for all 95 models into MATLAB. The minimum and maximum values are then extracted across these models, which will be used as spatially varying constraints to the multi-offset inversion. Likewise, inputs to the multi-monitor inversion are the pressure and saturation changes from each model, which are used in turn (Figure 6-2).

Figure 6-11 shows the simulated profiles for water cut (WCT) and gas-oil ratio (GOR) for the accepted 95 models, compared with that of the base model. The models show a similar trend and some models match history data better or worse than the base model. However, mismatches are still observed, especially towards the end of history in 2011,

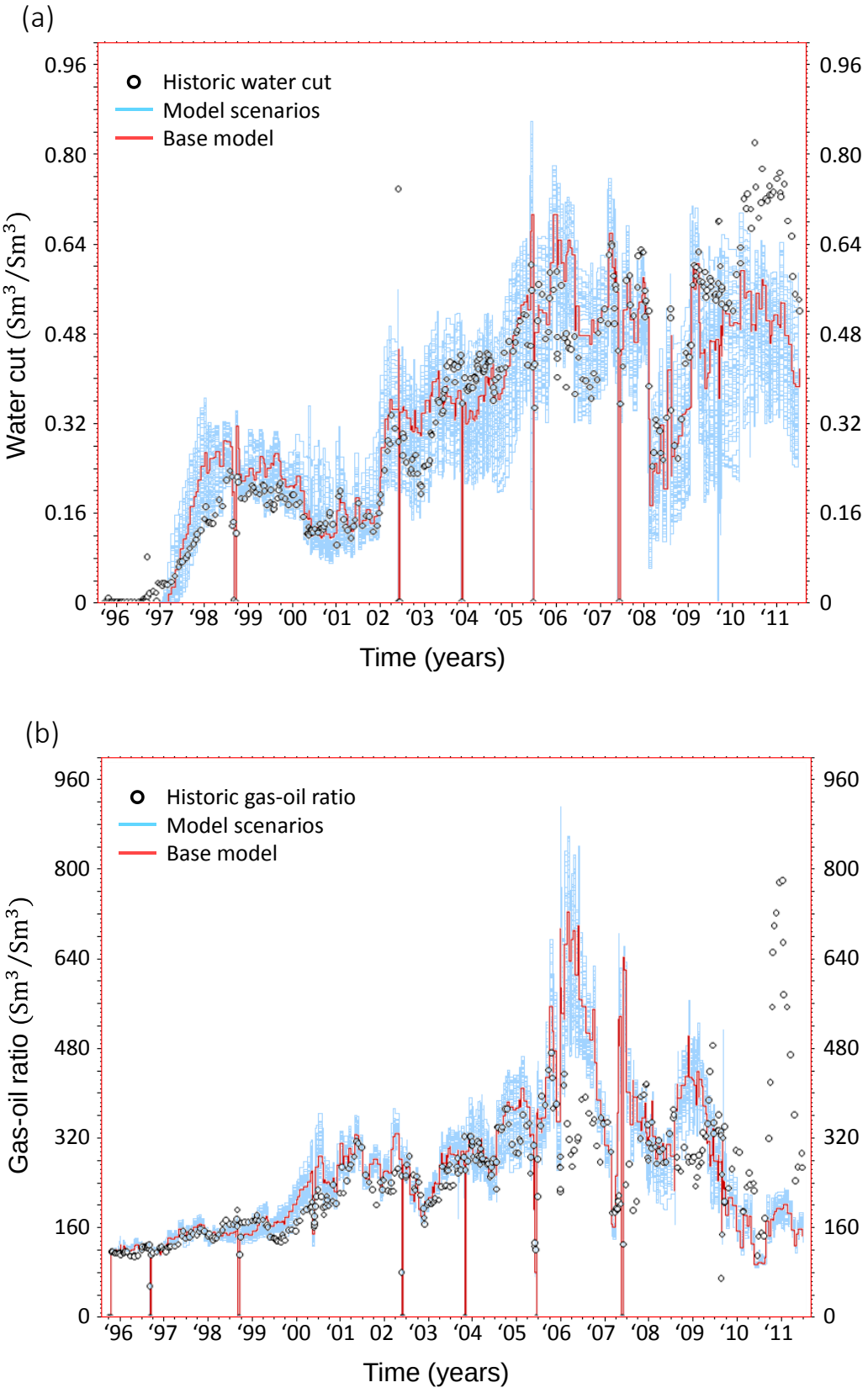

Figure 6-11 (a) Field water cut, FWCT (b) Field gas-oil ratio, FGOR, predicted from the restricted 95 model scenarios compared against history data, and the base model for the Fangst Group. The predicted models portray a similar trend as the historic data, also on the basis that the models were generated using global multipliers. Some models are closer to history than the base (original) model.

and particularly for GOR. In Figure 6-12, the corresponding partial objective function value as shown in Equation 6-11 are computed for each generated model including the base model, using the field water-cut and field gas-oil ratio data. It can be observed that most of the models match water-cut (Figure 6-12(a)) quite well, but strong mismatches occur for gas-oil ratio (Figure 6-12(a)). Likewise, some models match the historic data better than the base model. Apart from the base model (highlighted in red), a selected reference model (highlighted in green) is shown, for purposes to be discussed in section 6.3.5. The reference model (model number 23) matches GOR far better than the base model (model number 1), and for water-cut it is also better, although only slightly.

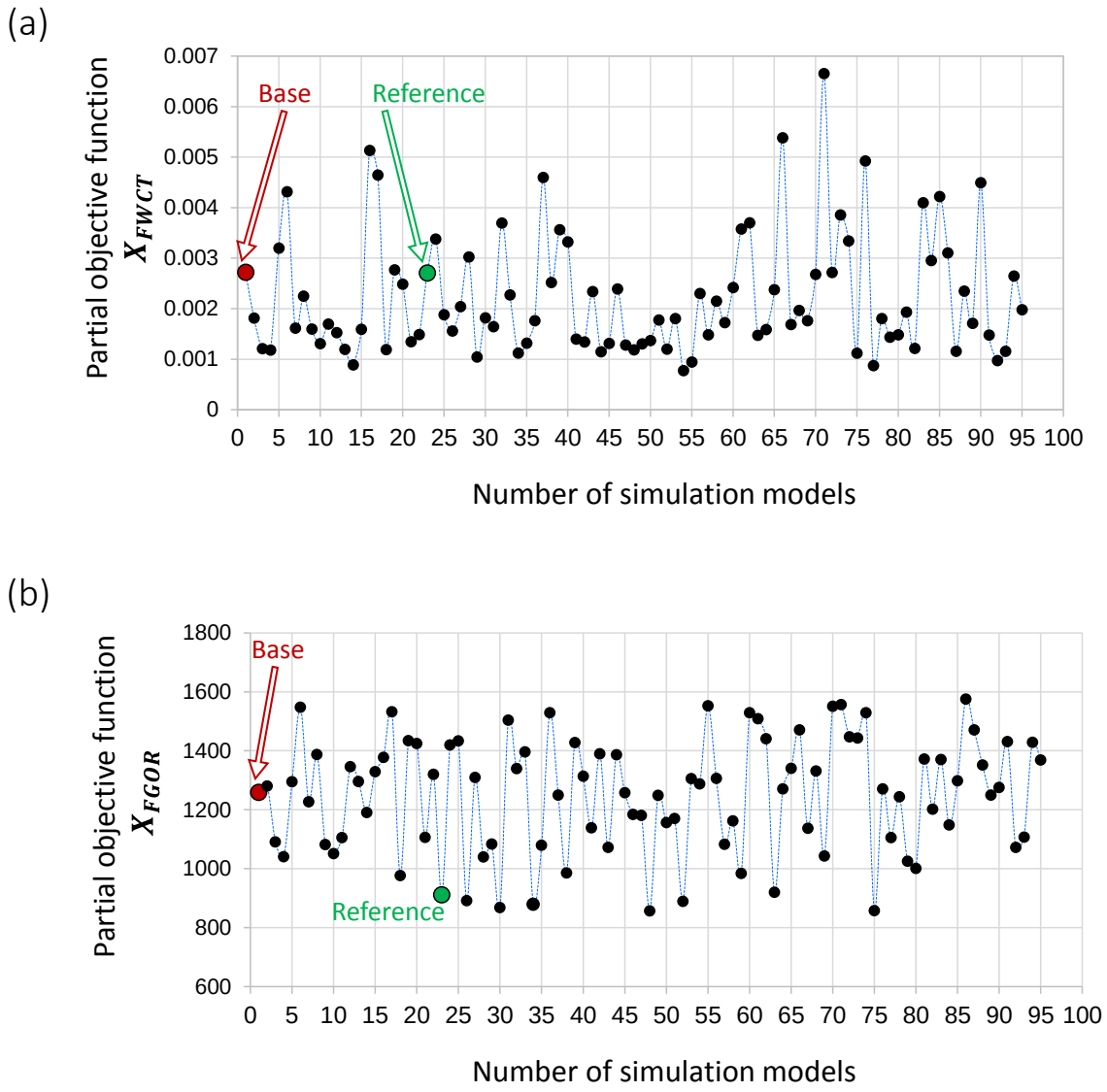

Figure 6-12 Quantification of match to historic data based on the partial objective function value, $\boldsymbol{X_d}$ (see Equation 6-11) computed for all generated models including the base simulation model, using (a) the field water-cut objective, X_{FWCT} and (b) the field gas-oil ratio objective, X_{FGOR}. The reference and base model are highlighted in red and green respectively.

The mismatches observed, particularly for GOR places a strong emphasis on the need for assigning an appropriate static model for better dynamic model predictions. This will thus involve defining more uncertain static properties, and performing not just a global perturbation (as is this case here) but also a local perturbation. Some of these include fault transmissibility multipliers, pore volume multipliers, endpoints of relative permeability curves etc. (Obidegwu, 2016), which will be a good extension of this study. For the Heidrun field, it is expected that a perturbation of the fault transmissibility will produce the biggest effect to match to the historical data. However, since the approach in this study does not update the reservoir static properties, the procedure to directly update the models will best be implemented via a joint history matching process using production data and 4D seismic data (for example, Fursov, 2015; Obidegwu, 2016; Yin, 2016).

6.3.5 Reference and base (original) model

A reference model is chosen for a synthetic application of the proposed inversion scheme, which is performed in Chapter 7. Going back to the inversion scheme (Figure 6-2), the observed seismic data from the seismic domain is now provided by this particular reference model. The reference model is kept aside and it is not among the generated models used to provide simulated pressure and saturation inputs to the multi-monitor inversion or pressure and saturation constraints to the multi-offset inversion. Note that the base model is also amongst the models used for the purposes above. In total, 95 models are used to perform step 1 and step 2 of the inversion scheme (Figure 6-2).

In this section I give details concerning the static and dynamic properties of the reference model from which synthetic seismic data are to be modelled. One of the 95 models that matches historic data 13% better than the base (original) model is chosen as a reference model (Figure 6-13). Other models can also be chosen as a reference model, as some models also match both water-cut and gas-oil ratio better than the chosen reference. However, for the purpose of the inversion scheme (Figure 6-2), the idea is not to choose a reference model based solely on the best match to historic data. Note that the reference model is chosen because the inversion scheme will be applied on synthetic 4D seismic data modelled from this reference model, in Chapter 7. If the inversion

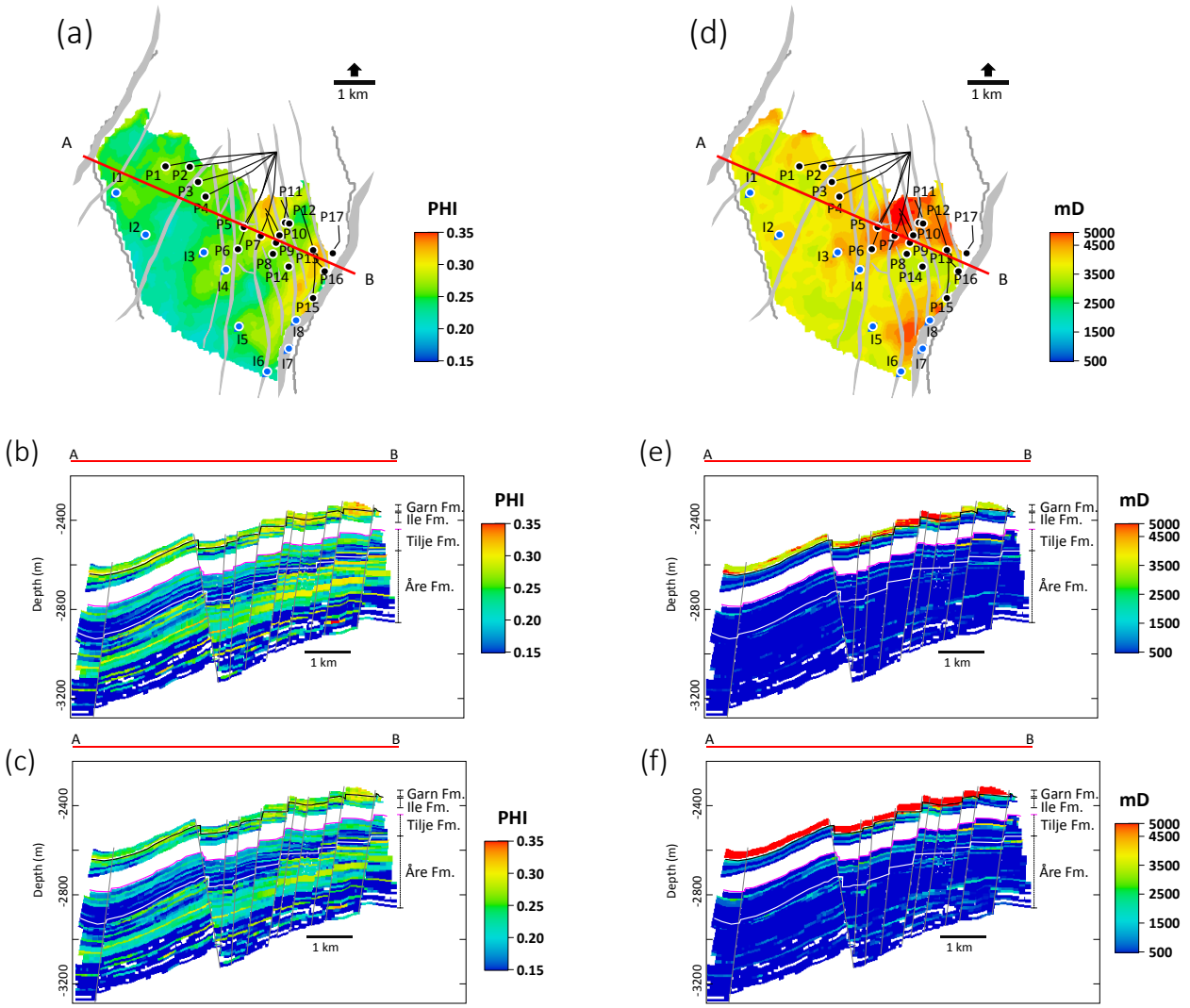

Figure 6-13 Reference and base model static properties. Depth-averaged maps of the base model for the Garn. Fm. are shown for (a) Porosity, PHI (d) Permeability along the X direction in mD. Cross-section view along line A-B for porosity are shown in (b) for the base model and (c) for the reference model. Section view for Permeability X are shown in (e) for the base model and ((f) for the reference model

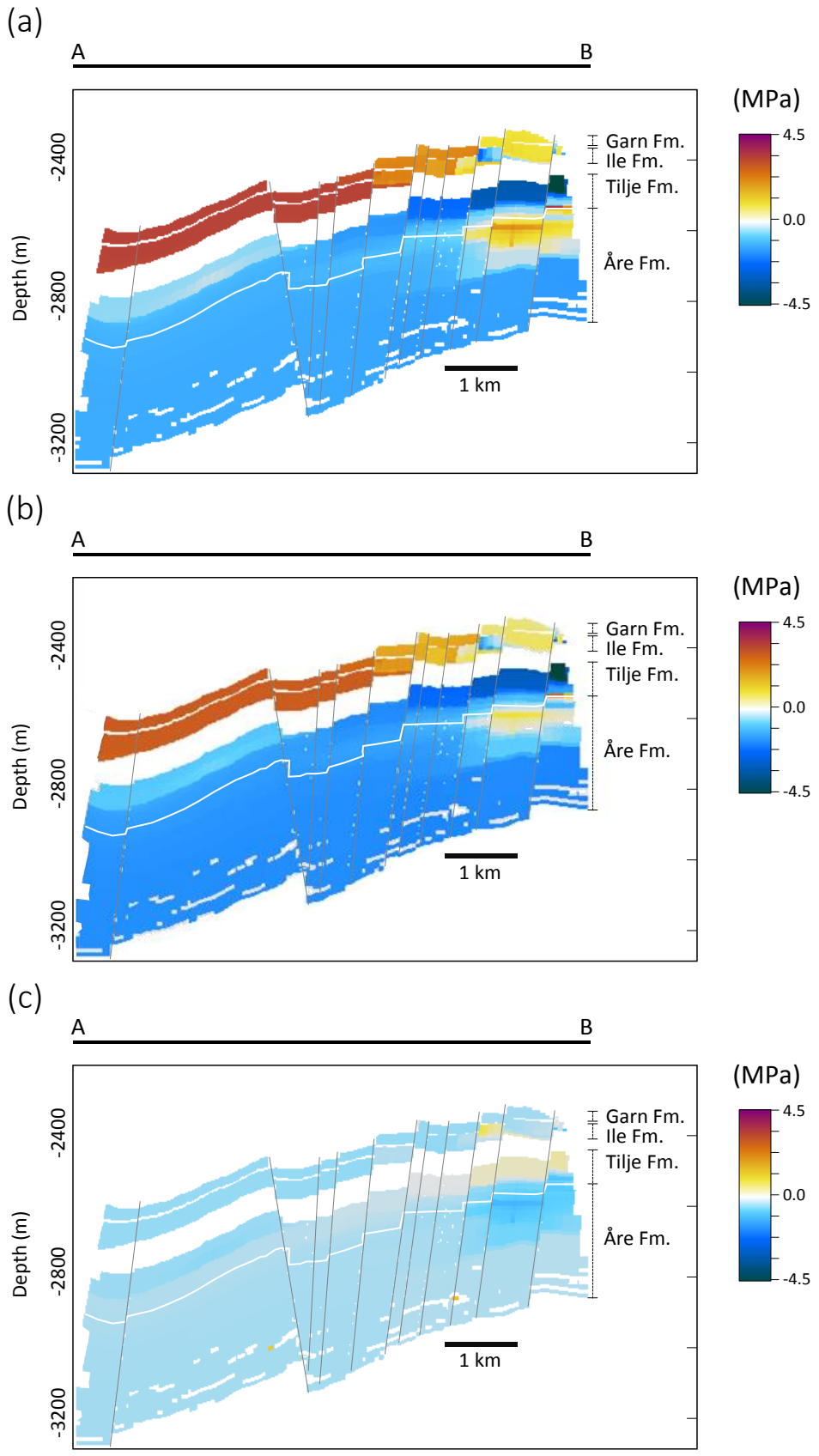

Figure 6-14 Prediction of pressure changes (2011-baseline) shown for (a) the base simulation model (b) the reference simulation model and (c) the difference in the simulated pressure change between both models, obtained by taking (b)-(a).

scheme was to be applied on the acquired observed 4D seismic dataset for the Heidrun field, there is no need to isolate a reference model. This chosen reference model is considered to be the true solution which is unknown (as is the case with observed 4D seismic data), and the inversion scheme would try to find other models that best match the reference model, in terms of the inverted sensitivity coefficients (see section 7.3.1) and in the final estimate of the inverted pressure and saturation changes (see section 7.3.2).

The reference and base model differ in terms of the four uncertain properties previously used to obtain the models (Table 6-2). In Figure 6-13, the porosity and permeability variations of the base and reference model are shown. The difference between the reference and the base model is further resolved by the simulated predictions for pressure (Figure 6-14), water (Figure 6-15) and gas (Figure 6-16) saturation changes, shown here for the 2011 – baseline monitor time. Both models show a similar scale of pressure changes, but because the reference model has a higher permeability than the base model, the magnitude of its pressure change is smaller, by up to 3.5 MPa. For water saturation changes, the major differences between the reference and base model occur in the top reservoir (Garn Fm.), with discrepancies in water saturation change of up to 40%. For gas saturation changes, the discrepancies are only very subtle, since vertical permeability between the reference and base model are the same, and the fault transmissibilities have been kept fixed across all the models. As a result, this is to be expected since very little dispersion in the simulated GOR across the qualified models is observed (Figure 6-11(b)), whereas for the outcome of water–cut, a wider dispersion is observed (Figure 6-11(a)).

6.4 Summary

This chapter introduces an engineering constrained map-based linear inversion scheme for the estimation of pressure, water and gas saturation changes from 4D seismic data. The estimation is a two-step inversion procedure, the first which is an innovative aspect of the scheme, is a multi-monitor inversion. This combines multiple monitor 4D seismic data to invert for offset-dependent spatially-varying sensitivity coefficients which relate the 4D seismic response to pressure and saturation changes. The second step is a multi-offset inversion which uses 4D seismic AVO data (partial-offset stacks of near, mid and

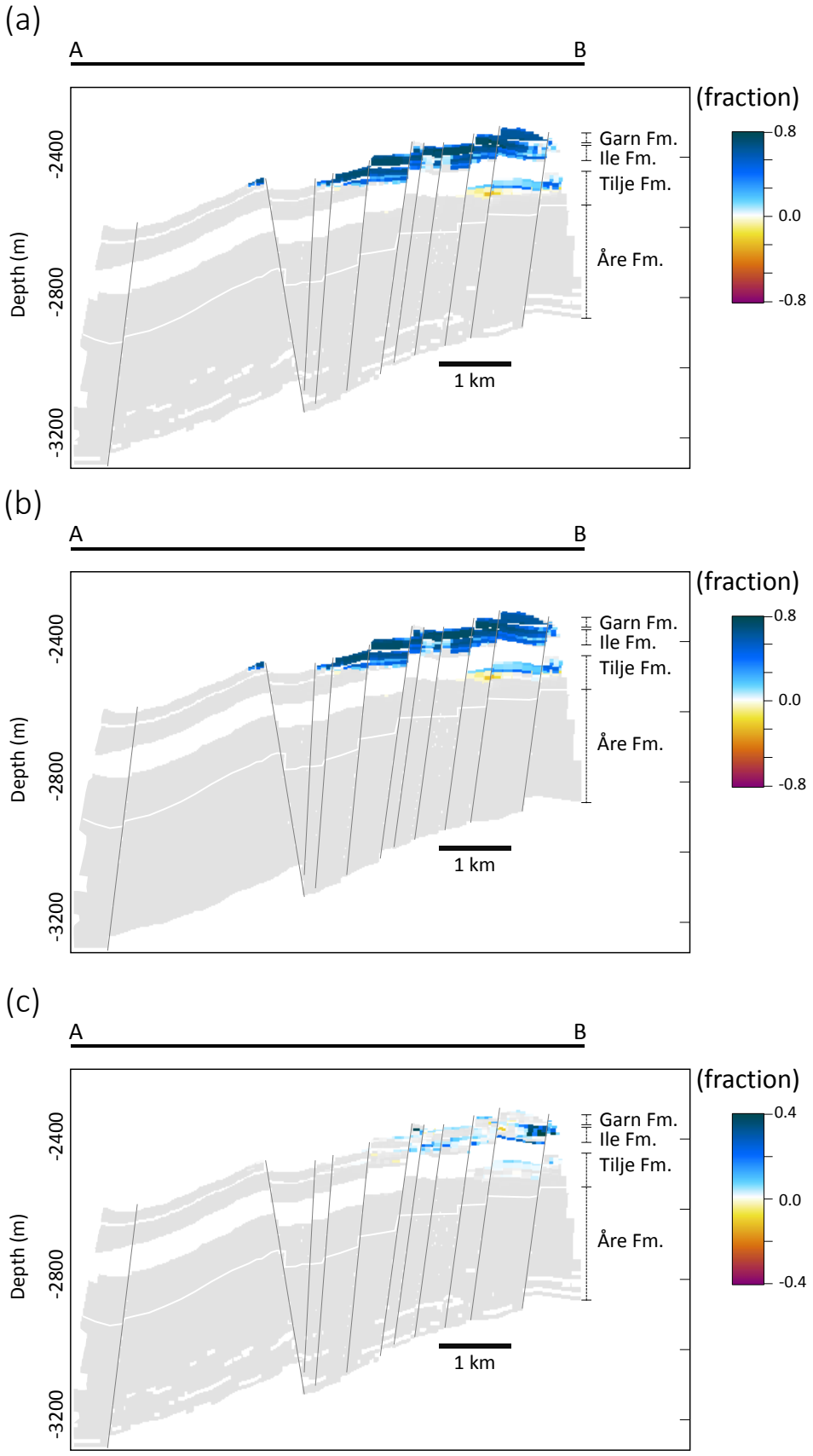

Figure 6-15 Prediction of water saturation changes (2011-baseline) shown for (a) the base simulation model (b) the reference simulation model and (c) the difference between both models obtained by taking (b)-(a).

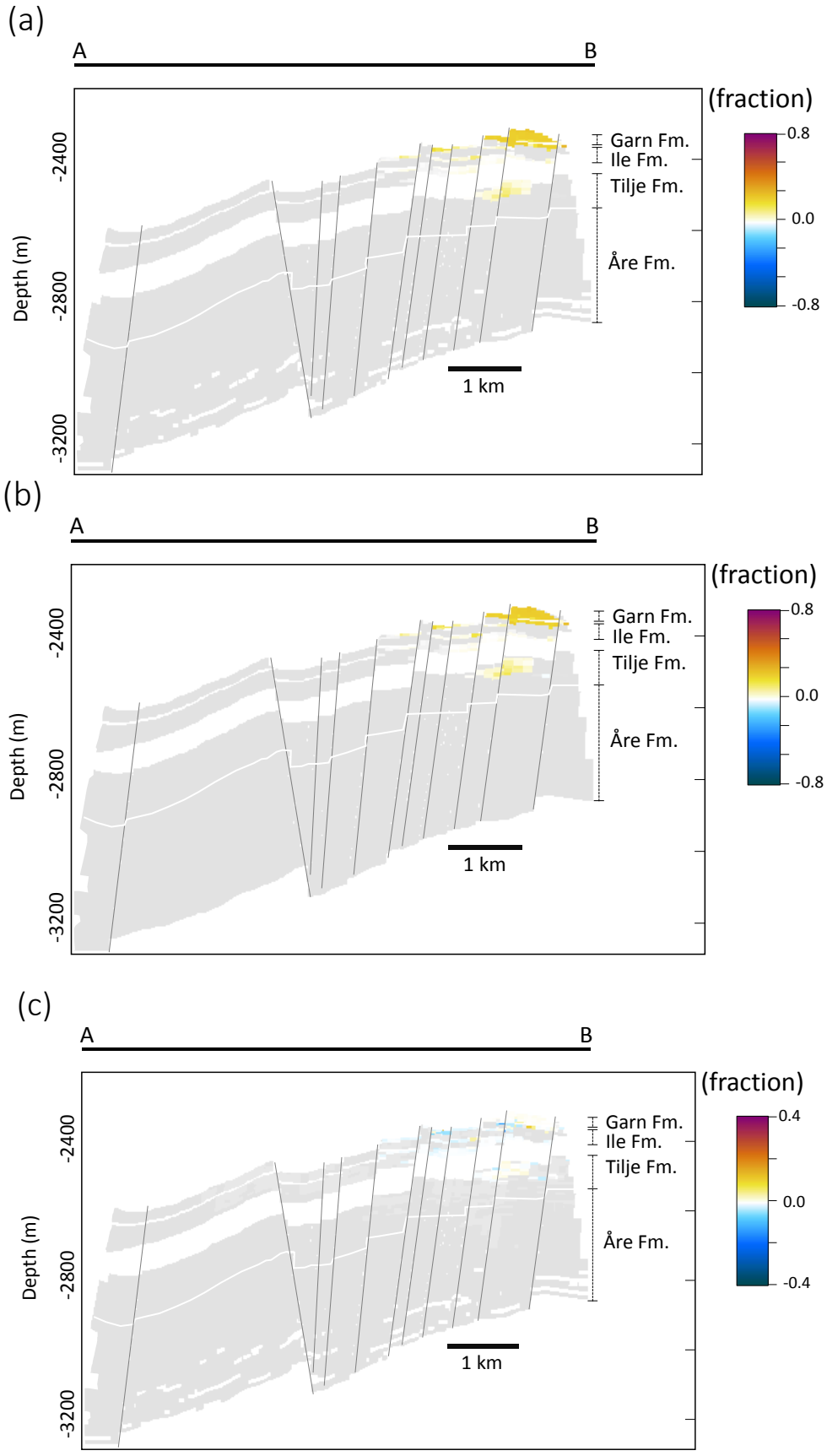

Figure 6-16 Prediction of Gas saturation changes (2011-baseline) shown for (a) the base simulation model (b) the reference simulation model and (c) the difference between both models obtained by taking (b)-(a).

far offsets) for a specific monitor time, combined with the estimate sensitivity coefficients, to invert for pressure and saturation changes at the same monitor time. Utilizing the information preserved across multiple monitor seismic data bypasses the need for rock-physics modelling, as the reservoir's sensitivity can be obtained directly via the inversion data calibration. The engineering constraints are obtained from multiple history-matched fluid-flow simulation models.

The first part of the inversion scheme which concerns the generation of the multiple models is described and applied to the Heidrun field reservoir model. This uses global multipliers to perturb static properties, such as porosity (and NTG), vertical and horizontal permeability from the geologically-consistent base (original) model. A set number of 200 simulation models were generated, out of which 95 models matched historic data to within a qualifying criterion. Using historic data to qualify the models reduced the dispersion across the models, a complement to the proposed inversion scheme. Across the monitor times, some of the models matched historic data better than the base model, but the models, however, fail to match historical data adequately in the last few months of the 16 year production history for the Heidrun field. This emphasises the need for assigning an appropriate static model for better dynamic forecast. An extension of this study will involve defining more uncertain static properties such as fault transmissibility multipliers, particularly for the Heidrun field. However, since the approach in this study does not update the reservoir static properties, model updates can be implemented via a joint history-matching process using well production data and 4D seismic data.

The next stage is to implement the inversion scheme by performing the multi-monitor and multi-offset inversion, incorporating the pressure and saturation changes from the qualified multiple simulation models. A synthetic application on the Heidrun field will be carried out using modelled 4D seismic data based on the reference model introduced in this chapter. This will be done in the next chapter.

Chapter 7

Application of the engineering-constrained inversion for the quantification of pressure and saturation changes on the Heidrun Field

In this chapter the inversion scheme earlier described in Chapter 6 is implemented on synthetic data (which includes offset amplitude stacks for each 4D monitor time), modelled with 4D seismic noise estimated from the observed 4D seismic data. Firstly, a preliminary assessment of the multi-monitor inversion which estimates the reservoirs sensitivity to the dynamic changes, and the multi-offset inversion which finally estimates the dynamic reservoir changes, fulfilled several objectives. These included assessing the influence of additional 4D monitor data in the multi-monitor inversion, assessing the effectiveness of spatially-varying or uniform solution constraints in the presence of strong 4D noise, and comparing the reliability of the conventional assumption of uniform reservoir sensitivity versus spatially-varying sensitivity derived from the multi-monitor inversion. Secondly, the inversion scheme is fully implemented and uncertainties for the inverted sensitivity coefficients, as well as for the inverted pressure and saturation changes are estimated and discussed. The added benefit of the multi-monitor inversion is that it allows for a soft "close-the-loop" between the engineering and the 4D seismic domain, as it is one way (but less direct way) to assess the best model from the generated multiple simulation models, besides the use of a history-matching objective.

7.1 Input data preparation for synthetic data application on Heidrun Field

7.1.1 Synthetic seismic modelling and 4D noise estimation

The observed 4D seismic data for the Heidrun field are extremely noisy across the offset stacks (Figure 6-6), with high data non-repeatability variations, corresponding to 4D signal-to-noise ratios less than 3 in most areas. Such data are not recommended for quantitative interpretation (Behrens et al. 2002). It was therefore decided that the inversion scheme (Figure 6-2) be demonstrated on a realistic synthetic dataset based on Heidrun field's properties. Having already generated the multiple simulation models in section 6.3.4, a reference model from one of the qualified 95 models, which matches historic data 13% better than the base model (Figure 6-12) is chosen to represent the observed 4D seismic response after seismic modelling. The difference between the reference and base (i.e. original) model and the reasons behind choosing a reference model are discussed in section 6.3.5. The simulated pressure and saturation at pre-production (i.e. baseline) and across the five monitor times (2001, 2004, 2006, 2008 and 2011) from the base and reference models are converted to amplitudes using the ETLP Reservoir Geophysics group's in-house Simulation to Seismic (Sim2Seis) code (Amini, 2014). This converts simulation model data (static and dynamic properties) into

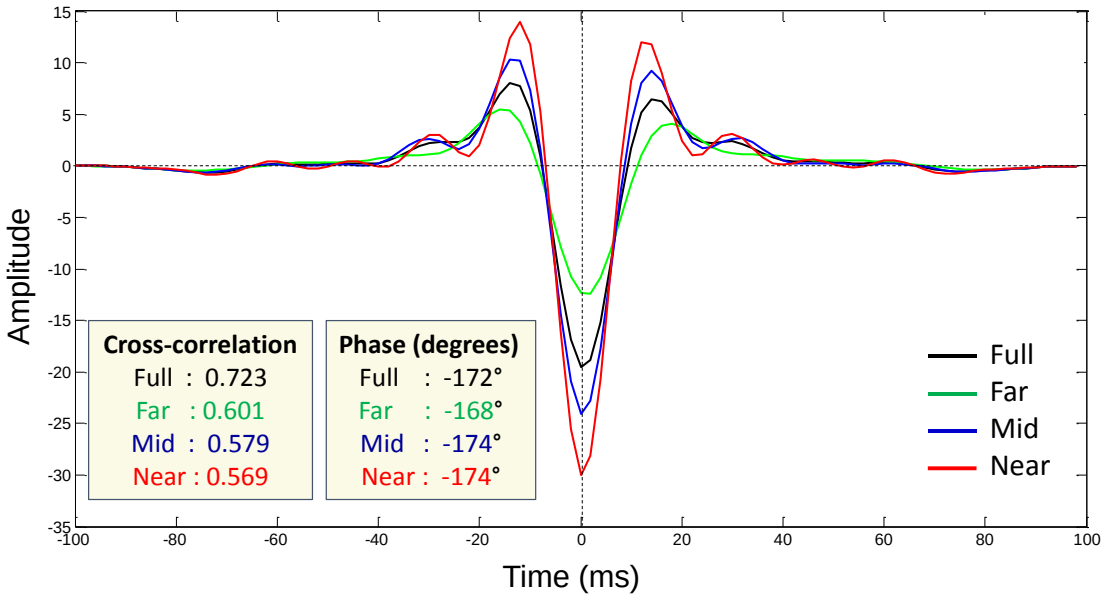

Figure 7-1 Offset-dependent wavelets used for synthetic seismic convolution modelling on the Heidrun Field. The wavelets were extracted from the observed baseline seismic data for the near, mid, far and full offset stacks through a seismic-to-well tie procedure,. Details of the wavelet phase are also provided in the inserted box. The seismic-to-well tie quality is also given by the cross-correlation value for each offset stack. The wavelets have a typical North Sea reverse polarity with a dominant frequency around 26 Hz.

impedances (via petro-elastic modelling), and then into synthetic seismic volumes (via 1D convolution). The wavelets (Figure 7-1) for performing the 1D convolution are extracted individually from the real field observed baseline seismic volumes of the near, mid, far and full offset stacks through a seismic-to-well tie procedure (Simm and Bacon, 2014). The quality of the seismic-to-well tie is given by the cross-correlation value ('1' implies a perfect tie, and '0' implies no correlation). The well-tie quality decreases as data quality decreases from full stack, followed by the far stack, and then the near stack which is the noisiest data. The simulator-to-seismic modelling outputs a synthetic seismic database, with 4D amplitudes for each monitor time (2001, 2004, 2006, 2008 and 2011) and for the near (0° to 14°), mid (14° to 28°), far (26° to 40°) and full (0° to 40°) angle stacks, which is the same angle range as in the observed seismic data.

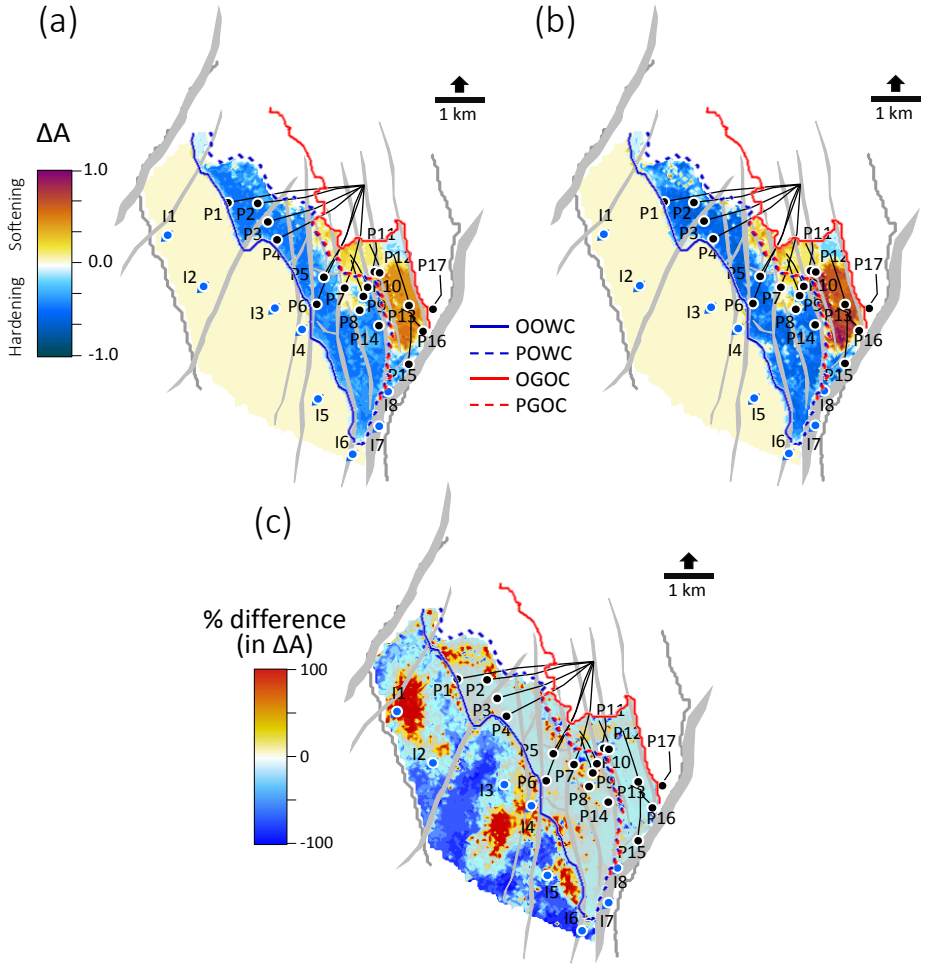

Figure 7-2 Noise-free full-stack synthetic 4D seismic amplitude response for the top reservoir, for the 4D year 2006-baseline, shown for (a) the reference model (b) the base model. The percentage difference in (a) relative to (b) is given in (c), calculated as, $\left(100\frac{(a)-(b)}{(b)}\right)$*. Producers are in black and water injectors in blue. Interpretations have been made in the maps for the original oil water-contact (OOWC), original gas-oil contact (OGOC), post-production oil-water contact (POWC), and gas-oil contact (PGOC) as of the 2001 monitor time. The softening response to pore pressure increase in the water leg (perforated by injectors) appears the same in (a) and (b), but the difference in (c) emphasises their dissimilarities.*

Figure 7-2 compares the synthetic 4D RMS amplitude response computed along top reservoir after implementing Sim2Seis separately for the base simulation model and the reference simulation model. In Figure 7-2(c) the disparity in the static reservoir properties between the reference and base model (Figure 6-12) is captured in the modelled 4D seismic responses with stronger differences in the water leg where only pressure increases occur. Changes in the gas leg are also weaker in Figure 7-2(a) compared to Figure 7-2(b).

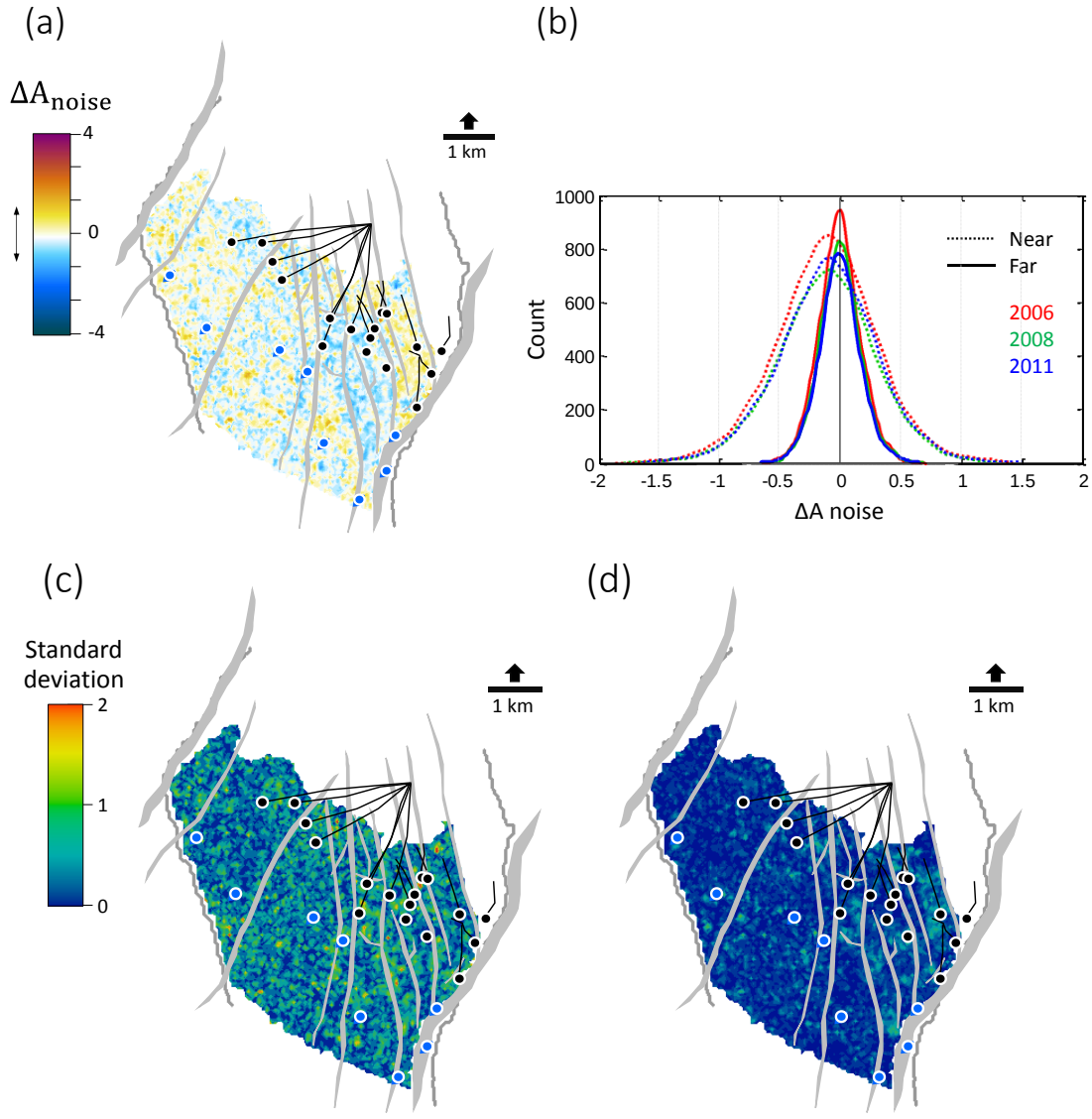

Figure 7-3 (a) The estimated 4D noise in amplitudes for Near offset stack (2006-base) at the reservoir level using observed 4D seismic amplitude response computed at top reservoir and NRMS maps computed in the overburden (see also Appendix A.2 for equations) (b) Histograms of the 4D noise at the near and far offsets for different monitor data, with mean value close to zero. 15% of this noise is added to the synthetic 4D amplitude maps. In absolute terms, the estimated 4D noise is the data uncertainty shown in (c) for the near offsets and in (d) for the far offsets, for the 2006-base amplitude response at top reservoir in the observed seismic data (Figure 7-4 (d) to (f)).

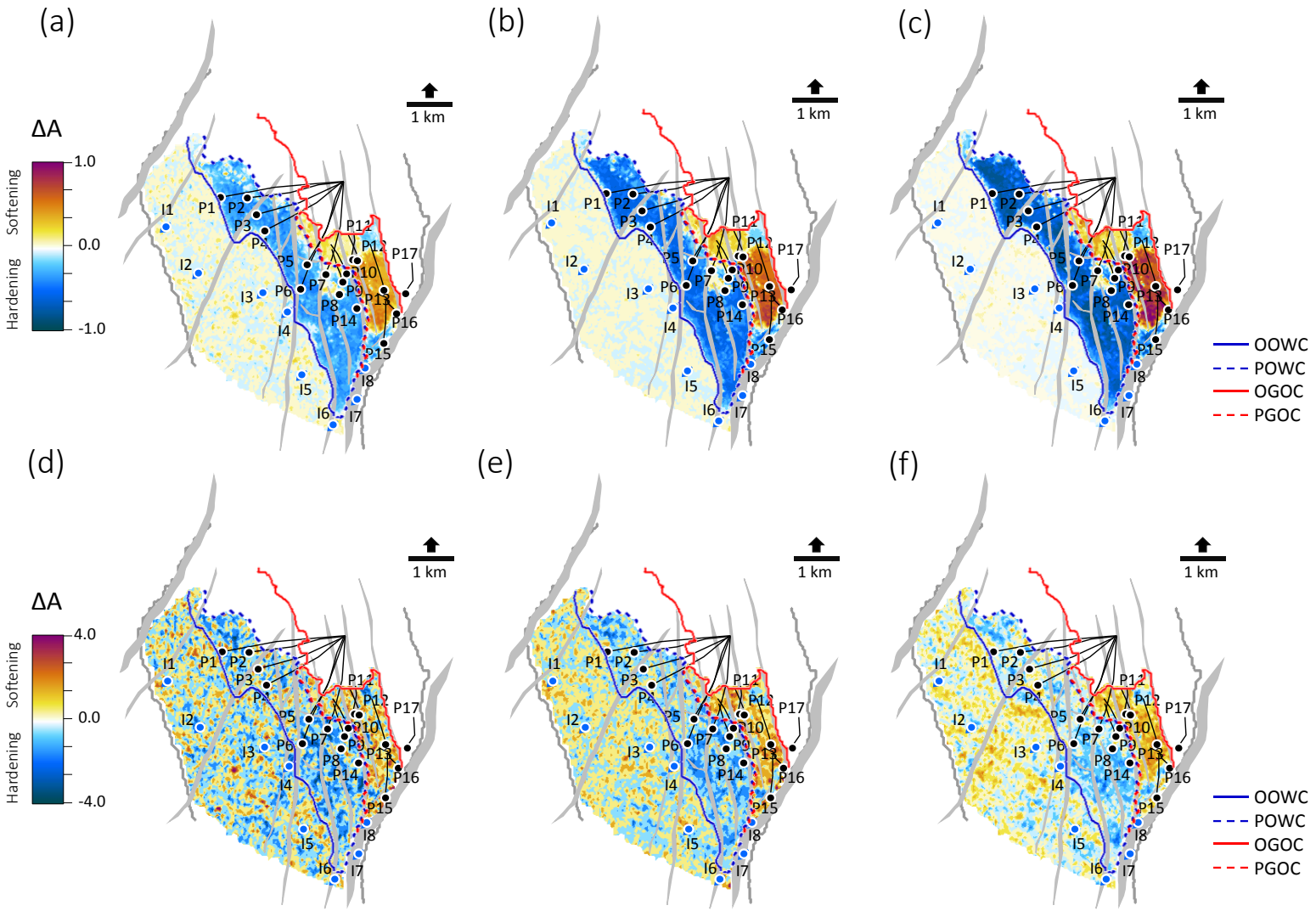

Figure 7-4 Top reservoir 4D amplitude response for 2006-baseline shown for the synthetic data from the reference model with noise added (top) and the observed data (bottom). In (a) or (d) near offset stacks (b) or (e) mid offset stacks, and in (c) or (d) far offset stacks. The synthetic data (top) reveal increasing 4D amplitude response with increasing offset in the saturation dominated areas, not easily interpreted in the observed data (bottom) due to strong noise. Fluid contacts are marked as in Figure 7-2.

The synthetic 4D amplitudes from the reference model are to be used in the inversion, taken as the observed measure of truth. The overall response is quite similar, as both models honour the historical data. The water leg as expected shows very weak amplitude response to the mild pressure increases (< 3.5 MPa), when compared to the response associated with saturation effects during this time.

To emulate real seismic data, 4D seismic noise (Figure 7-3(a) and (b)) is estimated from the observed 4D seismic data for each offset (i.e. angle). Non-repeatability (NRMS) maps computed above the reservoir and outside production areas, and the 4D amplitude response computed at top reservoir are combined to estimate the 4D seismic noise (see Appendix A-2 for calculations). In absolute terms, the estimated 4D seismic noise at the reservoir level is a measure of the uncertainty in the observed 4D seismic response (Figure 7-3(c) and (d)). The noise maps per offset stack are then scaled to smaller magnitudes (i.e. 15% of the estimated 4D seismic noise), and added to the synthetic 4D amplitude maps modelled from the reference model. This yields practically achievable 4D signal-to-noise ratios with mean around 5.8 (up to 16.7) for the near offsets and 7.6 (up to 20.3) for the far offsets. However, in the water leg where water injectors are located, the signal-to-noise ratio varies between 1.1 and 2.4 for the near offsets and are between 0.1 and 0.27 for the far offsets, due to very weak amplitude response to pressure changes at far offset relative to the magnitude of the added noise.

In Figure 7-4 the synthetic 4D seismic amplitudes maps from the reference model with noise added is shown, together with the observed 4D seismic amplitude maps. The observed 4D seismic response (Figure 7-4 (d) to (f)), particularly, the mid and far offset maps, show acquisition footprints in a northwest to southeast direction, evident as false softening (light yellow) signals, in the water leg region. This is where the effect of the injection related 4D softening response associated to mild pore pressure increases has not been detected. In the synthetic 4D seismic response (Figure 7-4 (a) to (c)), this region is mostly affected by the added noise, due to the modelled weak response to pressure. The 4D amplitude variation with offset character is difficult to interpret in the observed data due to the high noise levels, but in the synthetic data, the saturation dominated areas appear to increase with increasing offset, which agrees with the observed data.

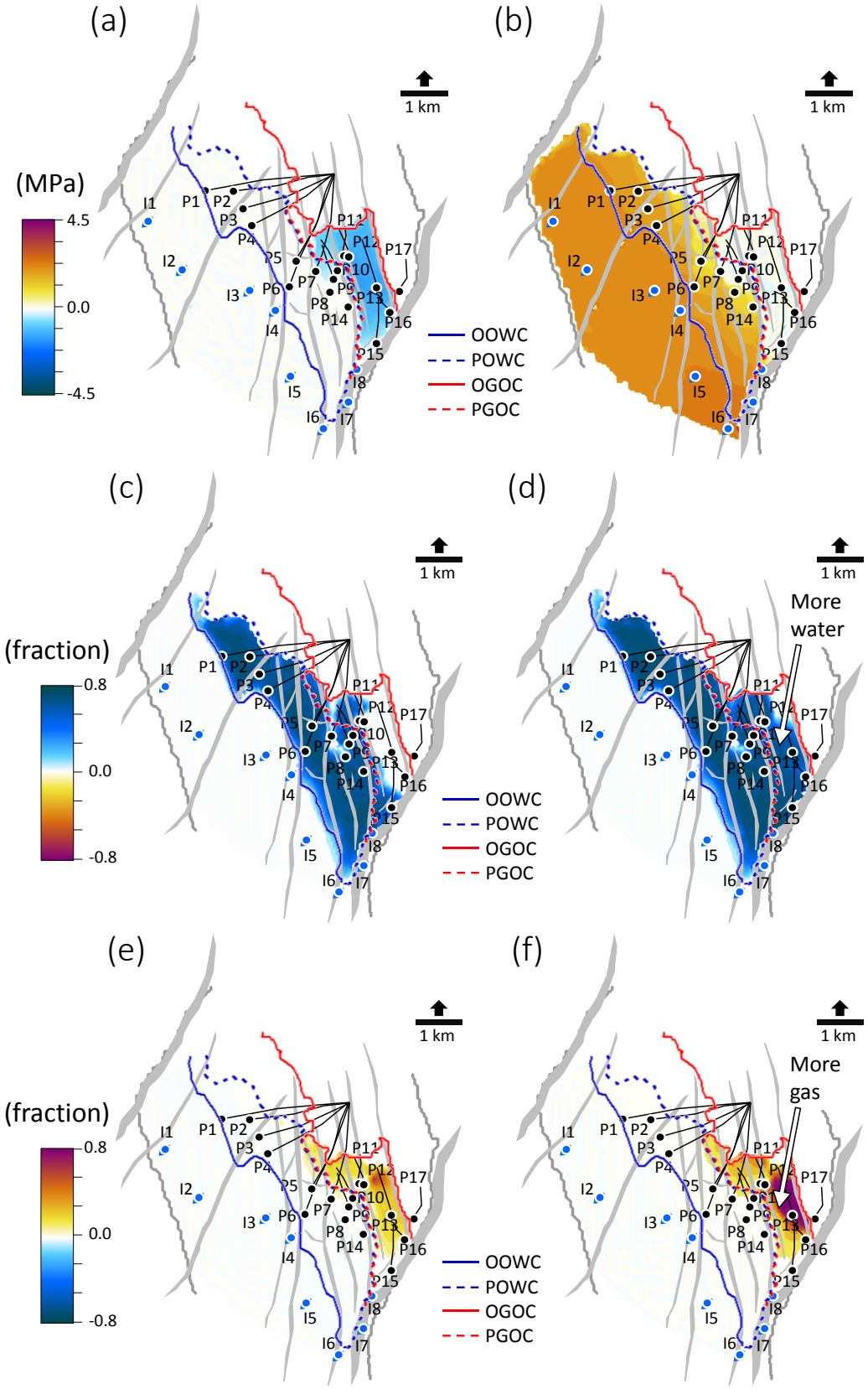

Figure 7-5 Spatially-varying bounds to be used as constraints for pressure and saturation inversion, extracted from the 94 models (although 95 models were generated, one model is kept as a reference). Depth-averaged maps over top reservoir for the 4D year 2006-baseline are shown for (a) Minimum pressure change (c) Minimum water saturation change (e) Minimum gas saturation change. (b), (d) and (f) are the same properties but for the maximum values. Fluid contacts are marked as in Figure 7-2.

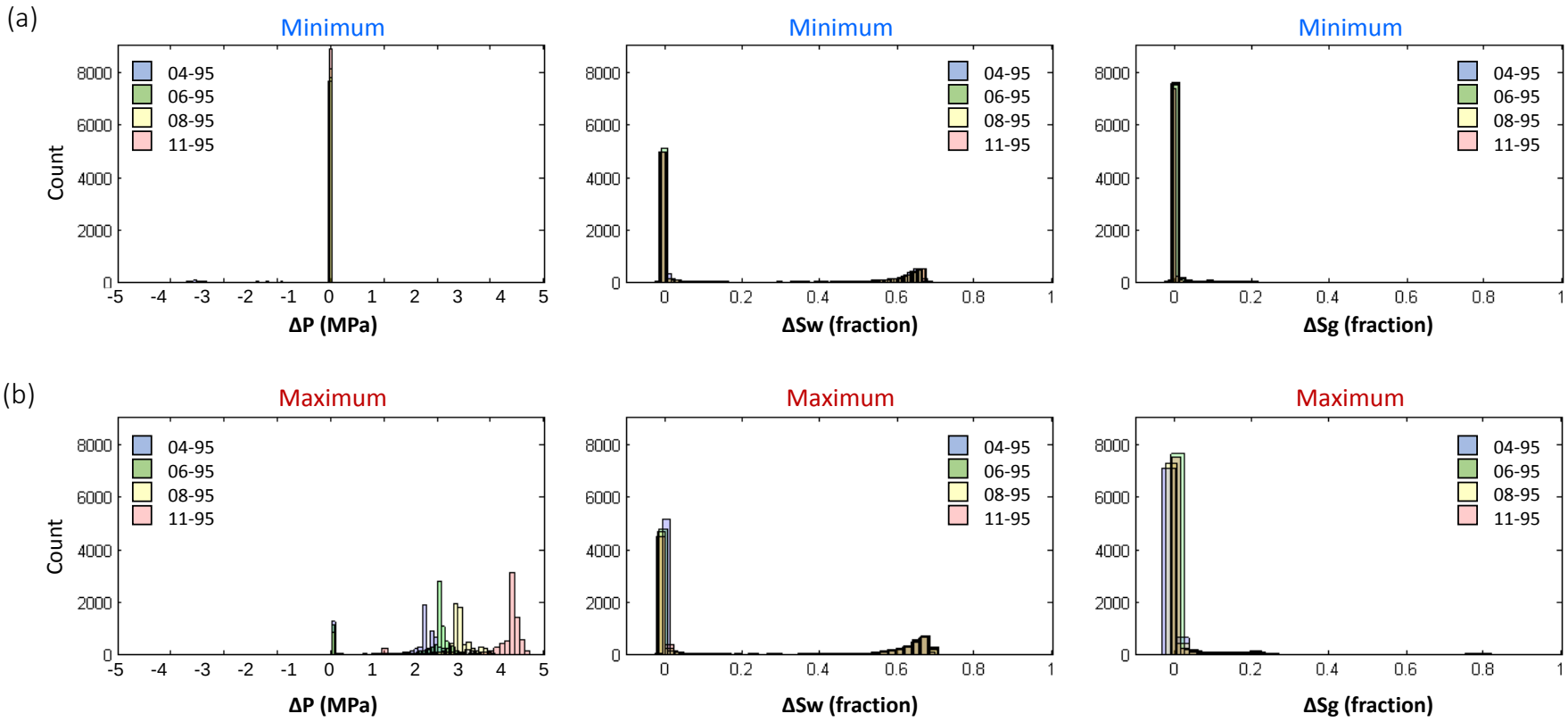

Figure 7-6 Histograms showing the range for the (a) minimum and (b) maximum depth-averaged predictions of pressure (left), water saturation (middle) and gas saturation (right) changes across the 4D monitor times, 2004, 2006, 2008 and 2011, relative to the 1995 pre-production state, extracted from the 94 simulation model scenarios (Note that 95 models were generated, but one model is kept aside as a reference model and it is not used to provide constraints, see also section 6.3.5). Though still conserved due to a strict qualifying criteria based on match to historical data, a bigger range between minimum and maximum for each of the monitor time is observed for pressure changes, than for saturation changes.

7.1.2 Multiple models: pressure and saturation spatially varying bounds

Depth-averaged maps of simulated pressure, water and gas saturation changes are computed over top reservoir for each of the 95 models earlier qualified by their match to historical data as described in section 6.2.3. Minimum and maximum values are then extracted only along 94 models (one model is kept aside as a reference model, see section 6.3.5), each for the 4D monitor times, which are spatially varying constraints, upper and lower limit to be used in the multi-offset inversion. Figure 7-5 shows the minimum and maximum values for the monitor time 2006-baseline. The variations in dynamic changes across the 94 models occur mostly in fault segment G and H for saturation, but for pressure this is across all segments, as to be expected. Histograms show similar variations between minimum and maximum saturations for other monitor times (Figure 7-6), across the 94 model scenarios, due to the strict qualifying criterion based on the match to historical data (Equation 6-12). Moreover, the study area was predominantly water flooded, with some gas cap expansion by the 2001 monitor time. For pressure changes, greater dispersion is observed, and the maximum limits increase at later monitor times due to injection.

7.1.3 Uniform bounds for pressure and saturation sensitivity

In the multi-monitor inversion for the sensitivity coefficients, uniform upper and lower bounds are used to constrain the solution space, (Equation 6-10). The uniform limits for the sensitivity coefficients were obtained following the procedure in Chapter 3. The noise-free synthetic 4D seismic data from the reference survey was used to calibrate the strongest and weakest 4D seismic signals around the injectors, and in saturation dominant areas, to the magnitudes of simulated pressure, water and gas saturation changes from the reference model at the same locations. Figure 7-7 plots the mean, upper, and lower range for pressure, water and gas saturation sensitivity for the near, mid, far and full offset stacks. The sensitivity is expressed as the percentage change in amplitude (relative to baseline) per unit change in the dynamic property. For saturations, the unit change is also in percentage, for pressure the unit change is MPa. For the inversion, the pressure sensitivity will need to be multiplied by 0.01, to maintain the same order as the saturation terms as in Equation 6-2. This reveals how small the C_P term is, compared to the C_{S_w} and C_{S_g} terms. Pressure sensitivity decreases with offset,

with approximately zero response at far offset, whereas the saturation sensitivity increases with offset. Notice also that the dispersion from the mean value reduces/ increases depending on the sensitivity direction with offset. Sensitivity to gas saturation changes is strongest, followed by water saturation, as already observed in Chapter 3.

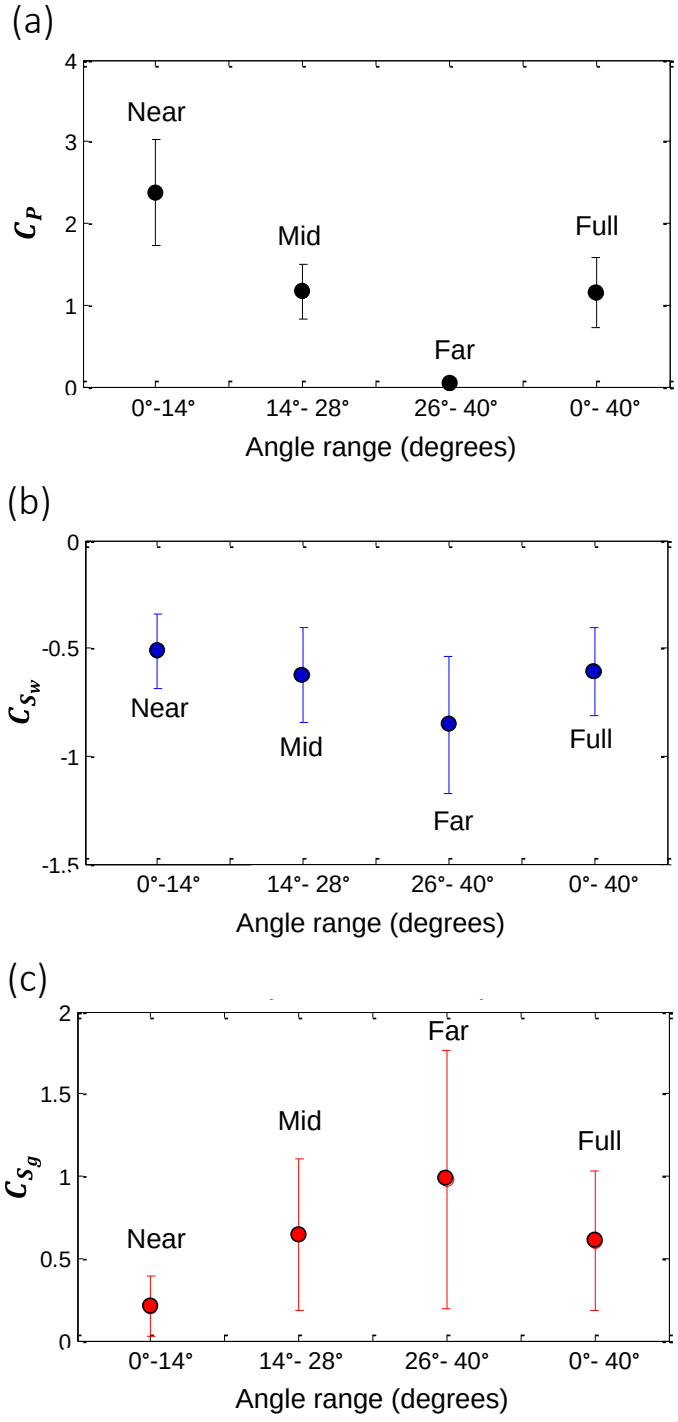

Figure 7-7 Synthetic derived uniform constraints (upper and lower limit) for the sensitivity for each offset (i.e. angle) stack (a) Pressure sensitivity, C_P , expressed as percentage change in amplitude per unit change in MPa. (b) and (c) are water, C_{s_w} and gas , C_{s_g} , saturation sensitivity, respectively, expressed as percentage in amplitude per unit change in saturation, measured in percentage. The dots represent the mean value, and the range represents the variation in sensitivity.

7.2 Preliminary assessment of the inversion scheme

7.2.1 The multi-monitor inversion

As Figure 7-8 illustrates, in this exercise I focus on three objectives:

- To compare the use of two 4D monitor dataset (which is the minimum number to use) versus three monitor dataset: I use the noise free synthetic data to test how well the sensitivity coefficients are obtained using two or three 4D monitors. I also compare the resulting pressure and saturation changes estimated from both cases, to those predicted from the reference simulation model, considered to be the truth.
- To assess the predictive ability of the multi-monitor inversion: I also check whether pressure and saturation changes can be reliably estimated for a particular 4D monitor time, not used in the multi-monitor inversion.
- To evaluate how robust the constrained inversion scheme is in the presence noise: I perform the multi-monitor inversion and multi-offset inversion using the noisy synthetic datasets.

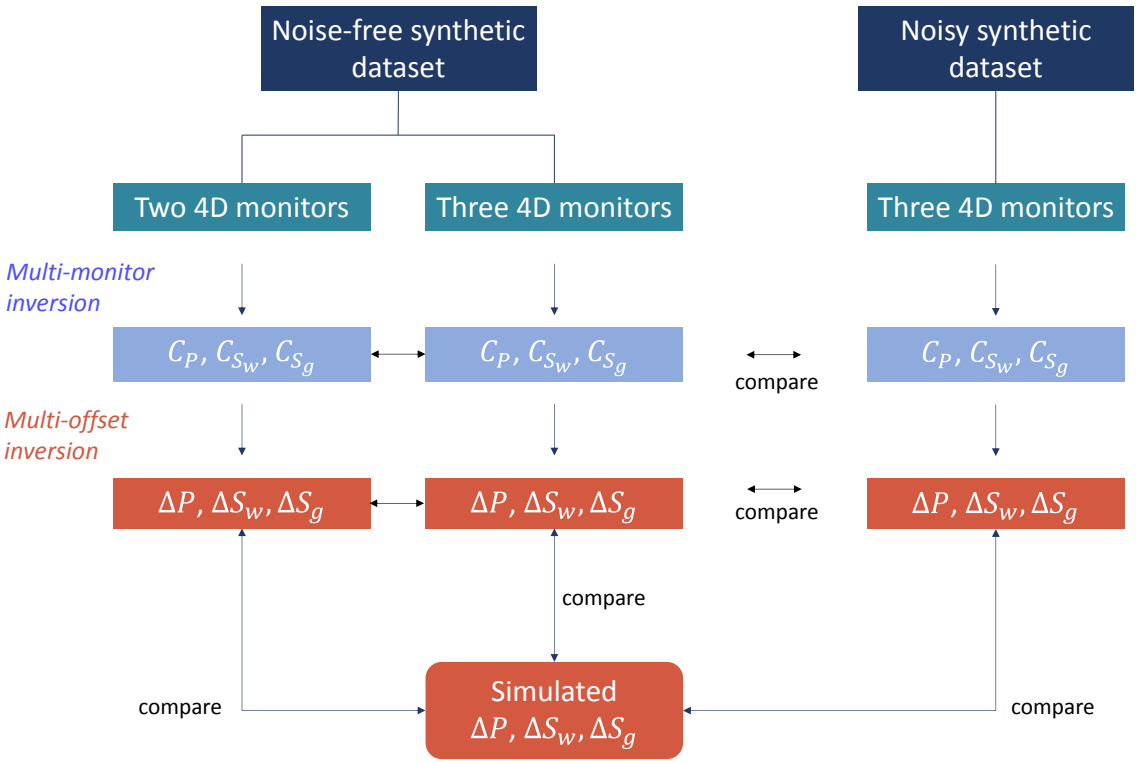

Figure 7-8 Illustration of the various ways for pilot application of the multi-monitor inversion, which feeds into the multi-offset inversion

In all test cases, the uniform upper and lower bounds (Figure 7-7) constrain the multi-monitor inversion. In the multi-offset inversion, the minimum and maximum pressure and saturation changes (Figure 7-5, Figure 7-6), obtained from the 95 simulation models provides spatially varying constraints to the solution space. Figure 7-9 shows the result of the multi-monitor inverted sensitivity coefficients obtained using noise-free synthetic 4D seismic data combined for the three monitor times, 2006, 2008 and 2011. The amplitude sensitivity to pressure changes decreases with offset, and the opposite is observed for saturation sensitivity. The sensitivity varies spatially depending on the underlying effects in the 4D seismic signatures (polarity and magnitude) from the combined monitor data. As to be expected, areas where there are no saturation changes (for example, the water injectors located in the water leg), the saturation sensitivity coefficients are zero. Areas where all the effects combine, then the multi-monitor inversion is able to resolve the sensitivity to the various effects.

To check that pressure and saturation changes can be estimated reliably for a particular 4D monitor time that was not used in the multi-monitor inversion, I show the results of the multi-offset inverted pressure and saturation changes for the 2004-baseline 4D time (Figure 7-10). The inversion combined the near, mid and far offset synthetic 4D seismic amplitude data with the corresponding offset sensitivity coefficients in Figure 7-9. The results are compared with the depth-averaged simulator predictions from the reference model (Figure 7-10 (d) to (f)). Subtle mismatches between the inverted and simulated saturation changes with differences of up to 0.1 (in fraction) are noted in the gas dominant area. For pressure changes, the mismatch is less than 0.3 MPa in both the water leg and water saturation dominant area, whereas in in the gas dominant area the mismatch is up to 1.5 MPa. It should also be noted, that the discrepancies between the inverted estimates and the flow simulator are in a small part contributed by the inversion. As a linear inversion equation (Equation 6-1a) was used, this may introduce small scale errors, especially, for the inverted gas saturation changes, although this is negligible. However, the error here is to a large extent contributed by the differences in scale/resolution between the 4D seismic domain and the flow simulator. The simulator-to seismic modelling procedure transforms the simulator grid (lateral and vertical cell sizes) to the seismic grid (lateral bin size) which carries uncertainties (Amini, 2014). More so, the 4D seismic maps are root-mean-square amplitudes calculated using a time

window along the top reservoir, whereas, the simulator maps are depth-averages.

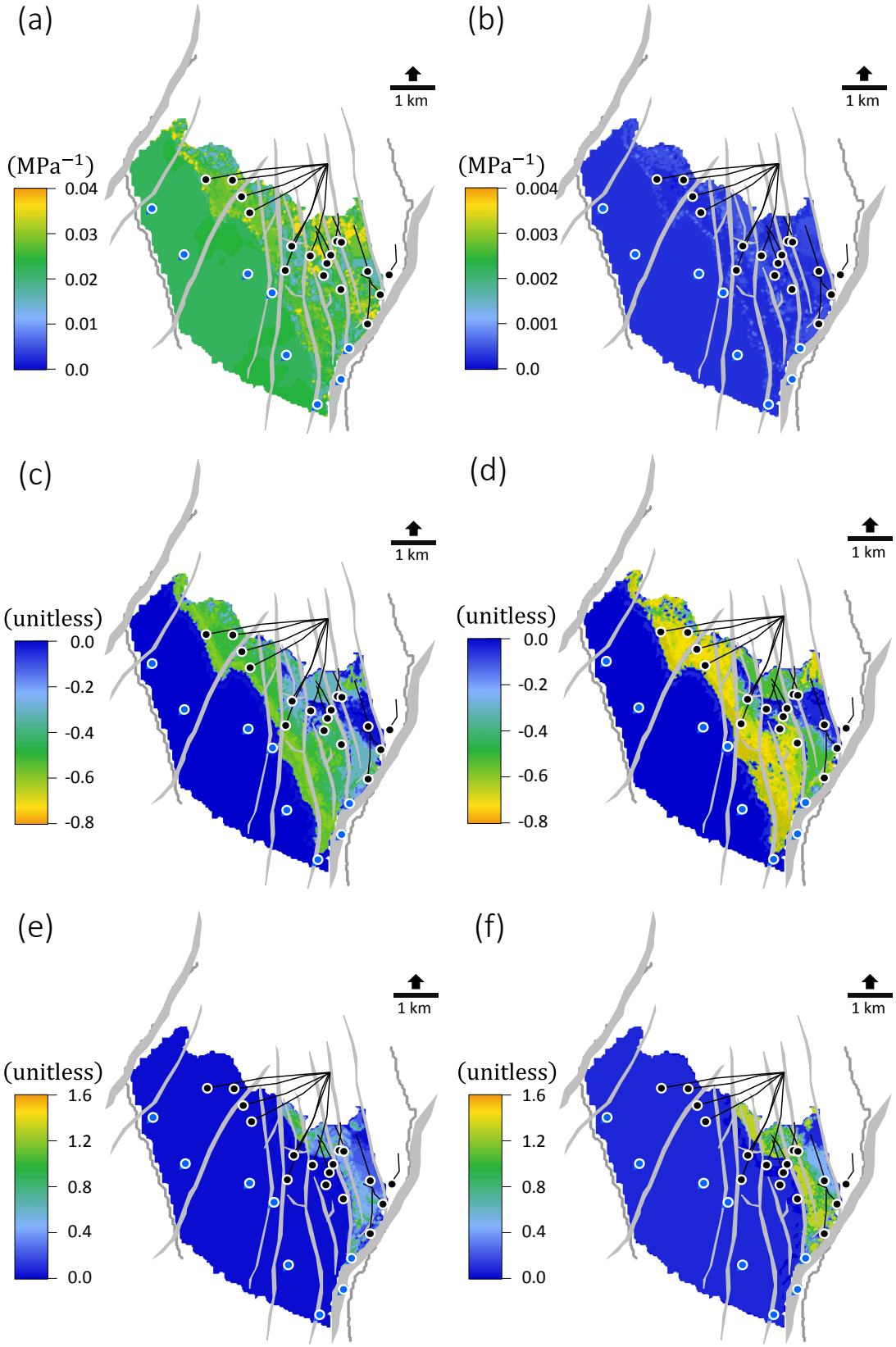

Figure 7-9 Inverted sensitivity coefficients using three monitors (2006, 2008 and 2011) from the noise-free synthetic 4D seismic amplitude stacks. Results are shown for (a) C_P for the near offset (b) C_P for the far offset (c) C_{S_w} for the near offset (d) C_{S_w} for the far offset (e) C_{S_g} for the near offset (f) C_{S_g} for the far offset.

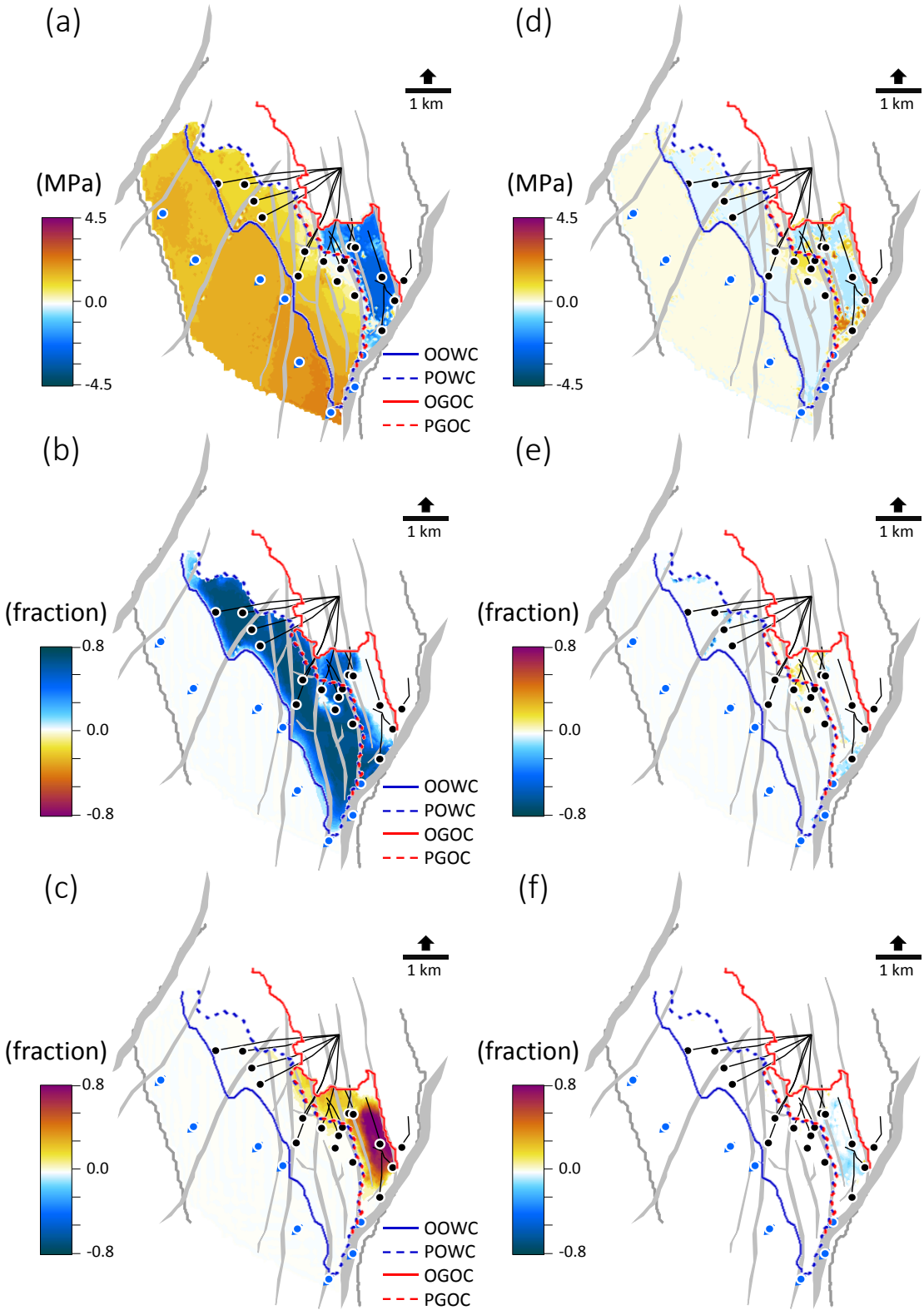

Figure 7-10 Constrained multi-offset inversion results for the 2004-baseline time using the spatially varying upper and lower limits from the 95 models, and the inverted sensitivity coefficients (Figure 7-9). Results are (a) Pressure changes (b) Water saturation changes (c) Gas saturation changes. The difference between the seismically-derived estimates in (a) to (c) and depth-averaged simulations from the reference model are shown in (d) to (f) for the respective properties in (a) to (c). For well labels and marked fluid contacts, see Figure 7-2.

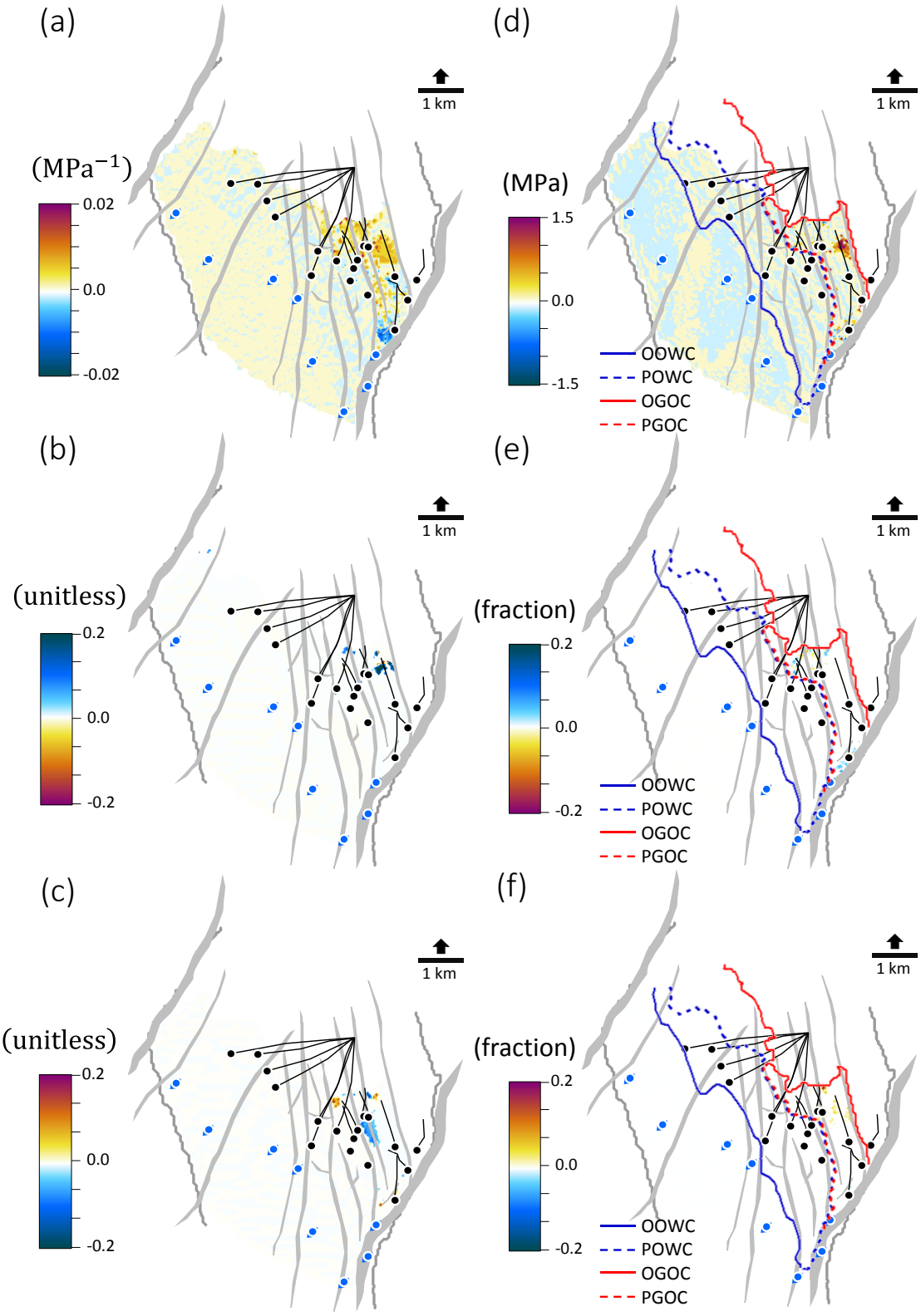

Figure 7-11 Comparing the influence of using two versus three monitors in the constrained inversion using noise-free synthetic data. The difference between the inverted sensitivity coefficients using three monitors (2006, 2008 and 2011) versus two monitors (2006 and 2008) are shown in (a) C_P for the near offset (b) C_{S_w} for the near offset and (c)) C_{S_g} for the near offset. The difference between the inverted dynamic results at the 2004 –baseline monitor time for the case of three monitors versus two monitors are shown for (d) Pressure changes (e) Water saturation changes (f) Gas saturation changes. For well labels and marked fluid contacts, see Figure 7-2.

Next, the inverted results obtained using three 4D monitor data (2006, 2008 and 2011) are compared against those obtained using only two 4D monitor data (2006 and 2008). In Figure 7-11 (a) to (c) the differences between the inverted sensitivity coefficients for the three monitor versus two monitor case are given. The differences reveal that the three monitor case estimates a stronger sensitivity to pressure changes than the two monitor case, in most areas. For sensitivity to water and gas saturation changes, both monitor cases are similar. In Figure 7-11 (d) to (f) the differences in the inverted pressure and saturation changes for the 2004-baseline monitor time are shown for the three monitor versus two monitor case. As the multi-offset inversion is spatially constrained in both cases, their estimated saturation changes are almost identical, hence very subtle differences (less than 0.04 in fraction) around a few producers in the gas dominant area. For pressure changes (Figure 7-11 (d)), the differences are typically less than 0.2 MPa. In areas where the discrepancies in the inverted pressure sensitivity (Figure 7-11(a)) are largest, particularly in the gas dominant area, the differences in the inverted pressure changes can be up to 2 MPa, between the three monitor and two monitor cases. It was also found that the three monitor case performs slightly better than the two monitor case when compared to the simulated predictions, particularly for pressure changes.

Finally, the multi-monitor inversion for the sensitivity coefficients is again performed for the three monitor case (2006, 2008 and 2011), but this time using the noisy synthetic 4D seismic data. The uniform upper and lower bounds (Figure 7-7) are again used to constrain the inversion. The multi-offset inversion follows this, also constrained by the spatially varying bounds (Figure 7-6). This final exercise is to assess the constrained inversion in the presence of noise. Figure 7-12 shows the inverted estimates of pressure and saturation changes, and compares these to the depth-averaged maps of pressure and saturation changes from the reference simulation model. As pressure is more affected by the noise due to the weaker sensitivity compared to saturation sensitivity, the inverted pressure changes are noisier (particularly in the water leg) than the saturation changes. Moreover, the spatially varying limits from the 95 models used to constrain the solution for saturations are less dispersed than for pressure. Hence, the inversion is better able to estimate the saturation changes within the tight bounds, with results almost identical to the noise-free case (Figure 7-10), than for pressure changes. Nevertheless, the pressure changes are still reliably estimated within the limits, close to the simulator predictions.

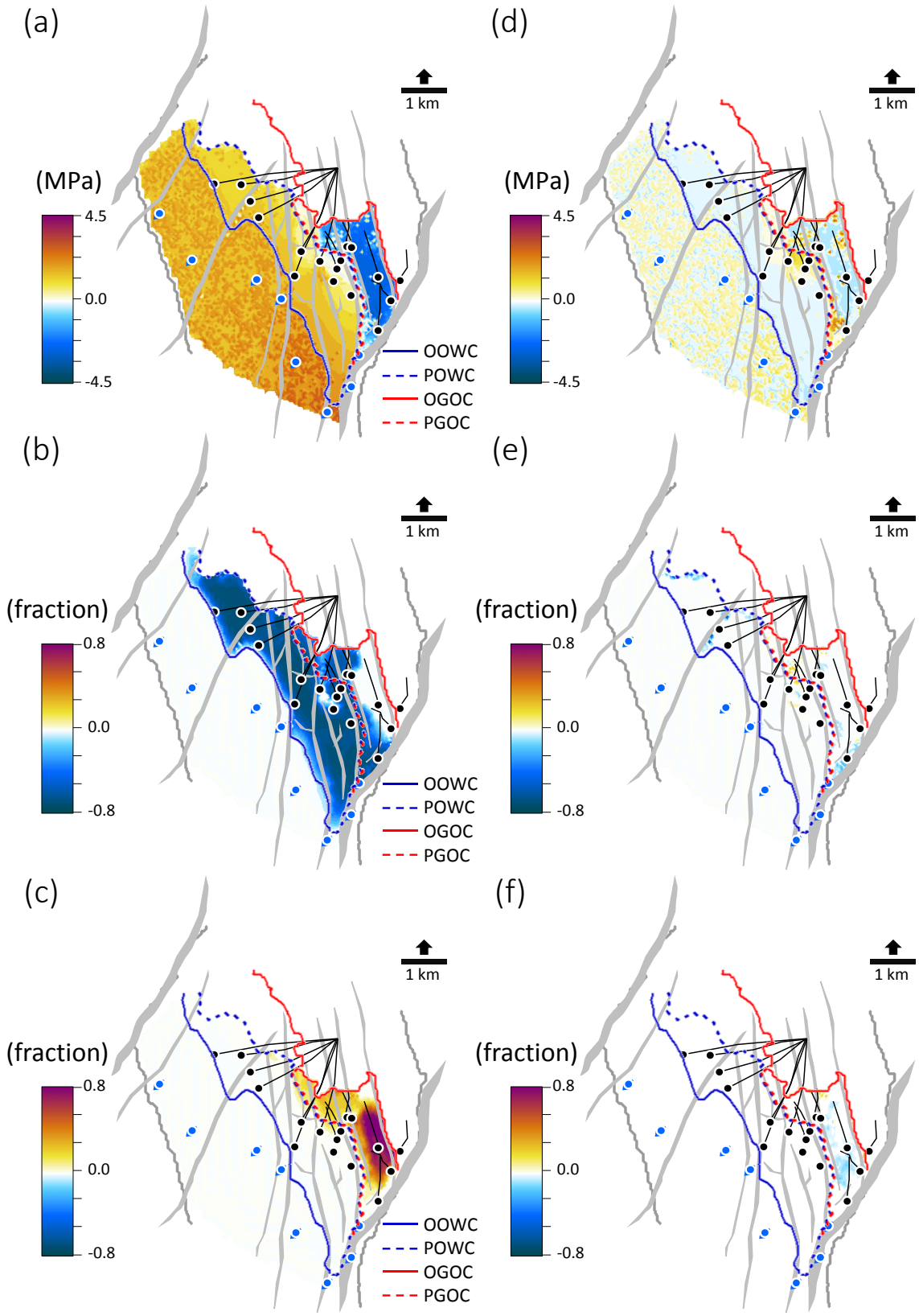

Figure 7-12 The results of the multi-offset inversion for the 4D monitor time, 2004-baseline, obtained using the noisy synthetic data, shown for (a) Pressure changes (b) Water saturation changes (c) Gas saturation changes. The difference between the seismically-derived inverted results and depth-averaged simulations from the reference model are shown in (d) to (f) for the respective properties in (a) to (c). For well labels and marked fluid contacts, see Figure 7-2. Also compare with the noise-free case in Figure 7-10.

7.2.2 The multi-offset inversion

Figure 7-13 illustrates the various implementations of the multi-offset inversion using noise-free synthetic data modelled from the reference simulation model.

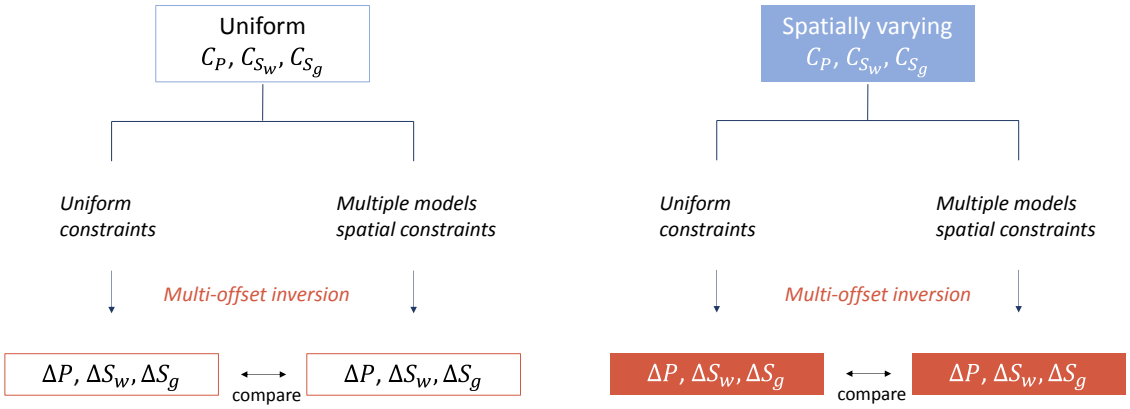

Figure 7-13 Illustration of the various ways for pilot application of the multi-offset inversion constrained using uniform values or spatially varying values extracted from multiple models. In each case, uniform (i.e. constant) and spatially varying C_P, C_{S_w} and C_{S_g} sensitivity coefficients are used.

In other studies (Floricich, 2006), the sensitivity coefficients were assumed uniform. Here I compare the use of uniform (i.e. constant) versus spatially varying sensitivity coefficients in the multi-offset inversion. The uniform sensitivity values are based on the mean derived from synthetic data calibration per offset stack (Figure 7-7). The case of the spatially varying sensitivities has been earlier obtained from the multi-monitor inversion (Figure 7-9). When utilising the uniform or non-uniform sensitivity coefficients, the multi-offset inversion compares two types of constraints to the ΔP and ΔS solution space:

- Uniform ΔP and ΔS bounds based on a single maximum and minimum value from the entire 95 models, specific to the 4D monitor time (Table 7-1).
- Spatially varying ΔP and ΔS bounds from the 95 models (Figures 7-5 and 7-6).

Uniform bounds	ΔP	ΔS_w	ΔS_g
Upper	4.14	0.89	0.97
Lower	-3.74	0	0

Table 7-1 Upper and lower bounds for the case of utilising uniform constraints in the multi-offset inversion, shown for the 2004-baseline monitor time. ΔP is in MPa and ΔS in fraction.

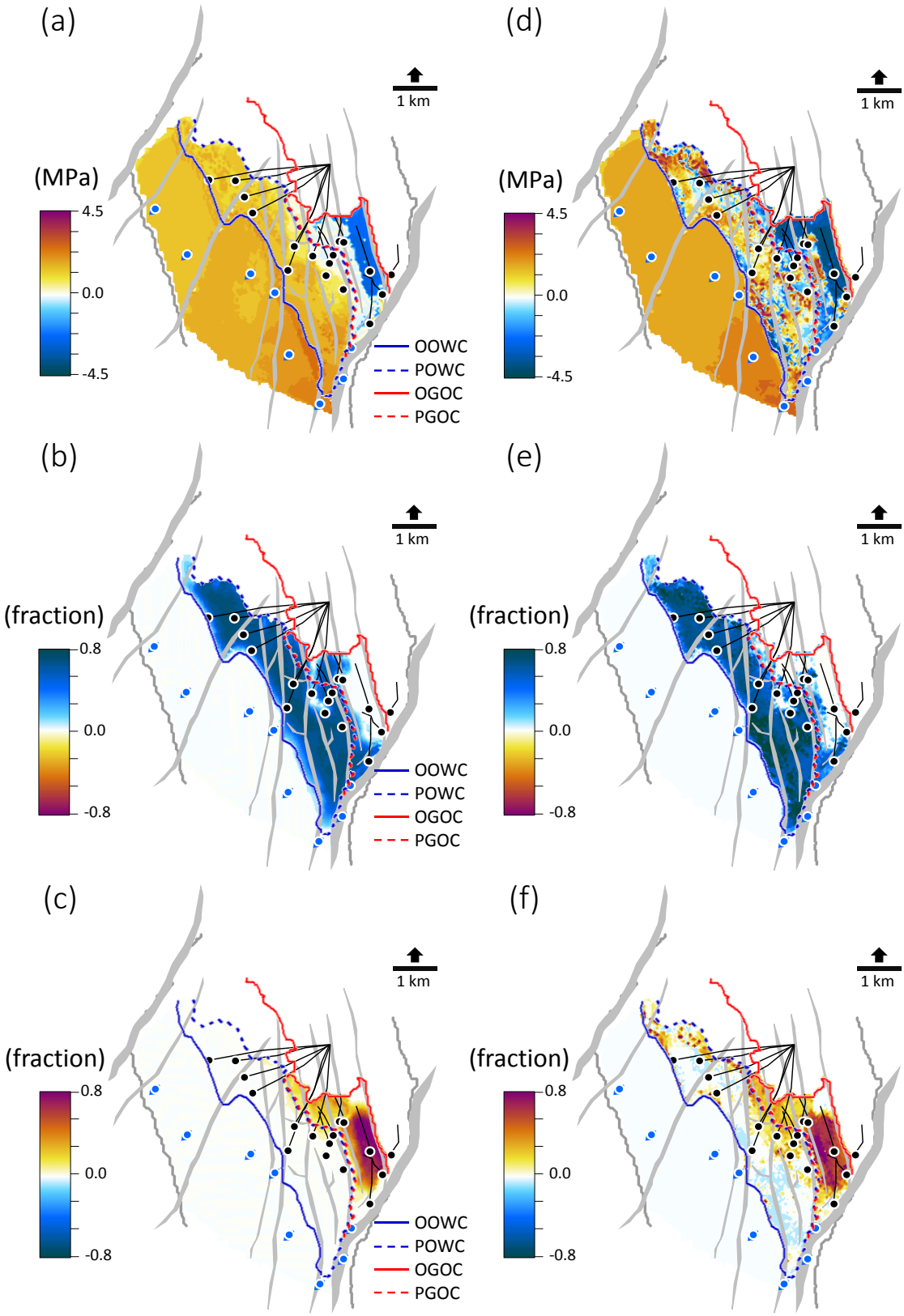

Figure 7-14 The 2004-baseline multi-offset synthetic inversion results for the case of uniform C_P, C_{S_w} and C_{S_g} sensitivities. Left column are estimated (a) Pressure changes (b) Water saturation changes and (c) Gas saturation changes, when the inversion is constrained using spatially varying upper and lower limits. The right column (d), (e) and (f) are the same but for the case where only uniform upper and lower limits are used. For well labels and marked fluid contacts, see Figure 7-2.

Figure 7-14 compares the multi-offset inversion results for the 2004-baseline monitor time when C_P, $C_{S_w}$and C_{S_g} are assumed uniform across the reservoir. In Figure 7-14 (a) to (c), spatially varying upper and lower limits from the 95 models (Figure 7-6) were used to constrain the inverted pressure and saturation changes, and in Figure 7-14 (d) to (f), uniform limits (Table 7-1), were instead used. In the case where only uniform constraints are used, the constant set of C_P, $C_{S_w}$and C_{S_g} fail to reproduce the expected changes, particularly, where pressure and saturation changes overlap beyond the water leg. This is clear for the inverted pressure changes (Figure 7-14 (d)) where pressure decreases are estimated where only pressure increases are expected and vice versa. For gas saturation changes (Figure 7-14 (f)), a leakage also occurs for the case of uniform constraint, as only gas saturation increases are predicted during this 4D monitor time, and the changes should be restricted to within the gas leg. For water saturation changes, only little discrepancies in the gas leg for both cases in Figure 7-14 (b) and (e) are observed. The comparisons above suggest that the use of uniform C_P, $C_{S_w}$and C_{S_g} can only yield reliable solutions when appropriate constraints are imposed in the multi-offset inversion. Better, if the constraints are spatially varying and honour material balance and flow conditions, as is the case for Figure 7-14 (a) to (c), otherwise a leakage between the inverted pressure and saturation changes is unavoidable, as is the case in Figure 7-14 (d) to (f).

Finally, in Figure 7-15 I show the multi-offset inversion results which uses the spatially varying sensitivity coefficients (Figure 7-9), but in this case only uniform pressure and saturation limits (Table 7-1) are used to constrain the inversion. Figure 7-15 (a) to (c) details the inverted pressure and saturation changes, and Figure 7-15 (d) to (f) details the difference between the inversion results and the predictions from the reference simulation model. Figure 7-10 is offered for comparison, as it represents the complete case of spatially varying sensitivity coefficients as well as spatially varying pressure and saturation constraints to the inversion, based on the 95 simulation models. Figure 7-15 (a) to (c) show that using the spatially varying C_P, $C_{S_w}$and C_{S_g} and uniform constraints, pressure and saturation changes are estimated reliably, when compared to the case of constant C_P, $C_{S_w}$and C_{S_g} and uniform constraints (Figure 7-14 (d) to (f)). The differences (Figure 7-15 (d) to (f)) also reveal how far off the inversion results are from reality. When compared to Figure 7-10 (d) to (f), the inconsistencies are largest in the

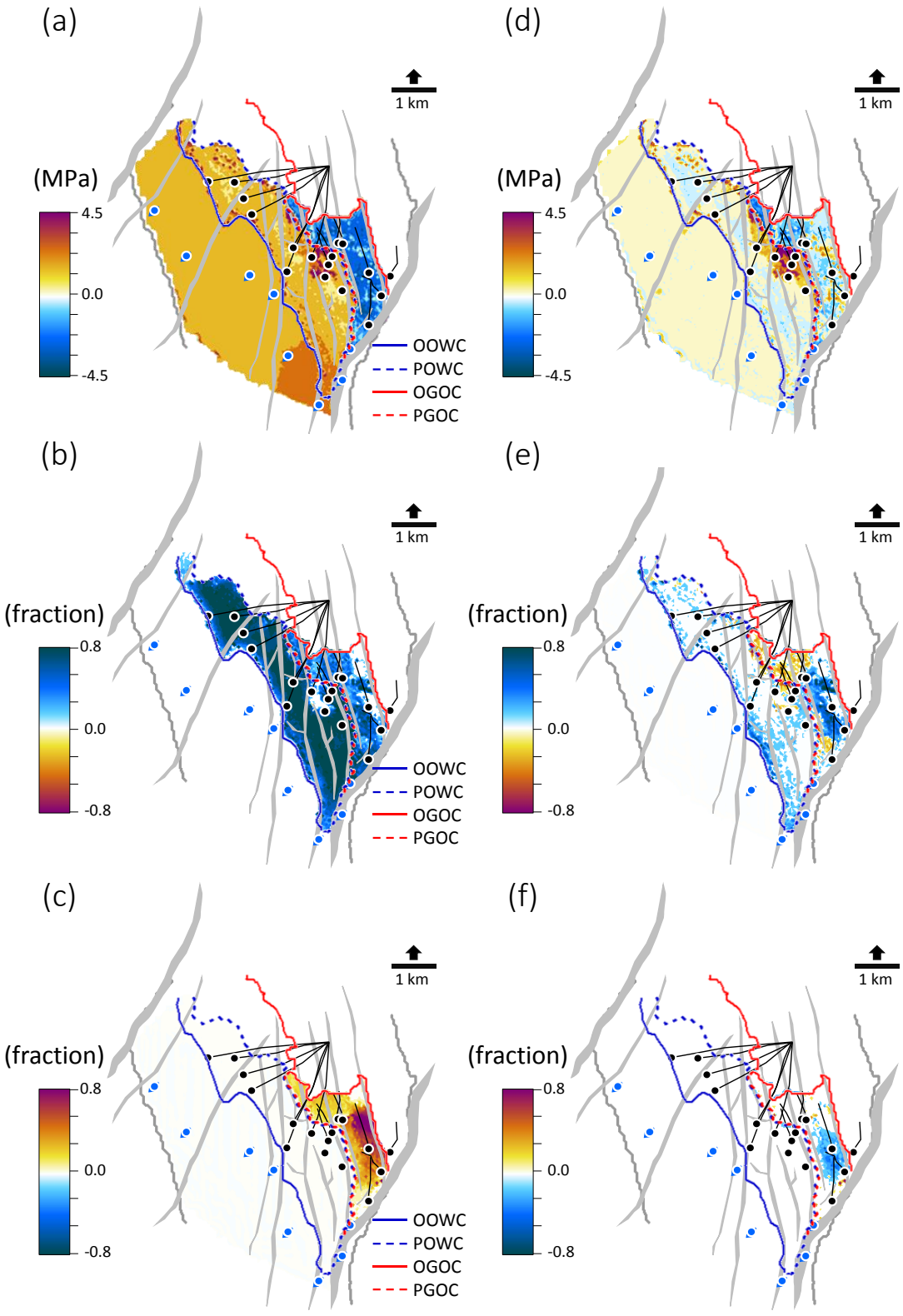

Figure 7-15 Constrained multi-offset inversion results for 2004-baseline time using uniform upper and lower limits (Table 7-1) for the case of spatially varying sensitivity coefficients (Figure 7-9). Results are (a) Pressure changes (b) Water saturation changes (c) Gas saturation changes. The difference between the seismically-derived inverted results and depth-averaged simulations from the reference model are shown in (d) to (f) for the respective properties in (a) to (c). For well labels and marked fluid contacts, see Figure 7-2.

gas leg. As the 2004-monitor dataset was not used in the multi-monitor inversion from which the C_P, $C_{S_w}$and C_{S_g} coefficients are derived, such large errors occur here, as changes in saturations across the later monitor times that were indeed used (2006, 2008 and 2011) occur mainly in the gas leg. In this gas leg area, the inversion estimates a higher magnitude in water saturation changes by up to 0.5 in fraction, while in reality, little or no water saturation changes occur here for the 2004-baseline monitor time. Likewise for gas saturation, the inverted gas saturation changes are smaller by up to -0.3 in fraction than in reality, because the 2006, 2008 and 2011 monitor times represent a period of gas saturation decrease, whereas earlier in 2004, the gas saturation had increased. These discrepancies suggest it is best to use all monitor data in the multi-monitor inversion, for which pressure and saturation changes are to be estimated, as this will give a more representative, C_P, $C_{S_w}$and C_{S_g} coefficients, albeit the success with the two monitor (Figure 7-11) and three monitor (Figure 7-10, Figure 7-15) case studies. In any case, the discrepancies also highlight the need for spatially varying pressure and saturation constraints to the multi-offset inversion and these can only be obtained from multiple models, as opposed to using uniform constraints. The pilot application of the inversion scheme therefore suggests the best case to be that of Figure 7-10, followed by Figure 7-15, in the absence of spatially varying pressure and saturation constraints.

7.3 Application of the inversion scheme for a soft "close-the-loop" on the Heidrun Field

The inversion scheme (Figure 6-2) detailed in section 6.2.1 is fully implemented here. The observed data from the Heidrun field is taken to be the noisy synthetic dataset previously modelled from the reference simulation model, which is considered here to be the truth. By using constraints such as the maximum and minimum limits extracted from the 95 history-matched models, a reliable solution for pressure and saturations changes can be reached via the multi-offset inversion. Additionally, the inversion estimates can also be compared to simulated pressure and saturation changes from the reference model. Prior to this, the scheme uses each of the 95 models in a multi-monitor inversion, which helps to find the model that is closest to the truth, preserved in the 4D seismic signals of the reference model across the monitor times. This added component is a strong benefit of the scheme, as it helps to address uncertainties by using multiple

models as well as a robust way of choosing the best model, hence a soft "close-the-loop".

7.3.1 The multi-monitor inversion scheme for best model validation

The multi-monitor inversion (Figure 6-2) helps to identify models that best honour the 4D seismic data. This is possible because the multi-monitor inversion combines all 4D monitor data and uses data according to each offset (near, mid, far and full) in turn. Such 4D seismic monitor data are spatially dense historical measurements from the field, which helps fill the gaps with spatially coarse well production data. Inputs to the multi-monitor inversion are also the simulated pressure and saturations for each model scenario, $\mathbf{G}^{[i]}$**,** with the inversion repeated per model (Equation 6-4). Therefore, by computing the norm of residuals, $\left\|\mathbf{d} - \mathbf{G}^{[i]}\mathbf{m}^{[i]}\right\|_2^2$ (terms earlier defined in Equation 6-4), the best model which estimates the unknown variables in **m (**i.e. C_P, $C_{S_w}$and C_{S_g}) closest to the observed 4D seismic response (provided here by the reference model) can be isolated. Note that C_P, $C_{S_w}$and C_{S_g} are already known for the reference model. This was achieved by running the multi-monitor inversion using all data solely from the reference model. The data are observed 4D seismic data (which has been modelled from the reference model), and simulated pressure and saturation changes contained from the reference model. For the rest of the 94 simulation models, **d** is kept the same (as it is the observed 4D seismic data) and $\mathbf{G}^{[i]}$ changes because this is provided by each model**,** from the 1st model to the 94th model So, besides the true solution of the sensitivity coefficients in **m** from the reference model, the multi-monitor inversion produces 94 estimates of $\mathbf{m}^{[i]}$ based on the other 94 simulation models**.** The inversion norm of residuals for each model is calculated, and which ever model that has the next smallest norm (besides the reference model which has the smallest norm) is identified as the best model. Three 4D seismic data for the monitor surveys 2006, 2008 and 2011 are combined for each offset stack (near, mid and far) as in Equation 6-2 to invert for $\mathbf{m}^{[i]}$, containing the sensitivity coefficients, $C_P{}^{[i]}$, $C_{S_w}{}^{[i]}$and $C_{S_g}{}^{[i]}$. The noisy synthetic 4D seismic dataset from the reference model, **d**, ((Figure 7-4 (a) to (c)) along with its data uncertainty (Figure 7-3(c) and (d)) is the data used in the inversion. The multi-monitor inversion is also constrained using the uniform limits (Figure 7-7), so as not to over-fit

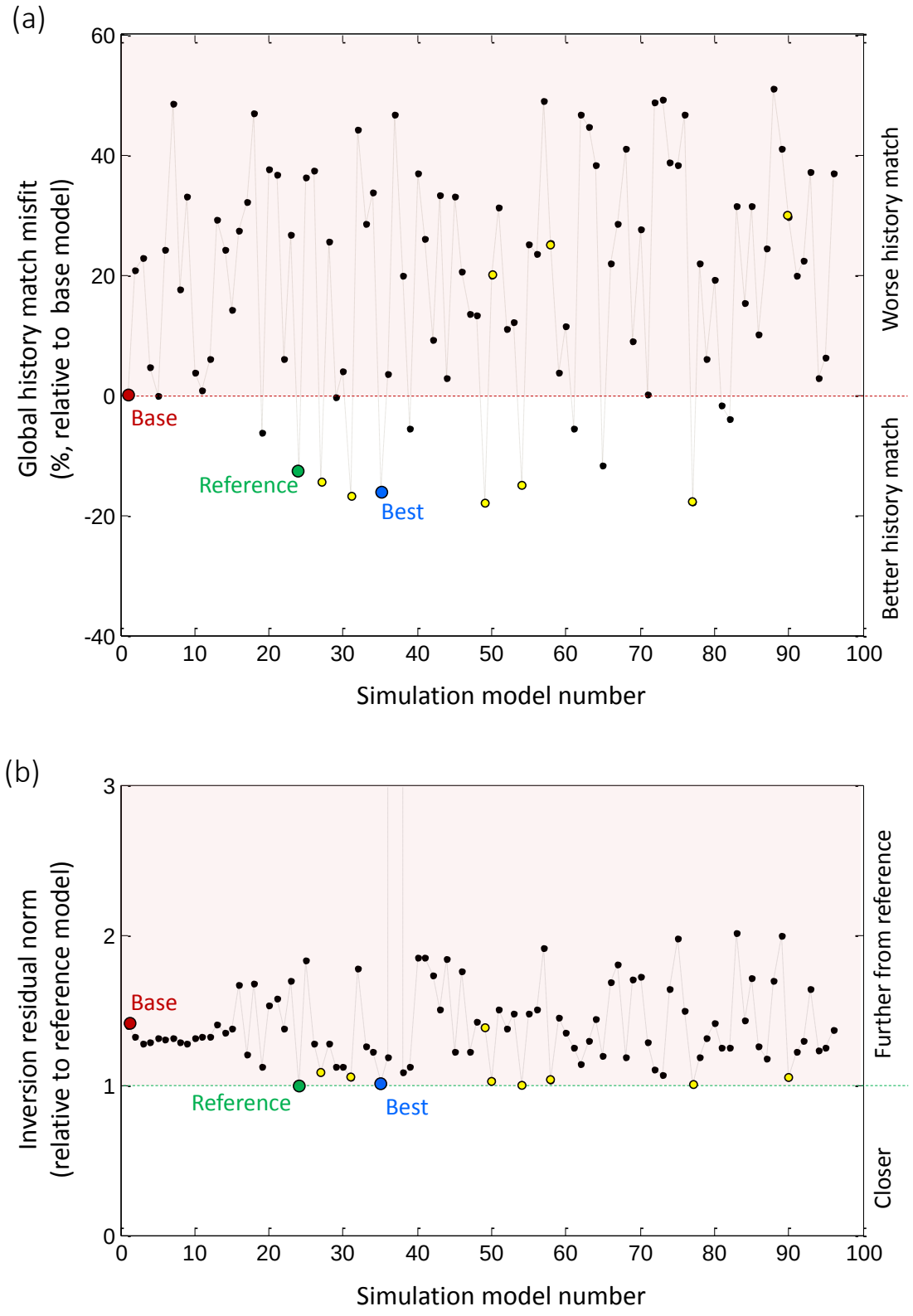

Figure 7-16 Cross-validating the match to historic production data with the multi-monitor inversion, to identify the best model closest to the reference model. (a) Plot of the global misfit from the history matching, based on the qualifying criterion, Equation 6-12, for all 95 models relative to the base model (b) plot of the total residual from the multi-monitor inversion (utilising all the offset stacks) for each of the models normalised by the reference model. Base, reference and best models are annotated. Other models are highlighted in yellow for inspection. Models 54 and 77 are close alternatives to the chosen best model.

noise in the 4D seismic data. The norm of residuals obtained can also be inspected alongside the global history-matching objective (Equation 6-11). On performing the multi-offset inversion for all 94 models, Figure 7-16 details this comparison, which also identifies other models closer to the reference model, apart from the best model. In Figure 7-16 (a), the global misfit from the history match, based on the qualifying criterion, Equation 6-12, is plotted for each of the models. A value less than zero, implies that the model is better history-matched than the base model. In Figure 7-16 (b), the total residual from the multi-monitor inversion (i.e. sum of all residual norms obtained per offset stack) for each of the models are normalised by the reference model. A value greater but close to 1, implies that the model is closer to the reference model. The base, reference and best models are identified on both plots. In Figure 7-16 (b), the best model differs from the reference model by 2.11%, whereas for the base model, this is 39.4%. Alternatives to the best model, for example, models 54 and 77 can be just as satisfactory. It can be argued that models with residual norm closer to the reference are also as close to the reference model in their history match objective function value. There are outliers to this trend, for example, model 49, matches historical data similar to the reference model, but the inversion residual norm is much higher, whereas for model 50, the opposite is observed.

This highlights possible trade-offs that may arise when simultaneously matching production data and the 4D seismic response (Obidegwu et al., 2015). However, in this case, the outliers are due to the fact that only results from the top reservoir (zones 3 to 7) have been used in the inversion, whereas the history matching accounts for all four reservoirs characterised in the Heidrun field's reservoir model (Figure 6-4). Nevertheless, the use of multiple models in the multi-monitor inversion scheme offers a way to identify better models, while at the same time deriving the best estimate of the sensitivity coefficients.

Figure 7-17 shows the cumulative field oil production over the 16 years of history for the field. The reference model simulation result is almost identical to the historical data. Compared to the base model, the best model which was identified by the inversion is not too far off from the reference. In terms of the static properties which define the reference and best model, this is given by global multipliers (Table 7-2).

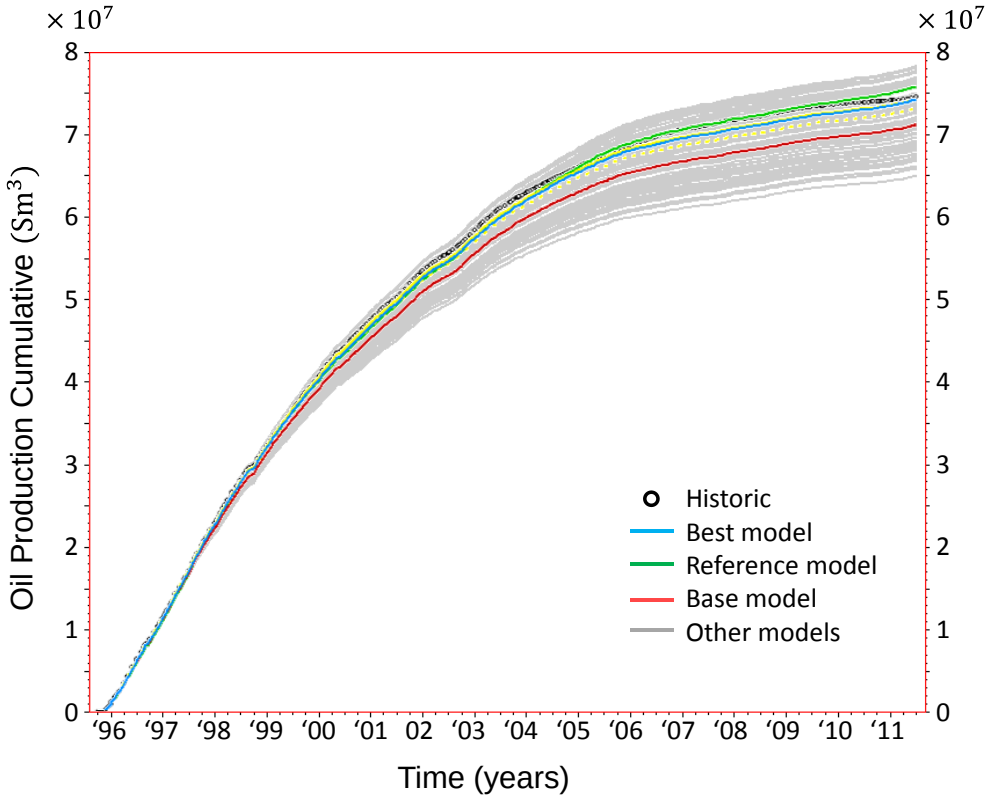

Figure 7-17 The benefit of multiple models to the inversion. Simulation results for cumulative oil production from the qualified 95 models highlighting the reference model (green), the best model (blue) identified by the inversion, and the base model (red), compared against historical data (black). Alternatives to the best model via the inversion are highlighted in yellow, and the rest of the models in grey. The reference and best model match history better than the base model.

Static property multipliers	Porosity	Permeability X	Permeability Y	Permeability Z
Base model	1	1	1	1
Reference model	0.932	1.488	1.435	1
Best model	1.018	1.507	1.381	1

Table 7-2 Base, reference and best model properties defined by global multipliers. A multiplier value of 1 means the property is the same, as in the base model.

7.3.2 Results of the completed inversion scheme

Once the model that best honours the observed 4D seismic signals is identified via the multi-monitor inversion, the estimated sensitivity coefficients are then used to invert for pressure and saturation changes across the 4D monitor times. For each 4D monitor time, the corresponding minimum and maximum spatially varying limits extracted from

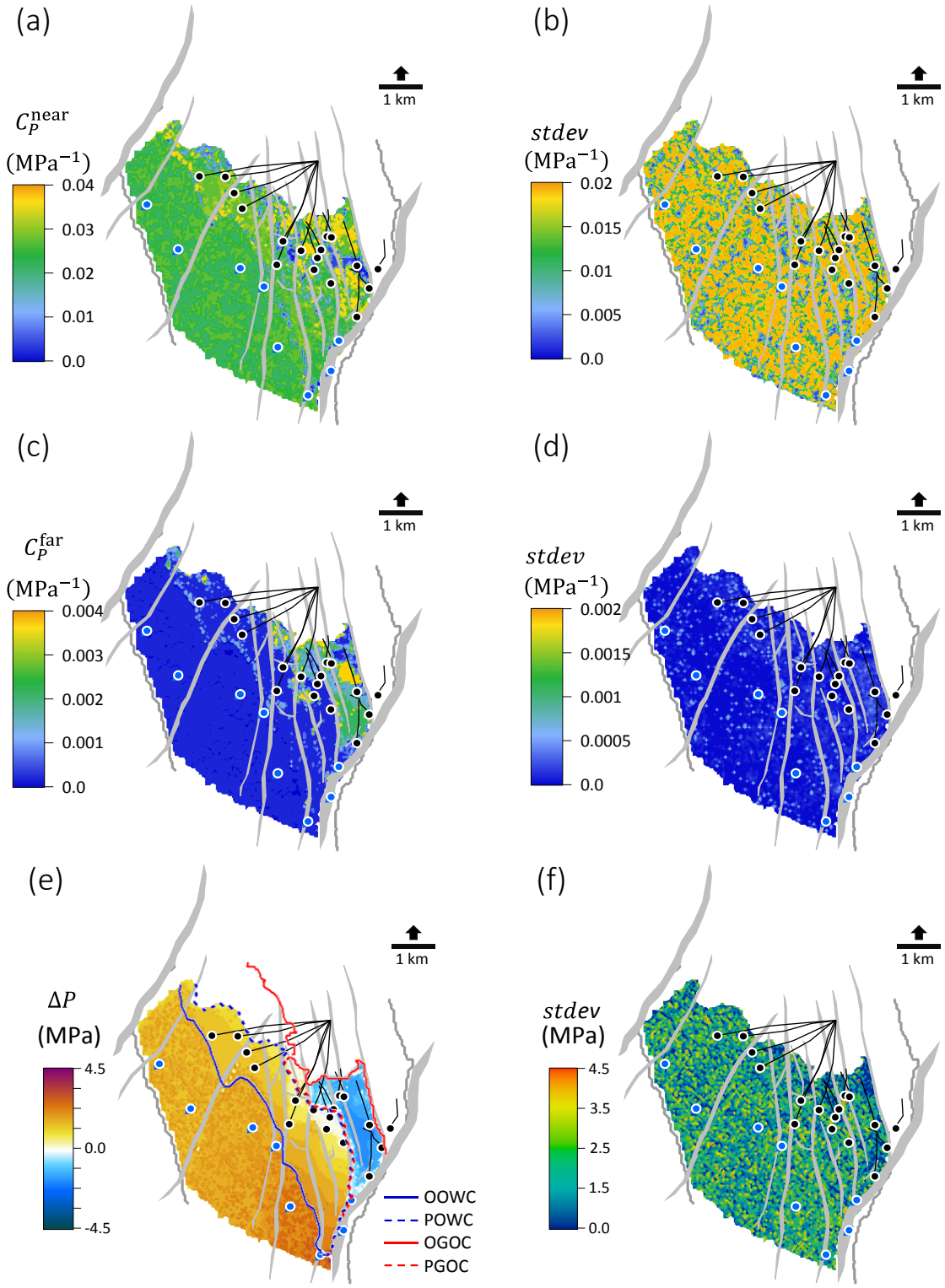

Figure 7-18 Results for pressure after implementing the overall inversion scheme The multi-monitor inverted pressure sensitivity for the near and far offsets are shown in (a) and (c) respectively, determined by the best model. The estimated uncertainty, stdev, for the results in (a) and (c) are shown in (b) and (d) respectively. The multi-offset inverted pressure change for the 2004-baseline monitor time is given in (e), and the estimated uncertainty, stdev, for the result in (e) is given in (f). For well labels and marked fluid contacts, see Figure 7-2.

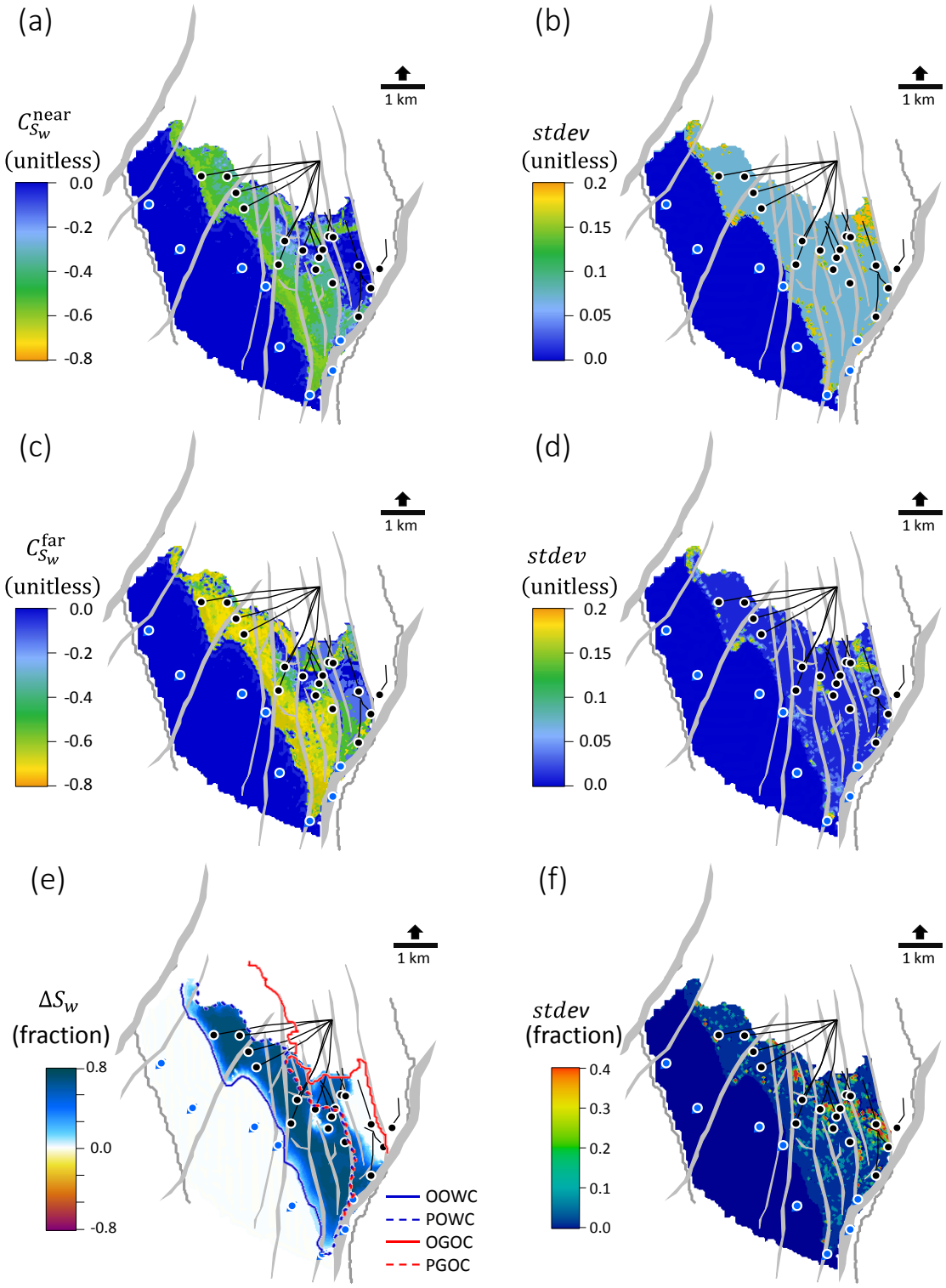

Figure 7-19 Results for water saturation after implementing the overall inversion scheme The multi-monitor inverted water saturation sensitivity for the near and far offsets are shown in (a) and (c) respectively, determined by the best model. The estimated uncertainty, stdev, for the results in (a) and (c) are shown in (b) and (d) respectively. The multi-offset inverted water saturation change for the 2004-baseline monitor time is given (e), and the estimated uncertainty, stdev, for the result in (e) is given in (f). For well labels and marked fluid contacts, see Figure 7-2.

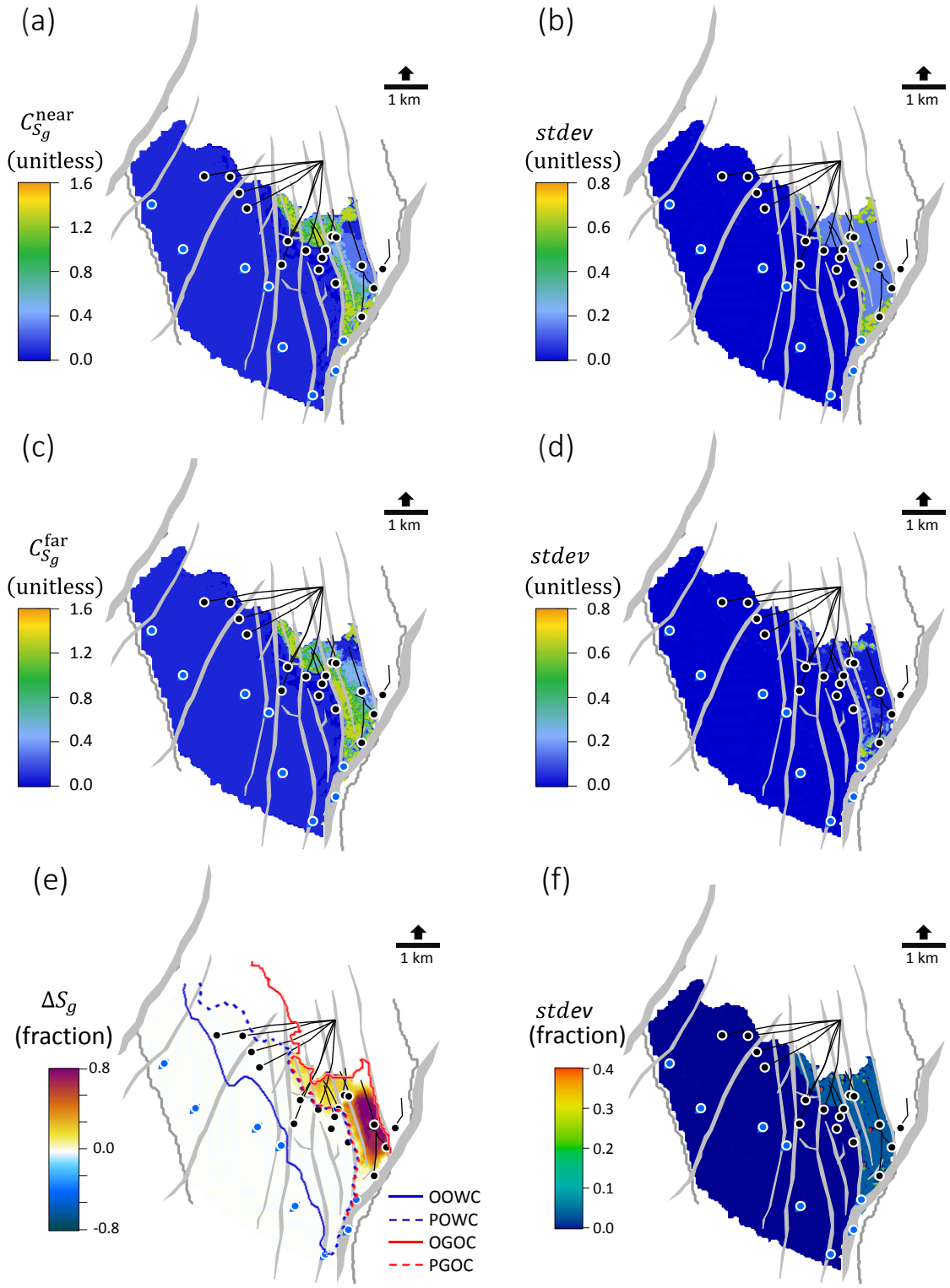

Figure 7-20 Results for gas saturation after implementing the overall inversion scheme The multi-monitor inverted gas saturation sensitivity for the near and far offsets are shown in (a) and (c) respectively, determined by the best model. The estimated uncertainty, stdev, for the results in (a) and (c) are shown in (b) and (d) respectively. The multi-offset inverted gas saturation change for the 2004-baseline monitor time is given (e), and the estimated uncertainty, stdev, for the result in (e) is given in (f). For well labels and marked fluid contacts, see Figure 7-2.

the 94 history-matched models, besides the reference model, (Figure 7-5 , Figure 7-6), are used to constrain the solution to the multi-offset inversion. The map-based inversion scheme combines 4D noise from different monitor data, as well as, from the near, mid and far offset stacks. It is necessary to also estimate the uncertainty in the inversion solution estimate (Equation 6-8), which is contributed mostly by noise in the data (Figure 7-3). Figure 7-18 shows the best model's inverted pressure sensitivity for the near and far stacks and the inverted pressure changes for the 2004-baseline monitor time, as well as their estimated uncertainties (i.e. standard deviation). Results for water saturation are shown in Figure 7-19, and for gas saturation in Figure 7-20.

Pressure sensitivity is strongest at the near offset (Figure 7-18(a)) and weakest at far offset (Figure 7-18(c)), the same for the 4D noise across the three monitor data used in the multi-monitor inversion. This also means that the uncertainty in pressure sensitivity is highest at the near offset (Figure 7-18(b)), and lowest at the far offset (Figure 7-18(d)). Since both pressure effects and the 4D noise are strongest and are of similar magnitudes at the near offset, the uncertainty in the inverted pressure changes (Figure 7-18(f)) mirrors the spatial variability of the noise for the near offset data (Figure 7-3). However, the inverted pressure changes (Figure 7-18(e)) honour the 4D seismic response (Figure 7-16 (b)) and are consistent with engineering constraints, due to the conditioning from multiple models. The uncertainty (Figure 7-18(f)) is up to 100% of the inverted pressure changes.

The sensitivity to saturation changes (Figure 7-19, Figure 7-20) is strongest at far offset and weakest at near offset, but the observed 4D noise (Figure 7-3) depicts the opposite. For any offset stack, the saturation sensitivity is also 20 times greater or more, than the pressure sensitivity. This explains the clear dominance of saturation effects even in the presence of the added noise (Figure 7-4(a) to (c)), leading to very high 4D signal to noise ratio. Since the influence of noise is very weak where saturations are concerned, regardless of offset, the estimated uncertainties are lower in magnitudes (less than 25%) than the inverted saturation sensitivities themselves. This is the same for the estimated uncertainties in the inverted saturation changes.

For the inverted water saturation changes (Figure 7-19(e)), areas with higher uncertainties (Figure 7-19(f)) of around 50% are associated to areas where either the

sensitivities at near, mid or far offset is near zero. This is due to a weak or a lack of 4D seismic signals on the 4D maps (Figure 7-4 (a) to (c)), relative to the magnitude of noise at these locations, particularly close to faults or small scale barriers in the simulation model from which the synthetic data was generated. For the inverted gas saturation changes (Figure 7-20 (e)), the uncertainty is around 10% (Figure 7-20 (f)).

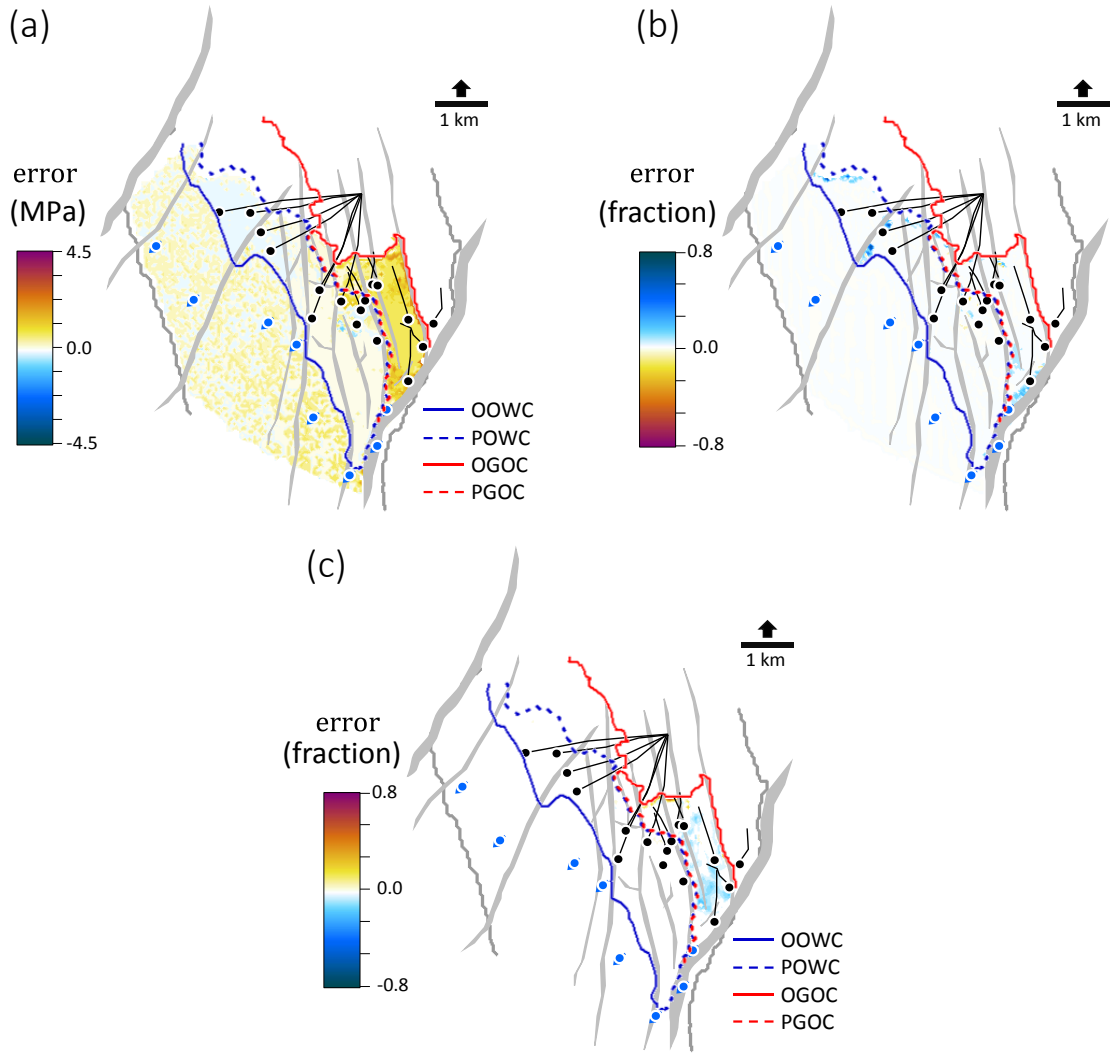

Figure 7-21 The effectiveness of the inversion scheme highlighted by the resulting error obtained by subtracting the depth-averaged maps of the dynamic reservoir changes simulated by the reference model, from the maps of inverted changes for the 2004-baseline monitor time, shown for (a) Pressure changes (b) Water saturation changes (c) Gas saturation changes. For well labels and marked fluid contacts, see Figure 7-2.

The inverted estimates of pressure and saturation changes for the 2004-baseline monitor time using the best C_P, C_{S_w} and C_{S_g} from the best model are then compared to the depth-averaged maps from the reference simulation model. Figure 7-21 shows the error (i.e.

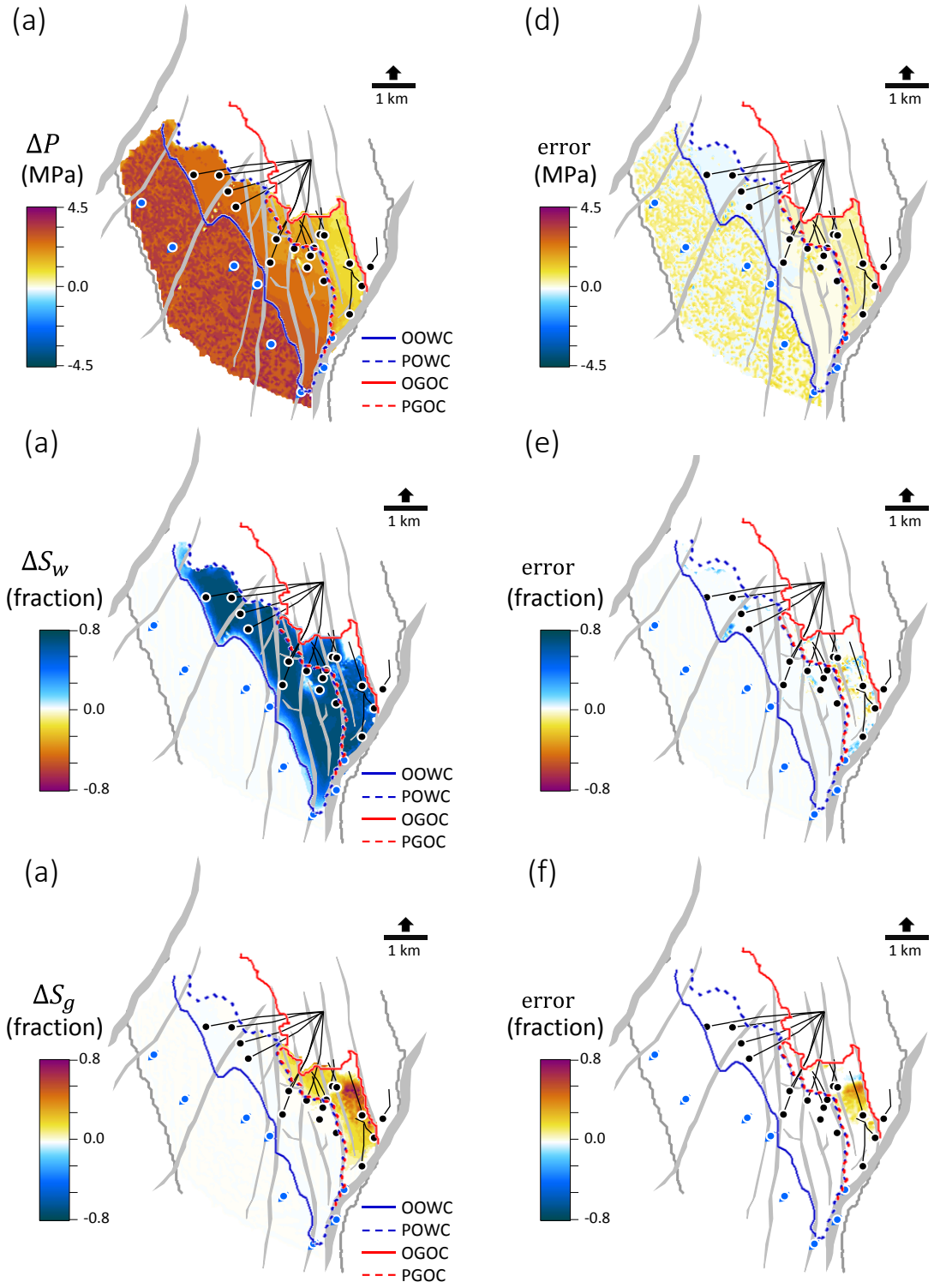

Figure 7-22 Results of the overall inversion scheme for the 2011-baseline monitor time. The multi-offset inversion results as determined by the best model are for (a) Pressure changes (b) Water saturation changes (c) Gas saturation changes. The error (i.e. difference) between the inversion estimates in (a) to (c) and depth-averaged simulations from the reference model are shown in (d) to (f) for the respective properties in (a) to (c). For well labels and marked fluid contacts, see Figure 7-2.

difference) which highlights the effectiveness of the inversion scheme with noisy 4D seismic data. The inverted estimates are lower in saturation changes (Figure 7-21 (b)

and (c)) by up to 0.1 in fraction, compared to the predictions of the reference simulation model. For pressure changes (Figure 7-21 (a)), weaker pressure decreases of up to -2.5 MPa error (in the gas leg) is estimated by the inversion compared to the reference simulations. Elsewhere, the error in inverted pressure change is around 0.4 MPa or less. The inverted estimates from the best model are not expected to match the reference model, as the static properties in both models are close but different (Table 7-2). It is however shown here that the inverted saturation changes are closer to the reference, than the pressure estimates. This is mostly due to the added noise which corrupts the already weaker response to pressure changes. Pressure is also sensitive to the slight differences in the static properties of both models, also true for gas saturation effects.

Figure 7-22 shows the inverted results for the 2011-baseline monitor time from the best model, which agree with the above findings. At this monitor time, only pressure increases occur, and the produced gas leg is also now waterflooded, which was not the case in the 2004 monitor time. The inversion scheme is able to separate reliably the various changes, and the error (Figure 7-22 (d) to (f)) with respect to the simulator results from the reference model are biggest for gas saturation and pressure changes. The error in pressure changes (Figure 7-22 (d)) is also smaller at the 2011 monitor time, than at the 2004 monitor time (Figure 7-21 (a)), due in part that only the 2006, 2008 and 2011 monitor data were used to estimate the sensitivity coefficients from the multi-monitor inversion, which fed into the multi-offset inversion. However, the ability of the inversion scheme to estimate the reservoir's dynamic changes across all 4D monitor times that are close enough to the truth (represented here by the reference model) is clear. The scheme can be viewed as a soft 'close-the-loop' through the use of multiple models, without directly updating the base model.

7.4 Summary

This chapter applied the map-based engineering-consistent inversion scheme which was introduced in Chapter 6 to a gas-oil-water system. A reference model was selected from one of the 95 models generated for the Heidrun field, from which simulator-to-seismic modelling created a realistic synthetic dataset for the Heidrun field by adding the observed 4D seismic noise to the modelled data.

- A preliminary assessment was performed for the multi-monitor inversion which estimates the sensitivity coefficients as spatially varying quantities. The multi-offset inversion which estimates pressure and saturation changes was also assessed.

- For the multi-offset inversion two cases are highlighted using noise-free synthetic data. The conventional inversion which assumes that the sensitivity coefficients are constant for the entire reservoir versus that which uses the spatially varying sensitivities derived from the multi-monitor inversion. Both cases solve the inversion by incorporating constraints based on a single upper and lower bound for pressure and saturation changes derived by computing the overall maximum and minimum from the 95 models. The inversion using spatially varying sensitivity coefficients performed much better and honoured the 4D seismic response. The case of constant sensitivity coefficients failed to reproduce the expected changes, particularly, where pressure and saturation changes overlap, yielding a leakage between the inverted pressure and saturation changes, with wrong polarity of change.

- For the multi-monitor inversion, two cases were tested on noise-free synthetic data. The inversion compared the use of three versus two 4D monitor data. In both cases, the inversion solution is constrained use a single upper and lower bound derived from prior calibrated sensitivities around wells for pressure, and in saturation dominated areas on the 4D seismic amplitude maps. Both cases gave similar results in terms of the overall magnitude and distribution of the inverted sensitivity coefficients. On comparing the result of using both cases in the multi-offset inversion, it was found that the three monitor case performs slightly better in its closeness to the simulation model maps, particularly for pressure change.

- After the preliminary assessment of the multi-monitor and multi-offset inversion, the constrained inversion scheme which also estimates uncertainties, was fully implemented on the Heidrun field. This used the noisy realistic synthetic data from the reference model, considered here to be the observed 4D

seismic amplitude data which represents the truth. Some findings and recommendations are summarised:

- The transformation of the 4D seismic amplitude response across multiple monitors into a single offset-dependent and spatially-varying sensitivity respective to pressure, water and gas saturation changes has been demonstrated via the multi-monitor inversion. The realistic synthetic data showed that the reservoir's sensitivity to gas saturation changes is strongest, followed by water saturation, and then pressure for the Heidrun field. This agrees with observations on the Heidrun field data in Chapter 3. Pressure sensitivity is strongest at the near offset and weakest at the far offset. The opposite is the case for saturation sensitivity. The sensitivity also varies spatially, capturing the reservoir heterogeneity as preserved in the 4D seismic response.

- At least two 4D monitor data are needed to solve for the sensitivity coefficients. It is recommended that all available 4D monitors, for which pressure and saturation changes are to be inverted for, should be used in the multi-monitor inversion. This gives more robust sensitivity coefficients which better represent the 4D monitor times. However, if the multi-offset inversion to follow is suitably constrained for engineering consistency, the need for this selection is unnecessary.

- The use of constraints, such as uniform upper and lower limits based on data calibrated sensitivities obtained prior to the inversion has proven effective in the multi-monitor inversion, particularly in the presence of 4D noise (which is different across the 4D monitor data, and also across offset stacks).

- A more robust form of constraints is exemplified by the use of multiple history-matched fluid-flow simulation models. These provided spatially varying maximum and minimum bounds of pressure and saturation changes to the solution of the multi-offset inversion at each 4D monitor time, and ensured engineering consistency at each seismic bin location.

- The quantitative integration of the reservoir engineering domain via multiple models, and the seismic domain via inversion lays the foundation for an effective model update via a joint 4D seismic-history matching procedure. The seismically-derived 4D attributes used in the history-matching could be either the inverted sensitivity coefficients from the best model, or the inverted pressure and saturation changes. Additionally, the best model identified by the multi-monitor inversion could be the starting point for direct model updating instead of the base (original) model.

- As an alternative to direct model updating, a soft "close-the-loop" was achieved by generating multiple history-matched simulation models, and using the constrained multi-monitor inversion to find the model out of the 95 models that best honours the observed 4D seismic response. This was achieved here, and the best model was found to be 97.8% close to the truth. The truth being an earlier chosen reference model from the 95 models, which was kept aside and was used to provide synthetic 4D seismic data for the inversion scheme.

Chapter 8

Conclusions and Recommendations

“The beautiful thing about learning is that no one can take it from you!”

-- unknown --

This chapter summarises the findings of this research on quantitative 4D seismic data interpretation for the quantification of pressure and saturation changes in clastic reservoirs, and then provides recommendations for future work that will enhance the efficiency and effectiveness of the workflow. The key objective of this thesis which is the enhancement of the data-driven inversion approach, the introduction of engineering-consistent constraints, and the analysis of uncertainties in quantitative 4D seismic data interpretation are examined, and the perceived limitations are prescribed as future recommendations.

8.1 Conclusions

The entire theme of this thesis demonstrates multiple data integration between the reservoir engineering and the 4D seismic data domain with direct consequences /application to seismic-assisted history matching. This was achieved at two fundamental levels: firstly, in the interpretation and inversion of 4D seismic data to quantify pressure and saturation changes in the reservoir, and secondly, in addressing more uncertainties in the acquired 4D seismic data by relating the spatio-temporal characteristics of two common offshore seismic acquisitions to the reservoir dynamic domain (see Figure 8-1).

In interpretation, quantitative estimates of the reservoir dynamic changes (pressure, and water and gas saturations) from 4D seismic data are often desired for reservoir management purposes. This is a challenge where pressure and saturation changes occur in the same place and their effects often compete, yielding an ambiguous 4D seismic response that is difficult to interpret qualitatively and quantitatively as being caused by either of the two effects. A first step in addressing this challenge is a quantitative measure of the reservoir's 4D seismic response to independent effects of pressure (increase and decrease) and fluid saturation (gas and water) changes; hence, a measure of the reservoir's sensitivity. In Chapter 2, a generalised rock-physics modelling is performed to build this understanding using standard 4D seismic attributes such as zero-offset amplitudes and time-shifts. This gives insights as to the complementary between 4D amplitudes and time-shifts, the specific nature of the reservoir's sensitivity at various magnitudes of dynamic changes, and the imbalance of sensitivity between pressure and saturation effects. Of further significance is the dependence of sensitivity on physical properties such as porosity, net-to-gross, and consolidation.

As the main focus of this research concerns 4D seismic data interpretation and its uncertainties, of greater concern is the pressure and saturation sensitivity measured directly from the acquired and processed 4D seismic data. This is of greater practical value as current measures are based on laboratory measurements on core plugs that have limited applicability to the in-situ field-scale reservoir response; and rock-physics modelling which are lacking in accuracy and replicability of the measured 4D seismic

response. In Chapter 3, a complementary technique for estimating pressure and saturation sensitivity is implemented which works by critically evaluating seismic and pressure-saturation measurements. This is possible in selected areas around and away from wells where pressure or saturation variations contribute predominantly to the observed 4D seismic response. Multiple monitor 4D seismic data are used to calibrate these areas as a function of field production time. This allowed the quantification of the sensitivity of the reservoir to pressure and saturation changes independently, at several monitor times. The technique uses both 4D seismic amplitudes and time-shifts from stacked (full offset) time migrated data acquired using towed streamer technology and is applied across a variety of producing North Sea clastic reservoirs. These fields included three normally pressured sandstones (Norne, Heidrun and Schiehallion fields) and a high-pressure-high-temperature (HPHT) sandstone (the Shearwater field). The results indicate that pressure and saturation sensitivity varies according to the geology of each reservoir, which favour rock-physics understanding. The purpose is to demonstrate a strategy by which the in-situ sensitivity can be reliably obtained from 4D seismic data. This gives a quantifiable understanding of different rocks, and provides a way of monitoring how the reservoir's sensitivity varies laterally, and also at different monitor times. Apart from non-repeatable noise, a limitation is that the quantified sensitivity is not fully laterally extensive, as only specific areas around or away from wells where an appropriately strong 4D seismic signal exists is used, which is in turn controlled by the production mechanisms of each field. In addition, lack of historical well pressure and repeated saturation measurements adds to the uncertainty.

In any quantitative 4D seismic study, the accuracy of the magnitudes of 4D seismic signals (amplitudes, time shifts or other 4D attributes) is often a concern. A joint workflow linking the seismic survey geometry and timings of shots of a towed streamer and permanent reservoir monitoring (PRM) acquisitions, to the spatio-temporal fluctuations of pressure and saturations in the Norne field reservoir under production is carried out in Chapter 4. This gives an interesting understanding of the uncertainties in the interpretability of the acquired 4D seismic data, beyond the multiple causes of non-repeatable noise, often tied to acquisition-geometry differences. Particularly, that conventional CMP stacking (i.e. averaging for post-stack data) which increases signal-to-noise ratio will be inadequate for 4D seismic data acquired when production

fluctuations occur during the shooting of seismic data. This is because the same CMP bin location will have been acquired at different times during the shooting, and therefore will have captured different reservoir changes. By averaging, there is a lack of truth in the resultant reservoir change.

Chapter 5 brings us to seismic modelling via 1D convolution and a migration operator on the Norne field simulation model, where it is observed that such reservoir fluctuations which occur during the shooting of the PRM and towed streamer monitor seismic acquisition creates a complicated spatio-temporal imprint on the pre-stack data, and errors when interpreting the 4D seismic data quantitatively. This signature does not translate into a clear post-stack seismic image of pressure effects, even when geometric non-repeatability is perfect. It is found that the true absolute reservoir changes could not be obtained, but instead a mixed version of reality which depends on the sequence and timings of the shots during the acquisition. Both pressure and fluid saturation changes are affected by this phenomenon – both suffer from lack of spatial location of the change, and quantification of the absolute value of that change. With fluid saturation changes, the main errors are concentrated around the fluid fronts, but with pressure the errors are more widely spread across field compartments due to its quick diffusive nature. The near, mid and far-offsets are found to sample both pressure and saturation changes differently and this affects the ability of time-lapse analysis to accurately separate changes of saturation and pressure. The outcome is a lack of accuracy in the measurement of reservoir changes using post-stack or offset sub-stacks from the 4D seismic data, as they are found to be in error. It is recommended that pre-stack 4D seismic data should be analysed using the time stamp of the acquisition within each CMP bin, and the data shot in a consistent pattern to optimise time coverage. This however has limitations for towed streamer acquisitions, which are of a considerably lower fold than PRM systems.

Intrigued with the quantitative integration of data from the reservoir engineering and seismic domain, a map-based inversion scheme for separating and estimating pressure and saturation changes from 4D seismic data is discussed in Chapter 6 and applied on the Heidrun field in Chapter 7. Inverse theory is applied using data-driven linear equations developed and validated for an oil-water-gas system within the ETLP group over the last 12 years. A common feature of my inversion scheme combines multiple

offset amplitude stacks (near, mid and far) to separate pressure, water saturation and gas saturation changes. A new feature, however, is the strategic use of repeated multiple monitor 4D seismic data, as a natural extension of the work carried out in Chapter 3 which bypasses the need for rock-physics modelling. Data acquired at different monitor times (three monitors used on the Heidrun field) are combined to invert for the laterally extensive reservoir's sensitivity. The estimated sensitivity is obtained for each offset stack and used as spatially varying weighting coefficients for pressure and saturation separation, which is shown to be more accurate and consistent, compared to using a single sensitivity value, as was the case in previous ETLP research. A weaker aspect of the multiple monitor data inversion is that it requires some prior knowledge of pressure and saturation changes at each monitor time, and this is obtained from a history-matched fluid-flow simulation model. The inversion scheme compensates for the inaccuracies in the original model by generating multiple reservoir models, obtained by global perturbation of static properties such as: lateral and vertical permeability and porosity (NTG). The models are simulated and qualified by their history match, and predictions from each of these models are used in turn in the multiple monitor inversion for the sensitivity coefficients. By generating multiple models, I address the uncertainties with using only one reservoir model (i.e. the model donated by sponsors), which may not be the best. Incorporating these into the map-based inversion also does a soft 'closing the loop', where a better model can be found based on the data misfit.

Apart from the reservoir engineering domain, uncertainties are also contributed by the 4D seismic data due to non-repeatable noise (and intra-survey fluctuations) which are different for the near, mid and far offset stacks, and are also different for each monitor 4D seismic data. The inversion scheme incorporates the noise uncertainty from each offset and for the monitor 4D seismic data, and outputs estimates of uncertainty in the solution of the inverted reservoir sensitivity, and also the inverted pressure and saturation changes.

In addition, the inversion problem is ill-posed as there is not enough information contained in the multiple offset 4D stacks (i.e. AVO stacks) to unambiguously invert for pressure and saturation changes (the determinant of the inversion matrix is zero); therefore it is fundamental for the inversion to incorporate a priori information that allows for an engineering-consistent solution. In this work, this challenge is resolved by

restricting the inversion solution space to known ranges of pressure, water and gas saturation changes. The restrictions are upper and lower bounds which are obtained a priori and could be either uniform (i.e. the same for each seismic bin location) or spatially varying. Uniform bounds are most common but have been found in this work to be inadequate to constrain each spatial location, particularly in noisy data. Such bounds are based on engineering material balance laws (for example, maximum and minimum water and gas saturation change) combined with bottom-hole-pressure measurements, if available.

Therefore, another key feature of my inversion scheme is the use of spatially varying upper and lower bounds, which addresses the pitfalls with uniform bounds. The spatially varying constraints for pressure and saturation changes are provided from the previously generated multiple history-matched fluid flow simulation models. The geologically consistent models honour material balance, flow conditions and well production history making the inversion solution at each seismic bin location more engineering consistent. The inversion scheme was successfully applied on a synthetic dataset built from the Heidrun field model and modelled with observed 4D seismic noise, where it was possible to analyse the reliability of the multiple monitor inversion for the reservoir's sensitivity, the pressure and saturation inversion, the robustness to noise, as well as the effectiveness of the multiple models constraints.

At least two 4D seismic monitor data are needed to solve for the sensitivity coefficients, but the use of more monitor data helps to reduce redundancy leading to more robust sensitivity estimates which can better represent any 4D monitor time. A minimum of three different offset stacks (near, mid and far) are needed to solve for the three dynamic changes, pressure, water saturation and gas saturation. Estimating pressure and saturation changes at each 4D monitor time (all together five monitors), when only three monitors were used to obtain the inverted sensitivity also demonstrated the robustness of the inversion scheme where the effects on the 4D seismic signatures are quite similar across monitor times, as was the case on the Heidrun Field. This remains to be applied on other only non-compacting sandstones, but it is expected that the multiple monitor approach is widely applicable to clastic fields. Other field types, such as carbonate and chalk reservoirs undergo compaction combined with changes in effective porosity during production. The requirement of non-changing effective porosity (which

predominantly determines the reservoir's sensitivity) in order to apply the multi-monitor inversion is invalid for these field types.

In applications to observed 4D seismic data, the challenge is that the generated models should be different enough to cover a wide range of uncertainties such that the observed 4D seismic signal can be explained within the bounds of predicted pressure and saturation changes from these models, but the models must be constrained by their history match quality, which in turn reduces the dispersion across the models. In addition, the bounds should not be too restrictive so as to give a higher degree of freedom to the solution of pressure and saturation space. This all depends on the confidence in the acquired and processed 4D seismic data, and in the generated models.

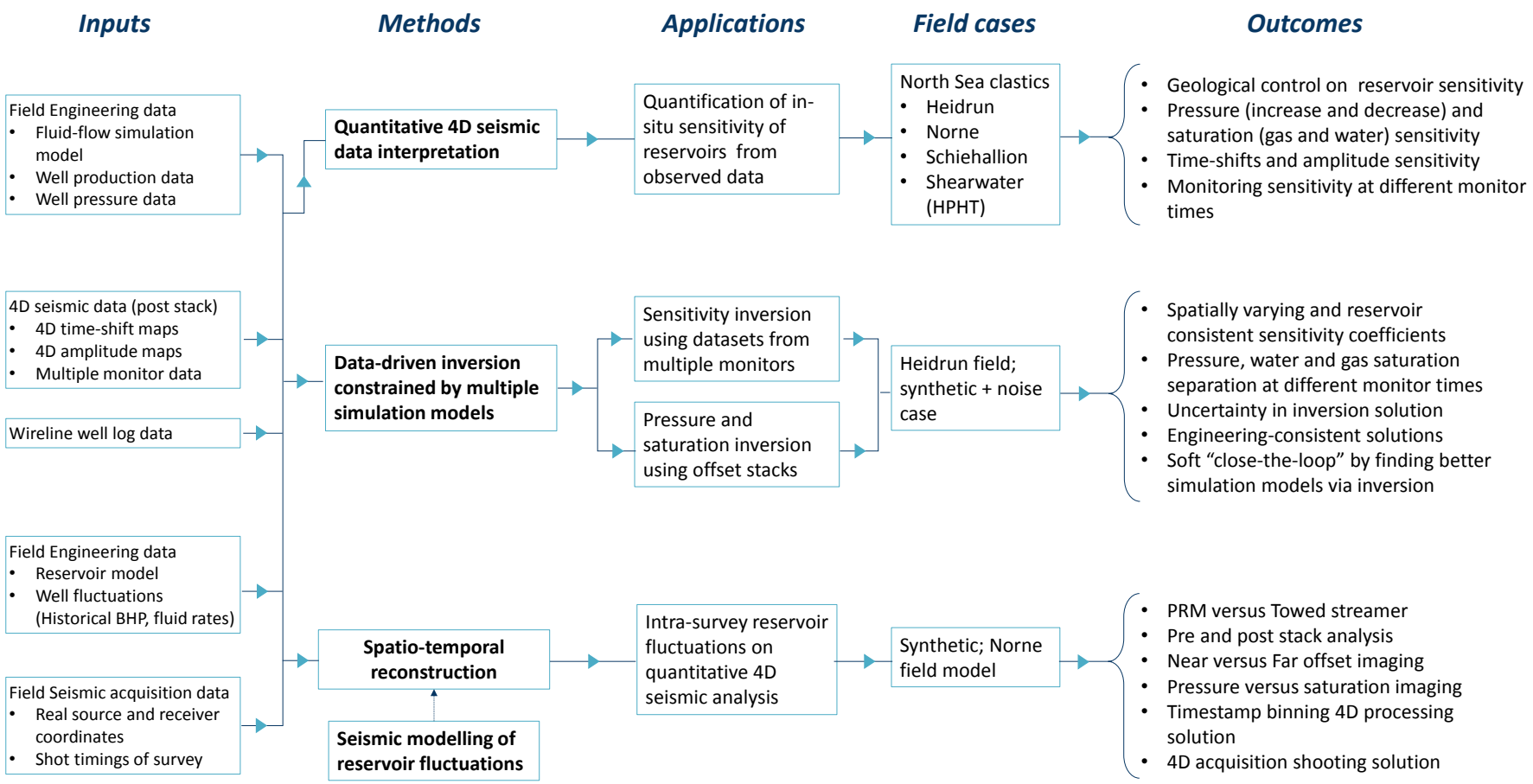

Figure 8-1 Summary of the accomplishments of this thesis.

8.2 Limitations and recommendations for future research

8.2.1 Key aspects of pressure and saturation quantification

In Figure 8-2 I summarise the main considerations for the separation and quantification of pressure and saturation changes in 4D seismic data. Some of these have been addressed (in bold) in this thesis, through the use of data-driven methods, but there is still much to be done in this area which are summarised below.

(1) Using different 4D seismic attributes:

Using two distinct 4D seismic attributes e.g. 4D seismic amplitudes as an interface property and 4D seismic time-shifts as an interval property can help to add further constraints to the inversion. Amplitude changes are caused by altered impedance contrasts in the vicinity of the bounding reservoir interfaces, and also depend on the reflection contrast of the reservoir interface. Such a response could therefore be influenced by local anomalies and intra-reservoir inhomogeneities. Time-shifts of seismic waves which have passed through the entire reservoir integrate the local velocity changes and can potentially provide a more robust measure of the average changes in the reservoir. In Chapter 2, it was shown that the reservoir's sensitivity quantified using amplitudes and intra-reservoir time-shifts are quite complementary. Through the field case studies in Chapter 3 where large intra-reservoir time-shifts of up to 3 ms and 1.7 ms were observed on the Shearwater and Norne field, respectively, it was also suggested that time-shifts are a more robust measure than amplitudes for these fields. In the inversion scheme in Chapter 6 and 7, only mapped 4D amplitudes were used, but intra-reservoir time-shifts can also be incorporated (Equation 6-1) still applies for each offset stack). Using time-shifts will depend how reliably these can be estimated from the 4D seismic data of the particular field, with respect to data quality (noise and resolution) and magnitude of the 4D seismic response. The 2D maps of the inverted sensitivity obtained using amplitudes and time-shifts can be compared side-by-side for each offset stack. Pressure and saturation changes can then be estimated as 2D maps using time-shift data and amplitude data separately, and the inversion results compared. Both results can also be normalised (for example, by taking the mean of the two results), to produce a

final estimate of pressure and saturation changes, constrained both by amplitudes and time-shifts.

(2) Using the linear/non-linear inversion equation:

Equation (6-1) shows the governing mathematical expressions relating the 4D seismic response to pressure and saturation changes through the reservoir's sensitivity terms. The inversion scheme used the linear approximation (Equation 6-1a) for the application on the Heidrun field in Chapter 7. The reasons for using the linear equation are also discussed in section 6.2.3, which depends on the magnitudes of pressure and saturation changes that occur across the monitor times of the field. This induced production will cause the 4D seismic response to lie within the linear or non-linear region in Figure 2-10 across the monitor times. If in doubt, then the quantified sensitivity (using Equation 2-23 and Equation 2-26) at each monitor time, as carried out in Chapter 3, will help to reveal whether to use a linear or non-linear equation. For the same location, if the calibrated sensitivities are of similar magnitudes between monitor times (i.e. less than 20% difference in sensitivity across all monitors), then the linear expression (Equation 6-1a) can be used. However, this calibration of sensitivity is usually localised, and may not always be representative of the entire reservoir. Thus, it is highly recommended to apply the inversion scheme using the non-linear equation (Equation 6-1b), and this may yield more accurate estimates of the reservoir's properties, both in the inverted sensitivity coefficients and in the inverted pressure and saturation changes.

(3) Using offset/angle gathers or timestamped post-stack 4D seismic data:

The inversion scheme in Chapter 7 has been applied using post-stack data (i.e. partial offset stacks of the near, mid and far offset) were conventional stacking has been done by common-midpoints (CMP) alone. In Chapters 4 and 5, the implications of intra-survey reservoir fluctuations was quantified to reveal NRMS errors of up to 7.5% between the near offset and far offset 4D seismic data which were stacked conventionally (Table 5-4). This adds to the inaccuracies in estimating pressure and saturation changes using offset stacks. If

a high quality and carefully processed 4D seismic dataset is available (i.e. NRMS < 10%), the use of pre-stack 4D seismic gathers instead of post-stack data might help to extract more accurate reservoir dynamic changes from 4D seismic data. Alternatively, as suggested in section 5.4.1, time binning of each trace within a CMP gather, and then stacking each group of time-binned traces separately can help reduce the error between timestamped stacks of the near, mid and far offset stacks (see Figure 5-20). The inversion can then be performed using timestamped and stacked offset data (also see section 8.2.5 for workflow).

(4) Bayesian formulation for uncertainty analysis:

In the application in Chapter 7, a deterministic inversion which accounted for uncertainties from the 4D seismic domain was implemented, however, a stochastic approach could instead be adopted by formulating the inversion scheme (section 6.2) within a Bayesian framework (see for example, Floricich, 2006; Buland and El Ouair, 2006; Veire et al., 2006; Fursov, 2015). This will allow the incorporation of the dependencies between different variables - 4D amplitudes, time-shifts, pressure/saturation, sensitivity coefficients, and allows the combination of data from different sources (wells, maps). For this, apart from 4D seismic data uncertainty, multiple simulation models will provide a priori statistical representations of pressure and saturation changes (a priori mean and standard deviation), and the uncertainty in well pressure/saturation production data (i.e. measurement error) can also be incorporated. Apart from the minimum and maximum values which was used as upper and lower bound constraints to the inversion carried out in Chapter 7, other statistical data such as the mean and standard deviation extracted from the multiple simulation models was not used in the inversion scheme. One other conventional way to incorporate constraints besides the use of upper and lower bounds, would be to introduce an a priori solution along with an a priori uncertainty for pressure and saturation changes. Here, the a priori solution and uncertainty represent the mean and standard deviation from the entire simulation models, respectively. The inversion objective is no longer to only minimize the fitness to the 4D seismic data accounting for data uncertainty, but also the closeness of the inversion solution to the a priori solution, with the a priori model uncertainty also taken into account (Menke, 1989). As the Bayesian scheme is well suited

for tracking uncertainties, from the multiple monitor inversion for the reservoir's sensitivity, to the final inversion for pressure and saturation changes, probabilistic maps of the inverted sensitivity and also the inverted pressure and saturation estimates can also be obtained.

(5) Volumetric inversion for thick reservoirs:

The data-driven approach in this thesis was performed on 2D maps which is quite appropriate for thin reservoirs. This definition of thickness is based on the seismic thickness of reservoirs which is dependent on the wavelength and frequency content of the seismic data at the target depth. Thus, depending on the seismic data quality, reservoirs of thicknesses of 10 to 70 m could be of half a wavelength cycle (i.e. peak to trough), which are considered seismically thin. Averaging across such a thin reservoir will not compromise the 4D seismic signals, as this can still be directly related to impedance changes, and thus, reflect the primary reservoir changes in pressure and saturation. On the other hand, seismically thick reservoirs are of a wavelength cycle or more. The reflectivity contrast at the top and base of the reservoir will have very different characters. Unlike thin reservoirs which are only affected by tuning effects (which can be catered for by using quadrature- phase difference seismic data to compute the mapped amplitudes), averaging over a thick reservoir introduces interference, tuning and side lobe complexities (Johnston, 2013). The averaged 4D signals can no longer represent the primary reservoir changes in pressure and saturation due to too many destructive and constructive seismic events within the thick reservoir. For reservoir changes such as pressure, which has a long wavelength spatial component, averaging the 4D seismic response across the entire reservoir will smear the signals where competing effects of pressure and saturation changes occur. The smearing also applies to water and gas saturations, as such effects generally concentrate on the bottom and top of the reservoir, respectively, depending on pressure gradients, gravity, mobility ratios and reservoir heterogeneity.

To apply the inversion scheme to thick reservoirs, the 4D seismic signals at the top and bottom reservoir interfaces can be computed separately, but this does not neglect the need for a volumetric inversion in three dimensions (3D).

Figure 8-2 Summarising the key aspects for an engineering-consistent pressure and saturation inversion from 4D seismic data. In bold are the key data-driven features of this thesis.

The inversion can be extended to 3D volumes if the inversion is performed inside the simulation grid. This is quite useful as most producing fields have multi-layered reservoirs. Performing the inversion on the simulation grid, is however a challenge, due to scale inconsistencies between the vertical and lateral resolution of seismic data and the irregular simulation model grid. This will involve transforming a band limited continuous information (the 4D signal extracted from 3D seismic data) into layered blocky information.

As of yet, the data-driven method which can use both 4D seismic amplitudes or time-shifts attributes have been applied on 2D maps, and it is not straightforward to directly transfer such attributes unto the reservoir simulation grid. Model-based techniques, however, have achieved this by inverting the 3D seismic traces to elastic properties via rock-physics inversion. Thore (2011) demonstrates a typical rock-physics based but layer-consistent inversion which requires a dense number of wells across the field to define the layering. Porosity and NTG wireline logs are used to define the blocky layers based on the vertical reservoir grid (since the vertical resolution of the seismic data is limited), and the layering is geologically compatible such that permeable layers and shaly layers are clearly delineated in the blocked logs. Inversion for elastic properties: density, P-wave velocity and S-wave velocity changes along the blocky layers are performed for seismic traces at wells using a simulated annealing technique based on rock-physics. The elastic properties could later be transformed into changes of pressure and saturation via a second inversion. The inverted property changes at the well positions are then extended to the rest of the seismic dataset by using a conjugate gradient algorithm to perform the inversion of each trace. The full inverted elastic property changes can then be in-filled into the reservoir grid, first by down-scaling and then up-scaling. The down-scaling uses an intermediate mapping object called Voxet which has the lateral resolution of the seismic data and the vertical resolution of the reservoir grid (i.e. block of layers of the Voxet corresponds to the inversion layers). The inverted properties are transferred to the Voxet, and lateral up-scaling of the Voxet to the reservoir grid is then performed, which has its associated loss of resolution.

Although Thore's (2011) model-driven procedure addresses the loss of vertical content associated with the data-driven map-based approach, it is however compute-intensive and complex, and defeats the purpose of readily available and reliable pressure and saturation change maps for quick decision making. From a reservoir management point of view, the 2D maps of inverted pressure and saturation changes from the data-driven technique implemented in this work are useful for monitoring sweep efficiency, defining the locations of new infill wells, identifying major inconsistencies in the reservoir model and accelerating joint history matching of production and seismic data. However, as we continue on the path of better quantitative integration between the 4D seismic domain and reservoir engineering domain, (for example, in seismic history matching), the transfer to the reservoir grid will become common place.

8.2.2 Limitations for the applicability of the inversion scheme in Chapters 6 and Chapter 7

The inversion scheme described in Chapter 6 and implemented in Chapter 7 is formed of two main parts - the engineering domain from which multiple history-matched simulation models are generated, and the seismic domain from which 4D seismic data are provided for the inversion which is of two steps. Step 1 is the multi-monitor inversion which combines (a) multiple monitor 4D seismic data for each offset stack (near, mid and far offset) and (b) simulated pressure and saturation changes from the multiple simulation models, to estimate (c) the reservoir's sensitivity as a spatial 2D map per offset stack. Step 2 is the multi-offset inversion which combines (a) multiple offset stacks (near, mid and far offset) of 4D seismic data for any monitor time and (b) the reservoir's sensitivity obtained from step 1, to estimate (c) the reservoir's pressure and saturation changes as a spatial 2D map at the monitor time. The limitations for the inversion scheme concern the available dataset: the availability of offset stacks of 4D seismic data at different monitor times; the availability of a geologically-consistent simulation model from which multiple models can be generated; and the availability of historic well production measurements for qualifying the match of the simulated

production data to historic production data. Here I note the limitations due to data availability and offer possible alternatives.

(1) *Only a single monitor 4D seismic data has been acquired on the field*:

In this case, the multi-monitor inversion (Equation 6-2) becomes a single-monitor inversion to obtain the sensitivity coefficients spatially. This single-monitor inversion is applicable if only a maximum of two types of effects have occurred in the reservoir. To clarify, the two types of effects imply pressure changes accompanied with either water saturation changes alone or gas saturation changes alone - so a two fluid-phase system. For example, depleting a HPHT gas condensate reservoir above dew point will only induce pressure changes accompanied with some saturation changes due to gas condensate displacement. Another example would be producing an oil-water reservoir above bubble point pressure - so the only changes that occur are pressure and water (or oil) saturation. The inversion scheme which applies multiple history-matched simulation models is still applicable for this case of a single monitor data.

(2) *If an original (base) history-matched simulation model is not available for the field:*

In this case, a spatial 2D map of the sensitivity coefficients cannot be obtained. However, by using a single value for each of the sensitivity coefficients (for example, a mean value as shown in Figure 7-7), pressure and saturation changes can still be estimated as a spatial 2D map. This was the case carried out in Section 7.2.2; see Figure 7.14 (a) to (c)). Alternatively, this single value of sensitivity can be obtained by least squares inversion (an example shown in Equation 1-14). Magnitudes of pressure and saturation changes, as well as the 4D seismic attribute changes are extracted around the well locations, and combined. This was the approach by Floricich (2006). In addition, it is necessary to constrain the multi-offset inversion which uses this single value of sensitivity, but spatially varying bounds in the form of maximum and minimum pressure and saturation changes defined for each spatial location can no longer be applied as inversion constraints. This is because these spatial constraints can only be obtained from multiple simulation models. Since a simulation model is not available, then the alternative is to apply a uniform bound constraint based on a

single minimum and maximum value of pressure and saturation changes. This was the case applied in section 7.2.2, but the results can be rather poor (see Table 7-1 and Figure 7.14 (d) to (f)). For pressure bounds, this can be derived from well pressure measurements by taking the maximum and minimum pressure change at the wells as this is where the biggest pressure changes occur. For saturation bounds, this will be based on material balance laws, using some practical maximum for saturation changes. For example, maximum water saturation changes can be calculated as $(1 - S_{wc} - S_{or})$, where S_{wc} is the connate water and S_{or} is the irreducible (or residual) oil saturation, and minimum taken to be zero or the negative of the maximum water saturation. Bounds for gas saturation changes could have similar limits as that for water saturation changes.

(3) If there are no usable well production/pressure measurements in the field:

It is unlikely that a field under 4D seismic surveillance (i.e. at least one monitor survey has been acquired) will lack usable well production data. Again, in this case, the sensitivity coefficients cannot be quantified at every spatial location, but its calibration is restricted to specific locations using Equation 2-23 for amplitudes and Equation 2-26 for time-shifts. This approach was carried out in Chapter 3 using multiple monitors of 4D seismic data, which, depending on production activity, gave the possibility of obtaining both saturation sensitivity and pressure sensitivity at the same location, but at different monitor times. This practical application on four fields was limited by the lack of well pressure measurements for all fields, but history-matched simulation models where available for all fields, which helped to provide both pressure and saturation changes at specific locations around and away from injectors and producers. The saturation changes around producers can also be estimated based on the magnitude of production data such as producing gas-oil ratio and water-cut measured in the producers (Floricich, 2006).

If these production data are not available and there are no repeated formation tester saturation logs, then the magnitude of saturation changes can be calculated using material balance equations (Dake, 1997). This type of model excludes fluid flow inside the reservoir, and considers fluid and rock

expansion/compression effects only, in addition, of course, to fluid injection and production. This requires knowledge of the reservoir which is field dependent: formation volume factor for gas/oil/water; rock (pore) compressibility; fluid (oil, water, gas) compressibility; pressure change (baseline – monitor time); cumulative oil, water, gas injected and produced; cumulative aquifer influx; cumulative producing gas-oil ratio; solution gas-oil ratio; preproduction (i.e. baseline) gas cap size, original oil in place; reservoir temperature, bulk volume and pore volume; density of reservoir fluids; and sand porosity. Also, if there are no pressure data for wells, material balance calculations can help to estimate pressure (Dake, 1997). This is most appropriate for an isolated compartment of the reservoir, but such an approach is highly biased.

After this, one can then estimate the sensitivity, and compute the mean and standard deviation of pressure sensitivity and also saturation sensitivity. This mean and standard deviation will be based on the contribution from multiple (or single) monitors and the contribution from various locations calibrated for separate effects of pressure and saturation. The inversion scheme can then use this computed mean of sensitivity (i.e. a non-spatially varying sensitivity) to estimate pressure and saturation changes at each spatial location (this was the case carried out in section 7.2.2, see 7.14 (a) to (c)). The computed standard deviation mentioned above signifies the variation in sensitivity across monitor time and across the locations calibrated. For example in Figure 3.22, the spread from the mean of sensitivity for each field is this variation in sensitivity, likewise, in Figure 7-7. This spread can also be incorporated as uncertainty in the inversion. In this case, the inversion using only the mean of sensitivity (i.e. one value for all spatial locations) is best carried out within a Bayesian framework to account for the variation in sensitivity computed as the standard deviation from the mean.

(4) If there are no available well production/pressure measurements in the field, no history-matched simulation model for the field, and not enough information for material balance calculations:

In this case, the data-driven approach in Chapter 3 cannot be carried out for the field. However, one can use the database of quantified sensitivity (Figure 3-22) based on one of the fields that can be considered an analogue to the new field in question. Alternatively, a model-driven approach should be sought. The sensitivity can be estimated by rock-physics modelling using a range of expected pressure and saturation changes which was carried out in its simplest form in Chapter 2. For reservoir applications, rock physics modelling requires petrophysical well log calibration and laboratory-based measurements on dry cores, with a variety of rock-physics models to choose from for a reservoir-based parameterisation (Briceno, 2017).

8.2.3 Recommendations for the intra-survey seismic modelling in Chapters 4 and 5

As the analysis of intra-survey reservoir fluctuations in Chapters 4 and 5 is a first, it was necessary to strip the seismic modelling down to its simplest form; a modified 1D convolution at a fixed angle of incidence, and an applied migration operator. However, future studies of this problem will need to consider the limitations behind the assumptions discussed in Section 5.2.1. More sophisticated seismic modelling such as Ray-tracing methods (for example, Burnes et al., 2002) or Finite difference (FD) elastic modelling (for example, Thore, 2006; Arts et al., 2007) in the pre-stack domain can now be considered. However, it will still be necessary to model using a homogenous overburden so as not to introduce any bias in the modelling results due to overburden complexity.

As a direct seismic modelling method, FD captures the different wave propagation effects, and source and receiver directivity that influence amplitudes. Such effects include spreading, reflection and transmission in discontinuities, diffractions, scattering, and focusing and defocusing. Pre-stack elastic FD modelling thus generates the closest response to wave propagation through the subsurface. For both the PRM and towed

streamer surveys, the seismic shot records at the baseline and monitor acquisitions obtained from FD modelling, can undergo typical steps in 4D seismic processing workflows (for example, Figure 8-6(b)), and thus will inherit the processing and imaging artefacts, in close realisation to observed seismic data. Although seismic acquisitions and processing/imaging algorithms aim to generate a clear and reliable seismic image at the reservoir interval, it is likely that some unwanted noise are left untreated in the final processed seismic data. The curiosity behind applying the FD modelling method is to investigate the intra-survey reservoir fluctuation problem and its significance in a realistic 4D seismic dataset. However, it will no longer be possible to separate AVO response, geometric non-repeatability errors and the intra-survey impact. The 4D seismic amplitude response at the reservoir interval will thus be affected by all of these.

The shot gathers at the baseline time is modelled using (1) its acquisition geometry, (2) a wavelet, and (3) the 3D earth model (V_P, V_S and ρ) at the pre-production state of the reservoir. The added complexity with the monitor survey is that it requires a dynamic 3D earth model (Figure 8-3). For simulating a shot record at a shot point, the FD modelling could use the 3D earth model (V_P, V_S and ρ) derived from the simulation model (static and dynamic properties) for the shot time corresponding to that shot point. Thus, within the timeframe of the monitor acquisition, each shot time can be considered as a monitor survey with the same geometry but with a different earth model. The difference between the earth models at each shot time is dependent on the production fluctuations during the acquisition. For simplicity, the elastic properties (V_P, V_S and ρ) in the homogenous overburden remains unchanged at the baseline and monitor time. So, FD modelling will generate N_{time} shot gathers; N_{time} being the total number of shot times (associated with the shot points) in the monitor acquisition. For the monitor survey of the towed streamer, N_{time}= 16,047 and for the PRM survey, N_{time}= 44,589 (Table 4-2). For the baseline, FD modelling will also generate N_{shot} shot gathers; where N_{shot} is the total number of shot points at the baseline acquisition. Since the baseline survey is assumed to be acquired at pre-production it uses only one earth model. The FD algorithm also requires an extended earth model with a regular Cartesian grid. As the fluid-flow simulation model is built with irregular corner-point geometry, its grid

must be converted to the Cartesian grid, with cell sizes of less than 1 m to minimize numerical dispersion effects.

The shot gathers from baseline and monitor are sorted according to CMP locations on a common grid and are processed (for example, using the workflow in Figure 8-6(b)). Pre-stack migration (e.g. Kirchoff time migration, Gray and May 1994; Sun et al., 2000) is applied on sorted offset gathers. The RMS velocities for pre-stack migration are derived from interval velocities based on the respective earth models. The complexity for the monitor data is that the shot gather for each shot point has been modelled using a dynamic earth model which is different for each shot time. To avoid this dilemma, the FD modelling can be repeated for the entire monitor acquisition geometry using a different earth model at a time (Figure 8-3).The time corresponds to each shot time of the monitor survey, so that the FD modelling is repeated for the total number of shot times, N_{time}. This way, by using the earth model for each shot time, pre-stack migration can be performed on the entire data modelled for that shot time. This means that within the monitor acquisition, seismic data over the entire acquisition/reservoir area is obtained and processed for each shot time.

Outputs for the monitor survey are pre-stack migrated CMP gathers for all shot times at each location on the grid. Using this common CMP grid of the baseline and monitor geometry obtained through processing, spatio-temporal binning combines the monitor outputs. Note that at each CMP location on the common grid, the time of shot from the monitor survey must also be known. Similar to the workflow in Figure 4-13, the CMP gathers at a particular location that do not correspond to the time of shot for that location are removed. The resulting seismic data will thus have the correct migrated CMP gathers at the correct location that the gathers were imaged. Both the baseline and monitor seismic data are then stacked according to different offset/angle groups, to obtain AVO stacks (near, mid, far and full offsets).

In theory, the proposed workflow (Figure 8-3) appears promising, but in practise the parameterisation and implementation of the FD modelling is compute intensive and very time consuming. The workflows (Figure 4-13 and Figure 5-2) implemented for the intra-survey analysis take less than 3 months combined for both the towed streamer and

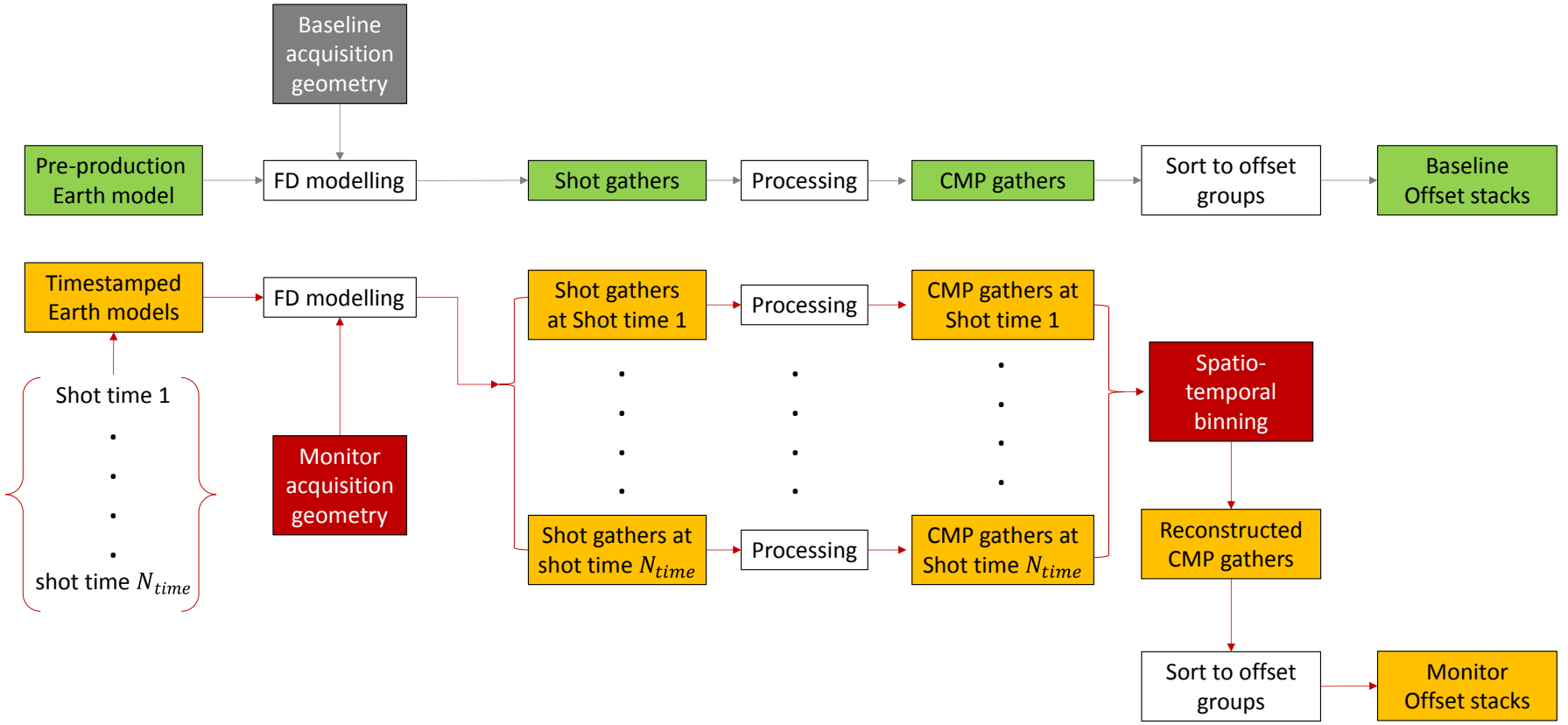

Figure 8-3 Recommended workflow for future study of the intra-survey reservoir fluctuation problem considering seismic wave propagation effects and geometric non-repeatability. Instead of 1D convolution followed by a migration operator, pre-stack elastic finite difference (FD) seismic modelling, followed by processing (which includes pre-stack time migration) is proposed. FD requires an earth model containing the elastic properties (P-wave and S-wave velocity and density). For simplicity, the overburden and underburden in the earth model are homogenous, and the overburden does not change. The reservoir's elastic properties is heterogonous, and is derived from the simulation model (static and dynamic). At baseline time, the earth model is simply based on the pre-production state of the reservoir. At monitor time, the dynamic behaviour of the reservoir fluctuates during the acquisition, requiring an earth model for each shot time, which in turn dictates the number of times FD modelling is run. This sets the order for the CMP-based processing using a common grid for the baseline data and monitor data (at each shot time). The time of shot at each midpoint location of the grid should also be known. Spatio-temporal binning uses this grid to reconstruct the monitor seismic data. This is achieved by keeping only the timestamped CMP gathers that are located on the common grid with the correct time of shot associated with that location.

PRM acquisitions, whereas, the FD modelling and processing workflow in Figure 8-3, using a powerful cluster system, are expected to take a minimum of 20 times the above mentioned for one type of survey, as it will have to repeated over the entire area with a different dynamic earth model for each shot time of the monitor acquisition.

Perhaps, the 1D convolution seismic modelling combined with a migration operator in Chapter 5 (Figure 5-2) is a more practical approach. Amini (2014) shows that 1D convolution including a range of incidence angles coupled with a migration operator, yields similar post-stack (full stack) seismic results to finite difference seismic modelling on a 2D line (Figure 8-4). This observation is however confined to thin reservoirs (30 to 100 m) and by modelling using the first two assumptions in Section 5.2.1.

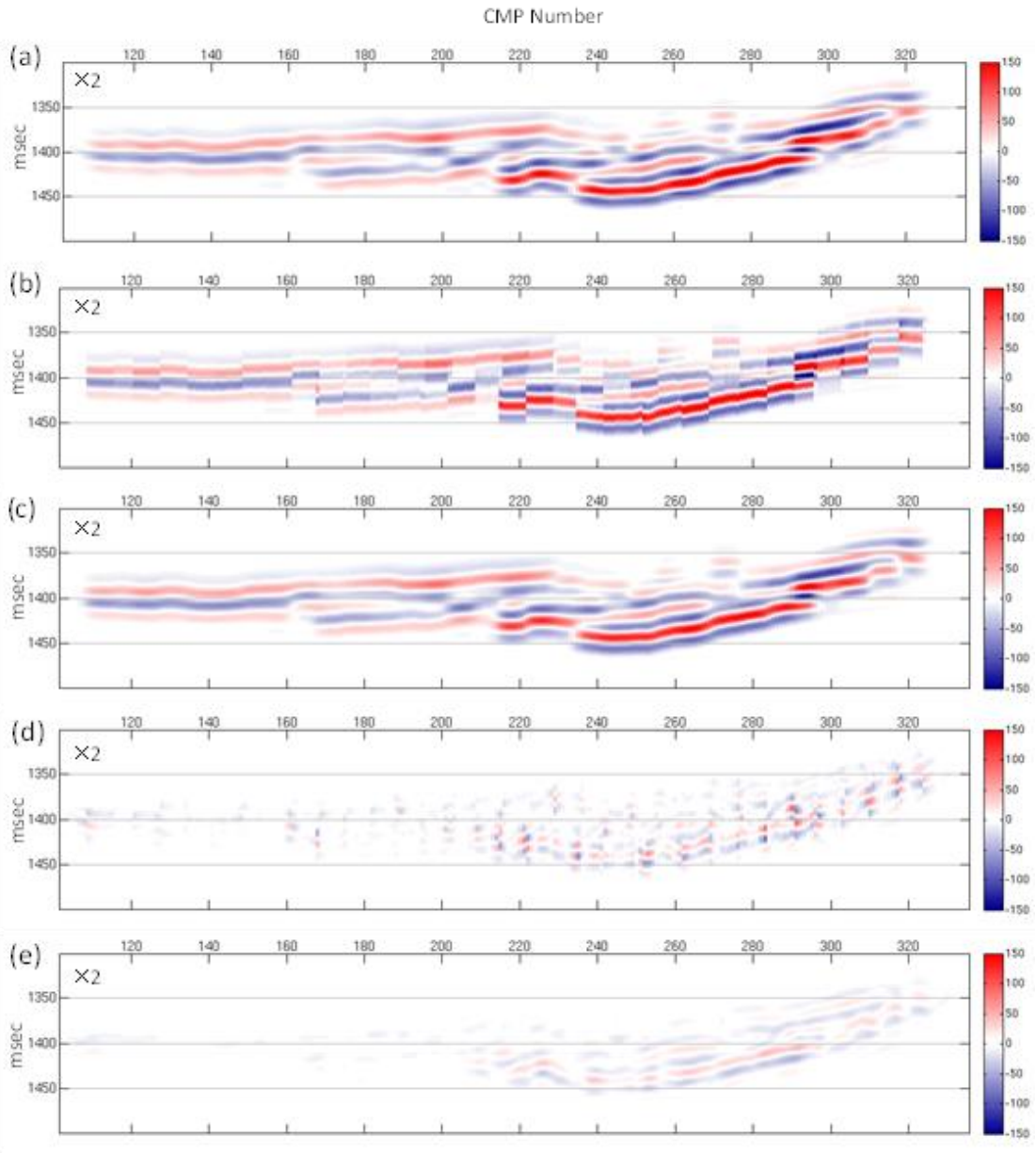

Figure 8-4 Seismic modelling comparison between finite difference (FD) for a single source and 2.5 km streamer configuration, and 1D convolution in terms of the monitor-baseline noise free 4D seismic response on post-stack (full offset) data; (a) the 4D seismic section from FD, (b) the 4D seismic section from ordinary 1D convolution, (c) the 4D seismic section from 1D convolution after application of the migration operator; it is visually similar to the section from FD modelling; (d) the difference between (a) and (b), (e) the difference between (a) and (c). To highlight the differences between the respective 4D seismic responses, the 4D amplitude in the difference result is multiplied by two, after Amini (2014).

8.2.4 Making post-stack 4D seismic data interpretation reliable by 4D timestamp binning

In 4D processing, monitor and baseline traces are binned using a common grid based on geometric criteria (for example, monitor and baseline traces with similar source and receiver positions) or on the basis of minimum azimuth difference (Figure A-2) or by selecting monitor traces closest to the bin centre of the baseline CMP bin. These are necessary steps in improving 4D data repeatability on the basis of spatial consistency, however, the complexities of intra-survey reservoir fluctuations are not considered. To cater for this, the timestamp binning strategy discussed in Chapter 5 can be embedded into 4D processing workflows. Figure 8-5(a) shows a proposed workflow for the time-binning of monitor data using the shot times and Figure 8-5(b) illustrates where this time-binning step could be applied within a typical 4D processing workflow. A way to embed this in such processing workflows would be to perform time-binning just after CMP binning. So, within each CMP bin, monitor traces are sorted based on the similarity of the time each monitor trace was shot. The criteria for similarity would be based on, for example, traces shot a few days apart. If wells are monitored during the acquisition, then the time interval for binning can be distributed according to the periods of significant production fluctuations. This time interval can also be irregular over the time frame of the monitor acquisition. This is in effect, a secondary binning that uses the shot timestamp of the monitor traces to address the temporal aspects of the 4D seismic signal as a result of intra-survey reservoir fluctuations.

The processing steps that follow timestamp binning will need to be applied to each group of time-binned traces within each CMP bin. The final stack at the end of the processing is thus specific to a timestamped group. Alternatively, one can implement timestamp binning at the end of the processing sequence (i.e. after pre-stack migration, and before stacking), however, it has been strategically placed in its current position of the processing workflow Figure 8-5(b). For example, it is suspected that acquisition footprints in 4D seismic data could be reduced after timestamp binning, thus, making "Footprint removal" unnecessary, however, it may still be best to perform timestamp binning as the last processing step. "*Although binning is used in 4D (and 3D) processing, it is not the only process that needs to be considered when analysing the total effect of intra-survey changes. Indeed, all multichannel processes that combine*

data recorded at different times need to be included as well. These include data regularisation, noise removal, and, most of all, migration.

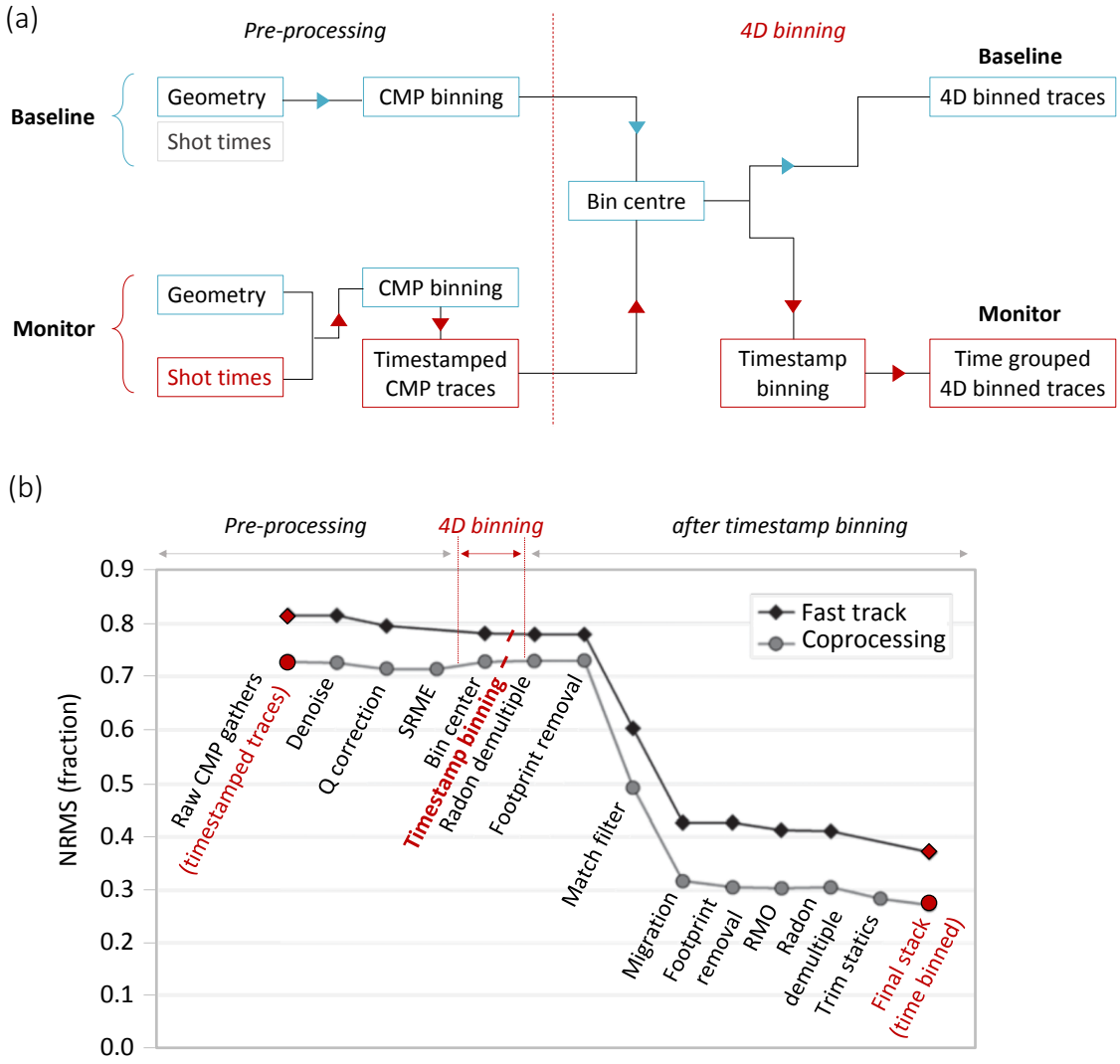

Figure 8-5 ***(a)*** *Baseline and monitor processing sequence for time-binning of the monitor data. Only the shot timestamps of the monitor data are required for 4D analysis. The 4D binning is not just a geometric (or spatial) aspect, but also considers the temporal aspect of the monitor acquisition.* ***(b)*** *A typical 4D processing workflow showing an example application on data from a Gulf of Mexico field (modified after Helgerud et al., 2011). 4D processing quality control for each processing step are tracked using NRMS values calculated between monitor and baseline seismic data (0-perfectly matched traces and 2- anti-correlated traces). A fast-track strategy helps to evaluate repeatability issues in the data and to produce early interpretation products. Coprocessing however results in better repeatability and less interpretation uncertainty. In the workflow, I have highlighted (in red) when my proposed timestamp binning should be implemented, and it is expected that this will improve the repeatability. The final stack is not a conventional CMP binned stack, but many stacks representing each common timestamp group within a CMP bin (see also Chapter 5, section 5.4)*

The requirements for those processes also need to be addressed, not least with respect to spatial sampling. For these reasons, any attempt to examine or ameliorate intra-survey effects would need to defer timestamp binning until the final step in processing, i.e. after (prestack) migration. The migration would also need to be performed shot by shot, and without summation across different shots. Some multichannel processes such as common receiver noise removal or Radon demultiple would also need to be excluded if the acquisition time of the traces in the gathers is too large. In addition, spatial sampling will need to be sufficient within each time bin used for the analysis, while the length of the (time) bin should be short enough that intra-survey effects can be neglected". (H. Jakubowicz, Personal communication, 4 July 2017).

The vertical axis on Figure 8-5(b) shows the improvements in 4D seismic data repeatability (NRMS) at each completed processing step. It is expected that the proposed 4D timestamp binning will improve the data repeatability across both Fast track and Coprocessing routes, but as of yet there is no telling by how much.

The shot timestamp of the baseline acquisition is not necessary if the baseline seismic data was acquired prior to production start, thus, the reservoir is in pressure equilibrium at this time. For mature fields, however, it is common for an older monitor survey to be assigned as the baseline (or reference), when, for example, the pre-production baseline survey was not a 4D dedicated survey. This is usually the case where more advanced acquisition technology, for example, from towed streamers to ocean-bottom-seismometers (nodes, OBN, or cables, OBC) has been implemented after production start-up. In this case, the reference monitor shot timestamp should also be considered.

In addition to this, it is suspected that if time-binning of the traces is performed before CMP stacking, this can help reduce the impact of other non-production effects such as water velocity changes and tidal variations which can fluctuate independently during monitor surveys. MacKay et al. (2003) show examples where temperature changes in a deep-water location introduce significant cross-line statics within a single survey. Baseline and monitor surveys are subject to this, and such non-production effects causes misalignments of long-period free surface and water-bottom multiples (which are in effect, non-repeatable) between monitor and baseline seismic data, which in turn produces a time-shift bias that depends linearly on the difference in tides and water

velocity between surveys. The resulting misalignments create artefacts that interfere with 4D seismic data interpretation. Calvert (2005a and 2005b) develops a method that removes multiple differences from observed 4D seismic data by shooting one (or both) of the surveys twice at different tidal or two-way water time states and by deriving an operator that removes the multiples on the 4D (monitor-baseline) seismic data. Hatchell et al. (2008) correct for this misalignment by using the correlation between water velocity differences and observed 4D seismic time-shifts between monitor and baseline.

As variations in tides and water velocity are of a temporal nature, it is common practice to measure the sea tidal states and water velocity during the shooting of the surveys. Timestamp binning can then be performed on the acquired seismic data (monitor or baseline), and tidal and water velocity corrections applied using the measurements taken at similar times to the shot timestamp groups of the seismic data. This will thus help to align multiples (and also primaries) in baseline and monitor seismic data and improve 4D seismic data repeatability. At later processing steps, the baseline (or assigned reference monitor) seismic data can be stacked conventionally according to CMP bins only. However, in order to address intra-survey reservoir fluctuations, the subsequent monitor data can be resorted into timestamp groups in agreement with production fluctuations time intervals.

Finally, from the perspective of seismic history matching, timestamp binning of 4D seismic data also addresses the timescale issues between the 4D seismic domain and the reservoir engineering domain. As the 4D seismic data is acquired over weeks or months, timestamp binning reduces uncertainties when comparing the acquired post-stack seismic data to synthetic post-stack seismic data modelled using the instantaneous predictions from the flow simulation model (see also section 5.4).

8.2.5 *An inversion scheme for "closing the loop" via seismic assisted history matching*

The inversion scheme (see Figure 6-2) which embodies the quantitative integration of the reservoir engineering domain via multiple models, and the seismic domain via inversion lays the foundation for model updating using a joint 4D seismic-history matching procedure (Figure 8-7). Calibrating the 4D signals via the inversion scheme, before running a history matching, helps to reduce incorrect information into the matching. This will help to improve the predictive capability of the reservoir simulation model. The history-matching could use the inverted pressure and saturation changes or the best estimate of the inverted sensitivity coefficients from multiple models approach.

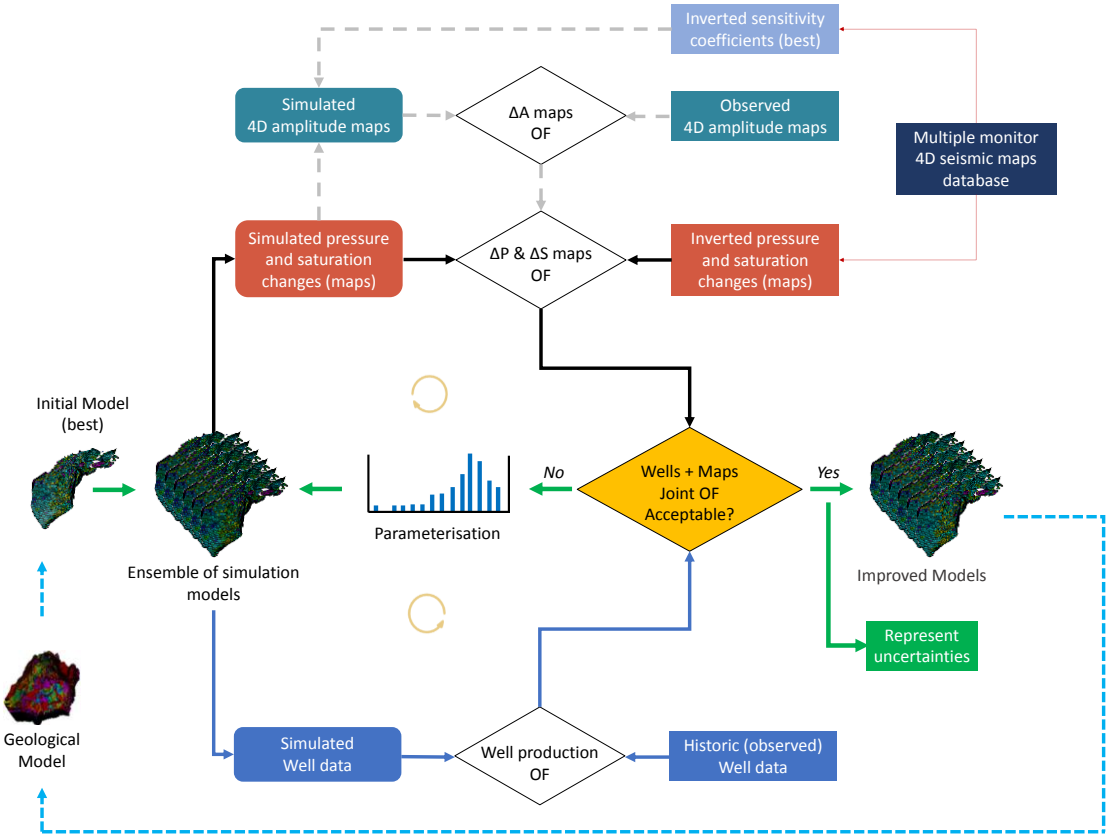

Figure 8-6 Proposed Seismic Assisted History Matching Workflow (modified after Obidegwu et al., 2015) after implementing the inversion scheme in Figure 6-2 - combining the production data with the 4D seismic data. The blue arrows (lower part) highlight the production history match loop; the black arrows (upper part) highlight the seismic history match loop using the inverted pressure and saturation changes; the green arrows (middle part) showcases their individual or combined path; while the orange arrows (circular arrows) shows the direction of the loop. The dashed grey arrows (upper most part) illustrate that 4D amplitudes obtained from the inverted sensitivity coefficients could instead be used in the seismic history match loop. The red arrows indicate the inversion part. There is also a potential for Geological model updating as indicated by the dashed light blue arrows.

If using the inverted sensitivity coefficients, it is best to convert these to synthetic amplitude maps (simulated) so as to avoid any inversion from the reservoir engineering domain via simulator-to-seismic modelling. The simulated 4D amplitude maps can instead be obtained quickly using the linear or non-linear inversion equations (Equation 6-1). The inverted sensitivity coefficients already derived from observed 4D seismic data can be combined with the simulated pressure and saturation changes from the model ensembles to generate 4D seismic synthetic maps at each monitor time.

The synthetic (i.e. simulated) 4D seismic maps can then be compared with the observed 4D seismic maps using an appropriate objective function (for example, least squares) for history-matching. However, it is recognised that the inverted pressure and saturation changes already obtained from the inversion scheme is the most direct attribute for seismic history-matching. Additionally, the best model identified by the inversion scheme could be the starting point from which ensembles of models are generated.

A second least-squares objective function (OF) is designed to compare the simulated and historic (i.e. observed) well production data. Together, both objective functions form a joint objective function for history matching with the aim of minimising the misfit between simulated parts and observed (or inverted) parts. The parameterisation usually involves the local or global perturbation of volumetric/ connectivity reservoir properties which include horizontal and vertical permeability multipliers, NTG multipliers, pore volume multipliers, endpoints of relative permeability curve (connate water saturation, critical gas saturation) and transmissibility multipliers for geobodies and/or faults depending on field geology. Uncertainties must be carried forward, both those estimated from pressure and saturation inversion of 4D seismic data, and also from measurement errors associated with historic well data. For comparing different resulting maps, vectors or initial realisations, estimating the norm of the differences should be used as a standard procedure. The Geological model can also be introduced into the history matching loop. This is necessary as more information is obtained about the reservoir, the initial assumptions about the fine scale geological model (from which the reservoir model is obtained by upscaling) will need to be addressed and updated.

8.3 Final remarks

The research output of this thesis has been driven by curiosity and passion with an attempt to raise relevant questions, conceptualise ideas to proffer solutions to them, as well as raise even more inquiries, all to push the boundaries of science. “Knowledge is of no value unless it is put into practice”. I hope that the knowledge that has been inspired through this research is taken forward in future studies, just as the many efforts in the past, have laid the foundation for the accomplishments of this thesis.

“The greatest challenge to any thinker is stating the problem in a way that will allow a solution”

-- Bertrand Russell, British philosopher, logician, mathematician, historian, writer, social critic, political activist & Nobel laureate (1872-1970) --

Appendix A

4D seismic data non-repeatability (NRMS) and estimation of 4D noise using maps

A.1 Measure of 4D seismic data repeatability, NRMS

The normalised root-mean-square (NRMS) metric is calculated as the RMS difference between two traces in a given window, divided by their average RMS, expressed as a percentage (Kragh and Christie, 2002). The window is above and away from the reservoir, outside any areas undergoing production. If a_t and b_t are the two traces, the NRMS is expressed as,

$$NRMS = \left\{ 100 \frac{2\left(RMS\left(a_t - b_t\right)\right)}{RMS\left(a_t\right) + RMS\left(b_t\right)} \right\},$$

where the *RMS* operator is calculated as:

$$RMS = \sqrt{\frac{\sum_{t_1}^{t_2} \left(x_t\right)^2}{N}}$$

and N is the number of samples of the trace x_t in the window $t_1 - t_2$

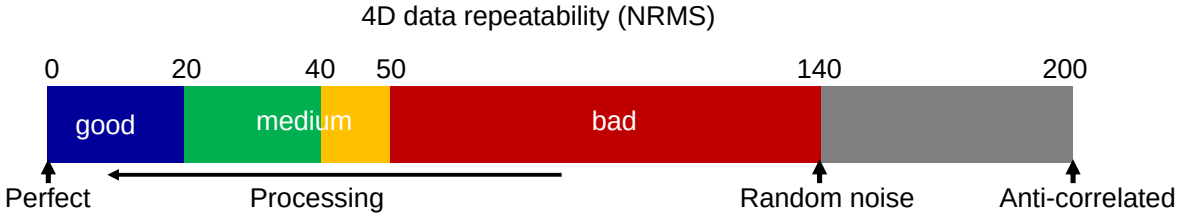

Figure A-1 NRMS colour chart. Theoretically, if two traces are identical, the NRMS is 0, if both traces contain random noise, NRMS is 141% and if they are 180° out of phase, the NRMS is 200%.

The NRMS is extremely sensitive to the smallest of changes between the two input traces, whether it is in the overall static, phase or amplitude.

From a very general point of view 4D noise can be assigned to three classes according to its source (Hubans, 2016):

- "Random noise" is the independent energy recorded by seismic sensors even when no seismic source is active. That is, it is environmental noise such as

swell, drilling, ground roll, seabed, rig noise, microseismic, etc. This noise has absolutely no relation or correlation with seismic survey.

- Repeatability noise is the 4D noise linked to the fact that the acquisition experiment cannot be perfectly repeated. The main source of non-repeatability in offshore streamer acquisition domain is the positioning error (Figure A-2) due to streamer feathering. Eiken et al. (2003) illustrates this simply by taking a seismic section, shifting it laterally by 25 m, and subtracting it from itself. The NRMS value of the difference in such a scenario averages approximately 40%. But in new domains or using new technology other non-repeatability effects may have greater impact than topographic errors: coupling, tidal impact on multiples, water bottom changes with season (velocity variations), seismic processing artefacts, focusing and defocusing effects and scattering etc. For example, water velocity variations between monitor and baseline of 10 m/s is equivalent to 1 ms two-way time at 100 m, and tidal changes of only 0.67 m is equivalent to 1 ms. Using the formula, $NRMS = 2\pi f.dt$ (Jakubowicz, 2012) then for $dt = 1$ ms and frequency of seismic data $f = 30$ hz, the NRMS between the monitor and baseline trace is 18.8%.

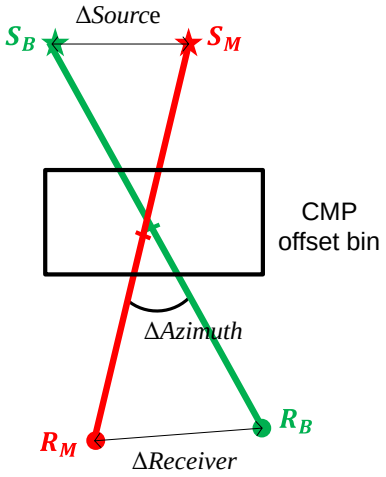

Figure *A-2 Geometric repeatability measure for time-lapse traces in a CMP bin. The source and receiver location,* $\boldsymbol{S_B}$ *and,* $\boldsymbol{R_B}$*, of one baseline trace are connected by the green line. The respective source and receiver location,* $\boldsymbol{S_M}$ *and,* $\boldsymbol{R_M}$*, for the monitor trace are connected by the red line. The measured distance between repeat source and receiver location is ΔSource and ΔReceiver, respectively. ΔAzimuth is the azimuth difference between the baseline and monitor source and receiver positions.*

- Coherent noise, very often related to non-repeated multiples.

It is therefore important that changes in the reservoir reflect in an NRMS measure greater than that outside the reservoir zone in order to detect a usable time-lapse signal.

Typical NRMS values for non-repeatability noise calculated outside and above the reservoir zone in post-stack seismic data are around 15-45% (offshore, towed streamer), 2-15% (offshore, PRM), 20-60% (Onshore, conventional), 0-1% (onshore, PRM).

References

Eiken, O., Haugen, G. U., Schonewille, M., and Duijndam A. (2003). A proven method for acquiring highly repeatable towed streamer seismic data. *Geophysics*, 68, 1303–1309, http://dx.doi.org/10.1190/1.1598123.

Jakubowicz, Helmut. Lecture on 4D Seismic Methods. Imperial College London, London, United Kingdom. March 5, 2012.

Kragh, E. D. and Christie, P. (2002). Seismic repeatability, normalized rms, and predictability. *The Leading Edge*, **21**(7), 640-647.

Hubans, C. (2016). 4D Noise Understanding to Validate 4D Anomalies. *78th EAGE Conference and Exhibition*, Vienna, Austria, Expanded Abstracts, We LHR2 15, https://doi.org/10.3997/2214-4609.201600950.

A.2 Estimation of 4D seismic data uncertainty

Let us consider two 2D amplitude maps A_{base}(x,y) and A_{mon} (x,y), such as base and monitor datasets. Each of them is composed of a geological (signal) part (G) and of a noise part (N):

$$A_{base}(x,y) = G_{base}(x,y) + N_{base}(x,y)$$
$$A_{mon}(x,y) = G_{mon}(x,y) + N_{mon}(x,y)$$

The noise parts correspond to acquisition and processing artefacts with specific structural characteristics: short scales for random noise and a strong spatial anisotropy ratio for an acquisition footprint for example (Magneron, 2016). In a 4D context N_{base} and N_{mon} are not correlated. Considering their structural content, the geological parts are generally well discriminated from the noise parts. Production effects result in differences between G_{base} and G_{mon} so that they are not 100% correlated.
The observed 4D seismic amplitude response, ΔA is a contribution from the pure 4D signals contributed by production effects, ΔG and 4D noise, ΔN. The noise is assumed additive:

$$\Delta G(x,y) = G_{mon}(x,y) - G_{base}(x,y)$$
$$\Delta N(x,y) = f(N_{mon}(x,y), N_{base}(x,y))$$
$$\Delta A(x,y) = \Delta G(x,y) + \Delta N(x,y)$$

To quantify the observed seismic 4D noise, ΔN, the seismic repeatability metric, NRMS as in section A-1, measured as a fraction between two 3D seismic datasets from the two surveys (which results in a 2D map), is applied as,

$$NRMS = \frac{2 \times RMS(3D_{mon} - 3D_{base})}{RMS(3D_{mon}) + RMS(3D_{mon})}$$

This is related to the 4D noise-to-signal ratio, N/S between the monitor and baseline seismic data (Grion et al., 2000; Behrens et al., 2002) as:

$$N/S = \frac{NRMS}{\sqrt{2 - NRMS^2}}$$

As seen in the above formula, N/S is the 4D noise-to-signal ratio, and it is the inverse of the signal-to-noise ratio (SNR or S/N).

Assuming non-repeatability noise is the main source of uncertainty, the 4D seismic noise, ΔN, as a 2D map can then be quantified as:

$$\Delta N(x,y) = \Delta G(x,y) \times N/S$$

$$\Delta N(x,y) = \frac{\Delta A(x,y)}{1 + N/S} \times N/S$$

$$\Delta N(x,y) = \frac{\Delta A(x,y) \times NRMS}{\sqrt{2 - NRMS^2} + NRMS}$$

The observed 4D seismic response, ΔA is the RMS amplitude map computed along the top reservoir, and the $NRMS$ attribute is computed above the reservoir outside any influence of production effects.

References

Behrens, R., P. Condon, W. Haworth, M. Bergeron, Z. Wang, and C. Ecker. (2002). 4D seismic monitoring of water influx at Bay Marchand: The practical use of 4D in an imperfect world. *SPE Reservoir Evaluation and Engineering*, 5, 410–420.

Grion, S., Keggin, J., Ronen, S. and Caldwell, J. (2000). Seismic repeatability benchmarks. *Offshore Technology Conference*, Houston, Texas, Expanded Abstracts, OTC-12099-MS, 499–504, https://doi.org/10.4043/12099-MS.

Magneron, C. (2016). Looking for the Lost Correlation. *78th EAGE Conference and Exhibition*, Vienna, Austria, Expanded Abstracts, We LHR2 16, https://doi.org/10.3997/2214-4609.201600951.

Appendix B

Literature review for pressure response observed in 4D seismic data from different fields

This appendix contains a literature review up until 2016 of reservoir pressure effects observed in 4D seismic amplitude and intra-reservoir time-shift data for various producing clastic fields taken from published papers where the magnitude of the pressure change (MPa) and the data noise levels expressed as "normalised RMS"(root-mean-square) were reported. The data included for each field have the limitation of being compiled from several papers, thus, multiple references. First, the table used to generate Figure 3-1 is provided, and then, the references are provided.

	RESERVOIR		MECHANISM AND TIME-LAPSE FOR EFFECT						DATA NOISE	REFERENCES	
Field name	**Location**	**geology**	**pressure up**	**time-shift**	**duration**	**pressure down**	**time-shift**	**duration**	**NRMS**	**Paper**	Full
TIMESHITS											
Trøll Ost	**Norwegian Sea**	**Shallow marine, gas field**				**-1.5 MPa**	**+0.2 to 1 ms**	**6 years**	**13%**	**Eiken et al. 2005**	
Shearwater	**Central North Sea**	**HPHT shoreface sand**				**-53 MPa**	**-2 ms**	**3 years**	**7%**	**Staples et al. 2007, Ji, 2016**	
South Gas Basin	**North Sea**	**Tight cemented gas sands with open fractures**				**-12.4 MPa**	**- 1.2 ms**	**7 years**	**~41%**	**Hall et al, 2006**	
Sarawak	**Offshore Sarawak,**	**Compacting reefal carbonate**				**-4.5 MPa**	**-1 ms**	**3 years**	**20%**	**Barker et al, 2008**	
Schiehallion	**UK continental sh**	**Turbidite**	**+17 MPa**	**2.4 ms**	**1.25 years**	**-15 MPa**	**-1.5 ms**	**8 months**	**31% and 24%**	**Floricich 2006, Dhiman Mondal 2012, Huang et al. 2012, Huang 2011**	
Troll East	**Norwegian Sea**	**Poorly consolidated**				**-4 MPa**	**-1**	**3 years**	**~15 %**	**Avseth et al, 2013**	
Elgin	**Central North Sea**	**HPHT, gas condensate**				**-50 MPa**	**-0.4**	**4 years**	**~12%**	**Grandi et al, 2010, Hawkins et al., 2007**	
Curlew D	**Central North Sea**	**Shallow marine, Gas condensate**				**-34 Mpa**	**-0.2**	**8 years**	**30%**	**Fehmers et al, 2007**	
Terra Nova	Offshore Canada,	Fluvial		1	5.5 years		-0.2 ms	5.5	~25%	Andersen et al, 2011	
Ekofisk	**North Sea**	**Chalk**	**+4.13 MPa**	**0.36 ms**	**6 months**	**-4.13 MPa**	**-0.26**	**6 months**	**5%**	**Lyngnes et al., 2013, Wong, 2016**	
Valhall	**North Sea**	**Chalk**	**+ 2 MPa ***	**1**	**3 years**	**-7 MPa**	**-3**	**3 years**	**8%**	**Corzo, 2009**	
Norne	**Norwegian Sea**	**Shallow marine**	**+20 MPa**	**1.3 ms**	**3 years**				**25%**	**Osdal et al. 2006**	
Svale	Norwegian Sea	Coastal plain env., heterolithic		~2	9 months				20%	Alsos et al, 2009	
Enfield	**Northwestern Aus**	**Clean unconsolidated**	**+11.7 MPa**	**6**	**7 months**				**20%**	**Saul and Lumley, 2015, Ali et al 2008**	
Peace river	**Onshore Canada, I**	**Unconsolidated**	**+ 5 MPa**	**0.55 ms**	**5 weeks**				**<2%**	**La Follet et al, 2015, Barker et al, 2015**	
Baobab	**Gulf of Guinea (Co**	**Turbidite with interbed**	**+14.7 MPa**	**4 ms**	**9 years**				**22%**	**Amini, 2016**	
AMPLITUDES											
Snorre	**Norwegian Sea**	**Fluvial**				**-11 to -15 MPa**		**12 years**	**15%**	**Røste et al. 2015**	
Mars	**Gulf of Mexico**	**Turbidite**				**-48 MPa**		**9 years**	**32%**	**Tura et al 2005**	
Europa	**Gulf of Mexico**	**Turbidite**				**-27 MPa**		**5 years**	**32%**	**Tura et al 2005**	
Holstein	**Gulf of Mexico**	**Turbidite**				**-17 to -29 MPa**		**5 years**	**21%**	**Ebaid et al. 2008**	
Genesis	**Gulf of Mexico**	**Turbidite**				**-35 MPa**		**3 years**	**45%**	**Hudson et al. 2005, Hogson et al. 2007, Magesan et al. 2005**	
Erskine	**Central North Sea**	**HPHT, gas condensate**				**-40 MPa**		**3 years**	**26%**	**Hajnasser 2012**	
Kristin	**Norwegian Sea**	**HPHT, gas condensate**				**-30 MPa**		**2 years**	**~29%**	**Dybvik et al, 2010, Hansen et al 2009**	
Forties	**North Sea**	**Turbidite**				**- 6 MPa**		**6 years**	**27%**	**Amoyedo et al. 2012**	
Cormorant	**North Sea**	**Fluvial-Deltaic sands**	**+ 8 MPa**		**7 years**	**- 8 MPa**		**4 years**	**40%**	**Floricich 2006**	
Gullfaks	**North Sea**	**Unconsolidated to cons**	**+9 MPa (85 - 99)**		**4 years**	**- 9 MPa**		**3 months (03-0**	**34 % and 28%**	**Strønen and Digranes 2004, El Ouair et al., 2007, Lumley et al. 2003, Landrø et al., 1999**	
Stybarrow	**Western Australia**	**Poorly consolidated tu**	**+ 13 MPa**		**1 year**				**18%**	**Hurren et al. 2012**	
South Arne	Danish North Sea	Chalk						5 years	15%	Herwanger et al, 2010	
Franklin		HPHT, gas condensate								De Gennaro et al, 2008	
Dan		Chalk								Hatchell et al, 2007	
Skua	Central North Sea	HPHT, gas condensate							13%	Staples et al, 2007	

Table B-1 Literature review of pressure increase and decrease effects in 4D seismic data for various producing fields. A combination of papers which reported the magnitude of pressure changes and the NRMS data repeatability are used.

References

Ali, A., Taggart, I., Mee, B., Smith, M., Gerhardt, A., and Bourdon, L. (2008). Integrating 4D Seismic Data with Production Related Effects at Enfield, North West Shelf, Australia. *Asia Pacific Oil and Gas Conference and Exhibition*, Perth, Australia, 20-22 October. Expanded Abstracts, SPE-116916-MS.

Alsos, T., Osdal, B., Hoias, A. (2009). The many faces of pressure changes in 4D seismic at the Svale field and its implication on reservoir management. *71st EAGE Conference & Exhibition*, Amsterdam, The Netherlands, 8 -11 June. Expanded Abstracts, Y004.

Amoyedo, S. O., Marfurt, K. J. and Roger, S. M. (2012). Time-lapse (4D) seismic effects: Reservoir sensitivity to stress and water saturation. *SEG Annual Meetin*g, Las Vegas. Expanded Abstracts, 1-6.

Andersen, T., Sinke, K., Wilcox, L., and Kelly, I. (2011). 4D Interpretation of the Terra Nova field, a structural and stratigraphical complex field with small 4D signals. *73rd EAGE Conference & Exhibition SPE EUROPEC 2011*, Vienna, Austria, 23-26 May. Expanded Abstracts, G029.

Avseth, P., Skjei, N., and Skalnes, A. (2013). Rock physics modelling of 4D time-shifts and time-shift derivatives using well log data – a North Sea demonstration. *Geophysical Prospecting*, **61**(2), 380-390.

Barker, T., Xue, Y. and Przybysz-Jarnut, J. (2015). Continuous seismic reservoir monitoring at Peace River: quantification of reservoir changes. *SEG Annual Meeting*, New Orleans, December, 2015. Society of Exploration Geophysicists. Expanded Abstracts, 5358 -5362.

Barker, T.B., Chen, B.N., Hague, P.F., Majain, J., and Wong, K. (2008). Understanding the time-lapse seismic response of a compacting carbonate field, offshore Sarawak, Malaysia. *International Petroleum Technology Conference*, Kuala Lumpur, Malaysia, 3-5 December. Expanded Abstracts, IPTC 12514, 1-14.

Barkved, O.I., Kommedal, J. H., Kristiansen, T.G., Buer, K., Kjeilstadli, R.M., Haller, N., Ackers, M., Sund, G., and Bakke, R. (2005). Integrating continuous 4D seismic data into subsurface workflows, *67th EAGE Conference & Exhibition*, Madrid, Spain, 13 -15 June. Expanded Abstracts, C001.

Benguigui, A., Roberts, G., and Shaw-Champion, M. (2012). Time-lapse 2D seismic steamflood monitoring - a case study from offshore republic of Congo, the Emeraude field, *74th EAGE Conference & Exhibition incorporating EUROPEC 2012*,Copenhagen, Denmark, 4-7 June. Expanded Abstracts, Y043.

Bergmann, P. and Chadwick, A. (2015). Volumetric bounds on subsurface fluid substitution using 4D seismic time shifts with an application at Sleipner, North Sea. *Geophysics*, **80**(5), 153-165.

Corzo Mojica, M., M. (2009). *Pressure estimation using time-lapse seismic in compacting reservoirs*, PhD Thesis, Institute of Petroleum Engineering, Heriot-Watt University.

De Gennaro, S., Grandi, A., Escobar, I., Onaisi, A., Ben-Brahim, L., Joffroy, G., Tindle, C., Neillo, V. (2008). Integrating 4D seismic, geomechanics, and reservoir simulations in the Elgin and Franklin fields, *70th EAGE Conference & Exhibition*, Rome, Italy, 9 - 12 June. Expanded Abstracts, E019.

Dybvik, O.P., Gemmer, L., Theune, U., and Ostmo, S. (2009). Establishing a geomechanical workflow for time-lapse modelling of an HPHT field, *71st EAGE Conference & Exhibition*, Amsterdam, The Netherlands, 8 – 11 June. Expanded Abstracts, P343.

Ebaid, H., Tura, A., Nasser, M., Hatchell, P., Smit, F., and Payne, N., Herron, D., Stanley, D., Kaldy, J., and Barousse, C. (2008). First dual-vessel high-repeat GoM 4D shows development options at Holstein field. *The Leading Edge*, **27**(12), 1622-1625.

Eiken, O. and Tøndel, R. (2005). Sensitivity of time-lapse seismic data to pore pressure changes: Is quantification possible? *The Leading Edge*, **24**(12), 1250-1254.

El Ouair, Y., Festervoll, A., K., Williams, J., Dræge, A., Strønen, L., S., and Digranes, P. (2007). Time-lapse seismic improves the reservoir management of the Gullfaks Field. *Oil & Gas Review*, OTC Edition, 44 – 46.

Falahat, R. (2012). *Quantitative monitoring of gas injection, exsolution and dissolution using 4D seismic*, PhD Thesis, Institute of Petroleum Engineering, Heriot-Watt University.

Fehmers, G.C., Hunt, K., Brain, J. P., Bergler S., Kaestner, U., Schutjens, P.M., Burrell, R.V. (2007). Curlew D - Pushing the boundaries of 4D depletion signal in a gas condensate field, UK Central North Sea. *69th EAGE Conference & Exhibition*, incorporating SPE EUROPEC 2007, London, United Kingdom, 11 – 14 June. Expanded Abstracts, P074.

Floricich, M. (2006). *An Engineering-Consistent Approach for Pressure and Saturation Estimation from Time-Lapse Seismic Data*. PhD thesis, Heriot-Watt University.

Grandi, A., Rahmanov, O., Neillo, V., Bourgeois, F., Deplanté, C., Ben-Brahim, L. (2010). Time lapse monitoring of the Elgin HPHT Field. *72nd EAGE Conference & Exhibition incorporating SPE EUROPEC 2010*, Barcelona, Spain, 14 – June. Expanded Abstracts, B040.

Grude, S., Landro, M., and Osdal, B. (2013). Time-lapse pressure-saturation discrimination for CO2 storage at the Snohvit field, *International Journal of Greenhouse Gas Control*, 19, 369-378.

Hajnasser, Y. (2012). *The implications of shale geomechanics and pressure diffusion for 4D interpretation*. PhD thesis, Heriot-Watt University.

Hall, S. A., MacBeth, C., Stammeijer, J., and Omerod, M. (2006). Time-lapse seismic analysis of pressure depletion in the Southern Gas Basin, *Geophysical Prospecting*, **54**(1), 63-73.

Hansen, O., Aronsen, H.A. and Østmo, S. (2009). 4D time shifts caused by depleting a HPHT reservoir–An example from the Kristin Field. *71st EAGE Conference and Exhibition incorporating SPE EUROPEC* 2009. Amsterdam, The Netherlands, 8 – 11 June. Expanded Abstracts, P344.

Hatchell, PJ, Jorgensen, O, Gommesen, L and Stammeijer, J. (2007). Monitoring reservoir compaction from subsidence and time-lapse timeshifts in the Dan field. *77th Annual International Meeting, SEG*, Expanded Abstracts, 2867-2871.

Hawkins, K., Howe, S., Hollingworth, S., Conroy, G., Ben-Brahim, L., Tindle, C., Taylor, N., Joffroy, G. and Onaisi, A. (2007). Production-induced stresses from time-lapse time shifts: A geomechanics case study from Franklin and Elgin fields. *The Leading Edge*, **26**(5), 655-662.

Herwanger, J.V., Schiøtt, C.R., Frederiksen, R., If, F, Vejbaek, O.V., Wold, R., Hansen, H.J., Palmer, E. and Koutsabeloulis, N. (2010). Applying time-lapse seismic methods to reservoir management and field development planning at South Arne, Danish North Sea. 7th Petroleum Geology Conference, Geological Society, London, 523-535.

Hodgson, N., MacBeth, C., Duranti, L., Rickett, J., and Nihei, K. (2007). Inverting for reservoir pressure change using time-lapse time strain: Application to Genesis, Field, Gulf of Mexico. *The Leading Edge*, **26**(5), 649-652.

Huang, Y. (2011). *Integration of well data into dynamic reservoir interpretation using multiple seismic surveys*. PhD thesis, Heriot-Watt University.

Huang, Y., MacBeth, C., Barkved, O., van Gestel, J.P. and Dybvik, O.P. (2011). Enhanced dynamic interpretation from correlating well activity to frequently acquired 4D seismic signatures. *The Leading Edge*, **30**(9), 1042-1050.

Hudson, T., Regel, B., Bretches, J., Condon, P., Rickett, J., Cerney, B., Inderwiesen, P., and Ewy, R. (2005). Genesis Field, Gulf of Mexico, 4-D project status and preliminary lookback. *SEG Int'l Exposition and 75th Annual Meeting*. Expanded Abstracts.

Hurren, C., Broad, C., Duncan, G., Hill, R., and Lumley, D. (2012). Successful application of 4D seismic in The Stybarrow Field, Western Australia. *SPE Asia Pacific Oil and Gas Conference and Exhibition*, Perth, Australia, 22-24 October 2012. Expanded Abstracts, SPE 158753.

Ivanova, A., Kashubin, A., Juhojuntti, N., Kummerow, J., Henninges, J., Juhlin, C., Luth, S., and Ivandic, M. (2012). Monitoring and volumetric estimation of injected CO2 using 4D seismic, petrophysical data, core measurements and well logging: a case study at Ketzin, Germany. *Geophysical Prospecting*, **60**(5), 957-973.

Jenkins, S.D., Waite, M.W., and Bee, M.F. (1997). Time-lapse monitoring of the Duri steamflood: pilot and case study, *The Leading Edge*, **16**(9), 1267-1274.

La Follet, J. R.,Wills, P., Lopez, J. L., Przybysz-Jarnut, J. K., van Lokven, M. (2015). Continuous seismic reservoir monitoring at Peace River: Initial results and interpretation. *85th Annual International Meeting*, SEG. Expanded Abstracts, 5440-5444.

Landrø, M., Solheim, O.A., Hilde, E., Ekren, B.O. and Strønen, L.K. (1999). The Gullfaks 4D seismic study. *Petroleum Geoscience*, **5**(3), 213-226.

Lumley, D., Adams, D., Meadows, M., Cole, S., and Ergas, R. (2003). 4D seismic pressure-saturation inversion at Gullfaks field, Norway. *First break*, **21**(9), 3-9.

Lyngnes, B., Landa, H., Ringen, K., and Haller, N. (2013). Life of Field Seismic at Ekofisk- Utilizing Seismic for Evaluating Well Target. *75th EAGE Conference & Exhibition incorporating SPE EUROPEC 2013*, London, UK, 10 - 13 June 2013. Expanded Abstracts, IPTC 16910

Magesan, M., Depagne, S., Nixon, K., Regel, B., Opich, J., Rogers, G. and Hudson, T. (2005). Seismic processing for time-lapse study: Genesis field, Gulf of Mexico. *The Leading Edge*, **24**(4), 364-373.

Ng, H. (2015). Monitoring fluid injection using seismic time-lapse analysis: a Rainbow Lake case study, MSc Dissertation, Department of Geology and Geophysics, University of Calgary, 1-98.

Osdal, B., Husby, O., Aronsen, H., Chen, N., and Alsos, T. (2006). Mapping the fluid front and pressure buildup using 4D data on Norne Field. *The Leading Edge*, **25**(9), 1134–1141.

Røste, T., Dybvik, O. P., and Soreide, O.K. (2015). Overburden 4D time shifts induced by reservoir compaction at Snorre Field. *The Leading Edge*, **34**(11), 1366-1374.

Saul, M., and Lumley, D. (2015). The combined effects of pressure and cementation on 4D seismic data. *Geophysics*, **80**(2),135-158.

Schutjens, P. M., Hindriks, K., Van der Horst, J., Hatchell, P., Van den Beukel, A., Barker, T., Wills, P., and Davis, J. (2005). Reservoir monitoring with seismic timeshifts: geomechanical modeling for its application in stacked pay, International Petroleum Technology Conference, Doha, Qatar, 21-23 November. Expanded Abstracts, IPTC-10511-MS.

Staples, R., Ita, J., Burrell, R. and Nash, R. (2007). Monitoring pressure depletion and improving geomechanical models of the Shearwater field using 4D seismic. *The Leading Edge*, **26**(5), 636-642.

Staples, R., Ita, J., Nash, R., Hague, P., and Burrell, R. (2007). Using 4D seismic data and geomechanical modelling to understand pressure depletion in HPHT fields of the Central N Sea. *69th EAGE Conference & Exhibition incorporating SPE EUROPEC 2007*, London, United Kingdom, 11-14 June 2007. Expanded Abstracts, A025.

Strønen, L. K. and Digranes, P. (2004). Time-lapse seismic extends the lifetime of the Gullfaks Field. *66th EAGE Conference & Exhibition*, Paris, France, 7-10 June 2004. Expanded Abstracts, A001.

Tura, A., Barker, T., Cattermole, P., Collin, C., Davis, J., Hatchell, P., Koster, K., Schutjens, P., and Wills, P. (2005). Monitoring primary depletion reservoirs using amplitudes and time shifts from high-repeat seismic surveys. *The Leading Edge*, **24**(12), 1214-1221.

Wong, M. Y. (2016). Presented at the Proceedings of the 34th Edinburgh Time-Lapse Project Meeting, Heriot-Watt University, Edinburgh, UK.

Wright, R. J. (2004). *Four-dimensional seismic analysis of the Hibernia oil field, Grand Banks*, Canada.

Appendix C

Matrix set-up, MATLAB in-built "*lsqlin*" function and the reflective-trust region algorithm for solving bounded linear inverse problems

Appendix C-1 summarises how the matrices are set up for the multi-offset and multi-monitor inversion introduced in section 6.2, and introduces the MATLAB in-built solver "*lsqlin*" which is used to solve the constrained linear inverse problem described in section 6.2.4. The solver is an optimisation technique based on the Interior-reflective Newton method via a Bounded Trust-Region approach. Appendix C-2 introduces optimisation algorithms and looks into how the "*lsqlin*" function attempts to solve the constrained linear inverse problem. This is based on the work by Coleman and Li (1993).

C.1 Matrix formulations

The general linear system

$$\mathbf{d} = \mathbf{Gm} + \mathbf{e}$$

satisfies the linear data-driven formulation for pressure and saturation inversion , and sensitivity coefficients inversion, in this thesis (see section 6.2.2):

$$\Delta A \approx \left(C_P \Delta P + C_{S_w} \Delta S_w + C_{S_g} \Delta S_g\right) A_b + \Delta N$$

where, ΔA is a 4D seismic amplitude map (monitor-baseline), ΔP is the change in pore pressure, ΔS_w is the change in water saturation, ΔS_g is the change in gas saturation, A_b is the baseline seismic amplitude map which captures the effects of the reservoir geology, porosity, net-to-gross and general static seismic properties. C_P, C_{S_w} and C_{S_g} are sensitivity coefficients and ΔN which is the same as $\mathbf{e}$ is the estimated 4D seismic noise in ΔA (see Appendix A-2).

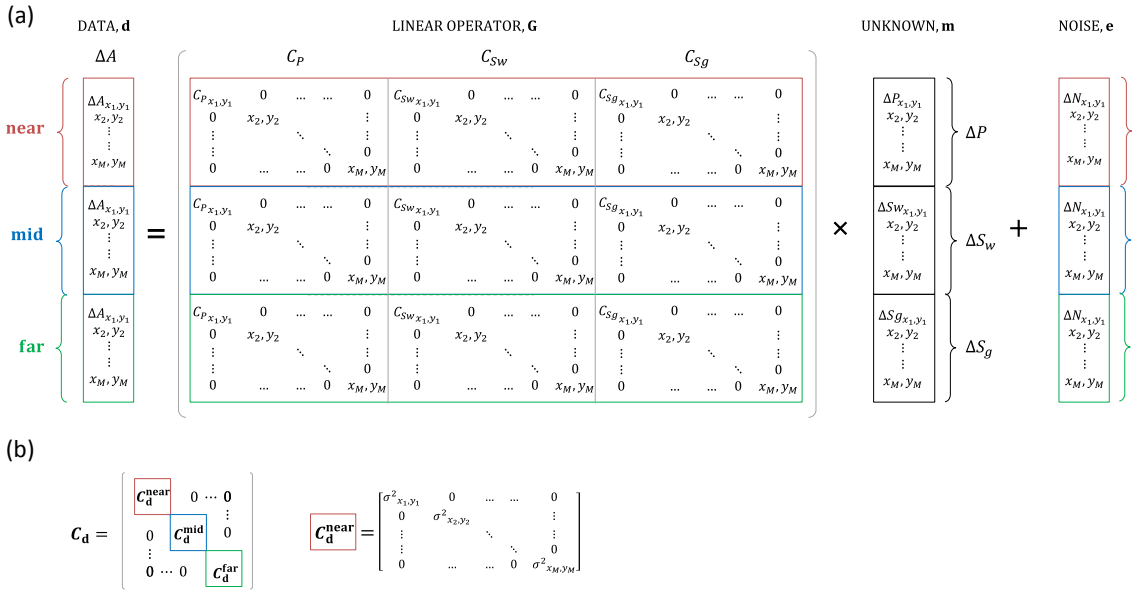

Figure C-1 Multi-offset simultaneous linear equation representation using three offset stacks (near, mid and far offset).(a) Matrix formulation as a general linear system $\boldsymbol{d} = \boldsymbol{Gm} + \boldsymbol{e}$. Note that (x,y) represents each seismic bin location, in this case there are "M" number of seismic bin locations. The linear mapping operator G which contains the sensitivity coefficients is a sparse matrix. Also note that its elements are internally pre-multiplied by the baseline amplitude map, A_b for each offset (see Equation 6-3). (b) Matrix representation of the data error covariance matrix, $\boldsymbol{C_d}$ for each offset stack. Note that only the diagonal entries are defined, whose elements are the noise estimates defined by their variance, $\sigma^2_{x,y}$ (i.e. a normal distribution of data errors with zero mean and non-zero standard deviation, σ) so that $\boldsymbol{C_d} = \sigma^2 \boldsymbol{I}$, where $\boldsymbol{I}$ is the identity matrix. Note that as the noise is spatially varying, the variance is also spatially, and that the noise is different for near, mid and far ΔA stacks.

For the formulations in the multi-offset inversion which combines near, mid and far offset amplitude stacks to obtain the unknown pressure and saturation changes at a monitor time, the above equation becomes a linear system of equations (Figure C-2). Likewise, for the multi-monitor inversion which combines 4D amplitude stacks at different monitor times, for a specific offset to obtain the unknown pressure and saturation sensitivity coefficients (Figure C-3). Note that the sensitivity coefficients will be different for each offset stack, as Figure C-2 indicates.

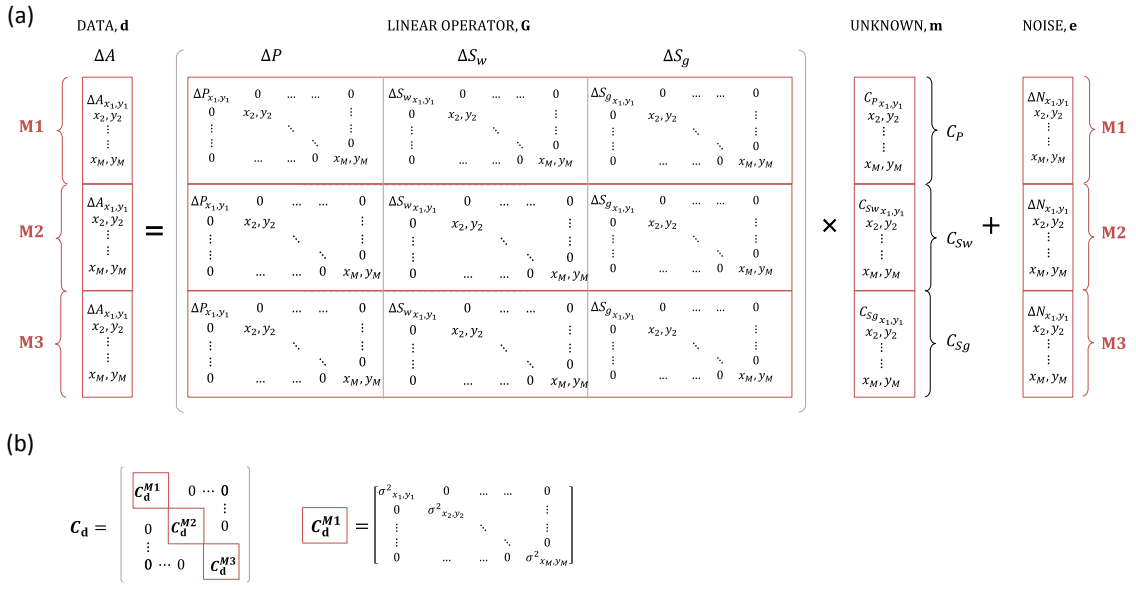

Figure C-2 Multi-monitor simultaneous linear equation representation for three monitor vintages. The monitor data, denoted by M1, M2 and M3 are for a specific 4D amplitude offset stack, ΔA. Note that (x,y) represents each seismic bin location, in this case there are "M" number of seismic bin locations. (a) Matrix formulation as a general linear system $\boldsymbol{d} = \boldsymbol{Gm} + \boldsymbol{e}$. *The linear mapping operator G which contains pressure and saturation changes is a sparse matrix. Also note that its elements are internally pre-multiplied by the baseline amplitude map,* A_i , *to satisfy the above equation. (b) Matrix representation of the data error covariance matrix,* $\boldsymbol{C_d}$ *for each monitor data. Note that only the diagonal entries are defined, whose elements are the noise estimates defined by their variance,* $\sigma^2_{x,y}$ *(i.e. a normal distribution of data errors with zero mean and non-zero standard deviation,* σ*), so that* $\boldsymbol{C_d} = \sigma^2\boldsymbol{I}$*, where* $\boldsymbol{I}$ *is the identity matrix. Note that as the noise is spatially varying, the variance is also spatially, and that the noise is different for each monitor time, M1 to M3.*

As discussed in section 6.2.1, also note that, in Figure C-3, the matrix mapping operator **G** contains "simulated" pressure and saturation changes for all monitor times, M1 to M3, which are taken one by one from multiple fluid-flow simulation models. One out of the several predictions of pressure and saturation changes from the models will provide the best estimate of C_P, C_{S_w} and C_{S_g} that honours the observed 4D seismic offset data, ΔA, combined for all monitor times. In Figure C-2, the matrix mapping operator **G** is

different, as it now contains this best estimate of C_P, C_{S_w} and C_{S_g} for each offset stack. This allows us to estimate $\Delta P, \Delta S_w$ and ΔS_g, for any monitor time, M1, M2 and M3.

C.1.1 MATLAB functions for solving constrained inverse problems

MATLAB offers several Optimisation Toolbox™ solvers for various types of functions, $\boldsymbol{f}(\mathbf{m})$ and constraints, with the objective of finding the vector solution, $\mathbf{m}$, (Table C-1). I use the "lsqlin" solver which implements the trust-region reflective algorithm described in section C.2 for a bounded linear problem. For more details see the references below.

Solver	$\boldsymbol{f}(\mathbf{m})$	**Constraints**
mldivide	$A\mathrm{m} - \mathrm{b}$	None
lsqnonneg	$A\mathrm{m} - \mathrm{b}$	$\mathbf{m} \geq 0$
lsqlin	$A\mathrm{m} - \mathrm{b}$	Bound, linear
lsqnonlin	General $f(\mathrm{m})$	Bound
lsqcurvefit	$f(m, mdata) - ydata$	Bound

Table C-1 Some built-in functions in MATLAB. The solver used in this thesis is the "lsqlin" solver highlighted in red. The lsqlin solver is applied because a linear inversion equation is used. If a non-linear equation is used, then the "lsqnonlin" solver should be used instead (see section 6.2.2)

C.1.2 The lsqlin function for a constrained linear inversion problem

In MATLAB, the in-built *lsqlin* function which is a linear least-squares solver with bounds or constraints minimizes the objective $f(\mathbf{m})$:

$$\min_{\mathbf{m}} f(\mathbf{m}) = \|\mathbf{b} - \mathbf{A}\mathbf{m}\|_2^2 \text{ so that } \{\mathbf{m}^{lower} \leq \mathbf{m} \leq \mathbf{m}^{upper}$$

where $\mathbf{A} = \left(\mathbf{G}^{\mathbf{T}}\mathbf{C}_{\mathbf{d}}^{-\mathbf{1}}\mathbf{G}\right)$ and $\mathbf{b} = \mathbf{G}^{\mathbf{T}}\mathbf{C}_{\mathbf{d}}^{-\mathbf{1}}\mathbf{d}$, which can be rewritten as,

$$\min_{\mathbf{m}} f(\mathbf{m}) = (\mathbf{d} - \mathbf{G}\mathbf{m})^{\mathbf{T}}\mathbf{C}_{\mathbf{d}}^{-\mathbf{1}}(\mathbf{d} - \mathbf{G}\mathbf{m}) \text{ such that } \{\mathbf{m}^{lower} \leq \mathbf{m} \leq \mathbf{m}^{upper}$$

with $\mathbf{m}$ as the unknown variables with an error covariance matrix for its solution estimated as $\mathbf{C_m} = \mathbf{A^{-1}}$ where the variance of the model variables, $\sigma_{\mathbf{m}}^2$ is given by the diagonal elements of $\mathbf{C_m}$, and σ is the standard deviation.

As shown in Figures C-2 and C-3, $\mathbf{G}$ is the $cM \times nM$ matrix mapping operator with n as the number of unknown variables to be estimated (such as C_i or Δi $(i = P, S_w, S_g)$) in $\mathbf{m}$ which is a vector with dimension, $nM \times 1$, containing the unknown variables; $\mathbf{d}$ is the 4D seismic data vector with dimension $cM \times 1$, where M is the number of seismic bin locations (x, y). The data could represent offset stacks for a particular 4D monitor time (so, using only near, mid and far offset stacks, $c = \mathbf{z} = 3$) or 4D monitor vintages for a particular offset stack (in this case, minimum number of monitors is $c = \boldsymbol{v} = 2$) . The 4D seismic noise, $\mathbf{e}$, which is estimated from 4D seismic data is a vector with dimension $cM \times 1$, which forms the diagonal elements of the data error covariance matrix $\mathbf{C_d}$. $\mathbf{C_d}$ has dimensions $cM \times nM$. Only the diagonal elements are defined, thus assuming that 4D seismic data measurement errors are independent. Similarly, $\mathbf{C_m}$ has dimensions $cM \times nM$. As with the unknown solution $\mathbf{m}$, the upper, $\mathbf{m}^{lower}$ and lower, $\mathbf{m}^{lower}$ bounds are vectors with dimension, $nM \times 1$, containing the maximum and minimum values respectively. In the case of the multi-monitor inversion for the sensitivity coefficients, C_P, C_{S_w} and C_{S_g}, a priori minimum and maximum values are defined in the bounds, and these are the same for every seismic bin location (see section 7.1.3). In the case of the multi-offset inversion for pressure and saturation changes, bounds containing maximum and minimum values for ΔP, ΔS_w and ΔS_g are defined, which can be the same or different for each seismic bin location (see section 7.1.2).

References

http://uk.mathworks.com/help/optim/ug/least-squares-model-fitting-algorithms.html
https://uk.mathworks.com/help/optim/ug/lsqlin.html#inputarg_options

C.2 Introduction to optimisation algorithms

- All optimisation algorithms start from an initial solution point, denoted by $\mathbf{m}_0$. For a non-linear problem, $\mathbf{m}_0$ must be provided by the user either starting at zero or some a priori values, but linear problems do not require initial values for $\mathbf{m}_0$, where $\mathbf{m}_0$ is the unknown.
- Beginning at $\mathbf{m}_0$, the optimisation algorithm generates a sequence of iterates $\mathbf{m}_1, \mathbf{m}_2, \mathbf{m}_3, \ldots\ldots, \mathbf{m}_k, \mathbf{m}_{k+1}, \ldots\ldots$
- The process of iteration terminates when either
    - No more progress can be made or
    - It seems that the solution has been approximated with sufficient accuracy, at a tolerance value supplied by the user
- For moving from the current iterate $\mathbf{m}_k$ to a new iterate $\mathbf{m}_{k+1}$, most of the continuous optimisation algorithms follow one of these approaches: Line Search methods or Trust-Region methods.

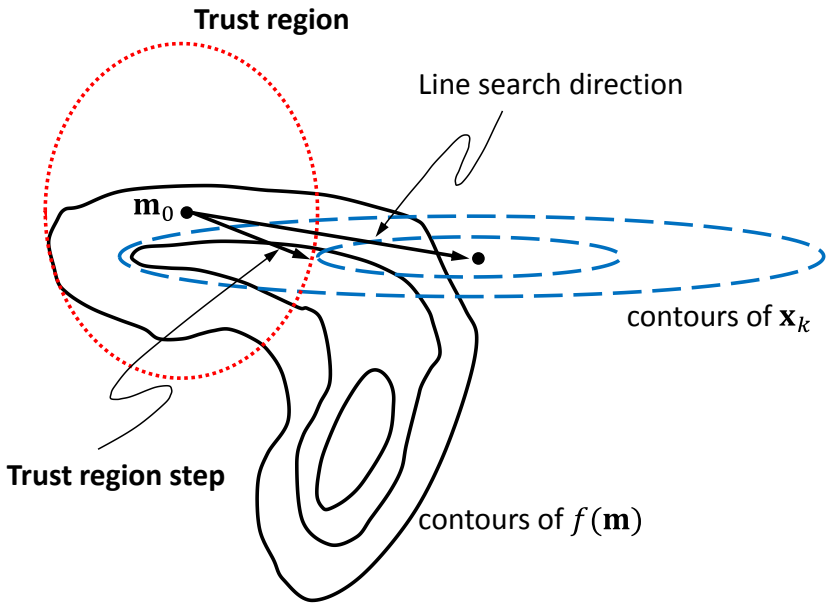

Figure C-3 Geometric interpretation between Line Search and Trust-Region Steps

C.2.1 Trust-Region method

Trust-region is a term used in mathematical optimisation to denote the subset of the region of the objective function that is approximated using a model function (often a quadratic). If an adequate model of the objective function is found within the trust region then the region is expanded; conversely, if the approximation is poor then the region is contracted.

- Trust-Region methods assume a quadratic model $\mathbf{x}^{(k)}$ that approximates the objective function, $f(\mathbf{m})$ in a finite region near the unknown $\mathbf{m}^{(k)}$
- This region, Δ, where the model, $\mathbf{x}^{(k)}$ is a good approximation of $f(\mathbf{m})$, is called the **trust-region**
- This method chooses the ***step length,*** Δ to move towards the approximate minimum of the model, $\mathbf{x}^{(k)}$ in this region
- The step length**,** Δ is also updated at each iteration using heuristics

Figure C-3 compares the approaches represented by Line Search and Trust-Region methods. Line Search methods, starting from the initial point, $\mathbf{m}_0$, move straight away towards the minimum of the model, $\mathbf{x}^{(k)}$, whereas the Trust-Region methods are moving in a somewhat different direction. Trust-Region methods first chooses step length and then a step direction, whereas, Line Search methods first chooses step direction and then a step length.

It can also be inferred from the representative objection function, $f(\mathbf{m})$, that the Trust-Region methods are not only minimising the model, $\mathbf{x}^{(k)}$, but they also remain near to the global minimum of the objective function, whereas, Line Search methods appear to deviate from the global minimum.

The model $\mathbf{x}^{(k)}$ in Trust-region methods is most often a quadratic obtained by a Taylor series expansion of $f(\mathbf{m})$ around $\mathbf{m}^{(k)}$, i.e.

$$\mathbf{x}^{(k)} = f\left(\mathbf{m}^{(k)}\right) + \frac{\partial f\left(\mathbf{m}^{(k)}\right)}{\partial \mathbf{m}^{(k)}} p + \frac{1}{2} p^{\mathrm{T}} \frac{\partial^2 f\left(\mathbf{m}^{(k)}\right)}{\partial {\mathbf{m}^{(k)}}^2} p,$$

For notation clarity, let $g\left(\mathbf{m}^{(k)}\right) = \frac{\partial f\left(\mathbf{m}^{(k)}\right)}{\partial \mathbf{m}^{(k)}}$ and $H\left(\mathbf{m}^{(k)}\right) = \frac{\partial^2 f\left(\mathbf{m}^{(k)}\right)}{\partial {\mathbf{m}^{(k)}}^2}$ which are matrices of first order and second order partial derivatives of the objective function $f\left(\mathbf{m}^{(k)}\right)$ relative to $\mathbf{m}^{(k)}$, at the current iterate, k, respectively. $H\left(\mathbf{m}^{(k)}\right)$ is also known as the Hessian matrix.

The subproblem to be solved to find the step length, Δ to take during the iteration is given by,

$$\min_{\|p\| \leq \Delta} f\left(\mathbf{m}^{(k)}\right) + g\left(\mathbf{m}^{(k)}\right) p + \frac{1}{2} p^{\mathrm{T}} H\left(\mathbf{m}^{(k)}\right) p,$$

The iteration step itself is

$$\mathbf{m}^{(k+1)} = \mathbf{m}^{(k)} + p_k,$$

where p_k is the step direction. The heuristic* to update the size of the trust-region depends on the ratio of the expected improvement from the model approximation with the actual improvement observed in the objective function, i.e.

$$\rho_k = \frac{f\left(\mathbf{m}^{(k)}\right) - f\left(\mathbf{m}^{(k)} + p_k\right)}{\mathbf{x}^{(k)} - \mathbf{x}^{(k)}(p_k)},$$

where the numerator is the actual objective function value at the current iterate minus the predictive objective function value at the current iterate. The denominator is the value of the quadratic model at the current iterate minus its predicted value.

- If there is a good agreement between predicted and actual values ($\rho_k \approx 1$), then the step length, Δ is increased;
- If the agreement is poor, i.e. ρ_k is small ($\rho_k \ll 1$), then Δ is decreased
- If ρ_k is smaller than a threshold value (e.g. $\approx 10^{-4}$), the step is rejected and the value of $\mathbf{m}^{(k)}$ is retained, but Δ is decreased accordingly.

** a heuristic is a technique designed for solving a problem more quickly when classic methods are too slow, or for finding an approximate solution when classic methods fail to find any exact solution. This is achieved by trading optimality, completeness, accuracy, or precision for speed. In a way, it can be considered a shortcut.*

C.2.2 Interior-reflective Newton method - a Bounded Trust-Region approach

The MATLAB in-built "lsqlin" function based on Coleman and Li (1993) and some explanations taken from (Mayorov, 2015), works as a box-constrained quadratic programming problem for a minimised inverse solution for linear problems as follows:

$$\min f\left(\mathbf{m}^{(k)}\right), \qquad \mathbf{m}^{(k)} \in \ \mathcal{F} = \left\{\mathbf{m}^{(k)}: \mathbf{m}^{lower} \leq \mathbf{m}^{(k)} \leq \mathbf{m}^{upper}\right\}$$

where $\mathbf{m}^{lower}$ and $\mathbf{m}^{upper}$ are vectors containing minimum and maximum values, respectively, so that the solution $\mathbf{m}^{(k)}$ lies within this bound. The bounds remain the same at any iteration, k.

Some of the components of $\mathbf{m}^{lower}$ and $\mathbf{m}^{upper}$ can be infinite meaning no bound in this direction, but this is not the case in this work, all components are defined within a reasonable expected bound. The notation $g\left(\mathbf{m}^{(k)}\right) = \frac{\partial f\left(\mathbf{m}^{(k)}\right)}{\partial \mathbf{m}^{(k)}}$ and $H\left(\mathbf{m}^{(k)}\right) = \frac{\partial^2 f\left(\mathbf{m}^{(k)}\right)}{\partial \mathbf{m}^{(k)^2}}$ which are the first order and second order partial derivatives of the objective function $f\left(\mathbf{m}^{(k)}\right)$ relative to $\mathbf{m}^{(k)}$, at the current iterate, k, respectively, is also used here. The Hessian, $H\left(\mathbf{m}^{(k)}\right)$ has to be a semi-positive symmetric matrix, which is an optimality condition to make sure it is a minimum.

The first order necessary conditions for $\mathbf{m}^{(k)}$ to be a local minimum are:

$$g\left(\mathbf{m}^{(k)}\right)_i = 0 \ \text{ if } \ \mathbf{m}^{lower}{}_i < \mathbf{m}^{(k)}{}_i < \mathbf{m}^{upper}{}_i$$
$$g\left(\mathbf{m}^{(k)}\right)_i \leq 0 \ \text{ if } \mathbf{m}^{(k)}{}_i = \mathbf{m}^{upper}{}_i$$
$$g\left(\mathbf{m}^{(k)}\right)_i \geq 0 \ \text{ if } \mathbf{m}^{(k)}{}_i = \mathbf{m}^{lower}{}_i$$

where i denotes a seismic bin location (x, y). The bounds $\mathbf{m}^{lower}$ and $\mathbf{m}^{upper}$ could be spatially varying or the same for each spatial location, *i*.

A vector, $v\left(\mathbf{m}^{(k)}\right)$ is then defined with the following components:

$$v\left(\mathbf{m}^{(k)}\right)_i = \begin{cases} \mathbf{m}^{upper}{}_i - \mathbf{m}^{(k)}{}_i & g\left(\mathbf{m}^{(k)}\right)_i < 0 \ \text{ and } \ \mathbf{m}^{upper}{}_i < \infty \\ \mathbf{m}^{(k)}{}_i - \mathbf{m}^{lower}{}_i & g\left(\mathbf{m}^{(k)}\right)_i > 0 \ \text{ and } \ \mathbf{m}^{lower}{}_i > -\infty \\ 1 & \text{otherwise} \end{cases}$$

The components of the vector, $v(\mathbf{m}^{(k)})$ are distances to the bounds at which anti-gradient points exists (if this distance is finite).

We then define a matrix $D(\mathbf{m}^{(k)}) = \text{diag}\left(v(\mathbf{m}^{(k)})^{1/2}\right)$, where the first order optimality can be stated as $D(\mathbf{m}^{(k)})^2\, g(\mathbf{m}^{(k)}) = 0$. This allows us think of our optimisation problem as the diagonal system of non-linear equations, which is the main idea here:

$$D(\mathbf{m}^{(k)})^2\, g(\mathbf{m}^{(k)}) = 0$$

The first order derivative (otherwise known as the Jacobian, J) of the left hand side exists whenever $v(\mathbf{m}^{(k)})_i \neq 0$ for all i, which is true when $\mathbf{m}^{(k)} \in \text{int}\,(\mathcal{F})$ (not on the bound). Assuming that this holds, then Newton step for this system satisfies:

$$\left(D(\mathbf{m}^{(k)})^2 H(\mathbf{m}^{(k)}) + \text{diag}(g(\mathbf{m}^{(k)})\, J^v\right) p = -D(\mathbf{m}^{(k)})^2\, g(\mathbf{m}^{(k)})$$

Here, J^v is the diagonal Jacobian matrix (i.e. first order derivative) of $v(\mathbf{m}^{(k)})$, its elements take values ± 1 or 0, note that all elements of the matrix $A(\mathbf{m}^{(k)}) = \text{diag}(g(\mathbf{m}^{(k)})\, J^v$ are non-negative.

Now we introduce the change of variables:

$$\mathbf{m}^{(k)} = D\, \hat{\mathbf{m}}^{(k)}$$

where D is a diagonal scaling matrix. In the new variables we have Newton step satisfying:

$$\hat{B}(\mathbf{m}^{(k)})\, \hat{p} = -\hat{g}(\mathbf{m}^{(k)})$$

$$\text{where } \hat{B}(\mathbf{m}^{(k)}) = D\, H(\mathbf{m}^{(k)}) D + A(\mathbf{m}^{(k)})$$

$$\text{and } \hat{g}(\mathbf{m}^{(k)}) = D\, g(\mathbf{m}^{(k)})$$

Note that $\hat{g}(\mathbf{m}^{(k)})$ is a proper gradient of $f(\mathbf{m}^{(k)})$ with respect to the "hat" variables. Looking at this Newton step we formulate the corresponding trust-region subproblem (i.e. a quadratic minimisation problem at each iteration):

$$\min_{\hat{p}} \hat{\mathbf{x}}^{(k)}(\hat{p}) = \hat{g}\left(\mathbf{m}^{(k)}\right)^{\mathrm{T}}\hat{p} + \frac{1}{2}\hat{p}^{\mathrm{T}}\hat{B}\left(\mathbf{m}^{(k)}\right)\hat{p}, \text{ such that } \|\hat{p}\| \leq \Delta,$$

where Δ is the step length and $\hat{p}$ is the step direction in the "hat" space..

In the original space, we have:

$$B\left(\mathbf{m}^{(k)}\right) = H\left(\mathbf{m}^{(k)}\right) + D^{-1}\,A\left(\mathbf{m}^{(k)}\right)D^{-1}$$

and the equivalent trust-region problem:

$$\min_{p} \mathbf{x}^{(k)}(p) = g\left(\mathbf{m}^{(k)}\right)^{\mathrm{T}}p + \frac{1}{2}p^{\mathrm{T}}B\left(\mathbf{m}^{(k)}\right)p, \text{ such that } \|D^{-1}p\| \leq \Delta,$$

where Δ is the step length and p is the step direction.

In large scale problems, the better approach is to solve the trust-region problem in "hat" space, so that D^{-1} would not need to be computed since it can become arbitrarily large when the optimum is on the boundary and the algorithm approaches it.
However, for small scale bounded linear problems (n, m < 100), where n is number of rows and m is number of columns, a simplified step to calculate p works just fine:

$$p = -\left(D\left(\mathbf{m}^{(k)}\right)^{2}H\left(\mathbf{m}^{(k)}\right) + \mathrm{diag}(g\left(\mathbf{m}^{(k)}\right)J^{v}\right)^{-1}D\left(\mathbf{m}^{(k)}\right)^{2}g\left(\mathbf{m}^{(k)}\right)$$

By iterating on the above step, the solution for a small scale bounded least squares problem should converge generally within a few iterations.

A modified improvement ratio of our trust-region solution is computed as follows:

$$\rho_k = \frac{f\left(\mathbf{m}^{(k)} + p_k\right) - f\left(\mathbf{m}^{(k)}\right) + \frac{1}{2}\hat{p}_k{}^{\mathrm{T}}A\left(\mathbf{m}^{(k)}\right)\hat{p}_k}{\hat{\mathbf{x}}^{(k)}(\hat{p}_k)}$$

Based on ρ_k we adjust a radius of trust-region using some reasonable strategy as outlined in section C.2.1, until convergence is attained. The quadratic model $\mathbf{x}^{(k)}$ has also been earlier introduced in section C.2.1.

In this section, we used a first-order optimality condition to introduce a scaling matrix D, which allowed us to reformulate the constrained problem as the system of non-linear equations. Then motivated by the Newton process for this system, we formulated the corresponding trust-region subproblem. The purpose of the matrix D is to prevent steps directly into bounds, so that other variables can also be explored during the step. This

does not mean that after introducing such a matrix, we ignore the bounds, specifically, our estimates $\mathbf{m}^{(k)}$must remain strictly feasible. Such feasibility can be achieved through reflective transformation.

Conceptually we apply a special transformation $\mathbf{m} = R(\mathbf{y})$, such that $\mathbf{y}$ is the unbounded variable and try to solve the unconstrained problem $\min_{\mathbf{y}} f\big(R(\mathbf{y})\big)$. Coleman and Li (1993) suggests a reflective transformation: a piecewise linear function, equal to identity when **y** satisfies the initial bound constraints, otherwise reflected from the bounds as a beam of light (hopefully, you get the idea!). They also show that their simple transformation does not also increase significantly the complexity of the function to minimize. It is not differentiable when **m** is on the bounds, requiring the moderate use of strictly feasible iterates. The general idea of the reflective Newton method is to do a Line Search along the reflective path (or a traditional straight line in **y** space).

A high level description of the Trust-Region Reflective algorithm goes like this (Mayorov, 2015):

1. Consider the trust-region problem in "hat" space as described in the above section.
2. Find its solution in the "hat" space and compute the corresponding solution in the original space $p = D^{-1}\hat{p}$.
3. Restrict this trust-region step to lie within bounds if necessary. Step back from the bounds by $\delta = \min(0.05,\ \|D^2 g\|)$ times the step length, Δ. Do it for all types of steps below.
4. Consider a single reflection of the trust-region step if bound was encountered in 3. Use 1-D minimisation of the quadratic model **x** to find the minimum along the reflected direction (this is trivial).
5. Find the minimum of the quadratic model along the $\hat{g}$.
6. Choose the best step among 3, 4, 5. Compute the corresponding step in the original space as in 2, update **m**.
7. Update the trust region radius by computing ρ as described in the above section.
8. Check for convergence and go to step 1 if the algorithm has not converged.

References

Coleman, T. F. and Li, Y. (1993). A reflective Newton method for minimizing a quadratic function subject to bounds on some of the variables. SIAM Journal on Optimisation, **6**(4), 1040-1058.

Wang, Yanghua. (2012). Lecture on Seismic inversion and quantitative analysis. MSc Petroleum Geophysics course notes, Imperial College London, 2011-2012.

Mayorov, Nikolay (2015). Trust Region Reflective Algorithm. [ONLINE] Available at: https://nmayorov.wordpress.com/2015/06/19/trust-region-reflective-algorithm/. [Accessed 13 February 2017].

https://en.wikipedia.org/wiki/Newton%27s_method [Accessed 13 February 2017].

Appendix D

Objective function results and global multipliers for the multiple simulation models generated on the Heidrun field

This appendix concerns Chapter 6 where the procedure for generating multiple models is described. This appendix details the global objection function, $\boldsymbol{OF_{model}}$ (Equation 6-11) results for each model that was found to meet the history-matching qualifying criteria, $\boldsymbol{Q}$, (Equation 6-12) relative to the original (i.e. base) model of the Heidrun Field that was provided by Statoil. Two history matching parameters are used, Field Gas-oil ratio (FGOR) and field water-cut (FWCT) in the global objective function (Equation 6-11). The models were generated via global multipliers for Permeability X, Y and Z and Porosity using the Multiple Reservoir Optimizer (MEPO) platform. An algorithm chosen was the Latin-Hypercube algorithm which samples the entire multiplier distribution and produces a set number of model scenarios. The following tables detail the multiplier values for all 95 models that were qualified out of the 200 models generated. The global objective function values labelled as '$\boldsymbol{OF_{model}}$' (as well as the partial objective function for the two history matching parameters, labelled as $\boldsymbol{X_{FGOR}}$ and $\boldsymbol{X_{FWCT}}$) and the qualifying value, $\boldsymbol{Q}$, (Equation 6-12) are also recorded for each model. Where a multiplier entry value is 0, it means that the specific property remains the same as in the base (starting) model. Models that match history better than the base model are highlighted in red.

Models	MULTPERMX	MULTPERMY	MULTPERMZ	MULTPOR	Global, $\mathbf{OF}_{model}$	Partial, X_{FGOR}	Partial, X_{FWCT}	Qualifier value, Q
1	0	0	0	0.935535	1259.008	1259.006	0.00272	20.72893
2	0	0	0	1.094644	1280.501	1280.5	0.001814	22.78995
3	0	0	0	1.044424	1090.63	1090.629	0.001213	4.582807
4	0	0	0	1.027291	1040.606	1040.605	0.001183	-0.21413
5	0	0	0	0.922566	1294.661	1294.658	0.003202	24.14776
6	0	0	0	0.898944	1547.7	1547.695	0.004316	48.41214
7	0	0	0	1.082696	1227.047	1227.046	0.001615	17.66411
8	0	0	0	1.115779	1387.001	1386.999	0.002252	33.00245
9	0	0	0	0.979091	1081.895	1081.893	0.001598	3.745138
10	0	0	0	1.000681	1050.738	1050.737	0.00131	0.757462
11	0	0	0	0.974319	1105.24	1105.238	0.001696	5.983778
12	1.288813459	0.614258625	0	1.102412	1346.276	1346.275	0.001526	29.09722
13	1.388324124	0.624513083	0	1.084287	1296.109	1296.108	0.001195	24.28663
14	1.239900276	0.688699649	0	1.034181	1190.287	1190.286	0.000889	14.13906
15	0.802772509	0.648190357	0	1.094228	1328.879	1328.877	0.001594	27.42894
16	1.004815639	1.247301164	0	0.884349	1377.624	1377.618	0.005132	32.10319
17	0.539055788	0.998283436	0	1.183922	1532.507	1532.502	0.004646	46.95525
18	1.220705122	1.30656014	0	1.027736	976.8074	976.8062	0.001193	-6.33191
19	0.886932221	0.707118233	0	1.142629	1434.068	1434.065	0.002772	37.51575
20	0.780291499	0.748909622	0	1.129694	1424.799	1424.797	0.002486	36.62696
21	0.945353365	0.950267229	0	0.996716	1105.77	1105.769	0.001348	6.034579
22	0.637071037	0.883034602	0	0.993819	1320.149	1320.148	0.00149	26.59187

Table D-1 Results of multiple model generation via global property multipliers on the Heidrun field model. Models that match history close to or better than the base model (donated by Statoil) are in red.

Models	MULTPERMX	MULTPERMY	MULTPERMZ	MULTPOR	Global, $\mathbf{OF}_{model}$	Partial, X_{FGOR}	Partial, X_{FWCT}	Qualifier value, Q
23	1.487502634	1.434744343	0	0.93202	911.0879	911.0852	0.002707	-12.6339
24	0.504108224	0.858641123	0	1.145929	1419.882	1419.878	0.003381	36.15541
25	1.469312492	0.669092577	0	1.118404	1433.638	1433.636	0.001883	37.47452
26	1.452767151	1.14145131	0	0.971963	891.5491	891.5475	0.00156	-14.5075
27	1.080535217	0.909615242	0	1.109095	1309.357	1309.355	0.002042	25.55694
28	1.122963372	1.447154697	0	0.924929	1039.818	1039.815	0.003026	-0.2897
29	1.422787897	1.008765714	0	1.041162	1083.729	1083.728	0.001045	3.921011
30	1.534541575	1.215473931	0	0.960956	868.3169	868.3151	0.001821	-16.7353
31	0.616698469	0.79935589	0	0.978988	1504.102	1504.101	0.001647	44.23149
32	1.071170296	1.03031004	0	0.911489	1339.726	1339.722	0.003695	28.46909
33	1.042041938	1.071434997	0	1.114874	1395.977	1395.974	0.002274	33.8631
34	1.506712716	1.381255944	0	1.017788	878.808	878.8069	0.001118	-15.7293
35	1.100121194	1.148009697	0	1.052739	1079.335	1079.334	0.001321	3.499684
36	0.726887475	0.736280915	0	0.965192	1529.489	1529.487	0.001762	46.6659
37	1.266210241	1.320141509	0	0.893825	1249.642	1249.637	0.004601	19.83074
38	1.149354089	1.389209354	0	0.939313	985.0569	985.0544	0.002522	-5.54084
39	0.509353081	0.820176074	0	1.153737	1428.263	1428.26	0.003564	36.95913
40	0.473096148	1.125191248	0	1.133075	1313.334	1313.331	0.003326	25.93835
41	0.717984091	1.085170756	0	1.013621	1138.351	1138.35	0.001398	9.158863
42	0.760692425	0.554895073	0	1.083106	1389.892	1389.891	0.001342	33.27967
43	1.032700664	1.226396843	0	0.946634	1072.29	1072.288	0.002339	2.824147
44	0.676359969	0.681048018	0	1.046963	1386.652	1386.65	0.001151	32.9689
45	1.309782628	0.851137147	0	1.075333	1257.336	1257.335	0.001315	20.56857
46	0.696691145	1.417985434	0	0.950142	1183.796	1183.794	0.002393	13.51671
47	0.908900986	0.903325753	0	1.057915	1180.734	1180.733	0.001283	13.22306
48	1.373808799	1.543250288	0	1.00866	856.9876	856.9864	0.001186	-17.8217
49	0.890908812	0.76370968	0	1.069029	1249.12	1249.119	0.001303	19.78072

Table D-2 Results of multiple model generation via global property multipliers on the Heidrun field model. Models that match history close to or better than the base model (donated by Statoil) are in red. The reference model from which synthetic data on the Heidrun field was modelled is highlighted in light green. The best model closest to the reference model that was identified after the multiple monitor inversion (see chapter 7.3) is highlighted in light blue.

Models	MULTPERMX	MULTPERMY	MULTPERMZ	MULTPOR	Global, $\mathbf{OF}_{model}$	Partial, X_{FGOR}	Partial, X_{FWCT}	Qualifier value, Q
50	1.042990368	0.841343625	0.670757634	1.072502	1156.744	1156.743	0.00137	10.92261
51	0.679700649	1.120114792	1.082913889	1.076998	1170.043	1170.042	0.001779	12.1979
52	1.504144718	1.540673964	0.593541222	1.035459	888.7092	888.708	0.001202	-14.7798
53	1.026825747	0.734008312	0.838669175	0.959584	1305.185	1305.183	0.001806	25.15691
54	1.355753757	0.506886802	1.268988487	1.05236	1287.56	1287.559	0.000777	23.46681
55	0.827921839	0.529670207	0.548078214	1.00585	1552.813	1552.813	0.000948	48.90251
56	1.3095147	1.497155094	0.518975501	1.107552	1306.521	1306.518	0.002303	25.28498
57	0.723355355	1.149088762	0.811611478	1.046768	1082.651	1082.649	0.001486	3.817618
58	0.910460188	1.087777056	0.775666198	0.957212	1162.286	1162.284	0.002152	11.45402
59	0.949457712	1.391167656	0.574425866	0.979135	983.8112	983.8095	0.001725	-5.6603
60	1.501795217	0.890943116	0.907132134	1.131236	1529.204	1529.202	0.00242	46.63855
61	1.11060439	0.869908692	0.608530004	1.167421	1509.015	1509.012	0.003581	44.70259
62	0.592884402	1.463840803	1.197834217	1.14427	1441.063	1441.059	0.003701	38.18651
63	1.149608778	1.192950463	0.723349918	0.98765	919.9097	919.9082	0.001476	-11.7879
64	0.687332122	0.791834798	0.632937732	1.079315	1270.638	1270.636	0.001591	21.84408
65	0.500874069	0.914754381	1.162856975	1.103629	1340.33	1340.328	0.00238	28.52704
66	1.007246737	1.281634483	1.28961047	0.880238	1470.467	1470.462	0.005383	41.00617
67	0.526333532	1.171712315	0.867824451	1.031111	1136.937	1136.935	0.001688	9.023208
68	0.990458757	0.524279217	0.488677675	1.123917	1331.834	1331.832	0.001967	27.71234
69	0.824513332	1.455184981	0.66921022	1.064924	1043.062	1043.06	0.001766	0.021355
70	1.168982965	1.243347516	1.392687623	1.126807	1551.417	1551.414	0.002682	48.76861

Table D-3 Results of multiple model generation via global property multipliers on the Heidrun field model. Models that match history close to or better than the base model (donated by Statoil) are in red.

Models	MULTPERMX	MULTPERMY	MULTPERMZ	MULTPOR	Global, $\mathbf{OF}_{model}$	Partial, X_{FGOR}	Partial, X_{FWCT}	Qualifier value, Q
71	1.428309225	1.218982715	0.844408143	0.862858	1556.858	1556.851	0.006658	49.29035
72	0.580993538	1.265361591	0.590147053	0.94625	1447.077	1447.074	0.002719	38.76319
73	0.568638477	0.642491964	0.537380141	1.170775	1443.312	1443.308	0.00386	38.40218
74	0.733106999	1.072785961	0.875811901	0.921002	1528.957	1528.954	0.003343	46.61487
75	1.519896927	1.429081391	0.972401435	1.013311	857.5069	857.5058	0.001123	-17.7719
76	1.127057379	1.048993551	1.514644317	0.887247	1270.421	1270.416	0.004925	21.82334
77	1.459179784	0.668372855	0.99503853	1.015835	1105.387	1105.386	0.000877	5.997877
78	0.874588599	0.940750875	1.414678193	0.967627	1243.77	1243.768	0.001807	19.26767
79	0.9019254	1.404701029	1.316944408	1.001011	1025.508	1025.507	0.001436	-1.66187
80	1.101782285	1.043238595	1.054772163	0.984432	1001.173	1001.172	0.001483	-3.99542
81	0.496378478	0.728386837	0.6516537	1.086122	1371.863	1371.861	0.001936	31.55077
82	0.982431682	0.801197294	1.429871088	0.993666	1201.758	1201.757	0.001214	15.23905
83	0.460160576	1.234632986	0.947438207	1.157495	1370.301	1370.296	0.004098	31.40097
84	0.862350599	1.483514172	1.47982026	0.925902	1148.578	1148.575	0.002956	10.13952
85	1.065890719	1.35481625	0.700443951	0.901917	1298.104	1298.099	0.004221	24.47786
86	0.551487	1.173106	0.763061	0.932456	1575.464	1575.461	0.003104	51.07449
87	0.661449553	0.55068214	0.79336368	1.060543	1471.075	1471.074	0.001158	41.06448
88	1.379607065	1.283958063	0.454095014	1.11815	1351.58	1351.578	0.002351	29.60581
89	1.25427782	0.933933666	0.712818816	1.095374	1249.643	1249.642	0.00171	19.8309
90	0.925556262	1.139507812	0.480706431	0.898557	1275.811	1275.806	0.004498	22.34014
91	0.843343702	0.688964752	1.214038444	0.972772	1431.377	1431.375	0.00148	37.25768
92	1.339287972	0.881549865	1.236617603	1.023432	1071.795	1071.794	0.000975	2.776613
93	1.049446362	1.000846939	1.222885306	1.041795	1107.078	1107.077	0.001158	6.160042
94	1.084399257	0.757759991	0.808869565	1.139289	1429.016	1429.014	0.002646	37.03136
95	1.451636732	1.373763701	1.036429413	1.097171	1368.557	1368.555	0.00198	31.2338

Table D-4 Results of multiple model generation via global property multipliers on the Heidrun field model. Models that match history close to or better than the base model (donated by Statoil) are in red.

Appendix E

Appended publications

E.1 Publications

- Omofoma, V. and MacBeth, C. (2015). Intra-survey Pressure Variations-Implications for 4D Seismic Interpretation. Paper presented at the 77th EAGE Conference and Exhibition-Workshops, Madrid, Spain, 1 – 4 June, 2015.

- Omofoma, V. E. and MacBeth, C. (2016). Quantification of Reservoir Pressure-sensitivity Using Multiple Monitor 4D Seismic Data. Paper presented at the 78th EAGE Conference and Exhibition, Vienna, Austria, 30 May – 2 June, 2016.

- Omofoma, V., MacBeth, C. and Amini, H. (2017). Intra-survey Reservoir Fluctuations – Implications for quantitative 4D seismic analysis. *Geophysical Prospecting (accepted, May 2017, under review)*

MADRID 2015
1-4 June 2015 | IFEMA Madrid

WS02-D04

Intra-survey Pressure Variations - Implications for 4D Seismic Interpretation

V. Omofoma* (Heriot-Watt University) & C. MacBeth (Heriot-Watt University)

SUMMARY

During the time taken for seismic data to be acquired, reservoir pressure and saturation may fluctuate as a consequence of field production and operational procedures. This has consequences for the quantitative analysis of 4D seismic data and particularly for understanding of the pressure signal that diffuses rapidly into the reservoir over a time-scale of hours or less. A modelling study using actual acquisition data (permanent seabed sensors and also towed streamers), reveals that the signature of pressure variations in the pre-stack domain is complex, and thus the resultant post-stack image is not representative of the true reservoir mechanisms that caused the pressure changes. This is of particular concern when trying to accurately resolve small pressure changes away from wells with post-stack data. It appears however that larger signals closer to the well may still be detected adequately. Our results have implications for post-stack quantitative 4D seismic analysis, as well as processing and acquisition workflows for detailed seismic time-lapse studies.

MADRID 2015
1-4 June 2015 | IFEMA Madrid

Introduction

Estimation of pressure changes across the reservoir is currently based on well measurement (for example: production logging tools and downhole gauges) and extrapolation using subsurface fluid flow simulation models. 4D seismic data may also sense these changes, and it is one of the main objectives for 4D seismic technology to perform the equivalent of a spatial pressure test on a field to determine its overall hydraulic connectivity. However, quantitative estimation of pressure changes across the reservoir using 4D seismic data is well known to be challenging (Eiken and Tøndel 2005). Many possible factors have been held responsible for this, such as: non-repeatability noise, rock stress sensitivity, geomechanical stress re-distributions, stress-unloading/damage of core plug samples, time scale of production versus laboratory, and shale effects (Alvarez and MacBeth 2014). In this study we introduce a new finding, which also adds to these arguments and warrants further future consideration. This relates to the time scale of seismic data acquisition relative to that of the pressure fluctuations themselves. During seismic acquisition (offshore or onshore) over many weeks, pressure variations induced in the field are captured in a non-obvious and irregular way across the pre-stack volume. Thus the post-stack (and migrated) data do not adequately reflect the spatial distribution of the true absolute pressure, but provide instead a complicated smeared and distorted average. The purpose of this study is to determine whether this effect is significant, and assess the impact it may have on our current 4D seismic interpretation practices. This is achieved by the use of modelling with real field acquisition and production data.

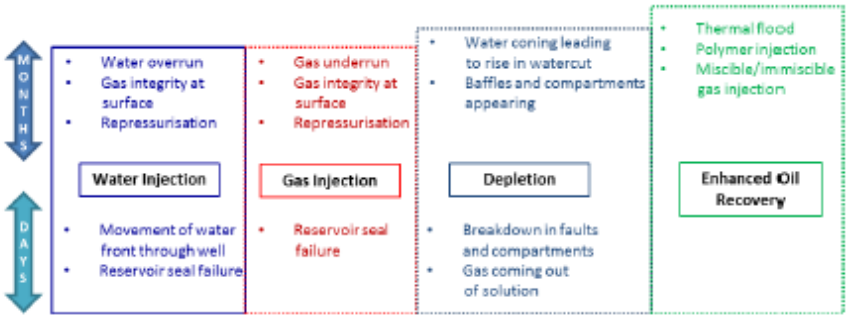

Figure 1 Examples of familiar processes that might occur in the reservoir at the same time as seismic data are acquired. Of particular interest are those effects with similar time scales to the surveying. For the water injector investigated in this study, the water front develops slowly, so that it can be viewed to be stationary over the period of acquisition. The pressure by contrast varies quickly over hours or less.

Time scale of acquisition versus production behaviour

Offshore seismic surveys shot to acquire data for monitoring purposes as part of a 4D seismic programme take many weeks to complete. The duration of the surveys is dependent on many practical factors such as the geometry of acquisition, boat speed, boat turn-around, spatial coverage required, and offset coverage. These are amidst other influences such as the effect of tides, platform and facility obstructions, general field activity and bad weather down-time which can typically run into days. Thus, for example, both towed streamer (Campbell et al., 2005) and permanent reservoir monitoring (Eriksrud 2014) surveys are most often acquired in a fairly randomized fashion with time scales ranging from 6 to 8 weeks. However, a range of random independent activities can also occur during the acquisition time that can induce pressure changes in the reservoir and its associated transients (Figure 1). These are controlled by operations management, and are specific to the well and field under consideration. Understandably, operations engineers would prefer that wells are in a steady state (constant flows), but in reality this is not the case. Some well activities possess similar time scales to the acquisition, for example: injector or producer well shut-off or re-start/start, alteration of a rate/choke setting, well tests, bumping/slugging, squeeze treatment where producers are typically shut-in for 12 hours. Turn-arounds, production optimisation, work-overs, evolving water cuts, and the introduction of new wells or re-introduction of old wells all add to this mix. Such well interventions can lead to localised pressure changes, and as pressure by its nature evolves/diffuses rapidly over a short time scale of hours after each significant change, the overall pressure field in the reservoir is

affected (depending on compartment size and properties). To illustrate this behaviour, the pressure variations of a single injector re-started during the actual acquisition of a permanent seabed system are superimposed upon the time scale of the acquisition (Figure 2(a)). Figure 2(b) shows the randomised nature of the shooting, which aimed to optimise time available and negotiate field operations and weather windows.

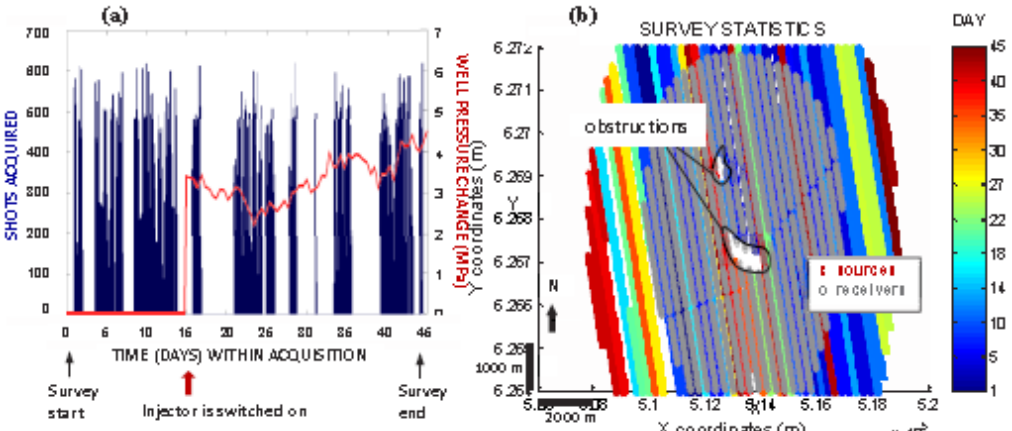

Figure 2 (a) Seismic acquisition activity histogram for a permanent reservoir monitoring survey superimposed on the pressure fluctuations of an injector well turned on during the acquisition. In the seismic survey, there are gaps at days when no data are acquired. (b) Geometry of seismic sources colour coded by the time sequence in days of shooting, with receivers overlain. The survey is not shot in a regular sequence covering the subsurface.

Modelling analysis

To understand the impact of the above intra-survey pressure variation on the time-lapse seismic data, we consider the example of an injector switched on 15 days into the shooting of a PRM survey as in Figure 2(a). Reservoir simulation is performed for a model of a uniform reservoir and a single injector, with a producer active outside the survey area (smaller than the seismic modelling area). The model is built based on the characteristics of a real North Sea field, but the reservoir simplified to a flat uniform reflector and homogenous overburden. The reservoir has a porosity of 21%, net-to-gross 0.7, reservoir thickness 30 m, permeability in X, Y and Z directions of 500 mD, 500 mD and 250 mD respectively.

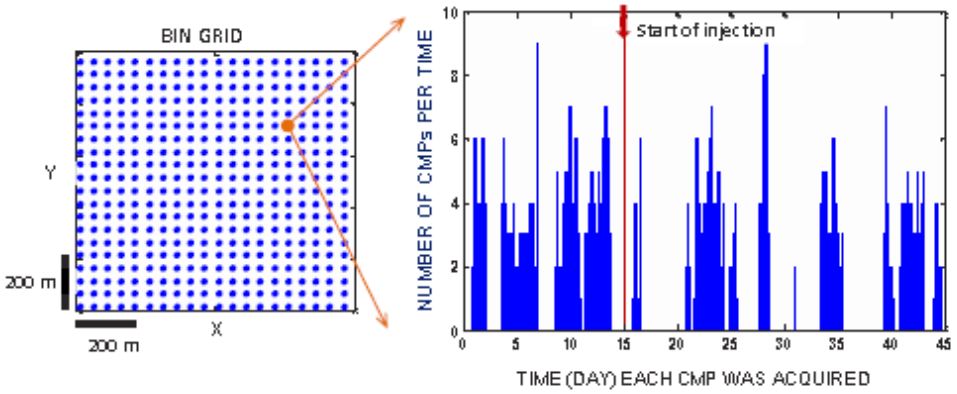

Figure 3 Histogram of time-stamped common midpoints (CMPs) sorted into each 50 x 50 m bin showing the time variability across a particular CMP bin. The resultant stacked trace in each CMP bin is an average from a combination of traces acquired at different times that have imaged different pressure variations before and after the injector is switched on.

The reservoir is under-saturated with initial water saturation 22% and initial pressure of 23.5 MPa. The simulation is run at fine-scale time steps of two hours to accurately determine the behaviour of a constantly injecting well with a rate 25,000 stb/day. The resulting field pressure and water saturation changes that occur during that time are then converted into seismic properties using a petroelastic model calibrated for the North Sea (Alvarez and MacBeth 2014), from which pre-stack reflection amplitude is computed. The source acquisition coordinates and timing of a real PRM survey are used to model the individual common mid-point data with the offset-dependent convolutional model (Amini 2014). Due to the large amount of available acquisition coordinates, source activations are decimated to every two hours and only these are considered. This also determines the numerical simulation time step above. The time stamped CMPs are then sorted into bins of 50x50m, corresponding to the simulation model grid, for ease of computation. A typical time distribution of CMPs in a bin is shown in Figure 3. CMPs are gathered into near-offset (less than 500m) and far-offset (1500m to 2500m), and then stacked. Finally, time-lapse amplitudes are created by differencing the resultant amplitude response from that prior to the production period. Similar results are found for higher fold images created by including sources that were activated every 10 minutes and finer simulation runs.

Results

The resulting map for the pressure-only seismic amplitudes is shown in Figure 4, together with the predicted responses for a fictitious 'instantaneous' acquisition, shot on the 25th and 44th day of production for reference. The injector creates a symmetric pressure distribution, spreading progressively outwards over time from the well, and eventually establishing an equilibrium with the boundaries of the model. The spatio-temporal character of this signal relative to the seismic acquisition, mixes the pressure sampling within each bin, which in turn causes the uneven time-lapse amplitude distribution. The time-lapse seismic amplitudes therefore do not represent either the situation before the injector, or after, but some complex spatio-temporal pre-stack mixture of the two. The images are distorted by the acquisition geometry and timing of the shooting. Qualitatively, the central image of the injector is clearly visible and can be interpreted, but quantitatively the overall shape is not correct, particularly with the smaller pressure changes. When coupled with non-repeatability noise, this would make interpretation difficult, and some features may be easily mistaken as having a geological origin. Furthermore, the near and far offset images sample the pressure change differently, which may be problematic for sophisticated time-lapse seismic analyses incorporating these data. Mean errors relative to the reference 'instantaneous' image at day 25 are of the order of 23% for near-offset amplitudes and 21% for the far-offset amplitudes - which are significant and cannot be ignored. The smallest error is around the injector itself, and error increases away from the injector location. Interestingly, due to the compact nature of the much slower water-flood progression during the intra-survey/injector period, water saturation (not shown) is relatively unaffected by the effects described above. That is, the pre-stack and post-stack time-lapse signatures appear very similar. Modelling studies for towed streamer and land acquisitions provide similar insight. In practice, the effect is locked into the post-stack image, smeared by migration and structural complexity.

Discussion and conclusions

Pressure variations caused by field operations during the shooting of a time-lapse acquisition can create a complicated spatio-temporal signature imprint on the pre-stack data. This signature does not translate into a clear post-stack image of the pressure. Therefore, during the acquisition of monitor surveys for time-lapse acquisition, care must be taken to understand the production engineering domain to avoid this occurring. The same is not true of water saturation changes. This modelling work with real acquisition data and fluid flow simulation reveals a number of important points:

- Ideally time-lapse acquisition must be performed during a quiet period of pressure equilibration in the reservoir lifecycle, can this be guaranteed? Should this be necessary?
- Quantitative analysis of pressure changes should be made in the pre-stack domain, not post-stack
- Quantitative analysis of water saturation changes may be accurate in the post-stack domain
- The time-scale of the survey relative to the well behaviour needs to be precisely defined in a time-lapse project – usually only one exact time is quoted for the survey, which is incorrect. Care must be taken in practice to assign times correctly to the survey.

- Near and far-offsets sample pressure differently, which may affect time-lapse analysis to separate changes of saturation and pressure.
- The comments above may also have a strong impact on pressure-related phenomena such as gas out of solution (Falahat et al. 2014).

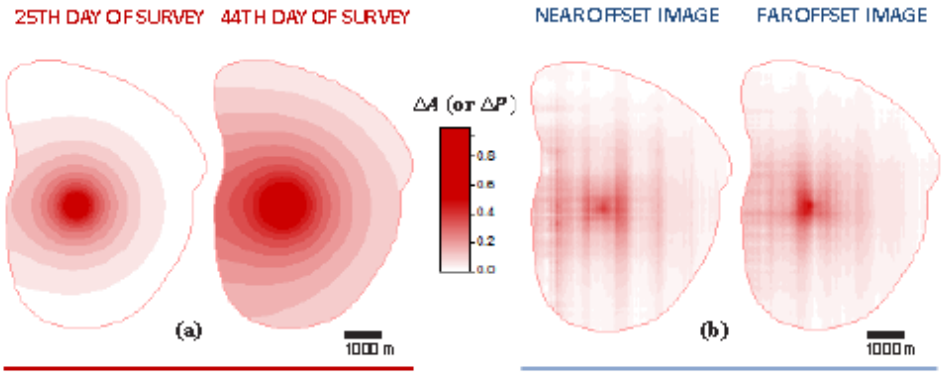

Figure 4. Pressure-driven time-lapse amplitude, taking into account acquisition timings relative to a single injector behaviour. Mapped amplitudes are individually normalized, and are shown at: (a) early and late life of the injector (assuming the survey was shot instantaneously), and (b) the resulting near and far offset images for a PRM survey. The dissimilarity at the near and far offsets suggests that the pressure image is significantly affected by the time sequence of shooting relative to well activity.

Acknowledgments

We thank the sponsors of the Edinburgh Time Lapse Project, Phase V, for their support (BG, BP, Chevron, CGG, ConocoPhillips, ENI, ExxonMobil, Hess, Ikon Science, Landmark, Maersk, Nexen, Norsar, RSI, Petoro, Petrobras, Shell, Statoil, Suncor, Taqa, TGS and Total). Thanks are extended to Schlumberger for providing the Petrel and Eclipse software. Special thanks to Alex Bertrand for providing the survey acquisition data, and Henning Hoeber for discussions.

References

- Alvarez, E. and MacBeth, C. (2014) An insightful parameterization for the flatlander's interpretation of time-lapsed seismic data. *Geophysical Prospecting* **62**, 75-96.
- Amini H. (2014) A pragmatic approach to simulator to seismic modelling for 4D seismic interpretation. PhD Thesis, Institute of Petroleum Engineering, Heriot-Watt University.
- Campbell, S., Ricketts, T. A., Davies, D. M., Slater ,C. P., Lilley, G. G., Brain, J., Stammeijer, J., and Evans, A.C. (2005) Improved 4D Seismic Repeatability — a West of Shetlands Towed Streamer acquisition case history. *SEG Technical Program Expanded Abstracts 2005*, pp. 2394-2397.
- Eiken, O. and Tøndel, R. (2005) Sensitivity of Time-lapse Seismic Data to Pore Pressure changes: Is Quantification Possible? *Society of Exploration Geophysicists*, **24 (12)**, 1250-1254.
- Eriksrud, M. (2014) Seabed permanent reservoir monitoring (PRM) – A valid 4D seismic technology for fields in the North Sea. *First Break*, **32 (5)**, 67 – 73.
- Falahat, R., Obidegwu, D., Shams, A., and MacBeth, C. (2014) The interpretation of amplitude changes in 4D seismic data arising from gas exsolution and dissolution, *Petroleum Geoscience*, **20**, 303 – 320.

VIENNA 2016

Th LHR2 04

Quantification of Reservoir Pressure-sensitivity Using Multiple Monitor 4D Seismic Data

V.E. Omofoma* (Heriot-Watt University) & C. MacBeth (Heriot-Watt University)

SUMMARY

Key to quantitative interpretation of 4D seismic data for the separation of pressure and saturation effects is accurate knowledge of their individual contributions to the 4D seismic signatures. Currently, pressure sensitivity is calibrated using laboratory measurements on core plugs that have limited applicability to the in-situ field-scale reservoir response. A complementary technique for estimating pressure sensitivity is to compare seismic and pressure measurements. This is possible in selected areas around and away from wells where pressure variations contribute predominantly to the 4D signatures. Multiple monitor 4D seismic data are utilised to sample these areas as a function of field production time. The technique is applied to seismic amplitudes across a variety of producing North Sea clastic reservoirs. The results indicate that pressure sensitivity varies according to the geology of each reservoir. Also, estimates around some water injectors appear to show elevated sensitivity, suggesting the presence of induced fractures.

78th EAGE Conference & Exhibition 2016
Vienna, Austria, 30 May – 2 June 2016

Introduction

The stress sensitivity of the reservoir rocks (due to fluid pore pressure change) though a mature subject, lacks proper in-situ calibration. Much of our current knowledge is based on laboratory experiments with core plug samples, where elastic moduli of the rock are measured under various isotropic or uniaxial applied loads. However, many studies have raised concern with these laboratory measurements and their suitability for replicating the in-situ reservoir response (Alvarez and MacBeth 2014). Alternative attempts have also been made to measure the stress sensitivity using other data. For example, Fürne et al. (2009) combined repeat formation tester and well log data to reveal weaker in-situ stress sensitivity than in the laboratory. Amini and MacBeth (2015) inferred the sensitivity by comparing observed 4D seismic data with synthetic data from a simulator to seismic study at areas around water injectors where pressure changes dominate. The purpose of this current study is to extend the latter approach by generalising the concept beyond just water injectors by including data acquired at different monitor times, and to apply the method to a wide range of offshore fields with different geological environments.

Method

Our method relies on the use of multiple repeated monitor surveys shot across a field undergoing production and recovery. We measure the magnitude of 4D seismic signals at different times and at specific locations in the reservoir where pressure changes are considered to be the over-riding influence, this is then cross-plotted against the estimated pressure changes. At these key locations, the hydrocarbon reservoir can experience a diversity of pressure changes, ΔP, over time and across the different monitor surveys (such as injection, depletion, re-pressurisation or relaxation). Sampling the seismic response over a sufficiently wide range of pressure changes enables us to evaluate the pressure sensitivity (Figure 1). The fields we have selected have up to five monitor surveys. For the method to work, there has to be significant pressure change between monitor surveys and good knowledge of the pressures at these reference locations. Estimated pressures are obtained from bottom-hole-pressure (BHP) for wells perforated in the reservoir, repeat-formation-tester (RFT) logs and depth-averaged maps of simulated pressures from a well history-matched reservoir model. These pressure data sources carry their own uncertainties, with the measured historical BHP or RFT pressure generally more reliable than simulated data (Beaumont et al. 1999). For the seismic data, our current work focuses around amplitudes sensitive to reservoir changes. Specifically, we work with top reservoir amplitude maps of post stack migrated data (full stack) computed using appropriate window parameters to suit each reservoir. Before proceeding, the seismic data are calibrated via 3D and 4D well ties (well production data co-located in space and time with the seismic response), and also calibrated for sim2seis studies (Amini 2014).

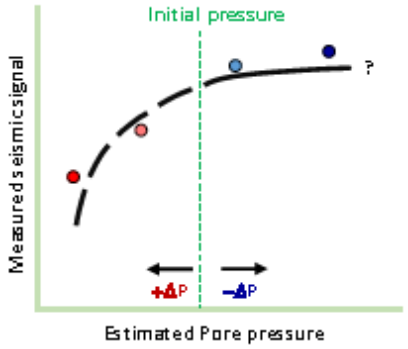

Figure 1 Generalised stress-sensitivity curve (black). Areas in the reservoir may exhibit a range of pore pressures for sampling across monitor times.

Although areas where pressure changes dominate are likely to be strongly field dependent, some generalisations are possible to guide our study: **(i)** *Inside water-flooded areas or regions of undisturbed fluid saturations* - areas water-flooded at a previous monitor time are likely to show pure pressure signals in subsequent monitor surveys. This result may however be biased by fractures existing around the borehole. We start by calibrating signals around water-flooded wells and expand outwards to larger water-flooded regions. Areas in the natural water or gas leg are useful as initial saturation levels are likely to remain fixed over time. **(ii)** *Outside areas undergoing significant saturation changes* - whilst theoretically small, pressure signals should still exist away from injectors and outside the influence of a growing water-flood front. Likewise, in areas away from producers undergoing depletion but no associated gas breakout in oil leg or negligible gas condensation effect in gas fields. These areas could be significant if the injection or depletion response is inside a compartment. One assumption is that other changes such as temperature, salinity or saturation changes are negligible, and this can be checked to some extent by modelling.

Application to field datasets

The method is applied to four North Sea clastic reservoirs with different characteristics. Pressure scenarios are identified by the polarity of the pressure change, reservoir location, and measurements at and away from wells. For measurements around wells, the 4D signals are taken within 200 m of the well perforation points. Measurements away from wells and in compartments are extracted by drawing polygons around the pressure signals on 4D maps. In Figure 2, we show pressure calibration using well pressure and injection data to interpret the 4D amplitude signatures for one scenario of a single water injector in an oil-leg compartment in field A. The analysis must be performed on a monitor by monitor basis per location as not all monitor surveys give clear pressure signals depending on well activity. Furthermore, complexities arise when calibrating pressure signals in other parts of field A because the signal variations predominantly relate to other effects across the reservoir. Below, we briefly describe each field and Table 1 details our results for their identified pressure scenarios.

- **Field A** is a tertiary deep water stacked turbidite reservoir composed of calcite cemented channel sands with average effective porosity 1 to 15%. The reservoir has black oil close to bubble point and production is by water injection to maintain pressure. Connectivity is a problem, and several compartments exists. Five monitor surveys (1999 to 2008) have been acquired with average non-repeatability noise 30 to 60%. Pressure effects are around water-flooded injectors, away from the water-flood front (outside wells) and in a compartment using the 2004, 2006 and 2008 surveys.

- **Field B** is a horst block of four segments divided into two separate compartments with good internal connectivity, composed of lower to middle Jurassic cemented fluvial sands with effective porosity 15 to 20%. Production of the oversaturated oil is by water injection and water-alternating-gas (WAG) injection. Four monitor surveys between 2001 (base) and 2006 have been acquired with non-repeatability 20 to 40%. Post 2001 re-pressurisation occurred and the pressure effects grew with time in the smaller compartment (a segment with a producer and water injector).

- **Field C** is a large fault-bounded dip closure with numerous fault segments but good connectivity composed of late Jurassic shallow marine sands. Reservoir sandstones are unconsolidated and homogenous with porosities 27 to 30%. Production of the oversaturated oil is by water injection and gas and WAG injection. Five monitor surveys (2001 to 2011) have been acquired with non-repeatability 20 to 30%. Oil had been produced by 2001 and subsequent surveys show mild pressure effects in the water leg (around injectors) and water-flooded oil leg (around producers).

- **Field D** is a highly stressed rotated fault block composed of deep water Jurassic stacked shoreface slightly consolidated sands with porosity 20 to 25%. The reservoir is a high-pressure-high-temperature (HPHT) gas condensate above dew point. Four seismic monitor surveys in 2001 (base), 2002, 2004 and 2013 with non-repeatability 5 to 15%. Production is by pressure depletion.

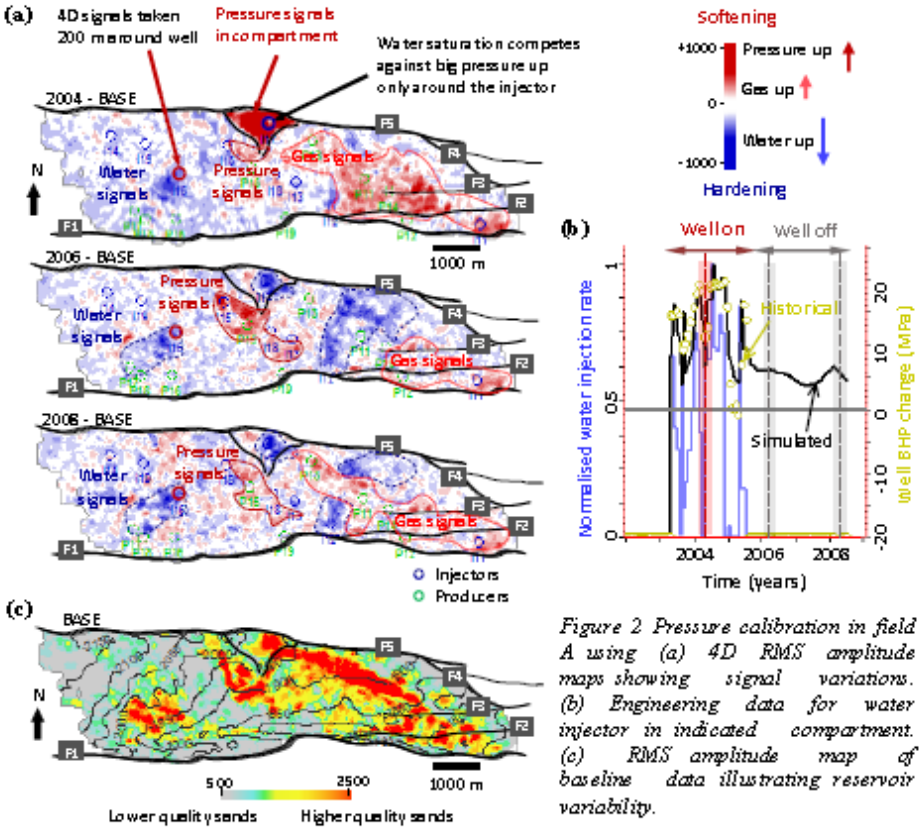

Figure 2 Pressure calibration in field A using (a) 4D RMS amplitude maps showing signal variations. (b) Engineering data for water injector in indicated compartment. (c) RMS amplitude map of baseline data illustrating reservoir variability.

Results and discussion

The results are shown in Table 1. We find pressure sensitivity varies quite considerably across the fields. The normally pressured unconsolidated sands of Field C are the most pressure sensitive while the slightly consolidated sands of the HPHT Field D are the least sensitive. Pressure sensitivity is certainly a seismic attribute dependent quantity, and we believe that the results may depend on the attribute measured, time gate, and also if time shifts are used instead. Interestingly, we observe an increased sensitivity around some water injectors in Field A, which may be due to induced fractures. The pressure sensitivity for amplitudes ranges from 4.5%/MPa to a much higher 17% for these fractured areas. Pressure sensitivity is 1.0%/MPa for Field B, 8.0%/MPa for field C and 0.3%/MPa for Field D. In comparison, laboratory-derived pressure sensitivity using bulk moduli (MacBeth, 2004) recorded a maximum of 10%/MPa for high porosity unconsolidated sands and 1%/MPa for the lower-porosity, cemented, and more-consolidated sands. All core sample measurements were assumed to be over-estimates. Whilst our measurements are consistent, limitations are: non-repeatability noise, assumption of the negligible influence of other phenomena in the areas studied and unreliability of available pressure measurements. In areas where there are no wells, depth-averaged maps of reservoir model simulated pressures are used, which may be in error. Likewise, analysis on Fields A, B and C used simulated well BHP and these are less accurate than historical pressures. Errors in simulated pressures are likely to be up to 25% - based on the misfit between their historical and simulated field production rates for gas, oil and water.

Conclusions

A technique for quantifying pressure sensitivity using multiple monitor seismic amplitude data has been successfully applied to four offshore clastic reservoirs. Our seismic-based method is transferable to other field types e.g. carbonates and could fill the gaps in rock-physics derived or laboratory-based measurements of pressure sensitivity. The method can also be extended for sensitivity measurements of other time-lapse effects such as saturations, temperatures etc. In doing so, we can better tackle the separation of pressure versus saturation for improved reservoir management. Finally, we note the implications of using post-stack data for pressure related studies (Omofoma and MacBeth, 2015) but justify our practical approach to be effective in areas with sufficiently large seismic signals.

Field	Pressure scenarios	No. of wells / monitors used	ΔP (MPa)		%ΔA	
			Mean	std	Mean	std
A	Compartment	1 injector / 1	18.0	0.35	122	71.6
	Water-flooded	4 injectors / 2	3.31*	1.81*	14.9	14.9
	Outside wells	None / 3	4.00	1.50	30.7	30.6
	Fractured	2 injectors / 2	-2.12*	0.84*	-36.4	8.80
B	Compartment	1 injector / 2	25.2*	5.40*	26.0	21.0
C	Water-flooded	7 producers / 4	-4.66*	3.21*	-21.0	5.10
	Water leg	5 injectors / 4	6.42*	3.80*	21.3	11.9
D	Gas leg	6 producers / 2	-53.3	4.40	-15.0	9.90

*Table 1 Mean and standard deviation (std) of amplitude-pressure sensitivity in four clastic reservoirs for each pressure scenario identified, number of wells and a number of monitor surveys. Pressure is well BHP (historical or simulated), or a depth-average prediction from the history-matched simulation model. *denotes simulated pressures.*

Acknowledgments

We thank the sponsors of the Edinburgh Time Lapse Project, Phase V and VI, for their support (BG, BP, Chevron, CGG, ConocoPhillips, ENI, ExxonMobil, Hess, Ikon Science, Landmark, Maersk, Nexen, Norsar, Petoro, Petrobras, RSI, Shell, Statoil, Suncor, Taqa, TGS, and Total). Thanks to Schlumberger for Petrel and Eclipse software and Hamed Amini for discussions.

References

- Amini H. 2014. A pragmatic approach to simulator to seismic modelling for 4D seismic interpretation. PhD Thesis, Institute of Petroleum Engineering, Heriot-Watt University.
- Amini, H. and MacBeth C., 2015. Calibration of rock stress-sensitivity using 4D seismic data. Extended abstract, 77th EAGE Conference and Exhibition, 1-4 June, Madrid, Spain.
- Alvarez E. and MacBeth C. 2014. An insightful parametrization for the flatlander's interpretation of time-lapse seismic data. *Geophysical Prospecting* 62(1), 75-96.
- Beaumont, A. E. and Foster, H. N. 1999. Treatise of Petroleum Geology/Handbook of Petroleum Geology: Exploring for Oil and Gas Traps. Chapter 5: Formation Fluid Pressure and Its Application. AAPG Special Volumes, Tulsa, OK., 64p.
- Fürre, A., Andersen, M., Moen, A. and Tønnessen, R. 2009. Deriving effects of pressure depletion on elastic framework moduli from sonic logs. *Geophysical Prospecting* 57(3), 427-437.
- MacBeth C. 2004. A classification for the pressure-sensitivity properties of a sandstone rock frame. *Geophysics* 69(2), 497–510.
- Omofoma, V., and MacBeth C., 2015. Intra-survey pressure variations – implications for 4D seismic interpretation. Extended abstract, 77th EAGE Conference and Exhibition 2015, 1-4 June, Madrid, Spain.

References

Aanonsen, S. I., Aavatsmark, I., Barkve, T., Cominelli, A., Gonard, R., Gosselin, O., Kolasinski, M., and Reme, H. (2003). Effect of Scale Dependent Data Correlations in an Integrated History Matching Loop Combining Production Data and 4D Seismic Data. *SPE Reservoir Simulation Symposium*, Houston, Texas. Expanded Abstract, SPE-79565-MS, https://doi.org/10.2118/79565-MS

Aarre, V. (2006). Estimating 4D velocity changes and contact movement on the Norne field. SEG Annual Meeting, 1-6 October, New Orleans, U.S.A. Expanded Abstracts, 3115-3119, https://doi.org/10.1190/1.2370175.

Aki, K. and Richards, P.G. (1980). *Quantitative seismology, Theory and methods*. W.H. Freeman & Co.

Alerini, M., Ayzenberg, M., Ek, T., Feng, T., Hustoft, L., Lie, E., Liu, S., Skjei, N. and Skjervheim, J.A. (2014). Utilisation of time-lapse seismic for reservoir model conditioning. *76th EAGE Conference and Exhibition*, Amsterdam RAI, The Netherlands, Expanded Abstracts, We G102 10, http://dx.doi.org/10.3997/2214-4609.20141144.

Alsos, T., Osdal, B. and Høiås, A. (2009). The many faces of pressure changes in 4D seismic at the Svale field and its implication on reservoir management. *71st EAGE Conference and Exhibition incorporating SPE EUROPEC 2009*, Expanded Abstracts, Y004, http://dx.doi.org/10.3997/2214-4609.201400532.

Alvarez, E. (2014). *Petroelastic approximations for quantitative 4D seismic interpretation*. PhD thesis, Heriot-Watt University.

Alvarez, E. and MacBeth, C. (2014). An insightful parametrisation for the flatlander's interpretation of time-lapse seismic data. *Geophysical Prospecting* **62**(1), 75-95.

Amini H. (2014). *A pragmatic approach to simulator to seismic modelling for 4D seismic interpretation*. PhD Thesis, Heriot-Watt University.

Andersen, C. F., Grosfeld, V., Van Wijngaarden, A.J. and Haaland, A. N. (2009). Interactive interpretation of 4D prestack inversion data using rock physics templates, dual classification, and real-time visualisation. *The Leading Edge*, **28**(8), 898-906.

Aouad, A., Taylor, R. and Millar, N. (2012). Seismic on the edge – a 3D transition zone seismic survey from concept to final volume. *22nd ASEG Conference and Exhibition*, Extended Abstracts, 1-5, http://dx.doi.org/10.1071/ASEG2012ab377.

Arts R. J., Chadwick R.A., Eiken O., Trani M. and Drotland S. (2007). Synthetic versus real time-lapse seismic data at the Sleipner CO2 injection site. *77th SEG meeting*, San Antonio, USA, Expanded Abstracts, 2974-2978.

Avseth, P., Mukerji, T. and Mavko, G. (2010). *Quantitative seismic interpretation: Applying rock physics tools to reduce interpretation risk*. Cambridge university press.

Avseth, P., Skjei, N. and Mavko, G. (2016). Rock-physics modeling of stress sensitivity and 4D time shifts in patchy cemented sandstones - Application to the Visund Field, North Sea. *The Leading Edge,* **35**(10), 868-878.

Avseth, P., Skjei, N. and Skålnes Å. (2013). Rock physics modelling of 4D time-shifts and time-shift derivatives using well log data — A North Sea demonstration: *Geophysical Prospecting*, **61**(2), 380–390, http://dx.doi.org/10.1111/j.1365-2478.2012.01134.x.

Ayzenberg, M. and Liu, S. (2014). Saturation and Pressure Inversion-From 4D Seismic to Reservoir Model Updating. *76th EAGE Conference and Exhibition*, Amsterdam RAI, The Netherlands, Expanded Abstracts, We G102 16, http://dx.doi.org/10.3997/2214-4609.20141150 .

Backus, G.E. (1952) Long-wave elastic anisotropy produced by horizontal layering. *Journal of Geophysical Research*, **67**(11), 4427-4440.

Bagaini, C., Bunting, T., El-Emam, A., Laake, A. (2010). Land Seismic Techniques for High-Quality Data. *Oilfield Review*, **22**(10), 28-29.

Barker, T. B., Chen, B. N., Hague, P. F., Majain, J. and Wong, K. (2008). Understanding the Time-Lapse Seismic Response of a Compacting Carbonate Field, Offshore Sarawak, Malaysia. *International Petroleum Technology Conference*, Extended Abstracts, http://dx.doi.org/10.2523/IPTC-12514-MS.

Barkved, O. I. (2004). Continuous Seismic Monitoring. *74th SEG Meeting*, Denver, Colorado, USA, Expanded Abstracts, 2537-2540, http://dx.doi.org/10.1190/1.1851258.

Barkved, O. I., Kristiansen, T. and Fjær, E. (2005). The 4D seismic response of a compacting reservoir – Examples from the Valhall Field, Norway. *75th SEG Annual International Meeting*, Expanded Abstracts, 2508-2511, http://dx.doi.org/10.1190/1.2148232.

Barkved, O. I., Van Gestel, J. P., Bergsvik, L. S., Stockden, I. and Kommedal, J. H. (2009). Seismic PLT–Linking Seismic Time-lapse Responses to Production and Injection Data. *71st EAGE Conference and Exhibition incorporating SPE EUROPEC*, Amsterdam, The Netherlands, 8-11 June. Expanded Abstracts.

Batzle, M. and Wang, Z. (1992) Seismic properties of pore fluids. *Geophysics*, **57**(11), 1395-1508.

Beaumont, E. A., and Fiedler, F. (1999). Treatise of Petroleum Geology/Handbook of Petroleum Geology: Exploring for Oil and Gas Traps. Chapter 5: Formation Fluid Pressure and Its Application. *AAPG Special Volumes*, Tulsa, OK, 64p.

Behrens, R., Condon, P., Haworth, W., Bergeron, M., Wang, Z. and Ecker, C. (2002). 4D seismic monitoring of water influx at Bay Marchand: The practical use of 4D in an imperfect world. *SPE Reservoir Evaluation and Engineering*, 5, 410 - 420.

Benguigui, A. (2010). *Quantitative evaluation of structural compartmentalisation in the Heidrun field using time-lapse seismic data*. Ph.D. thesis, Heriot Watt University.

Benguigui, A., Roberts, G., and Shaw-Champion, M. (2012). Time-lapse 2D seismic steamflood monitoring - a case study from offshore republic of Congo, the Emeraude field. *74th EAGE Conference & Exhibition incorporating SPE EUROPEC 2012*, Copenhagen, Denmark, 4-7 June, Expanded Abstracts.

Bergmann, P., and Chadwick, A. (2015). Volumetric bounds on subsurface fluid substitution using 4D seismic time shifts with an application at Sleipner, North Sea. *Geophysic*s, **80**(5), 153-165.

Bertrand, A., Folstad, P. G., Lyngnes, B., Buizard, S., Hoeber, H., Pham, N., Pierrepont de S., Schultzen, J. and Grandi, A. (2014). Ekofisk life of field seismic: Operations and 4D Processing. *The Leading Edge*, **33**(2), 142-148.

Bertrand, A., Mcquaid, S., Bobolecki, R., Leiknes, S. and Egil, H. (2005). Gas-oil contact monitoring at Troll using high resolution 4D analysis and neural networks. *67th EAGE Conference and Exhibition*, Expanded Abstracts, C040.

Björck, Å. (1988). A direct method for sparse least squares problems with lower and upper bounds. Numerische Mathematik, **54**(1), 19-32.

Blanchard, T. D. (2012). Inherent uncertainties in 4D AVO and the implications on pressure and saturation inversion. *74th EAGE Conference and Exhibition incorporating EUROPEC 2012*, Copenhagen, Denmark, Expanded Abstracts, Y020, http://dx.doi.org/10.3997/2214-4609.20148815.

Blanchard, T.D. and Thore, P (2013). Breaking the limitations of pressure and saturation inversion with a new dynamic constraint. *75th EAGE Conference and Exhibition incorporating SPE EUROPEC 2013*, London, UK, Expanded Abstracts, Th 14 13, http://dx.doi.org/10.3997/2214-4609.20130179.

Box, G. E., Hunter, J. S. and Hunter, W. G. (2005). *Statistics for experimenters: design, innovation, and discovery* (Vol. 2). *New York: Wiley-Interscience.*

Brain, J. (2011) *Shearwater: Intern project description*. Shell UK.

Brain, J. P., Coogan, S., Floricich, M., Goudswaard, J., Hake, H., Hunt, K., and McDonnell, P. (2009). 4D imaging beneath a gas chimney for quick identification of development opportunities. *71st EAGE Conference and Exhibition incorporating SPE EUROPEC 2009*, Amsterdam, The Netherlands, Expanded Abstracts, Y001.

Briceno, A. (2017). *Calibration and use of the Petroelastic Model for 4D Seismic interpretation.* PhD thesis, Heriot-Watt University.

Briceno, A., MacBeth, C. and Mangriotis, M. D. (2016). Towards an Effective Petroelastic Model for Simulator to Seismic Studies. *78th EAGE Conference and Exhibition*, Vienna, Austria, 30 May - 2 June. Expanded Abstracts, Th LHR2 08, http://dx.doi.org/10.3997/2214-4609.201601319

Brie, A., Pampuri, F., Marsala, A. F. and Meazza, O. (1995). Shear sonic interpretation in gas-bearing sands. *SPE Annual Technical Conference and Exhibition*. SPE30595, 701-710.

Brown, R. J. and Korringa, J. (1975). On the dependence of the elastic properties of a porous rock on the compressibility of the pore fluid. *Geophysics*, **40**(4), 608-616.

Buland, A. and El Ouair, Y. (2006). Bayesian time-lapse inversion. *Geophysics*, **71**(3), R43-R48.

Burns C. B., Aggio A., Gjøystdal, H. and Santos R. (2002). Facts from fiction-4D seismic model-based interpretation. *SPE International Petroleum Conference and Exhibition*, Villahermosa, Mexico, 10-12 February. SPE-74338-MS.

Byerley, G., Barham, G., Tomberlin, T. and Vandal, B. (2009). 4D seismic monitoring applied to SAGD operations at Surmont, Alberta, Canada. *79th SEG Annual International Meeting*, Expanded Abstracts, 3959–3953, http://dx.doi.org/10.1190/1.3255695.

Caldwell, J., Koudelka, E., Nesteroff, K., Price, R. and Zhang, P. (2015). Seismic permanent reservoir monitoring (PRM)–A growing market. *First Break*, 33(11), 65-73.

Calvert, M.A., Roende, H.H., Herbert, I.H., Za, J., Hickman, P. and Micksch, U. (2014). The impact of a quick 4D seismic survey and processing over the Halfdan Field, Danish North Sea. *First Break*, **32**(4), 43-50.

Calvert, R. (2005). 4D technology: Where are we, and where are we going? *Geophysical Prospecting*, **53**(2), 161-171.

Calvert, R.W. (2005a). *Marine time-lapse seismic surveying*. US patent #6906982 B2.

Calvert, R.W. (2005b). Insights and Methods for 4D reservoir monitoring and characterisation. *SEG/EAGE Distinguished Instructor Short Course.*

Campbell, S., Lacombe, C., Brooymans, R., Hoeber, H. and White, S. (2011). Foinaven: 4D processing comes up trumps. *The Leading Edge*, **30**(9), 1034-1040.

Campbell, S., Ricketts, T. A., Davies, D. M., Slater, C. P., Lilley, G. G., Brain, J., Stammeijer, J. and Evans, A. C. (2005). Improved 4D Seismic Repeatability - a West of Shetlands Towed Streamer acquisition case history. *75th SEG Annual International Meeting*, Expanded Abstracts, 2394-2397, http://dx.doi.org/10.1190/1.2148203.

Campbell, S., Schons, M., Mathew, S., Khalil, A., Riley, D., Hill, C., Allan, P., Gubbala, E., Alexe, M., Dervish-Uman, C. and Deschizeaux, B. (2015). Optimising Value through Improved 4D Seismic Processing on 10 Vintages-Foinaven-Schiehallion-Loyal Case History. *77th EAGE Conference and Exhibition*, Madrid, Spain, Expanded Abstracts, Tu N101 10, http://dx.doi.org/10.3997/2214-4609.201412553.

Canning, A. (2010). Some practical aspects of amplitude recovery before AVO and inversion. *SEG Technical Program*, Expanded Abstracts, 393-397, http://dx.doi.org/10.1190/1.351367.

Castro, S.A., Caers, J., Otterlei, C., Meisingset, H., Hoye, T., Gomel, P. and Zachariassen, E. (2009). Incorporating 4D seismic data into reservoir models while honoring production and geologic data: A case study. *The Leading Edge*, **28**(12), 1498-1505. http://dx.doi.org/10.1190/1.3272706.

Chapin, M., Terwoght, D. and Ketting, J. (2000). From seismic to simulation using new Voxel body and geologic modelling techniques, Schiehallion Field, West of Shetlands. *The Leading Edge*, **19**(4), 408–412.

Chen, J. and Schuster, G.T. (1999). Resolution limits of migrated images. *Geophysics*, **64**(4), 1046-1053.

Chu, D., and Gist, G. A. (2010). Inversion of 4D seismic data: U.S. Patent 2010/0142323 A1.

Chu, D., Burger, J. C. and Medema, G. F. (2012). Using Time Strain Volume for Improved 4D Interpretation - Methods and Case Studies. *74th EAGE Conference & Exhibition incorporating SPE EUROPEC*. Copenhagen, Denmark, 4-7 June. Expanded Abstracts, Y017.

Cole, S., Lumley, D., Meadows, M. and Tura, A. (2002). Pressure and saturation inversion of 4D seismic data by rock physics forward modelling: *SEG Technical Program*, Expanded Abstracts, 2475-2478, http://dx.doi.org/10.1190/1.1817221.

Coleman, T.F. and Li, Y. (1993). A reflective Newton method for minimizing a quadratic function subject to bounds on some of the variables. *SIAM Journal on Optimisation*, **6**(4), 1040-1058.

Cooper, M., Thorogood, E., O'Donovan, A., Kristiansen, P. and Christie, P. (1999). Foinaven active reservoir management: The time-lapse signal. *69th SEG meeting*, Houston, USA, Expanded Abstracts, 1640-1642.

Corzo, M., M. (2009). *Pressure estimation using time-lapse seismic in compacting reservoirs*. PhD Thesis, Heriot Watt University.

Cox, J. R and Hibbard, H. C, "Digital seismic recording." U.S. Patent 3,315,223, issued April 18, 1957.

Dadashpour, M., Echeverría-Ciaurri, D., Kleppe, J. and Landrø, M. (2009). Porosity and permeability estimation by integration of production and time-lapse near and far offset seismic data. *Journal of Geophysics and Engineering*, **6**(4), 325-344.

Dadashpour, M., Landrø, M. and Kleppe, J. (2007). Nonlinear inversion for estimating reservoir parameters from time-lapse seismic data. *Journal of Geophysics and Engineering*, **5**(1), 54-66.

Dake, L. P. (1997). The practice of reservoir engineering, *Developments in Petroleum Science*, 2nd edition, Amsterdam: Elsevier, **36**.

Davolio, A., Maschio, C. and Schiozer, D. J. (2013). A methodology to constrain pressure and saturation estimation from 4D seismic using multiple simulation models and observed data. *Journal of Petroleum Science and Engineering*, 105, 51-61.

Domenico, S.N. (1974). Effect of water saturation on seismic reflectivity of sand reservoirs encased in shale. *Geophysic*s, **39**(6), 759-769.

Domes, F. (2010). *The influence of overburden on quantitative time-lapse interpretation*. Ph.D. thesis, Heriot-Watt University.

Dong, Y., Dean, S.O. (2008). Reservoir simulation model updates via automatic history matching with integration of seismic impedance change and production data. IPTC 12550.

Dubrule, O. (2003). Geostatistics for seismic data integration in earth models. *EAGE Distinguished Instructor Series 6, 282.*

Dvorkin, J. and Nur, A. (1996). Elasticity of high-porosity sandstones: Theory for two North Sea data sets. *Geophysics*, **61**(5), 1363-1370.

Dyce, M., D. Whitcombe, C. McKenzie, and L. Hodgson, 2004, the quantification of 4D noise: 66th Conference and Exhibition, EAGE, 7 – 10 June, Extended Abstracts

Eiken, O. and Tøndel, R. (2005). Sensitivity of Time-lapse Seismic Data to Pore Pressure changes: Is Quantification Possible? *The Leading Edge*, **24** (12), 1250-1254, http://dx.doi.org/10.1190/1.2149538.

El Quair, Y., Lygren, M., Osdal, B., Husby, O., Springer, M. (2005). Integrated reservoir management approach: from time-lapse acquisition to reservoir model update at the Norne Field. IPTC 10894.

Eriksrud, M. (2014). Seabed permanent reservoir monitoring (PRM) – A valid 4D seismic technology for fields in the North Sea. *First Break*, **32** (5), 67-73.

Fahimuddin, A., Aanonsen, S.I. and Skjervheim, J.A. (2010). Ensemble based 4D seismic history matching: Integration of different levels and types of seismic data. *SPE EUROPEC/EAGE Annual Conference and Exhibition*, Barcelona, Spain, Expanded Abstracts, SPE131453.

Falahat, R. (2012). *Quantitative monitoring of gas injection, exsolution and dissolution using 4D seismic*. PhD Thesis, Heriot-Watt University.

Falahat, R., Obidegwu, D., Shams, A. and MacBeth, C. (2014). The interpretation of amplitude changes in 4D seismic data arising from gas exsolution and dissolution. *Petroleum Geoscience*, **20**(3), 303-320.

Falahat, R., Shams, A. and MacBeth, C. (2013). Adaptive scaling for an enhanced dynamic interpretation of 4D seismic data. *Geophysical Prospecting*, **61**(1), 231-247.

Farmer, H. G., Galarraga, M., Wang, K., Stammeijer, J. and Lydon M. (2015). BC10 LoFS - First Results and Year One Operations. *Third EAGE Workshop on Permanent Reservoir Monitoring 2015*, Expanded Abstracts, WeB03, http://dx.doi.org/10.3997/2214-4609.201411984.

Fehmers, G. C., Hunt, K., Brain, J. P., Bergler S., Kaestner, U., Schutjens, P. M., Burrell, R. V. (2007) Curlew D - Pushing the boundaries of 4D depletion signal in a gas condensate field, UK Central North Sea. *69th EAGE Conference & Exhibition*, Expanded Abstracts, P074.

Feng, T., Skjervheim, J. and Evensen, G. (2012). Quantitative use of different seismic attributes in reservoir modeling. ECMOR XIII-13th European Conference on the Mathematics of Oil Recovery, Biarritz, France, Expanded Abstracts, A11, http://dx.doi.org/10.3997/2214-4609.20143172.

Fischer, D., Sørenes, N., Teichmann, E., Blekastad, H., Moen, A.S., Sollie, I.H. and Smith, P. (2013). Value creation by a long-term time-lapse seismic processing approach on the Heidrun field. *First Break*, **31**(10), 93-99.

Fjaer, E., Horsrud, P., Raaen, A.M., Risnes, R. and Holt, R.M. (1992). *Petroleum related rock mechanics* (Vol. 33). Elsevier.

Floricich, M. (2006). *An engineering-consistent approach for pressure and saturation estimation from time-lapse seismic data*. PhD thesis, Heriot-Watt University.

Floricich, M., C. MacBeth, J. Stammeijer, R. Staples, A. Evans, and C. Dijksman. (2006). A new technique for pressure-saturation separation from time-lapse seismic — Schiehallion case study. *68th EAGE Conference and* Exhibition, Vienna, Austria, Expanded Abstracts, E017.

Floricich, M., Jenkins, G. and McCormick, D. (2012). Probabilistic inversion of multiple 4D seismic as applied on Schiehallion field. *74th EAGE Conference and Exhibition incorporating EUROPEC 2012*, Copenhagen, Denmark, Expanded Abstracts, Y021, http://dx.doi.org/10.3997/2214-4609.20148816.

Floricich, M., MacBeth, C. and Staples, R. (2005). An engineering-driven approach for separating pressure and saturation using 4D seismic: Application to a Jurassic reservoir in the UK North Sea. *75th SEG Annual International Meeting*, Expanded Abstracts, 2464–2467, http://dx.doi.org/10.1190/1.2148221.

Follett, J. R. L., Wills, P., Lopez, J. L., Przybysz-Jarnut, J. K. and van Lokven, M. (2015). Continuous seismic reservoir monitoring at Peace River: Initial results and interpretation. *SEG Annual Meeting*, New Orleans, Louisiana, USA, Expanded Abstracts, 5440-5444, http://dx.doi.org/10.1190/segam2015-5883275.1

Folstad, P., G., Bertrand, A., Lyngnes, B., Haller, N. and Grandi, A. (2013). Ekofisk Permanent Seismic Monitoring-Results after First 2 Years. *Second EAGE Workshop on Permanent Reservoir Monitoring 2013–Current and Future Trends*, Stavanger, Norway, 2-5 July. Expanded Abstracts.

Freeman, P. J., Kelly, S.,MacDonald, C., Millington, J. and Tothill, M. (2008). The Schiehallion field: lessons learnt modeling a complex deepwater turbidite. In: Robinson, A., Griffiths, P., Price, S., Hegre, J. & Muggeridge, A. (eds) *The Future of Geological Modelling in Hydrocarbons Development*, Geological Society, London, Special Publications, 309, 205-219.

Furre, A. K., Bakken, E., Kløv, T. and Nordby, L.H. (2006). Heidrun 2001-2004 time-lapse seismic project: Integrating geophysics and reservoir engineering. *First Break*, **24(**4), 33-39.

Furre, A., Munkvold, F. & Nordby, L. (2003). Improving reservoir understanding using time-lapse seismic at the Heidrun Field. *65th EAGE Conference & Exhibition*, Stavanger, Norway.

Fursov, I. (2015). *Quantitative application of 4D seismic data for updating thin-reservoir models.* PhD Thesis, Heriot-Watt University.

Gainski, M., Macgregor, A.G., Freeman, P.J. and Nieuwland, H.F. (2010). Turbidite reservoir compartmentalisation and well targeting with 4D seismic and production data: Schiehallion Field, UK. *Geological Society, London, Special Publications*, **347**(1), 89-102.

Galbraith, M. (2001). 3D Seismic Surveys – Past, Present and Future. *CSEG Recorder*, **26**(6), 1-7.

Gassmann, F. (1951) Über die elastizität poröser medien: Vierteljahrss-chrift der Naturforschenden Gesellschaft Zurich 95, 1-23. (English translation from http://sepwww.stanford.edu/sep/berryman/PS/gassmann.pdf)

Gervais, V. and Roggero, F. (2010). Integration of saturation data in a history matching process based on adaptive local parameterisation. *Journal of Petroleum Science and Engineering*, **73**(1), 86-98.

Gilham, R., Hercus, C., Evans, A. and De Haas, W. (2005), *Shearwater (UK Block 22/30b): managing changing uncertainties through field life,* paper presented at Geological Society, London, Petroleum Geology Conference series, Geological Society of London.

Gosselin, O., Aanonsen, S. I., Aavatsmark, I., Cominelli, A., Gonard, R., Kolasinski, M., Ferdinandi, F., Kovacic, L, and Neylon, K. (2003). History Matching Using Time-Lapse Seismic (HUTS). *SPE Annual Technical Conference*, Denver, Colorado, USA. Expanded Abstracts, SPE-84464-MS.

Grandi, A., Lyngnes, B. and Haller, N. (2013). Reservoir Management through Frequent Seismic Monitoring at Ekofisk Field. *75th EAGE Conference and Exhibition incorporating SPE EUROPEC*, London, UK, Expanded Abstracts, Th1409, http://dx.doi.org/10.3997/2214-4609.20130175

Grandi, A., Wnuquier, S., Cumming, H., Deplanté, C., and Hubans, C. (2009). Quantitative 4D time lapse characterisation: three examples. *SEG International Exposition and Annual Meeting*. Houston, Texas, 25-30 October, Expanded Abstracts.

Gray, S. H. and May, W. P. (1994). Kirchhoff migration using eikonal equation traveltimes. *Geophysics*, **59**(5), 810-817.

Greaves, R. J. and Fulp, T. J. (1987). Three-dimensional seismic monitoring of an enhanced oil recovery process. *Geophysic*s, **52**(9), 1175-1187.

Grude, S., Landrø, M., and Osdal, B. (2013). Time-lapse pressure-saturation discrimination for CO2 storage at the Snohvit field. *International Journal of Greenhouse Gas Control*, 19, 369-378.

Guilbot, J., and Smith, B. (2002), 4-D constrained depth conversion for reservoir compaction estimation: Application to Ekofisk field. *The Leading Edge*, **21**(3), 302–308, http://dx.doi. org/10.1190/1.1463782.

Gurevich, B. (2004). A simple derivation of the effective stress coefficient for seismic velocities in porous rocks. Geophysics, **69**, 393-397.

Hale, D. (2009). A method for estimating apparent displacement vectors from time-lapse seismic images. *Geophysics*, **74**(5), 99-107.

Hall, S. A., MacBeth, C., Barkved, O.I., Wild, P. (2005). Cross-matching with interpreted warping of 3D streamer and 3D ocean-bottom-cable data at Valhall for time-lapse assessment. *Geophysical Prospecting*, **53**(2), 283-297.

Harris, N. B. (1989). Reservoir geology of Fangst Group (Middle Jurassic) Heidrun Field, Offshore Mid-Norway. *AAPG Bulletin*, **73**, 1415 - 1435.

Hashin, Z. and Shtrikman, S. (1963). A variational approach to the theory of the elastic behaviour of multiphase materials. *Journal of the Mechanics and Physics of Solids*, **11**(2), 127-140.

Hatchell, P. J., Wang, K., Lopez, J. L., Stammeijer, J. G. F., and Davidson, M. (2013). Instantaneous 4D seismic (i4D) for water injection monitoring. *75th EAGE Conference and Exhibition*, Expanded Abstracts, Th-01-11, http://dx.doi.org/10.3997/2214-4609.20130430.

Hatchell, P., and Bourne, S. (2005). Rocks under strain: Strain induced time-lapse time shifts are observed for depleting reservoirs. *The Leading Edge*, **24**(12), 1222–1225, http://dx.doi. org/10.1190/1.2149624.

Hatchell, P., van den Beukel, A., Molenaar, M., Maron, K. P., Kenter, C. J., Stammeijer, J. G. F., van der Velde, J. J. and Sayers, C. M. (2003). Whole-earth 4D: Reservoir monitoring geomechanics. *73rd SEG Annual International Meeting*, Expanded Abstract, 1330–1333.

Hatchell, P., Wills, P. and Didraga, C. (2008). Identifying and removing effects of multiples on time-lapse interpretation at Vahall. *First Break*, **26**(5).

Haugvaldstad, H., Lyngnes, B., Smith, P. and Thompson, A. (2011). Ekofisk time-lapse seismic - A continuous process of improvement. *First Break*, **29**(9), 113–120.

Haverl, M. C., Aga, M. and Reiso, E. (2005). Integrated Workflow for Quantitative Use of Time-Lapse Seismic Data in History Matching–A North Sea Field Case. *67th EAGE Conference & Exhibition*, Madrid, Spain, Expanded Abstracts, SPE94453.

He, N., Inderwiesen, P., and Condon, P. (2004). Pressure and saturation inversion from 4D seismic constrained by production data. *66th EAGE Conference and Technical Exhibition,* Paris, France, Expanded Abstracts, A036.

Helgerud, M. B., Miller, A. C., Johnston, D. H., Udoh, M. S., Jardine, B. G., Harris, C. and Aubuchon, N. (2011). 4D in the deepwater Gulf of Mexico: Hoover, Madison, and Marshall fields. *The Leading Edge*, **30**(9), 1008–1018, http://dx.doi.org/10.1190/1.3640524.

Hicks, E., Hoeber, H., Houbiers, M., Lescoffit, S.P., Ratcliffe, A. and Vinje, V. (2016). Time-lapse full-waveform inversion as a reservoir-monitoring tool—A North Sea case study. *The Leading Edge*, **35**(10), 850-858.

Hoeber, H., Campbell, S., Dyce, M. and Whitecombe, D. (2008). Using complex trace analysis for 4D matching and 4D noise reduction. *First break*, **26**(5), 79-83.

Hofmann, R., Xu, X., Batzle, M., Prasad, M., Furre, A.K. and Pillitteri, A. (2005) Effective pressure or what is the effect of pressure?.*The Leading Edge*, ***24(***12), 1256-1260.

Hornman, K. and Forgues, E. (2013). Permanent reservoir monitoring with onshore surface seismic. *Second EAGE Workshop on Permanent Reservoir Monitoring – Current and Future Trends*, Expanded Abstracts, We-01-04, http://dx.doi.org/10.3997/2214-4609.20131292.

Huang, Y. (2011). *Integration of well data into dynamic reservoir interpretation using multiple seismic surveys*. PhD Thesis, Heriot-Watt University.

Huang, Y. and MacBeth, C. (2009). Direct correlation of 4D seismic and well activity for dynamic reservoir interpretation. *SEG Technical Program*, Expanded Abstracts, 3840-3844. Society of Exploration Geophysicists.

Huang, Y. and MacBeth, C. (2012). Direct correlation of 4D seismic with well activity for a clarified dynamic reservoir interpretation. *Geophysical Prospecting*, **60**(2), 293-312.

Huang, Y., MacBeth, C., Barkved, O., van Gestel, J. P. and Dybvik, O. P. (2011). Enhanced dynamic interpretation from correlating well activity to frequently acquired 4D seismic signatures. *The Leading Edge*, **30**(9), 1042-1050.

Huang, Y., MacBeth, C., Barkved, O., van Gestel, J.P. and Dybvik, O.P. (2011). Enhanced dynamic interpretation from correlating well activity to frequently acquired 4D seismic signatures. *The Leading Edge*, **30**(9), 1042-1050.

Hughes, J. K., (2000). Examination of seismic repeatability as a key element of time-lapse seismic monitoring. SPE Reservoir Eval. & Eng., **3**(6), 517-524.

Ivanova, A., Kashubin, A., Juhojuntti, N., Kummerow, J., Henninges, J., Juhlin, C., Luth, S., and Ivandic, M. (2012). Monitoring and volumetric estimation of injected CO2 using 4D seismic, petrophysical data, core measurements and well logging: a case study at Ketzin, Germany. *Geophysical Prospecting*, **60**(5), 957-973.

Jack, I. (1997). *Time-lapse seismic in reservoir management*. Distinguished Instructor Series, Society of Exploration Geophysicists.

Jenkins, S. D., Waite, M. W., and Bee, M., F. (1997). Time-lapse monitoring of the Duri steamflood: pilot and case study. *The Leading Edge*, **16**(9), 1267-1274.

Jin, L., van den Hoek, P.J., Alpak, F.O., Pirmez, C., Fehintola, T., Tendo, F. and Olaniyan, E.E. (2012). A comparison of stochastic data-integration algorithms for the joint history matching of production and time-lapse-seismic data. *SPE Reservoir Evaluation & Engineering*, **15**(04), 498-512.

Johnstad, S. E., Uden, R. C. and Dunlop, K. N. B (1993). Seismic reservoir monitoring over the Oseberg field. *First Break*, **11**(5), 177-185.

Johnston, D. H. (2013). *Practical applications of time-lapse seismic data*. Distinguished Instructor, Series, Society of Exploration Geophysicists.

Kahar, Y., Anno, P. D. and Haram, L. G. (2006). Fluid flow phenomena from 4D interpretation, Heidrun Field, Norwegian North Sea. *SEG Annual Meeting*, New Orleans, Louisiana, Expanded Abstracts, 3125 – 3129, http://dx.doi.org/ 10.1190/1.2370177.

Kanu, C., Toomey, A., Hodgson, L., Gherasim, M., L'Heureux, E., Du, B. and Zhang, Q. (2016). Evaluation of time-shift extraction methods on a synthetic model with 4D geomechanical changes. *The Leading Edge*, **35**(10), 888-893.

Kazemi, A., Stephen, K. and Shams, A. (2011). Seismic history matching of Nelson using time-lapse seismic data: An investigation of 4D signature normalisation. *SPE Reservoir Evaluation & Engineering*, **14**(05), 621-633.

Kiær, A.F., Eiken, O. and Landrø, M. (2016). Calendar time interpolation of amplitude maps from 4D seismic data. *Geophysical Prospecting*, **64**(2), 421-430.

Knapp, S., Maguire, D., Meng, X. and Sahai, S. (2014). 4D Acquisition and Processing of streamer and OBC data in West Africa: A case history to demonstrate how survey planning and advanced processing techniques improve repeatability for reservoir monitoring. *SEG Technical Program*, Expanded Abstracts, 4898-4902, http://dx.doi.org/10.1190/segam2014-0535.1.

Koster, K., Gabriels, P., Hartung, M., Verbeek, J., Deinum, G. and Staples, R. (2000). Time-lapse seismic surveys in the North Sea and their business impact. *The Leading Edge*, **19**(3), 286-293.

Kragh, E. D. and Christie, P. (2002). Seismic repeatability, normalized rms, and predictability. *The Leading Edge*, **21**(7), 640-647.

Kristiansen, P., Christie, P., Bouska, J., O'Donovan, A., Westwater, P., and Thorogood, E. (2000). Foinaven 4D: Processing and analysis of two designer 4Ds. *SEG Technical Program Expanded Abstracts*, 1456–1459.

Kumar, D., and Landa, J. L. (2008). A reliable 4D seismic attribute for joint inversion of seismic and production data. *SEG Annual Meeting*, Las Vegas, Nevada, U.S.A, SEG Technical Program Expanded Abstracts, 3164-3168, https://doi.org/10.1190/1.3064003.

Kvalheim, A.K., Sandø, I.A., Skogland, S.M., Vinje, V. and Carpenter, M. (2007). Impact of time and depth imaging methods on quantitative 4D reservoir management. *69th EAGE Conference and Exhibition incorporating SPE EUROPEC 2007*, London, UK. Expanded Abstracts, H017, http://dx.doi.org/10.3997/2214-4609.201401683.

La Follet, J., R.,Wills, P., Lopez, J., L., Przybysz-Jarnut, J., K., van Lokven, M. (2015). Continuous seismic reservoir monitoring at Peace River: Initial results and interpretation. 85th Annual International Meeting, SEG, Expanded Abstracts, 5440-5444.

Lacombe, C., Butt, S., Mackenzie, G., Schons, M. and Bornard, R. (2009). Correcting for water-column variations, *The Leading Edge*, **28**(2), 198-201, http://dx.doi.org/10.1190/1.3086058.

Landa, J. L. and Kumar, D. (2011). Joint inversion of 4D seismic and production data. SPE Annual Technical Conference and Exhibition, Denver, Colorado, USA, Expanded Abstracts, SPE-146771-MS, https://doi.org/10.2118/146771-MS

Landa, J., Meadows, M., Thacher, C., Waddle, R. and Williams, N. (2015). Map-Based Estimation of Reservoir Pressure and Saturation from 4D Seismic with a Data-Driven Procedure. *SPE Annual Technical Conference and Exhibition*, Houston, Texas, Expanded Abstracts, SPE-175100-MS https://doi.org/10.2118/175100-MS.

Landrø, M. (1999). Discrimination between pressure and fluid saturation changes from time-lapse seismic data. *69th Annual International Meeting*, SEG, Expanded Abstracts, 1651-1654, https://doi.org/10.1190/1.1820848

Landrø, M. (2001). Discrimination between pressure and fluid saturation changes from time-lapse seismic data. *Geophysics*, **66**(3), 836-844.

Landrø, M. (2002). Uncertainties in quantitative time-lapse seismic analysis. *Geophysical Prospecting*, **50**(5), 527–538, http://dx.doi.org/10.1046/j.1365-2478.2002.00330.x.

Landrø, M., and Øyvind, K. (2002) Pore pressure Estimation – what can we learn from 4D. CSEG RECORDER, **27**(7) 83-87.

Landrø, M., Veire, H. H., Duffaut, K. and Najjar, N. (2003). Discrimination between pressure and fluid saturation changes from marine multicomponent time-lapse seismic data. *Geophysics*, **68**(5), 1592–1599, http://dx.doi.org/10.1190/1.1620633.

Landrø, M., Solheim, O.A., Hilde, E., Ekren, B.O. and Strønen, L.K. (1999). The Gullfaks 4D seismic study. *Petroleum Geoscience*, **5**(3), 213-226.

Landrø, M., Strønen, L.K., Digranes, P., Solheim, O.A. and Hilde, E. (2001). Time-lapse seismic as a complementary tool for in-fill drilling. *Journal of Petroleum Science and Engineering*, **31**(2), 81-92.

Lasocki, J., Guemene, J., Hedayati, A., Legorjus, C. and Page, W. (1999). *The Elgin and Franklin fields: UK Blocks 22/30c, 22/30b and 29/5b*, paper presented at Geological Society, London, Petroleum Geology Conference series, Geological Society of London.

Lie, E. O. (2011). Constrained time shift estimation. *73rd EAGE Conference & Exhibition incorporating SPE EUROPEC*, Vienna, Austria, 23-26 May. Expanded Abstracts, G038.

Lu, J., Cook, J. P., Hosseini, A. S., Yang, C., Romanak, D. K., Zhang, T., Freifeld, M. B., Smyth, C. R., Zeng, H. and Hovorka, D. S. (2012). Complex fluid flow revealed by monitoring CO2 injection in a fluvial formation. *Journal of Geophysical Research*, **117**, 1 -13.

Lumley, D., Adams, D., Meadows, M., Cole, S. and Ergas, R. (2003). 4D seismic pressure-saturation inversion at Gullfaks field, Norway. *First Break*, **21**(9), 3-9.

Lumley, D.E. and Behrens, R.A. (1997). Practical Engineering Issues of 4D seismic reservoir monitoring. *SPE Annual Technical Conference and Exhibition*, San Antonio, Texas, Expanded Abstracts, SPE-38695-MS, 449 – 456, https://doi.org/10.2118/38695-MS.

Lumley, D.E., Nunns, A.G., Delorme, G., Adeogba, A.A. and Bee, M.F. (1999). Meren Field, Nigeria: A 4D seismic case study. *69th SEG meeting*, Houston, USA, Expanded Abstracts, 1628-1631.

MacBeth C. (2004). A classification for the pressure-sensitivity properties of a sandstone rock frame. *Geophysics* **69**(2), 497–510.

MacBeth, C., Floricich, M. and Soldo, J. (2006). Going quantitative with 4D seismic analysis. *Geophysical prospecting*, **54**(3), 303-317.

MacBeth, C., Stephen, K.D. and McInally, A. (2005). The 4D seismic signature of oil–water contact movement due to natural production in a stacked turbidite reservoir. *Geophysical Prospecting*, **53**(2), 183-203.

MacKay, S., Fried, J. and Carvill, C. (2003). The impact of water-velocity variations on deepwater seismic data. *The Leading Edge*, **22**(4), 344-350.

Magesan, M., Depagne, S., Nixon, K., Regel, B., Opich, J., Rogers, G., and Hudson, T. (2005). Seismic processing for time-lapse study: Genesis field, Gulf of Mexico. *The Leading Edge*, **24**(4), 364–373.

Maschio, C. and Schiozer, D. (2014). A method for reduction of uncertainties in reservoir model using observed data: application to a complex case. *Journal of the Brazilian Society of Mechanical Sciences and Engineering*, **36** (4), 901-918.

Maschio, C., de Carvalho, C.P.V. and Schiozer, D.J., (2010). A new methodology to reduce uncertainties in reservoir simulation models using observed data and sampling techniques. *Journal of Petroleum Science and Engineering*, **72(**1), 110-119.

Mateeva, A., Hornman, J. C., Hatchell, P., Potters, H. and Lopez, J. (2015). Frequent seismic monitoring for pro-active reservoir management. SEG Annual Meeting, New Orleans, Louisiana, USA, Expanded Abstracts, 4817-4821, http://dx.doi.org/10.1190/segam2015-5899850.1

Mavko, G., and Mukerji, T. (1995). Seismic pore space compressibility and Gassmann's relation, Geophysics, **60**, 1743-1749.

Mavko, G., Mukerji, T., and Dvorkin, J. (1998). *The Rock Physics Handbook – Tools for seismic analysis in porous media*: Cambridge University Press.

McWhorter, R., Schultz, G., Clark, A., Branch, T. and Lansley, M. (2012). 3D Seismic Operational Optimisation in the Lusitanian Basin, Portugal. *First Break*, **30**(1), 103-108.

Meadows, M. (2001). Enhancements to Landrø's method for separating time -lapse pressure and saturation changes. *SEG International Exposition and Annual Meeting*, San Antonio, Texas, Expanded Abstracts, 1652–1655.

Menke, W. (1989). *Geophysical Data Analysis: Discrete Inverse Theory*. Academic Press, Inc.

Mezghani, M., Fornel, A., Langlais, V., Lucet, N. (2004). History matching and quantitative use of 4D seismic data for an improved reservoir characterisation. *SPE Annual Technical Conference and Exhibition*, Houston, Texas, USA, Expanded Abstracts, SPE 90420.

Michou, L., Lafet, Y., Coléou, T. and Przybysz-Jarnut, J. (2013). 4D Seismic Inversion on Continuous Land Seismic Reservoir Monitoring of Thermal EOR. *75th EAGE Conference and Exhibition incorporating SPE EUROPEC 2013,* Expanded Abstracts, http://dx.doi.org/10.3997/2214-4609.20130427.

Mitchell, P., Paez, R., Johnston, D., Mohler, G. and da Cunha Neto, C. (2009). 4D seismic in deep water at the Dikanza field, offshore Angola, West Africa. *79th SEG Annual International Meeting*, Expanded Abstracts, 3924–3928, http://dx.doi.org/10.1190/1.3255688.

MV Geowave Master. (2008). Final survey report for BP's UK-Q204-Foinaven-Schiehallion Loyal fields. *Wavefield inseis.* Wavefield Job No. 4003-MST-BP-Foinaven.

Naeini, E. Z. (2013). TT domain time shift estimation. *75th EAGE Conference & Exhibition incorporating SPE EUROPEC*, 10-13 June, London, UK. Expanded Abstracts, Th P03 04.

Naess, O.E. (2005). The SOS source: testing and analysis of a 4D seismic source. *SEG Technical Program*, Expanded Abstracts, 68-71, http://dx.doi.org/10.1190/1.2144418

Nes, O.M., Holt, R.M. and Fjær, E. (2000). The reliability of core data as input to seismic reservoir monitoring studies. *SPE European Petroleum Conference*, Paris, France, 24-25 October. Expanded Abstracts, SPE-65180-MS.

Nickel, M. and Sonneland, L. (1999). Non-rigid matching of migrated time-lapse seismic. *69th Annual International Meeting, SEG*. Expanded Abstracts, 872-875, http://dx.doi.org/10.1190/1.1821191.

Nur, A. (1982). Seismic imaging in enhanced recovery: *SPE Enhance Oil Recovery Symposium*, SPE/DOE 10680, 99–109.

Nur, A. (1992). Critical porosity and the seismic velocities in rocks: *EOS, Transactions American Geophysical Union*, **73**, 43-66.

Nur, A., Mavko, G., Dvorkin, J. and Galmudi, D. (1998). Critical porosity: A key to relating physical properties to porosity in rocks. *The Leading Edge*, **17**(3), 357-362.

Nur, A., C. Tosaya, and D. Vo-Thanh. (1984). Seismic monitoring of thermal enhanced oil recovery processes. *54th SEG Annual International Meeting*, Expanded Abstracts, 337–340, http://dx.doi.org/10.1190/1.1894015.

Nur, A., and Z. Wang (1987). In-situ seismic monitoring EOR: The petrophysical basis. *SPE Annual Technical Conference and Exhibition*, Dallas, Texas, Expanded Abstracts, SPE 16865, https://doi.org/10.2118/16865-MS.

Obidegwu, D. (2016*). Seismic history matching using binary images*. PhD thesis, Heriot Watt University.

Obidegwu, D., Chassagne, R. and MacBeth, C. (2015). Seismic Assisted History Matching Using Binary Image Matching. SPE EUROPEC 2015, Madrid, Spain. Expanded Abstracts, SPE-174310-MS.

O'Brien, J., Moran, J., Wilbourn, G., Morris, S., Andersen, J. and Quezada, O. (2010). Monitoring a CO2 flood with fine time steps: Salt Creek 4D. The Leading Edge, 29(8), 912–919, http://dx.doi.org/10.1190/1.3480003.

Omofoma, V. and MacBeth C. (2015). Intra-survey pressure variations – implications for 4D seismic interpretation. *77th EAGE Conference and Exhibition*, Madrid, Spain, 1-4 June, Expanded Abstracts, WS02-D04, http://dx.doi.org/ 10.3997/2214-4609.201413467.

Omofoma, V. and MacBeth C. (2016). Quantification of reservoir pressure-sensitivity using multiple monitor 4D seismic data. *78th EAGE Conference and Exhibition*, Vienna, Austria, 30 May - 2 June, Expanded Abstracts, Th LHR2 04, http://dx.doi.org/10.3997/2214-4609.201601315.

Osdal, B., Husby, O., Aronsen, H., Chen, N. and Alsos, T. (2006). Mapping the fluid front and pressure buildup using 4D data on Norne Field. *The Leading Edge*, **25**(9), 1134–1141, http://dx.doi.org/10.1190/1.2349818.

Pazetti, B., Donno, D., Davolio, A., Grana, D. and Schiozer, D. (2016). The Impact of Time-shift Estimation and Correction on Two 4D Attributes-Amplitude Difference and Velocity Change. *78th EAGE Conference and Exhibition*, 30 May – 2 June. Expanded Abstracts, Th LHR2 07. http://dx.doi.org/10.3997/2214-4609.201601318

Pevzner, R., Urosevic, M. and Gurevich, B. (2015). Borehole Seismic Monitoring of a Small-scale CO2 Injection-The CO2CRC Otway Project Feasibility Study. *77th EAGE Conference and Exhibition,* Expanded Abstracts, http://dx.doi.org/10.3997/2214-4609.201412717.

Reid, B., Høyland, L., Olsen, S. & Petterson, O. (1995). The Heidrun Field-Challenges in Resetvoir Development and Production. *Offshore Technology Conference*, Houston, Texas, Expanded Abstracts, OTC-8085-MS, https://doi.org/10.4043/8085-MS.

Rickett, J. and Lumley, D. (2001). Cross-equalisation data processing for time-lapse seismic reservoir monitoring: A case study from the Gulf of Mexico. *Geophysics*, **66**(4), 1015 - 1025.

Rickett, J., Duranti, L., Hudson, T., Regel, B., and Hodgson, N. (2007). 4D time strain and the seismic signature of geomechanical compaction at Genesis. *The Leading Edge*, **26**(5), 644 – 647.

Risso, F. V. A., Risso, V. F. and Schiozer, D. J. (2011). Risk analysis of petroleum fields using Latin Hypercube, Monte Carlo and derivative tree techniques. Journal of Petroleum and Gas Exploration Research, 1 (1), 14 - 22.

Roggero F., Ding, D. Y., Berthet, P., Lerat, O., Cap, J., Schreiber, P. E. (2007). Matching of production history and 4D seismic data - application to Girassol Field, Offshore Angola. *SPE Annual Technical Conference and Exhibition*, Anaheim, California, U.S.A. 11 - 14 November, 2007, Expanded Abstracts, SPE 109929.

Ronen, S., van Waard, R., and Keggin, J. (1999). Repeatability of sea bed multi-component data. *69th Annual International Meeting*, *SEG*, Expanded Abstracts, 1695–1698, http://dx.doi.org/10.1190/1.1820860.

Ross, A., Viceer, S., Hildebrand, S., Morrison, C. and Jolley, E. (2010). A towed streamer 3D seismic survey in the Arctic marginal ice zone. *First Break*, **28**(12), 71-77.

Ross, C. P., Cunningham, G. B. and Weber, D. P. (1996). Inside the crossequalisation black box. *The Leading Edge*, **15**(11), 1233-1240.

Røste, T., Dybvik, P. O. and Søreide, K. O. (2015). Overburden 4D time shifts induced by reservoir compaction at Snorre field. *The Leading Edge*, **34**(11) 1366 – 1374.

Røste, T., Landrø, M. and Hatchell, P. (2007). Monitoring overburden layer changes and fault movements from time-lapse seismic data on the Valhall Field. *Geophysical Journal International*, **170**(3), 1100-1118.

Røste, T., Stovas, A. and Landrø, M. (2005). Estimation of layer thickness and velocity changes using 4D prestack seismic data. *67th EAGE Conference and Exhibition*, 13 – 16 June. Expanded Abstracts, C010.

Røste, T., Stovas, A. and Landrø, M. (2006). Estimation of layer thickness and velocity changes using 4D prestack seismic data. *Geophysics*, **71**(6), S219-S234.

Saul, M., and Lumley, D. (2015). The combined effects of pressure and cementation on 4D seismic data. *Geophysics*, **80(**2). 135-158.

Schulze-Riegert, R. and Ghedan, S. (2007). Modern techniques for history matching. *9th International Forum on Reservoir Simulation*, Abu Dhabi, United Arab Emirates, 9-13 December, 2007.

Sharma, N.C. (2002). History of Seismic Prospecting in ONGC: A Chronological Sketch of Events. *GEOHORIZONS*, 1-10. [Online] available: http://www.spgindia.org/geohorizon/jan2002/2002jan_n_c_sharma.PDF (Accessed 25 March 2017).

Sheriff, R. E. (1975). Factors affecting seismic amplitudes. *Geophysical Prospecting*, **23**(1), 125-138.

Sheriff, R. E. and Geldart, L.P. (1995). *Exploration Seismology*. 2nd ed. Cambridge: Cambridge University Press.

Shuey, R.T. (1985). A simplification of the Zoeppritz equations. *Geophysics*, **50**(4), 609 – 614.

Simm, R. (2007). Practical Gassmann fluid substitution in sand/shale sequences. *First Break*, **25(**12), 61-68.

Simm, R., Bacon, M., and Bacon, M. (2014). *Seismic Amplitude: An interpreter's handbook*. Cambridge University Press, Cambridge, United Kingdom.

Singer, L., Byerley, G. and Rose, P. (2017). Re-saturation targets identified from 4D seismic softening responses in the Forties Field. *Petroleum Geology Conference series*, 8, PGC8-25. Geological Society of London. http://dx.doi.org/10.1144/PGC8.25.

Smit, F., Brain, J., and Watt, K. (2005). Repeatability monitoring during marine 4D streamer acquisition. *67th EAGE Conference and Exhibition*, Madrid, Spain, 13-16 June, Expanded Abstracts, C015.

Smith, G. C. and Gidlow, P.M. (1987). Weighted stacking for rock property estimation and detection of gas. *Geophysical Prospecting*, **35**(9), 993-1014.

Souza, R. and Lumley, D. (2015). Estimation of reservoir fluid saturation from seismic data: amplitude analysis and impedance inversion as a function of noise. ASEG 24th International Geophysical Conference and Exhibition, Perth, Australia, Extended Abstracts, 1-4, https://doi.org/10.1071/ASEG2015ab146.

Stammeijer, J. G. F. and Hatchell, P. J., (2014). Standards in 4D feasibility and interpretation. *The Leading Edge*, **33**(2), 134-140.

Stammeijer, J. G. F., Davidson, M., Hatchell, P. J. and Lopez, J. L. (2013). Instantaneous 4D seismic (i4D) – an innovative concept to monitor offshore water injector well. *International Petroleum Technology conference*, Expanded Abstracts, IPTC 16901.

Staples, R., Cook, A., Braisby, J., Hodgson, B. and Mabillard, A. (2006). Integration of 4D seismic data and the dynamic reservoir model reveal new targets in Gannet C. *The Leading Edge*, **25**(9), 1126-1133.

Staples, R., Ita, J., Burrell, R. & Nash, R. (2007) Monitoring pressure depletion and improving geomechanical models of the Shearwater field using 4D seismic. *The Leading Edge*, **26**(5), 636-642.

Stephen K. D. and MacBeth C. (2008). Reducing reservoir prediction uncertainty by updating a stochastic model using seismic history matching. SSPE-100295-PA, SPE Journal, **11**(6), 991-999.

Stephen, K. D. and MacBeth, C. (2006). Seismic history matching in the UKCS Schiehallion field. First Break, **24**(4), 43 - 49.

Stephen, K. D., Soldo, J., MacBeth, C. and Christie M. (2006). Multiple Model Seismic and Production History Matching: A Case Study. SPE94173-PA. *SPE Journal,* **11**(4), 418-430.

Stephen, K.D. and Kazemi, A. (2014). Improved normalisation of time-lapse seismic data using normalized root mean square repeatability data to improve automatic production and seismic history matching in the Nelson field. *Geophysical Prospecting*, **62**(5), 1009-1027.

Sun, Y., Qin, F., Checkles, S. and Leveille, J. P. (2000). 3-D prestack Kirchhoff beam migration for depth imaging. *Geophysics*, **65**(5), 1592-1603.

Svay, J., Ni, Y., Bousquié, N., Sedova, A. and Mensch, T. (2013). Innovations for geophysical monitoring of 3D and 4D marine surveys. *First Break*, **31**(11), 83-88.

Tewari, R.D., Jeong, D., Khalid, R.M., Kittrell, C., Othman, T. and Rasidi, T. (2014). Quantification of Uncertainty of Reserves with High Quality History Matching Models in a Mature Field. *International Petroleum Technology Conference*, Kuala Lumpur, Malaysia, Expanded Abstracts, IPTC-18153-MS, https://doi.org/10.2523/IPTC-18153-MS.

Thedy, E. A., Dariva, P., Ramos Filho W. L., Maciel Jr., P. O, Silva, F. E. F. and Zorzanelli, B. (2015). First Results on Reservoir Monitoring in Jubarte PRM - Offshore Brazil. Third EAGE Workshop on Permanent Reservoir Monitoring 2014 – Proactive Reservoir Management: PRM and Beyond, Oslo, Norway, Expanded Abstracts, We B04.

Thore, P. (2006). Accuracy and limitations in seismic modelling of reservoir. *76th SEG meeting*, New Orleans, USA, Expanded Abstracts, 1674-1677.

Thore, P. (2011). A 4-D Seismic Inversion Scheme Ready-to-use for Updating Reservoir Grid. *EAGE/SPE Joint Workshop-Closing the Loop: Reservoir Simulation and Geophysical Measurements*, 4-6 April, Istanbul, Turkey, Expanded Abstracts, B04.

Tigrek, S., and Hatchell, P., J. (2006). Reservoir Compaction Quantification Using Geomechanical Inversion of Timelapse Time shifts. *68th EAGE Conference and Exhibition incorporating SPE EUROPEC*, Vienna, Austria, 12-15 June. Expanded Abstracts.

Tjetland, G., Kristiansen, T. G. and Buer, K. (2007). Reservoir Management Aspects of Early Waterflood Response after 25 Years of Depletion in Valhall Field. *International Petroleum Technology Conference*, Expanded Abstracts, IPTC 11276.

Tolstukhin, E., Lyngnes, B. and Sudan, H.H. (2012). Ekofisk 4D seismic-seismic history matching workflow. SPE Europec/EAGE Annual Conference, Copenhagen, Denmark. Exapnded Abstracts, SPE-154347-MS, https://doi.org/10.2118/154347-MS.

Tøndel, R., Schütt, H., Dümmong, S., Ducrocq, A., Godfrey, R., LaBrecque, D., Nutt, L., Campbell, A. and Rufino, R. (2014). Reservoir monitoring of steam-assisted gravity drainage using borehole measurements. *Geophysical Prospecting*, **62**(4), 760-778.

Toxopeus, G., Petersen, S. A. and Wapenaar, C. P. A. (2003). Improved geological modelling and interpretation by simulated migrated seismics. *SEG 73rd Annual International Meeting*, Expanded Abstracts, 2445-2448, http://dx.doi.org/10.1190/1.1817884.

Trani, M., Arts, R., Leeuwenburgh, O. and Brouwer, J. (2011). Estimation of changes in saturation and pressure from 4D seismic AVO and time-shift analysis. *Geophysics*, **76(**2), C1-C17, http://dx.doi.org/10.1190/1.3549756.

Tura, A. and Lumley, D. E. (1998). Subsurface fluid flow properties from time-lapse elastic wave reflection data: Proceedings of SPIE, Mathematical Methods in Geophysical Imaging V, 3453, 125-138, http://dx.doi.org/10.1117/12.323284

Tura, A. and Lumey, D. E. (1999). Estimating pressure and saturation changes time-lapse AVO data. 69th SEG meeting, Houston, USA, Expanded Abstracts, 1655-1758, https://doi.org/10.1190/1.1820849.

Tuttle, C., Pelissier, M., Barnes, M., Tribe, J., Persad, K. (2009). A seismically constrained reservoir modelling workflow: case study. *The Leading Edge*, **28**(12), 1492–1497.

van Gestel, J.-P., Olav I. Barkved and Kommedal., J. H. (2007). Valhall Life of Field Seismic Automated Workflow. *77th SEG meeting*, San Antonio, Texas, USA, Expanded Abstracts, 2898-2902, http://dx.doi.org/10.1190/1.2793068.

Vaxelaire, D., Kravik, K., Bertini, F. and Mougenot, J. M. (2007). Wide Azimuth 3D 4C OBC – A Key Breakthrough to Lead to the Development of Hild Field. *69th EAGE Conference and Exhibition incorporating SPE EUROPEC 2007*, London, UK, Expanded Abstracts,C009.

Veire, H. H., Borgos, H. G. and Landrø, M. (2006). Stochastic inversion of pressure and saturation changes from time-lapse AVO data. *Geophysics*, ***71***(5), C81-C92.

Verlo, S. B., and Hetland, M. (2008). *Development of a field case with real production and 4D data from the Norne Field as a benchmark case for future reservoir simulation model testing*. MSc Dissertation, Norwegian University of Science and Technology.

Vieira, J. M. B, Gomes, M. C., B., Camarão Junior, F. L., Lima, A. D. P. and Mathieson, A. (2011). Full azimuth OBC acquisition – A Campos Basin pre-salt case study. *12th International Congress of the Brazilian Geophysical Society*, Rio de Janeiro, Brazil, Expanded Abstracts.

Waal, d. H. and Calvert, R. (2003). Overview of global 4D seismic implementation strategy. *Petroleum Geoscience*, **9**(1), 1-6.

Waggoner, J.R., Cominelli, A., Seymour, R.H. (2002). Improved reservoir modeling with time-lapse seismic in a Gulf of Mexico Gas Condensate reservoir. SPE Asia Pacific Oil and Gas Conference and Exhibition held in Melbourne, Australia, Expanded Abstracts, SPE 77956.

Wang, K., Hatchell, P. J., Udengaard, C., Craft, K. and Dunn, S. (2013). Water velocity and tide measurement in marine seismic acquisition. *75th EAGE Conference and Exhibition incorporating SPE EUROPEC 2013*, Expanded Abstracts, Th 11 08, http://dx.doi.org/10.3997/2214-4609.20130135.

Watts, G., Jack, I. and Thompson, M. (2011). What do you think about 4D seismic? *First Break*, **29**(10), 109-112.

Watts, G. F. T., Jizba, D., Gawith, D.E. and Gutteridge, P. (1995). Reservoir monitoring of the Magnus Field through 4D time-lapse seismic analysis. *Petroleum Geoscience*, **2**(4), 361-372.

Watts, G. F. T., and Marsh, M. (2011). How often should you acquire 4D seismic surveys to optimise value? *EAGE Workshop on Permanent Reservoir Monitoring (PRM) - Using Seismic Data*, Trondheim, Norway. Expanded Abstracts, 10895, http://dx.doi.org/10.3997/2214-4609.20145217.

Wen, X.-H., Lee, S. and Yu, T. (2006). Simultaneous integration of pressure, water cut, 1 and 4-D seismic data in geostatistical reservoir modeling. *Mathematical geology*, **38** (3)**,** 301-325.

WesternGeco (2007). Data Processing Report for Statoil. Block 6608/10 (Norne). [ONLINE] Available at: http://www.ipt.ntnu.no/~norne/wiki/data/media/english/gfi/4d-seismic.pdf [Accessed 16 September 2015].

Western Monarch. (2006). Final field operation report on marine seismic reflection survey for BP's Foinaven, Schiehallion Loyal Fields, West of Shetlands, UK. *WesternGeco.* WesternGeco Job No. 9538.

Western Regent. (2004). Final field operation report on marine seismic reflection survey for BP's Schiehallion / Foinaven /Royal Fields, UKCS Blocks 204 / 205. *WesternGeco.* WesternGeco Job No. 9380.

WGP. (2010). WGP Caspian Sea Archives [Online] Available: http://www.wgp-group.com/tag/caspian-sea/ (Accessed 19 March 2017).

Whitcombe, D. N., Paramo, P., Philip, N., Toomey, A., Redshaw, T. and Linn, S. (2010). The correlated leakage method - its application to better quantify timing shifts on 4D data. *72nd EAGE Conference & Exhibition incorporating SPE EUROPEC*, Barcelona, Spain, 14-17 June. Expanded Abstracts, B037.

Widmaier, M., Hegna, S., Smit, F. and Tijdens, E. (2003). A strategy for optimal marine 4D acquisition. *73rd SEG Annual International Meeting*. Expanded Abstracts, 1533–1536, http://dx.doi.org/10.1190/1.1817587.

Widmaier, M., Long, A., Danielsen, B., and Hegna, S. (2005). Recent experience with 4D marine seismic acquisition. *First Break*, **23**(6), 77–82.

William, N. and Luis, T., (2002). Data and model uncertainty estimation for linear inversion. *Geophysical Journal International*, **149**(3), 625-632. https://doi.org/10.1046/j.1365-246X.2002.01660.x.

Williamson, P. R., Cherrett, A. J., and Sexton, P.A. (2007). A new approach to warping for quantitative time-lapse characterisation. 69th EAGE Conference & Exhibition incorporating SPE EUROPEC. London, UK, 11-14 June. Expanded Abstract, P064.

Xu, X., Hofmann, R., Batzle, M. and Tshering T. (2006). Influence of pore pressure on velocity in low-porosity sandstone: Implications for time-lapse feasibility and pore-pressure study. *Geophysical Prospecting*, **54**(5), 565–573

Yilmaz, Ö. (2001). Seismic data analysis: Processing, inversion, and interpretation of seismic data. Society of exploration geophysicists.

Yin, Z. (2016). *Enhancement of dynamic reservoir interpretation using the well2seis technique*. PhD thesis, Heriot-Watt University.

Yin, Z., Ayzenberg, M., MacBeth, C., Feng, T. and Chassagne, R. (2015). Enhancement of dynamic reservoir interpretation by correlating multiple 4D seismic monitors to well behavior. *Interpretation*, **3**(2), SP35-SP52.

Zabihi Naeini, E., and Hoeber, H. (2008) Improved time delay estimation. *70th EAGE Conference & Exhibition*, Rome, Italy, 9-12 June. Expanded Abstracts, P068.

Zabihi Naeini, E., Hoeber, H., Poole, G. and Siahkoohi, H. R. (2009). Simultaneous multivintage time-shift estimation. *Geophysics*, **74**(5), V109-V121.

Zadeh, H. M., Srivastava R. P., Vedanti, N. and Landrø M. (2010). Seismic monitoring of in situ combustion process in a heavy oil field. *Journal of Geophysical Engineering*, 7, 16-29.

Zubarev, D. I. (2009). Pros and Cons of Applying Proxy-models as a Substitute for Full Reservoir Simulations. *SPE Annual Technical Conference and Exhibition*, New Orleans, Louisiana, U.S.A, 4-7 October, 2009, Expanded Abstracts, SPE 124815.